# Transactions of the ASME

FLUIDS ENGINEERING DIVISION
Technical Editor
FRANK M. WHITE (1989)
Executive Secretary
L. T. NELSON (1989)
Calendar Editor
M. F. ACKERSON

Associate Editors
Fluid Machinery
WIDEN TABAKOFF (1988)
RICHARD F. SALANT (1987)
Fluid Measurements
ALEXANDER DYBBS (1987)
Fluid Mechanics
J. A. MILLER (1987)
HUGH W. COLEMAN (1987)
STANLEY F. BIRCH (1988)
WILLIAM W. DURGIN (1986)
Fluid Transients
FREDERICK J. MOODY (1986)
Numerical Methods
PATRICK J. ROACHE (1988)
Multiphase Flow
M. C. ROCO (1988)
GEORGES L. CHAHINE (1986)
Review Articles
K. N. GHIA (1986)

BOARD ON COMMUNICATIONS
Chairman and Vice President
K. N. REID, Jr.

Members-at-Large
W. BEGELL
J. T. COKONIS
W. G. GOTTENBERG
F. LANDIS
J. R. LLOYD
R. E. NICKELL
J. E. ORTLOFF
C. F. PHILLIPS
R. E. REDER
F. W. SCHMIDT

President, L. S. FLETCHER
Executive Director
PAUL ALLMENDINGER
Treasurer,
ROBERT A. BENNETT

PUBLISHING STAFF
Mng. Dir. Publ., J. J. FREY
Dep. Mng. Dir. Publ.,
JOS. SANSONE
Managing Editor,
CORNELIA MONAHAN
Editorial Production Assistant,
MARISOL ANDINO

**The Journal of Fluids Engineering** (ISSN 0098-2202) is published quarterly for $100 per year by The American Society of Mechanical Engineers, 345 East 47th Street, New York, NY 10017. Second class postage paid at New York, NY and additional mailing offices. POSTMASTER: Send address changes to The Journal of Fluids Engineering, c/o THE AMERICAN SOCIETY OF MECHANICAL ENGINEERS, 22 Law Drive, Box 2300, Fairfield, NJ 07007-2300.
**CHANGES OF ADDRESS** must be received at Society headquarters seven weeks before they are to be effective. Please send old label and new address.
**PRICES:** To members, $24.00, annually; to nonmembers, $100. Add $6.00 for postage to countries outside the United States and Canada.
**STATEMENT** from By-Laws. The Society shall not be responsible for statements or opinions advanced in papers or . . . printed in its publications (B7.1, Par. 3).



**INDEXED** by Engineering Information

# Journal of Fluids Engineering

**Published Quarterly by The American Society of Mechanical Engineers**

VOLUME 108 • NUMBER 2 • JUNE 1986





(Contents continued on page 140)

## Contents (continued)

# REVIEW—Mean Flow in Turbulent Boundary Layers Disturbed to Alter Skin Friction

**P. R. Bandyopadhyay**
NASA Langley Research Center,
Hampton, VA 23665-5225.
Mem. ASME

*Recent developments in methods of reducing drag in turbulent boundary layers have been briefly reviewed. The behavior of the mean flow in several drag reducing boundary-layer flows of current interest, viz., those over longitudinal surface riblets, outer-layer devices (OLD's), and longitudinal convex surface curvature, has been examined. The boundary layer on a surface with longitudinal concave curvature has been studied to complement the results of convex curvature. The riblets alter the flow in their vicinity only and cause no drag penalty. However, the OLD's disturb the entire boundary layer, and it is the slow downstream ($\simeq 150\,\delta_0$) relaxation back to the equilibrium state that produces a region of lower skin friction; a net drag reduction results when the wall-drag reduction exceeds the drag penalty due to the device. The net drag reduction achieved by the riblets and OLD's remains a modest 10 percent compared with the more spectacular levels reached by polymer addition and microbubble injection in water. Over mild convex curvatures, the outer-boundary-layer response is a function of the curvature ratio ($\delta_0/R$), and the relaxation rate after a length of convex curvature is a function of the curved length ratio ($\Delta s_0/\delta_i$). Boundary layers exhibit an asymmetric response to streamwise surface curvatures; the response is slower to a concave curvature than to a convex. Detailed turbulence and accurate wall shear stress measurements in the altered boundary layers are needed to understand the drag-reducing mechanisms involved.*

## Introduction

Reduction of drag in turbulent boundary layers has remained an active field of research for several decades. In the sixties and seventies, most of the effort was confined to the techniques of polymer addition in water and compliant wall motion. The recent oil embargo has generated additional interest, and the potential of new techniques like flow over riblets, outer-layer devices (OLD's) and longitudinal convex curvature in particular is being explored. References [1–6] provide a summary of all these approaches to drag reduction. A brief discussion of drag reduction techniques and mechanisms is given below.

(*a*) **Polymer Addition.** Research on the addition of a small quantity of polymer to a solvent like water to reduce its drag due to turbulent motion (below that of the solvent alone) owes its origin to B. A. Toms [2, 7]. In 1946 he discovered that, in the turbulent regime and at constant pressure, the rate of flow through a pipe increased with an increase in polymer concentration. The result indicated a lowering of the wall shear stress. After this discovery, more than 1000 papers have been written on this topic. Very large drag reductions (up to 80 percent) have been achieved. The progress has been reviewed in references [8–13].

(*b*) **Compliant Wall.** The complaint wall motion has been an equally popular topic of research on drag reduction. The review by Bushnell et al. [14] is the most recent summary of the progress made. The impetus to this approach to drag reduction was provided first by Gray and later by Kramer who suggested that the observed high speed of a dolphin was due to a lower viscous drag; Kramer added that a "distributed flow damping" or compliant wall motion could be the mechanism that produces a lower drag. Later theoretical studies have indicated that a delay in transition could result from this type of wall motion. The limited experiments of Wehrmann [15] support this prediction. However, it has not yet been conclusively demonstrated experimentally that a compliant wall motion could lead to a drag reduction in a fully turbulent boundary layer. Part of this failure may be due to the difficulty of constructing a wall having an extremely small damping and modulus of elasticity (especially for air flows) with today's technology.

On a relatively simplified level, it must be unambiguously demonstrated by experiment that a three-dimensional patch of wall having dimensions of the order of the inner layer can inhibit the production of turbulence when oscillated in the $y$-direction while being phase-locked to the bursting process [16]. Here, bursting is being defined in the sense of Kline and his coworkers [17, 18]. It covers the entire production cycle and consists of three events, viz., the liftup, oscillation, and breakup of the low-speed streaks near the wall. The above-mentioned experiment is difficult to perform because the mean bursting period has a large standard deviation. Addi-

Contributed by the Fluids Engineering Division and presented at AIAA/ASME 4th Fluid Mechanics, Plasma Dynamics and Lasers Conference, May 12-14, 1986, Atlanta, GA. as paper No. AIAA-86-1126. Manuscript received by the Fluids Engineering Division, January 12, 1984.

tionally, it is not clear to which event in the bursting cycle the wall oscillation should be phase-locked.

**(c) Coatings.** Attempts have been made to develop coatings for use in water flows that make use of the above-mentioned two techniques of drag reduction. Soluble coatings of polymer have shown a small drag reduction (5 percent) and have a short life time (10 min) [19]. Blick [20] quotes that a slightly higher reduction has been reported by the use of a commercially available, semipermeable, water-absorbing coating in ships. Very little information is available on these developments. Dickinson et al. [21] have described the results of a recent effort to develop a compliant coating for hydrodynamic application: no drag reduction could be achieved.

Attempts have also been made to develop surface coatings for use in air. Reductions of 12 and 1.4 percent in wing section profile drag have been measured in wind tunnel [100] and flight tests [101] respectively. However, these coatings reduce viscous drag by providing a smoother surface and not by altering the existing turbulent boundary layer structure. The available coatings are not ready for commercial use because they are not durable and corrosion resistant.

**(d) Microbubbles.** There has been a limited research effort on the use of microbubbles to reduce viscous drag in water flows [22–27]. Although the number of studies made is far less than for devices like the compliant wall, the flow description emerging is clearer. The microbubble technique involves the injection of bubbles of up to 50 $\mu$m in diameter through a porous wall and into the boundary layer. The bubbles must be small to stabilize the gas-liquid interface. The relationship between the pore size and bubble diameter is not well understood. Very high drag reductions – up to about 80 percent – have been measured on a plate downstream of a region of injection by both Bogdevich et al. [23] and Madavan et al. [24]. The Soviet scientists' use of several independent techniques to make redundant drag measurements [22, 23, 26], viz., a floating balance, hot film sensors, and measurement of $\partial U/\partial y\,|_{y=0}$ by laser Doppler anemometry improves the trustworthincss of the measurements. Unique drag-reduction relationships valid over a range of free-stream velocities and gas injection rates have been obtained by both the Soviet [23] and U.S. [24] groups. Over a considerable range, the data of Bogdevich et al. and Madavan et al., respectively, can be described empirically as

$$\frac{c_f'}{c_{f_0}} = \exp(-5\bar{C}_*^{\,2}) \tag{1}$$

and

$$\frac{C_f'}{C_{f_0}} = \exp\left(-47.8\,\frac{Q}{SU_\infty}\right) \tag{2}$$

Here, $Q/SU_\infty$ is the measure of the ratio of normal velocity of injection to the free-stream velocity. In addition, there appears to be a consensus that the high frequency part of the wall pressure and shear-stress fluctuations are damped when drag is reduced.

Very little is known about the downstream $c_f$ relaxation distance, bubble trajectories, and the turbulence characteristics. It is not fully understood why microbubble injection reduces drag. The decrease in density does not account for all the drag reduction. Two additional observations have to be taken into consideration. First, the region adjacent to the wall, extending over several viscous sublayer thicknesses, remains free of bubbles [22, 25]. Second, the limiting drag-reduction situation corresponds to the limiting sphere (bubble) package and the lowest Weber number ($\tau_w\, d/\mathfrak{I} = 0.012$). These observations suggest that the sublayer is stabilized because the closely packed layer of gas bubbles dampens the disturbances from the free stream and outer layer by a viscoelastic mechanism. Very recently, Legner [27] has incorporated these aspects of the flow in a remarkably simple stress model.

**(e) Spot Forcing.** Recently, drag-reduction studies have been performed on laminar-turbulent transition approaching from two different directions. In one approach, a similar but oppositely phased wave is introduced to cancel the Tollmien-Schlichting wave and thereby delay transition [28–31]. In the other approach, transition is made to occur by closely spaced Emmons' spots generated by external forcing in the area where, otherwise, transition would take place naturally [32,

## Nomenclature

$A, B$ = constants in the law of the wall: $U^+ = A \log_{10} y^+ + B$
$c$ = chord length of OLD
$c_f$ = local skin-friction coefficient, $\tau_w/(1/2\ \rho\ U_\infty^2)$ or $\tau_w/(1/2\ \rho\ U_{pw}^2)$
$C_f$ = $c_f$ integrated over a flat plate of finite length
$c_{fN}$ = local skin-friction coefficient of the "normal" part of the altered boundary layer, $\tau_w/(1/2\ \rho\ U_{N\infty}^2)$
$\bar{C}_*$ = maximum gas concentration in the layer
$D$ = diameter of a pipe
$d$ = diameter of a microbubble
$f$ = Fanning friction factor
$G$ = Clauser's profile shape parameter,

$$\int_0^\delta \left(\frac{U_\infty - U}{U_\tau}\right)^2 dy \Big/ \int_0^\delta \left(\frac{U_\infty - U}{U_\tau}\right) dy$$

$H$ = shape factor of the layer, $\delta^*/\theta$
$h$ = height (peak to valley) of a riblet
$k$ = von Kármán's constant
$l$ = mixing length
$p$ = local static pressure
$Q$ = gas injection rate
$R$ = radius of longitudinal curvature
$\mathrm{Re}_c$ = chord Reynolds number of OLD, $U_\infty c/\nu$
$\mathrm{Re}_D$ = pipe flow Reynolds number, $VD/\nu$
$\mathrm{Re}_x$ = Reynolds number, $U_\infty\, x/\nu$
$\mathrm{Re}_\theta$ = Reynolds number, $U_\infty \theta/\nu$
$S$ = surface area of gas injection
$s$ = streamwise distance in flow over a curved surface or spanwise spacing of riblets
$s_0$ = streamwise distance from start of curvature
$T$ = period between bursting
$t$ = thickness of a flat ribbon (OLD)
$U$ = streamwise time mean velocity
$U_N$ = streamwise time mean velocity of the "normal" or Newtonian part of the altered boundary layer
$U_p$ = potential velocity in flow over a curved surface
$U_{N\infty}$ = free-stream velocity of the "normal" part of the altered boundary layer;
$U_s$ = slip velocity at a station
$U_\tau$ = friction velocity, $(\tau_w/\rho)^{1/2}$
$U_\infty$ = free-stream velocity in boundary layer on a flat surface
$\underline{u}$ = RMS of streamwise velocity fluctuation
$\overline{uv}$ = time-mean shear stress
$V$ = cross-sectional average flow velocity in a pipe

33]. This apparently produces smaller scales of turbulence whereby lower $c_f$ levels pertaining to higher $Re_\theta$ are produced. In principle, the use of flush-mounted surface heaters in water flows to control disturbances [29, 30] offers some unique advantages, viz., three-dimensionality and microprocessor programmability. Their potential in fully turbulent flows have not been explored. Average drag reductions of about 15 percent on a finite length plate have been reported in the spot forcing method [33]. In its current state, this technique is highly inefficient and better methods of producing spots would be useful. Detailed turbulence measurements are also not available. Although the efficiency of techniques like spot forcing or microbubble injection may be questionable, further research is justified because they could permit a vehicle to attain higher speeds for a short time.

*(f)* **Bursting.** Several unsuccessful attempts have been made in the past aimed at altering the turbulence production in a boundary layer. The motivation has been that since bursting (the so-called production cycle) is quasiperiodic, a single frequency perturbation should have some success in controlling the production of turbulence. This can also be seen as an attempt to organize the flow. Arakeri and Narasimha [34] applied a periodic suction, the period being equal to or below the mean bursting frequency at the station. No drag reduction attributable to the concept was observed. Blackwelder and Woo [35] introduced a periodic pressure pulse in the free stream to simulate that created by the passage of the free stream past the large structures of the boundary layer. Although the burst frequency was reduced by up to 20 percent at certain frequencies of the pressure pulse, the authors did not regard the result as conclusive.

*(g)* **Riblets.** Out of all the techniques studied most recently, the flow over longitudinal surface riblets and boundary layers altered by an outer-layer device (OLD) have, by far, the immediate potential of being applied in practice. Additionally, they could be retrofitted [6]. Walsh and Lindemann [36–38] have made direct measurements of drag on a 28-cm-wide and 90-cm-long flat plate covered with longitudinal surface riblets whose height and spacing were of the order of the thickness of the viscous sublayer. The experiments were performed in air. Various riblet geometries were tested. A maximum drag reduction of 8 percent, compared with that on a smooth flat plate, was observed in two riblet geometries in a zero-pressure gradient boundary layer – a symmetric v-groove with $h^+ = s^+ = 12$ and one having a sharp peak and a valley curvature with $h^+ = 8$ and $s^+ = 16$. The drag measurements were repeatable to 1 percent and a reduction existed up to an $s^+$ of 30. The optimum riblet dimensions do not scale with any known organized structure of the boundary layer. For example, an $s^+$ of 12–16 is much smaller than the mean wall-layer low-speed streak spacing of 90. A satisfactory explanation of the optimum riblet spacing is not yet available. Reif and Dinkelacker [39] have noted that the scales of fast sharks are similar to riblets with a sharp peak. Bechert et al. [40] have constructed artificial shark scales and performed drag balance measurements. The drag reduction versus $s^+$ behavior was found to be virtually the same as found by Walsh. Hooshmand et al. [41] have examined the drag reduction behavior of v-groove riblets. Measurements of $\partial U/\partial y\,|_{y=0}$ show that, compared with that on a smooth flat plate, $c_f$ is reduced by 40 percent at the valleys and increased by 10 percent at the peaks. The large drop in $c_f$ at the valleys explains why riblets produce a net drag reduction inspite of the increase in surface area as well as the increase in $c_f$ at the peaks. Bacher and Smith [42] also have shown by $\theta$-measurements that a reduction in drag occurs for v-groove riblets. However, the $\theta$-measurements of Gallagher and Thomas [43] on v-groove riblets have not revealed any drag reduction. Note that a drag reduction of 8 percent requires a drop in $\theta$ of 4 percent. Since it is not unusual for a so-called two-dimensional boundary layer to contain a spanwise variation in $\theta$ of this order, resolving the drag-reduction behavior by a measurement of $\theta$ along one longitudinal plane would be questionable. A large-area drag balance measurement would be more desirable.

Nitschke [44] has examined the drag-reduction performance of riblets in a developed pipe flow of air. In principle, it is more desirable to do such experiments in a pipe because the wall shear stress is directly related to the pressure drop along the pipe, a quantity that is easier to measure accurately than wall shear stress. Nitschke has examined only one riblet geometry having a rounded peak, which is also different from

## Nomenclature (cont.)

$x$ = streamwise distance
$x_0$ = streamwise distance from end of curvature
$y$ = distance normal to the wall
$z$ = spanwise distance
$\beta$ = Clauser's pressure gradient parameter, $\frac{\delta^*}{\tau_w}\frac{dp}{dx}$
$\delta$ = boundary-layer thickness
$\delta_0$ = $\delta$ at start of curvature or device (OLD) location
$\delta_i$ = $\delta$ at end of curvature
$\delta^*$ = displacement thickness of the boundary layer, $\int_0^\delta \left(1-\frac{U}{U_\infty}\right)dy$
$\Delta c_f$ = change in local skin-friction coefficient compared with that in a flat plate at the same $s$ or $x$
$\Delta U/U_\tau$, $U+$ = strength of the wake component
$\Delta s_0$ = total turning length of the curved surface
$\pi$ = wake strength parameter
$\rho$ = density of the working fluid
$\theta$ = momentum thickness of the boundary layer, $\int_0^\delta \frac{U}{U_\infty}\left(1-\frac{U}{U_\infty}\right)dy$
$\Im$ = coefficient of surface tension
$\tau$ = viscous plus turbulent shear stress
$\tau_w$ = wall shear stress
$\nu$ = kinematic viscosity of the working fluid

**Subscript**

$N$ = normal (= unaltered) flat-plate boundary layer
$s$ = slip condition near wall
$0$ = refers to unaltered boundary layer when used in $c_f$ or $C_f$
$p$ = potential flow condition (appears in curved flows)
$w$ = at the wall

**Superscript**

$+$ = nondimensionalized by wall-layer velocity ($U_\tau$) and length ($\nu/U_\tau$) scales
$'$ = refers to altered boundary layer when used in $c_f$ or $C_f$

those examined by Walsh [36, 37]. This geometry resulted in a maximum reduction of about 3 percent in the resistance, the uncertainty being ± 1.5 percent. This reduction is lower presumably because her riblet peaks are not sharp [36–38, 40]. Nitschke has found that the drag reduction occurs between an $s^+$ of 8 and 30, which is in excellent agreement with Walsh. Nitschke did not find any large difference in the streamwise mean velocity and turbulence distributions between the smooth and riblet pipes. It should be noted that determining the appropriate value of the pipe diameter applicable to the calculation of wall shear stress from the pressure drop in the riblet pipe is a serious matter since the pipe diameter is raised to the power of 5 in the relevant expression of shear stress. Nitschke obtained the effective diameter from mass flow and not any near-wall flow consideration. Schlichting (see [45]), in his notable study on rough walls, had also used a similar approach to obtain the effective wall location. Coleman et al. [45] have pointed out that although this approach is logical on physical grounds, "it is unrelated to any characteristics (assumed or proven) of the velocity profile."

Walsh and Lindemann [38] have shown that the riblet drag reduction is insensitive to yaw angles of up to 15 deg but, at 30 deg, they no longer reduce drag. They also performed experiments combining two different drag-reducing devices, viz., the riblets and the outer-layer devices. Limited tests with a stack of three ribbons show that the reduction is approximately additive. The performance of riblets in the presence of a longitudinal pressure gradient is unknown.

**(*h*) Outer-Layer Devices.** Since the early work of Yajnik and Acharya [46], interest has grown in the direct manipulation of the turbulence structure in the outer part of the boundary-layer to achieve a sustained lowering in skin friction [47–69, 102–105]. Thus, a net drag reduction results after the drag penalty due to the device causing the manipulation has been taken into consideration. A net drag reduction is achieved when a pair of low-drag devices of chord $\delta_0$, viz., thin flat ribbons ($t/\delta_0 < 0.02$) or airfoils, are positioned at an $y/\delta_0$ of about 0.8 in tandem, spanning the entire boundary layer and having a spacing of 5–10 $\delta_0$ between the devices. The net drag reduction reported by Corke et al. [47, 48] is 20 percent: Anders and co-workers [49–52] reported 7 percent and Narasimha and Sreenivasan [68] reported about 10 percent.

Typically, a maximum $c_f$ reduction of 20 to 40 percent is achieved within about 15 $\delta_0$ downstream of the device. Here $\delta_0$ is the boundary-layer thickness of the unaltered flow at the device location. This reduced level persists up to about 40 $\delta_0$.

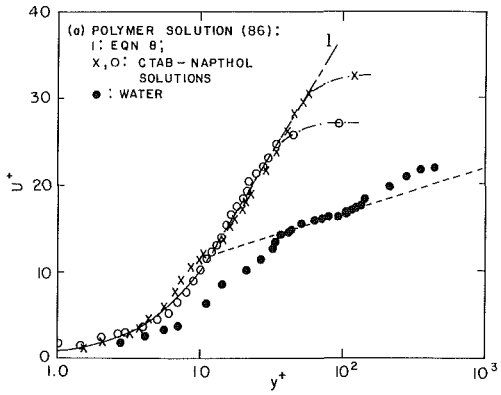


Fig. 1(*a*)

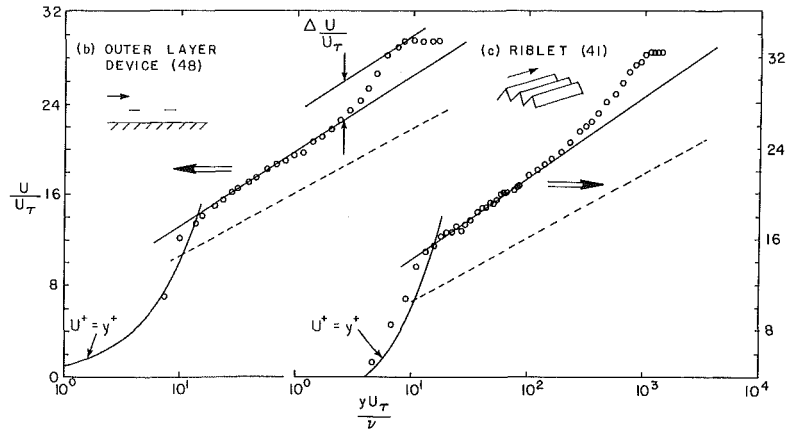


Fig. 1(*b*) and (*c*)

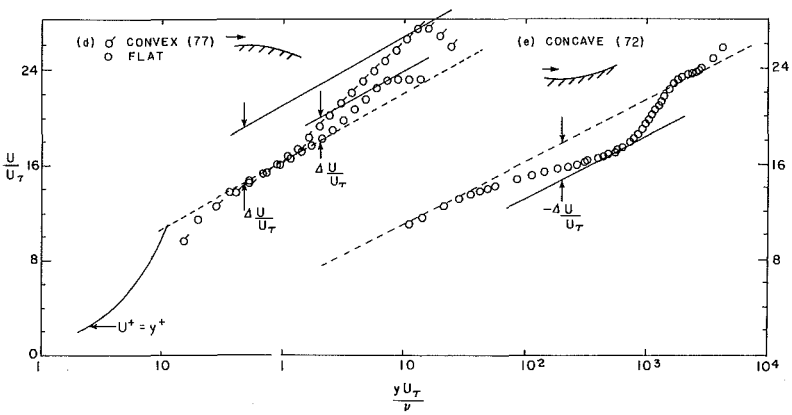


Fig. 1(*d* and *e*)

**Fig. 1 Mean velocity profiles in drag-reducing/drag-increasing boundary layers; broken line: $U^+ = 5.6 \log y^+ + 4.9$; in Fig. 1(*c*), the origin in *y* is at the valley**

Thereafter, the $c_f$ relaxes back slowly to the unaltered level at about 150 $\delta_0$ [49, 52, 56, 65, 67]. These trends in $c_f$ reduction appear to hold in mild favorable and adverse pressure gradients as well [57, 65]. The demonstration by Anders and Watson [49] that the devices having an airfoil section (NACA 0009) perform as well as flat ribbons has brought this technique closer to flight tests. This is so because the stiffness of an airfoil device is higher than that of a flat ribbon by about three orders of magnitude. Earlier, Bertelrud's [58] flight tests had shown that locating profiled ribbons on the wing did not pose any serious safety hazard. In rough wall boundary layers, to a first order, the devices have been found to reduce wall resistance to similar absolute levels as in smooth walls [64]. This is to be expected because the outer layers of smooth and rough walls are known to be similar and the devices introduce the same amount of momentum defect no matter what the wall condition is. Therefore, the end result is that the devices would yield approximately the same absolute levels of net drag reduction in both smooth and rough walls.

*(i)* **Convex Curvature.** It has been known for many years that, when a surface having a longitudinal convex curvature follows a length of flat plate, $c_f$ in the curved length drops to levels lower than that would occur on the flat plate if it had continued to the same streamwise distance. (See references [70 and 71] for reviews and references [72–85] for recent developments in boundary layers over curved surfaces.) However, it is only very recently that the potential of a convex surface to offer a net drag reduction is being evaluated [6]. In the underlying concept, the boundary layer is periodically (in space) subjected to a convex curvature so that a drag reduction results with respect to an appropriately defined reference surface having no curvature. Smits and Joubert [83] and Smits [84] have shown that in a body of revolution, the drag-reducing behavior of a convex curvature could be enhanced by combining it with streamline divergence over the nose. The effect of the combined strain rates is favorable, although, applied singly streamline divergence is known to be destabilizing. The application of convex curvature requires the introduction of short regions of concave curvature ahead of each region of convex surface as well. The qualitative behavior of $c_f$ in a concave surface is opposite to that in a convex surface. Thus the possible sources of drag penalty are the higher viscous friction in the concave region and the pressure drag due to the curved surfaces. Currently, there is no data on whether a net drag reduction can be achieved by employing curvature on an axisymmetric body.

**Measurements of $c_f$ in Altered Boundary Layers.** In drag-reducing flows with OLD's or riblets, the accurate measurement of the coefficient of local skin friction, $c_f$ is difficult. Two popular methods of measuring $c_f$, viz., the Preston tube and the Clauser chart method, rely on the existence of a "normal" law of the wall. Since it is believed that the constants in the law of the wall in the above two altered flows might have been disturbed (to be discussed in the following section), these two popular methods may be inapplicable. If the distributions of $\theta$ and static pressure are accurately known, $c_f$ in the altered flows can be obtained from a momentum balance. The accuracy of $\tau_w$ obtained in this way is limited by: (*a*) the uncertainty in the calculation of $\theta$ (because this method requires reliable near-wall measurements) and, in riblets, in the ambiguity of the $y = 0$ location, (*b*) the fact that a differentiation process for $d\theta/dx$ and $dp/dx$ is involved, which introduces some uncertainty, and (*c*) any mean three-dimensionality that might exist in the flow field. As is known from studies on "normal" flat-plate boundary layers, if attention is paid to these problems, the uncertainty in $c_f$ can be reduced substantially from the ±20 percent level that is often reported otherwise. Another technique, viz., the measurement of $\partial U/\partial y|_{y=0}$, is highly desirable, although such measurements are difficult when, at high $Re_\theta$ and in air, the sublayer thickness becomes very small. The use of a small-area skin-friction balance to measure $c_f$ holds promise if it is designed to be sensitive to the low $\tau_w$ that commonly occurs in the low dynamic head laboratory facilities [67]. The local skin friction can also be measured directly by the oil-viscosity balance method of Tanner [106] which does not require any calibration (also see [107 and 103]). Since the net drag-reduction levels are rather small in riblet and OLD flows, their measurement by more than one independent technique is essential and the uncertainties in the measurements must be stated. New methods of measuring $c_f$ in the altered flows due to riblets and OLD's are needed. Special attention must be paid to the spanwise variations in $c_f$ and $\theta$ to ensure that the net drag reduction is achieved over the span. In the curved surfaces, on the other hand, the measurement of $c_f$ does not pose a special problem because the "normal" law of the wall applies.

**Mean Flow.** In the drag reduction techniques employing riblets, OLD, and convex curvature, the "normal" development of the boundary layer is carefully disturbed. These studies are useful not only from a practical point of view but also because, by altering the "normal" balance of forces, the aspects of the turbulence production process that are universal in nature can be brought to light. As far as the drag-reducing mechanism is concerned, a comparison of the mean and turbulence characteristics between the various drag reducing flows would be instructive.

In the following paragraphs, the behavior of the mean flow in the drag-reducing boundary-layer flows of most recent interest, viz., those over riblets, OLD's, and convex surface curvature, has been examined. A limited reference has been made to the near-wall region of polymer-additive flows. The mean flow in boundary layers over a concave surface has also been studied to complement the results of convex curvature.

**(*a*) Law of the Wall.** Five typical mean velocity profiles are shown in Fig. 1 in terms of the wall-layer variables for (*a*) flows of dilute polymer solutions in a boundary layer at the condition of maximum drag reduction [86], flat-plate boundary layers altered by (*b*) OLD's [48] and (*c*) riblets [41], and boundary layers over longitudinal (*d*) convex [77] and (*e*) concave [72] curvatures. The zero-pressure gradient equilibrium flat-plate boundary-layer velocity profile is included in Fig. 1(*d*) for comparison. The figures show the regions of the boundary layer over which the velocity profiles in the drag-reducing/drag-increasing flows depart from the normal distributions. The log law in a flat-plate boundary layer is given by

$$U/U_\tau = A \log_{10}(yU_\tau/\nu) + B \tag{3}$$

where the commonly used values of $A$ vary from 5.5 to 5.6 and of $B$ from 4.9 to 5.45. Barring this minor variation in the values of $A$ and $B$, the existence of a logarithmic layer in a normal flat-plate boundary can now be considered to be firmly established. Such a layer does exist in all the flows, although in the flows having no surface curvature the values of $A$ and $B$ appear to be higher than normal. For example, in OLD flows, Corke et al. [48] quote $A = 6.61$, $B = 6.53$ and $A = 6.61$, $B = 7.56$ in two sets of ($Re_\theta$) experiments. The data of Lemay et al. [67] show that in the region immediately downstream of the devices (10 $\delta_0$), the normal law of the wall is altered and Preston tube measurements do not agree well with the small-area (about 30 mm diameter) balance measurements. However, their data also show that when the reduction in $c_f$ is less than about 20 percent, the normal law of the wall holds in the altered flow as well. De and Squire [61] in their modelling of the altered flow, have concluded that $k$ drops to 0.24 downstream of the devices and then recovers slowly. Figure 1(*c*) (from reference [41]) indicates that $A$ and $B$ are 6.6 and 7.15 in flow over a riblet surface if the $U_\tau$ obtained at the

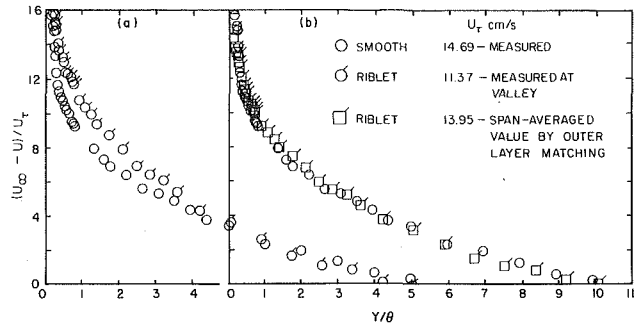


Fig. 2 Boundary-layer defect profiles in smooth, flat surfaces and riblet surfaces

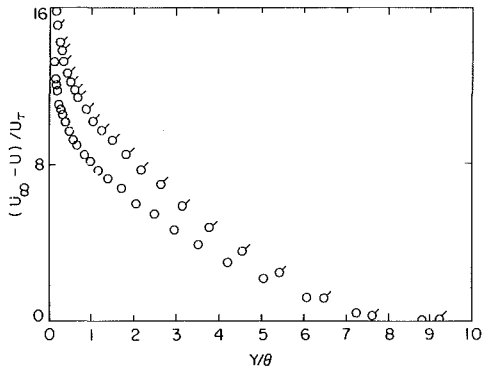


Fig. 3 Defect profiles in normal (○) and OLD flows (♂)

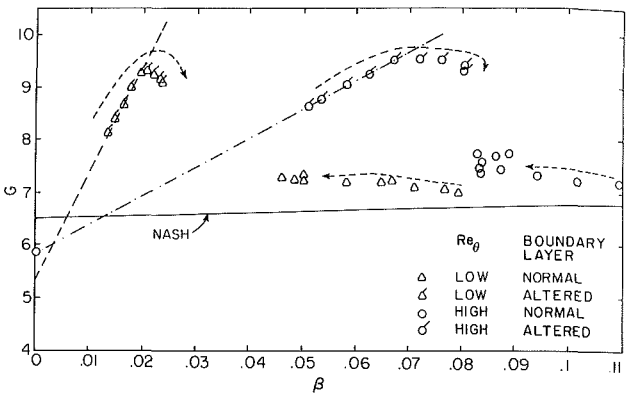


Fig. 4 Boundary-layer trajectories in normal and OLD flows [48]; arrows indicate x-direction

valley is used. However, if the span-averaged measurements are considered [42], the change in the law of the wall is much smaller. In the flow of a polymer solution in a pipe, depending on the concentration, $A$ and $B$ are known to be different from the normal values [13]; Fig. 1($a$) shows the law of the wall for the limiting case of the maximum drag reduction [86]. Therefore, the evidence so far, although by no means conclusive, is that the von Kármán's constant, $k$, is lower than the normal flat-plate value of 0.40–0.41, in drag-reducing flows having no surface curvature. The lowest $k$ of 0.197 is reached in polymer flow at the condition of maximum drag reduction. Since the mixing length, $l$, near a wall bears a linear relationship to the distance from the wall, $y(l = ky$, where $k = \log_e 10/A)$, a higher value of $A$ suggests a lower mixing length in the drag-reducing flows, shown in Figs. 1($a$)–($c$). A lower $l$ could be interpreted to mean that the outward ejections at the wall associated with the turbulence production process are narrower which results in a lower skin friction. On the other hand, the higher values of $B$ imply the existence of a thicker viscous sublayer.

In flows over curved surfaces, the law of the wall remains unchanged from the normal distributions found in a smooth flat plate; however, the outer layers are quite different in the convex and concave surfaces, Unlike that in a flat-plate boundary layer, the flow over a convex surface with zero streamwise pressure gradient contains a static pressure gradient normal to the wall which causes the velocity reduction in the outermost part of the profile as shown in Fig. 1($d$). The difference between the convex surface law of the wall and that on a flat plate is that the wake profile departs from the log layer at a lower $y^+$ [77, 73], resulting in a thinner log layer and law-of-the-wall layer. This suggests that the body force does not affect the near-wall region in a direct manner. Thus, the phase in the turbulence production cycle that is being directly disturbed in flows with longitudinal surface curvature lies in the outer layer, in other words, in the large structures of the flow. Since large structures involve long time scales, the relaxation length downstream of a region of curvature can be expected to be $0(\delta)$. This behavior is desirable in achieving a substantial drag reduction [6]. Conversely, in the case of the near-wall manipulators, for example, in the downstream of a length of riblet surface, the drag-reducing effect would not persist beyond a few sublayer thicknesses. No drag penalty is involved with the riblets and the maximum net drag reduction achieved is about 10 percent. On the other hand, a similar level of net drag reduction has been achieved in flows altered by OLD's as well, although the $c_f$ is reduced by as much as 40 percent over lengths of about 25 $\delta_0$. This happens because of the drag penalty paid by the device. The drag reduction is much higher, up to 80 percent, in both polymer flows and microbubble injection. Though the net drag reduction achieved by riblets and OLD's is modest in comparison, the devices are of significance to civil aviation and the net drag reduction is large enough to result in savings of billions of dollars in fuel annually in the U.S. [6].

**($b$) Defect Profile.** The above section shows that the drag-reducing flows having no surface curvature exhibit a qualitatively similar law-of-the-wall behavior. Being largely a near-wall agent, perhaps, this is to be expected in polymer solutions and riblets. However, this is not obvious in OLD flows because the devices are believed by some authors [52] to break up the large eddies which reside in the outer layer and apparently no direct near-wall manipulation is involved. (The popular acronym LEBU, which stands for large eddy breakup, was thus coined.)

Virk et al. [13] have shown that in the flow of polymer solutions, the defect law ($(U_\infty - U)/U_\tau$ versus $y/R$) agrees with that found in the flow of the solvent in a pipe. This similarity indicates that the inner layer parameter $U_\tau$ is a relevant velocity scale in the outer layer and $(U_\infty - U)$ drops to the same extent as $U_\tau$ does compared with the flow of the solvent in a pipe, resulting in a fuller velocity profile. The defect profiles for riblet and OLD flows are shown in Figs. 2 and 3. The profiles of the altered layers have been compared with those obtained at the same station in the normal flat-plate boundary layers. Figure 3 shows that in boundary-layers disturbed by OLD's, the normal defect law is not obeyed; additionally, the trend in $c_f$ reduction stated earlier means that the flow is not in a state of local self-preservation.

The measurements in the normal and altered (OLD) flows by Corke et al. [48] have been examined in terms of their departure from the equilibrium boundary layer. This departure can be described by boundary layer trajectories [87], viz., $G$ versus $\beta$, where $G$ is Clauser's [88] profile shape parameter and $\beta$ is the ratio of pressure and friction forces. If we rate a $\beta$ of 5 as strong and 0.5 as mild, then the $\beta$ of about 0.05 in Corke et al.'s plate should be termed weak. The $G$ versus $\beta$ trajectories are shown in Fig. 4; the arrows indicate the $x$-direction. The unaltered layers have $d\beta/dx < 0$ but the OLD flows have $d\beta/dx > 0$. Nash [87] terms them as the "allevia-

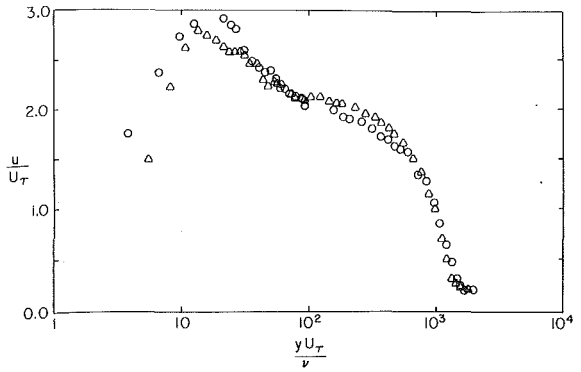


Fig. 5 Turbulence-intensity distributions in boundary-layers over smooth (○) and riblet surfaces (△)

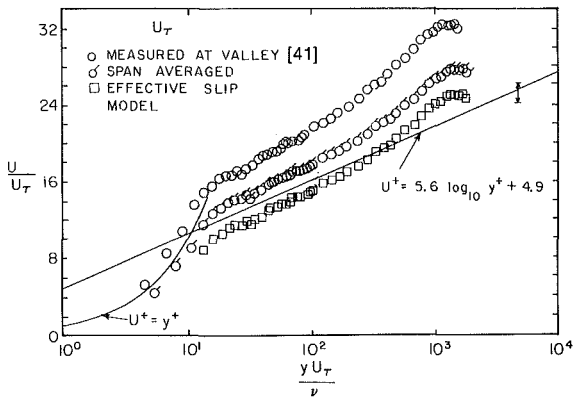


Fig. 6 Effective slip model in boundary-layers over riblet surface; solid lines: smooth, flat plate; arrows indicate uncertainty limits in the model

tion of pressure gradient" and the "augmentation of pressure gradient" type respectively. Consideration of $G$ as a dependent variable and $\beta$ as an independent variable was done by Clauser to understand the behavior of adverse pressure gradient boundary layers from a systems point of view [89, 90]. Nash has shown that it is the sign of $d\beta/dx$ that determines the relaxation of $G$. For $d\beta/dx > 0$, the trajectories remain close to the equilibrium locus; however, for $d\beta/dx < 0$, they tend to depart. The positive nature of $d\beta/dx$ in these OLD flows suggests that given a sufficient length, they would approach the equilibrium locus. This behavior indicates that if departure from equilibrium is an essential element, larger drag reduction may be possible when OLD's are used in $d\beta/dx < 0$ flows.

Figure 4 also shows that after the flows are altered by OLD's, their early effect is to increase the sensitivity of $G$ to $\beta$. The nonequilibrium nature of the OLD flows under consideration makes the $G$ versus $\beta$ trajectories sensitive to the flow history. This has to be borne in mind, for example, while comparing the results of wind tunnels and flight tests.

Tani and Motohashi [91] have observed that the pattern of return to equilibrium in OLD flows, in terms of $\pi$ versus $\mathrm{Re}_\theta$, is similar to that of tripped boundary layers. Based on similarity considerations, they are examining if the departure from equilibrium could be expressed by the integral shear stress parameter, viz., $\int_0^\delta (2\pi/\rho\, U_\infty^2 \delta)\, dy/c_f$.

Figure 2(*a*) shows that the defect law breaks down in the case of the flow over a riblet surface if, for the velocity profile measured over the valley, the $U_\tau$ measured at the valley is used as the velocity scale. The appropriate value of $U_\tau$ in riblets can be determined by studying the flow in the immediate vicinity of the riblets because it is in this neighborhood that the change in the riblet flows primarily takes place. Hooshmand et al. [41] have shown that at the $x$-station under consideration in Fig. 2 (over the riblet surface), the friction velocity $U_\tau$ is 11.4 cm/s over the valley and 15.3 cm/s over the peak but 14.7 cm/s on the smooth flat plate. Thus, at this flow condition, the local skin friction is lower by 40 percent at the riblet valleys and 10 percent higher at the peaks compared with that in a flat plate, and the net span-averaged effect is a lower skin friction. The riblet profile shown in Fig. 2(*a*) has been measured over a valley, and therefore it is logical to use $U_\tau$ at the valley as the velocity scale for the entire layer. Although on the face of it this choice of $U_\tau$ is logical, in the following paragraph it is shown to be inapplicable to the profile in view of a spanwise variation in the mean flow created by the riblets in their vicinity.

The large difference in the friction velocity at the peaks and valleys of the riblets creates a situation that has no counterpart in smooth-wall boundary layers. Figure 5 in reference [41] shows that the mean velocity at a constant $y$ (taking $y = 0$ at the valley) and along the span is like a sine function; the velocities are lower over a peak than over a valley. The difference between the mean velocities at a fixed $y$ over the peaks and valleys decreases away from the wall. There is no phase change with $y$ but there is a monotonic drop in the difference between the mean velocities at points above the peak and valley. At $y^+ = 13$ ($y/\delta = .01$), a barely perceptible difference in velocity still exists. Following Clauser [88], the inner layer is taken to extend up to $y/\delta = 0.15$ from the wall and the outer layer to cover from 0.05 to 1.0 with a region of overlap in between. The spanwise nonuniformity in the mean velocity can therefore be safely assumed to have been eliminated at $y/\delta = .05$ ($y^+ = 60$), the inner edge of the outer layer. In other words, as far as the inner boundary condition of the outer layer is concerned, it is immaterial whether the profile taken is above the peak or the valley. The spanwise nonuniformity is confined to the sublayer and buffer layer alone. It is therefore concluded that as far as the outer layer is concerned, the appropriate $U_\tau$ is neither the value that occurs at the valley nor at the peak; it must lie in between. However, the appropriate $U_\tau$ cannot be equal to the flat-plate value either, although it is an intermediate value, simply because the riblet drag (averaged over the span) has been well established to be lower. Thus, the appropriate $U_\tau$ for the outer layer lies between the $U_\tau$ measured over the valley and that of the smooth flat plate. A more specific statement is difficult to make at this stage. A detailed measurement of $U_\tau$ over one wavelength of the riblet must be done to get the average $U_\tau$, that is, the $U_\tau$ impressed upon the outer layer at its inner boundary. Figure 2(*b*) shows that a $U_\tau$ of 13.95 cm/s with an uncertainty of $\pm 4$ percent makes the defect profiles of the riblet and smooth flat plate collapse on each other. The following discussion of the $u$-turbulence distribution also shows that this value of $U_\tau$ leads to a consistent result. The $U_\tau$ of 13.95 cm/s is therefore effectively a span-averaged value.

If a defect profile does not change as the flow moves downstream, the outer layer is said to have reached local self-preservation. Virk et al.'s [13] solution for flow of a polymer in a pipe has reached such a state. It has been shown above that the defect profiles in riblets and smooth flat plates collapse, which indicates that the mean flow in the outer layer is not altered by the riblets. Figure 5 shows the $u$-turbulence profiles at the same ($x$, $z$) station, with and without the riblet surface, plotted using wall-layer scales. The collapse in the outer layer indicates that the riblets do not alter the turbulence in the outer layer as well. The data of Bacher and Smith [42] also support this conclusion.

A technique of estimating the $c_f$ on a riblet surface in external flows can be developed based on the fact that the riblets do not alter the outer-layer flow. Note that the channel data of Grass [92] and the compilation of boundary-layer data by Antonia and Luxton [93] also indicate that, in the region of self-perservation, the $U$-defect, $u$-turbulence, and $v$-turbulence

profiles in rough and smooth walls collapse on each other in the outer layer when $U_\tau$ is taken as the velocity scale. Therefore, the mean velocity and turbulence profiles in both the flat-plate and riblet surfaces should first be measured at identical $x$-stations. The $U_\tau$ for the riblet surface could then be estimated by determining the value that gives the best agreement of the riblet data with the flat-plate defect profile and $u$-turbulence when expressed in wall-layer variables. A comparison of the drag obtained from the $\tau_w$ distribution along $x$ with the drag balance measurement must be completed to firmly establish this technique.

The relationship between bursts and skin friction is unknown. For example, if the viscous drag is to be reduced, should the effort be directed at reducing the burst frequency? However, if bursting is indeed directly related to the skin friction, both the change in the period between bursting $T$ and the strength of the burst should be considered. The importance of the strength of bursts has been ignored, perhaps because of the preoccupation with the measurement of $T$ over the last decade or two. The riblet and OLD flows offer the unique opportunity of comparing the value of $T$ at a station with and without the disturbance at the same free-stream velocity without performing any kind of nondimensionalization. This bypasses the seemingly endless controversy of whether $T$ scales with the inner or outer variables or a combination of both. Corke et al. [48] have concluded that in a boundary layer altered by OLD, when the skin friction drops by 30 percent, the bursting frequency drops by 17 percent. Note that by bursting frequency the authors mean the quantity $U_\tau^2 T/\nu$. When their measurements of $T$ alone are compared with those obtained with and without OLD, $T$ is found to remain unchanged. Therefore, the change in skin friction is not related to $T$. The measurements of Walsh [37], Hooshmand et al. [41], and Gallagher and Thomas [43] in flow over riblets also show that there is no clear change in $T$ compared with that on a smooth flat plate. A number of investigators agree that in OLD and riblet flows, near the wall, there is a drop in the absolute $u$-turbulence level [53, 48, 37, 41, 42]. Experiments should be performed to determine the change in the dispersion of the strength, spanwise spacing, and time between bursts in the altered boundary layers. In the OLD flows such measurements should be phase-referenced to the passage of the wake vortices from the device to determine if the wake is responsible for the slow relaxation presumably back to equilibrium.

Although it is not well understood why the outer-layer devices lead to a drag reduction, a coherent description of the changes created in the turbulence structure is beginning to emerge. Nagib and co-workers [55, 48, 66] have shown that the presence of the devices leads to a suppression of the large-scale intermittency in the boundary layer. As is indicated by a lower $d\delta/dx$, the entrainment is reduced [49]. The turbulence level near the wall is also reduced. The inclined hairpin vortices, found in normal boundary layers [94], continue to appear in the altered flow, but they do so in the inner region only and in a more orderly fashion [55, 56, 61]. It needs to be inquired (*a*) if the high frequednсy vortex shedding due to the devices (high compared to the frequency of the energy containing eddies of the boundary layer) is related to the turbulence suppression near the wall and, (*b*) if the appearance of the modulated structures is also accompanied by a decrease in the spatial growth rate of the energy containing disturbances [108].

The defect law in flows over longitudinal convex and concave curvatures has been examined by Ramaprian and Shivaprasad [74] and more recently by Prabhu et al. [80]. Prabhu et al. have observed that in strong convex and concave curvatures, the defect law is independent of the friction velocity. This led them to conclude that a strong curvature "loosens" the coupling between the inner and outer layers that exists in a flat-plate boundary layer. There are differences in the rate ($\delta/R$) at which this coupling is loosened when the curvature is convex or concave. For example, the data of Prabhu et al. (Fig. 6 in reference [80]) show that $B$, the intercept in the log law, is dropping at a $\delta/R$ of 0.04 (convex); on the other hand, even at a $\delta/R$ of $-0.08$ (concave), $B$ remains at the flat-plate level. The data of Ramaprian and Shivaprasad [74] for a mild $\delta/R$ of 0.01 also show interesting differences in the response of a boundary layer to convex and concave curvatures. Their measurements of defect profiles show that the boundary layer quickly approaches self-preservation over the concave surface much like on a flat plate, but that it shows no such tendency when the wall curvature is convex. Additionally, they observe "that compared to the flat wall boundary layer. . . , the non-dimensional mixing length and Reynolds shear stress are considerably reduced over most of the convex wall boundary layer and increased, though *less* (present author's italics) spectacularly, in the concave wall boundary layer." In summary, the available data, although limited, clearly indicate that a boundary layer is slower to respond to a concave curvature than to a convex. This can be termed as an asymmetric response of the boundary-layer large structures to external forces. A similar behavior has been observed in positive and negative pressure gradients [95]. Such an asymmetric behavior has useful potential in fluids engineering applications. For example, if a boundary layer is subjected to successive regions of equal concave and convex curvatures, it is likely to result in a lower viscous drag compared with that on a flat plate of equal length.

**(*c*) Effective Slip Model.** Regardless of the differences between the types of disturbances imposed on the flows without a surface curvature, the fact remains that the law of the wall and the strength of the wake component behaviors (to be discussed later) in these flows bear striking similarities. This suggests that the effective slip model [13], which has been found to be so successful in the modelling of mean velocity in polymer flows, may be applicable to OLD [48] and riblet flows as well. This model is simple to use but does not explicitly consider the role of the turbulence that seems to determine the extent of the viscous drag reduction.

Virk et al. [13] have proposed that for the flow of a drag-reducing polymer solution in a pipe, the mean velocity, $U$, at any point in the outer layer as defined by Clauser [88] is the sum of the velocities contributed by two plugs, viz., (1) the velocity, $U_N$, that would exist in the Newtonian solvent but at the prevailing (low) wall shear stress and (2) the constant effective slip velocity, $U_s$, given by the difference between the actual cross-sectional average velocity and that of the Newtonian plug. Excellent agreement between the polymer solutions and solvent was obtained.

The following analogy can be drawn from the point of view of the mean flow only. The flow of drag-reducing polymer solutions is similar to the drag-reducing OLD and riblet flows, and the Newtonian plug in polymer solutions discussed above is like a plug of normal flat-plate boundary layer in the altered flows. We define a normal flat-plate boundary layer to be one that obeys the friction law of Ludwieg and Tillmann. In this sense, the altered flows are not normal. Here, the model of Virk et al. [13] has been applied without any recourse to the average velocities through the layer. The measured Reynolds number, $\mathrm{Re}_\theta$, and shape factor, $H$, of the altered boundary layer, when put into the well known Ludwieg-Tillmann relationship, viz.,

$$c_{fN} = (0.246/10^{0.678H})\mathrm{Re}_\theta^{-0.268} \tag{4}$$

predicts the skin-friction coefficient, $c_{fN}$, of the "normal" flat-plate plug appropriate to the station under consideration. The coefficients of local skin friction measured in the altered flows and calculated for the normal plug in the slip model are

**Table 1 Coefficient of local skin friction in altered flows**

| | Riblets [41] | OLD flows [48] | | | |
|---|---|---|---|---|---|
| | | $Re_\theta$ in unaltered flow | | | |
| | | 2000 | 4000 | 3000 | 5500 |
| | | $x(m)$ | | | |
| | | 2.59 | 4.68 | 2.59 | 4.68 |
| $c_f$ Measured | 0.0026 | 0.0025 | 0.0021 | 0.0021 | 0.0018 |
| $c_{fN}$ calculated for normal plug in effective slip model | 0.0032 | 0.0034 | 0.0030 | 0.0032 | 0.0029 |

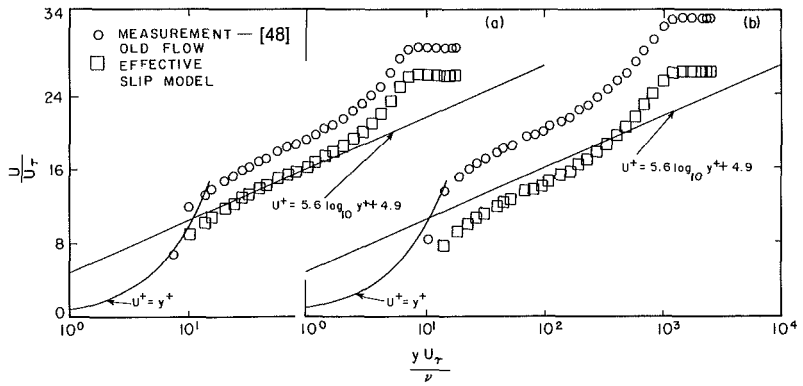


**Fig. 7 Effective slip model in boundary-layers altered by OLD**

shown in Table 1. Note that $c_{fN}$ calculated in the normal plug is greater than the $c_f$ measured as required in a slip model. Now $c_{fN}$ can be used to calculate $U_{N\infty}/U_\tau$, where $U_{N\infty}$ is the freestream velocity of the normal part of the altered boundary layer and $U_\tau$ is the friction velocity of the layer. The $U_\tau$ remains the same in both the altered boundary layer and its normal flat-plate plug model. Therefore, $c_f = 2\,U_\tau^2/_\infty^2$ and $c_{fN} = 2\,U_\tau^2/U_{N\infty}^2$. Since the slip velocity is constant all through the layer at a station, we obtain

$$U_s/U_\tau = U_\infty/U_\tau - U_{N\infty}/U_\tau \tag{5}$$

The relationship

$$U_N/U_\tau = U/U_\tau - U_s/U_\tau \tag{6}$$

can be used to obtain the mean velocity profile of the normal plug across the layer. The results for riblet and OLD flows are shown in Figs. 6 and 7, respectively. The Clauser line for the normal flat-plate boundary layer has been included for comparison with the effective slip model. The agreement is reasonable, although, often it is not as impressive as in the polymer solutions of Virk et al. [13] (to 1 percent). Following the recommendation of Walsh [37] and Hooshmand et al. [41], the $y = 0$ location in riblet surfaces has been taken at the midlevel between the peak and the valley of a longitudinal rib. The effective slip model, when applied to the normal flow, indicates the uncertainty inherent in the data and is marked in Fig. 6. It is not presented here, but the fact that one could choose a constant $U_s/U_\tau$ even by trial and obtain an excellent agreement between the log law and the normal plug in both of these flows must be of physical significance. This strong correlation means that the essential aspects of the effective slip model are as applicable to riblet and OLD flows as they are to the polymer solution.

The applicability of the effective slip model can be interpreted to mean that the disturbances introduced have made a major change in the inner layer ($y+ < 50$–$60$). However, the same end result is reached by three different routes in the polymer, riblet, and OLD flows. In the case of the polymer solution, a molecular change takes place in the inner layer [96] leading to a nonisotropic behavior of the viscosity [13, 97]. On

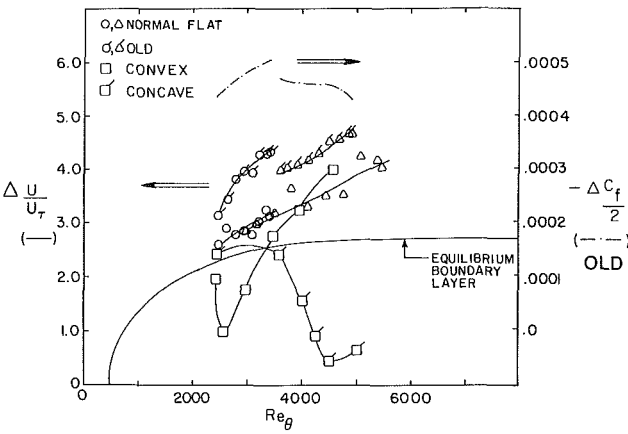


**Fig. 8 Strength of the wake component and skin-friction reduction in OLD [48] and curved boundary layers [74]**

the other hand, in both riblets and OLD flows, the mechanisms are entirely hydrodynamic. However, the details of the mechanisms are unclear and these two flows are yet to be successfullly modelled. Meanwhile, in an effort to explain the drag-reduction mechanisms involved the experimenters have stressed the role of various aspects of the flows. For example, in OLD flows, Anders and Watson [49] have emphasized the modification in the large eddies at the devices. Nagib and co-workers [48, 65, 66] have identified four mechanisms, viz., restriction of the $v$-component by the devices (also emphasized by Narasimha and Sreenivasan [68]), unsteady circulation generated by the device in the fluctuating turbulent flow causing "unwinding" of normal boundary-layer vorticity (also emphasized by Bushnell [6]), generation of new small scales in the outer layer, and the wake of the devices; the role of the wake in the slow recovery of the altered flow has been particularly emphasized by Mumford and Savill [56]. More recently, Sreenivasan [102] has argued that the

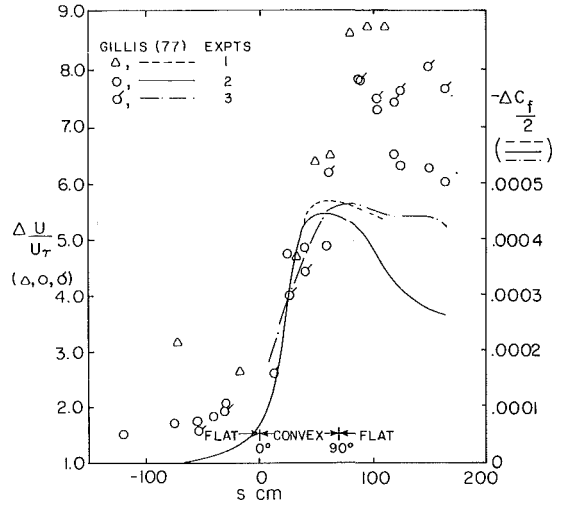


**Fig. 9 Streamwise variations of the strength of the wake component and skin-friction reduction in flow over a convex surface at zero-pressure gradient**

primary drag reducing mechanism in OLD flows is inviscid in nature and the devices must produce a lift force to yield any net drag reduction. In riblet flows, in the near-wall region, the restriction of the normal spanwise motion, vortex stretching, and the development of a "viscous-like pool" have been emphasized by a number of researchers [39, 42, 43, 97].

**(*d*) Strength of the Wake Component.** The so-called wake layer [98], which is the outer part of the boundary layer that lies beyond the log layer, will now be examined. Note that in curved flows, for examlple, the wake deviates from the universal wake function for flat walls due to Coles [74]. A comparison between the flows is thus easier when it is based on (the strength of) the wake component and not the shape of the wake function through the layer. The absolute strength of the wake component is a measure of the average energy of the large eddies [98] and is defined to be the maximum (positive) or minimum (negative) velocity departure ($\Delta U/U_\tau$) of the wake layer from the log law as shown in Fig. 1. This definition has been extended to flows where the log layer constants ($A$ and $B$) are different from their normal values and to boundary layers over large concave curvatures which exhibit curious negative and double (having both a positive and a negative $\Delta U/U_\tau$) wakes. (See Fig. 7 in references [73 and 76] for examples.) Such negative wakes are not present when the concave curvature is weak [74]. The wake component $\Delta U/U_\tau$ was obtained by plotting the velocity profiles as shown in Fig. 1 and not calculated from $\pi$, the wake strength parameter of Coles which implies the universal wake function to apply.

The downstream variations of the strength of the wake component in the various altered flows have been plotted in Figs. 8–11. The uncertainty in the measurements of mean velocity is usually about 1 percent and in $\Delta U/U_\tau$ is about 5–10 percent [98]. Also plotted is the drag reduction ($-\Delta c_f/2$) or increase ($\Delta c_f/2$) compared with normal flat-plate levels. The wake component increases when there is a drag reduction and decreases when there is a drag increase. Similar behavior is known to exist in adverse and favorable pressure gradients, respectively, although a balance of considerably different forces is involved. Figures 10(*a*) and (*b*) show that the rise in $\Delta U/U_\tau$ is an order of magnitude higher when pressure forces are involved. In Fig. 8, the wake component of equilibrium boundary layers due to Coles [98] has been included. The equilibrium value of 2.7 is reached in normal boundary layers at $Re_\theta > 6000$. Boundary layers not approaching this level were originally termed anomalous by Coles. By this definition, all drag-reducing flows are anomalous in nature. Historically,

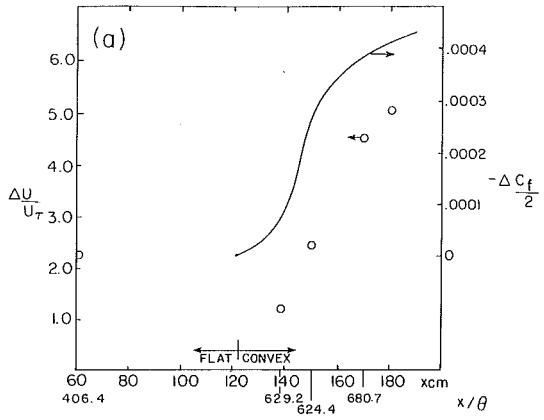


**Fig. 10(*a*)**

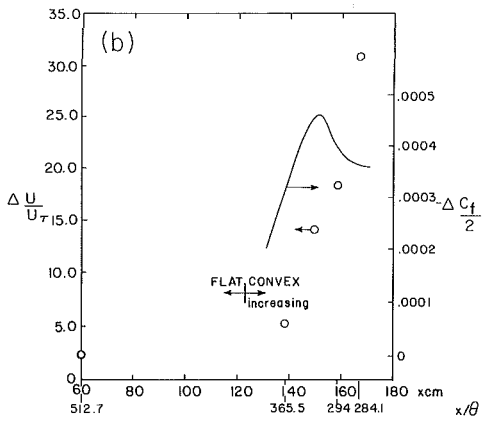


**Fig. 10(*b*)**

**Fig. 10 Strength of the wake component and skin-friction reduction in flow over a convex surface in (*a*) zero-pressure gradient and (*b*) separating boundary layers [72]**

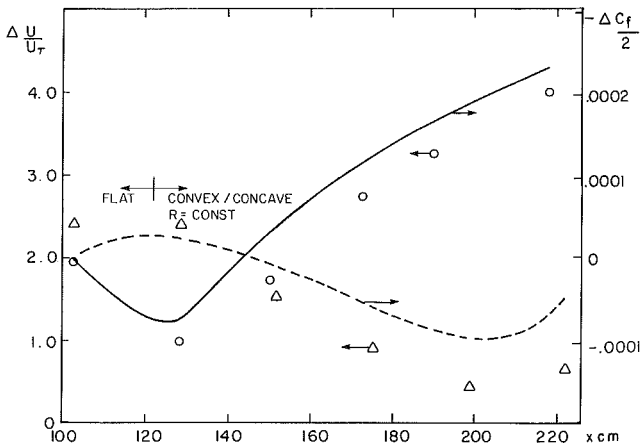


**Fig. 11 Strength of the wake component and skin-friction reduction/increase in flow over a convex (○, solid line) and a concave (△ and broken line) surface [74]**

studies on anomalous flows have not been very popular. However, in view of their engineering applications there is a need to create and study all kinds of anomalous flows in a controlled manner.

It has been shown that the riblets do not disturb the outer layer. Thus, as in undisturbed flow, the outer layer of the riblet flow could indeed be in a state of local near self-preservation, although the wake component (see Fig. 1) in-

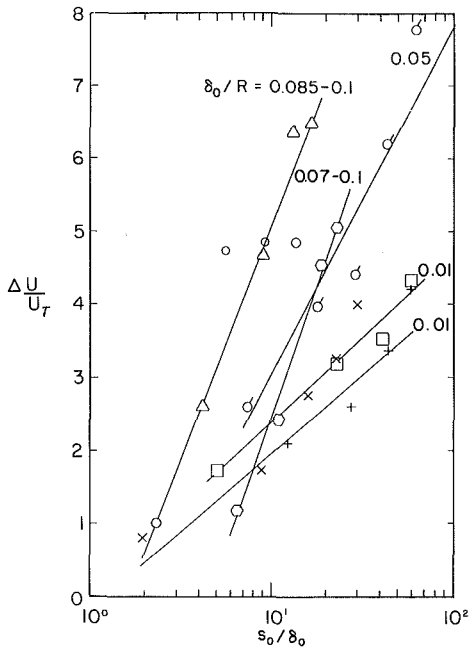


Fig. 12 Outer layer response to convex surface curvature; (symbol, source, *dp/dx*, starting $Re_\theta$, $\delta_0/R$, $dR/ds_0$) are: (△, Gillis first, 0., 5000, .085, 0.), (○, Gillis second, 0., 3800, .10, 0.), (♂, Gillis third, 0., 2300, .05, 0.), (□, Hoffmann and Bradshaw, ≃ 0., 4500, .01, 0.), (◯, So and Mellor, 0., 2000, .06, positive), (+, Gibson et al., mild favorable, 3000, .01, 0.) and (X, Ramaprian and Shivaprasad, mild favorable, 2500, .013, 0.)

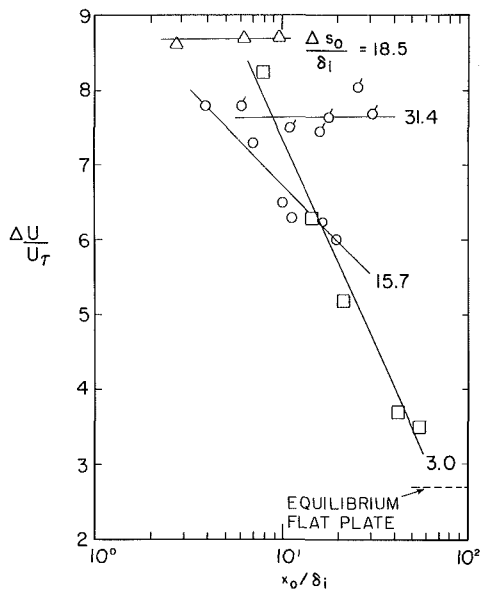


Fig. 13 Outer-layer relaxation downstream of a region of convex curvature; (symbol, source, $Re_\theta$, $\Delta s_0/\delta_i$, $\delta_i/R$) are: (△, Gillis first, 5000, 18.5, .085), (♂, Gillis third, 2300, 31.4, .05), (○, Gillis second, 3800, 15.7, .10) and (□, Smits et al., 6000, 3.0, .18).

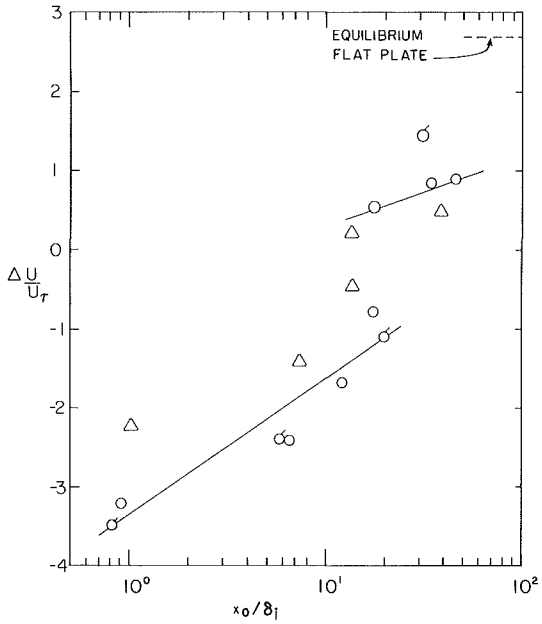


Fig. 14 Outer-layer relaxation downstream of a region of concave curvature; source: Smits et al. [76], (symbol, flow identification, $\Delta s_0/\delta_i$, $\delta_i/R$, $Re_\theta$) are: (○, cc30c, 5.3, .08, 5500), (♂, cc30T, 4.7, .10, 5500) and (△, cc20c, 4, .11, 4500).

dicates otherwise. Gillis has shown (Figs. 50 and 51 of reference [77]; also see reference [78]) that when the shear stress, $uv/U_\tau^2$, is plotted against the distance from the wall normalized by the wall radius, $R$ (not $\delta$), the profiles collapse for $\delta/R = 0.05$ and 0.10. In a similarly strong curvature, the data of So and Mellor [72] also fall on the same profile. (It will be shown that the outer layer response to convex surface curvature is also similar in the experiments of Gillis and of So and Mellor.) Gillis has concluded that "there may be an asymptotic shear stress profile, at least for zero pressure-gradient flow over convex dsurfaces with $\delta/R$ greater than 1/20." But such asymptotic behavior must mean that a local self-preservation exists. Figure 9 shows that the wake component is far from the equilibrium value. Therefore, in turbulent boundary layers with no streamwise pressure gradient more than one type of locally self-preserving state is indeed reachable. Thus, the asymptotic wake component can identify the equilibrium state and some of the so-called anomalous flows are in a locally self-preserving state. The boundary layer can thus be said to exhibit a protean nature. In any case, such orderliness, albeit limited, makes the term "anomalous" inappropriate.

Figure 9 shows the streamwise variation of the wake component in the convex curvature experiments of Gillis [77] at a free-stream velocity of about 15 m/s. The boundary-layer trip was removed in the third experiment, producing a lower $\delta/R$. It is interesting that in the range considered, the variations in $\delta/R$ and $Re_\theta$ have no effect on the strength of the wake component over the region of convex curvature. However, it is the relaxation rate over the following flat plate that is different, at least between the second and third experiments.

To establish the parameters of interest in design, the response of the outer layer to a convex surface curvature and its subsequent relaxation downstream have been studied by comparing the experimental data from various curved boundary layers. The results are plotted in Figs. 12 and 13 in semilogarithmic axes. Figure 12 shows that the response is semilogarithmic, the slope being positive and dependent on $\delta_0/R$, the curvature ratio, up to about 0.07. Linearity is followed better in the data of Gillis [77], So and Mellor [72], and Hoffmann and Bradshaw [75] because the pressure gradient is nearly zero in their experiments. On the other hand, the data of both Gibson et al. [79] and Ramaprian and Shivaprasad [74] shows some deviation because their flows had a mild favorable-pressure gradient. The Reynolds number, $Re_\theta$, in the range of 2000 to 5000 has little effect. Figure 12 shows an important result: an asymptotic state is reached by the outer layer when $\delta_0/R > 0.05$. As stated earlier, Gillis and Johnston [78, 77] also have made a similar observation. They further state that, when $\delta_0/R > 0.05$, turbulent shear stress is rapidly destroyed, largely by negative shear-stress production. The fact that $\delta_0/R \simeq 0.05$ denotes the

boundary between two qualitatively different flow regimes has been utilized by Adams and Johnston [85], who have successfully modelled the two regimes by employing two different mixing length models.

Figure 13 shows the outer-layer relaxation after a region of convex curvature. Very few experiments have been done in this range. The first experiment of Gillis [77] has a rather short downstream length and lacks any sign of relaxation, which could be explained as an effect of the three-dimensionality caused by the sidewalls. Barring this run, Fig. 13 shows that the response is semilogarithmic, the slope being negative and dependent on $\Delta s_0/\delta_i$, the curved-length ratio. Note that $\Delta s_0/R$, which is determined by the surface geometry alone, is the same in all three experiments of Gillis and therefore does not control the rate of relaxation. Thus, the present results mean that a boundary layer that has been subjected to a greater curved-length ratio $\Delta s_0/\delta_i$ will relax more slowly.

A similar study of the response of a concave curvature could not be done due to a lack of data. Limited data from Smits et al. [76] are shown in Fig. 14 in semilogarithmic axes, and the interpretations are tentative. The curious double wake strengths (one each of positive and negative) have been included. The negative wake component can be thought of as the result of outer flow destablization due to a concave curvature, and it seems to relax somewhat faster. This response is also semilogarithmic. There is little difference in the response between the three data sets, possibly because $\Delta s_0/\delta_i$ is nearly the same. The importance of $\delta_0/R$ over and $\Delta s_0/\delta_i$ after a region of curvature suggests that care has to be taken in designing a model if the full-scale viscous flow is to be reproduced.

## Limit of Drag Reduction

In studies on drag reduction in turbulent boundary layers, it is of interest to know the limit of drag reduction. In polymer flows, on semi-empirical grounds, Virk [12] has shown that the limit is described by the following relationship, irrespective of the type and concentration of polymer:

$$\frac{1}{\sqrt{f}} = 19.0 \log_{10}\sqrt{f}\,\mathrm{Re}_D - 32.4 \tag{7}$$

The corresponding asymptotic velocity profile is given by

$$U^+ = 11.7 \ln y^+ - 17.0 \tag{8}$$

This asymptote has been experimentally verified in a boundary layer [86] (see Fig. 1(*a*)).

In injection of microbubbles in water in a flat-plate boundary layer, the work of Bogdevich et al. [23] indicate that the limit is described by the laminar flow of a homogeneous mixture at the same Reynolds number. The relationship is as follows:

$$c_f' = 0.664/\sqrt{\mathrm{Re}_x} \tag{9}$$

The limits in the remaining drag-reducing flows are not known. There is an indication that a limit exists in the flow over a convex curvature because the shear stress across the boundary layer appears to approach an asymptotic distribution [77]. At the condition of maximum drag reduction, it is known both from Eqn. (8) and turbulence measurements [13, 99] that the boundary layer of a polymer flow is not laminar. The state reached by the turbulence is limiting in nature. On the other hand, the reduction in $c_f$ achieved so far in riblet and OLD flows is well below that described by equation (8).

## Concluding Remarks

The drag reduction experiments discussed in this paper pertain to relatively low Reynolds numbers and there is a need to perform experiments at much higher Reynolds numbers. Since the drag reduction levels achieved are small in some cases, measurements by more than one independent technique are desirable and attention should be paid to spanwise flow nonuniformities. The OLD flows in particular present many unanswered questions. Very little is known about small chord airfoil sections which can be used as outer layer devices. A nominally two-dimensional boundary layer usually has only a small (1 percent) spanwise variation in the momentum thickness; but, as the experiments of Anders and Watson [49, 102] show, it is intriguing how a seemingly two-dimensional outer layer device, especially of the airfoil type, can accentuate these spanwise flow nonuniformities.

## Acknowledgments

This work was supported by NASA Contract NAS1-17296. Helpful discussions with Mr. D. M. Bushnell and other members of the Viscous Flow Branch of Langley Research Center are acknowledged. Thanks are also due to Professors T. C. Corke and J. M. Wallace for the generous supply of tabulated data.

## References

1 "Viscous Drag Reduction," Ed. C. S. Wells, 1969, Plenum, London.

2 *Proc. Int. Conf. on Drag Reduction* held at Univ. Cambridge, Sept. 4-6, 1974. Ed.: N. G. Coles, Published by BHRA Fluid Engg., Cranfield, U. K.

3 *Drag Reduction*, 2nd Int. Conf. Drag Reduction held at Univ. Cambridge, Aug. 31-Sept. 2, 1977. Eds.: H. S. Stephens and J. A. Clarke, Published by BHRA Fluid Engg., Cranfield, U. K.

4 "Viscous Drag Reduction," Ed. G. R. Hough, Vol. 72, *Progress in Astronautics and Aeronautics*, 1980.

5 "Special Course on Concepts for Drag Reduction," AGARD Rep. No. 654, 1977.

6 Bushnell, D. M., "Turbulent Drag Reduction for External Flows," AIAA Paper No. 83-0227, 1983.

7 Toms, B. A., "On the Early Experiments on Drag Reduction by Polymers," *Phys. Fl.*, Vol. 20, No. 10 Part II, Oct. 1977, pp. 53-55.

8 Lumley, J. L., "Drag Reduction by Additives," *Ann. Rev. Fluid Mech.*, Vol. 1, 1969, pp. 367 ff.

9 Hoyt, J. W., "The Effect of Additives on Fluid Friction," *Trans. ASME*, Vol. 94, June 1972, pp. 258-285.

10 Lumley, J. L., "Drag Reduction in Turbulent Flow by Polymer Additives," *J. Polymer Sci. Macromolecular Reviews*, Vol. 7, 1973, pp. 263-290.

11 Hoyt, J. W., "Polymer Drag Reduction—A Literature Review, 1975-6," *Drag Reduction*, 2nd Int. Conf. on Drag Reduction, held at Univ. Cambridge, p. A1-1, Aug. 1979; Published by BHRA Fluid Engg., Cranfield, U. K.

12 Virk, P. S., "Drag Reduction Fundamentals," *A.I.Ch.E.J.*, Vol. 21, No. 4, 1975, pp. 625-656.

13 Virk, P. S., Merril, E. W., Mickley, H. S., and Smith, K. A., "The Toms Phenomenon: Turbulent Pipe Flow of Dilute Polymer Solutions," *J. Fluid Mech.*, Vol. 30, 1967, pp. 305-328.

14 Bushnell, D. M., Hefner, J. N., and Ash, R. L., "Effect of Compliant Wall Motion on Turbulent Boundary Layers," *Phys. Fl.*, Vol. 20, No. 10, Part II, 1977, pp. S31-S48.

15 Wehrmann, O. H., "Tollmien-Schlichting Waves Under the Influence of a Flexible Wall," *Phys. Fl.*, Vol. 8, 1965, pp. 1389-1390.

16 Wilkinson, S. P., and Balasubramanian, R., "Turbulent-Burst Control Through Phase-Locked Travelling Surface Depression," Paper No. AIAA-85-0536, 1985.

17 Kim, H. T., Kline, S. J., and Reynolds, W. C., "The Production of Turbulence Near a Smooth Wall in a Turbulent Boundary Layer," *J. Fluid Mech.*, Vol. 50, 1971, pp. 133-160.

18 Kline, S. J., "Ad hoc Committee Report 4," *Workshop on Coherent Structure of Turbulent Boundary Layers*, 1978, Lehigh Univ., pp. 485-488.

19 Thew, M. T., Lee, Y. T., Long, R. F., and Bragg, R., "Experiments With Soluble Polymeric Drag-Reducing Coatings," *Drag Reduction*, 2nd Int. Conf. Drag Reduction, 1977, p. G2-23, Published by BHRA Fluid Engg., Cranfield, U. K.

20 Blick, E. G., "Skin Friction Drag Reduction by Compliant Coatings," *Proc. Int. Conf. Drag Reduction*, Sept. 1974, p. F2-23, Published by BHRA Fluid Engg., Cranfield, U. K.

21 Dickinson, S. C., Power, J. L., and Eynck, J., "Design, Manufacture and Testing of Compliant Coatings for Reduction of Turbulent Drag," Naval Ship Res. and Dev. Center Rep. DTNSRDC-84/060, Aug. 1984.

22 Dubnishchev, Yu. N., Evseev, A. R., Sobolev, V. S., and Utkin, E. N., "Study of Gas-Saturated Turbulent Streams Using a Laser Doppler Velocity Meter," *J. App. Mech. Tech. Phys.*, Vol. 16, 1975, pp. 114-119.

23 Bogdevich, V. G., Evseev, A. R., Marlyuga, A. G., and Migirenko, G. S., "Gas Saturation Effect on Near-Wall Turbulence Characteristics," *Proc. Second Int. Conf. Drag Reduction*, Aug. 31-Sept. 2, 1977, held at Univ. Cambridge, p. D2-25, Published by BHRA Fl. Engg., Cranfield, U. K.

24 Madavan, N. K., Deutsch, S., and Merkle, C. L., "Reduction of Tur-

bulent Skin Friction by Microbubbles," *Phys. Fl.*, Vol. 27, No. 2, 1984, pp. 356-363.

25 Merkle, C. L., and Deutsch, S., "Drag Reduction by Microbubbles: Current Research Status," Paper No. AIAA-85-0537, 1985.

26 Lyamshev, L. M., Chelnokov, B. I., and Shustikov, A. G., "Pressure Fluctuations in the Turbulent Boundary Layer of a Water Flow with Gas Injection," *Sov. Phys. Acoust.*, Vol. 29, No. 6, Nov.-Dec. 1983, pp. 477-480.

27 Legner, H. H., "A Simple Model for Gas Bubble Drag Reduction," *Phys. Fl.*, Vol. 27, No. 12, 1984, pp. 2788-2790.

28 Milling, R. W., "Tollmien-Schlichting Wave Cancellation," *Phs. Fl.*, Vol. 24, No. 5, 1981, pp. 979-981.

29 Liepmann, H. W., Brown, G. L., and Nosenchuck, D. M., "Control of Laminar-Instability Waves Using a New Technique," *J. Fl. Mech.*, Vol. 118, 1982, pp. 187-200.

30 Liepmann, H. W., and Nosenchuck, D. M., "Active Control of Laminar-Turbulent Transition," *J. Fl. Mech.*, Vol. 118, 1982, pp. 201-204.

31 Thomas, A. S. W., "The Control of Boundary-Layer Transition Using a Wave-Superposition Principle," *J. Fluid Mech.*, Vol. 137, 1983, pp. 233-250.

32 Chambers, F. W., "Preliminary Measurements of a Synthetic Turbulent Boundary Layer," Lockheed-Georgia Company, Rep. LG82RR0009, Sept. 1982.

33 Goodman, W. L., "Emmons' Spot Forcing for Turbulent Drag Reduction," *AIAA J.*, Vol. 23, No. 1, 1985, pp. 155-157.

34 Arakeri, J., and Narasimha, R., "Effect of Pulsed Slot Suction on a Turbulent Boundary Layer," *AIAA J.*, Vol. 21, No. 2, 1983, pp. 306-307.

35 Blackwelder, R. F., and Woo, H. H. W., "Pressure Perturbation of a Turbulent Boundary Layer," *Phys. Fl.*, Vol. 17, No. 3, 1974, pp. 515-519.

36 Walsh, M. J., "Riblets as a Viscous Drag Reduction Technique," *AIAA J.*, Vol. 21, No. 4, 1983, pp. 485-486.

37 Walsh, M. J., "Turbulent Boundary Layer Drag Reduction Using Riblets," AIAA Paper No. 82-0169, Jan. 1982.

38 Walsh, M. J., and Lindemann, A. M., "Optimization and Application of Riblets for Turbulent Drag Reduction," AIAA Paper No. 84-0347, Jan. 1984.

39 Reif, W.-E., and Dinkelacker, A., "Hydrodynamics of the Squamation in Fast Swimming Sharks," Neues Jahrbuch fuer Geologie und Palaeontologie. Abhandlungen Band 164, pp. 184-187, Stuttgart E. Schweizerbart'sche Verlagsbuchhandlung, 1982.

40 Bechert, D. W., Hoppe, G., and Reif, W.-E., "On the Drag Reduction of the Shark Skin," Paper No. AIAA-85-0546, 1985.

41 Hooshmand, A., Youngs, R., Wallace, J. M., and Balint, J.-L., "An Experimental Study of Changes in the Structure of a Turbulent Boundary Layer Due to Surface Geometry Changes," AIAA Paper No. 83-0230, 1983.

42 Bacher, E. V., and Smith, C. R., "A Combined Visualization-Anemometry Study of the Turbulent-Drag Reducing Mechanisms of Triangular Micro-Groove Surface Modifications," Paper No. AIAA-85-0548, 1985.

43 Gallagher, J. A., and Thomas, A. S. W., "Turbulent Boundary Layer Characteristics Over Streamwise Grooves," Paper No. AIAA-84-2185, 1984.

44 Nitschke, P., "Experimental Investigation of the Turbulent Flow in Smooth and Longitudinal Grooved Tubes," NASA TM77480, 1984. Translation of "Experimentelle Untersuchung der turbulenten Stroemung in glatten und laengsgerillten Rohren," Max-Planck Institute fuer Stroemungsforschung, Goettingen, West Germany, 1983.

45 Coleman, H. W., Hodge, B. K., and Taylor, R. P., "A Re-evaluation of Schlichting's Surface Roughness Experiment," ASME JOURNAL OF FLUIDS ENGINEERING, Vol. 106, 1984, p. 65.

46 Yajnik, K. S., and Acharya, M., "Non-equilibrium Effects in a Turbulent Boundary Layer Due to the Destruction of Large Eddies," *Structure & Mechanisms of Turbulence*, Vol. 1, p. 249, Lect. Notes in Phys. No. 76, Springer-Verlag, 1979.

47 Corke, T. C., Guezennec, Y., and Nagib, H. M., "Modification on Drag of Turbulent Boundary Layers Resulting from Manipulation of Large Scale Structures," *Sympo. Viscous Drag Reduction*, Dallas, Texas, Nov. 7-8, 1978 appears in pp. 128-143 of reference [4].

48 Corke, T. C., Nagib, H. M., and Guezennec, Y. G., "A New View on Origin, Role and Manipulation of Large Scales in Turbulent Boundary Layers," NASA CR165861, 1982.

49 Anders, J. B., and Watson, R. D., "Airfoil Large-Eddy Breakup Devices for Turbulent Drag Reduction," Paper No. AIAA-85-0520, 1985.

50 Anders, J. B., Hefner, J. N., and Bushnell, D. M., "Turbulent Skin Friction Reduction Using Large-eddy Breakup Devices," *Bull. Amer. Phys. Soc.*, Vol. 28, No. 9, 1983, p. 1386.

51 Hefner, J. N., Anders, J. B., and Bushnell, D. M., "Alteration of Outer Flow Structures for Turbulent Drag Reduction," Paper No. AIAA-83-0293, 1983.

52 Anders, J. B., Hefner, J. N., and Bushnell, D. M., "Performance of Large-Eddy Breakup Devices at Post-Transitional Reynolds Numbers," Paper No. AIAA-84-0345, 1984.

53 Hefner, J. N., Weinstein, L. M., and Bushnell, D. M., "Large Eddy Breakup Scheme for Turbulent Viscous Drag Reduction," *Viscous Flow Drag Reduction*, Ed. G. R. Hough, Vol. 72, Progress in Astro. and Aero., 1980, pp. 110-127.

54 Hefner, J. N., and Bushnell, D. M., "Turbulent Boundary-Layer Relaxation with Application to Skin-Friction Drag Reduction," *AIAA J.*, Vol. 22, No. 7, 1984, pp. 871-872.

55 Corke, T. C., "Digital Image Filtering in Visualized Boundary Layers," *AIAA J.*, Vol. 22, No. 8, 1984, pp. 1124-1131.

56 Mumford, J. C., and Savill, A. M., "Parametric Studies of Flat Plate Turbulence Manipulators Including Direct Drag Results and Laser Flow Visualization," *Laminar Turbulent Boundary Layers* – FED Vol. 11, Eds. E. M. Uram and H. E. Weber, Book No. 100167, ASME 1984, pp. 41-51.

57 Bertelrud, A., Truong, T. V., and Avellan, F., "Drag Reduction in Turbulent Boundary Layers Using Ribbons," Paper No. AIAA-82-1370, 1982.

58 Bertelrud, A., "Full Scale Experiments into the Use of Large-Eddy-Breakup Devices for Drag Reduction on Aircraft," AGARD CP365, Fl. Dyn. Sympo., Brussels, 21-23 May 1984.

59 Takagi, S., "The Structure of Turbulent Boundary Layer Controlled by the Plates," *Proc. 15th IUTAM Sympo.*, Tokyo, July 1983.

60 Nguyen, V. D., Dickinson, J., Jean, Y., Chalifour, Y., Anderson, J., Lemay, J., Haeberle, D., and Larose, G., "Some Experimental Observations of the Law of the Wall Behind Large Eddy Break-up Devices Using Servo-Controlled Skin Friction Balances," Paper No. AIAA-84-0346, 1984.

61 De, Z. M. and Squire, L. C., "The Interaction of a Wake With a Boundary Layer," *IUTAM Symp. Structure of Complex Shear Flow*, Marseille, 1982, Eds. R. Dumas and L. Fulachier, pp. 376-387, 1983, Springer.

62 *Yajnik*, K. S., Sundaram, S., and Acharya, M., "Observations on Large Scale Motions in Highly Disturbed Boundary Layers," *Structure of Complex Turbulent Shear Flow*, Eds. R. Dumas and L. Fulachier, IUTAM Sympo. Marseille, France, 1982, p. 366, Springer.

63 Bandyopadhyay, P. R. and Watson, R. D., "The Pressure Field due to Drag Reducing Outer Layer Devices in Turbulent Boundary Layers," *Exp. Fluids*, 1986 (to be published).

64 Bandyopadhyay, P. R., "Drag Reducing Outer-Layer Devices in Rough Wall Turbulent Boundary Layers," *Exp. Fluids*, 1986 (to be published).

65 Plesniak, M. W., and Nagib, H. M., "Net Drag Reduction in Turbulent Boundary Layers Resulting from Optimized Manipulation," Paper No. AIAA-85-0518, 1985.

66 Guezennec, Y. G., and Nagib, H. M., "Documentation of Mechanisms Leading to Net Drag Reduction in Manipulated Turbulent Boundary Layers," Paper No. AIAA-85-0519, 1985.

67 Lemay, J., Provencal, D., Gourdeau, R., Nguyen, V. D., and Dickinson, J., "More Detailed Measurements Behind Turbulence Manipulstors Including Tandem Devices Using Servo-Controlled Balances," Paper No. AIAA-85-0521, 1985.

68 Narasimha, R., and Sreenivasan, K. R., "The Control of Turbulent Boundary Layer Flows," Paper No. AIAA-85-0517, 1985.

69 Poddar, K., and Van Atta, C. W., "Turbulent Boundary Layer Drag Reduction on an Axisymmetric Body Using LEBU Manipulators," *5th Sympo. Turb. Shear Flows*, Cornell Univ., 1985, pp. 1.1-1.6.

70 Bradshaw, P., "Effect of Streamline Curvature on Turbulent Flow," AGARD-AG-169, 1973.

71 Bradshaw, P., "The Analogy Between Streamline Curvature and Buoyancy in Turbulent Shear Flow," *J. Fluid Mech.*, Vol. 36, 1969, pp. 177-191.

72 So, R. M., and Mellor, G. L., "An Experimental Investigation of Turbulent Boundary Layers Along Curved Surfaces," NASA CR-1940, 1972.

73 So, R. M. C., and Mellor, G. L., "Experiment on Turbulent Boundary Layers on a Concave Wall," *Aero. Qrly.*, Vol. 26, 1975, p. 25.

74 Ramaprian, B. R., and Shivaprasad, B. G., "Mean Flow Measurements in Turbulent Boundary Layers Along Mildly Curved Surfaces," *AIAA J.*, Vol. 15, 1977, p. 189.

75 Hoffmann, P. H., and Bradshaw, P., "Turbulent Boundary Layers on Surfaces of Mild Longitudinal Curvature," Imperial College, London, IC Aero. Rep. 78-04, 1978.

76 Smits, A. J., Young, S. T. B., and Bradshaw, P., "The Effect of Short Regions of High Surface Curvature on Turbulent Boundary Layers," *J. Fluid Mech.*, Vol. 94, 1979, pp. 209-242.

77 Gillis, J. C., "Turbulent Boundary Layer on a Convex, Curved Surface," *Ph.D. thesis*, Stanford Univ., 1980.

78 Gillis, J. C., and Johnston, J. P., "Turbulent Boundary Layer Flow and Structure on a Convex Wall and its Redevelopment on a Flat Wall," *J. Fluid Mech.*, Vol. 135, 1983, pp. 123-153.

79 Gibson, M. M., Verriopoulos, C. A., and Nagano, Y., "Measurements in the Heated Turbulent Boundary Layer on a Mildly Curved Convex Surface," *3rd Sympo. on Turbulent Shear Flows*, Univ. Calif., Davis, 1981, pp. 4.7-4.11.

80 Prabhu, A., Narasimha, R., and Rao, B. N. S., "Structure and Mean Flow Similarity in Curved Turbulent Boundary Layers," Proc. IUTAM Sympo. on *Structure of Complex Turbulent Shear Flows*, held at Marseille in 1982; Ed. R. Dumas and L. Fulachier, Springer, 1983.

81 Savill, A. M., "A New Structural Model of Turbulent Shear Flow and Its Application to a Selection of Curved Flows Including Recovery," *Proc. I.A.H.R. Sympo. Refined Modelling of Flows*, Vol. 1, 1982, pp. 219-237. Proc. held at Paris, Sept. 7-10, 1982.

82 Gibson, M. M., and Verriopoulos, C. A., "Turbulent Boundary Layer on a Mildly Curved Convex Surface. Part 2: Temperature Field Measurements," *Expts. Fluids*, Vol. 2, 1984, pp. 73-80.

83 Smits, A. J., and Joubert, P. N., "Turbulent Boundary Layers on Bodies of Revolution," *J. Ship. Res.*, Vol. 26, 1982, pp. 135-147.

84 Smits, A. J., "The Control of Turbulent Boundary Layers by the Application of Extra Strain Rates," Paper No. AIAA-85-0538, 1985.

85 Adams, E. W., and Johnston, J. P., "A Mixing-Length Model for the Prediction of Convex Curvature Effects on Turbulent Boundary Layers," *Trans. ASME*, Vol. 106, 1984, pp. 142-148.

86 Frederick, P. S., and A. White, "Structure of Turbulent Boundary Layers at Maximum Drag Reduction," *Nature*, Vol. 256, 1975, pp. 30-31.

87 Nash, J. F., "Turbulent-Boundary-Layer Behavior of the Auxiliary Equation," AGARDograph 97, pp. 245–279, May 1965.

88 Clauser, F. H., "The Turbulent Boundary Layer," *Advances in App. Mech.*, Ed.: H. L. Dryden and Th. von Kármán, V. IV, p. 1, New York Academic Press, 1956.

89 Clauser, F. H., "Turbulent Boundary Layers in Adverse Pressure Gradients," *J. Aero. Sci.*, Feb. 1954, pp. 91–108.

90 Clauser, F. H., "The Behavior of Nonlinear Systems," *J. Aero. Sci.*, May, 1956, pp. 411–434.

91 Tani, I., and Motohashi, T., "Some Thoughts on Non-Equilibrium Turbulent Boundary Layer Flows," *Proc. 16th Turbulence Sympo.*, Tokyo, July 1984.

92 Grass, A. J., "Structural Features of Turbulent Flow Over Smooth and Rough Boundaries," *J. Fluid Mech.*, Vol. 50, 1971, p. 233.

93 Antonia, R. A., and Luxton, R. E., "The Response of a Turbulent Boundary Layer to a Step Change in Surface Roughness Part 1. Smooth to Rough," *J. Fluid Mech.*, Vol. 48, 1971, p. 721.

94 Head, M. R., and Bandyopadhyay, P., "New Aspects of Turbulent Boundary-Layer Structure," *J. Fluid Mech.*, Vol. 107, 1981, pp. 297–338.

95 Leontev, A., and Fomichev, V. M., "Heat Transfer and Drag in a Turbulent Boundary Layer with a Pressure Gradient," *Inzhenerno-Fizicheskii Zhurnal* (in Russian), Vol. 45, July 1983, pp. 5–11.

96 Merril, E. W., and Horn, A. F., "Scission of Macromolecules in Dilute Solution: Extensional and Turbulent Flows," *Polymer Comm.*, Vol. 25, 1984, p. 144.

97 Landahl, M. T., and Henningson, D. S., "The Effects of Drag Reduction Measures on Boundary Layer Turbulence Structure – Implications of An Inviscid Model," Paper No. AIAA-85-0560, 1985.

98 Coles, D. E., "The Turbulent Boundary Layer in a Compressible Fluid," Rand Rep. R-403-PR, 1962.

99 Bertshy, J. R., and Abernathy, F. H., "Modifications to Laminar and Turbulent Boundary Layers Due to the Addition of Dilute Polymer Solutions," *Drag Reduction*, 2nd Int. Conf., p. G1-1, Aug. 31–Sept. 2, 1977, Published by BHRA Fluid Engg., Cranfield, U. K.

100 Beasley, W. D., and McGhee, R. J., "An Exploratory Investigation of the Effects of a Thin Plastic Film Cover on the Profile Drag of an Aircraft Wing Panel," NASA TM74073, Oct. 1977.

101 Kreitinger, R. L., and Middleton, D. B., "Aircraft Surface Coatings for Drag Reduction/Erosion Protection," Tech. Paper No. SAE 811070, 1981.

102 Drag Reduction and Boundary Layer Control Symposium, sponsored by ONR/NSSC/AFOSR/ NASA; National Academy of Sciences, Washington, DC, 22–25 Oct. 1985 (abstracts only).

103 Westphal, R. V., "Skin Friction and Reynolds Stress Measurements for a Turbulent Boundary Layer Following Manipulation Using Flat Plates," Paper No. AIAA-86-0283, 1986.

104 Govindaraju, S. P., and Chambers, F. W., "Direct Measurements of Drag of Ribbon Type Manipulators in a Turbulent Boundary Layer," Paper No. AIAA-86-0284, 1986.

105 Blackwelder, R. F., and Chang, S-I., "Length Scales and Correlations in LEBU Modified Turbulent Boundary Layers," Paper No. AIAA-86-0287, 1986.

106 Tanner, L., "A Skin Friction Meter, Using the Viscosity Balance Principle, Suitable for Use with Flat or Curved Metal Surfaces," *J. Phys. E.*, Vol. 10, 1977, pp. 278–284.

107 Manson, D. J., "A Nonintrusive Laser Interferometer Method for Mesurement of Skin Friction," *Exp. Fluids*, Vol. 1, 1983, pp. 15–22.

108 Kudryashov, A. V., Mansfel'd, A. D., Rabinovich, M. I., and Sushchik, M. M., "Modulation mechanism of suppression of turbulence in shear flows," *Sov. Phys. Dokl.*, Vol. 29, No. 7, 1984, pp. 530–532.

**J. C. Dutton**
Associate Professor.
Mem. ASME
Department of Mechanical and Industrial Engineering,
University of Illinois at Urbana-Champaign,
Urbana, IL 61801

**P. Piemsomboon**
Graduate Research Assistant.
Mechanical Engineering Department,
Texas A&M University,
College Station, TX 77843

**P. E. Jenkins**
Professor and Chairman.
Department of Mechanical Engineering,
University of Nebraska-Lincoln,
Lincoln, NB 68588
Fellow ASME

# Flowfield and Performance Measurements in a Vaned Radial Diffuser

*The flow characteristics of a vaned diffuser typical of those currently used in centrifugal compressors have been determined experimentally by using a static diffuser test rig. The vortex test vehicle (VTV) portion of this rig was used to simulate the essential features of the flow leaving the impeller of an actual compressor. The mean flow phenomena at the diffuser entrance and the static pressure recovery along the diffuser passage have been determined. In addition, the flow angle and Mach number distributions at several key locations throughout the diffuser channel have been obtained. The most notable feature of the diffuser flowfield is the high degree of nonuniformity in the inlet/leading edge region.*

## Introduction

Today many small gas turbine engines which utilize centrifugal compressors are increasingly being used in applications such as powerplants for smaller service jets or helicopters. In addition, they are being considered as replacements for piston engines in the automotive and utilities industries. However, the development of radial flow compressors for these engines has now led to the point where a key item for improved system performance is the vaned diffuser. Thus, it is imperative for the development of future high performance radial equipment that additional design information on diffuser performance be obtained and that the qualitative understanding of the detailed flow mechanisms occurring in vaned diffusers be improved. The objective of the present paper is to provide such information obtained under well-controlled experimental conditions using a static diffuser test rig. The advantage of this facility is that it provides the capability to isolate and investigate the vaneless space/diffuser flowfields without the unsteady, distorted flow imposed by the impeller.

Previous attempts [1, 2] have been made to simulate the exit flow from an impeller by using a cascade of radial nozzles. However, stationary radial nozzles produce wakes and shock wave systems which propagate into the vaned diffuser in a manner which is different from that of the flow exiting a rotating impeller. Baghdadi [3–5] used a vortex rig similar to the one employed in this study to generate a swirling flow at the diffuser inlet. Baghdadi, however, concentrated his efforts on overall diffuser performance and not on detailed measurements. A nonrotating "static blow test" apparatus was employed by Russo and Blair [6] to investigate the flow in

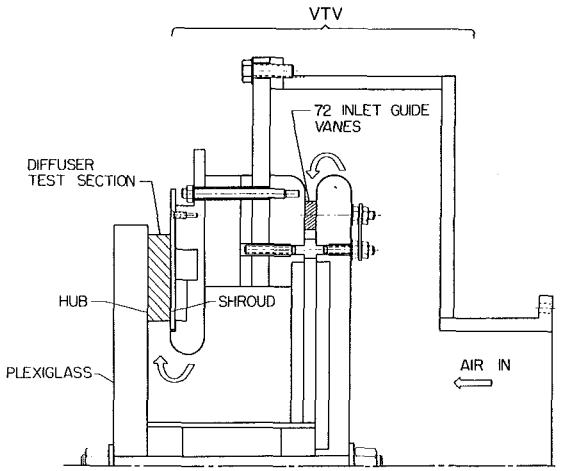


**Fig. 1 Schematic diagram of the static diffuser test rig**

conical and controlled-contour diffusers. As discussed by these authors, the region from the diffuser throat to the exit of an actual centrifugal compressor diffuser is probably reasonably well modeled by this static apparatus. However, the complex flowfield in the critical region between the impeller tip and diffuser throat is not likely to be adequately simulated by the nonswirling flow from this device.

Recently, several experimental investigations [7–14] have been aimed at obtaining measurements in vaned radial diffusers which are supplied by actual centrifugal compressor impeller flow. Rather than obtaining detailed flowfield measurements, these studies have generally concentrated on obtaining overall diffuser performance and/or overall compressor performance maps (which include the diffuser). The most detailed measurements taken to data on actual centrifugal compressor diffuser flows are those of Krain

Contributed by the Fluids Engineering Division of THE AMERICAN SOCIETY OF MECHANICAL ENGINEERS and presented at the Winter Annual Meeting, New Orleans, La., December 9–14, 1984. Manuscript received by the Fluids Engineering Division, June 28, 1984.

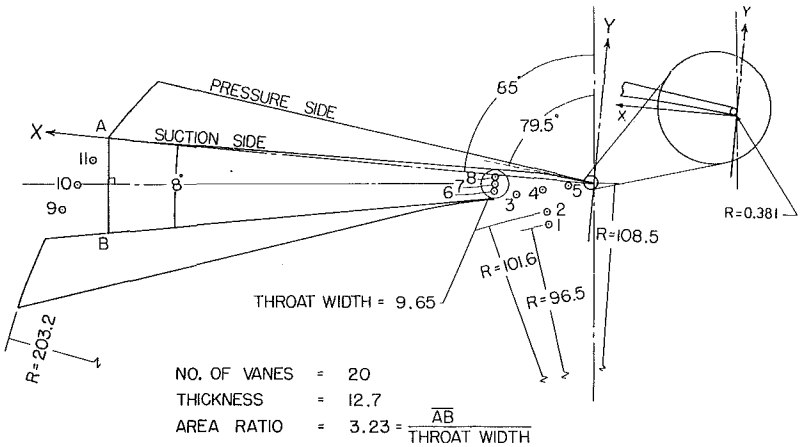


**Fig 2 Drawing of the constant thickness, composite, vaned radial diffuser used in the experiments (all dimensions in mm). The numbered points shown are the probe survey locations.**

**Table 1 Vane pressure and suction side contours**

| $X$ (mm) | $Y_s$ (mm) | $Y_p$ (mm) |
|---|---|---|
| 0.000 | 0.343 | 0.343 |
| 2.540 | 0.089 | 0.978 |
| 7.620 | 0.406 | 1.638 |
| 15.240 | 0.889 | 2.662 |
| 22.860 | 1.372 | 3.619 |
| 30.480 | 1.854 | 4.623 |
| 38.100 | 2.159 | 5.626 |
| 45.720 | 2.286 | 6.629 |
| 53.340 | 2.184 | 7.620 |
| 60.960 | 2.032 | 8.611 |
| 68.580 | 1.880 | 9.601 |
| 76.200 | 1.714 | 10.579 |
| 83.820 | 1.575 | 11.570 |
| 91.440 | 1.422 | 12.560 |
| 99.060 | 1.257 | 13.551 |
| 106.680 | 1.105 | 14.554 |
| 114.300 | 0.940 | 15.532 |
| 121.920 | 0.787 | 16.523 |
| 129.540 | 0.660 | 17.526 |
| 137.160 | 0.495 | 18.504 |
| 146.215 | 0.292 | 19.660 |
| 154.940 | 0.127 | - - - - |
| 162.560 | 0.000 | - - - - |

[11] and Jansen and Rautenberg [13]. Krain used a laser doppler velocimeter system to obtain instantaneous velocity and flow angle profiles across a plane in the quasi-vaneless inlet region and across the throat plane. The diffuser investigated by Jansen and Rautenberg consisted of a set of three-dimensionally twisted blades which were matched to the measured flow angle distribution at the impeller exit. The influence of the diffuser inlet shape on the performance of a centrifugal compressor stage has been further investigated by Bammert, Jansen, and Rautenberg [14].

Due to the critical nature of the vaneless region, as reported by many investigators such as Dean and Young [7], Rodgers [12], and Rayan and Yang [10], the present investigation has focused on measurements in this region. The mean flow phenomena at the diffuser entrance and the pressure recovery along the diffuser passage have been measured. In addition, a yaw probe and pitot probe have been used to obtain the flow angle and Mach number distributions at various locations along the diffuser channel, including the entrance region.

## Equipment and Apparatus

A blowdown air flow facility was constructred for these experiments. Compressed air was supplied to a 16 $m^3$ (550 $ft^3$) storage tank by means of an Ingersoll-Rand piston compressor. A Masoneilan Camflex control valve was used to regulate this compressed air so that a constant supply pressure was maintained at the test rig during the blowdown tests. A 48-port Scanivalve was used with an associaaed controller and decoder which, in turn, were coupled to a MINC microcomputer so that the Scanivalve could be automatically controlled by the computer. The microcomputer was programmed to record the pressure data, temperature data, and to step the Scanivalve. An ASME standard square-edged orifice plate was used to measure the mass flow rate.

Figure 1 shows a schematic diagram of the static diffuser test rig which was used in this study. The rig consists of two major sections: the vortex test vehicle (VTV) and the diffuser test section. The purpose of the VTV is to simulate the exit

## Nomenclature

$A$ = area
$AR$ = exit-to-throat diffuser area ratio
$B_F$ = blockage factor, $B_F \equiv$

$$1 - \frac{\dot{m}\sqrt{RT_t/\gamma}}{\mathrm{PAcos}\alpha\, M\left(1+\frac{\gamma-1}{2}M^2\right)^{1/2}}$$

$C_p$ = coefficient of pressure, equation (1)
$L$ = hub-shroud width
$\dot{m}$ = mass flow rate
M = Mach number
$P$ = pressure
$PS$ = pressure side
$R$ = radius, specific gas constant
Re = Reynolds number
$SS$ = suction side
$T$ = temperature
$VTV$ = vortex test vehicle
$x$ = coordinate measured from shroud to hub
$X$, $Y_s$, $Y_p$ = coordinates used to define vane geometry, Fig. 2 and Table 1
$\alpha$ = flow angle measured from the tangential direction
$\gamma$ = specific heat ratio

**Subscripts**

$P$ = pressure
$S$ = suction
$t$ = total
1 = throat center location

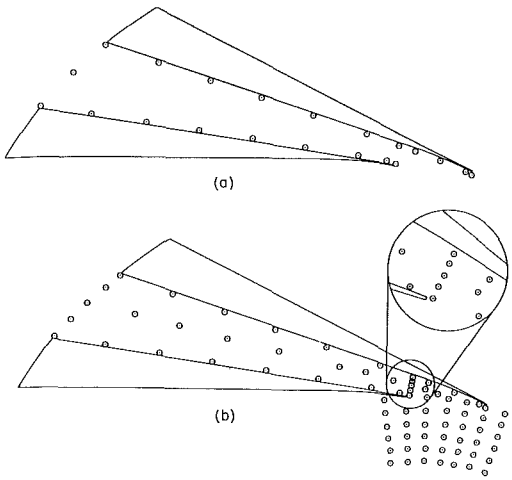


Fig. 3 Static pressure tap locations: (*a*) shroud side; (*b*) hub side

flow from a high pressure ratio centrifugal compressor impeller. After being regulated down by the control valve, the compressed air from the supply tank was used to pressurize the VTV shroud which contains a set of 72 inlet guide vanes positioned at approximately 45 degrees from the tangential direction. As the flow is forced radially inward through these guide vanes, a swirl velocity component is induced. The flow then traverses axially to the vaned diffuser test section where it swirls radially outward through the diffuser passages. A 19.1 mm (3/4 in.) thick plexiglass sheet was located on the back side (hub) of the diffuser test section to visually observe the flowfields and to provide access for the yaw and stagnation probes.

The geometry of the diffuser test section is shown in Fig. 2. The diffuser consists of 20 composites blades which have a constant thickness of 12.7 mm (1/2 in.). Other geometrical parameters for the diffuser are given in the figure. Note that the 79.5 deg angle shown in Fig. 2 is the angle between the radial direction and the mean vane camber line at the leading edge. The contours of the pressure and suction sides of a typical vane are given in Table 1 in the local $X$-$Y$ coordinate system shown in Fig. 2. All dimensions in Fig. 2 and vane surface coordinates in Table 1 have been taken from machining drawings and coordinate tables supplied by the manufacturer.

Two kinds of probes were used in these experiments: a yaw probe and a stagnation probe. The yaw probe was used to measure the flow angles while the pitot probe was used to measure stagnation pressures which, when combined with static pressure data, can be used to obtain Mach number information. The yaw probe used was a miniaturized boundary layer probe consisting of two 1.07 mm (0.042 in.) diameter tubes soldered on top of each other with their tips sheared off at opposing 45 deg angles to the plane of the probe stem. The probe tip (sensing element) was located approximately 3 mm from the stem. When the probe is exactly aligned with the flow, the pressure difference between the two tubes is zero and the yaw angle is thereby determined. The null position of the yaw probe was found in a previous experiment by placing it on the axis of a fully-developed pipe flow. The total pressure data was obtained using a standard miniaturized pitot probe, also 1.07 mm in diameter. The probes were inserted into the diffuser test section at the 11 locations shown in Fig. 2 (not all in the same diffuser channel), including two in the entry region, three across the vane leading edge location, three at the diffuser throat, and three across the diffuser exit. The yaw probe measurements were obtained first in order to get the local flow directions. After obtaining all of the flow direction data, the pitot probe was placed in the flow and set at the yaw angle for that particular location in order to obtain the local stagnation pressure. For both the yaw angle and pitot pressure data, the

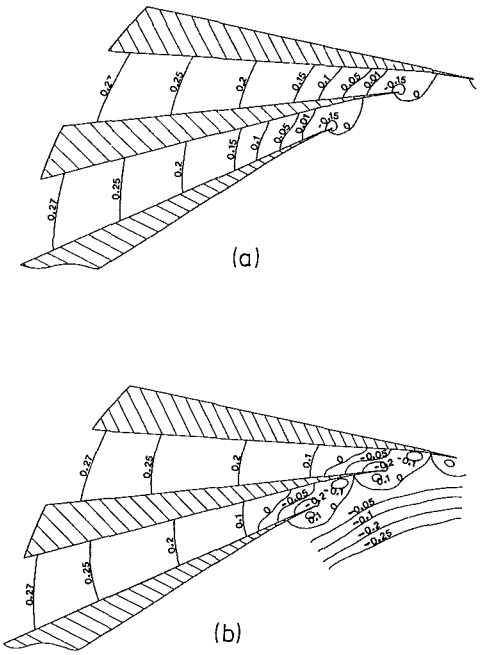


Fig. 4 Sidewall static pressure contours for the low flow rate case: (*a*) shroud side; (*b*) hub side (uncertainty in $C_p$ = ± .002)

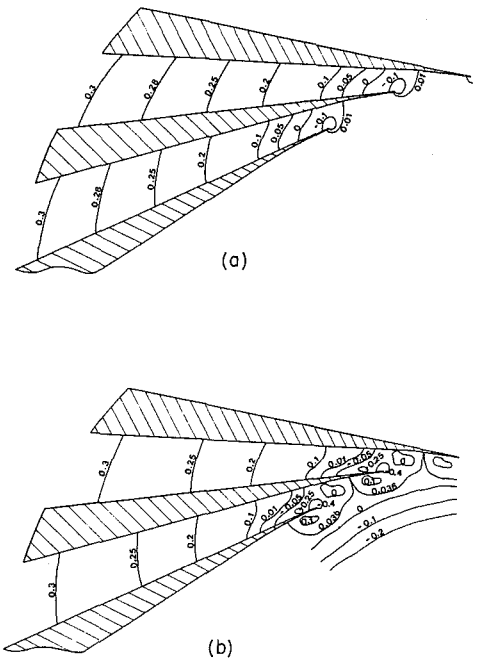


Fig. 5 Sidewall static pressure contours for the high flow rate case: (*a*) shroud side; (*b*) hub side (uncertainty same as Fig. 4)

hub-to-shroud profiles at the 11 measurement locations were obtained one at a time in different runs with plugs inserted at the other 10 locations to provide flush surfaces at the diffuser walls. THus, only a single probe was inserted in the flow at a time, with a maximum blockage of 11 percent occurring when fully inserted at the throat. For other probe locations and smaller insertion depths the blockage was much less, and no second throat was believed to be generated due to stem blockage.

Static pressure taps were placed both on the hub and shroud sides of the diffuser passage, as shown in Fig. 3, so that wall static pressure distributions along the diffuser channel could be obtained. Because the vanless space/inlet region

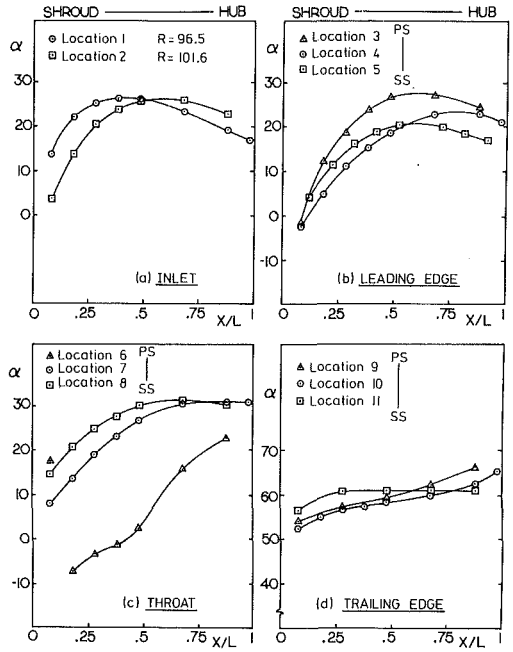


**Fig. 6 Shroud-to-hub yaw angle distributions at 11 diffuser locations for the low flow rate case: (*a*) inlet; (*b*) leading edge; (*c*) throat; (*d*) trailing edge (uncertainty in $\alpha = \pm 4°$; uncertainty in $x/L = \pm .001$)**

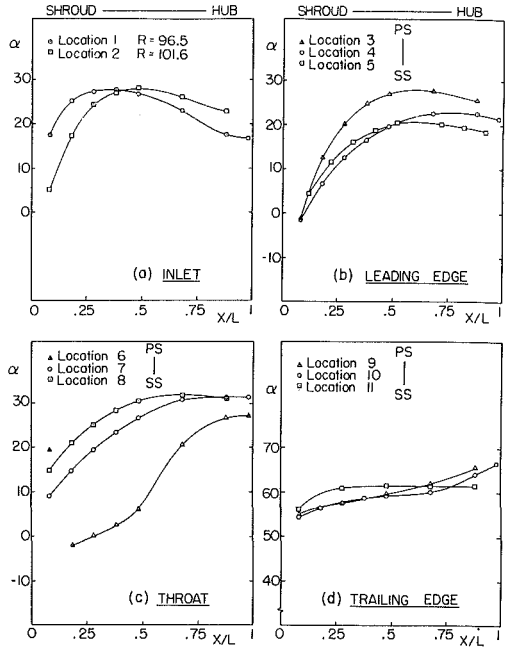


**Fig. 7 Shroud-to-hub yaw angle distributions at 11 diffuser locations for the high flow rate case: (*a*) inlet; (*b*) leading edge; (*c*) throat; (*d*) trailing edge (uncertainties same as Fig. 6)**

of the diffuser is considered to be a senstive area and plays a dominant role in dictating diffuser performance, a concentration of static pressure taps was installed in this area on the plexiglass hub plate. Altogether 80 taps were used on the hub side. Due to the design of the VTV, the shroud side of the diffuser is relatively inaccessible; in this case 21 static taps were used on the shroud side, again with a concentration of instrumentation in the inlet region.

## Experimental Results

During the course of the experimentation, two supply pressures were used for the VTV: 13.8 kPa gage (2 psig) and 34.5 kPa gage (5 psig), which resulted in measured mass flow rates of 0.226 kg/s (0.499 lbm/s) and 0.396 kg/s (0.873 lbm/s), repsectively. The blockage factor (defined as one minus the actual mass flow rate divided by the ideal mass flow rate) based on average conditions at the diffuser leading edge was only weakly dependent on flow rate level for these two experiments with $B_F = 5.8$ percent for the low flow rate and $B_F = 6.4$ percent for the high flow rate experiments. The Reynolds number, also based on average conditions and the hydraulic diameter at the leading edge, was $\mathrm{Re} = 1.1 \times 10^5$ and $\mathrm{Re} = 1.9 \times 10^5$ for these two experiments, respectively. These values for both blockage factor and Reynolds number are typical of those occurring behind impellers in modern centrifugal equipment. Both quantities have been based on leading edge values rather than the more usual throat values because of rather uncertain probe blockage effects experienced at the throat in these experiments, as will be discussed further. Due to the measured flow incidence in the inlet/leading edge region (see Figs. 6(*a*)-(*b*) and 7(*a*)-(*b*), the two operating points discussed herein are typical of those in the design point-choke range.

The first data sets obtained were the hub and shroud sidewall static pressure distributions along the diffuser channel. The static pressure contours on the shroud side and the hub side are shown in Figs. 4 and 5 for the low and high flow rate cases, respectively. The variable plotted in these figures is the coefficient of pressure,

$$C_p \equiv \frac{P - P_1}{P_{t1} - P_1} \tag{1}$$

where reference location 1 is at the center of the throat. It can be seen that the static pressure contours are much more uniform downstream from the diffuser throat than in the vane leading edge region. Near the leading edge, the fluid dynamics is extremely complicated as the flow undergoes the transition from a highly tangential jet-like swirling flow to a channel flow. The pressure gradients in this region are also fairly strong. The pressure contours for both the hub and shroud look somewhat similar especially after passing the throat. However, weak hub-to-shroud pressure gradients do exist and, in fact, persist all the way to the diffuser exit. The static pressure on the shroud side is generally slightly higher than on the hub side at the inlet station. From the hub side contours in the inlet region, Figs. 4(*b*) and 5(*b*), it can be seen that the flow is highly axisymmetric before being influenced by the vanes in the leading edge region. Furthermore, there are some pockets of local acceleration in the vane leading edge region where the static pressure is very low. From the leading edge region on downstream the flow diffuses and appears to become more and more one-dimensional in nature as the exit is approached. By comparing Figs. 4 and 5, the effect of flow rate on the shape of the static pressure contours does not appear to be strong but the higher flow rate does give a higher pressure recovery at the exit of the diffuser. Note that the shroud side isobars are necessarily less detailed than those on the hub side since less instrumentation was available on the shroud wall.

Figures 6(*a*)-(*d*) and 7(*a*)-(*d*) show the flow angle data for the low and high flow rate cases, respectively, at the various probe locations detailed in Fig. 2. At each streamwise station, i.e., inlet, leading edge, throat, and exit, data was obtained at three locations distributed from the pressure side of one vane to the suction side of the next except at the inlet station where two radial locations were used. At location 6, which is 2.54 mm (0.1 in.) away from the pressure side at the throat, the flow angle data is inconsistent with that of stations 7 and 8. This is probably due to the fact that the flow in the immediate vicinity of the leading edge of a vane is extremely sensitive to disturbances such as the presence of a probe. In essence the probe at this location increases the effective bluntness of the leading edge, resulting in local flow separation and causing the validity of the data at this location to be questionable.

For both flow rate levels, the shroud-to-hub yaw angle

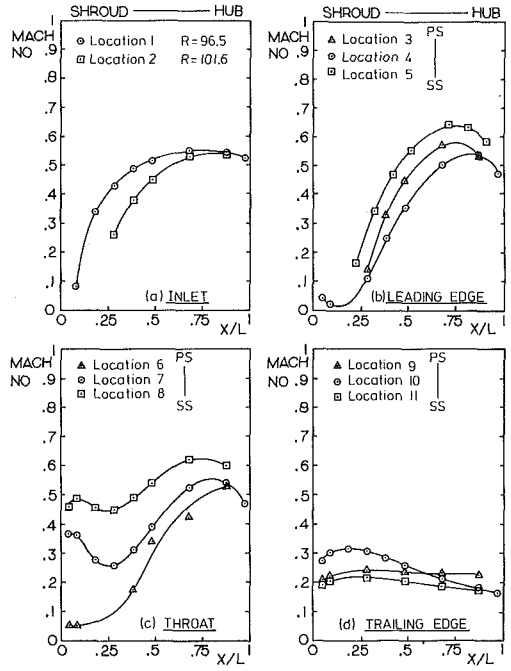


**Fig. 8 Shroud-to-hub Mach number distributions at 11 diffuser locations for the low flow rate case: (*a*) inlet; (*b*) leading edge; (*c*) throat; (*d*) trailing edge (uncertainty in $M = \pm .001$; uncertainty in $x/L = \pm .001$)**

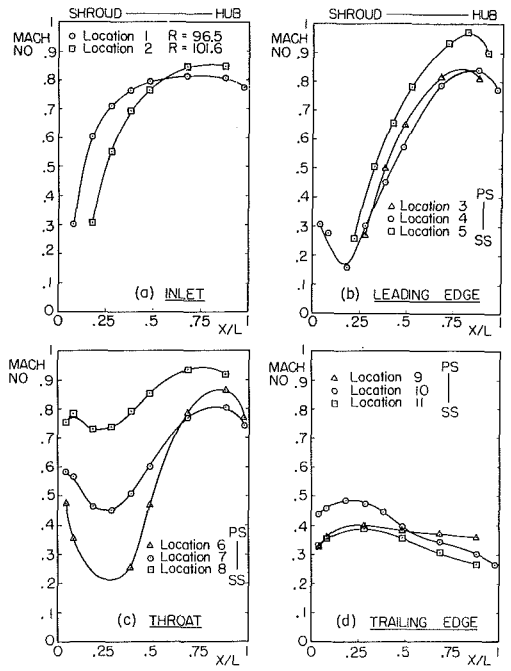


**Fig. 9 Shroud-to-hub Mach number distributions at 11 diffuser locations for the high flow rate case: (*a*) inlet; (*b*) leading edge; (*c*) throat; (*d*) trailing edge (uncertainties same as Fig. 8)**

distributions at the two inlet stations (Figs. 6(*a*) and 7(*a*)) are fairly symmetric about the channel centerline with the average value being on the order of 15 to 20 degrees. This value is typical of the flow exiting the impellers of modern high pressure ratio centrifugal compressors. At the leading edge (Figs. 6(*b*) and 7(*b*)) the flow is very nearly tangential, i.e., $\alpha \cong 0$ deg, at the shroud side with the angle increasing (and therefore the flow direction becoming more radial) near the hub side. There are fairly large differences in the flow angles between the shroud side and the hub side at this station with the difference approaching 30 degrees for both flow rates. At the throat locations (Figs. 6(*c*) and 7(*c*)) the yaw angle distributions are somewhat more uniform than at the leading edge locations although the shroud side angles are still up to 20 degrees less than the hub side angles.[1] At the diffuser exit (Figs. 6(*d*) and 7(*d*)) the distributions are fairly uniform although, surprisingly, $\alpha$ increases by 5 to 10 degrees from shroud to hub even at this location.

By comparing the yaw angle profiles for the three probe locations distributed across the leading edge, throat, and exit locations, the cross channel variations from the pressure side to the suction side can be determined. Clearly, these variations are largest at the leading edge with the maximum value being of the order of 10 degrees. As the flow traverses downstream to the throat[1] and exit, these pressure side-suction side variations decay, becoming no more than 5 degrees at the diffuser exit. Another interesting observation is that the yaw angles near the suction side of the channel (locations 5, 8, and 11) generally exceed those at the centerline (locations 4, 7, and 10), particulary for the half of the channel nearest the shroud wall.

A careful comparison of Figs. 6 and 7 shows that at the inlet station the flow angles for the high flow rate case are about 10 percent larger than those for the low flow rate, especially near the shroud side of the channel. The effect of the flow rate level on the yaw angle distributions decreases as the flow proceeds down the diffuser until, finally, there is no significant effect at the trailing edge.

[1] As previously mentioned, the data at location 6 are suspect due to possible probe blockage and separation effects.

Unlike the flow angle, differences in flow rate have a strong influence on the Mach number distributions. Obviously, the higher the flow rate, the higher the Mach number data obtained throughout the diffuser channel. As shown in Fig. 8 for the low flow rate, and especially in Fig. 9 for the high flow rate, Mach numbers in the transonic range were obtained near the hub side at the inlet and leading edge stations and across most of the channel at the throat station. Although high subsonic Mach numbers were measured, no supersonic velocities were enountered so that it is not felt that local shock waves were introduced into the flowfield by means of the probes. At the inlet (Figs. 8(*a*) and 9(*a*)) and leading edge (Figs. 8(*b*) and 9(*b*)), velocities near the shroud side are very much lower than near the hub side, and the differences are larger when the flow rate is increased. The velocity distributions at these stations increase rapidly near the shroud side becoming flat or even dropping slightly as the hub side is approached. At the throat (Figs. 8(*c*) and 9(*c*)), the Mach number distributions are more uniform than in the inlet or leading edge regions but the velocity at the shroud side is still lower than at the hub side. Again at location 6, the velocity data looks somewhat suspicious for the same reasons as mentioned in connection with the yaw angle data, particularly near the shroud side of the channel. The peak velocity always occurs near the hub side for the inlet, leading edge, and throat stations. At the trailing edge (Figs. 8(*d*) and 9(*d*)), on the other hand, the peak velocities occur near the shroud side and the Mach numbers are generally very much lower than at the other three locations due to the diffusion which occurs between the throat and exit.

Examining the pressure side-suction side cross channel variation in the Mach number distributions, it is seen that these variations are quite large at the diffuser throat, particularly for the higher flow rate. However, these large velocity differences between the pressure and suction sides of the channel are strongly damped by the time the flow reaches the diffuser exit where the Mach numbers are much lower. Another feature of the Mach number distributions evident in Figs. 8 and 9 is that the suction side velocities are higher than those near the pressure side at the leading edge and throat locations, as would be expected, and in agreement with the static pressure data.

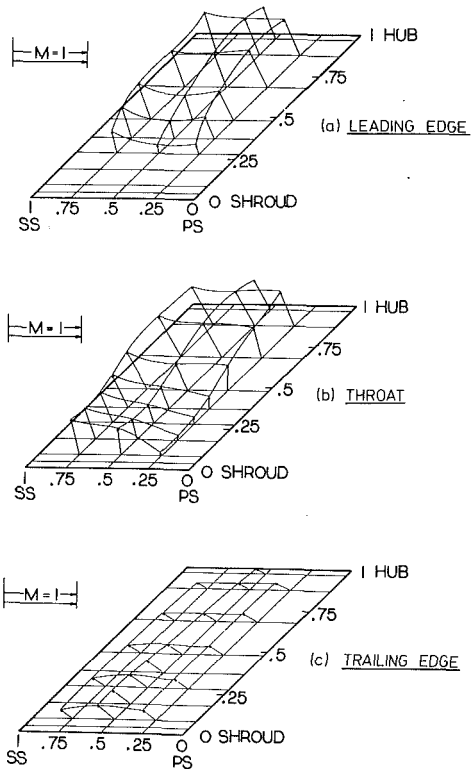


**Fig. 10 Three-dimensional Mach number surfaces for the low flow rate case: (*a*) leading edge; (*b*) throat; (*c*) trailing edge (uncertainties in M, $\alpha$, and locations same as Figs. 6 and 8)**

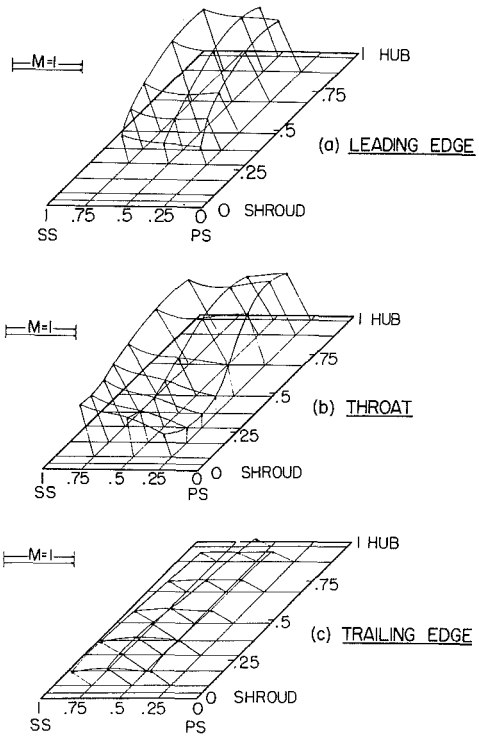


**Fig. 11 Three-dimensional Mach number surfaces for the high flow rate case: (*a*) leading edge; (*b*) throat; (*c*) trailing edge (uncertainties in M, $\alpha$, and locations same as Figs. 6 and 8)**

By comparing the low flow rate data of Fig. 8 and the high flow rate data of Fig. 9, it is also apparent that although the Mach number magnitudes are clearly affected by the flow rate level, the shapes of the Mach number profiles are relatively independent of flow rate.

The preceding yaw angle and Mach number data for the low and high flow rate cases have been combined in the three-dimensional diagrams shown in Figs. 10 and 11, respectively. These figures provide a graphical representation of the velocity data across the entire leading edge, throat, and trailing edge cross-sections. The length of each arrow is proportional to the magnitude of the local Mach number while its angle of inclination from vertical is equal to the local yaw angle (positive counterclockwise). This figure shows the variations of the flow from both hub-to-shroud and pressure side-to-suction side and can be used to re-emphasize the trends noted earlier in connection with Figs. 6–9. For both flow rates it is clearly seen that the velocity decreases more rapidly from the suction side to the pressure side near the shroud than near the hub at the leading edge and throat stations. At the throat there is a low velocity region at about a quarter of the way from the shroud side to the hub side which is particularly pronounced near the pressure surface of a vane. It is also clearly seen that the yaw angle at the trailing edge is much more radial (the arrows are far away from vertical) and that the flow is much more uniform than at the other two stations. Comparing Figs. 10 and 11, the major effect of increasing the flow rate is simply an increase in the Mach number mangitude while the shapes of the profiles are relatively unchanged.

Although the detailed measurements of Krain [11] behind an actual impeller were carried out only across a plane in the quasi-vaneless region and across the diffuser throat plane and those of Jansen and Rautenberg [13] immediately in front of and immediately behind the vane row, many similarities to the present experimental results are evident. The wall static pressure contours presented in Figs. 4 and 5 are quite similar to those reported in references [11 and 13]. In addition, the large shroud-to-hub increases in the yaw angle shown in Figs. 6 and 7 are also characteristic of the flow angle measurements of Krain [11] and Jansen and Rautenberg [13]. The low velocity region apparent near the pressure-shroud side corner at the leading edge and throat in Figs. 10 and 11 is also typical of the flow exiting an actual impeller [11, 13]. The magnitude of this velocity defect is somewhat more pronounced in the present VTV experiments although, as previously discussed, this may be partially due to probe blockage effects.

Future work planned for the static diffuser test rig includes the application of boundary layer suction and/or blowing near the diffuser inlet so that the effects of inlet velocity profile shape on the diffuser performance and flowfields can be determined. In addition, the use of a non-intrusive laser doppler velocimeter (LDV) system to further investigate the mean flowfields and to provide information on fluctuating and turbulence effects is a logical extension of the present work.

## Conclusions

The following conclusions may be drawn from this experimental investigation of flow in a vaned radial diffuser supplied by a vortex test vehicle:

(1) The hub and shroud sidewall static pressure contours are much more uniform downstream from the diffuser throat than in the vane leading edge region.

(2) The flow is highly axisymmetric in the diffuser inlet region which corresponds to the vaneless space in an actual machine. The fluid dynamics in the leading edge region is complicated as the flow transitions from an axisymmetric jet flow to a two-dimensional channel flow and the pressure gradients are fairly strong here. Also there are some pockets of local acceleration in this region.

(3) The flow rate level has little effect on the shape of the static pressure contours, the yaw angle profiles, and the Mach number distributions.

(4) For the yaw angle and Mach number measurements, the size of the probe is a major concern in obtaining reliable data.

(5) The VTV produces a fairly symmetrical flow angle

distribution in the inlet region. At the leading edge large shroud-to-hub differences in $\alpha$ exist, although the yaw angle distributions become more and more uniform as the flow proceeds from the vane leading edge to the diffuser exit.

(6) Flow angles near the suction side of the channel are generally slightly higher than at the centerline at all locations, especially near the shroud side.

(7) The Mach number distributions also become more uniform as the flow passes through the diffuser channel from the leading to trailing edge. In addition, Mach numbers in the transonic range have been obtained at the high flow rate condition investigated.

(8) The velocity near the suction side of the channel is generally higher than near the pressure side, and the region of higher velocity moves from the hub side to the shroud side as the flow travels downstream.

## Acknowledgments

The authors would like to thank the Garrett Turbine Engine Company for its donation of the static diffuser test rig and the Texas A&M University Turbomachinery Research Consortium for financial support of this research.

## References

1 Faulders, C. R., "Aerodynamic Design of Vaned Diffusers for Centrifugal Compressors," ASME Paper No. 56-A-213, July 1956.

2 Giraud, F. L., and Platzer, J., "Theoretical and Experimental Investigations on Supersonic Free Vortex Flow," Gas Turbine Laboratory, Massachusetts Institute of Technology, Report No. 36, Apr. 1954.

3 Baghdadi, S., "Study of Vaned Radial Diffusers Using Swirling Transonic Flow Produced by a Vortex Nozzle," Ph.D. thesis, School of Mechanical Engineering, Purdue University, Dec. 1973.

4 Baghdadi, S., and McDonald, A. T., "Performance of Three Vaned Radial Diffusers with Swirling Transonic Flow," ASME JOURNAL OF FLUIDS ENGINEERING, Vol. 97, No. 2, June 1975, pp. 155–173.

5 Baghdadi, S., "The Effect of Rotor Blade Wakes on Centrifugal Compressor Diffuser Performance," ASME JOURNAL OF FLUIDS ENGINEERING, Vol. 99, No. 1, Mar. 1977, pp. 45–52.

6 Russo, C. J., and Blair, L. W., "Effect of Size and Reynolds' Number on Centrifugal Diffuser Performance," ASME Paper No. 81-GT-8, 1981.

7 Dean, R. C., Jr., and Young, L. R., "The Fluid Dynamic Design of Advanced Centrifugal Compressors," Creare Technical Note TN-244, Creare Technical Information Service, Hanover, New Hampshire, Aug. 1976.

8 Verdonk, G., "Vaned Diffuser Inlet Flow Conditions for a High Pressure Ratio Centrifugal Compressor," ASME Paper No. 78-GT-50, Apr. 1978.

9 Yoshinaga, Y., Gyobu, I., Mishina, H., Koseki, F., and Nishida, H., "Aerodynamic Performance of a Centrifugal Compressor with Vaned Diffusers," ASME JOURNAL OF FLUIDS ENGINEERING, Vol. 102, No. 4, Dec. 1980, pp. 486–493.

10 Rayan, M. A., and Yang, T. T., "An Investigation of Vane-Island Diffusers at High Swirl," ASME Paper No. 80-GT-148, Mar. 1980.

11 Krain, H., "A Study on Centrifugal Impeller and Diffuser Flow," ASME Paper No. 81-GT-9, Mar. 1981.

12 Rodgers, C., "The Performance of Centrifugal Compressor Channel Diffusers," ASME Paper No. 82-GT-10, Mar. 1982.

13 Jansen, M., and Rautenberg, M., "Design and Investigations of a Three Dimensionally Twisted Diffuser for Centrifugal Compressors, ASME Paper No. 82-GT-102, Mar. 1982.

14 Bammert, K., Jansen, M., and Rautenberg, M., "On the Influence of the Diffuser Inlet Shape on the Performance of a Centrifugal Compressor Stage," ASME Paper No. 83-GT-9, June 1983.

# A New Diffuser Mapping Technique

## Part 1: Studies in Component Performance

**D. Japikse**
Concepts ETI, Inc.,
Norwich, Vt.

*A rigorous derivation of the $K = Cp_i - Cp$ diffuser recovery and loss equation is presented and the critical assumptions to yield this simplified relationship are critiqued. Qualified confirmation of the equation is achieved using precise laboratory data. A new diffuser loss-map is presented which facilitates engineering diffuser design work, even when a recovery map is unavailable. Numerous application examples for turbomachinery analysis are given including the application to a turbomachinery cascade with strong turning.*

### Introduction

The relationship between the static pressure recovery and the total pressure loss of a diffuser has been of considerable interest to users and designers of all classes of diffusers, particularly turbomachinery design and development engineers. Although several references have been published suggesting methods to compute the total pressure loss of a diffuser, a simple technique has not been widely accepted. Based on the author's formal teaching in the turbomachinery field over the past several years, it has become clear that very few engineers are aware of the possible, and surprisingly simple, relationship between total pressure loss and static pressure recovery given by the following equation:

$$K = Cp_i - Cp \tag{1}$$

This relationship between the total pressure loss coefficient ($K$) and the ideal ($Cp_i$) and actual ($Cp$) pressure recovery of a diffuser is rarely used by engineers, although a few[1] are aware of the suggested validity and occasionally apply it. The only formal presentations of this relationship, currently known, are the extensive use made of it in the BHRA Reference "Internal Flow Systems" (Miller, 1978), a simplified derivation by Kline et al. (1959), and a similar derivation by several English authors (for example Stevens, 1970, page 5) which introduced velocity profile terms into a form of equation (1). The latter work seems to have stopped when profile or distortion parameters proved to have marginal practical value and the utility of equation (1) did not emerge from this earlier work. In Miller (1978), it is stated (without detailed derivation) that one can describe diffusers either in terms of static pressure recovery or in terms of a total pressure loss coefficient and readily relate between the two options with equation (1) given above. In spite of the extensive use of this concept in Miller (1978), the idea has not progressed very far beyond this single reference.

In this paper, we present a complete derivation of equation (1), explain the approximation required to get equation (1), test the validity of the concept against experimental data, and then demonstrate the development of an alternative diffuser mapping technique. In addition, numerous examples are given of the resultant map and its use in turbomachinery engineering.

**Fundamental Derivation.** The derivation is started by working with the definition of total pressure loss coefficient and the static pressure recovery coefficient. These must be carefully defined using mass average parameters. The mass average parameters are employed so that these coefficients will serve their traditional and important function of realistically relating the energy transport between two stations in a flow element. This is essential for correct state-point calculations in turbomachinery. Beginning then with a definition of total pressure loss coefficient one can manipulate the various terms to the point where one can introduce the static pressure recovery coefficient with certain remaining residual terms (incompressible case).

$$K = \frac{(\overline{p_{01}} - \overline{p_{02}})}{(\overline{p_{01}} - \overline{p_1})} \tag{2}$$

where $\overline{p_{01}}$ and $\overline{p_{02}}$ must be evaluated from mass averaged values:

$$\overline{p_{01}} = \frac{1}{m}\int_m \left(p_1 + \frac{1}{2}\rho C_1^2\right) dm \tag{3}$$

$$\frac{m\overline{p_{01}}}{\rho} = \int_m p_1 d(C_1 A) + \int_m \frac{1}{2}\rho C_1^2 d(C_1 A)$$

$$= \bar{p}_1 C_1 A_1 \Big]_m + \frac{1}{2}\rho\left[\int C_1^3 dA + \int A C_1^2 dC_1\right] \tag{4}$$

($\bar{p}_1$ is defined by the mean value theorem)

[1] Of 350 practicing turbomachinery engineers at Concepts courses in the U.S. and Europe, only 3 or 4 were aware of equation (1).

Contributed by the Fluids Engineering Division of The American Society of Mechanical Engineers and presented at the 29th International Gas Turbine Conference and Exhibit, Amsterdam, The Netherlands, June 4-7, 1984. Manuscript received by the Fluids Engineering Division, September 24, 1984. Paper No. 84-GT-237.

where:

$$\int AC^2 dC = \int \left\{ \frac{d(A\ C^3)}{3} - \frac{C^3}{3}\, dA \right\} = \frac{1}{3} A\ C^3 \Big]_A - \int_A \frac{C^3}{3}\, dA \tag{5}$$

The first term on the right-hand side in equation (5) is zero by evaluation at its limits of integration. This follows since $C = 0$ at the walls for a channel or annular diffuser. $C$ is also zero at the wall for a conical diffuser but not at the centerline; the term is still zero for a conical diffuser since $A = \pi r^2 = 0$ at the centerline ($r = 0$). Substituting equation (5) into (4) we get:

$$\bar{p}_{01} = \frac{\rho C A \bar{p}_1}{m} \Big]_m + \frac{\rho}{m} \frac{\rho}{3} \int_{A_1} C^3 dA = \bar{p}_1 + \frac{\rho^2}{3m} \int_{A_1} C^3 dA \tag{6}$$

and similarly for $p_{02}$, thus using equation (6) with equation (2):

$$K = \frac{\int_1 C_1^3 dA_1 - \int_2 C_2^3 dA_2}{\int_2 C_1^3 dA_1} - Cp \tag{7}$$

we can simplify equation (7) by noting that:

$$(\overline{C^2}) = \frac{1}{m} \int_m C^2 dm = \frac{\rho}{m} \int_A C^3 dA \tag{8}$$

hence equation (7) becomes:

$$K = \frac{\overline{C_1^2} - \overline{C_2^2}}{\overline{C_1^2}} - C_p \tag{9}$$

In fact, relationship (9) cannot be completely reduced to simple terms and equation (1) above does not result directly. At this point, followers of the historical approach have not paid attention to the proper averaging implied by the mass average definitions. The conservation-of-mass relationship has been (incorrectly) introduced into equation (9) to obtain equation (1) above. It should be perfectly clear that the use of the continuity equation places a strong limitation on the basic derivation. We can simplify the relationship equation (9) between total pressure loss and static pressure recovery only when the following condition is met:

$$(\bar{C}_2)^2 = \overline{C_2^2} \text{ and } (\bar{C}_1)^2 = \overline{C_1^2} \tag{10}$$

If and only if these conditions are met, can we then simplify the derived equation (9) to the equation (1) form:

$$K = Cp_i - Cp \text{ where } Cp_i = 1 - 1/AR^2 \tag{11}$$

This equation is not generally applicable but applies only when the mass average of the inlet velocity squared is equal to the square of the mass average inlet velocity and the same at the exit.

Thus the limited historical use of the simple, equation (1), relationship between total pressure loss and static pressure recovery of a diffuser is applicable only when very simple flow fields exist and the averaging principle can be accepted. In fact, this averaging relationship, shown by equation (10), will presumably apply only if the flow is perfectly uniform at inlet and outlet or the profiles are similar. Other forms of distribution will depart from this simple averaging relationship which would invalidate, in strict terms, the applicability of equation (1). Thus under conditions where the flows are tending to be quite uniform both at inlet and outlet, one might anticipate the equation to have fair validity, but as the flow becomes more and more distorted one would expect less satisfactory agreement. The latter is the real case for practical diffusers. From an engineering standpoint, it is always interesting to see how far the real world forces departure from ideal conditions. Thus equation (1) *can be accepted as a possible reference, albeit perhaps an ideal reference*, which should be tested with actual data from both the laboratory and real machine experience. This is the objective of subsequent portions of the paper.

**Evaluation With Laboratory Diffusers.** In order to test the validity of equation (1), the data from several laboratory diffusers was carefully integrated to establish the required mass average parameters. Fortunately, conical diffuser and annular diffuser data of various geometric configurations was available. After integrating the traverses at the diffuser exit and using similar data at the diffuser inlet, it was possible to evaluate both the inlet and the outlet average conditions including, particularly, the exit mass average total pressure. These data were then used to compute the loss coefficient and the pressure recovery coefficient. The ideal pressure recovery coefficient was, of course, known from the basic geometry. Examples of three different conical diffusers are shown in Fig. 1.[2] Data from three different geometries (Area Ratio = 2.5, 3.5, and 5.0 all with $2\theta = 5.8$ deg) are given. These include many cases tested at different levels of fluid dynamic blockage and at different levels of Mach number. The flags or tick

[2] Figures 1, 2, and 6 were first published by the author in "Anon" (1979) using data from Goebel and Patel (1976), Japikse (1977), and Wood and Henry (1958). Only Wood and Henry (1958) gave $K$ and $Cp$ data; this author, assisted by Mr. T. W. Carney, integrated all the available traverse data from Goebel and Patel (1976) and Japikse (1977) in order to get $K$ values which were not heretofore available. All traverses which satisfied conservation of mass (compared to an orifice measurement) to within about 5 percent are believed to be included herein. Whenever a traverse failed to pass the correct mass flow, the case was rejected. For Goebel and Patel (1976), 29 out of 32 test cases were included when the "Anon" (1979) study was prepared.

## Nomenclature

$A$ = area
$AR$ = area ratio = $A_2/A_1$
$b$ = passage width
$B$ = fluid dynamic blockage = $(1 - A_{flow}/A_{geometric})$
$C$ = velocity
$C_m$ = meridional component of velocity
$C_\theta$ = tangential component of velocity
$Cp$ = pressure recovery coefficient $= (\bar{p}_2 - \bar{p}_1)/(\bar{p}_{01} - \bar{p}_1)$
$Cp_i$ = ideal pressure recovery
$D$ = inlet diameter
$K$ = loss coefficient $= (\bar{p}_{01} - \bar{p}_{02})/(\bar{p}_{01} - \bar{p}_1)$
$k$ = ratio of specific heats $c_p/c_v$
$L$ = diffuser length
M = Mach number
$p$ = static pressure
$p_0$ = total pressure
$pr$ = pressure ratio for a compressor stage
$r$ = radius
Re = Reynolds number
$SC$ = swirl coefficient = $r_2 C_{\theta 2}/r_1 C_{\theta 1}$
$W$ = diffuser throat width
$X$ = inlet length
$\alpha$ = swirl angle
$\epsilon^*$ = boundary layer displacement thickness
$\eta$ = stage efficiency
$\eta_D$ = diffuser effectiveness
$2\theta$ = channel or conical diffuser total divergence angle
$\lambda$ = $C_\theta/C_m$
$\rho$ = density

**Subscripts**

1 = inlet
2 = outlet

**Superscripts**

( $\bar{}$ ) = mass average value

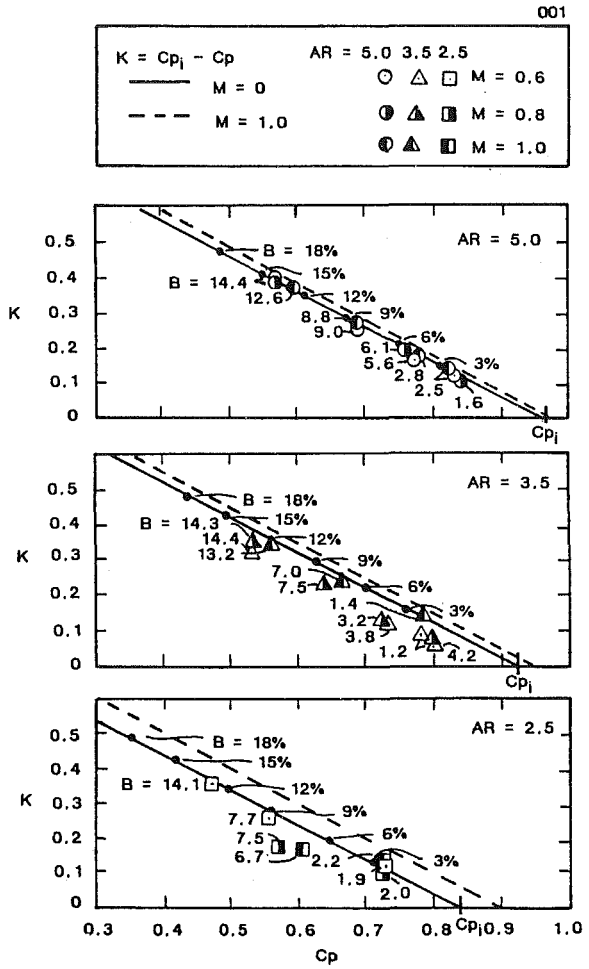


**Fig. 1 Examples of mass averaged loss (*K*) data versus pressure recovery (*Cp*) for three different conical diffusers with $2\theta = 5.8$ deg and various inlet tube lengths. "Anon" (1979)**

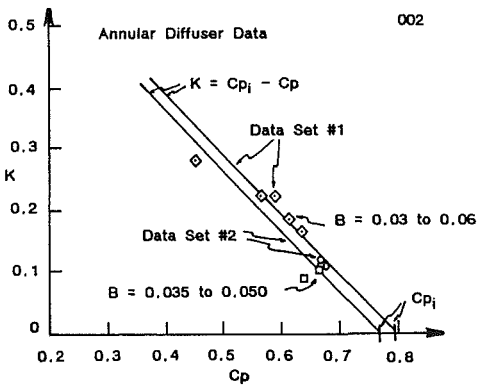


**Fig. 2 Examples of mass averaged loss (*K*) data versus pressure recovery (*Cp*) for two different axial annular diffusers, various divergence angles. "Anon" (1979)**

marks labeling blockage level on Fig. 1 are used later in this paper. It can be observed that all the data follows the basic trend of equation (1) quite reasonably. Indeed, there seems to be no particular departure from the trend either at low fluid dynamic blockage or high fluid dynamic blockage, or with Mach number, or with the area ratio. A second example is given in Fig. 2 where data from several different annular diffusers is displayed. Again, acceptably good agreement between theory and data is shown. Of course, some departures from the actual trend are in evidence, which would be expected based on the critical analysis of the fundamental derivation above.

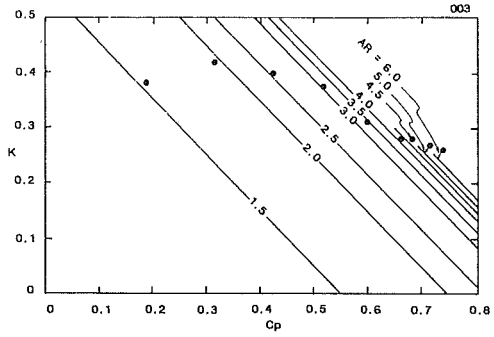


**Fig. 3 Loss-map using data of Yahya and Gupta (1975) for a radial annular diffuser**

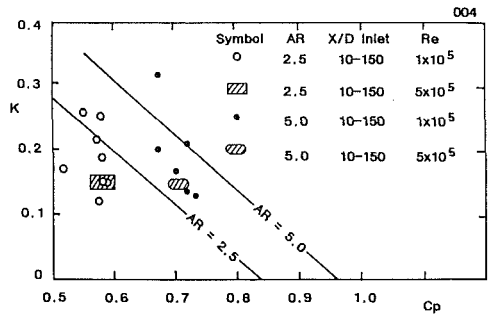


**Fig. 4 Loss-map using data of Sharan (1976) for varying inlet conditions (conical)**

A further example of *K* versus *Cp* data for a radial flow annular diffuser has been prepared, see Fig. 3, using the data of Yahya and Gupta (1975) and rather close agreement has again been found. *K* versus *Cp* data are given in Fig. 4 for conical diffusers (Sharan, 1976) of different inlet lengths and hence different inlet blockages and different inlet turbulent shear stress distributions. This data falls within ± 0.1 of the reference line (Fig. 4) but shows some scatter. The results are quite different when the Reynolds number is raised from $10^5$ to $5.0 \times 10^5$.

## Diffuser Performance Mapping

For several decades, the recovery map (Reneau et al., 1966), as shown for example in Fig. 5, has received very wide attention for mapping the basic performance characteristics of any particular class of diffusers. This map is an extremely important tool for diffuser and turbomachinery design and it is not supplanted by anything presented in this paper. However, the historical recovery map does not show any information concerning the total pressure loss of the diffuser used. In addition, it is necessary to have separate maps for each level of fluid dynamic blockage. As an alternative, equation (1) can be used to inspire a supplementary diffuser map. Figure 1 shows actual blockage values labeled and general blockage levels marked by ticks. These ticks marks are good to about ± 1.5 percent blockage compared to the actual points (experimental accuracy on *B* was ± 0.6 percent). Figure 6 shows a composite of the individual characteristics, with contours of the fluid dynamic blockage sketched on from the Fig. [1][3] tick marks.

[3] Actual test Mach numbers deviated slightly from those shown on Fig. 1. The range of values is as follows:

| Nominal M | Established with a centerline static pressure tube | Established with a wall pressure tap |
|---|---|---|
| 0.6 | 0.58 to 0.61 | 0.58–0.60 |
| 0.8 | 0.77 to 0.81 | 0.76–0.84 |
| 1.0 | 1.0 | 0.91–1.0 |

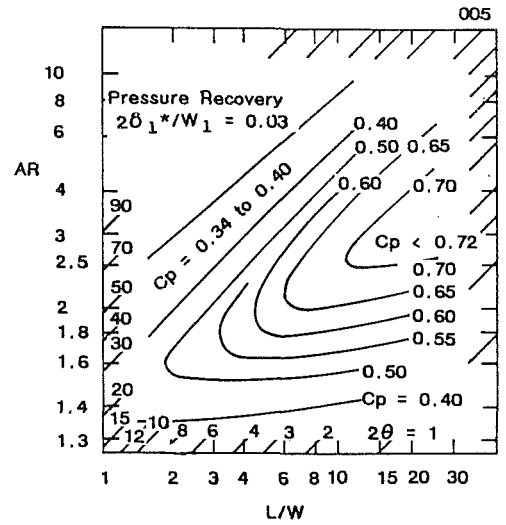


Fig. 5 Recovery map of pressure recovery coefficient (*Cp*) as a function of *AR*, *L/W* for a given inlet blockage (0.03) (Reneau et al., 1966)

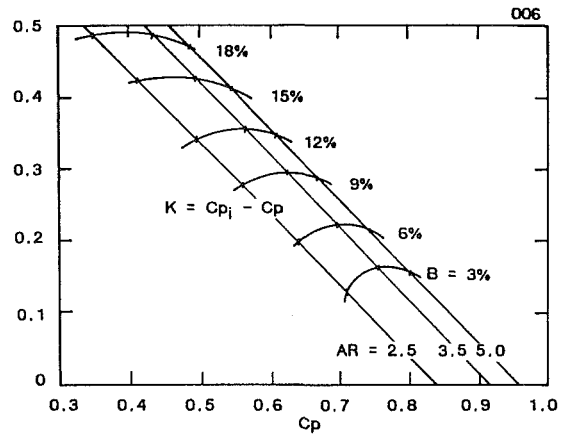


Fig. 6 Incompressible loss-map showing *K* versus *Cp* with constant aerodynamic blockage lines added (based on Fig. 1 data) for a series of conical diffusers with $2\theta = 5.8$ deg

Hence, this is a map based on equation (1), confirmed by laboratory data, and extended to include fluid dynamic blockage based on the measured experimental results.

A second characteristic of this mapping is shown in Fig. 7 where additional ideas are introduced. By utilizing the definition of diffuser effectiveness (the ratio between actual pressure recovery and ideal pressure recovery), we can put lines of constant effectiveness on the new diffuser map. The vertical axis has an effectiveness of zero and the horizontal axis has an effectiveness of unity. The various rays emanating from the origin of the map show different levels of diffuser effectiveness. This form of mapping shows the static pressure recovery of a diffuser, the total pressure loss coefficient of a diffuser, the diffuser effectiveness, and the level of fluid dynamic blockage associated with the particular diffuser. The map can be created simply from the basic equation (1) principle. However, equation (1) is not precisely correct and the maps should be modified slightly to reflect measured data when available. Alternatively, the map can be based solely upon equation (1) with a limited amount of (expensive) test data added to guide users in the proper interpretation and correction of levels inspired by equation (1).

Both the recovery map and the loss-map are to be used together. For example, if a designer is concerned with a particular diffuser application, he would estimate the expected pressure recovery coefficient from the recovery map using the details of the diffuser geometry, including area ratio and *L/W*

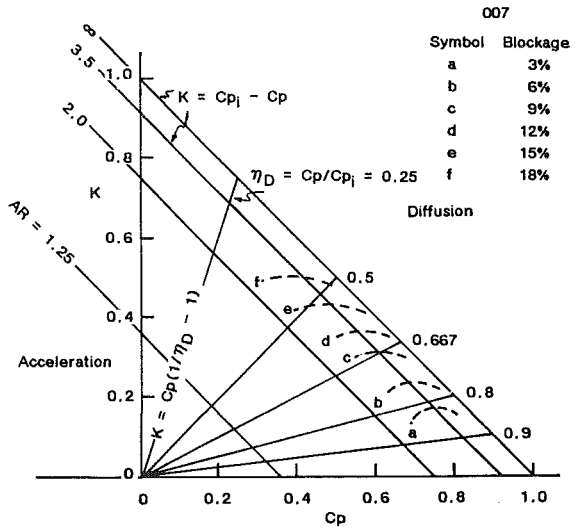


Fig. 7 Loss-map as per Fig. 6 but with lines of constant effectiveness added

or $2\theta$ and blockage. After obtaining the chosen values of *AR* and *Cp*, the designer can then enter the loss-map, Fig. 7, and establish a very reasonable estimate of diffuser loss and effectiveness.

In other instances, an engineer may very well work with the loss-map directly without consulting the recovery map, but in an approximate engineering fashion. In many instances, it is necessary to deal with diffusers which have highly distorted inlet conditions, unknown levels of inlet fluid dynamic blockage, and geometric departures from the simple diffuser forms for which the recovery type diffuser maps are available. In this case, an engineer can make a first estimate of the probable performance by consulting the appropriate loss-map. Given the area ratio of the diffuser and a reasonable estimate of diffuser effectiveness (based on familiarity with numerous other diffusers), one can then anticipate approximately what level of loss is to be expected and what the equivalent laboratory inlet fluid dynamic blockage might be. This of course is approximate and requires a meaningful estimate or guess as to the level of diffuser effectiveness. However, this is the first parameter available to an applied engineer for reasonable estimating. For example, it is well known that a sudden expansion of area ratio 2 (the Borda-Carnot problem) has a diffuser effectiveness of 0.667. High performance channel diffusers usually have an effectiveness in the range of 0.75 to 0.85. Conical diffusers with stabilizing inlet swirl may reach effectivenesses on the order of 0.95. Hence an engineer can ballpark the effectiveness level approximately and then obtain an estimate of the expected pressure recovery and loss coefficient using total pressure loss-mapping techniques. To be sure, approximate usage of this type should be avoided whenever possible but many engineering problems must be solved when detailed data and computational methods are not available.

**Loss-Map Utilization.** Several examples can be made of the usage of the loss-map technique in turbomachinery stage evaluation. The particular examples are taken from centrifugal compressors and radial inflow turbines since this is an area receiving much of the author's immediate attention. To be sure, similar exercises can be developed for axial flow staging as well.

The first example applies to the vaneless diffuser portion of a centrifugal compressor stage. All the data shown were processed by the author, using the same methods as implemented above, for the available data from Eckardt for his vaneless diffuser, see Fig. 8. It will be observed that the pressure recovery and total pressure loss data follow the equation (1) to better than ± 0.1 on *K* and *Cp*.

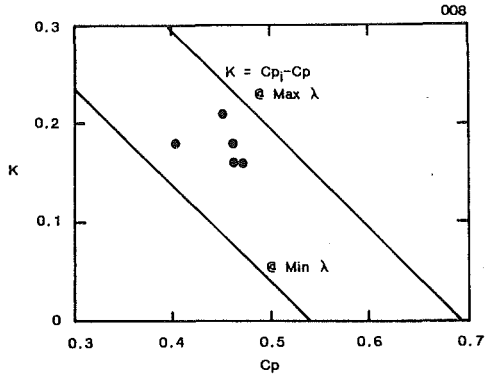


Fig. 8 Loss-map for Eckardt's compressor data. $Cp_i$ computed according to Appendix I.

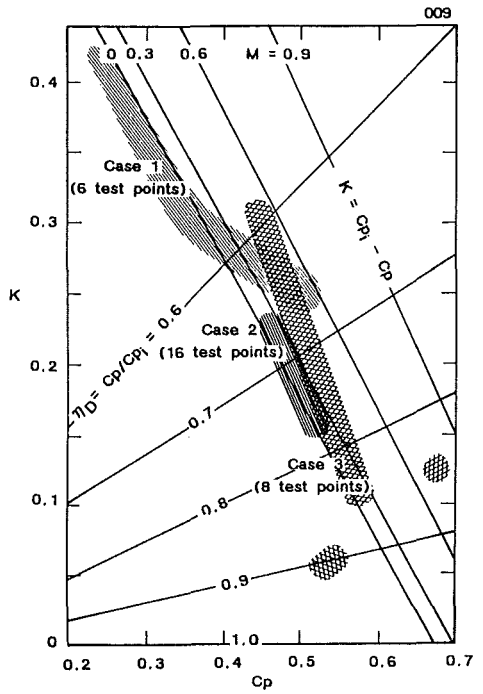


Fig. 9 Loss-map for the vaneless diffuser study (Creare Consortium, Japikse and Osborne, 1982)

A second example is shown for a series of vaneless diffusers tested at Creare Incorporated for the Return Channel and Vaneless Diffuser Consortium, Japikse and Osborne (1982). The basic measured data and the loss-map format are shown in Fig. 9. However, in this particular case, we have a slightly different representation of the lines of $K$ versus $Cp$. This is due to the compressibility[4] of the medium which shows up in the fundamental derivation (see Appendix I). As a result, we obtain the relationship given below:

$$K = \left(1 - \frac{\bar{\rho}_1/\bar{\rho}_2}{AR^2}\right) - Cp$$

In this form, we can appreciate that the Mach number becomes a mild variable and can be portrayed in the fundamental mapping. We also observe that all measured data fall within the Mach range applicable to the actual data sets.

In addition, the same principle was used for the return channel cascade portion which followed the diffuser. An example is shown in Fig. 10 and it can be observed that the same basic characteristics illustrated before in Figs. 1, 2, 8, and 9 are

[4]The same compressibility effect was included in Fig. 1 as a dashed line. It was not emphasized before in order to stress the essential issues and since the effects were comparatively smaller.

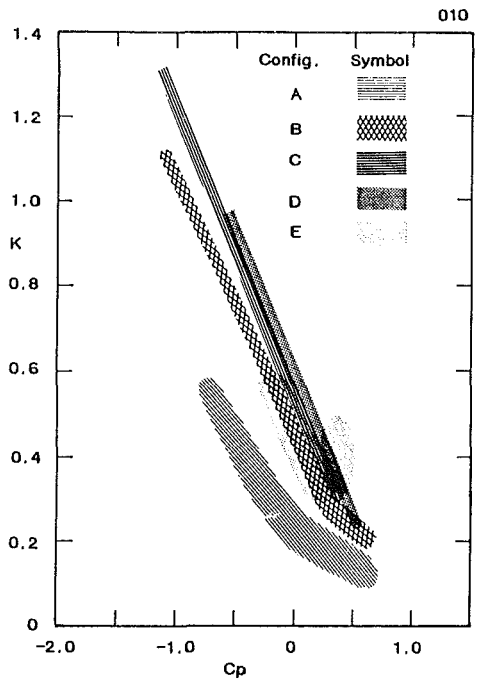


Fig. 10 Loss-map for return channel cascade (Creare Consortium, Japikse and Osborne, 1982)

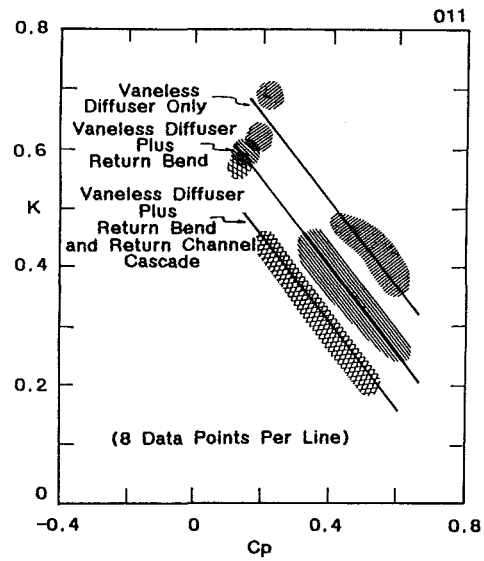


Fig. 11 Loss-map for vaneless diffuser, return bend and return channel (Creare Consortium, Japikse and Osborne, 1982)

again revealed in this particular case. In this instance, we have no particular reason to insist on the utilization of this loss-map procedure since we are dealing with an airfoil cascade which, in some modes, behaves in an overall sense as a diffuser and in other instances the flow actually accelerates to get through it. Thus Fig. 10 is actually an off-design point representation of the performance of an entire cascade in terms of the important parameters, $Cp$ and $K$. It is clear that all of these sets of data measured perform as though they follow the basic equation (1) relationship, even though we have not yet established a method for computing the $Cp_i$ value! The preparation of Fig. 10 was simply done as an exercise to test the overall validity of the approach and to see how far it might be used in turbomachinery cascade work.

An additional example to test the overall validity of the loss-map procedure is shown in Fig. 11 where the overall

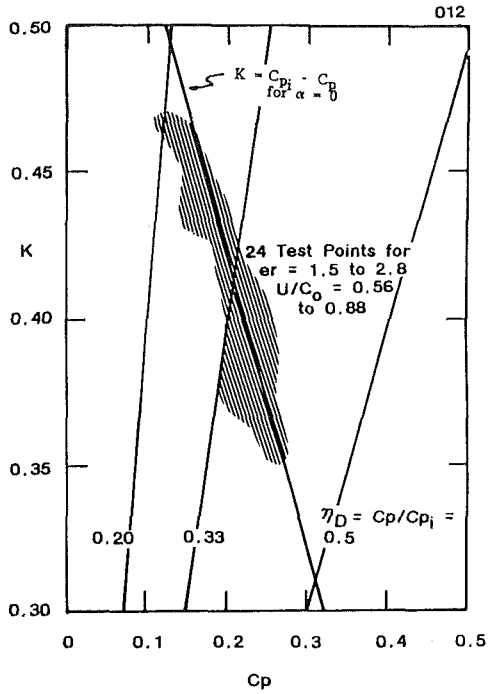


*Fig. 12* **Loss-map for radial turbine exhaust diffuser (Creare Consortium, Japikse, 1982)**

characteristics of the vaneless diffuser, return bend, and return channel referred to above are now included in a single value of *Cp* and *K* for the entire system. These results are revealed in Fig. 11 and again the basic loss-map procedure provides a useful method of representing the data. The extent to which this mapping procedure applies is somewhat surprising and suggests that it could probably be refined and implemented even further for future cascade studies.

A final example is given in Fig. 12 where the diffuser performance of an exhaust diffuser operating behind a radial turbine is illustrated (Japikse, 1982). Similar methods could be used for a diffuser operating behind an axial turbine. In this case, we see comparatively low values of pressure recovery and high values for diffuser loss. The diffuser is operating with a highly distorted inlet flow, sometimes including backflow. We can immediately appreciate that the diffuser effectiveness ranges between 0.2 and 0.4, the lowest values ever experienced by this author in turbomachinery work. It is clear that this diffuser does not perform well when compared against all other classes of common conical, channel and annular diffusers. The problem has been associated with a severely distorted inflow condition.

## Usage and Accuracy

As a basic rule, the experimental data employed in the preceding tests[5] have been accurate to approximately ± 0.03 on both *Cp* and *K*. Conceivably, a few points (5 percent of the data or less) would fall in a looser band of accuracy but still within ± 0.06 on both *Cp* and *K*. Integrated traverse data has been used herein whenever the integration yields mass flow agreement to within about ± 5 percent or when a physically sensible data correction can be made.

The fundamental question which led to the entire concept of the diffuser loss-map was to question the accuracy of equation (1). It can therefore be seen that the equation is surprisingly accurate even with various inlet conditions and significant nonuniformities. Surprisingly, all cases considered by the

[5] The estimated cost of the test programs which yielded the detailed, and comparatively rare, traverse data is in excess of $500,000.

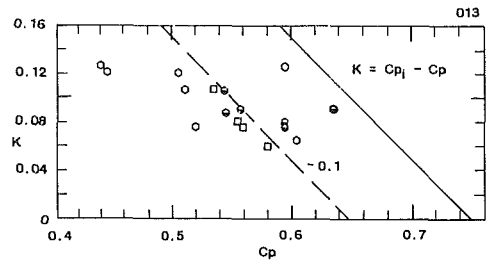


**Fig. 13 Loss-map for two straight center-body annular diffusers (*AR* = 2) plotted with data from Stevens and Williams (1980). Note important deviation of data from equation (1), with points outside the ± 0.1 band.**

author show good agreement with the basic equation (1) relationship or errors that are almost always less than ± 0.1 on either *K* or *Cp* from the reference line, equation (1). More extreme deviations are evident in Fig. 13. Figure 13 was replotted from the data of Stevens and Williams (1980) which reveals lower losses than would be anticipated by the equation (1) principle. In this case significant alterations have been made to diffuser performance. The author has recently learned that this data may not be as accurate as the tolerances given in the preceding paragraph.

At least 95 percent of the author's measured *K* versus *Cp* data fall within ± 0.05 of the equatoin (1) line, but some points miss by as much as ± 0.1. If special effects (vorticity, turbulence, inlet gradients) are present, larger deviations may be expected as illustrated by Steven's case. To appreciate this uncertainty, a $pr = 2.0$ and a $pr = 7.5$ centrifugal compressor stage was designed using an impeller followed by a channel diffuser. On a total-to-total basis, *pr* changes by 4 and 5 percent for the two cases, respectively, when *K* is increased by 0.1. The efficiency changes by 4.7 and 2.0 points, respectively. Fortunately most cases won't be this severe, but some may be. Hence careful measurements of the actual process are essential; the use of the loss-plot to correlate the resulting data has proven most helpful for each class of diffuser.

This work can be summarized by modifying equation (1) to read:

$$K = Cp_i - Cp \pm \delta \tag{12}$$

which covers nearly all qualified data available. Most of the time, $\delta = \pm 0.05$ but can be as high as $\delta = \pm 0.1$. Unfortunately, some workers have used equation (1), without documenting such usage, and reported their *K* values based only on *Cp* measurements. Such claims for *K* can easily be in error by as much as ± 30 to 100 percent! Published *K* values should only be trusted if the measurement technique is documented.

## Closure

It appears that the use of equation (1) is a realistic method for a preliminary estimate of the loss in a diffuser of any class if the static pressure recovery coefficient is known. For engineering purposes, it is constructive to estimate diffuser performance using the loss-map. Whenever a recovery map is available, it should be used first followed by the loss-map. The loss-map procedure provides a valuable method for displaying the static pressure recovery and the total pressure loss information for diffusing elements, whether they be simple straight wall laboratory diffusers, complex turbomachinery diffusers or even (evidently) airfoil cascades.

## Acknowledgment

The author wishes to acknowledge Creare Incorporated for their permission to use Figs. 9, 10, 11, and 12 from their various consortium reports and to acknowledge the author's professional colleagues C. Osborne, T. W. Carney, J. H.

Goebel, B. R. Patel, D. M. Karon, and R. Balch for their stimulating critiques and expert assistance during the five years of this work.

## References

Anon, 1979, "Report of the Hydrodemonstration Committee—Draft No. 2," prepared for Naval Underwater Systems Center, Newport, RI, (pp. 3-54 to 3-89 entitled "Diffuser/Duct" prepared and authored by D. Japikse).

Eckardt, D., Personal Communications.

Goebel, J. H., and Patel, B. R., 1976, "Performance Data for 6° Conical Diffusers," Creare TM-527. Proprietary.

Japikse, D., 1977, "The Design and Evaluation of Restricted Length Annular Exhaust Diffusers," Creare TN-257. Proprietary.

Japikse, D., and Osborne, C., 1982, "Vaneless Diffuser, Return Bend and Return Channel Performance Investigation," Creare TN-346. Proprietary.

Japikse, D., 1982, "The Comprehensive Performance Evaluation of a Radial Inflow Turbine," Creare TN-348. Proprietary.

Kline, S. J., Abbott, D. E., and Fox, R. W., 1959, "Optimum Design of Straight-Walled Diffusers," ASME *Journal of Basic Engineering*, pp. 321-330.

Miller, D. S., 1978, *Internal Flow Systems*, BHRA Fluid Engineering.

Reneau, L. R., Johnston, J. P., and Kline, S. J., 1966, "Performance and Design of Straight, Two-Dimensional Diffusers," ASME Paper No. 66-FE-10.

Sharan, V. Kr., 1976, "An Exponential Investigation of the Behavior of Conical Diffusers in Turbulent Flow," *Journal of Applied Mathematics and Physics (ZAMP)*, Vol. 27.

Stevens, S. J., 1970, "Turbulent Incompressible Flow in Annular Diffusers," PhD thesis, Loughborough University of Technology, Department of Transport Technology.

Stevens, S. J., and Williams, G. J., 1980, "The Influence of Inlet Conditions on the Performance of Annular Diffusers," ASME JOURNAL OF FLUIDS ENGINEERING, Vol. 102, pp. 357-363.

Wood, C. C., and Henry, J. R., 1958, "Effects of Shock-Boundary-Layer Interaction on the Performance of a Long and a Short Subsonic Annular Diffuser," NACA RML58A31.

Yahya, S. M., and Gupta, R. L., 1975, "A Test Rig for Testing Radial Diffusers," *International Journal of Mechanical Science*, pp. 415-490.

## APPENDIX I

The equation (1) relationship can be conveniently extended to other cases. For example:

Compressibility:

$$K = (\overline{p_{01}} - \overline{p_{02}})/(\overline{p_{01}} - \overline{p_1})$$
$$= (\overline{p_1 F(M_1)} - \overline{p_2 F(M_2)})/(\overline{p_1 F(M_1)} - \overline{p_1})$$

$$F(M) = \left(1 + \frac{k-1}{2} M^2\right)^{\frac{k}{k-1}}$$

$$F(M) = 1 + \frac{kM^2}{2} + \ldots \text{ by Taylor Series}$$

Hence

$$K = -Cp + \left(1 - \frac{\overline{\rho_1}/\overline{\rho_2}}{AR^2}\right) + \ldots$$

the density ratio can be approximately estimated from the isentropic equations and an approximate continuity relationship:

$$\frac{\bar{\rho}_1}{\bar{\rho}_2} = \left[\frac{1 + \frac{k-1}{2}(\overline{M_1}/AR)^2}{1 + \frac{k-1}{2}\overline{M_1}^2}\right]^{\frac{1}{k-1}}$$

or more accurately from the complete equations which are a function of the total pressure loss from 1 to 2.

**Radial Vaneless Diffuser (Incompressible)**

$$K = (\overline{p_{01}} - \overline{p_{02}})/(\overline{p_{01}} - \overline{p_1})$$
$$= \left[\overline{p_1} + \frac{1}{2}\rho C_1^2 - \overline{p_2} - \frac{1}{2}\rho C_2^2\right]/\left[\overline{p_1} + \frac{1}{2}\rho \overline{C_1^2} - \overline{p_1}\right]$$
$$= -Cp + \frac{\overline{C_{\theta 1}^2} + \overline{C_{m1}^2} - (\overline{C_{\theta 2}^2} + \overline{C_{m2}^2})}{\overline{C_{\theta 1}^2} + \overline{C_{m1}^2}}$$
$$= -Cp + \left\{1 - \left[\frac{\overline{C_{\theta 2}^2}}{\overline{C_{m1}^2}} + \frac{\overline{C_{m2}^2}}{\overline{C_{m1}^2}}\right]/\left[\frac{\overline{C_{\theta 1}^2}}{\overline{C_{m1}^2}} + 1\right]\right\}$$
$$= -Cp + [1 - (1/AR^2 + (\lambda_1 SC\, r_1/r_2)^2)/(1 + \lambda_1^2)]$$

if we should choose (arbitrarily) to idealize the geometry related recovery process then we can set $SC = 1$. For constant depth diffusers we would then get:

$$K = Cp_i - Cp \text{ where } Cp_i = 1 - 1/AR^2$$

## DISCUSSION

### W. A. Spraker[6]

We are indebted to Dr. Japikse for this paper. The discusser must own up to being one of the multitude not familiar with the concept presented by Dr. Japikse.

The discusser was struck by the possibility that this analysis might be useful in understanding the performance of centrifugal compressor volutes.

Centrifugal compressor volutes are usually designed from the continuity and angular momentum equations resulting in the $A/R$ descriptor which is almost universally used to define volute geometry. This results in good match point performance but tells nothing about the variation of losses or static pressure rise coefficient as flow varies.

An earlier report by Japikse [1] presents an analysis of the volute by L. R. Young. Young derives the ideal static pressure rise coefficient for the volute as:

$$Cp_i = 1 - \frac{1}{AR^2(1+\lambda^2)} \tag{1}$$

where, $\lambda$ is the ratio of the mass average tangential to meridional velocity at the volute inlet and $AR$ is the ratio of volute exit to inlet area.

Young then assumes that the energy content of the meridional velocity entering the volute is lost from sudden expansion. He derives the static pressure rise coefficient for the case where the product $\lambda \times AR$ is greater than 1 as:

$$Cp = \frac{2(\lambda - 1/AR)}{AR(1+\lambda^2)} \tag{2}$$

Schwitzer recently completed a detailed test of a turbocharger compressor having a large number of static pressure taps located along the compressor contour, the vaneless diffuser, and the volute. The impeller was 3.6 in. in diameter, the volute $A/R$ was 0.56, and the volute area ratio at the static pressure measuring station was 0.721.

Volute inlet total pressure and flow angle were calculated from the measured volute inlet static pressure using the analysis of Stanitz [2] and the volute discharge total pressure was calculated from the measured airflow rate, total temperature, static pressure and flow area. This allowed the calculation of the volute pressure recovery coefficient and loss coefficient as defined by Japikse in his present paper. Note that since no traverses were made, the criteria described by Japikse's equation (10) may not be met.

The experimental values of loss coefficient were then plotted versus static pressure rise coefficient as shown in Fig. 14. We note that the data falls along a single line for a range of data which included five values of compressor rotational speed and flow variation from close to surge to high flow for each speedline.

[6]Manager, Turbomachinery Aerodynamics, Schwitzer Indianapolis, Indianapolis, Ind. 46206.

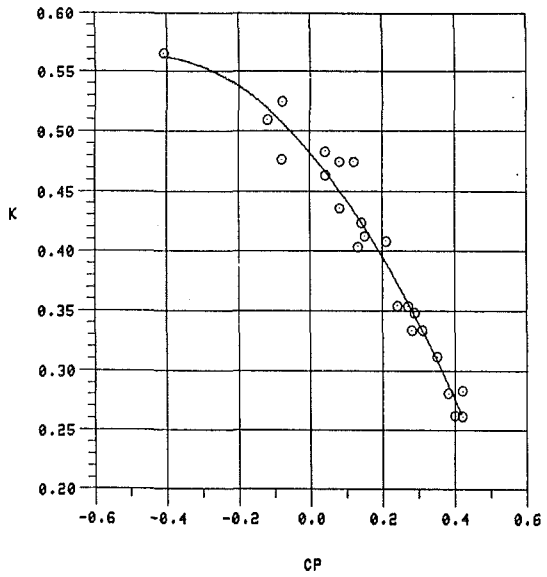


Fig. 14 Experimental static pressure rise versus total pressure loss coefficients for a volute

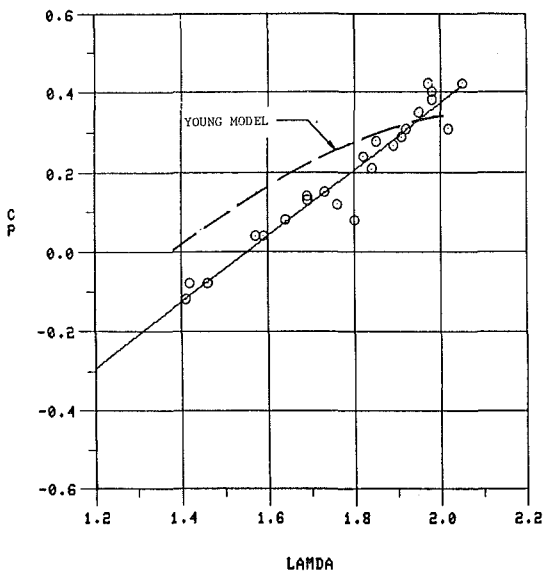


Fig. 16 Static pressure rise coefficient versus lambda

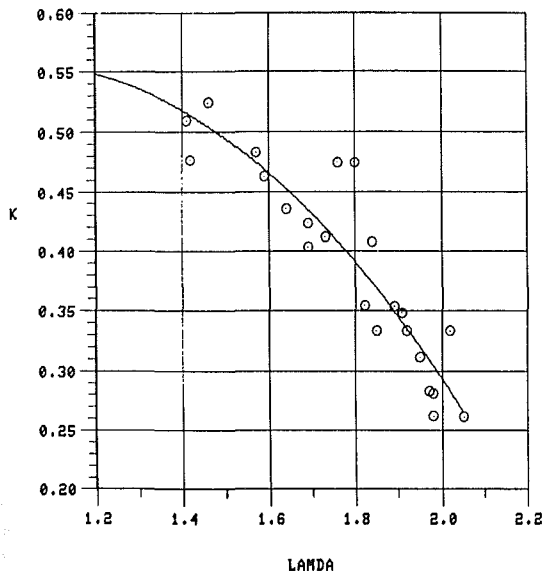


Fig. 15 Total pressure loss coefficient versus lambda

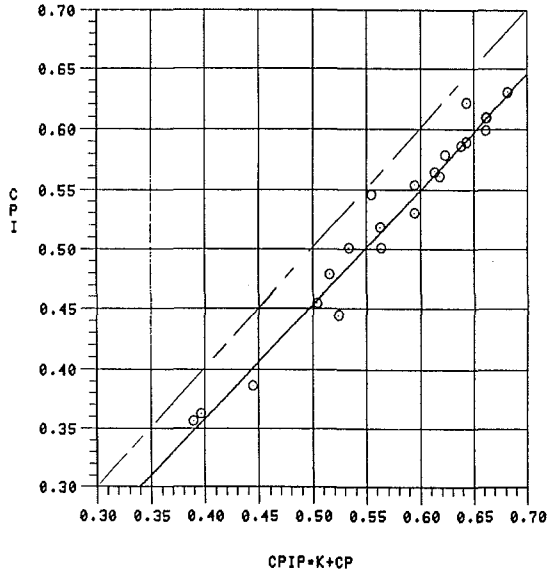


Fig. 17 Ideal static pressure rise coefficient versus experimental data

Next, the loss coefficient and static pressure rise coefficient was plotted versus the flow angle parameter Lambda as shown on Figs. 15 and 16. Figure 16 also shows the Young performance prediction for static pressure rise coefficient from equation (2) for comparison.

Finally, the sum of the static pressure rise coefficient and loss coefficient were plotted against the ideal static pressure rise from equation (1) as shown in Fig. 17.

Reasonable agreement is seen between experimental and ideal performance in Fig. 17. Some of the difference may be the result of the fact that the experimental data were calculated using compressible flow whereas the ideal performance is for incompressible flow. Young's performance prediction in Fig. 16 is optimistic at high flow rates and crosses the measured data at lower flow rates.

The relationships revealed in Figs. 14 through 17 may be expected to vary with the volute area ratio, details of the volute design, and perhaps with the $A/R$. The point of view suggested by Japikse offers a promising avenue for understanding and performance prediction not only of diffusers but, surprisingly enough, such complicated flow structures as volutes.

## Additional References

1 Japikse, D., "Advanced Diffusion Levels in Turbocharger Compressors and Component Matching," *Proceedings of Conference, Turbocharging and Turbochargers*, Institution of Mechanical Engineers, London, 1982.

2 Stanitz, J. D., "One Dimensional Compressible Flow in Vaneless Diffusers of Radial and Mixed Flow Compressors, Including Affects of Friction, Heat Transfer and Area Change," NACA TN-2610, 1952.

## Author's Closure

Mr. Spraker's examination of the contents of this study is a very constructive contribution to the turbomachinery industry. He has provided a solid case study of the application of the basic concepts to an additional, and complicated, turbomachinery fluid element: the scroll or volute. As Mr. Spraker notes, the data which he uses is a hybrid experimental/analytical type of data since the static state parameters are known and the total state parameters were deduced at the inlet and outlet of the volute by conventional analytical techniques. As he fully recognizes, some error is implied as a result and

our recent investigations show that the Stanitz (Spraker's reference [2]) calculation method will yield some error in total pressure and flow angle at the end of the vaneless diffuser (i.e., the volute inlet). Nonetheless, the four figures presented by Mr. Spraker are surely valid for illustrating the basic application of the idea to the complex volute flow field and any errors, should they be discovered later after more detailed experimental investigation, will likely only amount to a modest shift in the trends he presents.

Figure 14 of the discussion is the direct application of the loss map concept for the volute. It represents an industrial turbomachinery component and therefore is similar to Figs. 8–12 of the paper. The data on this map include both accelerating and decelerating flow regimes, thus illustrating some of the map structure in the negative $C_p$ range, similar to the results shown previously in Fig. 10 for a return channel cascade. An important point must be made for Fig. 14, as well as Fig. 8 of the paper. In each case, the ideal pressure recovery depends on a fundamental fluid dynamic parameter: an inlet swirl parameter ($\lambda$). Hence there is no one unique intercept of the $x$-axis, that is, there is not one unique $C_{p\,\text{ideal}}$. Thus in each case, one must actually consider a family of $K = C_{pi} - C_p$ lines intersecting the various data rather than a single overall trend. It is interesting to note that, in spite of this fact, the data tends to form a band with nearly the correct slope and a sensible $C_p$ axis intercept.

Figure 17 of Mr. Spraker's discussion is a useful comparison and one which, in retrospect, should have been used also for the data of Figs. 8, 9, and 10. He has effectively removed the swirl angle dependence from the loss map data comparison by plotting $K + C_p$, which give the experimentally implied value of $C_{pi}$, versus a theoretical determination of $C_{pi}$ from Young's model. The fact that excellent correlation is found provides a very dramatic confirmation of the $K = C_{pi} - C_p$ model and indirectly suggests a good way to find the theoretical $C_{pi}$ value which eluded us with the Figs. 10 and 11 data.

The author appreciates this contribution and trusts that more data sets will be forthcoming for industrial turbomachinery components. When data of the type presented in the discussion and Figs. 8–12 are thoroughly interpreted in terms of the basic parameters shown on Fig. 7 of the paper, it will be possible to develop a coherent loss and recovery modeling system for these turbomachinery elements.

**A. M. Abdelhalim**[1]
Assistant Professor,
Department of Aeronautical and Astronautical Engineering,
Air Force Institute of Technology,
WPAFB, Ohio 45433

**U. Ghia**
Professor.

**K. N. Ghia**
Professor.
Mem. ASME

Department of Mechanical and Industrial Engineering,
Department of Aerospace Engineering and Applied Mechanics,
University of Cincinnati,
Cincinnati, OH 45221

# Analysis of Turbulent Flow Past a Class of Semi-Infinite Bodies

*This study was undertaken with the primary purpose of developing an analysis for flow past a class of two-dimensional and axisymmetric semi-infinite bodies. The time-averaged Navier-Stokes equations for these flows are derived in surface-oriented conformal coordinates ($\xi$, $\eta$) in terms of similarity-type vorticity and stream-function variables. Turbulence closure is achieved by means of a two-equation turbulence model utilizing the kinetic energy k and its dissipation rate $\epsilon$ which enable determination of the isotropic eddy viscosity. The coupled vorticity and stream-function equations are solved simultaneously using an incremental formulation of the factored alternating-direction implicit scheme. The turbulence equations for k and $\epsilon$ are solved by the standard ADI method. Numerical solutions are obtained for the thin flat plate and compared with available experimental and analytical data. Also, results are obtained for flow over a parabola and compared with the flat-plate results in order to assess the effects of longitudinal curvature on the flow results. Finally, solutions are obtained for flow past a two-dimensional semi-infinite body with a shoulder, at $Re_d = 24{,}000$. The computed results have the same general trend as the experimental data; possible causes for the differences within the separated-flow region are cited.*

## Introduction

Turbulent flow over semi-infinite bodies has generally been analyzed using the boundary-layer assumptions. These assumptions are reasonably valid far downstream along the body, so that the results obtained in that region are quite acceptable. A considerable body of literature is available for modelling and solution of turbulent flow in the downstream region of two-dimensional as well as axisymmetric bodies, using the boundary-layer equations. Cebeci [1] as well as White [2] have provided a fairly comprehensive set of results for turbulent flow along a flat plate and along a longitudinal cylinder.

A realistic generalization of the thin flat plate is a plate with finite thickness as considered earlier by U. Ghia and Davis [3] for laminar flow. Figure 1 shows this geometry as well as a conformal coordinate system useful for analyzing these flows. Turbulent flow past the thick flat plate, as well as the corresponding axisymmetric case, namely, the longitudinal cylinder, have been studied experimentally by Ota and his coworkers. Measurements have been reported by Ota and Itasaka [4] for the mean-flow velocity profiles in the separated and reattached regions downstream of the shoulder for $Re_d = 2.69 \times 10^4$ based on the plate thickness $d$ (i.e., $Re_d = U_\infty d/\nu$). The measurements for the corresponding turbulence quantities have been presented by Ota and Narita [5] at $Re_d = 2.4 \times 10^4$. Mean-flow velocity profiles were also measured by Ota [6] for the axisymmetric flow along a longitudinal cylinder at $Re_d = 5.6 \times 10^4$ based on the cylinder diameter. In all cases, the length of the separated-flow region was observed and documented. As expected, the axisymmetric case exhibited a milder as well as shorter separated-flow region as compared to the two-dimensional case. Moreover, in the turbulent-flow range of Re examined, the reattachment length was found to be independent of Re and was observed to be between 4 and 5 plate thicknesses for the two-dimensional cases and about 1.6 times the cylinder diameter for the axisymmetric case.

It is important to recognize that the thin plate is obtained as a special case of the thick flat plate in the present formulation. Moreover, this configuration does not encounter flow separation. Hence, the thin flat plate was studied in detail in the present work. To the best knowledge of the authors, Navier-

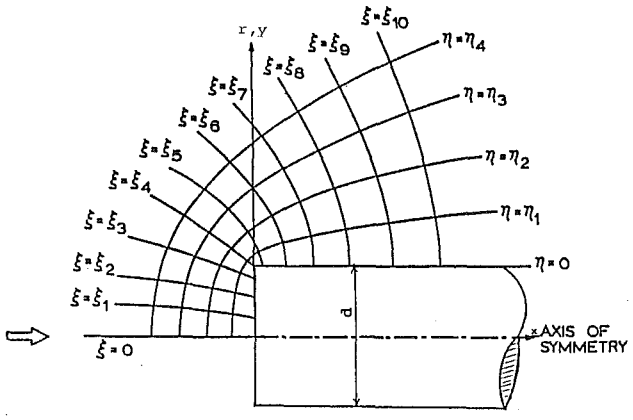


*Fig. 1 Flow configuration and coordinate system (axisymmetric or two-dimensional symmetric)*

[1] Formerly, Graduate Assistant at University of Cincinnati.

Contributed by the Fluids Engineering Division of THE AMERICAN SOCIETY OF MECHANICAL ENGINEERS and presented at the Fluids Engineering Conference, Houston, Texas, June 20–22, 1983. Manuscript received by the Fluids Engineering Division, November 21, 1983. Paper No. 83-FE-32.

  

Stokes solutions for turbulent flow over a thin semi-infinite plate have not been obtained previously. Wu [7] has recently investigated the turbulent flow over a thin finite flat plate using the Navier-Stokes equations in Cartesian coordinates. Turbulence was considered via the ($k$, $\epsilon$) two-equation model of Launder and Spalding [8], together with the wall-function approach for treating the near-wall region. The predictions of Wu [7] at the mid-section of the finite plate considered, agreed well with the measurements of Klebanoff [9] and Smith and Walker [10] for the turbulence kinetic energy and mean velocity, respectively. Singhal and Spalding [11] used the boundary-layer form of the equations for the mean flow as well as for the turbulence quantities $k$ and $\epsilon$ to predict boundary-layer flows for several configurations that were examined at the Stanford Conference (see Kline et al. [12]). Without modification of the $k$, $\epsilon$ equations or changes in any of the empirical constants in the turbulence model, the predictions agree well with the experimental data for the cases studied. For example, for the flat plate, good agreement was obtained with the mean-velocity profiles measured by Weighardt and Tillman [13]. This further establishes the wide applicability of the ($k$, $\epsilon$) two-equation turbulence model.

The present research is aimed at developing a generalized formulation of the Navier-Stokes equations in conformal coordinates for the analysis of turbulent flow, for the family of two-dimensional and axisymmetric semi-infinite bodies represented by the $\eta$ = constant curves in Fig. 1. The Navier-Stokes equations are used for the analysis in terms of the mean-flow vorticity and stream function. The eddy-viscosity concept is employed to relate the turbulent stresses (Reynolds stresses) to the deformation tensor (rate-of-strain tensor) in order to express the turbulent stresses in a manner similar to the viscous stresses. Hence, the resulting mean-flow stream-function equation for the turbulent flow is the same as the corresponding laminar-flow equation. Also, the resulting mean-flow vorticity equation is similar to the vorticity equation for a laminar flow with variable fluid viscosity.

The turbulent eddy viscosity is evaluated from the turbulence kinetic energy $k$ and its dissipation rate $\epsilon$ which are determined from their respective transport equations in the form suggested by Jones and Launder [14] so as to be applicable in the wall region also. Results are obtained first for the family of parabolas. Calculations are then made for the flat plate and are compared with existing predictions as well as with available measurements. The results of an attempt made to compute the flow past a two-dimensional body for which measurements are available are also included. This configuration consists of a flow at $\mathrm{Re}_d = 24{,}000$ past a thick plate with a shoulder and includes a finite region of separated flow immediately downstream of the shoulder.

## Analytical Formulation of Problem

**Geometry of the Problem.** The analysis developed here is that of the flow past a class of axisymmetric bodies, the geometry of which is shown in Fig. 1. Also depicted in the figure is a conformal coordinate system, ($\xi$, $\eta$) used to represent this geometry. The relation between the cylindrical coordinates ($r$, $x$) in the meridional plane of the flow configuration and the conformal coordinates ($\xi$, $\eta$) is given by the Schwarz-Christoffel transformation:

$$z = \frac{1}{2}\left[\zeta(\mathrm{Re} - \zeta^2)^{1/2} + \mathrm{Re}\,\sin^{-1}(\zeta/\sqrt{\mathrm{Re}})\right] \tag{1}$$

where $z = r - ix$, and $\zeta = \xi + i\eta$.

The $r$ and $x$ coordinates have been nondimensionalized by the viscous length $\nu/U_\infty$, where $\nu$ is the kinematic viscosity of the fluid and $U_\infty$ is the free-stream velocity. The Reynolds number, Re, is defined as $\mathrm{Re} = (2U_\infty d/\pi\nu)$, with $d$ taken to be the lateral dimension of the sharp-shouldered body, which, in fact, corresponds to a blunt plate or a circular cylinder in axial flow. This transformation also permits the study of flow past the family of bodies formed by any curve of constant $\eta = \eta_w$. The parameter $\eta_w$ is a measure of the longitudinal curvature of the body surface at the shoulder where $\xi = \sqrt{\mathrm{Re}}$. Hence, $\eta_w = 0$ corresponds to the sharp shouldered body, while $\eta_w \neq 0$ yields various blunt-shouldered bodies.

The scale factors for this transformation are defined as

$$h_1 = h_2 = h = \left|\frac{dz}{d\zeta}\right| = [(\xi^2 + \eta^2 - \mathrm{Re})^2 + 4\mathrm{Re}\eta^2]^{1/4}$$
$$h_3 = H = r^j \tag{2}$$

where $j$ is an index, that is equal to zero for two-dimensional flow and is equal to unity for axisymmetric flow. The transformation given in equation (1) is the same as that used by Ghia and Davis [3] in their study of flow past two-dimensional bodies. Moreover, with $\mathrm{Re} = 0$, it reduces to the parabolic transformation used by Davis[15] for his study of flow past parabolas, of which the flat plate is a special case.

**The Governing Equations.** The governing equations are the time-averaged full Navier-Stokes equations, together with the equation for conservation of mass for incompressible flow. For two-dimensional and axisymmetric flow, it is more convenient to formulate the problem in terms of the vorticity and stream function. In this formulation, the equation for conservation of mass is identically satisfied by defining the stream function as follows:

$$u \triangleq \frac{1}{hH}\frac{\partial\psi}{\partial\eta}, \quad v \triangleq -\frac{1}{hH}\frac{\partial\psi}{\partial\xi} \tag{3}$$

where $u$ and $v$ are the velocity components in the $\xi$ and $\eta$ directions, respectively. Although turbulent flow does not exhibit self-similarity for asymptotically large $\xi$, the similarity variables derived by U. Ghia and Abdelhalim [16] for the corresponding laminar flow have also been used here to study turbulent flow. This is useful in real configurations where the flow is laminar in the vicinity of the stagnation point and goes through transition, to become turbulent further downstream. The introduction of similarity-type variables helps to analytically incorporate some of the known behavior of the flow, thereby reducing the spatial variation in the problem. The form of the similarity-type variable for the stream function has been guided by the inviscid solution for the stream function for flow against a vertical wall and is taken to be

$$\psi = \xi^{j+1} f(\xi, \eta). \tag{4}$$

In terms of the similarity-type stream function $f$, the stream function equation is given by

$$f_{\xi\xi} + f_{\eta\eta} + \frac{2(j+1)}{\xi} f_\xi + \frac{j(j+1)}{\xi^2} f - \frac{H_\eta}{H} f_\eta - \frac{H_\xi}{H}\left(f_\xi + \frac{j+1}{\xi} f\right) = -\frac{Hh^2}{\xi^{j+1}}\Omega. \tag{5}$$

Based on the right-hand side of equation (5), a similarity-type variable for the vorticity is introduced as

$$\Omega(\xi, \eta) = -\frac{\xi^{j+1}}{Hh^2} g(\xi, \eta). \tag{6}$$

Before presenting the vorticity equation, the nondimensionalization used for the physical variables is given as follows:

$$u = u^*/U_\infty, \; v = v^*/U_\infty, \; \tau = \tau^*/\rho U_\infty^2,$$
$$\psi = \psi^*/\nu, \; \Omega = \Omega^*\nu/U_\infty^2, \; \nu_e = 1 + \nu_t/\nu. \tag{7}$$

Now, the use of equation (6) in the vorticity transport equation for $\Omega$ leads to the vorticity equation in terms of the similarity-type vorticity function $g$ and is given as

$$(\nu_e g)_{\xi\xi} + (\nu_e g)_{\eta\eta} + (\nu_e g)_{\xi}\left[\frac{2(j+1)}{\xi} - \frac{H_\xi}{H} - \frac{4h_\xi}{h}\right]$$

$$+ (\nu_e g)_{\eta}\left[\frac{H_\eta}{H} - \frac{4h_\eta}{h}\right] + (\nu_e g)\left[\frac{(j+1)}{\xi}\left\{\frac{j}{\xi} - \frac{H_\xi}{H} - \frac{4h_\xi}{h}\right\}\right.$$

$$\left. + \frac{2h_\xi}{h}\frac{H_\xi}{H} + \frac{h_\eta}{h}\frac{H_\eta}{H} - \frac{2}{h}(h_{\xi\xi} + h_{\eta\eta}) + \frac{6}{h^2}(h_\xi^2 + h_\eta^2)\right]$$

$$+ g_\eta \frac{\xi^j}{H}[\xi f_\xi + (j+1)f] - g_\xi \frac{\xi^{j+1}}{H} f_\eta$$

$$+ g\left(\frac{2}{H}\xi^j\right)\left[-\{\xi f_\xi + (j+1)f\}\left(\frac{h_\eta}{h} + \frac{H_\eta}{H}\right)\right.$$

$$\left. + f_\eta\left\{\xi\frac{H_\xi}{H} + \xi\frac{h_\xi}{h} - \frac{(j+1)}{2}\right\}\right]$$

$$+ a_1 f_{\xi\xi} + a_2 f_{\eta\eta} + a_3 f_{\xi\eta} + a_4 f_\xi + a_5 f_\eta + a_6 f = h^2 g_t \qquad (8)$$

where the coefficients $a_1$ through $a_6$ are given by the following expressions:

$$a_1 = 2\left[-\frac{\partial^2\nu_e}{\partial\eta^2} + \frac{h_\eta}{h}\frac{\partial\nu_e}{\partial\eta} - \frac{h_\xi}{h}\frac{\partial\nu_e}{\partial\xi}\right],$$

$$a_2 = 2\left[-\frac{\partial^2\nu_e}{\partial\xi^2} - \frac{h_\eta}{h}\frac{\partial\nu_e}{\partial\eta} + \frac{h_\xi}{h}\frac{\partial\nu_e}{\partial\xi}\right],$$

$$a_3 = 4\left[\frac{\partial^2\nu_e}{\partial\xi\partial\eta} - \frac{h_\xi}{h}\frac{\partial\nu_e}{\partial\eta} - \frac{h_\eta}{h}\frac{\partial\nu_e}{\partial\xi}\right],$$

$$a_4 = \frac{\partial^2\nu_e}{\partial\xi\partial\eta}\left[\frac{4(j+1)}{\xi} - 2\left(\frac{2h_\xi}{h} + \frac{H_\xi}{H}\right)\right] + \frac{2\partial^2\nu_e}{\partial\xi^2}\left[\frac{h_\eta}{h} + \frac{H_\eta}{H}\right]$$
$$- \frac{2\partial^2\nu_e}{\partial\eta^2}\frac{h_\eta}{h} + 2\frac{\partial\nu_e}{\partial\eta}[a_7 - a_8] + 2a_9\frac{\partial\nu_e}{\partial\xi},$$

$$a_5 = -\frac{2\partial^2\nu_e}{\partial\xi\partial\eta}\left[2\frac{h_\eta}{h} + \frac{H_\eta}{H}\right] + \frac{2\partial^2\nu_e}{\partial\eta^2}\left[\frac{h_\xi}{h} + \frac{H_\xi}{H} - \frac{2(j+1)}{\xi}\right]$$
$$- \frac{2\partial^2\nu_e}{\partial\xi^2}\frac{h_\xi}{h} - 2a_9\frac{\partial\nu_e}{\partial\xi}[a_7 - a_8],$$

and

$$a_6 = \frac{2(j+1)}{\xi}\left[-\frac{\partial^2\nu_e}{\partial\xi\partial\eta}\left(\frac{2h_\eta}{h} + \frac{H_\eta}{H}\right) + \frac{\partial^2\nu_e}{\partial\eta^2}\left(\frac{h_\xi}{h}\right.\right.$$
$$\left. + \frac{H_\xi}{H} - \frac{2j}{\xi}\right)$$
$$- \frac{\partial^2\nu_e}{\partial\xi^2}\frac{h_\xi}{h} - \frac{\partial\nu_e}{\partial\eta}\left\{a_9 + \left(\frac{j+2}{\xi}\right)\frac{h_\eta}{h}\right\}$$
$$\left. + \frac{\partial\nu_e}{\partial\xi}\left\{a_7 + \left(\frac{j+2}{\xi}\right)\frac{h_\xi}{h} - 2a_8\right\}\right]. \qquad (9)$$

Furthermore, the quantities $a_7$, $a_8$ and $a_9$ introduced in the coefficients $a_4$, $a_5$ and $a_6$ are defined as follows:

$$a_7 = \frac{h_\eta}{h}\left(\frac{h_\eta}{h} + \frac{H_\eta}{H}\right) + \frac{h_\xi}{h}\left(\frac{h_\xi}{h} + \frac{H_\xi}{H} - \frac{2(j+1)}{\xi}\right),$$

$$a_8 = \frac{h_{\xi\xi} + h_{\eta\eta}}{2h} + \frac{h_\xi^2 + h_\eta^2}{h^2}$$

and

$$a_9 = \frac{h_\eta}{h}\left(\frac{h_\xi}{h} + \frac{H_\xi}{H} - \frac{2(j+1)}{\xi}\right) - \frac{h_\xi}{h}\left(\frac{h_\eta}{h} + \frac{H_\eta}{H}\right). \qquad (10)$$

The derivation of equations for $f$ and $g$ can be found in the work of Abdelhalim, U. Ghia and K. Ghia [17]. The effective kinematic viscosity, $\nu_e$, appearing in equation (8), is evaluated from the two-differential equation model which consists of transport equations for the turbulent kinetic energy $k$, and its dissipation rate, $\epsilon$.

**The Turbulence Equations.** Modeling turbulence through the eddy viscosity concept has been shown to be adequate for most two-dimensional or axisymmetric attached flows of interest. The $(k, \epsilon)$ model of Launder and Spalding [8] involves a minimum number of empirical constants. It has been tested by several researchers for a variety of flow problems and has been found to yield acceptable results over a wide range of the problem parameters without adjustment of the empirical constants in the model. Researchers have also used the $(k, \epsilon)$ model with reasonable success for studying separated flows in confined configurations (e.g., Rodi [18]). These advantageous features of this model suggested its use in the present study also. However, it is valid only in the region of fully turbulent flow, so that the wall regions require special treatment (see Goyal, K. Ghia and U. Ghia [19]). Hence, the present study employs the $(k, \epsilon)$ model of Jones and Launder [14] which is applicable up to the wall. Abdelhalim, U. Ghia and K. Ghia [17] have derived the turbulence equations in conformal coordinates using the general vector form. These equations are given as follows.

*Equation for Turbulent Kinetic Energy:*

$$\frac{h^2}{\nu_e}\frac{\partial k}{\partial t} = \frac{\partial^2 k}{\partial\xi^2} + \frac{\partial^2 k}{\partial\eta^2} + A\frac{\partial k}{\partial\xi} + B\frac{\partial k}{\partial\eta} - \frac{h^2\epsilon}{\nu_e} + \frac{h^2 D}{\nu_e}$$
$$- \frac{1}{2k\nu_e}\left[\left(\frac{\partial k}{\partial\xi}\right)^2 + \left(\frac{\partial k}{\partial\eta}\right)^2\right] \qquad (11)$$

*Equation for Dissipation Rate of Turbulent Kinetic Energy:*

$$\frac{h^2}{\nu_e'}\frac{\partial\epsilon}{\partial t} = \frac{\partial^2\epsilon}{\partial\xi^2} + \frac{\partial^2\epsilon}{\partial\eta^2} + A_1\frac{\partial\epsilon}{\partial\xi} + B_1\frac{\partial\epsilon}{\partial\eta}$$
$$+ \frac{h^2}{\nu_e'}\frac{\epsilon}{k}(c_1 D - c_2\epsilon) + D_1 \qquad (12)$$

The coefficients $A$, $B$, $A_1$, $B_1$, $D$, and $D_1$ appearing in equations (11) and (12) are defined as follows.

$$A = \left(-hu + \frac{\partial\nu_e}{\partial\xi} + \nu_e\frac{H_\xi}{H}\right)/\nu_e, \qquad (13a)$$

$$B = \left(-hv + \frac{\partial\nu_e}{\partial\eta} + \nu_e\frac{H_\eta}{H}\right)/\nu_e, \qquad (13b)$$

$$A_1 = \left(-hu + \frac{\partial\nu_e'}{\partial\xi} + \nu_e'\frac{H_\xi}{H}\right)/\nu_e', \qquad (13c)$$

$$B_1 = \left(-hv + \frac{\partial\nu_e'}{\partial\eta} + \nu_e'\frac{H_\eta}{H}\right)/\nu_e' \qquad (13d)$$

$$D = \frac{\nu_t}{h^2}\left[2\left\{\left(\frac{\partial u}{\partial\xi}\right)^2 + \left(\frac{\partial v}{\partial\eta}\right)^2 + \left(v\frac{H_\eta}{H}\right)^2\right.\right.$$
$$\left. + \left(u\frac{H_\xi}{H}\right)^2\right\} + \left(\frac{\partial v}{\partial\xi} + \frac{\partial u}{\partial\eta}\right)^2$$
$$+ u^2\left\{\left(\frac{h_\eta}{h}\right)^2 + 2\left(\frac{h_\xi}{h}\right)^2\right\} + v^2\left\{2\left(\frac{h_\eta}{h}\right)^2 + \left(\frac{h_\xi}{h}\right)^2\right\}$$
$$+ 4\left(v\frac{h_\eta}{h}\frac{\partial u}{\partial\xi} + u\frac{h_\xi}{h}\frac{\partial v}{\partial\eta}\right) - 2\left(u\frac{h_\xi}{h} + v\frac{h_\xi}{h}\right)\left(\frac{\partial v}{\partial\xi} + \frac{\partial u}{\partial\eta}\right)$$
$$\left. + 2uv\left(\frac{h_\xi}{h}\frac{h_\eta}{h} + 2\frac{H_\xi}{H}\frac{H_\eta}{H}\right)\right], \qquad (13e)$$

$$D_1 = -\frac{2\nu_t}{\nu_e'}\{\nabla\cdot\nabla^*\mathbf{v}\}\cdot\{\nabla\cdot\nabla^*\mathbf{v}\} \qquad (13f)$$

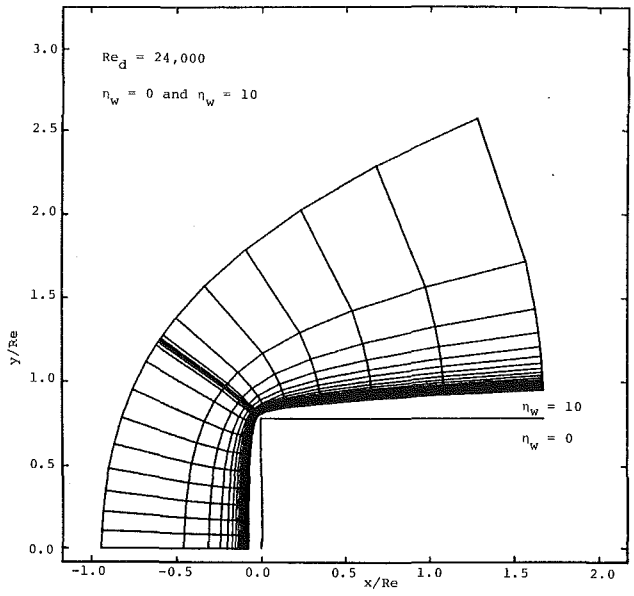


**Fig. 2 Typical coordinate distribution near surface of thick plate**

where

$$\nabla \cdot \nabla^* \mathbf{v} = \frac{1}{h^2}\left[\frac{\partial^2 u}{\partial \xi^2} + \frac{H_\xi}{H}\frac{\partial u}{\partial \xi} + u\left(\frac{h_\eta^2}{h^2} - \frac{h_{\eta\eta}}{h} - \frac{h_\xi^2}{h^2} - \frac{h_\eta}{h}\frac{H_\eta}{H} - \frac{H_\xi^2}{H^2}\right) + \frac{\partial^2 v}{\partial \xi \partial \eta} + \frac{\partial v}{\partial \xi}\left(\frac{h_\eta}{h} + \frac{H_\eta}{H}\right) - \frac{h_\xi}{h}\frac{\partial v}{\partial \eta} + v\left(\frac{h_{\xi\eta}}{h} - 2\frac{h_\eta h_\xi}{h^2} + \frac{h_\eta}{h}\frac{H_\xi}{H} - \frac{H_\xi H_\eta}{H^2}\right)\right]\vec{e}_1 + \frac{1}{h^2}\left[\frac{\partial^2 v}{\partial \eta^2} + \frac{H_\eta}{H}\frac{\partial v}{\partial \eta} + v\left(\frac{h_\xi^2}{h^2} - \frac{h_{\xi\xi}}{h} - \frac{h_\eta^2}{h^2} - \frac{h_\xi}{h}\frac{H_\xi}{H} - \frac{H_\eta^2}{H^2}\right) + \frac{\partial^2 u}{\partial \xi \partial \eta} + \frac{\partial u}{\partial \eta}\left(\frac{h_\xi}{h} + \frac{H_\xi}{H}\right) - \frac{h_\eta}{h}\frac{\partial u}{\partial \xi} + u\left(\frac{h_{\eta\xi}}{h} - 2\frac{h_\eta h_\xi}{h^2} + \frac{h_\xi}{h}\frac{H_\eta}{H} - \frac{H_\xi H_\eta}{H^2}\right)\right]\vec{e}_2. \quad (13g)$$

Also, other quantities appearing in equations (11) and (12) are as follows,

$$\nu_e = 1 + c_D\frac{k^2}{\epsilon},\quad \nu_e' = 1 + c_D k^2/(\sigma\epsilon),$$
$$c_D = 0.09\exp[-2.5/\{1 + k^2/(50\epsilon)\}],$$
$$\sigma = 1.3,\qquad c_1 = 1.42$$
$$c_2 = 1.92[1.0 - 0.3\exp(-k^4/\epsilon^2]. \quad (14)$$

**Transformation of Dependent and Independent Variables.** For improved accuracy, it is recommend that numerical computations be performed using bounded dependent variables of order of magnitude of unity. For the present problem, the vorticity function $g$ is of order unity for the case of two-dimensional flow, but not for the case of axisymmetric flows. Based upon the asymptotic behavior of the vorticity function $g$, the following new dependent variable for the vorticity is introduced

$$G = g/(\mathrm{Re} + \eta_w^2)^{j/2} \quad (15a)$$

so that $G$ is expected to be of order unity. The stream function $f$ goes to infinity as $\eta$ goes to infinity. For the purpose of numerical solution, the new stream function variable used is defined as

$$F = f - (\eta^{j+1} - \eta_w^{j+1})/(j+1) \quad (15b)$$

so that $F$ remains bounded and of order unity everywhere.

For the independent variables, in terms of the conformal coordinates $(\xi, \eta)$, the flow region extends over a quarter infinite plane when use is made of the symmetry of the flow across $\xi = 0$. It is desirable to impose the far-field boundary conditions at true infinity, i.e., as $\eta \to \infty$. Similarly, the downstream boundary condition should also be imposed, ideally, as $\xi \to \infty$. Imposing these asymptotic boundary conditions at finite values of $\xi$ or $\eta$, however large, can lead to inaccuracy in the solution. Moreover, this inaccuracy can be estimated only by carrying out a higher-order asymptotic analysis of the problem; this is, in general, not a simple process. Hence, in the present study, as in previous related studies, the asymptotic boundary conditions are applied at true infinity. However, the computational domain must remain bounded. This was initially accomplished by the introduction of the following new independent variables $S$ and $N$, suggested by Ghia and Davis [3].

$$S = 1 - \frac{A_t}{\xi}\ln\left(1 + \frac{\xi}{A_t}\right) \quad (16a)$$

and

$$N = (\eta - \eta_w)/(C + \eta - \eta_w). \quad (16b)$$

These transformations map the unbounded domain $0 \le \xi$, $\eta < \infty$ onto the bounded range $0 \le S, N \le 1$. The mapping functions are monotonic so that uniform increments along $S$, or $N$ correspond to progressively increasing increments along $\xi$, or $\eta$, thereby providing some grid-point clustering near the stagnation point as well as in the high gradient region near the body surface. In fact, the constants $A_t$ and $C$ appearing in equation (16) are a measure of this clustering as they represent the slopes of the transformation functions near $\xi = 0$ and $\eta = \eta_w$, where $S_\xi = 1/(2A_t)$ and $N_\eta = 1/C$, respectively.

In the present problem of flow past bodies with a shoulder, it was found that, although the $\eta$-$N$ transformation is satisfactory, the mesh-point distribution along the $\xi$-direction resulting from equation (16$a$) is not suitable for the present geometry, especially near the shoulder. Hence, the following modified transformation has been used in the present study:

$$S = 1 - a\left(\frac{A_t}{\xi}\right)\ln\left(1 + \frac{\xi}{A_t}\right) + e\tan^{-1}(\xi - \xi_c) + c \quad (16c)$$

where $\xi_c = \sqrt{\mathrm{Re}}$, the value of $\xi$ at the shoulder, and $a$, $A_t$, $e$, and $c$ are parameters evaluated from specified conditions for the transformation and the degree of the resolution required. The transformation given by equation (16$c$) also provides some clustering of mesh points in the vicinity of the shoulder as shown in Fig. 2. Ideally, it is highly desirable to have good resolution near the point of reattachment also, but perhaps this has to be achieved via a solution-adaptive mesh-clustering procedure wherein the mesh is adjusted as the solution develops. It should be mentioned that, in this study, longitudinal grid clustering is employed only near the stagnation point and near the shoulder. The latter location coincides with the separation point as $\eta_w$ approaches zero or as Re increases.

The final form of the stream function and vorticity equations obtained by introducing equations (15) and (16) in equations (5) and (8) is considerably complex and is given in detail by Abdelhalim, U. Ghia, and K. Ghia [17]. The necessary boundary conditions for the final form of the governing differential equations are discussed next.

**Boundary Conditions**

*At the Wall $\eta=\eta_w$, i.e., at $N=0$ and $S\geq 0$.* At the body surface, molecular diffusion dominates and, with the condition of zero-slip at the surface, leads to

$$F=0, F_N=-C\eta_w^j, k=0, \epsilon=0. \tag{17a}$$

*At the Far-Field Boundary $\eta\to\infty$, i.e., at $N=1$ and $S\geq 0$.* The free-stream conditions prevail at this boundary and lead to

$$F_N=0, G=0; k=k_\infty, \epsilon=\epsilon_\infty \tag{17b}$$

where $k_\infty$ and $\epsilon_\infty$ correspond to free-stream turbulence. The inclusion of this free-stream turbulence also aids in lowering the transition Reynolds number as well as in limiting the region of non-turbulent flow, so that turbulent flow can be assumed to prevail throughout the computational domain.

*At the Line of Symmetry $\xi=0$, i.e., at $S=0$* and $N\geq 0$. On the symmetry line, $F_\xi$, $G_\xi$, $k_\xi$, and $\epsilon_\xi$ are zero. Instead of using these conditions directly, they are employed in the governing equations to obtain special forms of the equations which are then solved to determine the solution at this boundary.

*At the Downstream Boundary $\xi\to\xi_\infty$, i.e., at $S=1$ and $N\geq 0$.* Far downstream, the governing equations are only weakly elliptic, i.e., the second derivatives of all the dependent variables with respect to $\xi$ are negligible. Rather than using these conditions directly to extrapolate the solution at the downstream boundary, they are employed in the governing differential equations to yield the reduced (parabolic) form of the equations valid at the downstream boundary. Their solution yields the flow variables at the downstream boundary. Clearly, this solution depends on the solution in the interior of the computational domain and, hence, needs to be continuously updated in the pseudo-transient iterative solution procedure employed in the present work.

## The Numerical Solution Scheme

The governing equations (5), (8), (11), and (12) form a set of coupled nonlinear partial differential equations which are solved using a semi-implicit iterative scheme. The vorticity equation (5) and the two turbulence equations (11) and (12) for $k$ and $\epsilon$, respectively, are time-dependent, whereas the stream function equation is time independent. A fictitious time-derivative term is added to the stream-function equation so as to make it amenable to solution by the numerical scheme used. With this modification, all four governing equations are rendered parabolic in both the $\xi$–$t$ and $\eta$–$t$ planes, while still retaining their ellipticity in the $\xi$–$\eta$ plane. Accordingly, boundary conditions along all four boundaries of the ($S$, $N$) computational domain were provided in the earlier section.

**On the Factored Alternating-Direction Implicit (FADI) Scheme.** The FADI scheme of Beam and Warming [20], as generalized by Hill et al. [21], has been used for the numerical solution of the incompressible Navier-Stokes equations, whereas the alternating-direction implicit (ADI) method of Ghia and Davis [3] has been used to solve the turbulence equations for $k$ and $\epsilon$ written in conformal coordinates. The FADI scheme is second-order-time accurate and spatially factored. The time derivative is written as a 3-point backward difference. Thus, it is a three time-level scheme and, hence, requires more computer storage as compared to the ADI scheme, which is primarily a two time-level scheme. To retain the advantage of using three time levels and, at the same time, not increase the computer storage beyond that used by the conventional ADI scheme, the factored scheme is constructed in a "delta" form (i.e., in terms of increments of the unknown variables). This provides a direct derivation of the scheme and leads to an efficient computational algorithm. The treatment

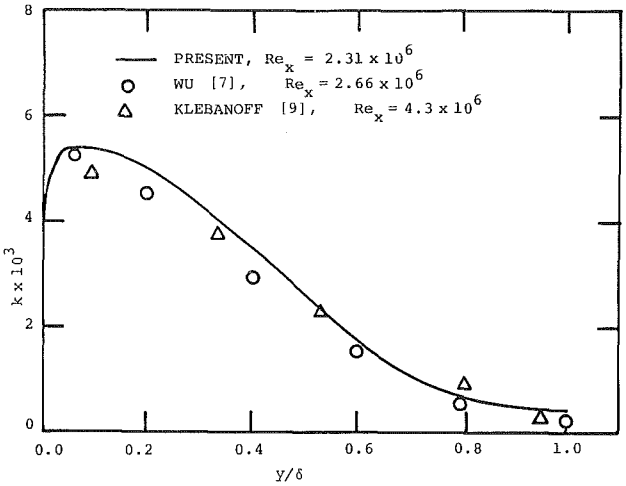


**Fig. 3 Typical profile of turbulent kinetic energy in boundary-layer over flat plate**

of the non-linear terms in the vorticity equation is also simplified by using the delta form in the factored scheme. In addition, the delta form has the advantageous property of a steady state (if one exists) independent of the time step. The FADI scheme is basically suitable for equations that are parabolic with respect to one of the independent variables.

**Convergence Criterion.** The following convergence criterion is used in the present study

$$\sum_{I=1}^{I_{\max}}\sum_{J=1}^{J_{\max}}\frac{[\Delta f^n]}{I_{\max}\cdot J_{\max}\Delta t}<\delta_f, \tag{18}$$

where $f$ denotes any of the variables $F$, $G$, $k$, or $\epsilon$. For most of the cases studied, $\delta_f$ was taken to be $10^{-5}$. It was found that, with this value of $\delta_f$, the solution had converged to within three decimal-place accuracy.

**Enhancing the Convergence Rate.** In an effort to reduce the computation time, some steps were taken toward enhancing the convergence rate of the solution. Following K. Ghia [22], different values were used for the time steps in the vorticity and the stream function equations. For the stream-function equation, the time step used is expressed as

$$\Delta t_1=\lambda_1/N_\eta^2 \tag{19}$$

where $\lambda_1$ is taken to be 90 for all the computations. For the vorticity equation, the time step used is given as

$$\Delta t=\lambda_2/(1-N) \tag{20}$$

where $\lambda_2$ is assigned different values, depending upon factors such as the grid size, the grid distribution, the Reynolds number and $\eta_w$. For example, at downstream infinity, $\lambda_1$ and $\lambda_2$ were taken to be 90 and 50, respectively, and for laminar flow, 13 iterations were required to obtain a convergent solution with a tolerance of $10^{-13}$ per point at that location.

The finite-difference representation used for the convective terms is known to affect the stability properties and the convergence rate for most numerical solutions. As reported by Hill et al. [21], the convective terms in the incremental variables can be represented by an upwind difference, which is first-order accurate, while retaining second-order accurate central differences for the convective terms in the variable itself. This leads to two advantages; firstly, it enhances the convergence rate, in general, and secondly, the resulting steady-state solution is still second-order accurate even after treating the delta convective terms by upwind differencing. The reason for this is that, at the limit of steady state, $\Delta G$ and $\Delta F$ approach zero, so that the truncation error in the steady-state solution is governed by that for the right-hand sides con-

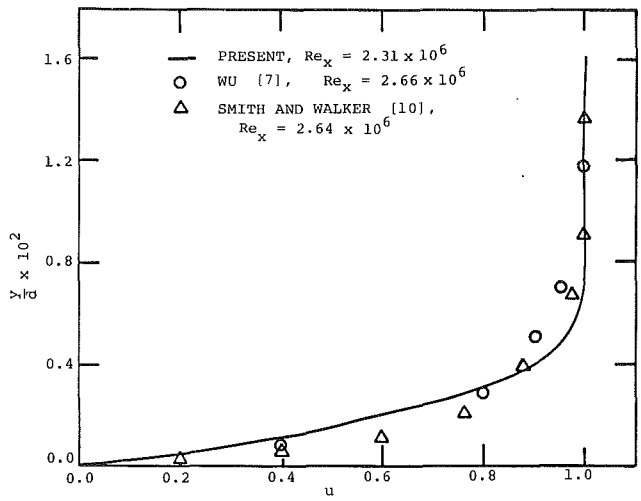


Fig. 4 Typical mean-velocity profile in boundary-layer over flat plate

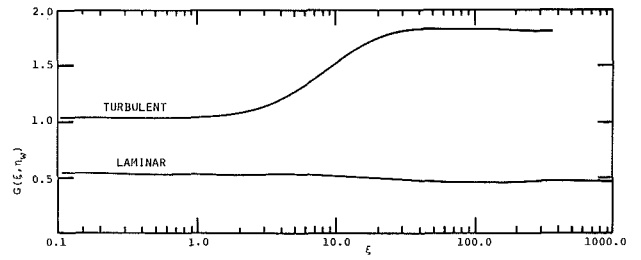


Fig. 5 Comparison of the vorticity function for laminar and turbulent flow over flat plate

taining the flow variables themselves and not the incremental variables. Similarly, in the equations for $k$ and $\epsilon$, the streamwise convective terms are treated implicitly in the $\eta$-direction sweep.

## Results and Discussion

The emphasis of this study is on the development of the two-dimensional/axisymmetric analyses for turbulent flow using conformal coordinates. Results are presently obtained only for two-dimensional flow configurations. In all of the cases studied, the wall-region near the surface is treated via the low-Reynolds-number modelling technique of Jones and Launder [14] rather than the wall-function approach used by Launder and Spalding [8]. In the wall-function approach, the law of the wall is used to provide the boundary conditions at a point adjacent to the boundary. Use of this logarithmic law introduces some assumptions which are well valid for flow over a flat plate at large values of $Re_x$ but are not valid, in general, for the flow cases considered in the present study. The presence of strong longitudinal curvature as that exhibited by sharp shouldered bodies precludes the use of the law of the wall. The law of the wall also encounters difficulty at the stagnation point as well as at the points of flow separation and reattachment where $g_w$ vanishes. Hence, the present calculations employ the $(k, \epsilon)$ turbulence model in the form that is also applicable in the inner region where the effects of laminar viscosity are not negligible. The present formulation integrates the governing differential equations up to the actual surface, where the exact boundary conditions $k=0$ and $\epsilon=0$ are applicable. The main difficulty with the integration of the $(k, \epsilon)$ equations up to the wall is the high resolution required to represent the inner layer.

**Semi-Infinite Thin Plate.** The flow past a semi-infinite thin plate is analyzed first since both experimental as well as numerical results are available for this flow. Different types of

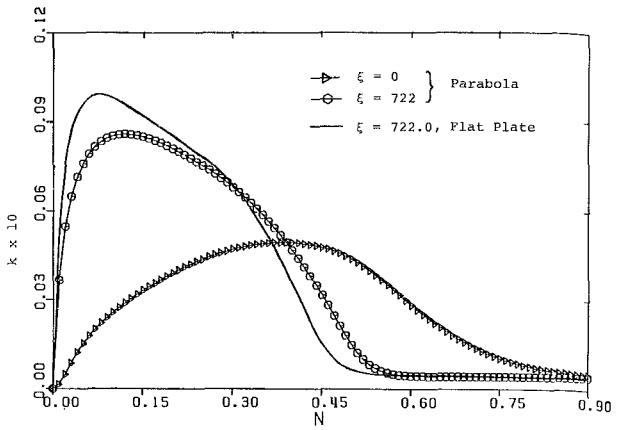


Fig. 6 Turbulent kinetic-energy distribution for flow past a parabola

initialization were tried for this problem. The one found to be most suitable consisted of the corresponding laminar solution, while the turbulence quantities $k$, $\epsilon$, and $\nu_t$ were initially set at their corresponding free-stream values. Then, $k$ and $\epsilon$ were first updated using the laminar solution.

Figure 3 shows the profile of the computed nondimensional turbulent kinetic energy $k$ for a Reynolds number, $Re_x = 2.31 \times 10^6$. On the same graph, the computational results of Wu [7] as well as the experimental data of Klebanoff [9] are shown. The computations of Wu [7] were carried out for a finite flat plate whose mid-section corresponds to $Re_x = 2.66 \times 10^6$, while the experiment of Klebanoff [9] was performed at $Re_x = 4.3 \times 10^6$. The present results show the same trend as the data of Wu [7] and Klebanoff [9]. It should be mentioned that the data of Wu [7] was obtained using the fully turbulent version of the $(k, \epsilon)$ equations, with the "inner" region being represented by the law of the wall, i.e., the computation did not start from the solid surface itself. Accordingly, the first point of computation in the work of Wu [7] was placed at $y_+ = 50$ where $y_+ = y\,\tau_w/(\rho\nu)$. With the transformations used in the present work, the results presented in Figs. 3 and 4 are obtained using $y_+ = 3.17$ at the first computational point away from the wall. Furthermore, the eleventh computational point away from the wall corresponds to $y_+ = 50$ at which Wu [7] had applied the law of the wall. Thus, the resolution of the inner region appears to be adequate.

The corresponding velocity profile for the thin flat plate at $Re_x = 2.31 \times 10^6$ is shown in Fig. 4. Also shown in the same figure are the results of Wu [7] corresponding to $Re_x = 2.66 \times 10^6$ and the experimental data of Smith and Walker [10] at $Re_x = 2.64 \times 10^6$. The present results agree reasonably well with both these sets of available data, thus further confirming the accuracy of the present solutions.

Figure 5 shows the predicted vorticity function along the surface of the flat plate as well as the corresponding vorticity function for laminar flow. As seen from this figure, the laminar calculation is continued till $\xi \to \infty$, where the laminar self-similar solution prevails, but this is not the case for the turbulent flow which does not proceed to self-similar solution as $\xi \to \infty$ in terms of the present variables. Hence, the computations for turbulent flow did not proceed to $\xi \to \infty$ as indicated by the result in Fig. 5. The first observation to be made from the results presented in Fig. 5 is that the vorticity function at the surface of the flat plate is larger for turbulent flow than for the corresponding laminar flow at any station $\xi$. This is in agreement with the physics of the problem since the vorticity function is directly related to the shear stress, and the turbulent shear stress is always larger than the laminar shear stress. Secondly, the difference between the two values is smaller near the stagnation point, and this difference increases with downstream distance. In reality, the flow over a flat-plate would be laminar up to a distance corresponding to $Re_x = 5 \times$

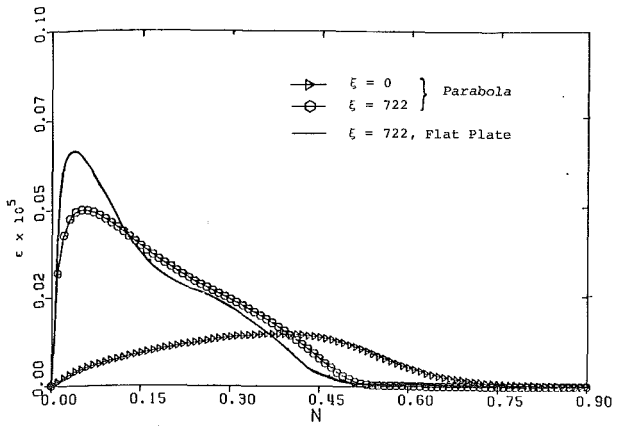


Fig. 7 Turbulent energy-dissipation distribution for flow past a parabola

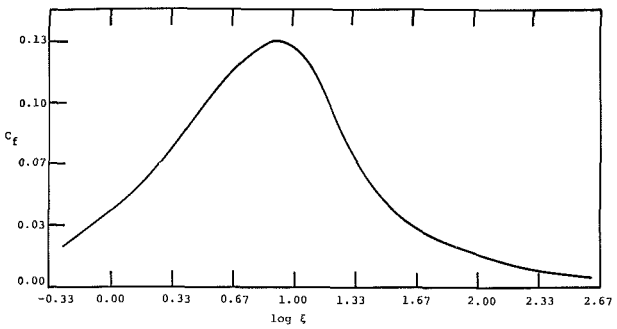


Fig. 8 Skin-friction coefficient for a parabola

$10^5$, followed by a transition region, with fully turbulent flow prevailing downstream thereof. But for the present computations, a certain low level of turbulence was introduced in the free stream in order to avoid the numerical difficulty that would otherwise be encountered while evaluating the eddy viscosity in the region of the free stream. The introduction of this free stream turbulence enables the entire computational domain to be considered as corresponding to turbulent flow. In fact, the ($k$, $\epsilon$) turbulence model has not so far been successfully tested for flow in the transition region, although a relaminarizing turbulent flow has been accurately computed with this model (Jones and Launder [14]). On the other hand, the values used for the turbulence quantities in the free-stream, as well as the choice of the location at which the far downstream boundary conditions are applied, may influence the flow solution. These may perhaps be the reasons for the somewhat too large value of the turbulent vorticity function at the leading edge of the plate (Fig. 5) for which the flow should be nearly laminar near the leading edge.

**Flow Past Parabolas.** Next, the turbulent flow over parabolas is analyzed. This serves two main purposes. Firstly, it enables examination of the behavior of the turbulence quantities $k$ and $\epsilon$ in the vicinity of the stagnation point. Secondly, since a parabola asymptotes to a flat plate at downstream infinity, comparison with the flat plate results at large downstream distances enables assessment of upstream history effects in turbulent flows. The initialization used for this case is as described earlier for the calculation of flow past a thin semi-infinite plate.

Figure 6 shows the predicted turbulent kinetic energy profiles for two streamwise locations, $\xi = 0$ and $\xi = 722$ for a parabola with $\eta_w = 10$, i.e., with nose radius of curvature equal to 100. The distribution of $k$ at $\xi = 0$ (i.e., along the stagnation line) shows a relatively milder growth in the turbulence kinetic energy as compared to that at the further downstream location $\xi = 722.0$. Also, the maximum value at-

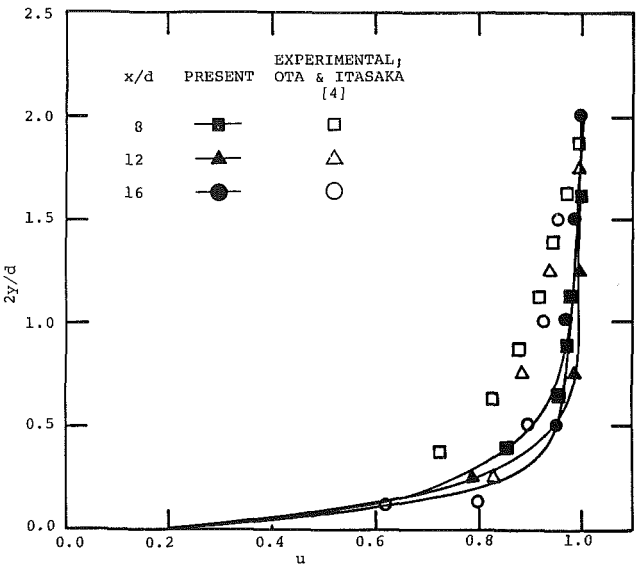


Fig. 9 Comparison between predicted and experimental data for velocity profiles for thick plate

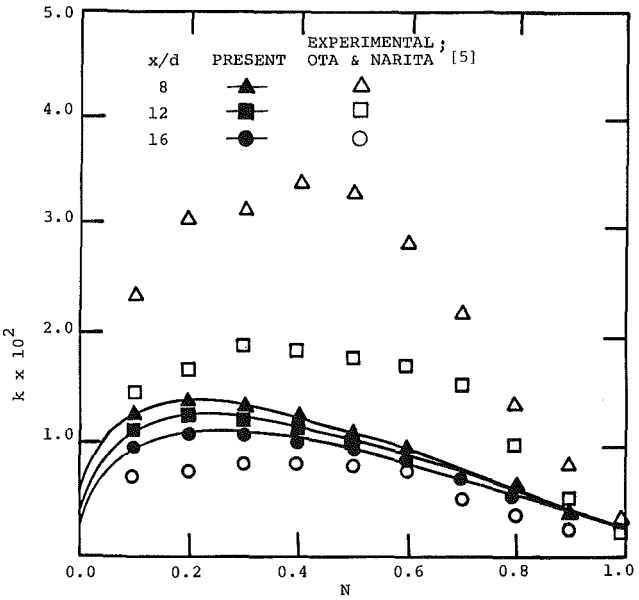


Fig. 10 Comparison between predicted and experimental data for turbulence kinetic energy for thick plate

tained in the $k$ profile at $\xi = 0$ is considerably lower and occurs much further away from the wall at $\xi = 0$ than at $\xi = 722.0$. These observations are as should be expected since a boundary layer in the vicinity of a stagnation point should contain less turbulent kinetic energy than at further downstream locations. On the same figure, the corresponding distribution of the turbulent kinetic energy over the flat plate at $\xi = 722.0$, i.e., at $\mathrm{Re}_x = 2.6 \times 10^5$, is shown. Comparison of this profile for the parabola reveals, primarily, the effect of upstream history on the kinetic energy of turbulence. At large values of $\xi$, the geometry of the parabola approaches that of a flat plate. Viewed as the limit of a parabola, the flat plate possesses infinite longitudinal curvature at the stagnation point $\xi = 0$ and zero longitudinal curvature for $\xi \geq 0$. On the other hand, at $\xi = 0$, a parabola possesses finite longitudinal curvature, related to $\eta_w$, and decreases smoothly for $\xi > 0$ and vanishes as $\xi \to \infty$. The effects of these upstream differences in the longitudinal curvatures of the two geometries is, as seen from the graphs in Fig. 6, that $k$ rises more sharply and approaches

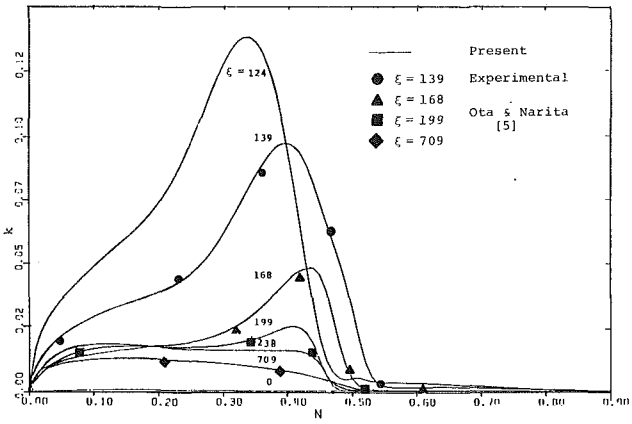


**Fig. 11 Comparison between predicted and experimental variation of turbulent kinetic energy within reduced separation bubble for thick plate**

the free-stream condition more rapidly for the flat plate than for the parabola.

Figure 7 shows the same comparison for the dissipation rate $\epsilon$ as is performed in Fig. 6 for the turbulent kinetic energy, and the same trends as in Fig. 6 are observed again in Fig. 7. Finally, the predicted distribution of the coefficient of friction along the surface of the parabola is shown in Fig. 8. The coefficient of friction increases from its value at the stagnation point, reaches a maximum value at $\xi = 9.94$, and then decreases monotonically with increase in streamwise distance.

**The Thick Plate.** Finally, some results are presented for flow over the general two-dimensional bodies considered in the present formulation. Of particular interest is the flow configuration considered experimentally by Ota and his coworkers [4, 5]. For the two-dimensional case, Ota and Itasaka [4] have presented experimental data for turbulent flow over a sharp-shouldered thick plate at $\mathrm{Re}_d = 2.69 \times 10^4$. An attempt was made to compute this flow configuration but numerical difficulties, consisting primarily of extremely slow convergence rate, were encountered for this value of $\mathrm{Re}_d$, with $\eta_w = 0$. A possible alternative was to consider a somewhat modified geometry at the same value of $\mathrm{Re}_d$. Hence, a body with a slightly blunted shoulder ($\eta_w = 10$) has been considered in the present study. This, of course, precludes the possibility of detailed quantitative comparison of the present results with the available experimental data. Nevertheless, qualitative trends can still be compared. Both of these configurations are shown in Fig. 2, which also depicts the clustered grid distribution for the blunted shoulder configuration. For this case, a lower-Re turbulent solution was first obtained. This was used as the initial solution for a higher-Re turbulent flow solution. More than one intermediate Re (turbulent) solutions were necessary in order to achieve the final value of Re at which the solution was actually required. The intermediate-Re solutions were not iterated to complete convergence, but rather only until the initial errors were smoothed and their decreasing trend established.

Figure 9 shows the velocity profiles at three different stations downstream of the shoulder region of the plate. On the same figure, the velocity profiles obtained experimentally by Ota and Itasaka [4] for the corresponding sharp-shouldered body are also shown. It is observed that the general trend for both sets of these results is the same. The results also show that the boundary-layer thickness as well as the velocity gradient at the surface are smaller for the predicted results than for the experimental results. This may primarily be due to the difference in the geometry of the body considered in the experiments of Ota and Itasaka [4] ($\eta_w = 0$) and in the present predictions ($\eta_w = 10$).

Figure 10 shows the corresponding distributions of the turbulent kinetic energy obtained from the predicted results and compared with the measurements of Ota and Narita [5]. The general trend for both these sets of results is that $k$ increases from zero at the surface to a maximum value and then decreases again to approach the free-stream value. The comparison is fair at the stations far downstream, but there is significant difference in the magnitudes of $k$ at the stations upstream. These differences may be due to the use of an isotropic eddy-viscosity model, coupled with the difference in the geometry used in the prediction ($\eta_w = 10$) and in the experiments ($\eta_w = 0$). Further discussion about this point is presented in the next paragraph. Both the geometries under consideration encounter a separated flow region immediately downstream of the shoulder. But, as expected, the size of the separation bubble for the present case with $\eta_w = 10$ is smaller, by a factor of about 4, as compared to the separation bubble observed experimentally for the case with $\eta_w = 0$. The streamwise stations at which the velocity profiles are presented in Fig. 9 are all downstream of the experimental separation bubble. A station-for-station comparison of the predicted results with the experimental data could not be made within the separated flow region, because of the different size of the predicted and measured separation bubbles. However, when the streamwise dimension of the predicted separation bubble was scaled up to match with the measured separation bubble, the computed results within the separated-flow region compared well with the corresponding measured data as shown in Fig. 11.

It is recognized that, in the vicinity of the shoulder, the combined effects of pressure gradient and longitudinal surface curvature become important. A turbulence model employing the wall-function approach, based on the law of the wall for a flat plate, cannot adequately account for these effects. On the other hand, the low-Reynolds-number modelling used in the present study partially accounts for these effects. Further, a separation bubble is embedded in the turbulent boundary layer aft of the shoulder. In this region, anisotropy of the normal stresses is important and the discrepancy, which is maximum in this region, can partly be alleviated by a modified anisotropic form of the two-equation model suggested by Launder and Spalding [8]. Chieng and Launder [23] recently studied a separated-flow model problem using the ($k$, $\epsilon$) two-equation model. For the backward-facing-step configuration, for which the separation point is fixed, the strong pressure gradients downstream of the step led to under-prediction of the reattachment length by as much as 30 percent. In the absence of turbulence data within the viscous sublayer, they had to examine their heat-transfer predictions in order to provide means for assessing and improving the near-wall turbulence model. For a separated-flow configuration, the use of low-Reynolds-number form of the ($k$, $\epsilon$) model led to heat-transfer rates that were about five times too high in the vicinity of the maximum heat-transfer point. This was attributed to larger length scales that emerge from the solution of the $\epsilon$ equation and lead to higher turbulent viscosity. These issues lead to the fact that further experimentation is needed to improve the turbulence modelling. Finally, even the (41 × 101) grids, with clustering, used in the present study are not entirely adequate for providing a high degree of accuracy in the separated-flow region. However, increase in the grid size would be accompanied by a corresponding increase in the computer time. For efficient solutions on highly refined meshes, the use of the multi-grid scheme of U. Ghia, K. Ghia, and Shin [24] should be explored for the present problem.

## Conclusions

An analysis and numerical solution procedure have been formulated for determining the incompressible viscous flow past a class of two-dimensional or axisymmetric semi-infinite bodies. The analysis is based on using the full Navier-Stokes

equations in terms of vorticity and stream function, written in an orthogonal surface-oriented coordinate system. The turbulence effects are considered by using the $(k, \epsilon)$ two-equation model, together with the low-Reynolds number modelling approach for treating the near-wall region. These equations have been carefully and accurately derived, perhaps for the first time, in terms of general conformal coordinates for two-dimensional as well as axisymmetric flows. The vorticity and stream-function equations are solved simultaneously by a factored ADI scheme formulated in terms of the increments in these variables during each iteration. The turbulence equations for $k$ and $\epsilon$ are solved by the conventional ADI method in order to update the eddy viscosity during each iteration. The use of different spatially-variable time steps for the individual equations was found to significantly affect the convergence rate of the solutions. The use of the appropriate initialization also affected the efficiency of the numerical solutions considerably.

Solutions are obtained for flow over a semi-infinite thin plate as well as a parabola in order to partially verify the analysis developed. Finally, the turbulent flow over a blunt flat plate has been computed and the results presented in terms of turbulent kinetic energy and velocity profiles for $Re_d = 24 \times 10^3$. The results obtained are in agreement with the experimental data at far downstream locations, but not in the separated-flow region. This is believed to be primarily due to the difference in the geometry of the thick plates considered in the experiment ($\eta_w = 0$) and in the present prediction ($\eta_w = 10$). The sharp-shouldered geometry with $\eta_w = 0$ has a finite thickness at downstream infinity and is expected to exhibit a larger and stronger separation bubble as compared to a blunt-shouldered body with $\eta_w = 10$ as its lateral dimension approaches infinity at downstream infinity (Fig. 2). Part of the difference between the predicted and the measured data is also due to the turbulence model itself which needs to be modified for use with separated flows in order to account for the anisotropy of the eddy viscosity. Also, still finer grids than those used here are needed in order to resolve the multiple scales present in the problem. The (41 × 101) grid used in the present computations requires 600 K bytes of main memory. The attached-flow calculations for the flat plate and the parabola needed about 15 minutes of CPU time of the AMDAHL 470 V/6 computer; the corresponding time for the separated flow past the thick plate was about 40 minutes. It is planned to refine the numerical scheme and modify and improve the turbulence model before obtaining results for the axisymmetric configurations for which experimental data are available [6].

## Acknowledgment

This research was supported partially by the Air Force Office of Scientific Research Grant No. AFOSR 80-0160.

## References

1 Cebeci, T., "Laminar and Turbulent Incompressible Boundary Layers on Slender Bodies of Revolution in Axial Flow," ASME *Journal of Basic Engineering*, Vol. 92, 1970, pp. 545–554.

2 White, F. M., "An Analysis of Axisymmetric Turbulent Flow Past a Long Cylinder," ASME *Journal of Basic Engineering*, Vol. 94, 1972, pp. 200–206.

3 Ghia, U., and Davis, R. T., "Navier-Stokes Solutions for Flow Past a Class of Two-Dimensional Semi-Infinite Bodies," *AIAA Journal*, Vol. 12, No. 12, 1974, pp. 1659–1665.

4 Ota, T., and Itasaka, M., "A Separated and Reattachment Flow on a Blunt Plate," ASME JOURNAL OF FLUIDS ENGINEERING, Vol. 98, No. 1, 1976, pp. 79–86.

5 Ota, T., and Narita, M., "Turbulence Measurements in a Separated and Reattached Flow Over a Blunt Flat Plate," ASME JOURNAL OF FLUIDS ENGINEERING, Vol. 100, 1978, pp. 224–228.

6 Ota, T., "An Axisymmetric Separated and Reattached Flow on a Longitudinal Blunt Circular Cylinder," ASME *Journal of Applied Mechanics*, 1975, pp. 311–315.

7 Wu, J. C., "A Method for the Numerical Solution of Turbulent Flow Problems," AIAA Paper No. 77-649, 1977.

8 Launder, B. E., and Spalding, D. B., "Numerical Computation of Turbuelnt Flows," *Computer Methods in Applied Mechanics and Engineering*, Vol. 3, 1974, pp. 269–289.

9 Klebanoff, P. S., "Characteristics of Turbulence in a Boundary Layer with Zero Pressure Gradient," *NACA* Technical Note 3178, 1954.

10 Smith, D. W., and Walker, J. H., "Skin-Friction Measurements in Incompressible Flow," NASA TR R-26, 1959.

11 Singhal, A. K., and Spalding, D. B., "Prediction of Two-Dimensional Boundary Layers with the Aid of the k-ϵ Model of Turbulence," *Computer Methods in Applied Mechanics and Engineering*, Vol. 25, 1980, pp. 365–383.

12 Kline, S. J., Morkovin, M. V., Sovran, G., and Cockrell, D. J., "Computation of Turbulent Boundary Layers," *AFOSR-IFP-Stanford Conference Proceedings*, 1968.

13 Weighardt, K., and Tillmann, W., "On the Turbulent Friction Layer for Rising Pressure," NACA TM 1314, 1944.

14 Jones, W. P., and Launder, B. E., "The Prediction of Laminarization with Two-Equation Models of Turbulence," *International Journal of Heat and Mass Transfer*, Vol. 15, 1972, pp. 301–314.

15 Davis, R. T., "Numerical Solution of the Navier-Stokes Equations for Symmetric Laminar Incompressible Flow Past a Parabola," *Journal of Fluid Mechanics*, Vol. 51, Pt. 3, 1972, pp. 417–433.

16 Ghia, U., and Abdelhalim, A., "Navier-Stokes Solutions for Longitudinal Flow Along Circular Cylinder, Including Blunt-Leading-Edge Separation," AIAA Paper 82-0024, presented at *AIAA 20th Aerospace Sciences Meeting*, Orlando, Fla., 1982.

17 Abdelhalim, A., Ghia, U., and Ghia, K. N., "Navier-Stokes Solutions for Incompressible Separated Flow Past a Class of Two-Dimensional and Axisymmetric Semi-Infinite Bodies," *Aerospace Engineering Report AFL* 81-9-59, University of Cincinnati, Cincinnati, Ohio, 1981.

18 Rodi, W., "Progress in Turbulence Modelling for Incompressible Flows," AIAA Paper No. 81-0045, 1981.

19 Goyal, R. K., Ghia, K. N., and Ghia, U., "Numerical Simulation of Three-Dimensional Turbulent Flow in Curved Ducts Using Parabolized Navier-Stokes Equations," presented at *Third International Conference on Mathematical Modeling*, Los Angeles, Calif., 1981.

20 Beam, R. M., and Warming, R. F., "An Implicit Factored Scheme for the Compressible Navier-Stokes Equations," AIAA Paper 77-645, presented at AIAA 3rd Computational Fluid Dynamics Conference, Albuquerque, N.M., 1977.

21 Hill, J., Davis, R. T., and Slater, G., "Development of a Factored ADI Scheme for Solving the Navier-Stokes Equations in Streamfunction-Vorticity Variables," *Aerospace Engineering Report* No. AFL 79-12-49, Univ. of Cincinnati, Ohio, 1979.

22 Ghia, K. N., "Incompressible Streamwise Flow Along an Unbounded Corner," *AIAA Journal*, Vol. 13, No. 7, 1975, pp. 902–907.

23 Chieng, C. C., and Launder, B. E., "On the Calculation of Turbulent Heat Transport Downstream from an Abrupt Pipe Expansion," in *Momentum and Heat Transfer Processes in Recirculating Flows*, ASME Publication, Editors: J. A. C. Humphrey and B. E. Launder, 1980.

24 Ghia, U., Ghia, K. N., and Shin, C. T., "High-Re Solutions for Incompressible Flow Using the Navier-Stokes Equations and a Multi-Grid Method," *Journal of Computational Physics*, Vol. 48, 1982, pp. 387–411.

# Measurements of Wall Shear Stress in Axial Flow in a Square Lattice Rectangular Rod Bundle

**M. Abdelghany**
Assistant Professor.

**R. Eichhorn**[1]
Dean, College of Engineering.

Department of Mechanical Engineering,
University of Kentucky,
Lexington, KY 40506

*Hot film probe measurements of the distribution of the wall shear stress were made for axial flow along a rectangular 3 × 6 array of rods with a pitch to diameter ratio, P/D=4/3, and a wall to diameter ratio, W/D=2/3. Measurements were performed on rods at several locations and on two duct side walls at a position 62 hydraulic diameters from the entrance. Local shear stress maxima occur near the largest subchannel flow areas with the lowest maximum local shear stress on rods nearest the sidewalls. Maximum to the minimum shear stress ratio on an individual rod is largest for the corner rod. Side wall maximum local shear stress occurs in the first wall subchannel. Overall friction factors calculated from the wall shear stress measurements agree with those calculated from pressure drop data.*

## Introduction

Axial flow in rod bundles occurs in a number of industrial processes, most notably in nuclear reactors. The design of such devices depends critically on an ability to predict the pressure drop and heat transfer under the conditions in which they are expected to operate. One parameter that is important to these considerations is the local wall shear stress on the surface of the rods and the bounding enclosure.

There have been a number of prior studies that relate to this work [1-12]. The early studies, such as the pioneering work of Deissler and Taylor [1], used modifications of the universal velocity profile for pipe flow to predict the velocity distribution, the shear stress and the heat transfer coefficient in noncircular channels. Later work has produced detailed measurements of the velocity distributions, some of the turbulence parameters and the wall shear stress in rod bundles of both triangular and square pitch.

Most of the experimental studies have used a finite array of rods, usually without consideration of the bounding walls, whereas the analytical studies have assumed infinite arrays. The most complete studies have been on a single flow subchannel so solid boundaries have been used to replace the planes of symmetry that occur in real arrays.

There is little information in the literature on the contribution made by individual rods and the bounding walls in a finite array to the overall pressure gradient. The semi-empirical analysis of Rehme [13,14] and Malak [15] can be used to predict the overall friction factor from a knowledge of the subchannel geometries, and they seem to work well, but they offer no information on the local variation of the shear stress or the magnitudes of the shear stress maxima and minima and their relative locations.

The present paper reports the results of wall shear stress measurements in a 3 × 6 rectangular array of rods bounded by plane walls making a rectangular cross section 406 mm × 203 mm. The rods were 50.8 mm in diameter by 3.35 m in length providing an overall hydraulic diameter of 45.1 mm. The fluid medium was air and measurements of the wall shear stress are reported for Reynolds numbers of 6.70 and 7.92 × $10^4$.

## Experimental Apparatus and Procedure

The test section, Fig. 1, is a rectangular channel (406.4 × 203.2 mm) with 18 rods (50.8 mm O.D.) arranged in a square lattice with a pitch to diameter ratio, $P/D = 4/3$, and a wall to diameter ratio, $W/D = 2/3$.

The rods are constructed from cold drawn stainless steel tubes. The outer surfaces of the rods was smoothed with fine emery paper. All of the rods are circular to within ±6 μm. One rod is outfitted as a test rod to carry instrumentation as described below. This rod can be inserted in place of any one of the other rods. The rods are straight to within 3 mm over a 3.2 mm span.

The two sides and the top of the channel were fabricated from plexiglas. The top plate is fixed to the bottom plate by 12 external tie rods to allow its removal while the location of the test rod is changed.

The total length of the test section is 2.96 m; measurements were performed at 2.79 m, or 62 hydraulic diameters, from the entrance. This measurement plane is located 63.5 mm from the exit.

The rods are supported horizontally at the ends only. Spacers were not used and flow blockage was avoided at the measurement plane. To minimize the rod sag, the length of the rods (62 $D_h$) was chosen as the shortest possible length that still allowed close to fully developed flow at the test section. The maximum rod sag was found to be less than 2 mm at 1.524 m (34 $D_h$) from the measurement plane. The

[1]Present address: Dean, Cullen College of Engineering, University of Houston, TX.

Contributed by the Fluids Engineering Division for publication in the JOURNAL OF FLUIDS ENGINEERING. Manuscript received by the Fluids Engineering Division, October 22, 1982.

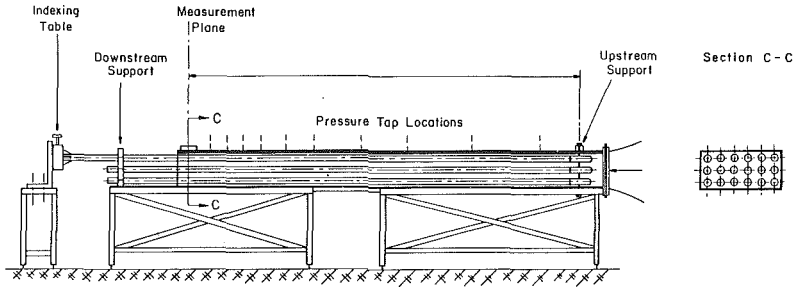


**Fig. 1 Sketch of test section**

deflection at the measurement plane is about 1.1 mm. The test section is described in detail in [16].

The wind tunnel described by Eichhorn and Fox [17] was used to supply air flow to the rod bundles. At the beginning of the present work, the uniformity of the flow and the variation of the nozzle discharge coefficient with Reynolds number were checked and found to be in agreement with ASME standards for flow nozzles. The pressure drop across the nozzle was used to measure the flow rate of air to the test section. The probable uncertainty in the mean flow velocity was less than $\pm 0.65$ percent.

Pressure drop in the rod bundle was determined from pressure measurements with ten pressure taps drilled along the center line of the test section top plate. The distance between pressure taps decreased in the flow direction from 457.2 mm to 101.6 mm from the entrance to the measurement plane.

The pressure taps were connected to a Meriam micromanometer through a Scanivalve pressure selector switch. Pressures were measured to $\pm 0.025$ mm of water. The slope of the best fit line to the pressure gradient, $dp/dx$, was used to determine the average friction factor from the formula

$$f_p = \frac{8\bar{\tau}_{wp}}{\rho \bar{U}^2} = \frac{2D_h}{\rho \bar{U}^2} \frac{dp}{dx} \tag{1}$$

where $D_h$ is the hydraulic diameter and $\bar{U}$ is the average flow velocity in the rod bundle. The uncertainty in the calculated friction factor was estimated to be less than $\pm 1.33$ percent.

Two DISA D55 R47 glue-on hot film probes were used to measure the wall shear stress. These probes have elements 1 mm long by 0.1 mm wide. One probe was glued to one of the rods with the shortest element dimension in the flow direction. This rod was used as the test rod and was held by an indexing table at the downstream end. The indexing table was used to rotate the rod and adjust its angular position to $\pm 0.25$ deg.

The probe used to measure the wall shear stress on the side walls was glued in the same flow orientation to a flexible rubberized magnetic sheet (228.9 × 101.6 mm and 0.8 mm in thickness). The magnetic sheet was used to allow calibration of the probe in a circular tube. After calibration, the magnetic sheet was simply transferred to the plane traversing mechanism used for the side wall measurements as shown in Fig. 2. The traversing mechanism is an aluminum plate machined on the bottom side with a steel plate screwed to it to form a recess equivalent to the magnetic sheet thickness. The plate movement was detected with a linear variable differential transformer (LVDT). Because the active length of the sensor was 1 mm measurements were not attempted closer than 3 mm from the corner.

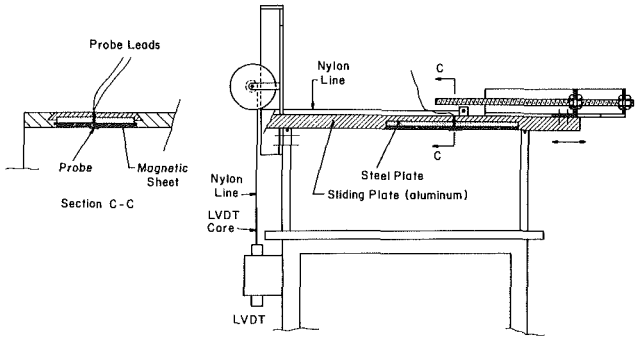


**Fig. 2 Cross-section of traversing mechanism used for plane wall shear stress measurements**

The probes were calibrated simultaneously in a concentric annulus with a diameter ratio = 1.434. The annulus outer tube is a seamless stainless steel tube whose inner surface was honed to a diameter uniform to within ± 0.6 $\mu$m. A steel sleeve attached to the downstream end of the tube was machined with a recess to receive the magnetic sheet. With this recess it is possible to have a continuous and smooth surface when the magnetic sheet is placed inside the sleeve for probe calibration. The inner tube of the annulus is simply the test rod with the probe glued to its surface. The inner tube is supported concentrically near its upstream end by three bolts screwed through 3 nuts welded to the outer tube wall. The

## Nomenclature

$a$ = half the channel width, mm
$D$ = rod diameter, mm
$D_h$ = hydraulic diameter, mm
$f$ = friction factor
$f_p$ = friction factor calculated from pressure measurement data
$f_\tau$ = friction factor calculated from wall shear stress data
$P$ = rod pitch, mm
$R_0$ = zero shear radius of the annulus, mm
$R_1$ = inner radius of the annulus, mm
$R_2$ = outer radius of the annulus, mm
Re = Reynolds number $= \rho \bar{U} D_h / \mu$
$\bar{U}$ = bundle average velocity, m/s
$\bar{u}$ = local mean axial velocity, m/s
$u'$ = fluctuating velocity in the axial direction, m/s
$u_*$ = local friction velocity $= \sqrt{\tau_w/\rho}$, m/s
$W$ = distance from the plane wall to the adjacent rod center, mm
$X$ = distance from corner along long plane wall, mm
$Y$ = distance from corner along short plane wall, mm
$y$ = distance normal to plane wall, mm
$\tau_w$ = local wall shear stress, N/m$^2$
$\bar{\tau}_{wp}$ = average shear stress from pressure measurements, N/m$^2$
$\bar{\tau}_{ave}$ = average shear stress from integration of the local shear, N/m$^2$
$\rho$ = density, kg/m$^3$
$\mu$ = viscosity, kg/ms
$\nu$ = kinematic viscosity, m$^2$/s

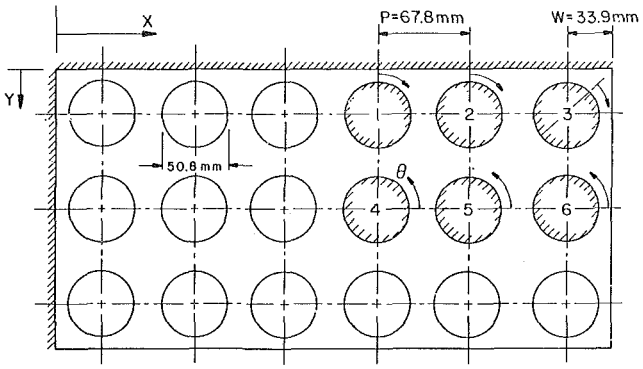


**Fig. 3 Cross-section of rod array showing measurement locations (hatched surfaces) and coordinates**

portion of the bolts within the annulus are faired to minimize flow disturbances. The upstream end of the tube is also streamlined. An aluminum stand with three leveling screws is used to support the inner tube at its downstream end at about 500 mm from the annulus exit. The sensors were located approximately 126 $D_h$ from the annulus entrance, comfortably in a region of fully developed flow. The calibration flow rates were set to achieve shear stress levels close to those expected in the rod bundles.

The pressure gradient along the annulus was measured using seven pressure rings arranged on the outer wall. The pressure rings are connected to a Meriam macromanometer through the Scanivalve pressure selector switch. The overall friction factors agree well with the results of Brighton and Jones [23] and Jones and Leung [26].

The slope of the best fit line to the annulus pressure gradient was used to calculate the inner and the outer wall shear stresses, $\tau_{w_1}$ and $\tau_{w_2}$, using the relations:

$$\tau_{w_1} = -\frac{R_0^2 - R_1^2}{2R_1}\frac{dp}{dx} \tag{2}$$

$$\tau_{w_2} = -\frac{R_2^2 - R_0^2}{2R_2}\frac{dp}{dx} \tag{3}$$

where $R_0$ is the radius of zero shear and $R_1$ and $R_2$ are the inner and outer radii, respectively. The radius of the zero shear stress, $R_0$, was determined from the formula given by Kays and Leung [18] as

$$\frac{R_0/R_2 - R_1/R_2}{1 - R_0/R_2} = (R_1/R_2)^{0.343} \tag{4}$$

With the present diameter ratio, the inner and outer wall shear stresses differ by 5.9 percent. The uncertainties in the shear stresses were estimated to be less than ± 1.08 percent.

Power was supplied to the glue-on hot film probes by a TSI constant temperature anemometer which provides the required heating current and bridge circuit and control functions. The bridge voltage – shear stress relation at an overheat ratio of approximately 1.44 was found to folow closely the well-known law that relates the square of the bridge voltage to the one-third power of the shear stress [27-32]. However, the coefficients in this relation are quite sensitive to ambient temperature. The method of temperature compensation proposed by Kanevĉe [33] was used in this work. Sufficient reproducibility of the measurements and a high enough overall accuracy through both the calibration and measurement phases of the program was achieved by determining the bridge voltage to within ± 1.25 parts in $10^4$ (± 0.5 mv) and the ambient temperature to within ± 0.14°C.

The ambient temperature of the flow was varied during the calibration of the sensors and was monitored with an iron-constantan themocouple. The bridge voltage was measured with a specially constructed signal conditioning unit comprising three op-amps, a d-c offset circuit and a 0.1HZ low pass filter.

To study the effect on the wall shear stress distribution of the rod location relative to the side walls, measurements were

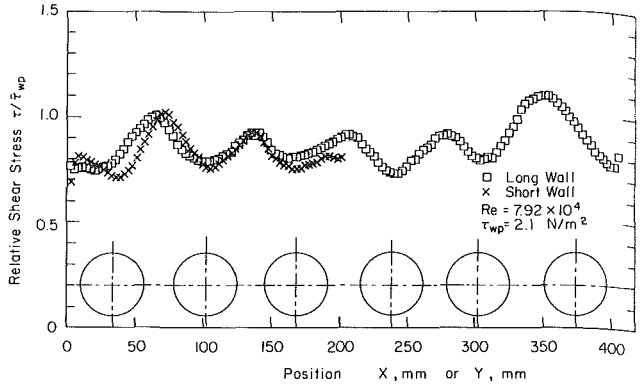


**Fig. 4(a) Wall shear stress distribution on plane walls**

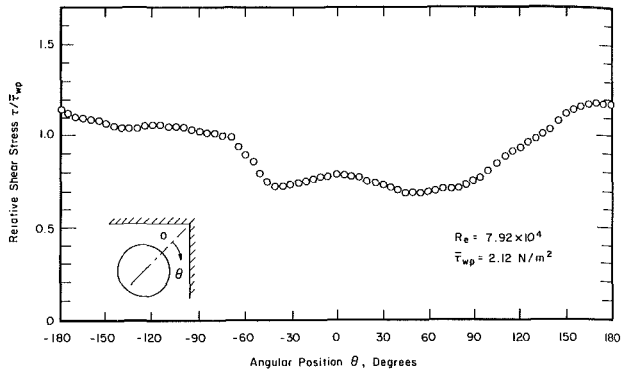


**Fig. 4(b) Wall shear stress distribution on corner rod**

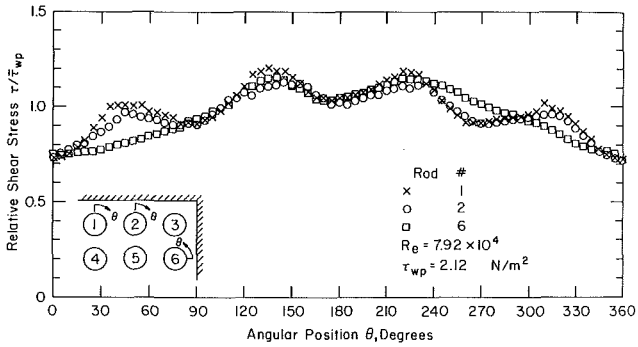


**Fig. 4(c) Wall shear stress distribution on wall adjacent rods**

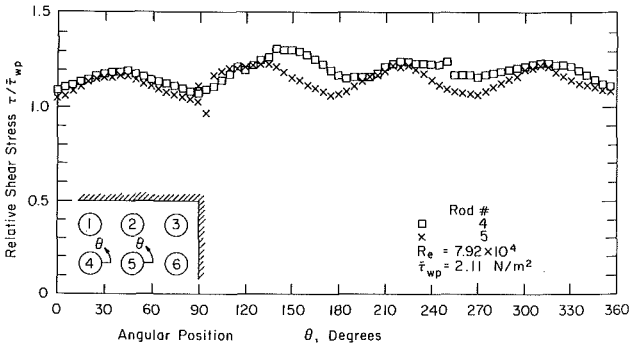


**Fig. 4(d) Wall shear stress distribution on central rods**

performed on six rods as shown in Fig. 3. Also, measurements were performed on two of the side walls. Circumferential measurements on the test rod were taken at 5 degree intervals from 0 to 360 deg for the six chosen locations. Along both the vertical and horizontal side walls, measurements were taken at 3 mm intervals starting 3 mm from the corner.

The results of measurements of velocity profiles along the upper long plane wall and a contour plot of the axial turbulence intensity are included to provide a rationale for the shear stress results. These data wewre obtained with a DISA hot wire probe No. 55P15 and the TSI linearized anemometer.

The results in the balance of the paper have the following uncertainties: our estimates of the probable error (uncertainty) for the dimensionless variables are ± 3.8 percent in the shear stress ratio, $\tau_w/\bar{\tau}_{wp}$, and ± 3.9 percent in the friction factors, $f$, and in the Reynolds number.

## Results

Distributions of the dimensionless local wall shear stress, $\tau_w/\bar{\tau}_{wp}$, on selected wall surfaces are shown in Fig. 4 for Re = $7.92 \times 10^4$. In each case, the average shear stress, $\bar{\tau}_{wp}$, was calculated from axial pressure drop measurements. Figure 4(*a*) compares the shear stress on the long (horizontal) plane wall with that on the short (vertical) plane wall. The shear stress on the corner rod is shown in Fig. 4(*b*). The zero of the abscissa in Fig. 4(*b*) is fixed on the bisector of the corner angle to allow an assessment of the symmetry of the flow about the bisector. Figures 4(*c*) and 4(*d*) compare the shear stress on three of the wall-adjacent rods and on two of the centrally located rods, respectively.

The velocity distribution in the wall layer at selected positions along the long wall was measured with a DISA 55P15 hot wire probe. These distributions were used in conjunction with a Clauser plot [34] and the smooth wall law-of-the-wall [22],

$$\frac{\bar{u}}{u_*} = 5.75 \log \frac{y u_*}{\nu} + 5.5 \tag{5}$$

to find independent estimates of the wall shear stress. In equation (5), $\bar{u}$ is the mean velocity, $y$ is the distance normal to the plane wall and $u_*$ is the local friction velocity, $\sqrt{\tau_w/\rho}$. In the application of Clauser plot, as described in [34], the logarithmic law of the wall, equation (5) is expressed in terms of the friction factor, $f$, as follows:

$$\frac{\bar{u}}{U}\sqrt{\frac{8}{f}} = 5.75 \log \frac{y \bar{U}}{\nu}\sqrt{\frac{f}{8}} + 5.5 \tag{6}$$

The resulting relation is used to plot a family of curves of $u/\bar{U}$ against $y\bar{U}/\nu$ for incremented values of the friction factor. Then, the measured velocity distribution is overlayed on the plot and $f$ is determined by interpolation between the family of curves that are closest to the data points. The friction factors determined in this way are compared in Fig. 5 with those calculated from the directly measured wall shear stress presented in Fig. 4(*a*). Agreement between the two measurement techniques is excellent and is within the uncertainty limits of the two separate measurements, except close to the corner where we expect a significant effect of the adjacent wall.

Figure 6 shows the dimensionless velocity distributions compared with each other, with the smooth wall law-of-the-wall and with a modified law-of-the-wall formula discussed later. The values of $u_*$ needed to construct Fig. 6 were taken from the hot-film shear stress measurements. The extreme sensitivity of the velocity profiles to the values of $u_*$ is evident in Fig. 6 for the velocity profiles at $X = 3.2$, 4.25, 33.9, and 50.8 mm. These, of course, are the positions in Fig. 5 that show the greatest difference between shear stress values determined from the Clauser plot and the hot-film sensor.

In Fig. 7, we show a contour plot of the axial turbulence intensity in the subchannels surrounding the corner rod. This figure, and Figs. 5 and 6 are parts of an extensive experimental program to study the turbulent flow field in the rod bundle using hot wire anemometers as described in [16]. They are included here to help explain the results of the wall shear stress measurements.

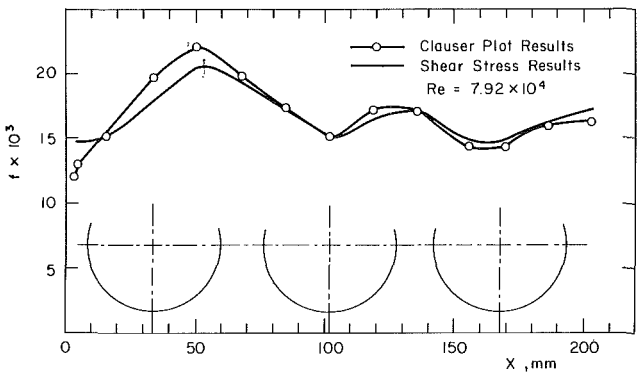


**Fig. 5 Clauser plots for nondimensional velocity distribution near the long wall**

## Discussion of Results

Figure 4(*a*) shows that the shear stress on the short wall, although not completely symmetrical about the center line, increases with the distance from the corner until it reaches a maximum, at about 8 mm from the corner, near the center of

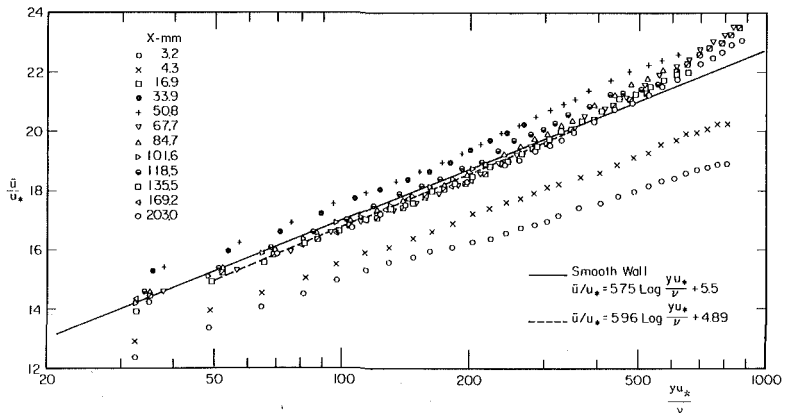


**Fig. 6 Dimensionless velocity distribution on the long plane wall**

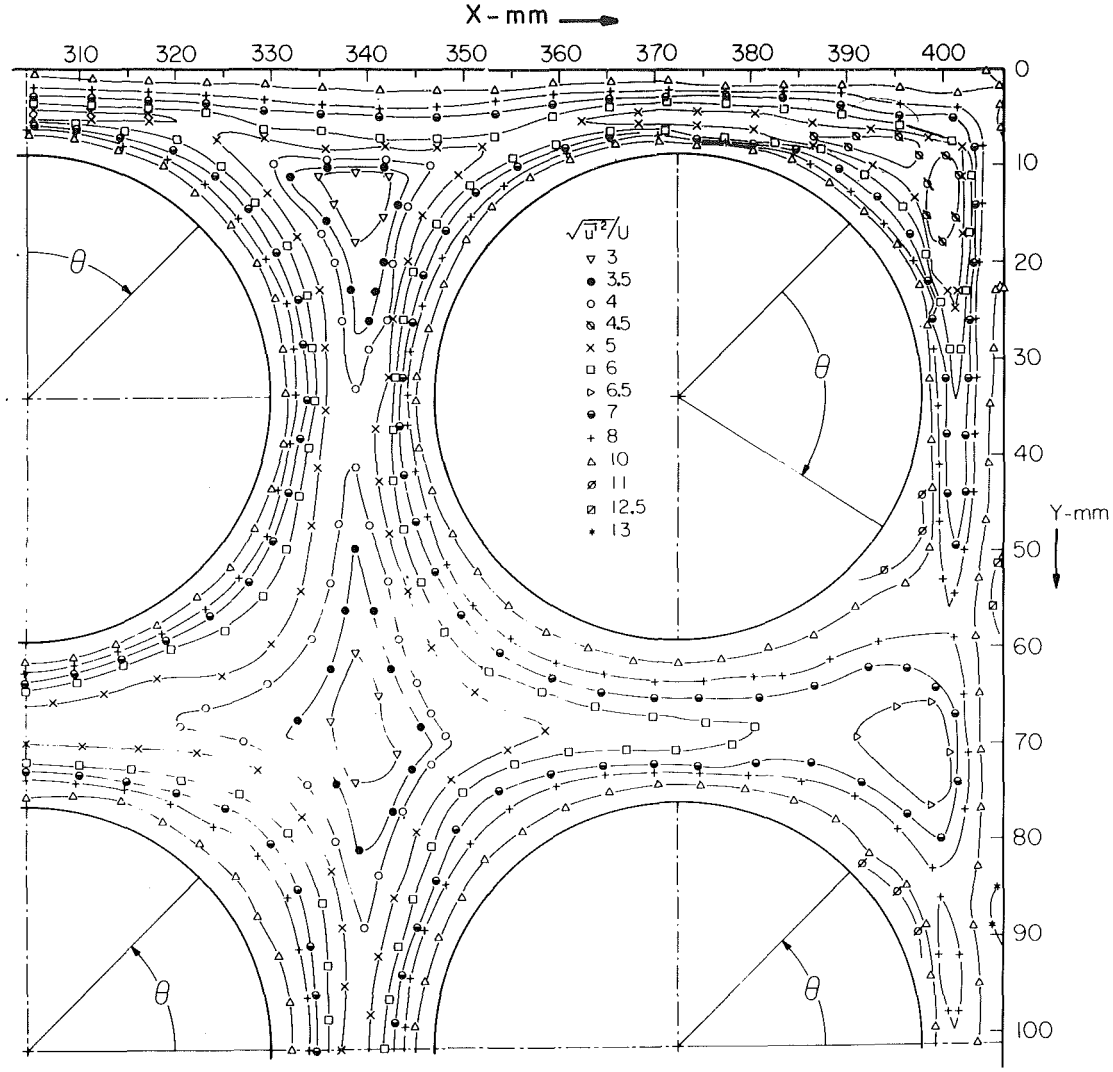


**Fig. 7 Contour plot of axial turbulence intensity**

the maximum flow area of the corner subchannel. Then, the shear stress decreases with the decrease in the flow area until it reaches a minimum near the narrowest gap between the wall and the corner rod. The magnitude of the maximum in the corner subchannel is much less than the magnitude of other maxima away from the corner and in one corner is hardly visible at all. This reduction in the magnitude of the maxima in the corner would result from stronger secondary flows in the corner subchannel than in the other subchannels. Strong secondary flows help to smooth the distribution of the wall shear stress. The distortion of distribution of the axial turbulence intensity in the corner subchannel, Fig. 7, also suggests the existence of the secondary flow cells as discussed below.

The wall shear stress distribution on the long wall does not have a maximum near the maximum flow area of the corner subchannel. Also, this distribution is much more uniform than the distribution on the short wall in the same subchannel. This suggests that the secondary flows near the long wall are stronger than those near the short wall. This difference in the size and strength of the secondary flows can be attributed to the geometry of the test section, which with a height of one-half the width, helps to increase the strength of the secondary flow cells and push them into the corner subchannel, close to the long wall.

The existence of the secondary flows is detected from the distortions of the turbulence intensity and wall shear stress distributions; however, the complete pattern of the secondary flow can not be described without direct measurements of the secondary flow velocities. As the velocities are less than 1 percent of the mean axial velocity their direct measurement is difficult as well as uncertain and was not attempted.

Away from the corner, the distribution of the shear stress on both walls is more or less periodic with maxima near the maximum flow areas, and minima close to the gaps between the rods and the walls. The differences in the magnitudes of the maxima relative to each other, and the relative difference in the magnitudes of the minima, are probably the result of differences in the sag and/or out-of-roundness of the rods.

For the corner rod, Fig. 4(*b*) indicates that the wall shear stress distribution is more or less uniform along the part of the rod surface facing the corner for $\Theta$ between $-45$ and 45 deg. The absence of a significant increase in the wall shear stress, on the part of the rod wall toward the bisector, is further evidence of the existence of strong secondary flows in the corner. This effect, we believe, indicates that the secondary flow cells circulate fluid away from the rod surface toward the corner along the bisector and back along the plane walls. This supposition is supported by the distortion in the axial turbulence intensity as shown in Fig. 7. The bulge in the intensity contour lines away from the rod at the bisector ($\Theta = 0$ deg) indicates that high intensity fluid is carried away from the rod toward the channel center. Near the gap with the side walls, the contour lines bulge toward the rod surface. This indicates

**Table 1 Comparison of friction factor results**

| Reference and Friction Factor Equation | Re = 7.92 x $10^4$ | | |
|---|---|---|---|
| | Friction factor f | % difference $\frac{f_p - f}{f_p} \times 100$ | % difference $\frac{f_\tau - f}{f_\tau} \times 100$ |
| Present work, from pressure drop measurements $f_p$ | 0.0190 | – | -3.61 |
| Present work, from wall shear stress measurements $f_\tau$ | 0.0184 | 3.75 | – |
| Blasius Equation [21] $f = 0.316\ Re^{-0.25}$ | 0.0188 | 1.18 | -2.48 |
| Maubach's Equation [7] $\frac{1}{\sqrt{f}} = 2.035 \log Re\sqrt{f} - 0.989$ | 0.0191 | -0.34 | -3.94 |
| Malak [15] $\sqrt{\kappa_t/f} = 2 \log Re\sqrt{f}/\kappa_t^{3/2} - 0.8$ | 0.0231 | -21 | -25.5 |
| Prandtl [22] $1/\sqrt{f} = 2 \log Re\sqrt{f} - 0.8$ | 0.0189 | 0.64 | -2.99 |
| Rehme [13] $\sqrt{8/f} = A[2.5 \ln Re\sqrt{f}/8 + 5.5] - G^*$ | 0.0191 | -0.33 | -3.93 |

that low intensity fluid is carried toward the rod surface thus pushing the high intensity lines toward it.

The overall distribution of the wall shear stress on the corner rod was expected to be symmetrical around the bisector. However, as shown in Fig. 4(*b*), symmetry is not quite achieved as the distribution is distorted by a hump in the wall subchannel along the long wall. Two factors may contribute to this result. The first is that the test section geometry makes the corners closer to each other in the direction of the short wall than in the direction of the long wall. This could cause the corner influence and consequently the secondary flows to be more pronounced in the short wall subchannels than in the long wall subchannels. Further evidence of this effect is seen in Fig. 7 where the turbulence intensity is distorted by a hump near the rod surface. This distortion is consistent with secondary currents carrying fluid with high turbulence intensity away from the rod. On the other hand, no such distortion that can be related to the effect of secondary flows is detected in the wall subchannel with the long wall. Such an effect will help to smooth the wall shear stress distribution on the part of the rod surface in the short wall subchannel (45 deg $< \Theta <$ 135 deg) compared to the distribution on its geometrically symmetrical section in the long wall subchannel ($-135$ deg $< \Theta < -45$ deg). The other factor may be the effect of slight differences between the size of the two gaps with the two walls as a result of rod sag. Such a geometric defect will increase the difference between the two subchannel wall shear stress distributions.

The wall shear stress distributions on the wall-adjacent rods, as shown in Fig. 4(*c*), indicate that the largest maximum shear stress is found where the flow area is the largest, at $\Theta = 135$ and 225 deg. Also, the distribution is symmetrical around the vertical diameter for rods 1 and 2 and around the horizontal diameter for rod 6. The symmetry of the distribution on rod 2 indicates a weak influence of the short wall on the flow in the long wall subchannels and the central channels. The shear stress distribution on rod 6 is somewhat different from the other distributions, especially in the wall subchannels ($\Theta = 0$ to 90 deg and 270 to 360 deg). This difference between the distributions confirms the greater influence of the corners and the side walls on the flow in the vertical wall subchannels than on the flow in the horizontal wall subchannels as mentioned above and in the discussion of the corner rod results.

For the rods near the channel center the distribution of the wall shear stress has a periodic nature as shown in Fig. 4(*d*). In any subchannel of the eight geometrically symmetric subchannels surrounding each rod, the wall shear stress on the rod surface increases steadily with the flow area. The local minimum is located near the gap between the rods and the local maximum is located near the largest flow area. The regularity and the similarity of the distribution on the rod surface in all subchannels indicate that the effect of the duct walls is not detectable for those subchannels that do not have boundaries with the duct walls.

**Table 2 Summary of wall shear stress measurements results**

| Surface number and location | Re = 7.92 x $10^4$ | |
|---|---|---|
| | Ave. Shear, $N/m^2$ | Max/Min shear stress |
| Rod # 1 (wall rod) | 2.092 | 1.665 |
| # 2 (wall rod) | 2.071 | 1.586 |
| # 3 (corner rod) | 1.947 | 1.739 |
| # 4 (center rod) | 2.528 | 1.211 |
| # 5 (center rod) | 2.415 | 1.2 |
| # 6 (wall rod) | 2.045 | 1.547 |
| Horizontal Wall | 1.828 | 1.509 |
| Vertical Wall | 1.736 | 1.528 |

The friction factor was calculated from the pressure drop data using equation (1). Also, the results of the wall shear stress measurements were integrated numerically for the whole channel as shown in [16]. The result of this integration was used to calculate the friction factor from the equations:

$$\bar{\tau}_{\text{ave}} = \frac{1}{A} \int \tau_w dA \tag{7}$$

$$f_\tau = \frac{8\bar{\tau}_{\text{ave}}}{\rho \bar{U}^2} \tag{8}$$

The friction factor calculated from the wall shear stress is smaller than the one calculated from the pressure drop data by about 3.61 percent but the agreement is well within experimental uncertainty. In Table 1, we compare our results with friction factors calculated from semi-empirical relations for circular tube and annuli [7, 21, 22], and infinite square array of rods [15], and a rod bundle similar to the one used in the present work using the method proposed by Rehme [13, 14]. The second column gives the percentage differences of all results relative to the friction factor calculated from the pressure drop data of the present work as a reference. The third column gives the differences relative to the friction factor calculated from the wall shear stress measurements as a reference. These comparisons indicate that the results of the semi-empirical relations are in excellent agreement with the experimental friction factors of the present work except Malak's [15] result which is very large compared to all the others.

The application of a Clauser plot, as described above and in [34], to determine the friction coefficient, $f$, from the velocity data was used in the present work. As shown in Fig. 5, there is good agreement between the friction coefficients determined from the Clauser plot and the coefficients calculated from the shear stress measurements along the long wall except near the corner. Very close to the corner the large curvature of the iso-velocity lines causes a velocity gradient along the hot wire. This fact and possibly the presence of secondary flows could cause the observed difference in friction factor.

A summary of the results of the shear stress calculations for all surfaces is given in Table 2. The results indicate that the average shear stress on the rod surface decreases as the rod location becomes closer to the corner. The minimum average is found on the corner rod, and the maximum average is on the center rod. On the other hand, the ratio of the local maximum to the local minimum of the wall shear stress is

larger for the rods closer to the plane walls and the corners than it is for the rods near the channel center. The differences in the average and in the magnitude of the local maxima and the local minima from one rod to the other are the result of the test section configuration. Because the size of the gap between the rods and the plane wall is one-half the size of the gap between two adjacent rods, the variation in the local wall shear stress is much larger for the rods close to the plane wall than it is for the rods nearest the channel center where all the gaps with all neighboring rods are equal.

The nondimensional velocity profiles on the long wall, Fig. 6, away from the corner subchannel and the first wall-subchannel after the corner, are slightly lower than the velocities determined from the law-of-the-wall for a smooth wall given in equation (4). The velocity data, for $50 < yu_*/\nu < 350$ and for $X > 51$ mm, were fitted with the logarithmic relation:

$$\bar{u}/u_* = 5.96\log(yu_*/\nu) + 4.89 \quad (9)$$

Considering all the probable errors in the velocity, the shear stress and the displacement measurements, we estimate the uncertainties in the coefficients in equation (9) to be ± 3.1 percent and ± 5 percent, respectively. This indicates that within the experimental uncertainty the measured velocity profiles have the same slope (5.75) as the smooth wall velocity distribution, but the $y$-intercept is always smaller than 5.5. This is in agreement with Rehme's results [7] which fit a logarithmic relation with a slope of 5.75 and $y$-intercept equal to 5.0.

The measured velocities deviate from the logarithmic law at large $yu_*/\nu$. This deviation could be the result of the curvature in the isovelocity lines owing to the presence of the rods. Close to the corner the logarithmic velocity profiles deviate from the law-of-the-wall for smooth walls as shown in Fig. 6. The velocity gradient along the hot wire that results from the curvature of the isovelocity lines combined with the effect of secondary flows on both the velocity and shear stress measurement could cause such a deviation.

## Conclusions

Wall shear stress measurements were performed for a 3 × 6 rectangular rod bundle with square lattice and $P/D = 4/3$. From the results the following conclusions can be drawn:

1. The shape of the distribution and the percentage variation of the wall shear stress on a rod depend on its location relative to the plane walls. The peak to peak variation is largest for rods closest to the corner. But the local average wall shear stress for the rods and consequently the contributions to the overall pressure drop is smallest for rods closest to the corner.

2. The distribution of the local friction factor on the side wall determined from the wall shear stress measurements agrees with the distribution determined from the velocity measurements using Clauser plots [36]. Close to the corner the distribution of the friction factor was not accurately determined in this study. However, the overall friction factor calculated from the integration of wall shear stress agrees within the experimental uncertainties (≤ 3.94 percent) with the friction factor calculated from the pressure drop data and with the results available in the literature [7, 13, 21, 22].

## References


1 Deissler, R. G., and Taylor, M. F., "Analysis of Axial Turbulent Flow and Heat Transfer through Banks of Rods or Tubes," Reactor Heat Transfer Conference of 1956, TID-7529, Part 1, Vol. 2, Nov. 1957, pp. 416–460.

2 Rowe, D. S., "Measurements of Turbulent Velocity Intensity and Scale in Rod Bundle Flow Channels," BNWL-1736, UC-80, 1973.

3 Rowe, D. S., and Johnson, B. M., "Implications Concerning Rod Bundle Cross-flow Mixing Based on Measurements of Turbulent Flow Structure," *Int. J. of Heat and Mass Transfer*, Vol. 17, 1974, pp. 407–419.

4 Trupp, A. C., and Azad, R. S., "The Structure of Turbulent Flow in Triangular Array Rod Bundles," *Nuc. Eng. and Design*, No. 32, 1975, pp. 47–84.

5 Carajilesov, P., and Todreas, N. E., "Experimental and Analytical Study of Axial Turbulent Flows in an Interior Subchannel of a Bare Rod Bundle," ASME 75-WA/HT-51, 1975.

6 Slagter, W., "Finite Element Analysis for Turbulent Flows of Incompressible Fluids in Fuel Rod Bundles," *Nuc. Sc. and Eng.*, Vol. 66, 1978, pp. 84–92.

7 Rehme, K., "The Structure of Turbulent Flow Through a Wall Subchannel of a Rod Bundle," *Nuc. Eng. and Design*, No. 45, 1978, pp. 311–323.

8 Rehme, K., "The Structure of Turbulent Flow Through Subchannels of Rod Bundles," Symposium on Fluid Flow and Heat Transfer over Rod or Tube Bundles, ASME Winter Annual Meeting, New York, Dec. 1979, pp. 67–81.

9 Rowe, D. S., "Progress in Thermal Hydraulics for Rod and Tube Bundle Geometries," Symposium on Fluid Flow and Heat Transfer over Rod or Tube Bundles, ASME Winter Annual Meeting, New York, Dec. 1979, pp. 1–12.

10 Trupp, A. C., and Aly, A. M. M., "Predicted Secondary Flows in Triangular Array Rod Bundles," Symposium on Fluid Flow and Heat Transfer over Rod or Tube Bundles, ASME Winter Annual Meeting, New York, Dec. 1979, pp. 85–94.

11 Fakory, J., and Todreas, N., "Experimental Investigation of Flow Resistance and Wall Shear Stress in the Interior Subchannel of a Triangular Array," Symposium on Fluid Flow and Heat Transfer over Rod or Tube Bundles, ASME Winter Annual Meeting, New York, Dec. 1979, pp. 77–84.

12 Eichhorn, R., Kao, H. C., and Neti, S., "Measurements of Shear Stress in a Square Array Rod Bundle," *Nuc. Eng. and Design*, No. 56, 1980, pp. 385–391.

13 Rehme, K., "Simple Method of Predicting Friction Factors of Turbulent Flow in Non-Circular Channels," *Int. J. of Heat and Mass Transfer*, Vol. 16, 1973, pp. 933–950.

14 Rehme, K., "Laminarströmung in Stabbündeln," *Chemie—Ing. Technik*, Vol. 43, 1971, pp. 962–966.

15 Malak, J., "Pressure Losses and Heat Transfer in Non-Circular Channels with Hydraulically Smooth Walls," *Int. J. Heat and Mass Transfer*, Vol. 18, 1975, pp. 139–149.

16 Abdelghany, M., "Experimental Study of Axial Flow in a Finite Array of Rods and the Application of Finite Element Techniques to Flow in Ducts and Rod Bundles," Ph.D. thesis, Mechanical Engineering, University of Kentucky, Lexington, May 1982.

17 Eichhorn, R., and Fox, T. S., "A Method for the Construction of Flow Nozzles and Wind Tunnel Contraction Sections," ASME JOURNAL OF FLUID ENGINEERING, Vol. 99, 1977, pp. 772–774.

18 Kays, W. M., and Leung, E. Y., "Heat Transfer in Annular Passages, Hydrodynamically Developed Turbulent Flow with Arbitrarily Prescribed Heat Flux," *Int. J. Heat and Mass Transfer*, Vol. 6, 1963, pp. 537–557.

19 Rehme, K., "Turbulent Flow in Smooth Annuli with Small Radius Ratios," *J. of Fluid Mechanics*, Vol. 64, Part 2, 1974, p. 263.

20 Maubach, K., and Rehme, K., "Negative Eddy Diffusivities for Asymmetric Turbulent Velocity Profiles," *Int. J. Heat and Mass Transfer*, Vol. 15, 1972, pp. 425–432.

21 Lawn, C. J., and Elliott, C. J., "Fully Developed Turbulent Flow Through Concentric Annuli," *J. of Mech. Eng. Science*, Vol. 14, No. 2, 1972, pp. 195–204.

22 Schlichting, H., *Boundary Layer Theory*, McGraw-Hill, sixth ed., 1968.

23 Brighton, J. A., and Jones, J. B., "Fully Developed Turbulent Flow in Annuli," ASME *Journal of Basic Engineering*, 1964, pp. 835–844.

24 Okiishi, T. H., and Serovy, G. K., "An Experimental Study of the Turbulent-Flow Boundary-Layer Development in Smooth Annuli," ASME *Journal of Basic Engineering*, 1967, pp. 823–836.

25 Rehme, K., "Simple Method of Predicting Friction Factors of Turbulent Flow in Non-Circular Channels," *Int. J. of Heat and Mass Transfer*, Vol. 16, 1973, pp. 933–950.

26 Jones, O. C. Jr., and Leung, J. C. M., "An Improvement in the Calculation of Turbulent Friction in Concentric Annuli," ASME JOURNAL OF FLUID ENGINEERING, Vol. 103, 1981, pp. 615–623.

27 Bellhouse, B. J., and Schultz, D., "Determination of Mean and Dynamic Skin Friction, Separation and Transition in Low Speed Flow with a Thin Film Heated Element," *J. of Fluid Mechanics*, Vol. 24, 1966, pp. 374–400.

28 Bellhouse, B. J., and Schultz, D., "The Measurement of Fluctuating Skin Friction in Air with Heated Thin Film Gauges," *J. of Fluid Mechanics*, Vol. 32, 1968, pp. 675–680.

29 Brown, G. L., "Theory and Application of Heated Films for Skin Friction Measurement," *Proc. of 1967 Heat Transfer and Fluid Mech. Inst.*, pp. 361–381.

30 Davies, P., and Kimber, G. R., "Skin Friction Measurements with a Heated Film," I. Mech. E., No. C105/76, 1976, pp. 39–44.

31 Liepmann, H. W., and Skinner, G. T., "Shearing Stress Measurements by Use of Heated Elements," NACA TN#3268, 1954, pp. 1–27.

32 Tanner, R. I., "Theory of a Thermal Fluxmeter in Shear Flow," ASME *Journal of Applied Mechanics*, Vol. 89, 1967, pp. 801–805.

33 Kanevcê, G., and Oka, S., "Correcting Hot Wire Readings for Influence of Fluid Temperature Variations," DISA Information, No. 15, Oct. 1973, pp. 21–24.

34 Clauser, F. H., "Turbulent Boundary Layer in Adverse Pressure Gradients," *Journal of the Aeronautical Science*, Vol. 21, 1964, pp. 91–108.

## DISCUSSION

### K. Rehme[2]

Wall shear stresses in non-circular channels are usually meausred by Preston tubes, with air as the working fluid. Therefore wall shear stress measurements with a hot-film probe are of interest as an independent tool, despite their sensitivity to ambient temperature changes.

The authors' results may be affected by the short test section and the considerable sag of the rods. Sixty-two hydraulic diameters of flow development is quite short for such a complicated channel as the authors used. One indication may be the deviation of the non-dimensional velocity profiles in the corner subchannel. The discussion of secondary flow influences on wall shear, mean velocity, and turbulence intensity may also be affected. Detailed measurements of the structure of turbulent flow through rod bundles [35] have shown that distortions in the distribution of Reynolds stresses may be caused by a powerful intersubchannel instability, without any evidence of secondary flow.

### Additional Reference

35 J. D. Hooper, "The Development of a Large Scale Structure in the Rod Gap Region for In-line Flow Through Closely Spaced Rod Arrays," *Proc. 4th Symposium on Turbulent Shear Flows*, Sept. 12–14, 1983, pp. 1.23–1.27.

## Authors' Closure

We wish to thank Dr. Rehme for his interest and comments on our paper.

The paper contains a discussion of the length of the rod bundle and the probable effect of rod sag. We considered the length chosen (62 $D_h$), to be long enough for nearly fully developed flow at the end of the rod bundle, but short enough to produce only a slight rod sag. The maximum rod sag occurs near the mid-point of the rod bundle and there it corresponds to a maximum change in the rod to wall gap of less than 25 percent. All rods should have sagged by about the same amount so only the upper and lower wall regions would have been affected. The position of the rods was carefully maintained at both ends. We wished to avoid flow blockage, so spacers were not used. The results presented in the paper should be useful in their own right, even if the flow is not quite fully developed.

The deviation of the dimensionless velocity profiles in the corner region can be attributed to the measurement technique and the fact that the hot wire probe was traversed normal to the long wall and (therefore necessarily) parallel to the short wall. For $x$ positions closest to the short wall (3.2 and 4.3 mm), the corner bisector is reached at $yu^*/\nu = 190$ and 260, respectively. Thus we do not expect the hot wire to yield good results in that region.

Rehme suggests that interchannel mixing is a result of "coherent structures" of the type found by Hooper [35]. Whether or not the events found by Hooper can be classified that way, it is certainly ture that they would have a profound effect on interchannel mixing. It is also true, that prior to Hooper's work, published results [3, 4, 7, and 10] usually attributed the variation in the wall shear stress to secondary flows, however small they might be. Hooper's studies were carried out in either two parallel subchannels consisting of two half rods and four quarter rods or a row of rods bounded by two plane walls. It is unclear whether the same results would be obtained in larger rod arrays such as the one reported on here. Our own power spectral measurements of the axial velocity component [16] were not made at low enough frequencies to reveal such an effect, but we did not observe the regularity in the hot wire signals that Hooper did (Fig. 4, reference [35]).

[2]Kernforschungszentrum, Karlsruhe, West Germany

  

# Scrutinizing the k-ϵ Turbulence Model Under Adverse Pressure Gradient Conditions

**W. Rodi**
University of Karlsruhe,
Karlsruhe, FRG

**G. Scheuerer**
University of Erlangen-Nürnberg,
Erlangen, FRG.

*The k-ϵ model and a one-equation model have been used to predict adverse pressure gradient boundary layers. While the one-equation model gives generally good results, the k-ϵ model reveals systematic discrepancies, e.g. too high skin friction coefficients, for these relatively simple flows. These shortcomings are examined and it is shown by an analytical analysis for the log-law region that the generation term of the ϵ-equation has to be increased to conform with experimental evidence under adverse pressure gradient conditions. A corresponding modification to the ϵ-equation emphasizing the generation rate due to deceleration was employed in the present investigation and resulted in improved predictions for both moderately and strongly decelerated flows.*

## Introduction

One of the conclusions of the 1980-81 AFOSR-HTTM-Stanford Conference on Complex Turbulent Flows was that the effects of adverse pressure gradients on shear layers were not predicted very well by most turbulence models. This conclusion applies not only to the simple mixing-length approach, but especially to the two-equation and Reynolds stress equation models, employing a transport equation for a characteristic turbulence length scale. Indeed it is vexing to see the now widely used $k$-$\epsilon$ turbulence model to be seriously in error for relatively simple adverse pressure gradient equilibrium boundary layers. The differences between this model and existing data manifest themselves mainly in consistently overpredicted skin friction values and a tendency of the calculated flow to remain attached where experiments indicate separation. The poor predictions can be traced to the fact that the length scale determined by the $\epsilon$-equation rises steeper near the wall than in the case of zero pressure gradient, while experimental data suggest that the length-scale gradient is virtually independent of the pressure gradient over a wide range. For this reason, one-equation models using an empirical length-scale specification yield much better predictions for adverse pressure gradient boundary layers than does the $k$-$\epsilon$ model.

Adverse pressure gradient shear layers are of great practical interest, as they occur on aerofoils, turbomachinery blading or in diffusers. The Evaluation Committee of the Stanford Conference suggested therefore that special attention be focussed on acquiring a higher predictive ability for these flows. In particular, it would be desirable to improve the accuracy of the $k$-$\epsilon$ model which has been found to work well in a large variety of other flow situations. The purpose of the present paper is to trace in detail the reasons for the poor performance of the $k$-$\epsilon$ model when applied to decelerated boundary layers and, based upon this knowledge, to modify the model such that it leads to improved predictions for these flows.

A few suggestions for modifying the $k$-$\epsilon$ model have been published, which aimed at the $\epsilon$-equation. Hanjalic and Launder [1] pointed out the special role that irrotational straining plays in the spectral transport from the large, energy-containing to the small dissipating eddies. The generation term in the modelled $\epsilon$-equation involves in its most general form both rotational and irrotational strain rates. In order to bring the irrotational part into prominence, Hanjalic and Launder [1] multiplied this term by a larger empirical coefficient than the rotational term. For decelerated flows, the modification gives rise to larger $\epsilon$-values, thereby reducing the length scale and also the shear stress $-\rho uv$. This model has been used in the present investigation, and it will be shown to yield improved results.

Another modification suggested by Hanjalic and Launder (see Launder [2]) is to replace the constant $\sigma_\epsilon$ in the diffusion term of the $\epsilon$-equation by a function of the ratio of production to dissipation of kinetic energy. According to Launder [2], however, this modification improves the model calculations only to a minor extent. Launder [2] further suggested to limit the growth of $L$ by simply increasing the computed values of $\epsilon$ to yield $L = 2.5y$ whenever the computed values give rise to larger length scales. This suggestion is certainly a rather crude measure that is not really consistent with the concept of a two-equation model. In summary, none of the model extensions suggested is satisfactory, and the basic failure of the $k$-$\epsilon$ model to yield the observed universal near-wall length scale gradient also under adverse pressure-gradient conditions still lacks an explanation.

In the present paper, the shortcomings of the $k$-$\epsilon$ model in adverse pressure gradient situations are investigated systematically. First, calculations with the one-equation turbulence model proposed by Norris and Reynolds [3] and the low-Reynolds number version of the $k$-$\epsilon$ model of Lam and Bremhorst [4] are compared for two equilibrium adverse

Contributed by the Fluids Engineering Division for publication in the JOURNAL OF FLUIDS ENGINEERING. Manuscript received by the Fluids Engineering Division, February 10, 1984.

pressure gradient boundary layers. While the one-equation model yielded good overall agreement with the data, the $k$-$\epsilon$ model reveals the known discrepancies. In order to trace the reasons for these an analytical analysis was carried out for the log-law region which shows that the set of empirical coefficients in the $\epsilon$-equation, which have been determined by reference to zero pressure gradient boundary layers, are not compatible with the experimental observations in decelerated flows. Finally, the modified $\epsilon$-equation proposed by Hanjalic and Launder [1] is applied and shown to yield improved results.

## Mathematical Models

The mathematical models used in the present investigation employ the usual continuity and momentum equation for two-dimensional shear layers (see e.g., Patel et al. [5]) together with a turbulence model. Calculations have been carried out with the following turbulence models: the standard $k$-$\epsilon$ model (Launder and Spalding [6]), the low-Reynolds number version of the $k$-$\epsilon$ model by Lam and Bremhorst [4], denoted LB, and the one-equation-model given by Norris and Reynolds [3] and denoted NR. With the standard $k$-$\epsilon$ model the viscous near wall zone was bridged by wall-functions, see Launder and Spalding [6], where the velocity at the first grid node is linked to the wall shear stress by the logarithmic law of the wall. For the LB- and NR-model calculations, the no-slip-condition was employed at the wall. In the free stream, the variation of the external velocity inferred from data served as boundary condition.

**The Standard $k$-$\epsilon$ Model.** The $k$-$\epsilon$ model calculates the shear stress with the eddy viscosity hypothesis in the following way:

$$-\overline{uv} = \nu_t \frac{\partial U}{\partial y}; \quad \nu_t = c_\mu \frac{k^2}{\epsilon} \tag{1}$$

where $k$ is the turbulent kinetic energy, $\epsilon$ is its dissipation rate and $c_\mu$ is an empirical constant. The local values of $k$ and $\epsilon$ are determined from transport equations, which read

$$U\frac{\partial k}{\partial x} + V\frac{\partial k}{\partial y} = \frac{\partial}{\partial y}\left(\frac{\nu_t}{\sigma_k}\frac{\partial k}{\partial y}\right) + P_k - \epsilon \tag{2}$$

$$U\frac{\partial \epsilon}{\partial x} + V\frac{\partial \epsilon}{\partial y} = \frac{\partial}{\partial y}\left(\frac{\nu_t}{\sigma_\epsilon}\frac{\partial \epsilon}{\partial y}\right) + \frac{\epsilon}{k}(c_{\epsilon 1}P_k - c_{\epsilon 2}\epsilon) \tag{3}$$

The term $P_k$ is the production rate of $k$ and is given by

$$P_k = -\overline{uv}\frac{\partial U}{\partial y} - (\overline{u^2} - \overline{v^2})\frac{\partial U}{\partial x} \tag{4}$$

The second (underlined) term in equation (4) which involves the irrotational strain rate $\partial U/\partial x$ is neglected in the models introduced here but will be needed when an improved model is suggested below. For the empirical constants the values $c_\mu = 0.09$, $c_{\epsilon 1} = 1.44$, $c_{\epsilon 2} = 1.92$, $\sigma_k = 1.0$, $\sigma_\epsilon = 1.3$ given for instance by Rodi [7] have been adopted. As near wall boundary conditions values of $k$ and $\epsilon$ at the first grid node are related to the wall shear stress by assuming local equilibrium in the $k$-equation, see Launder and Spalding [6].

**The Low-Reynolds Number $k$-$\epsilon$ Model (LB).** The low-Reynolds number version resolves the flow field down to the wall and hence accounts directly for viscous effects. To this end the empirical constants $c_\mu$, $c_{\epsilon 1}$, and $c_{\epsilon 2}$ are multiplied by functions $f_\mu, f_1, f_2$ which involve the molecular viscosity. The exact formulae may be found in Rodi et al. [8] and are not repeated here.

**The One-Equation-Model (NR).** In the one-equation model of Norris and Reynolds [3] the eddy viscosity concept (equation (1)) is used as well, however with a different function $f_\mu$. This model calculates only the turbulent kinetic energy $k$ from a transport equation, whereas the dissipation rate is now obtained from

$$\epsilon = \frac{k^{3/2}}{L}\left(1 + \frac{c_\epsilon}{k^{1/2}L/\nu}\right) \tag{5}$$

where $L$ is prescribed algebraically in the form of a ramp distribution like in the mixing-length approach

$$L = c_D \min\{\kappa y, \lambda\delta\} \tag{6}$$

and $\delta$ is the boundary layer thickness. The empirical constants have the values $c_\mu = 0.084$, $c_D = 6.41$, $c_\epsilon = 13.2$, $\kappa = 0.41$, $\lambda = 0.085$. It should be noted that the same transport equation for $k$ is used as in the LB-two-equation model. In all cases the resulting set of equations is solved with an adapted version of the GENMIX code described by Spalding [9]. Computational details may be found in Rodi et al. [8].

## Results and Discussion

**Comparison of NR- and LB-Predictions.** In this section the results obtained with the LB-model and the NR-model are compared for two experimental situations investigated by Andersen et al. [10]. The first relates to a zero pressure gradient (ZPG) boundary layer and the second to an equilibrium adverse pressure gradient (APG) boundary layer. In these experiments, the freestream velocity was varied according to $U_e \propto x^m$ and the test conditions refer to $m = 0.0$ and $m = -0.20$. At $x = 2.08$ $m$, where the bulk of the comparison with the calculations was made, momentum-thickness-

## Nomenclature

$a_1$ = structural coefficient
$c_f$ = skin friction coefficient
$c_\mu, c_\epsilon, c_{\epsilon 1}, c_{\epsilon 2}, c_{\epsilon 3}, c_D$ = turbulence model constants
$k$ = turbulent kinetic energy
$K$ = acceleration parameter
$P$ = static pressure
$P_k$ = production rate of turbulent kinetic energy
$u_\tau$ = shear velocity
$U, u$ = mean and fluctuating velocity in the stream-wise direction
$V, v$ = mean and fluctuating velocity in the normal direction
$x$ = streamwise coordinate
$y$ = normal coordinate
$y^*$ = nondimensional wall distance
$\delta$ = boundary layer thickness
$\epsilon$ = dissipation rate
$\kappa$ = von Karman - constant
$\lambda$ = turbulence model constant
$\nu_t$ = eddy viscosity
$\rho$ = density
$\sigma_k, \sigma_\epsilon$ = diffusion constants in the turbulence model
$\tau_w$ = wall skin friction

**Subscripts**

e = free stream conditions

**Superscripts**

$-$ = time averaged quantity

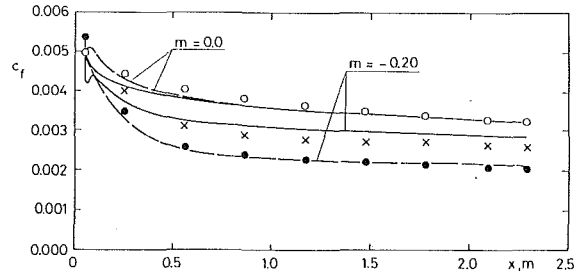


**Fig. 1 Comparison of model predictions and experimental $c_f$-values; data: ○ m = 0.0, ● m = —0.20; predictions: – LB, — — NR, x standard $k$-$\epsilon$ model**

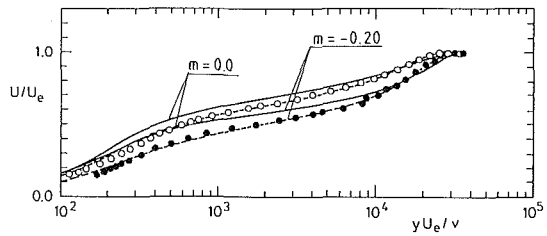


**Fig. 2 Mean velocity profiles at $x = 2.08$ m; key as for Fig. 1**

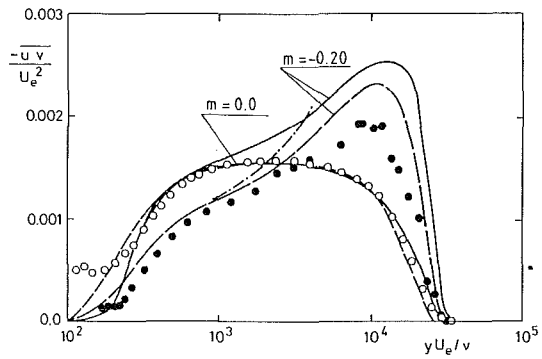


**Fig. 3 Shear stress profiles at $x = 2.08$ m; key as for Fig. 1**

Reynolds numbers of 2900 and 4100 were achieved, so that viscous effects were negligible to first order.

Figure 1 shows the computed skin friction coefficients $c_f = 2\tau_w/\rho U_e^2$. The calculations were started using the experimental mean velocity profiles. For the turbulent kinetic energy and its dissipation rate no data were available, and representative zero-pressure gradient distributions were applied as initial profiles. This explains the rapid variation of $c_f$ close to the starting location. In the ZPG-case, the LB- and NR-model produce almost identical $c_f$-values which are in excellent agreement with the data, at least for $x > 1.5$ m. While the NR-model simulates the influence of the adverse pressure gradient on $c_f$ satisfactorily, the LB-model yields markedly too high $c_f$-values for this case. At the last measurement station the differences amount up to 40 percent. To shed some light on this behavior Fig. 2 compares the computed velocity profiles with the data at $x = 2.08$ m. The NR-model gives an excellent representation of the velocity distribution for both, the ZPG and APG-case. For the ZPG-case the LB-model over-predicts the velocities especially in the near wall region ($y^* = yU_e/r < 1000$), but still gives the correct $c_f$-values. For the APG condition the discrepancies become more severe: the $k$-$\epsilon$ model predictions do not respond sufficiently to the deceleration in the viscous near wall zone and display too rapid an increase of the velocity, which is almost as strong as for the ZPG-flow. This increase in the near wall region leads

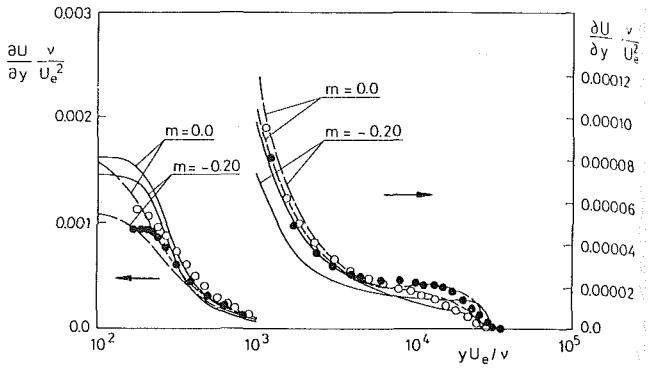


**Fig. 4 Velocity gradients at $x = 2.08$ m; key as for Fig. 1**

to an overprediction of the velocity in the log-law and outer part of the boundary layer.

The corresponding shear stress distributions are presented in Fig. 3 which shows that the poor performance of the $k$-$\epsilon$ model is caused by an overprediction of the shear stress. While both turbulence models yield shear stress profiles in very good agreement with the data for the ZPG-flow, differences become apparent for the decelerated flow. Again it is the one-equation model which gives a very good representation of the shear stress distribution near the wall and overpredicts the shear stress peak in the outer zone only slightly. The discrepancies displayed by the two-equation model are more important: it shows virtually no response to the pressure gradient and produces a steep increase of the shear stress in the immediate vicinity of the wall ($y^* < 1000$). Accordingly, the measured data are considerably overpredicted in this region, and the high level is maintained further outwards in the boundary layer. However, the predicted slope $\partial\overline{uv}/\partial y$ (which in fact enters the momentum equation) is similar to the measured one. The chain-dotted line in Fig. 3 shows $\overline{uv}$ according to equation (7)

$$\frac{-\overline{uv}}{U_e^2} = \frac{c_f}{2} - Ky^* - \sqrt{\frac{c_f}{2}}\frac{1}{\kappa y^*} \tag{7}$$

which may be derived from the momentum equation upon neglect of the convective terms. The acceleration parameter $K$ is defined as $K = \nu(dU_e/dx)/U_e^2$. Relation (7) can be seen to provide a fair approximation to the data in the log-law region.

According to equation (1) the shear stress $-\rho\overline{uv}$ in the $k$-$\epsilon$ model is calculated from the turbulent kinetic energy $k$, its dissipation rate $\epsilon$ and the local velocity gradient $\partial U/\partial y$; it is therefore interesting to see how these quantities are influenced by the pressure gradient. The nondimensionalized velocity gradient is plotted in Fig. 4. At the wall this quantity reduces to $c_f/2$ and the $c_f$-behavior is therefore reflected directly in the near wall zone, i.e., the one-equation model shows a stronger response to the deceleration. Further away from the wall the computed and the measured gradients become similar in magnitude for both the ZPG and the APG case and reveal the typical $y^{-1}$-behavior. It is important to note that, except very close to the wall, the gradients predicted with the $k$-$\epsilon$ model are smaller than those obtained with the NR-model so that they cannot be responsible for the overprediction of the shear stress.

The predicted profiles of the turbulent kinetic energy $k$ are compared with the data in Fig. 5. The distributions for ZPG-flow are discussed first. The calculations with the LB- and NR-model agree only in the log-law and outer part ($y^* > 3000$) of the boundary layer and reproduce the data quite well in this region. Near the wall, the computed profiles differ considerably. Due to probe limitations there are unfortunately no measurements available in this region. The calculations

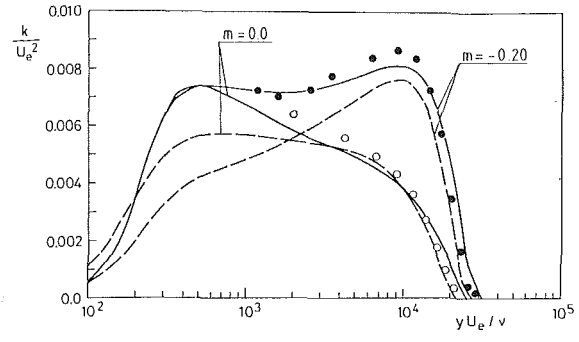


Fig. 5 Turbulent kinetic energy at $x = 1.78$ m; key as for Fig. 1

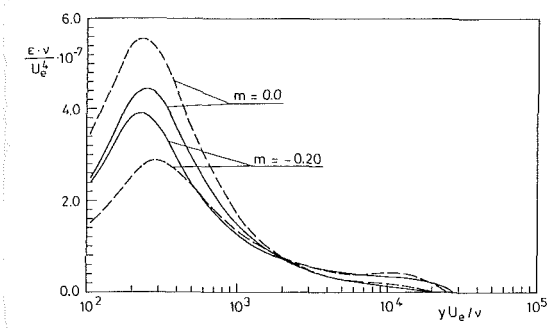


Fig. 6 Dissipation rate of turbulent kinetic energy at $x = 1.78$ m, key as for Fig. 1

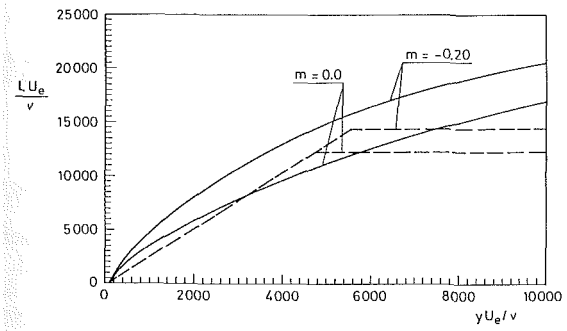


Fig. 7 Turbulence length scales at $x = 2.08$ m; key as for Fig. 1

presented by Patel et al. [5] show however, that the LB-model predictions fit very well existing data in the peak-region ($y^* \approx 500$) while the one-equation model gives too low $k$-values. Therefore, the two-equation model mimics reality better for the ZPG-flow. When an adverse pressure gradient is applied, this model produces an almost identical near wall increase and displays a reaction only beyond $y^* = 800$. On the other hand, the NR-one-equation model yields a distinctly different behavior for the two pressure gradient conditions insofar as it gives a much slower rise in the vicinity of the wall for the APG-case. In the log-law region the existing data are better fitted by the $k$-$\epsilon$ model, while in the outer zone both models produce similar $k$-distributions in good agreement with the data. It appears that the main differences between the two models and also discrepancies with the data originate from the region very close to the wall ($y^* < 1000$). The fact that the NR-model predicts a reduction of $k$ in this region under the influence of an adverse pressure gradient, while the LB-model does not, can be explained by the relative change of production of $k$, $P_k$, and dissipation rate $\epsilon$. Figures 6 and 8 below, will show that in the NR-calculations, $P_k$ is reduced more than $\epsilon$ by the deceleration while both are reduced by approximately the same amount in the LB-calculations.

The third quantity that determines the shear stress in the $k$-$\epsilon$ model is the dissipation rate $\epsilon$. Its variation with wall distance is shown in Fig. 6. The first feature to notice is that for the ZPG-case the LB- and NR-models yield similar shapes but substantially different peak-values for the $\epsilon$-profiles. It has been demonstrated by Patel et al. [5] that it is again the two-equation model that simulates existing data better. In the log-law region, the two curves behave similar. For the decelerated flow both models yield a reduction in $\epsilon$. It may seem somewhat surprising that this reduction is much stronger in the case of the one-equation model as one might expect that this would lead to an increase of the shear stress (according to equation (1)), which is not the case (see Fig. 3). In fact $-\overline{uv}$ actually decreases because the fall in $\epsilon$ is more than offset by the parallel decrease of $k$ shown in Fig. 5.

A more instructive picture emerges when $k$ and $\epsilon$ are combined to yield the length-scale $L = k^{3/2}/\epsilon$, whose distribution is shown in Fig. 7. For the one-equation model the near wall distribution is prescribed independently of the pressure gradient and is given by equation (6). In the most important near wall and log-law regions this variation is reproduced to a good approximation by the $k$-$\epsilon$ model for the ZPG case. In the APG-case a steeper increase of the length scale results, which is mainly caused by the fact that too high $k$-levels persist near the wall.

As was mentioned already, the high $k$-values are due to the dissipation rate $\epsilon$ being too small relative to the production $P_k$ shown in Fig. 8, and this may be traced to the production of $\epsilon$ being too small. The word "relative" is very important here for, as can be seen from Fig. 6, the $\epsilon$-values predicted by the LB-model are actually larger than those resulting from the NR-model (for the APG-flow). In any case, an increase in $\epsilon$ would directly reduce $-\overline{uv}$ and $L$ via equation (1) but what is much more important, would reduce also $k$ and hence again $-\overline{uv}$ and $L$. Further, according to equation (4), $P_k$ would decrease which would also act to reduce $k$ and finally $-\overline{uv}$. Due to the strong interlinkage and feedback, a relatively small increase in the production of $\epsilon$ can have a significant effect on the predictions.

**Analysis.** The results presented above have demonstrated that the poor performance of the $k$-$\epsilon$ model under APG-conditions can be traced to the $\epsilon$-equation. It will now be shown by an analytical analysis for the log-law region that the empirical coefficients used in this equation are not really compatible with experimental observations in decelerated flows. In order that the $k$-$\epsilon$ model is consistent for ZPG-flow the constants in the $\epsilon$-equation must satisfy the following condition:

$$c_{\epsilon 1} = c_{\epsilon 2} - \frac{\kappa^2}{\sigma_\epsilon \sqrt{c_\mu}} \tag{8}$$

To obtain this relation from the $\epsilon$-equation (3) the following assumptions have been invoked: (i) the convection of $\epsilon$ is negligible, (ii) the local shear stress $-\overline{uv}$ is approximately equal to the friction velocity $u_\tau^2$, (iii) the production of $k$ balances the dissipation rate and (iv) the logarithmic law of the wall applies. A corresponding relation is now derived for APG-flows. Assumption (i) is kept, while the shear stress is now approximated by equation (7) which involves an explicit dependence on the pressure gradient. Experiments have shown that the logarithmic law of the wall prevails even under APG-conditions, so that the log-law is retained to describe the variation of $U$. The final assumption is that the near-wall length scale is independent of the pressure gradient and is described (as in the one-equation model) by

$$L = \frac{\kappa}{c_\mu^{3/4}} y \tag{9}$$

For $c_\mu = 0.09$ and $\kappa = 0.41$ this yields the experimentally observed variation $L = 2.5y$. When these conditions are in-

serted into the $\epsilon$-equation and $k$ is eliminated via a structural coefficient

$$a_1 = \frac{-\overline{uv}}{k} = c_\mu^{1/2}$$

independent of the pressure gradient (as found experimentally by Bradshaw [11]) the following relation results:

$$c_{\epsilon 1} = c_{\epsilon 2}\sqrt{\frac{-\overline{uv}}{u_\tau^2} - \frac{\kappa^2}{\sigma_\epsilon c_\mu^{1/2}} + \frac{\kappa^2}{\sigma_\epsilon c_\mu^{1/2}}} \cdot \left[\frac{3}{2}\cdot\frac{dP/dx}{-\overline{uv}/y} - \frac{3}{4}\cdot\left(\frac{dP/dx}{-uv/y}\right)^2\right] \quad (10)$$

The variation of the shear stress $-\overline{uv}$ in the log-law region is given by equation (7). From this it can be seen that $-\overline{uv}/u_\tau^2$ rises (above unity) with increasing adverse pressure gradient so that $c_{\epsilon 1}$ also has to be increased in order that the $\epsilon$-equation be consistent with experimental observations entering the derivation of (10). The bracketed term in (10) has a similar, but smaller effect on $c_{\epsilon 1}$. In the calculations presented above, $c_{\epsilon 1}$ as determined from the ZPG-formula (8) was used, and hence it is not surprising that the APG observations were not recovered.

**Test of Model Improvements.** From the preceding two subsections two features become obvious: The first is that the disagreement with the data for APG-flow originates mainly from the viscous near wall region. Computations were therefore carried out also with the standard $k$-$\epsilon$ model in which this region is bridged by wall functions. The second feature, which may be delineated from the preceding discussion is that an increase in the generation rate of $\epsilon$ may lead to a better simulation of APG-boundary layers. Therefore additional calculations were carried out with the model of Hanjalic and Launder [1]. In this model the irrotational contribution to the production $P_k$ is retained (underlined term in equation (4)), but in the $\epsilon$-equation this contribution is multiplied with a constant $c_{\epsilon 3}$ instead of $c_{\epsilon 1}$ multiplying the rotational part. The modified $\epsilon$-equation reads

$$U\frac{\partial \epsilon}{\partial x} + V\frac{\partial \epsilon}{\partial y} = \frac{\partial}{\partial y}\left(\frac{\nu_t}{\sigma_\epsilon}\frac{\partial \epsilon}{\partial y}\right) - c_{\epsilon 1}\frac{\epsilon}{k}\overline{uv}\partial U/\partial y - c_{\epsilon 3}(\overline{u^2} - \overline{v^2})\frac{\partial U}{\partial x} - c_{\epsilon 2}\epsilon^2/k \quad (11)$$

The empirical constant $c_{\epsilon 3}$ was given the value 4.44 by Hanjalic and Launder [1]. For decelerated flows both production terms are positive and enhance the values of $k$ and $\epsilon$, respectively, the latter having the desired effect. Due to the relatively large value of $c\epsilon_3$ (compared with $c_{\epsilon 1} = 1.44$), the modified $k$-$\epsilon$ model becomes much more sensitive to deceleration than the standard model. It should be noted that the modified dissipation-rate equation (11) is not invariant to rotations of the coordinate system, whereas the original $\epsilon$-equation (3) is. This restricts the general applicability of the modified model equation. As the $k$-$\epsilon$ model does not provide values of $\overline{u^2}$ and $\overline{v^2}$ explicitly, Hanjalic and Launder [1] suggested to relate these quantities empirically to the turbulent kinetic energy via the experimentally known structural coefficients $\overline{u^2}/k = 1.1$ and $\overline{v^2}/k = 0.25$.

The two model versions just described were first applied to the moderately decelerated flow used previously as test case (experiments of Andersen et al. [10]). Relative to the LB-prediction the standard $k$-$\epsilon$ model gives already an improved prediction of $c_f$ (see Fig. 1). This is achieved by the fact that at least at one point in the logarithmic zone (where the wall functions are specified), the velocity is forced to have the "correct" value. However, there is still substantial disagreement with the data. The Hanjalic-Launder-model on the other hand

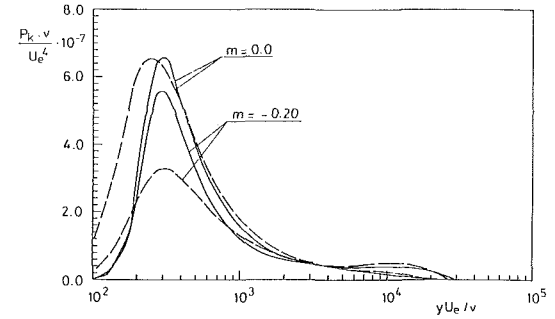


**Fig. 8 Production rates of turbulent kinetic energy $k$ at $x = 2.08$ m; key as for Fig. 1**

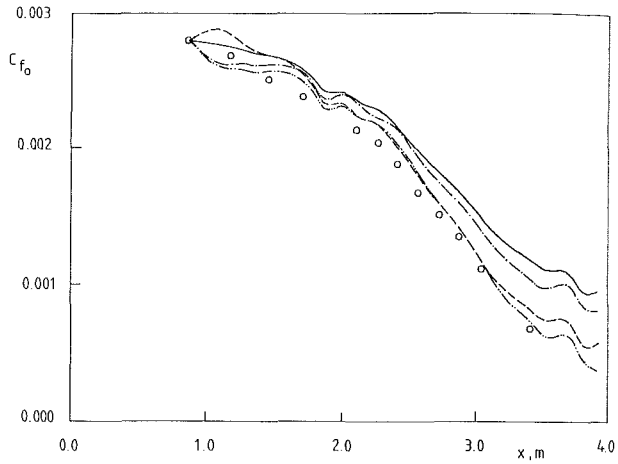


**Fig. 9 Skin friction coefficient for the experiments by Samuel and Joubert: data: ○; predictions: — LB, — — NR, — · standard $k$-$\epsilon$, — · · — Hanjalic-Launder model.**

yielded very good agreement with the data and the resulting $c_f$-variation coincides with the NR-curve in Fig. 1.

A similar picture evolved for a case with stronger deceleration, namely the experiment of Samuel and Joubert [12], in which the flow was close to separation. The variations of skin friction coefficient for this test case are shown in Fig. 9. Note that $c_{f0}$ is defined as $2\tau_w/(\rho U_0^2)$ where $U_0$ is the reference velocity at the wind tunnel entrance. The LB-model reproduces the experimental situation rather poorly. For $x > 3$ m the predicted values are too large by a factor of two. The standard $k$-$\epsilon$ model using wall functions gives only minor improvements. Good overall agreement is obtained with the NR-model, which yields only slightly too high values for the last measurement station. The best reproduction of the data is achieved with the Hanjalic-Launder-model. For moderate adverse pressure gradients ($x < 2$ m) the results are nearly identical with those of the NR-model, as was also the case for the previous test problem. For the stronger deceleration towards the end of the test section the Hanjalic-Launder-model proves to be superior to the one-equation model.

## Conclusion

The present investigation allows the following conclusions. The $k$-$\epsilon$ turbulence model gives consistently too high $c_f$-values when applied to decelerated boundary layers. It was shown that this originates from too steep an increase of the turbulent kinetic energy $k$ and consequently the shear stress $-\overline{uv}$ near the wall. This steep increase is caused by $\epsilon$-values which are too small relative to the production rate of $k$ and contribute therefore directly via the eddy viscosity relation and indirectly

via the resulting higher $k$-values to the described behavior. An analytical treatment has shown that an enhancement of the $\epsilon$-generation in adverse pressure gradient situations is necessary in order to correct this feature. A modification of the $\epsilon$-equation to this effect, proposed by Hanjalic and Launder [1], was employed. It yielded good predictions for moderately and strongly decelerated flows. Finally, the one-equation model used for comparison purposes produced excellent results for all test cases.

## Acknowledgments

The authors are grateful to Miss A. Messner for her expert typing of the manuscript.

## References

1 Hanjalic, K., and Launder, B. E., 1980, "Sensitizing the Dissipation Equation to Irrotational Strains," ASME JOURNAL OF FLUIDS ENGINEERING, Vol. 102, p. 34.

2 Launder, B. E., 1984, "Second Moment Closure: Methodology and Practice," *Turbulence Models and Their Applications*, Vol. 2, Edition Eyrolles, Saint-Germain Paris.

3 Norris, L. H., and Reynolds, W. C., 1975, "Turbulent Channel Flow with a Moving Wavy Boundary," Rept. No. FM-10, Stanford Univ., Dept. Mech. Eng., Stanford, CA.

4 Lam, C. K. G., and Bremhorst, K. A., 1981, "Modified Form of the k-$\epsilon$-Model for Predicting Wall Turbulence," ASME JOURNAL OF FLUIDS ENGINEERING, Vol. 103, p 456.

5 Patel, V. C., Rodi, W., and Scheuerer, G., 1985, "A Review and Evaluation of Turbulence Models for Near Wall and Low-Reynolds-Number Flows," *AIAA Journal*, Vol. 23, p. 1308.

6 Launder, B. E., and Spalding, D. B., 1974, "The Numerical Computation of Turbulent Flow," *Comp. Meth. in Appl. Mech. and Eng.*, Vol. 3, p. 269.

7 Rodi, W., 1980, "Turbulence Models and Their Application in Hydraulics," International Association for Hydraulic Research Publ.

8 Rodi, W., Celik, I., Demuren, A. O., Scheuerer, G., Shirani, I., Leschziner, M. A., and Rastogi, A. K., 1982, *Proc., 1980-81 AFOSR-HTTM-Stanford Conference on Complex Turbulent Flows*, ed. S. J. Kline, B. J. Cantwell, G. M. Lilley, Vol. III, 1495.

9 Spalding, D. B., 1979, *GENMIX; A General Computer Program for Two-Dimensional Parabolic Phenomena*, Pergamon Press, Oxford.

10 Andersen, P. S., Kays, W. M., and Moffat, R. J., 1972, "The Turbulent Boundary Layer on a Porous Plate: An Experimental Study of the Fluid Mechanics for Adverse Free-Stream Pressure Gradients," Rept.-No. HMT-15, Stanford Univ., Dept. Mech. Eng., Thermosc. Div., Stanford, CA.

11 Bradshaw, P., 1967, "The Turbulence Structure of Equilibrium Boundary Layers," *J. Fluid Mech.*, Vol. 29, p. 625.

12 Samuel, A. E., and Joubert, P. N., 1974, "A Boundary Layer Developing in an Increasingly Adverse Pressure Gradient," *J. Fluid Mech.*, Vol. 66, p. 481.

# Effect of a Vibrating Upstream Cylinder on a Stationary Downstream Cylinder

**M. Moriya**
Research Scientist.

**H. Sakamoto**
Professor.

Department of Mechanical Engineering,
Kitami Institute of Technology,
Kitami, 090, Japan

*The flow around two circular cylinders in tandem arrangement in uniform flow where the upstream cylinder is forcibly vibrated in direction normal to the approach flow was experimentally studied at Reynolds number of $6.54 \times 10^4$. The spacing ratio $l/d$ ($l$: distance between centers of cylinders, $d$: diameter of circular cylinders) and the ratio of amplitude to cylinder diameter $a/d$ ($a$: amplitude of transverse vibration of cylinder) were varied from 2 to 6 and 0 to 0.029 respectively. The effects of the vibration of the upstream cylinder on the downstream cylinder were discussed. In particular, two distinct "lock-in" regions were observed when the upstream cylinder was vibrated with a spacing ratio of $l/d = 3.0$. The cylinder vibration was so effective even for $a/d$ as small as 0.017 to cause two different flow patterns.*

## 1 Introduction

Many studies have been done on the flow around two circular cylinders, and most of those have been devoted to examining the time-mean aerodynamic forces and vortex shedding. The engineering importance of this subject has been pointed out by Zdravkovich [1], when he investigated the flow around two circular cylinders in various arrangements. However, the fluctuating pressure and aerodynamic forces acting on the cylinder are not well understood.

Recently, Arie et al. [2] revealed the behavior of the fluctuating pressure around two circular cylinders in tandem arrangement from the studies of rms values of the fluctuating pressure on the surface of the circular cylinders and spanwise correlation between pressures at two points. They also revealed the behavior of the fluctuating aerodynamic forces from the circumferential correlation. The authors [3] revealed the behavior of the fluctuating force from the ensemble-averaging of the pressure fluctuation on the surface of the circular cylinder based on the velocity signal of the periodic vortex shedding. Tanida et al. [4] studied experimentally on tandem circular cylinders in uniform flow at low Reynolds numbers. There, one of the two cylinders was oscillated in either transverse or longitudinal direction. It was reported that the transverse oscillation of downstream cylinder became unstable in the region of synchronization.

Two circular cylinders placed in a flow need not always be steady; they can be vibrated by the unsteady aerodynamic forces. Vibration and noise problems of heat exchangers belong to this category. In the case of two circular cylinders, unlike a single cylinder, vibration is caused by aerodynamic force arising from the flow interference between the closely placed cylinders, and the vibrations of two cylinders are linked together. Hence it is called "bundle vibration." Tanaka [5] and Conners [6] studied cylinder bundle vibrations in cross-flow and model tests were conducted to measure the fluid forces.

In this paper, flow around two circular cylinders in tandem arrangement in uniform flow, where the upstream cylinder is forcibly vibrated in direction normal to the approach flow, is dealt with and the effects of the vibration of the upstream cylinder on the downstream cylinder are discussed.

## 2 Experimental Apparatus and Procedure

In this experiment a recirculation type wind tunnel which has 0.5m × 0.5m cross section and 2.5m long rectangular test section was used. The approaching velocity at the test section was measured at the location of the upstream circular cylinder by means of a Pitot-static tube without presence of the cylinders. Flow two-dimensionality at the test section was well maintained within $6.2d$ ($d$: diameter of the circular cylinder) from the center plane of the wind tunnel and the error was less than 1 percent. The freestream velocity in this experiment was maintained constant at $U_\infty = 20 \pm 0.2$ m/s and the rms longitudinal velocity fluctuation was about 0.4 percent of the approach velocity.

The downstream and upstream cylinders tested were machined brass and aluminum respectively with 49mm diameter, $d$, with smooth surface finish. The cylinders were placed at the test section at right angles to the approach flow, and the clearance between the cylinders and wind tunnel walls were sealed with "O" rings. The flow blockage due to the presence of the cylinder is 9.8 percent in area. A 0.8mm diameter pressure tap was located at the center of the span to measure the time-mean pressure on the surface of the cylinder by Betz type manometer with its accuracy of 0.2 mmAq. The time-mean pressure distribution was obtained by rotating the cylinder in every 10 degrees from 0 to 180 deg. Also the fluctuating pressure at the surface of the cylinder was measured by

Contributed by the Fluids Engineering Division for publication in the JOURNAL OF FLUIDS ENGINEERING. Manuscript received by the Fluids Engineering Division, April 9, 1984.

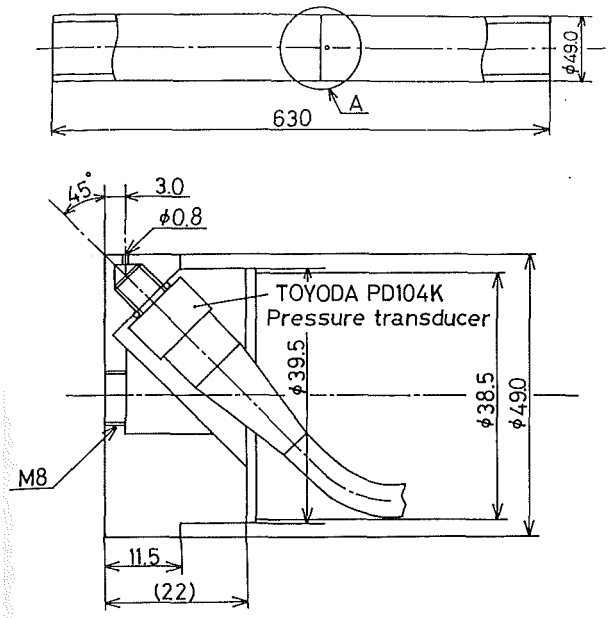


Fig. 1 Sketch of the installation of pressure transducer

a semiconductor pressure transducer. As shown in Fig. 1, the pressure sensing element was mounted in a cavity on the surface of the cylinder, and the gain factor was found to be $1 \pm 0.06$ from the test of frequency response.

The entire upstream cylinder made from aluminum was forcibly vibrated by an electro magnetic vibrator (EMIC F050-C). Frequency of the vibrator (EMIC 901-F type) can be varied continuously from 5 Hz to 5 KHz, and the frequency of the forced vibration of the upstream cylinder was chosen on the basis of the frequency of the vortex shedding from the cylinder at rest. The vortex shedding frequency was determined from the power spectra of the surface pressure fluctuation as the frequency corresponds to a spectrum peak. The vibration behavior of the forcibly vibrated cylinder was monitored by a vibration meter (EMIC 508 type, DM-005 pick up). The output signal from the vibration meter very well fit to a sinusoidal curve. The rate of the positional deviation of the cylinder from neutral position due to the forced vibration to the diameter of the circular cylinder was varied from 0 to 2.9 percent.

In order to evaluate the fluctuating force acting on the cylinder, first ensemble-averaged fluctuating pressure was obtained for each angular position of the pressure transducer. Then the instantaneous pressure distribution along the circumference for each phase was obtained. The fluctuating velocity signal in the irrotational flow outside the wake behind the upstream cylinder was taken as a base signal for ensemble-averaging. In order to avoid the disturbance on the flow field around the cylinders due to the presence of the hot wire probe, from trial and error, the base signal was obtained at the location where the base signal shows the most periodical velocity fluctuation without causing disturbance on the flow field

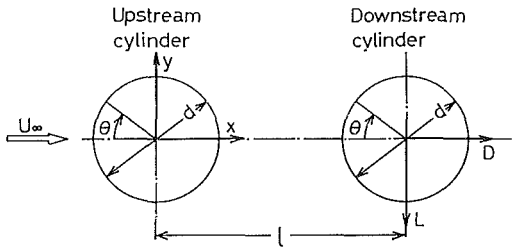


Fig. 2 Schematic diagram of the two circular cylinders in tandem arrangement

around the two cylinders. Signals from both the pressure transducer and hot wire probe were digitized simultaneously at a rate to obtain 80 samples per period of the vortex shedding from the upstream cylinder. Hence the fluctuating pressure coefficient at $j$th phase for a particular angular position $\theta$ is defined as

$$C_p'(\theta, j) = <p'(\theta, j)> \Big/ \frac{1}{2}\rho U_\infty^2 \quad \begin{matrix}(\theta = 0,\ 10,\ ,\ ,180 \text{ deg}) \\ (j = 1,2,\ ,\ ,\ ,\ ,\ ,\ 80)\end{matrix}$$

where $< >$ denotes ensemble mean. The time for the signal analysis for the ensemble-averaging by digital computer is approximately 15 seconds and the number of averages is 400 to 500. Thus the fluctuating lift can be calculated from integration of the fluctuating pressure at $j$th phase obtained from the ensemble-averaging along the circumference.

$$C_L'(j) = \frac{1}{2}\int_0^{2\pi} C_p'(\theta, j)\sin\theta d\theta \quad (j = 1,2,\ ,\ ,\ ,\ ,\ ,\ ,\ 80)$$

## 3 Results and Discussions

The placement of the two circular cylinders, the coordination system and the definitions of the symbols are shown in Fig. 2. The Reynolds number based on the diameter of the cylinder is $6.53 \times 10^4$ and no adjustments are made for the flow blockage on the experimental data. Experiments were carried out for the spacing ratio $l/d = 2.0$ to 6.0 but discussed mainly for $l/d = 3.0$ and 3.5 where the effects of the vibration of the upstream cylinder is significant.

In many experimental investigations on the flow around two circular cylinders in tandem arrangement at rest, it was reported that there are typically two different types of flow patterns [Zdravkovich [1], Arie [2], etc.]. The flow field within the spacing between the two cylinders exhibits different flow patterns beyond the critical spacing (about 3.5 diameters). For the spacing smaller than the critical spacing, the separated shear layer from the upstream cylinder reattaches onto the downstream cylinder, before vortex streets form, hence this kind of flow is defined as reattachment flow. On the other hand, for the spacing greater than the critical spacing, the vortex streets form behind both the cylinders. This type of flow is defined as jump flow.

**3.1 Lock-in Region.** Koopman [7], Bishop and Hassan [8], and Griffin and Ramberg [9] etc. made experimental in-

## Nomenclature

$a$ = amplitude of transverse vibration of cylinder
$\bar{C}_D$ = time-mean drag divided by $qd$
$C_L'(\text{rms})$ = rms lift divided by $qd$
$\bar{C}p$ = time-mean pressure divided by $qd$
$C_p'$ = rms pressure divided by $q_\infty d$
$d$ = diameter of circular cylinder
$f$ = frequency used in power spectrum
$f_k$ = frequency of overtex shedding
$f_h$ = frequency of transverse vibration of cylinder
$l$ = distance between centers of two cylinders
$q$ = free-stream dynamic pressure $= (1/2)\rho U_\infty^2$
$R$ = Reynolds number $= U_\infty d/\nu$
$S_t$ = Strouhal number $= fd/U_\infty$
$U_\infty$ = time-mean freestream velocity
$x,y$ = Cartesian coordinate system (see Fig. 1)
$\theta$ = angle measured from stagnation point of cylinder
$\nu$ = kinematic viscosity
$\rho$ = density of fluid

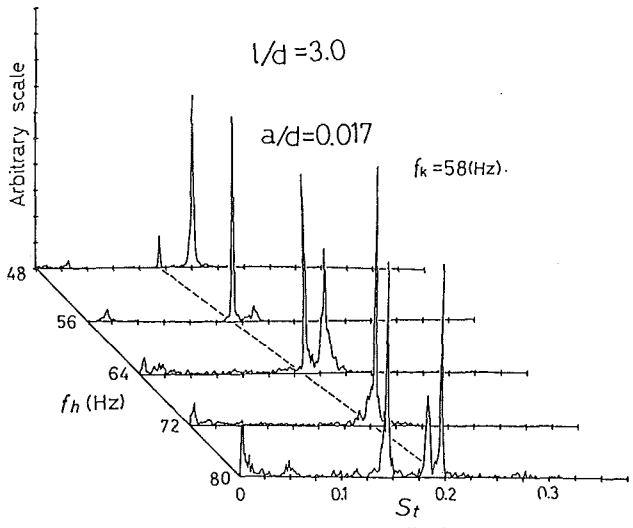


Fig. 3 Power spectra distributions

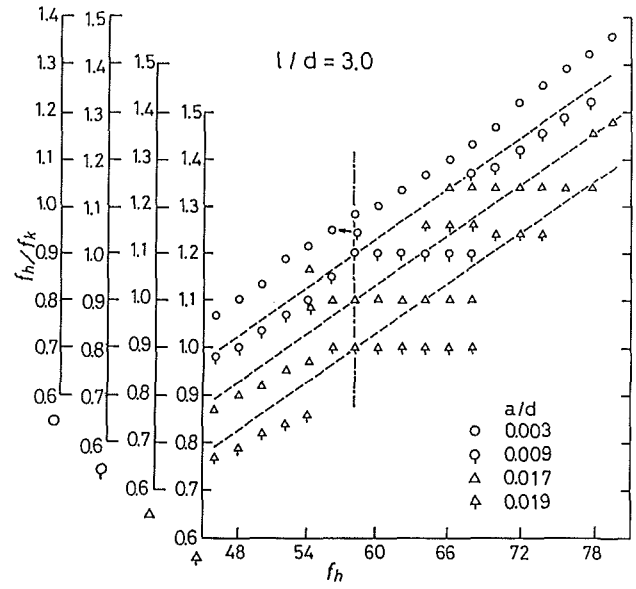


Fig. 4 Relationship between $f_h/f_k$ and $f_h$. The uncertainty in the ordinate is ±0.02 and that in the abscissa is ±0.001

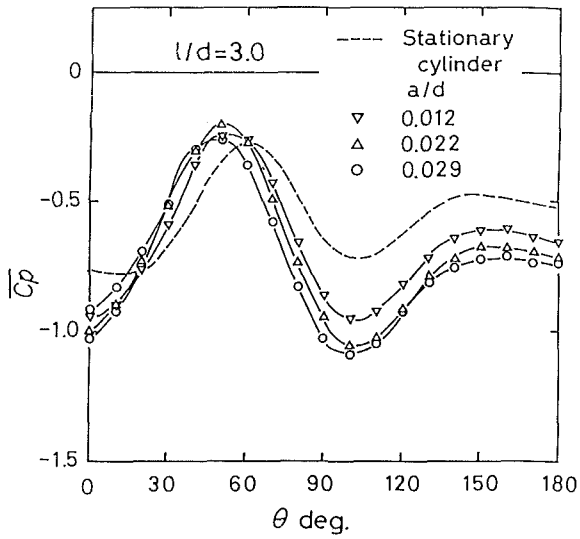


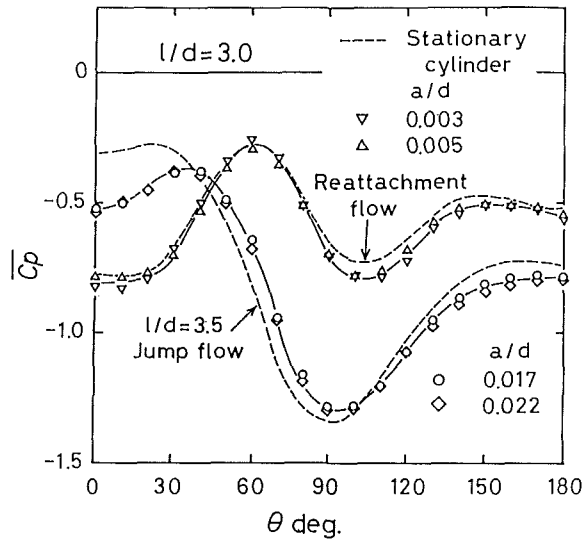


Fig. 5(*a*) and (*b*) Time-mean pressure distributions along the surface of the downstream cylinder for $1/d = 3.0$. (*a*) is for $f_h/f_k = 1.0$ and (*b*) is for $f_h/f_k = 1.24$. The uncertainty in the ordinate is ±0.01 and that in the abscissa is ±0.2 deg. Lines are for visual aids only.

vestigations on the flow around a single circular cylinder vibrating in the direction normal to the approach flow, and it was reported that there is a domain where the cylinder vibration and vortex shedding frequency are synchronized.

In the present study, characteristics of the fluctuating pressure acting on the downstream cylinder were studied when the upstream cylinder is vibrated in the direction normal to the approach flow. When the frequency of vibration of the upstream cylinder is close to the vortex shedding frequency of the downstream cylinder, the lock-in phenomenon on the fluctuating pressure on the surface of the downstream cylinder was observed. In particular, in the case of $1/d = 3.0$ there were two lock-in regions of the fluctuating pressure of the downstream cylinder for certain amplitudes of the vibration of the upstream cylinder. Figure 3 shows the power spectra of fluctuating pressure on the surface of the downstream cylinder at $\theta = 90$ deg against the Strouhal number $S_t$ ($S_t = fd/U_\infty$; $f$ is the frequency of a spectrum) for various frequency of the forced vibration $f_h$ when $a/d = 0.017$. The broken line corresponds to the frequency of the forced vibration. When the upstream cylinder is vibrated near its natural vortex shedding frequency, say at $f_h = 56$Hz, because of lock-in phenomenon, a peak of the power spectrum occurs at the frequency of the forced vibration, namely, first lock-in region. The second lock-in region occurs at much higher frequency of forced vibration, say at $f_h = 72$Hz. When the frequency of forced vibration is taken at the frequency between first and second lock-in region, two spectrum peaks can be seen. As the frequency of the forced vibration is increased beyond the second lock-in region, a spectrum peak of natural vortex shedding reappeared, then becomes dominant as the frequency of the forced vibration further increased. Therefore in Fig. 4, $f_h/f_k$ ($f_k$ is the vortex shedding frequency when the cylinders are at rest) is plotted against $f_h$ so that the lock-in region can be seen clearly. The vertical broken line with a dot corresponds to the natural vortex shedding frequency. When the amplitude of the vibration is small ($a/d = 0.009$), there is only one lock-in region at $f_h/f_k = 1.0$, but for $a/d \gtreqless 0.017$ there are two lock-in regions at $f_h/f_k = 1.0$ and 1.24. In the present experiment, Strouhal number for the jump flow and the reattachment flow are 0.176 and 0.142 respectively and ratio of the two Strouhal numbers corresponds to $f_h/f_k = 1.24$ for the second lock-in region. This implies that the reattachment flow with the upstream cylinder at rest switched to jump flow as the upstream cylinder is vibrated.

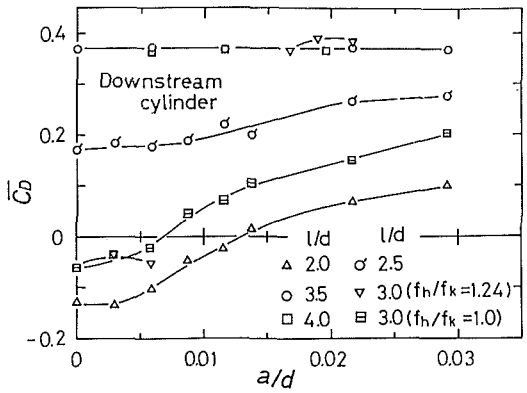


**Fig. 6 Time-mean drag coefficient $\bar{C}_D$ plotted against the amplitude ratio *a/d*. The uncertainty in the ordinate is ±0.01 and that in the abscissa is less than ±0.001. Lines are for visual aids only.**

**3.2 Time-Mean Pressure and Drag.** Figures 5 show that the time-mean pressure distribution on the downstream cylinder for $1/d = 3.0$ is significantly affected by the vibration of the upstream cylinder. Figure 5(*a*) shows the time-mean pressure distribution when the frequency of the forced vibration is the same as that of vortex shedding from cylinder at rest, $f_h/f_k = 1.0$. When the separated flow from upstream cylinder reattaches onto the surface of the downstream cylinder, the flow would be decelerated to cause larger pressure coefficient. Therefore, when the amplitude ratio of the vibration $a/d$ exceeds a certain value, it is notable that the location of the reattachment of the flow separated from the upstream cylinder on the surface of the downstream cylinder changes from 60 to 50 deg. On the other hand, Fig. 5(*b*) shows the time-mean pressure distribution for the frequency ratio $f_h/f_k = 1.24$. When the amplitude ratio of the vibration $a/d \geqq 0.017$ the time-mean pressure distribution becomes similar to that of jump flow for $1/d = 3.5$ with the cylinder at rest in the range 30 deg $< \theta <$ 180 deg. From the time-mean pressure distributions, it is seen that the switch of the flow from reattachment flow to jump flow depends on the state of the vibration of the upstream cylinder.

Time-mean drag coefficient of the downstream cylinder obtained from the time-mean pressure distributions against $a/d$ are presented in Fig. 6. The characteristics of the distribution of $\bar{C}_D$ for $1/d = 3.0$ are altered by the different characteristics of the vibration. In the range $0.006 < a/d < 0.017$ with $f_h/f_k = 1.24$, it is difficult to measure $\bar{C}_D$ because the flow of two kinds changes intermittently at irregular time intervals. Also within the range of the amplitude of the vibration employed in the present experiment, there are no effects of the vibration when the flow around the two circular cylinders at rest is already jump flow ($1/d \geq 3.5$).

When the two circular cylinders are at rest the value of $1/d$ near 3.5 is the critical value for the flow switched from reattachment to jump, but it is considered that the critical value shifts to near 3.0 when the upstream cylinder is vibrated. As reported by Koopman [7], this is attributed that the geometry of the vortex wake is altered appreciably by the vibration of the cylinder and causes a reduction in the lateral spacing. Hence it can be pointed out that the vibration of the circular cylinder affects mainly the region of the wake formation and the profile of the separating shear layer.

**3.3 Fluctuating Pressure and Fluctuating Lift.** Figures 7 show rms values of the fluctuating pressure on the surface of the circular cylinder against the angle from the stagnation point in the front surface of the cylinder for various amplitudes of vibration of the upstream cylinder. For $1/d = 3.0$, as in the case of the time-mean pressure distributions, two different distributions of rms values are observed at certain frequencies of the forced vibration. In Fig. 7(*a*) the frequency of the forced vibration is the same as that of the vortex shedding from the cylinder at rest ($f_h/f_k = 1.0$). The distribution of rms value of the fluctuating pressure acting on the circular cylinder has the same tendency as that of the cylinder at rest, but all the values increase as the amplitude of the vibration increases. In Fig. 7(*b*) the frequency of the forced vibration is the frequency of the vortex shedding when the flow around the two circular cylinders is jump flow ($f_h/f_k = 1.24$). When the amplitude of the vibration is small, the distribution of the rms value of the fluctuating pressure on the surface of the downstream cylinder is that of reattachment flow, but it switches to that of jump flow as the amplitude of the vibration increases. Hence similar behavior is observed in fluctuating pressure as expected from the time-mean pressure.

The rms values of the fluctuating lift obtained from the

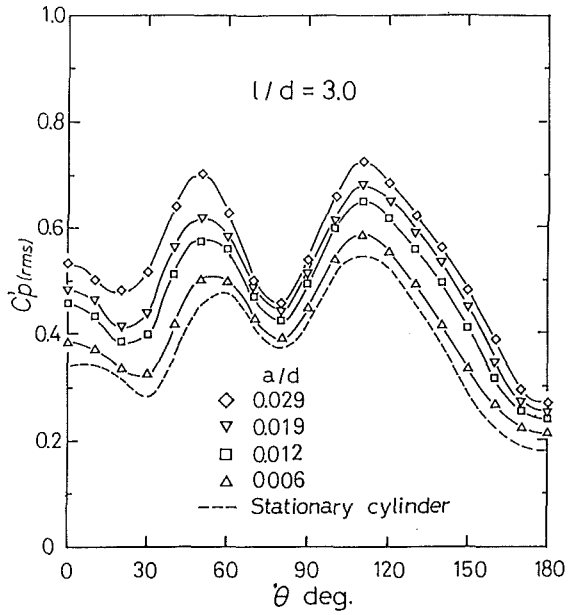


**Fig. 7(*a*)**

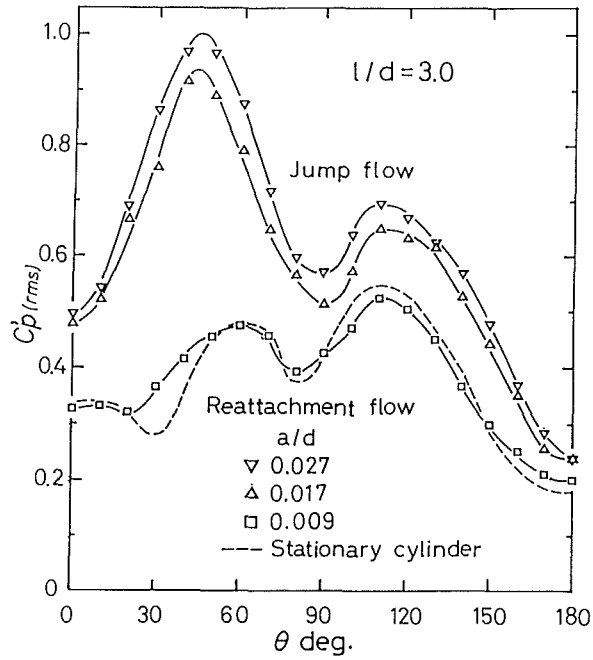


**Fig. 7(*b*)**

**Fig. 7(*a*) and (*b*) rms pressure distribution along the surface of downstream cylinder for $1/d = 3.0$. (*a*) is for $f_h/f_k = 1.0$ and (*b*) is for $f_h/f_k = 1.24$. The uncertainty in the ordinate is ±0.01 and that in the abscissa is ±0.2 deg. Lines are for visual aids only.**

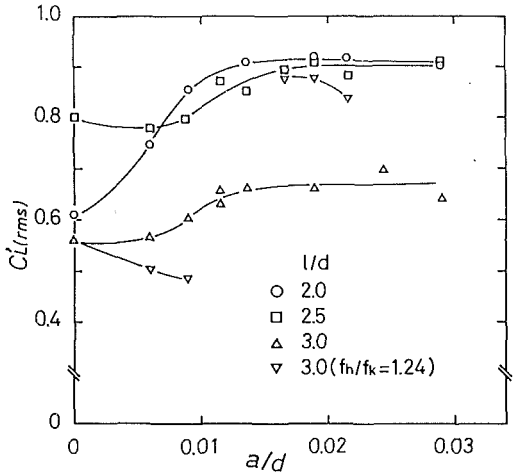


**Fig. 8 RMS lift coefficient plotted against the amplitude ratio *a/d*. The uncertainty in the ordinate is ±0.03 and that in the abscissa is less than ±0.001. Lines are for visual aids only.**

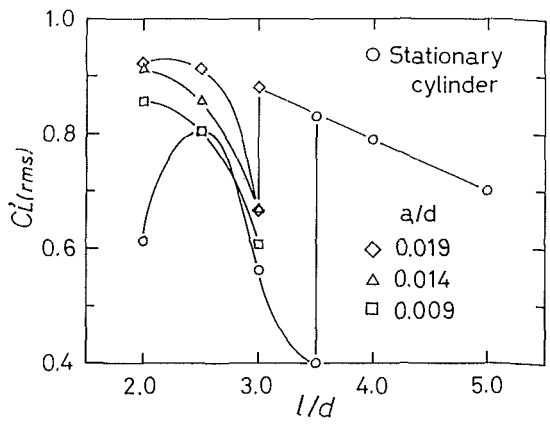


**Fig. 9 RMS lift coefficient plotted against nondimensional spacing *1/d*. The uncertainty in the ordinate is ±0.03 and that in the abscissa is less than ±0.01. Lines are for visual aids only.**

ensemble-averaging against the amplitude ratio of the vibration, $a/d$, of the upstream cylinder are presented in Fig. 8. In the present experiment, when the amplitude of the vibration for $1/d=2.0$ is rather small, the fluctuating lift acting on the downstream cylinder is significantly large. This will be arising from the fact that the cylinder is the closest to the vibrating cylinder in the range of the present experiment. Furthermore, as expected from the time-mean pressure and fluctuating pressure distributions, the fluctuating lift distribution for $1/d=3.0$ shows different tendencies for different frequencies of the forced vibration.

RMS intensities of fluctuating lift obtained from the ensemble-averaging for each amplitude ratio of the forced vibration are shown in Fig. 9 as functions of the spacing of the two circular cylinders, $1/d$. The distribution of the fluctuating lift on the downstream cylinder when the upstream cylinder is at rest has the tendency to show a peak value in the vicinity of $1/d=2.5$. The fluctuating lift for $1/d=3.0$ shows different values for two different frequencies of forced vibration when the amplitude ratio of the vibration is $a/d=0.019$. The smaller value of the fluctuating lift is the value for the reattachment flow around two cylinders and the larger one is the one for the flow switched to jump flow. Within the range of the flow around the two cylinders remains jump flow, for the smallest spacing of the cylinders, $1/d$, the fluctuating lift acting on the downstream cylinder is the largest and it decreases as $1/d$ increases. This result agrees with Arie et al. (3) ($2.0 \leq 1/d \leq 10.0$). This is considered to be originated from the fact that the vortex shedding from the upstream cylinder gradually dissipates downstream.

## 4 Conclusions

The present study has led to the following major conclusions.

(1) In the case of the two circular cylinders in a tandem arrangement, as the upstream cylinder is forcibly vibrated at frequency near that of the vortex shedding from the cylinder at rest, the fluctuating pressure on the surface of the downstream cylinder is synchronized with the forced vibration. In particular, there are two lock-in regions for $1/d=3.0$.

(2) When the flow around the two cylinders is synchronized with the vibration of the upstream cylinder, the aerodynamic forces are significantly different from the case when one of the cylinders is at rest.

(3) While $1/d \simeq 3.5$ is the critical value for the flow to be switched from reattachment flow to jump flow when the cylinders are at rest, the critical value shifts to $1/d \simeq 3.0$ when the upstream cylinder is vibrated.

## Acknowledgment

We would like to express special thanks to Professor Masaru Kiya of The Hokkaido University who gave us very helpful advice. We also would like to express our thanks to Mr. Obata and Mr. Abe of the workshop of our college for their assistance in the completion of the experimental equipment.

## References

1 Zdravkovich, M. M., "Review of Flow Interference Between Two Circular Cylinders in Various Arrangement," ASME JOURNAL OF FLUIDS ENGINEERING, Vol. 99, Ser. I., No. 4, 1977, pp. 618–633.

2 Arie, M., Kiya, M., Moriya, M., and Mori, H., "Pressure Fluctuations on the Surface of Two Circular Cylinders in Tandem Arrangement," ASME JOURNAL OF FLUIDS ENGINEERING, Vol. 105, No. 2, 1980, pp. 161–167.

3 Moriya, M., Sakamoto, H., Kiya, M., and Arie, M., "Fluctuating Pressures and Forces on Two Circular Cylinders in Tandem Arrangement," *Transaction of JSME*, Vol. 49, No. 443, 1983, pp. 1364–1374.

4 Tanida, Y., Okajima, A., and Watanabe, Y., "Stability of a Circular Cylinder Oscillating in Uniform Flow or in a Wake," *Journal of Fluid Mechanics*, Vol. 61, 1973, pp. 769–784.

5 Tanaka, H., "Fluid Elastic Vibration of Tube Array in Cross Flow," *Journal of Sound and Vibration*, Vol. 77, No. 2, 1981, pp. 19–37.

6 Conners, H. J., "Fluidelastic Vibration of Tube Arrays Excited by Cross Flow," *Symposium on Flow Induced Vibration in Heat Exchangers*, ASME Winter Annual Meeting, Dec. 1970.

7 Koopmann, G. H., "The Vortex Wakes of Vibrating Cylinder at Low Reynolds Numbers," *Journal of Fluid Mechanics*, Vol. 28, No. 3, 1967, pp. 501–512.

8 Bishop, R. E. and Hassan, A. T., "The Lift and Drag Forces on an Oscillating Cylinder," *Proceeding of the Royal Society of London*, Series A, Vol. 277, 1964, pp. 51–75.

9 Griffin, O. M., and Ramberg, S. E., "The Vortex-Street Wakes of Vibrating Cylinders," *Journal of Fluid Mechanics*, Vol. 66, 1974, pp. 553–576.

10 Bearman, P. W., "Vortex Shedding from Oscillating Bluff Bodies," *Annual Reviews of Fluid Mechanics*, Vol. 16, 1984, pp. 195–222.

11 King, R., and Jones, D. J., "Wake Interaction Experiments with Two Flexible Circular Cylinders in Flowing Water," *Journal of Sound and Vibration*, Vol. 45, No. 2, 1976, pp. 259–283.

12 Bruun, H. H., and Davies, P.O.A.L., "An Experimental Investigation of the Unsteady Pressure Forces on a Circular Cylinder in a Turbulent Cross Flow," *Journal of Sound and Vibration*, Vol. 40, No. 4, 1975, pp. 535–559.

H. G. Polderman[1]

G. Velraeds[2]

W. Knol

Department of Mechanical Engineering,
Twente University of Technology,
Enschede, The Netherlands

# Turbulent Lubrication Flow in an Annular Channel

*An analytical and experimental study is presented of the lubrication flow in an annular channel with a moving core. Velocity profiles and wall friction were determined over a Reynolds number range up to $3 \times 10^4$ and radius ratios of 0.6 and 0.85. The experimental results are shown to be in good agreement with the predictions of a three-layer gradient-diffusion model.*

## 1 Introduction

This paper presents an analytical and experimental examination of lubrication flow in an annular channel which was carried out at Twente University of Technology as part of a research program to support the design of hydraulic capsule transport systems.

Capsule transport is a technique proposed for conveying bulk solids in pipes: the commodities to be transported are encapsulated in circular cylindrical containers and pumped with a liquid as carrier through a pipeline with a slightly larger diameter. The concept is due to Canadian investigators who studied the pipe flow of oil water mixtures. At high oil water ratios the oil was observed to form slugs which moved through the pipe faster than the surrounding water, whereas the pressure drop over the line was reduced even below the one for a single phase oil or water flow at the same flow rate. Similarly, a capsule transport line can be expected to operate at favourable hold-up and pressure gradients [1]. Applications of capsule transport which have been considered recently include capsule pipelines for the transport of coal in the U.S. from the Colorado area to the west coast [2] and for the vertical haulage of ore in the deep ocean mining of manganese nodules [3].

In the hydrodynamics of capsules the flow in the annular gap between the capsule and the pipe wall plays an important part. This flow can be classified as a combination of Couette and Poiseuille flow. Following Townsend [4] it will be referred to as lubrication flow. Apart from capsule pipelines it occurs in other transport systems, for example along trains in tunnels and in devices such as bearings and equipment for wire-coating. In the following attention is restricted to the annular flow proper. The integral hydrodynamics of capsule flow has been considered in more detail elsewhere [5].

## 2 Theoretical

Figure 1 shows the geometry considered, a section of an annular channel with a rigid core moving at velocity $v_c$. A wide variety of velocity and shear stress distributions is possible. Some of them are indicated in Fig. 2. Large negative pressure gradients are accompanied by pressure flow type velocity profiles (Fig. 2(*a*)). Under small positive or negative pressure gradients a Couette flow type velocity profile establishes itself

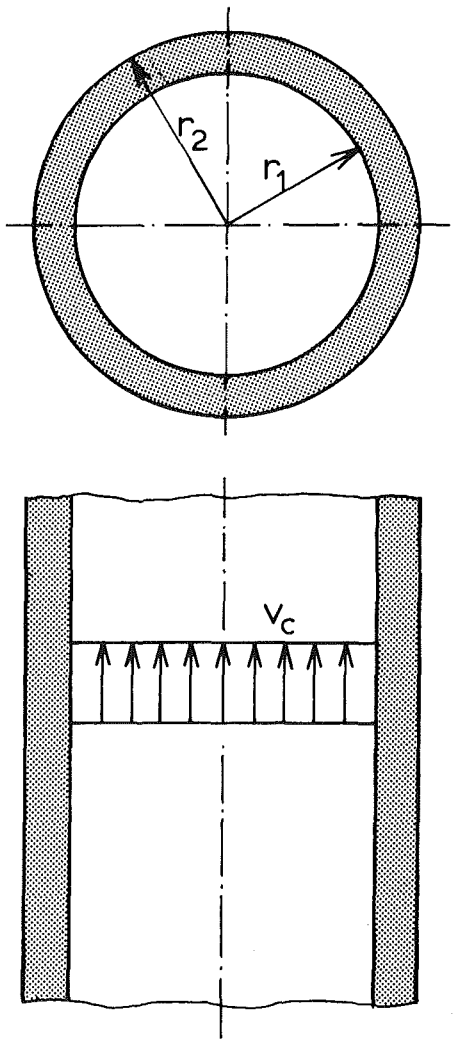


Fig. 1 The geometry considered

[1] Present address: Koninklijke/Shell Laboratorium Amsterdam.
[2] Now at Océ Nederland B.V., Venlo.

Contributed by the Fluids Engineering Division for publication in the JOURNAL OF FLUIDS ENGINEERING. Manuscript received by the Fluids Engineering Division, April 9, 1984.

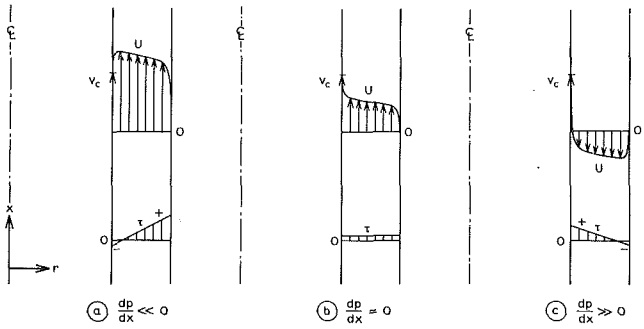


**Fig. 2 The range of velocity profiles and shear stress distributions occurring in lubrication flow**

(Fig. 2(*b*)), and in case of a large positive pressure gradient the flow can be in opposite directions in the inner and the outer part of the channel (Fig. 2(*c*)).

In capsule flow systems the annular pressure gradient prevailing is the result of the balance of the external forces acting on the capsules. In horizontal systems it will be the most efficient to make the capsules approximately neutrally buoyant. In this case the pressure difference over the capsule ends only has to overcome the shear force on the side walls. The annular pressure gradient is small and the velocity profile of the Couette flow type. In vertical pipelines the capsules can be heavier and the pressure difference over the capsule has to balance the nett capsule weight as well. The resulting pressure gradient increases with increasing capsule weight and the corresponding velocity profile will vary between those of Fig. 2(*a*) and 2(*b*).

Although the horizontal flow regime has been the subject of most of the earlier publications on capsule flow, no sufficiently accurate description of the annular flow was put forward. Charles [6] considered the capsule as an integral part of the flow. He assumed that the annular velocity was proportional to the 1/7th power of the distance to the pipe wall, extending the wall layer from the pipe wall to the capsule, thus entirely neglecting the wall layer along the capsule wall. Kennedy [7] partly improved this model taking into account the viscous sublayer at the capsule wall. Garg [8] suggested a superposition of a pressure flow and a Couette flow velocity profile. In the case of turbulent flow this will certainly lead to substantial errors because of the nonlinearity of the governing equations.

The flow along a train moving in a tunnel can be idealized as annular lubrication flow as well. In this case the pressure gradient will be small and positive, the velocity profile being of a Couette flow type, lying in between those of Fig. 1(*b*) and Fig. 1(*c*). Sud and Chaddock [9], who described the fully developed part of the flow between train and tunnel as annular pressure flow, probably under-estimated the contribution of the relative motion of the walls.

In the following the theory of turbulent lubrication as developed by Constantinescu [10] Reynolds [11] and Elrod and Ng [12] will be generalized to derive equations for the annular flow from the equations of motion.

**2.1. The Equation of Motion.** For a parallel flow in an annular channel the Navier Stokes equations reduce to

$$\tau - \frac{\frac{1}{2}(r^2 - r_1^2)}{r} \frac{dp}{dx} + \frac{r_1 \tau_1}{r} = 0 \tag{1}$$

with

$$\tau = -\mu \frac{dU}{dr} + \rho_f u_x u_r \tag{2}$$

$\rho_f u_x u_r$ is a shear stress acting in a plane parallel to the wall caused by turbulent transport of momentum in the radial direction, $\mu\, dU/dr$ is the viscous shear stress.

To solve for the velocity profile from equations (1) and (2) the turbulent shear stress is, according to Boussinesq, converted into a diffusion term

$$\rho_f u_x u_r = -\mu_t \frac{dU}{dr} \tag{3}$$

in which the diffusion coefficient $\mu_t$ is the turbulent viscosity. Substituting equations (2) and (3) in (1) results in

$$-\frac{r^2 - r_1^2}{2r} \frac{dp}{dx} + \frac{r_1 \tau_1}{r} = -(\mu + \mu_t) \frac{dU}{dr} \tag{4}$$

$\mu_t$ is not a fluid property. In the wall layer, i.e., that part of the flow which is influenced by the presence of the wall, it is gradually increasing with the distance to the wall. Beyond that layer, in the core it is almost constant. In the following we will consider the distribution of $\mu_t$ in the wall layer and the core, and the corresponding velocity profiles.

**2.2 The Wall Layer.** A practical expression which describes the variation of $\mu_t$ in the wall layer accurately was proposed by van Driest [13]. It is based on Prandtl's mixing length equation:

$$\mu_t = \rho_f l^2 \left| \frac{dU}{dr} \right| \tag{5}$$

$l$ is the mixing length, the "mean free path" of the turbulent eddies. In the fully turbulent part of the wall layer the mixing length is about proportional to the wall distance:

## Nomenclature

$A$ = Van Driest constant, $\simeq$ 26, equation (7)
$D$ = pipe diameter, (m)
$P_a$ = nondimensionalized annular pressure gradient, $h \frac{dp}{dx} / \rho_f v_c^2$
$\mathrm{Re}_a$ = annular flow Reynolds number, $\rho_f v_c h/\mu$
$R$ = core viscosity flow constant, $\rho_f v^* h/\mu_t$
$S$ = sign of the velocity gradient
$U$ = local fluid velocity, (m/s)
$c_f$ = friction coefficient, $\tau/\rho_f v_c^2$
$g$ = gravitational constant, (m/s$^2$)
$h$ = annulus width, (m)
$k$ = radius- or diameter ratio, $r_1/r_2$
$l$ = mixing length, (m)
$p$ = pressure, (N/m$^2$)
$r$ = radial coordinate, (m)
$r_\tau$ = wall stress ratio
$u$ = velocity fluctuation, (m/s)
$v_c$ = core velocity, (m/s)
$v^*$ = wall friction velocity, (m/s)
$x$ = axial coordinate, (m)
$y$ = distance from the inner wall, (m)
$y'$ = distance from the outer wall, (m)
$y_m$ = wall distance of the matching point between wall layer, (m) and core
$y_0$ = wall distance of the zero shear stress plane, (m)
$\kappa$ = von Karman constant, $\simeq$ 0.4, equation (6)
$\mu$ = dynamic viscosity, (Ns/m$^2$)
$\mu_t$ = turbulent viscosity, (Ns/m$^2$)
$\nu$ = kinematic viscosity, (m$^2$/s)
$\rho_f$ = fluid density, (kg/m$^3$)
$\tau$ = shear stress, (N/m$^2$)
$\tau_w$ = wall shear stress, (N/m$^2$)

**Subscripts**

$c$ = pertaining to core wall
$p$ = pipe wall
$r$ = radial direction
$x$ = axial direction
1 = inner wall
2 = outer wall

**Table 1 Core viscosity flow constants**

| Type of flow | $r_\tau$ | $R$ |
|---|---|---|
| Plane pressure flow [21] | −1 | 25.8 |
| Open channel flow [22] | 0 | 13 |
| Plane Couette flow [15, 16] | 1 | 7–9 |

$$1 = \kappa y,\ \kappa \simeq 0.4 \tag{6}$$

where $\kappa$ is the von Karman constant. Van Driest suggested an extension of equation (6) to include the regions immediately near the wall

$$1 = \kappa y[1 - \exp(-y^+/A)],\ A \simeq 26 \tag{7}$$

$y^+$ is the nondimensionalized wall distance, $y^+ = y\,v^*/\nu$ with $\nu$ the kinematic viscosity, and $v^*$ is the wall friction velocity, $v^* = \sqrt{\tau_w/\rho_f}$ where $\tau_w$ is the wall shear stress. The term between braces in equation (7) describes the damping effect on the turbulence caused by the vicinity of the wall.

From equations (4), (5), and (7) and substituting the wall distance $y = r - r_1$ instead of $r$ we find the following expression for the velocity gradient:

$$-\mu \frac{dU}{dy} - \rho_f 1^2 S\left(\frac{dU}{dy}\right)^2 = \tau_y \tag{8}$$

where

$$\tau_y = -\frac{dp}{dx}\frac{y}{2}\left(1 + \frac{r_1}{r_1 + y}\right) + \frac{r_1\tau_1}{r_1 + y}$$

$S$ = sign $(dU/dy)$ and takes into account the absolute value of the velocity gradient. Equation (8) is a quadratic equation in $dU/dy$ with the solution

$$\frac{dU}{dy} = \frac{-2\tau_y}{\mu + \sqrt{(\mu^2 - 4S\rho_f 1^2 \tau_y)}} \tag{9}$$

The other root has to be discarded for physical reasons.

An expression similar to equation (9) can be derived for the profile at the outer wall

$$\frac{dU}{dy'} = \frac{-2\tau_y'}{\mu + \sqrt{(\mu^2 - 4S\rho_f 1^2 \tau_y')}} \tag{10}$$

with $y' = r_2 - r$ and

$$\tau_{y'} = -\frac{dp}{dx}\frac{y'}{2}\left(1 + \frac{r_2}{r_2 - y'}\right) + \frac{r_2\tau_2}{r_2 - y'}$$

**2.3. The Core.** In the fully turbulent core in between the wall layers $\mu_t$ appears to be approximately constant. A flow constant $R$ is defined

$$R = \rho_f v^* h/\mu_t \tag{11}$$

which can be regarded as a Reynolds number representative of the turbulence in the core. $h = r_2 - r_1$ is the channel width. $R$ depends on the geometry of the flow which can be characterized by the ratio of the wall stresses. The wall stress ratio $r_\tau$ is introduced with the following definition:

$$\begin{aligned} r_\tau &= \tau_1/\tau_2 \text{ if } \tau_1 < \tau_2 \\ &= \tau_2/\tau_1 \text{ if } \tau_1 > \tau_2 \end{aligned} \tag{12}$$

$r_\tau$ is negative for pressure flow type velocity profiles and positive for Couette flow type profiles, see Fig. 2.

At the time this investigation was carried out almost no information was available on the variation of $R$ with $r_\tau$. From the experimental data published in the literature, values could be established for the special cases $r_\tau = -1$, 0 and 1. These are summarized in Table 1. For intermediate values of $r_\tau$ $R$ had to be determined by interpolation. Procedures for interpolation have been proposed by Reynolds [11] and by Townsend [4]. For negative values of $r_\tau$ we followed the more physical argument of Townsend. He assumes that pressure flows are made up of two separate layers on each side of the zero stress plane, which he considers to be impermeable to the turbulent motion. In each layer $\mu_t$ is specified by the relevant wall stress, the thickness of the layer and the value of R for open channel flow,

$$\begin{aligned} y < y_0 &: \ \mu_t = \frac{\rho_f v_1^* y_0}{R_{|r_\tau = 0}} \\ y > y_0 &: \ \mu_t = \frac{\rho_f v_2^* (h - y_0)}{R_{|r_\tau = 0}} \end{aligned} \tag{13}$$

where $y_0$ is the distance of the zero stress plane to the inner wall. When $r_\tau$ is positive there is no zero stress plane. For this case $R$ was estimated by linear interpolation between $R_{|r_\tau = 0}$ and $R_{|r_\tau = 1}$:

$$R = 13 - 5r_\tau,\ 0 \le r_\tau \le 1 \tag{14}$$

To evaluate $\mu_t$ from equations (11) and (14) the wall friction at the wall with the largest shear stress was used as velocity scale as this satisfies for both $r_\tau = 0$ and $r_\tau = 1$:

$$\mu_t = \rho_f v^* h/R, \text{ with } v^* = \max(v_1^*, v_2^*) \tag{15}$$

Summarizing, we find the velocity gradient in the central part of the flow to be

$$\frac{dU}{dy} = -\tau_y/(\mu + \mu_t) \tag{16}$$

with $\mu_t$ given by equations (13) for $r_\tau \lesssim 0$ and by (14) and (15) for $r_\tau \gtrsim 0$.

**2.4. The Location of the Matching Point of Wall Layers and Core.** For flows which are reasonably symmetrical the distance to the wall where the wall layer adjoins the core can be determined by the assumption that $\mu_t$ is continuous. The transition is located at the wall distance $y_m$ where the viscosity of the wall layer equals that of the core:

$$\rho_f \kappa^2 y_m^2 \frac{dU}{dy} \simeq \frac{\rho_f v^* h}{R}$$

or equivalently

$$y_m \simeq \frac{1}{\kappa}\left(\frac{v^* h}{R\dfrac{dU}{dy}}\right)^{\frac{1}{2}} \tag{17}$$

$y_m'$ is given by a similar equation.

However, a problem arises when the shear stress at one of the walls becomes very small. Then both $v^*$ and $dU/dy$ vanish and equation (17) becomes indeterminate. For negative wall stress ratios there is no difficulty: if $\tau_w \to 0$, the wall layer disappears completely. To approach $r_\tau = 0$ from the positive side a relation between $y_m$ and $r_\tau$ was postulated. The relation to be determined has to satisfy $y_m = 0$ for $r_\tau = 0$ to be in agreement with equation (13). On the other side equation (17) gives $y_m \simeq 0.3$ h for $r_\tau \to 1$. Therefore for $0 < r_\tau < 1$ the matching point was determined from

$$y_m = 0.3 r_\tau h \tag{18}$$

A consequence of this approach is that $\mu_t$ and thus the velocity gradient are not necessarily continuous in $y_m$. In the following chapter it will be shown that an eventual discontinuity in $\mu_t$, resulting in a kink in the velocity profile, has only a minor influence on the accuracy of the results.

**2.5. The Annular Velocity Profile.** The velocity profile is calculated by numerical integration of equations (9), (10), and (16). The boundary conditions are

$$y = 0 \ : \ U = v_c \text{ and } y' = 0 \ : \ U = 0 \tag{19}$$

The annular flow is determined by $v_c$, $dp/dx$, $r_1$, $r_2$, $\mu$, and $\rho_f$. To reduce the number of variables and to bring the results in a more general form dimensionless groups are introduced. From six variables in three dimensions three independent dimensionless groups can be formed. The groups chosen are:

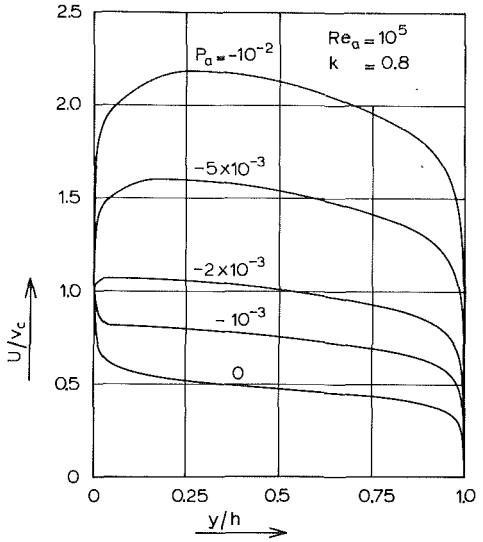


**Fig. 3 Dependence of the annular velocity profile on the pressure gradient**

– the radius ratio $k = r_1/r_2$
– a Reynolds number $\mathrm{Re}_a = \rho_f v_c h/\mu$
– the nondimensionalized annular pressure gradient $P_a$

$$P_a = \frac{h}{\rho_f v_c^2}\frac{dp}{dx}$$

The variation of the velocity profile with $\mathrm{Re}_a$, $P_a$, and $k$ is illustrated in Figs. 3, 4, and 5. In Fig. 3 the dependence of the profile on the pressure gradient can be seen: small pressure gradients are accompanied by Couette flow type velocity profiles and large pressure gradients with pressure flow type velocity profiles. Figure 4 shows that the flow resistance decreases with increasing $\mathrm{Re}_a$ resulting in an increased annular flow rate. From Fig. 5 it can be seen that the asymmetry of the velocity distribution increases with decreasing $k$.

## 3 Annular Lubrication Flow Experiments

In the model described above rather gross assumptions had to be made concerning the core viscosity and the thickness of the wall layers. As at the time this investigation was carried out no sufficiently general experimental information was available in the literature, it was decided to design experiments to verify the theoretical results.

The difficulty to generate a measurable turbulent shear flow is most clearly illustrated by the fact that experimental investigations make up only a small part of the extensive literature on this subject. Couette [14] was the first to study the flow caused by the relative movement of parallel walls. He investigated the circular shear flow in the narrow gap between two closely spaced coaxial cylinders created by the rotation of the outer cylinder. The wall friction was determined from the torque on the inner cylinder. Reichardt [15] investigated turbulent Couette flow in a plane channel in which a moving wall was featured by a rubber belt. His experiments showed the validity of the 'law of the wall' for this type of flow. Comparable experiments have been reported by Robertson [16], Robertson and Johnson [17] and Chue and McDonald [18].

Until then only pure shear flow without pressure gradient had been considered. Huey and Williamson [19] examined plane shear flow with positive pressure gradients. By inserting blockage elements in a channel with one moving wall a circulating flow was established with zero net flow. In this way the flow in a heavily loaded bearing or in the pocket of a hydrostatic bearing could be simulated. In the lubrication flow along capsules in capsule pipelines the pressure gradient will be negative in most cases. To study this flow over a wide range

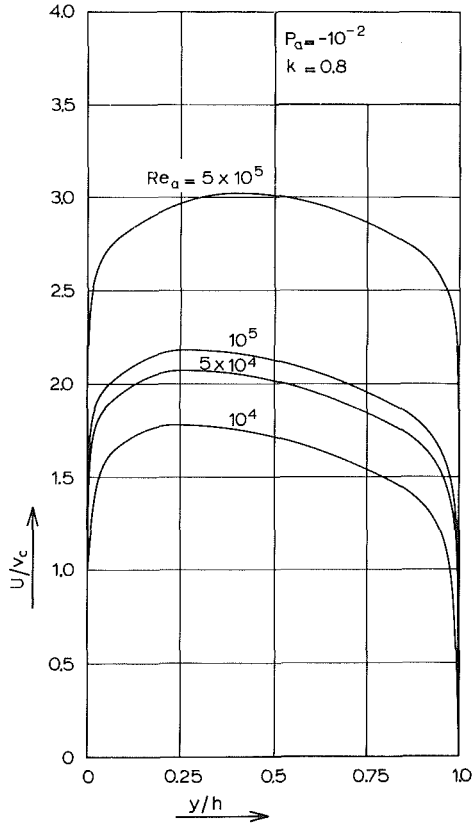


**Fig. 4 Influence of Reynolds number**

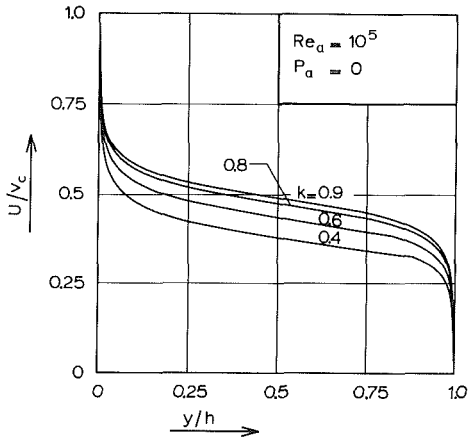


**Fig. 5 Influence of the radius ratio**

of pressure gradients and in an annular geometry the test rig and the experiments described in the next section were realized. Recently El Telbany and Reynolds [20] published similar experiments covering the whole range of shear flows carried out in a plane channel.

**3.1 The Annular Flow Test Rig.** The test facility is drawn schematically in Fig. 6. The annular test section consists of a 2m. long stainless steel pipe of 55.4 mm inner diameter in which a rubber string is moving. Both string and pipe wall surfaces are hydraulically smooth. The outer pipe connects fluid reservoirs filled with water. With a speed controlled centrifugal pump different water levels can be established in these reservoirs, and in this way the annular pressure gradient can be varied. The pressure gradient is limited by the height of the reservoirs between $-8$ and $+4$ kPa/m.

The string was assembled from circular rubber profiles of 1 m. in length which had been machined after manufacturing to bring the accuracy of the outer diameter to $\pm 0.2$ mm. The

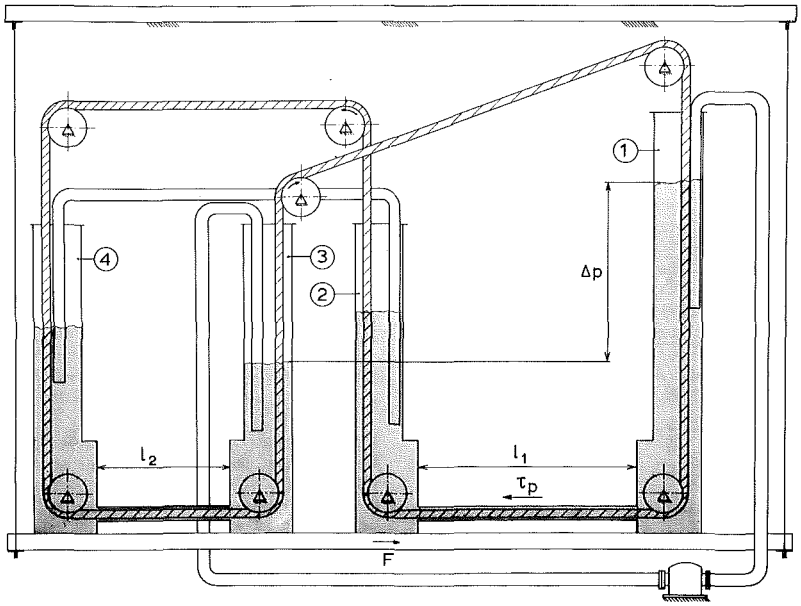


**Fig. 6 Diagram of the annular flow test rig, illustrating the measurement of the wall shear stress**

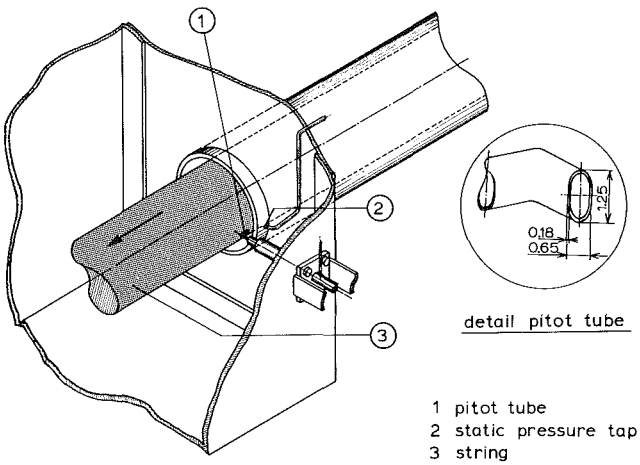


**Fig. 7 Velocity profile measurement with a Pitot tube**

segments were joined with cyanoacrylate adhesives. The string was made hollow to make it neutrally buoyant in water, the density of neoprene being about 1300 kg/m$^3$. The string circulates over 0.4 m diameter pulleys one of which is driven by a controllable electromotor. Its tension can be varied by displacement of a straining pulley. One of the a priori requirements was a concentricity of the string within 0.5 mm. Therefore the positioning of the lower pulleys was made adjustable and much attention was given to assure sufficient stiffness of the whole construction.

Strings of 33.5 and 46.9 mm diameter were used, resulting in diameter ratios of 0.6 and 0.85. The velocity of the string could be varied continuously up to 3 m/s. The flow rate was measured with a magnetic inductive flowmeter. The pressure gradient was determined with ordinary U-tube fluid manometers connected with 0.5 mm pressure taps in the wall of the outer pipe. For this purpose the best least squares fit to the manometer readings was calculated.

**3.2 Wall Friction Measurements.** The reservoirs and the measuring section are mounted independent of the string and the pulleys on a separate section which is attached to the frame with four vertical strips of 2 mm sheet iron. See Fig. 6. This part can move in the horizontal direction. It is displaced from its original position by the shear force exerted on the outer pipe by the fluid flow and the nett horizontal force resulting from the different pressures acting on the vertical side walls. The influence of end effects is eliminated by the addition of an identical compensation section in a direct line with the measuring section with a horizontal pipe of 0.5 m length. In this pipe the flow and string move in the opposite direction. Thus a net force results, apart from the pressure force, being the effect of the wall friction exerted by fully developed flow on a pipe section of 1.5 m. length. From the total force on the movable section and the pressure differences the wall shear stress can be calculated:

$$F_{\text{tot}} = \Delta p \tfrac{1}{4}\pi D^2 - \tau_p \pi D(l_1 - l_2)$$

with $\Delta p = (p_1 - p_2) + (p_3 - p_4)$. Or equivalently

$$\tau_p = -\frac{F_{\text{tot}} - \Delta p \tfrac{1}{4}\pi D^2}{\pi D(l_1 - l_2)} \tag{20}$$

To assure a correct force measurement the quadrangle formed by the horizontal beams and the suspending strips has to be an exact parallelogram, otherwise a change of the water levels in the reservoirs will cause undesirable retroactive forces that bias the measured force. For the same reason a force transducer has been chosen with a small displacement ($\lesssim 3$ $\mu$m/N) to avoid the influence of gravity on the considerable mass of the moving part. The horizontal pipes have been brought into one line very carefully to avoid torque.

The fluctuating signals of flowmeter and force- and pressure transducers were plotted on a 4-channel recorder and were averaged over several minutes. The absolute error in the force measurements was $\lesssim 0.02$ N. The pressure difference could be read within 10 N/m$^2$. It is acting on a surface of $2.4 \times 10^{-3}$m, resulting in a pressure force $\lesssim$ 0.025 N. So according to equation (20) the uncertainty in the measured shear force is $\lesssim 0.05$ N and in the shear stress $\lesssim 0.2$ N/m$^2$, i.e., 0.5% of the largest shear stress.

**3.3 Velocity Profile Measurements.** Velocity profiles have been measured with a Pitot tube at the end of the measuring section. This is illustrated in Fig. 7. The Pitot tube was made of 1.5 mm outer diameter stainless steel tubing, flattened to a width of 0.65 mm. It could be positioned in the horizontal midplane of the annulus within 0.01 mm with a micrometer traversing arrangement. The pressure difference between the Pitot tube and the wall tap was measured with a Honeywell pressure transducer. If necessary the profiles were normalized

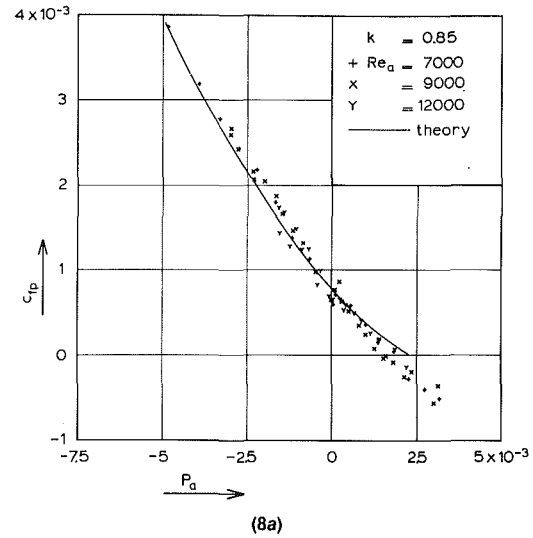


(8a)

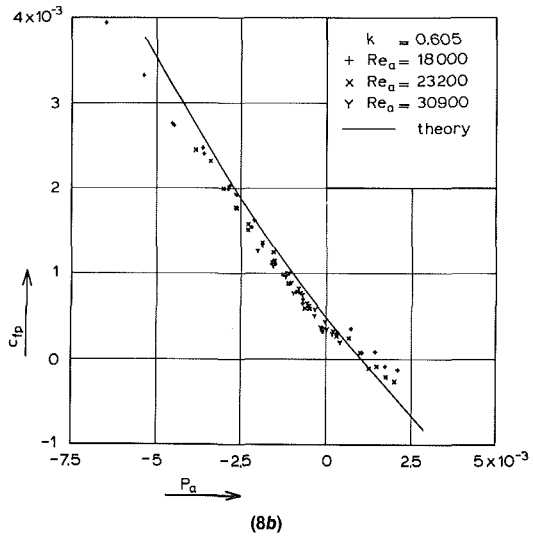


(8b)

**Fig. 8 Comparison of the measured and predicted wall shear stress (Uncertainty in $c_f = \pm 0.03 \times 10^{-3}$, in $P_a = \pm 0.12 \times 10^{-3}$, in $Re_a = \pm 800$)**

on the average velocity measured with the magnetic inductive flowmeter. For this purpose the average velocity was determined from the profile measurements by fitting a curve through the measured velocities by spline approximation and subsequent numerical integration.

**3.4 Experimental Results.** The measured wall friction at the outer wall is compared with the predictions of the mathematical model in Fig. 8. The wall friction coefficient $c_{fp}$ is plotted as a function of $P_a$,

$$c_{fp} = \frac{\tau_p}{\rho_f v_c^2}$$

The Reynolds dependence of $c_{fp}$ over the investigated range is so small that the theoretical curves for different Reynolds numbers almost coincide. For $k = 0.85$ the agreement is good except near $\tau_p \simeq 0$. Because of the poor description of the wall layer for small wall stresses the prediction is less accurate there. For $k = 0.6$ there is some difference. This is considered to be the effect of the limited length of the compensation section, which is probably too short to completely compensate for the entrance effect for this wide channel ($l_2/h \simeq 40$).

In Fig. 9 the variation of $c_{fp}$ with $Re_a$ is plotted for the zero pressure gradient case. For $k = 0.85$ the calculated wall friction agrees with the measurements. The plane flow case is also included. It is the limiting case of annular flow for $k \to 1$. The

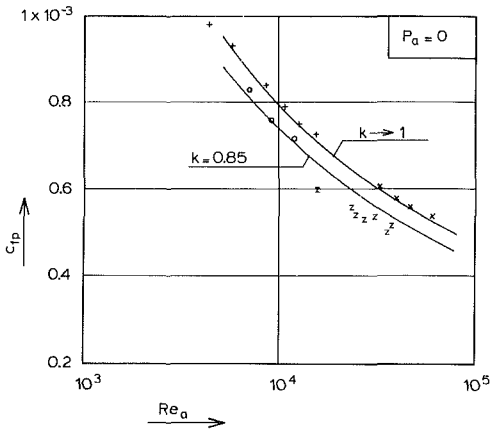


**Fig. 9 Comparison of the calculated wall shear stress with experimental data from various sources for pure Couette flow ($P_a = 0$): (a) Plane flow ($k \to 1$): + Couette, z Reichardt, x Robertson, (b) Annular flow ($k = 0.85$): o Annular test rig data, cf. Fig. 8(a) (Uncertainty estimates: see Fig. 8)**

measurements of Couette, Reichardt and Robertson in plane channels are compared with calculations in which $k = 1$ was approximated by setting $k = 0.99$ in the computer program. In Couette's experiment the spacing between the cylinders was small relative to their diameters and the circular flow can also be considered as almost plane. The calculations are supported by the measurements of Couette and Robertson. There is a discrepancy between the prediction and the data of Reichardt. Robertson determined the wall friction from his velocity profile measurements, whereas Reichardt measured it directly with a hot wire anemometer, a method which is in general more accurate. But, as Robertson already objected, Reichardts wall friction results are not consistent with his velocity profile measurements.

The measured and calculated velocity profiles are presented in Fig. 10. On the whole the agreement is better for $k = 0.6$. For $k = 0.85$ the pitot tube with its outer diameter of 0.65 mm is in fact too large for the narrow annulus of 4.3 mm width. In this case normalization on the measured average velocity was necessary. For positive wall stress ratios – Couette flow type velocity profiles – the velocity distribution is in general accurately predicted. It is clear that the interpolation given by (14) and (18) is accurate enough. As already mentioned there is a kink in the calculated profiles in some cases, but its effect on the results is not significant.

For negative wall stress ratios where Townsends interpolation method – equation (13) – has been used there is some discrepancy. This is not too surprising. The pressure gradient that could be achieved being limited, $r_\tau$ was negative but still close to zero for the maximum pressure gradient. The asymmetry of the flow is considerable then. It is known that in asymmetrical flows there is a substantial distance between the location of the zero stress plane and the location of the maximum of the velocity profile. However, any gradient diffusion model predicts that these locations coincide. So it can be expected that the model is somewhat inaccurate here. For the same reason it can be expected that the agreement improves if $Re_a$ or $P_a$ of the flow increases. In the first case the influence of the wall layers diminsishes, in the latter the flow is more symmetrical and the calculation is more exact.

## 4 Conclusion

The experimentally determined velocity profiles and wall friction coefficients are in good agreement with the theoretical prediction except where the wall stress ratio is close to zero. It can be concluded that turbulent lubrication flow can be calculated accurately at least over the investigated range of parameters: $Re_a \lesssim 3 \times 10^4$, $P_a \lesssim 5 \times 10^{-3}$ and $0.6 \lesssim k \lesssim 1$.

Although commercial transport systems will be operating at Reynolds numbers and pressure coefficients which are higher by an order of magnitude, it is to be expected that upscaling to this range is justified as the variation of the velocity profiles with the operating parameters is very gradual.

## 5 Acknowledgment

The authors wish to acknowledge the continuous interest of Prof. H. Van Den Kroonenberg in the present work. They are most grateful to Messrs. B. Boone and J. Kaspers for their technical assistance.

## References

1 Govier, G. W., and Aziz, K., *The Flow of Complex Mixtures in Pipes*, Van Nostrand Reinhold, New York 1972.

2 Legal, C., "The Aquatrain Concept," Unpublished Contribution to the Fourth International Symposium on Freight Pipelines, Atlantic City, Oct. 1982.

3 Van Den Kroonenberg, H. H., "A Novel Vertical Underwater Lifting System for Manganese Nodules Using a Capsule Pipeline," Paper 3365 presented at the Eleventh Annual Offshore Technology Conference, Houston 1979.

4 Townsend, A. A., *The Structure of Turbulent Shear Flow*, Cambridge University Press, Cambridge 1976.

5 Polderman, H. G., "Design Rules for Hydraulic Capsule Transport Systems," *Journal of Pipelines*, Vol. 3, 1982, pp. 123-136.

6 Charles, M. E., The Pipeline Flow of Capsules, Part 2: Theoretical Analysis of the Flow of Concentric Forms," *Can. J. Chem. Eng.*, Vol. 41, Apr. 1963, pp. 46-51.

7 Kennedy, R. J., "Towards an Analysis of Plug Flow through Pipes," *Can. J. Chem. Eng.*, Vol. 44, Dec. 1966, pp. 354-356.

8 Garg, V. K., "Capsule Pipelining – an Improved Theoretical Analysis," ASME JOURNAL OF FLUIDS ENGINEERING, Vol. 99, Dec. 1977, pp. 763-771.

9 Sud, I., and Chaddock, J. B., "Drag Calculations for Vehicles in Very Long Tubes from Turbulent Flow Theory," ASME JOURNAL OF FLUIDS ENGINEERING, Vol. 103, June 1981, pp. 361-366.

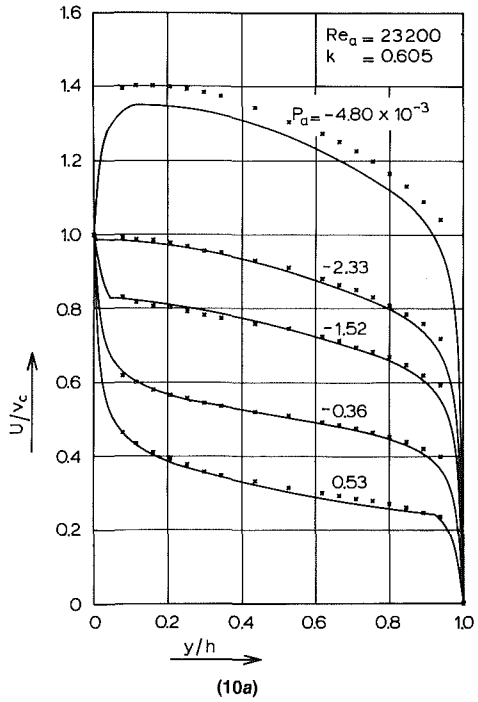


(10a)

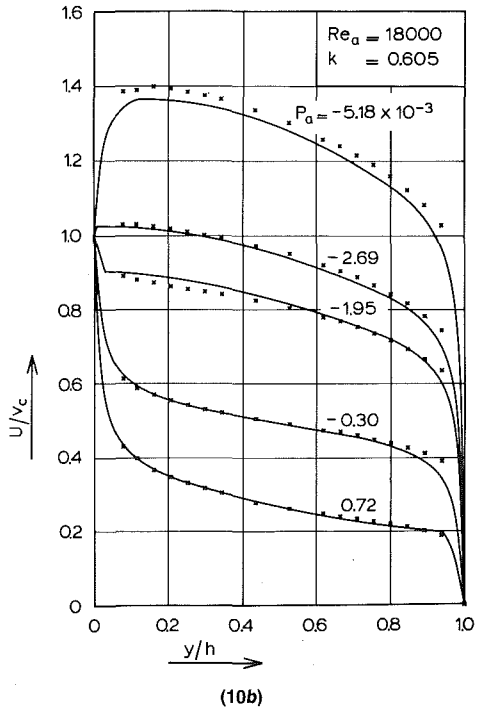


(10b)

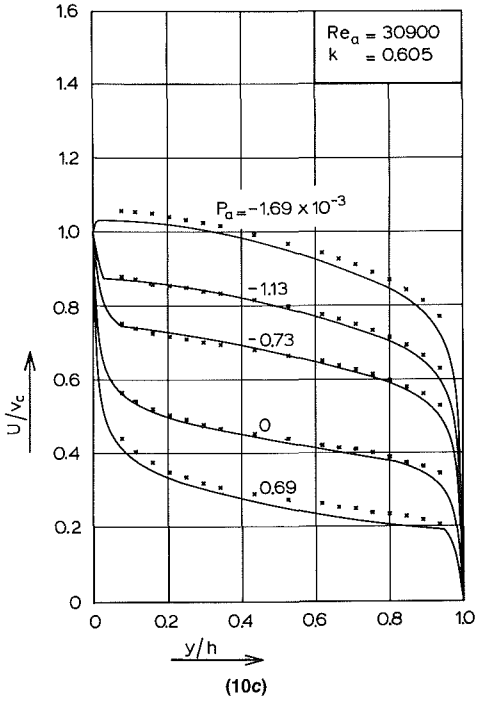


(10c)

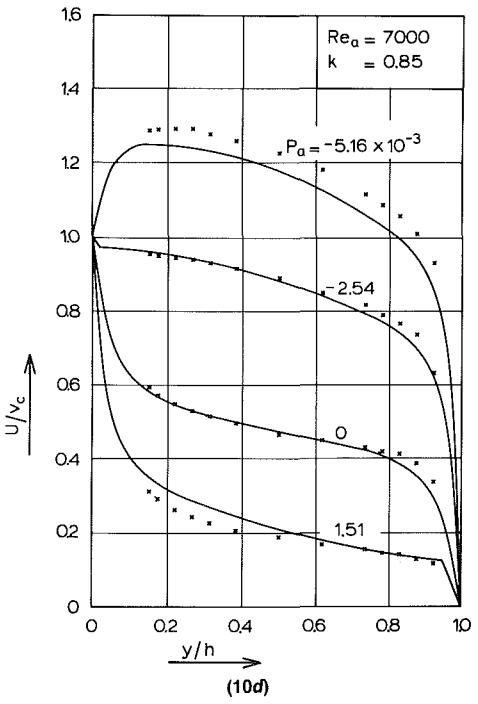


(10d)

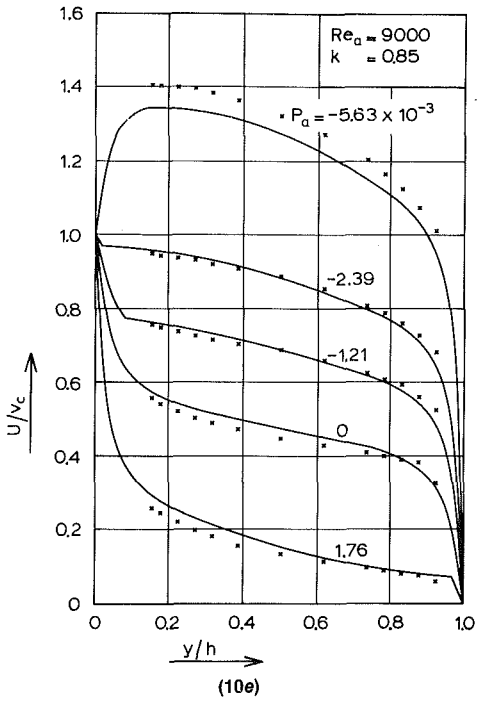


(10e)

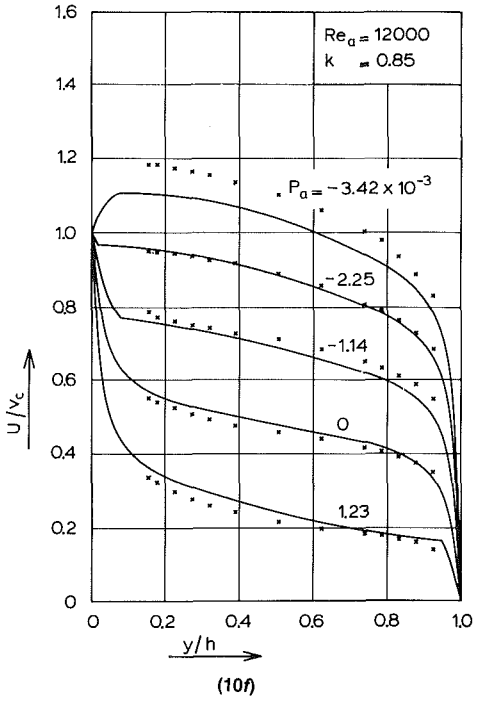


(10f)

**Fig. 10 Comparison of measured and predicted velocity profiles (Uncertainty in $U/v_c = \pm 0.02$, in $y/h = \pm 0.01$, $Re_a = \pm 800$, in $P_a = \pm 0.12 \times 10^{-3}$)**


10 Constantinescu, V. N., "On Turbulent Lubrication," *Proc. Instn. Mech. Engrs.*, Vol. 173, 1959, pp. 881–893.

11 Reynolds, A. J., "Analysis of Turbulent Bearing Films," *J. Mech. Eng. Sci.*, Vol. 5, 1963, pp. 258–272.

12 Elrod, H. G., and Ng, C. W., "A Theory for Turbulent Fluid Films and its Application to Bearings," ASME *Journal of Lubrication Technology*, Vol. 89, July 1967, pp. 346–362.

13 Van Driest, E. R., "On Turbulent Flow near a Wall," *J. Aeron. Sci.*, Vol. 23, 1956, pp. 1007–1011.

14 Couette, M., "Etudes sur le frottement des Liquides," *Ann. Chem. Phys.*, Vol. 21, 1890, pp. 433–510.

15 Reichardt, H., Gesetzmässigkeiten der geradlinigen turbulenten Couetteströmung, Mitt. Max Planck Institut für Strömungsforschung No. 22, Göttingen 1959.

16 Robertson, J. M., "On Turbulent Plane Couette Flow," *Proceedings Sixth Mid-Western Conference on Fluid Mechanics*, University of Texas 1959, p. 169–182.

17 Robertson, J. M., and Johnson, H. F., "Turbulence Structure in Plane Couette Flow," *Proc. ASCE/J. Eng. Mech. Div.*, Vol. 96, Dec. 1970, pp. 1171–1182.

18 Chue, S. H., and McDonald, A. T., "Application of a New Effective Viscosity Model on Turbulent Plane Couette Flow," *AIAA Journal*, Vol. 8, Nov. 1970, pp. 2076–2078.

19 Huey, J., and Williamson, J. W., "Plane Turbulent Couette Flow with Zero Net Flow," ASME *Journal of Applied Mechanics*, Vol. 95, Dec. 1974, pp. 885–890.

20 El Telbany, M. M. M., and Reynolds, A. J., "Velocity Distributions in Plane Turbulent Channel Flows," *J. Fluid Mech.*, Vol. 100, 1980, pp. 1–29.

21 Laufer, J., "Investigation of Turbulent Flow in a Two-Dimensional Channel," NACA report no. 1053, Washington 1951.

22 Finley, P. J., et al., "Velocity Measurements in a Thin Horizontal Water Layer," *Houille Blanche*, Vol. 21, 1966, pp. 713–721.

# A Single-Flexible-Cylinder Analysis for the Fluidelastic Instability of an Array of Flexible Cylinders in Cross-Flow

**S. J. Price**
Mem. ASME

**M. P. Paidoussis**
Fellow ASME

Department of Mechanical Engineering,
McGill University,
Montreal, Québec
Canada, H3A 2K6

*A quasi-static fluidelastic analysis is developed for a single flexible cylinder surrounded by rigid cylinders and subject to cross-flow. Although the analysis is quasi-static, it includes a frequency-dependent term which arises because of flow retardation around the front stagnation region of the cylinder. The combined effect of this flow retardation and of the fluid force field is to produce, for some intercylinder patterns of motion, a negative fluid damping, acting in the sense normal to the flow direction. Using this analysis, the effect of array pattern of the adjacent rigid cylinders is investigated, and it is shown that for some geometries a single flexible cylinder will become unstable while for others it will not. For those array patterns which the theory indicates to be potentially unstable, the variation of critical flow velocity with mass-damping parameter is obtained and compared with available experimental data. In general, the comparison is good, indicating the validity of this analysis.*

## 1 Introduction

Cylinder arrays, in the form of closely packed tube banks, subject to cross-flow are found in many types of heat exchangers, boilers and steam generators. It has been known for over two decades that this cross-flow may cause violent vibrations of the arrays [1]. Thus, it is not surprising that there has been a great deal of effort devoted to developing design criteria to prevent this vibration from occurring [2, 3].

Up till fairly recently, the majority, if not all, of the design criteria were broadly based on the now familiar Connors expression [4]. However, in the past few years a number of new theoretical models have been obtained [5–13], which may be divided into two broad categories: (i) the truly analytical models requiring little or no experimental fluid force data [11, 12], and (ii) analyses requiring experimental fluid force data, which may be either the full unsteady data [6–8] or steady time-averaged data [5, 9, 10, 13]. In general, agreement between the theoretically predicted flow velocities for instability and those obtained experimentally is better for the analyses in which the unsteady force coefficient data is employed; however, because of the vast amount of experimental data these analyses require as input, it is doubtful if they will even become practical for use as design tools. A reasonable degree of success has been obtained with quasi-static type analyses; these require only the time-averaged static fluid force coefficient and their spatial derivatives in two orthogonal directions. Even for these analyses, however, the amount of fluid-force coefficient data required as input, which must be measured for each particular type of array and inter-cylinder spacing under consideration, is prohibitive.

Thus, the appeal for the truly analytical models is obvious. As yet, these have met with limited success and, in fact, require one very important piece of data: the phase lag between the tube displacement and resultant change in the fluid forces. This phase lag will undoubtedly be dependent on a number of parameters, e.g., the tube non-dimensional frequency, $fd/U$, the Reynolds number of the flow, the array geometry and the inter-cylinder separation. In view of this, the "truly" analytical solutions must be regarded as being in their infancy; however, they are well deserving of further attention.

In this paper an intermediate approach is taken: an attempt is made to determine the critical flow velocity of a full array of flexible cylinders by analyzing a single flexible cylinder in the middle of an array of rigid cylinders. The justification for this approach comes from both theoretical and experimental sources. Experimentally, Lever and Weaver [11] show that a single flexible cylinder in the midst of an array of rigid cylinders becomes unstable at sensibly the same flow velocity as when all the cylinders are flexible; the combined mass-damping parameter, $m\delta/\rho d^2$, for these experiments was 1.8. Theoretically, both Chen [7, 8] and the present authors [13] show that the instability mechanism for multiple flexible cylinders subject to cross-flow is, for some array geometries, of two distinct types: (i) for low $m\delta/\rho d^2$ the instability is primarily due to negative fluid damping, which is mainly produced by motions of a cylinder on itself, rather than by coupling effects; (ii) for high $m\delta/\rho d^2$ the instability is predominantly due to a fluidelastic-stiffness-type mechanism, where fluid coupling between the cylinders is necessary. The authors found the boundary between these two regimes to be

Contributed by the Fluids Engineering Division for publication in the JOURNAL OF FLUIDS ENGINEERING. Manuscript received by the Fluids Engineering Division, October 16, 1984.

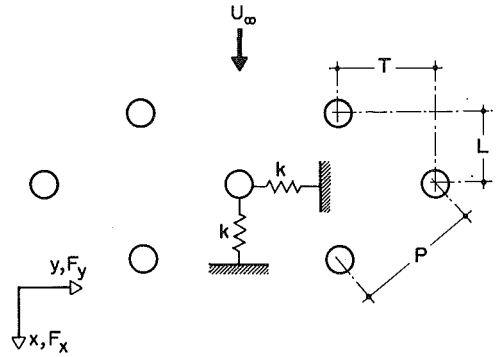


**Fig. 1 Schematic of the orthogonal spring system used to represent cylinder flexibility**

approximately $m\delta/\rho d^2 = 300$. Thus, for $m\delta/\rho d^2 < 300$, one flexible cylinder in any array of rigid cylinders will go unstable at approximately the same flow velocity as an array of flexible cylinders, at least for some geometrical array patterns.

The fluidelastic analysis employed in this paper for a single flexible cylinder is by the usual quasi-static method, with the addition of one very important frequency-dependent term, which was first introduced by Simpson and Flower [14] in an analysis of wind induced vibrations of overhead power conductors. Using this analysis, stability boundaries are calculated for a number of different array geometries and the results obtained are compared with available experimental data.

The analysis for a single flexible cylinder in an otherwise rigid array is not claimed to be a priori better than that for a fully flexible array, which is presented in [13]; the aim here is to explore the limitations of this simpler analysis, for the following reasons: (i) because it is simpler and experimentally and computationally cheaper, (ii) because the results are easier to interpret physically, and (iii) in view of the controversy as to whether a single flexible cylinder in an otherwise rigid array can become unstable for both low and high $m\delta/\rho d^2$, which contrasts Chen's [7, 8] and Lever and Weaver's [11] theories.

## 2 Theory

Consider a single flexible cylinder in the midst of an array of rigid cylinders subject to a cross-flow normal to the cylinder axis (Fig. 1). In the analysis, the so-called "semi-rigid" approach is taken in which the cylinder deformation is specified by a number of pertinent mode shapes. In fact, the cylinder is considered as being rigid, with the system flexibility being provided by an orthogonal spring system supporting the cylinder, as shown in Fig. 1. The equations of motion of the cylinder may easily be written as

$$[M]\ddot{\mathbf{z}} + [C]\dot{\mathbf{z}} + [E]\mathbf{z} = \mathbf{F}, \tag{1}$$

where $[M] = ml[I_2]$ is the mass matrix, $m$ being the mass per unit length, $l$ the cylinder length, and $[I_2]$ the unit matrix of order 2; $[C] = c[I_2]$ is the mechanical damping matrix, $c$ being an equivalent modal viscous damping coefficient; $[E] = k[I_2]$ is the mechanical stiffness matrix, $k$ being an equivalent modal stiffness; $\mathbf{z} = \{x, y\}^T$, $x$ and $y$ being the in-flow and cross-flow cylinder displacements, repectively; and $\mathbf{F}$ represents the fluid forces acting on the cylinder.

**2.1 Fluid Forces and Flow Retardation.** Using a standard quasi-static analysis [9, 13] the fluid forces acting on the cylinder in the $x$- and $y$-directions may be written as

$$F_x = \tfrac{1}{2}\rho U_\infty^2 ld\left(C_D\left[1 - \frac{2}{U_\infty a}\dot{x}\right] + C_L\frac{\dot{y}}{U_\infty a}\right),$$

$$F_y = \tfrac{1}{2}\rho U_\infty^2 ld\left(C_L\left[1 - \frac{2}{U_\infty a}\dot{x}\right] - C_D\frac{\dot{y}}{U_\infty a}\right), \tag{2}$$

where $\rho$ is the fluid density; $a$ is the ratio between the flow velocity impinging on the cylinder and the free stream velocity, $U_\infty$, which may be obtained from continuity: $a = T/(T - \tfrac{1}{2}d)$; and $C_L$ and $C_D$ are the lift and drag coefficients, respectively, and are functions of $x$ and $y$. Assuming that it may be expressed in linear form, $C_L$ may be written as

$$C_L = C_{L_0} + x\frac{\partial C_L}{\partial x} + y\frac{\partial C_L}{\partial y} \tag{3}$$

and similary for $C_D$, where $x$ and y are assumed small.

Before substituting these expressions into equations (2), it is necessary to establish exactly what $x$ and $y$ are—the complication being that as the flow approaches the cylinder it is retarded, producing a time delay, $\Delta t$. Thus, the fluid impinging on the body at time $t$ is that which, if the velocity had been steady, would have impinged at time $t - \Delta t$, so producing a time delay between the cylinder arriving at a given position and achieving the static forces acting on it associated with that position. This can be particularly important in cases such as the present one, where large changes in the fluid force coefficients may occur as a result of small cylinder displacements, particularly for motions in the $y$-direction.

The effect of this flow retardation on the fluid dynamics has

## Nomenclature

$a$ = ratio of reference gap velocity to free stream velocity, $U_G/U_\infty$
$c$ = equivalent modal mechanical-damping viscous coefficient
$C_D$, $C_L$ = drag and lift coefficients, respectively
$d$ = cylinder diameter
$e$ = equivalent modal mechanical stiffness term
$f$ = natural frequency of oscillation for the cylinder in vacuum (Hz)
$\mathbf{F}$ = fluid force vector for the cylinder
$\bar{g}$ = frequency-dependent time delay term
$i$ = $\sqrt{-1}$
$l$ = cylinder length
$L$ = equilibrium separation between cylinders in the in-flow direction
$m$ = mass per unit length of the cylinder
$\bar{m}$ = nondimensional mass of the cylinder, $m/\rho d^2$
$P$ = equilibrium pitch separation between cylinders (Fig. 1)
$R$ = cylinder radius
$t$ = time
$T$ = equilibrium separation between cylinders in the cross-flow direction
$U_c$ = critical value of $U_\infty$ for oscillatory instability
$U_G$ = reference gap velocity, $U_\infty T/(T - \tfrac{1}{2}d)$
$U_p$ = "pitch" flow velocity, $U_\infty P/(P-d)$
$U_\infty$ = free stream velocity
$\bar{U}$ = nondimensiosnal velocity, $U_\infty/\omega d$
$x$, $y$ = cylinder displacements in the in-flow and cross-flow direction, respectively
$\bar{x}$, $\bar{y}$ = nondimensional cylinder displacements; $x/d$ and $y/d$, respectively
$\mathbf{z}$ = cylinder displacement vector
$\beta$ = fluid damping term
$\delta$ = cylinder logarithmic decrement in vacuum
$\kappa$ = fluid stiffness term
$\lambda$ = complex eigenvalue
$\mu$ = flow retardation parameter
$\rho$ = fluid density
$\tau$ = dimenionless time, $\omega t$
$\omega$ = circular frequency of oscillation for the cylinder in vacuum

already been obtained by Simpson and Flower [14]; it is presented here in abbreviated form. If the fluid velocity, $U$, impinging on a cylinder is constant, then the time taken to traverse from $x = x_1$ to $x = R + \Delta R$ is $t = (x_1 - R - \Delta R)/U$; but in fact the viscous fluid slows down as it nears the cylinder. If the approach velocity is taken as variable and is denoted by $U_v$, then the time taken to traverse the same distance is

$$t + \Delta t = \int_{R+\Delta R}^{x_1} \frac{1}{U_v}\, dx;$$

now, if $U_v$ is taken to be the same as that given by potential flow theory around an isolated cylinder,[1] then $U_v = U(1 - R^2/x^2)$, yielding

$$\Delta t = \frac{R}{2U}\left[\ln\left(\frac{x_1 - R}{x_1 + R}\right) - \ln\left(\frac{\Delta R}{2R + \Delta R}\right)\right].$$

Following Simpson and Flower [14], $x_1 \sim 0(2R)$ and $\Delta R \sim 0(R/100)$ are taken, yielding

$$\Delta t = \mu d/U; \quad \mu \sim 0(1).$$

In reference [13] the effect of varying $\mu$ on stability was investigated; for a rotated triangular array ($P/d = 1.375$), it was found that $\mu = 1$ indeed appears to give the best agreement between theory and experiment. Thus, $\mu = 1$ will be used in all of the calculations in this paper.

The effect of this flow retardation on the $y$-motion is such that the cylinder suffers an apparent displacement of $\Delta y = y(t) - y(t - \Delta t)$. Assuming the cylinder motions to be of damped harmonic form, then

$$\Delta y = y(t)(1 - \bar{g}); \quad \bar{g} = \exp(-\lambda \mu d/U).$$

It should be noted that if the cylinder is in an upstream row, then the pertinent flow velocity $U$ is $U_\infty$, but for all other rows $U = aU_\infty$.

If the retardation effects are considered to be equally operative in both the $x$- and $y$-motions, then the modified form of equation (3) is

$$C_L = C_{L_0} + \bar{g}\left(x\frac{\partial C_L}{\partial x} + y\frac{\partial C_L}{\partial y}\right),$$

and similary for $C_D$. Thus after substitution of these expressions into equations (2), the fluid forces become

$$\mathbf{F} = \tfrac{1}{2}\rho U_\infty^2 ld\left\{\frac{\tfrac{1}{2}\pi d}{U_\infty^2}[A]\ddot{\mathbf{z}} + \frac{1}{U_\infty a}[B]\dot{\mathbf{z}} + \bar{g}[K]\mathbf{z} + \mathbf{F}_0\right\}, \quad (4)$$

where $[A]$ is the added mass matrix, which may be calculated by the method of Paidoussis et al. [15]; the fluid damping matrix, $[B]$, the fluid stiffness matrix, $[K]$, and the static force coefficient vector, $\mathbf{F}_0$, are

$$[B] = \begin{bmatrix} -2C_{D_0}, & C_{L_0} \\ -2C_{L_0}, & -C_{D_0} \end{bmatrix}, \quad [K] = \begin{bmatrix} \partial C_D/\partial x, & \partial C_D/\partial y \\ \partial C_L/\partial x, & \partial C_L/\partial y \end{bmatrix},$$

$$\mathbf{F}_0 = \{C_{D_0}, C_{L_0}\}^T.$$

Substitution of equation (4) into (1) yields the equations of motion of the system.

**2.2 Solution of the Equations.** The equations of motion may, of course, be solved using standard eigenvalue techniques; however, they may also be sovled in a much more convenient manner. For a single flexible cylinder, symmetrically positioned with respect to adjacent cylinders, it is clear both from physical intuition and from experimental results that $C_{L_0} = \partial C_L/\partial x = \partial C_D/\partial y = 0$. Thus, the off-diagonal terms in $[B]$ and $[K]$ of equations (4) vanish. Now, if the coupling terms in the added mass matrix, which are generally small, are neglected, then equations (1) and (4) may be written as two uncoupled equations of the form

$$ml\ddot{\bar{z}} + c\dot{\bar{z}} + e\bar{z} = \frac{\pi}{4} d^2 l\rho A\ddot{\bar{z}} + \tfrac{1}{2}\rho U_\infty^2 ld\{(d/U_\infty a)\beta\dot{\bar{z}} + \bar{g}\kappa\bar{z}\}, \quad (5)$$

where $\bar{z}$ may be either $\bar{x}$ or $\bar{y}$ (defined as $\bar{x} = x/d$ and $\bar{y} = y/d$); $\beta$ and $\kappa$ are the appropriate fluid damping or stiffness terms: $-2C_{D_0}$ and $\partial C_D/\partial\bar{x}$, respectively, if $\bar{z} = \bar{x}$; or $-C_{D_0}$ and $\partial C_L/\partial\bar{y}$, respectively, if $\bar{z} = \bar{y}$.

Equation (5) may be written in terms of nondimensional time, $\tau$, as follows:

$$\bar{z}''\left[1 - \frac{\pi}{4}\frac{A}{\bar{m}}\right] + \bar{z}'[\delta/\pi - \beta\bar{U}/2a\bar{m}] + \bar{z}[1 - \kappa\bar{g}\bar{U}^2/2\bar{m}] = 0,$$

where $(\,)' = (d/d\tau)$, $\bar{m} = m/\rho d^2$, $\bar{U} = U_\infty/\omega d$, $\omega = (e/ml)^{1/2}$ being the circular natural frequency in vacuum, and $\delta$ is the modal logarithmic decrement.

If the analysis is restricted to obtaining a stability boundary, then a solution of the form $\bar{z} = \bar{z}_0 \exp(ip\tau)$ may be taken, where $p$ is a real number. Thus, $\bar{g}$ will be given by $\bar{g} = \exp(-ip\mu/\bar{U}a)$, and the above equations may be written as

$$-p^2\left[1 - \frac{\pi}{4}\frac{A}{\bar{m}}\right] + ip\left[\frac{\delta}{\pi} - \frac{\beta}{2a}\frac{\bar{U}}{\bar{m}}\right] + \left[1 - \frac{\kappa}{2}\frac{\bar{U}^2}{\bar{m}}\left\{\cos\left(\frac{-p\mu}{\bar{U}a}\right) + i\sin\left(\frac{-p\mu}{\bar{U}a}\right)\right\}\right] = 0. \quad (6)$$

Equating real and imaginary parts of (6) to zero yields the critical values for neutral stability: $\bar{U} = \bar{U}_c$, $p = p_c$.

**2.3 Solutions for Large and Small $\bar{U}$.** In general, the solution of equation (6) has to be obtained iteratively, because $p/\bar{U}$ is the argument of the trigonometric functions. However, for sufficiently large values of $U$ (gaseous flows), i.e., for small $p\mu/\bar{U}a$, these functions are simplified to yield the closed-form, single-valued solutions: $\bar{U} = 2a\bar{m}\delta/[\pi(\beta - \mu\kappa)]$; in more conventional form, this may be written as

$$\left.\begin{aligned} U_c/fd &= \{4a/(-2C_{D_0} - \mu\partial C_D/\partial\bar{x})\}(m\delta/\rho d^2) \\ &\quad \text{for } x\text{-motions,} \\ U_c/fd &= \{4a/(-C_{D_0} - \mu\partial C_L/\partial\bar{y})\}(m\delta/\rho d^2) \\ &\quad \text{for } y\text{-motions.} \end{aligned}\right\} \quad (7)$$

These expressions hold for $U_c/fd > 10$, approximately. Since $C_{D_0} > 0$, for oscillatory instability to exist it is necessary that $\partial C_D/\partial\bar{x}$ or $\partial C_L/\partial\bar{y}$ be negative and sufficiently large; the other condition, that $p_c \neq 0$, is then automatically satisfied.

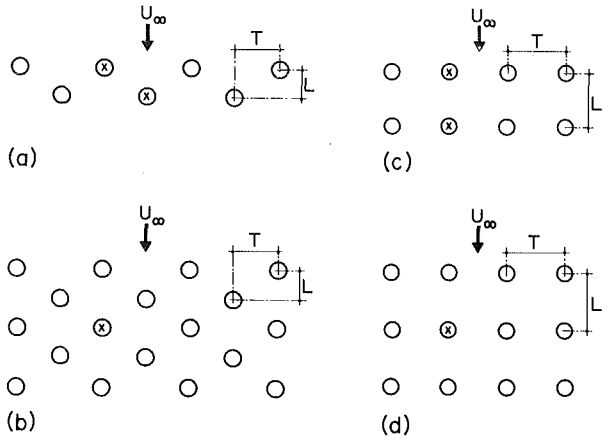


**Fig. 2 Schematic representation of the cylinder geometries analyzed. (a) a double staggered row; (b) a full staggered array; (c) a double in-line row; (d) a full in-line array.**

[1] Obviously this will not be correct but, in view of the other assumptions made with regard to this retardation effect, the complexity of a more exact expression is not warranted.

**Table 1 Fluid-force coefficients for the different array geometries investigated**

| Array | Rotated square $P/d=2.12$ | | | Rotated triangular $P/d=1.375$ | | | In-Line square $P/d=1.5$ | | |
|---|---|---|---|---|---|---|---|---|---|
| No. of rows<br>Row location | Two<br>Front | Two<br>Back | Five<br>Middle | Two<br>Front | Two<br>Back | Five<br>Middle | Two<br>Front | Two<br>Back | Three<br>Middle |
| $C_{D_0}$ | 2.8 | 3.2 | 2.0 | 7.7 | 6.1 | 6.8 | 10.6 | 2.2 | 2.3 |
| $\partial C_L/\partial \bar{y}$ | −0.2 | 1.7 | 3.7 | −7.8 | 0.9 | −243 | −28.6 | −25.7 | −73 |
| $\partial C_D/\partial \bar{x}$ | −0.9 | 0.3 | −0.3 | −6.8 | −1.0 | −5.2 | −12.0 | 0.9 | −6.3 |
| $\left\{\frac{4a}{-C_{D_0}-\partial C_L/\partial \bar{y}}\right\}$ | −ve | −ve | −ve | 68.9 | −ve | 0.029 | 0.22 | 0.51 | 0.17 |

For small $U$, on the other hand, it is no longer perimissible to linearize $\sin(-p\mu/\bar{U}a)$ which then oscillates between $-1$ and 1, and hence yields multiple values of $U_c$; moreover, in this case it may be shown that instabilities may arise, not only for $\partial C_L/\partial \bar{y}$ or $\partial C_D/\partial \bar{x}$ negative and large, but also positive and large. In this case, $U_c/fd$ is obtained by solving equations (6).

## 3 Results

The stability of a single flexible cylinder in the midst of six geometrical arrangements was investigated. Four of the staggered arrangements tested are represented by the two- and five-row arrays shown in Figs. 2(*a*) and 2(*b*): either of a rotated square geometry ($L/d = T/d = 1.5$; $P/d = 2.12$), or of a rotated triangular geometry ($L/d = 1.191$, $T/d = 0.688$; $P/d = 1.375$). Figs. 2(*c*) and (*d*) are two- and three-row in-line square arrays ($L/d = T/d = P/d = 1.5$). The flexible cylinder was positioned in any of the rows marked with an "$x$" in Figs. 2.

The necessary force coefficients and their derivatives were measured for these geometric patterns, using static models mounted in a wind tunnel; complete details of the wind tunnel and the measurement techniques used are given in [16]; the numerical results are presented in Table 1. In view of equations (7) and of the values of $\partial C_L/\partial \bar{y}$ and $\partial C_D/\partial \bar{x}$ in the table, it is clear that, in the range of applicability of equation (7), instability will occur in the $y$-direction, if at all. The last line of the table gives the factor relating $U_c/fd$ to $m\delta/\rho d^2$ for $\mu = 1$; if this is negative, obviously instability is not possible.

The results obtained by this analysis will be compared with available experimental data [17–33].

**3.1 Results for the Rotated Triangular Array ($P/d = 2.12$).** As shown in Table 1 and as confirmed by solutions of equation (6), no instability is possible in these arrays—for the locations of the flexible cylinder shown in the table. This surprising result was confirmed by experiments conducted in air flow, in all three cases shown in Table 1, and in water flow for the case of a seven-row array [32, 33]. Similar results were obtained [33] with a tighter array ($P/d = 1.5$).

This is an important result, for it shows that, for at least one array geometry, a single flexible cylinder in the array will *not* be subject to fluidelastic instability. On the other hand, it is known that all-flexible arrays do become fluidelastically unstable (e.g., [25]); also, it was shown that, if more than one cylinder is allowed to be flexible, then fluidelastic instability *is* predicted [13].

Hence, single-flexible-cylinder analysis (this one, or others' [11, 34]) cannot be used to analyze the stability of fully flexible rotated square arrays. Evidently, in this case, fluid-stiffness coupling effects are instrumental in precipitating instability. It is nevertheless gratifying that the present theory predicts the same as was obtained experimentally, in the case of a single flexible cylinder in the array, as it should.

**3.2 Results for the Rotated-Triangular Array ($P/d = 1.375$).** As shown in Table 1, instability in the front row of a two-row array is just possible, but $U_c/fd$ in this case would be

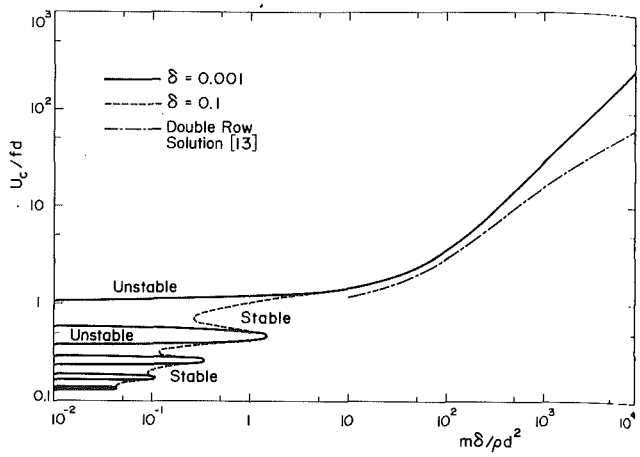


**Fig. 3 Variation of critical flow velocity with combined mass-damping parameter for a single flexible cylinder in the middle of a rotated triangular array of rigid cylinders with $P/d = 1.375$.**

$\sim 0(10^3)$, very much higher than any of the other instabilities in the table, or reported in the literature. Thus, it may be said that this two-row array is efffectively stable. No experiments were conducted to test this result.

The five-row array, on the the hand, is highly unstable, and $U_c/fd = 0.029(m\delta/\rho d^2)$ in this case. The existence of fluidelastic instability was confirmed experimentally, by the authors [33] and other investigators, e.g. [21].

From equations (7) is appears that $U_c/fd$ is linearly proportional to $m\delta/\rho d^2$, and for a single flexible cylinder at high values of $m\delta/\rho d^2$ this, in fact, is so. However, for low values of $m\delta/\rho d^2$, this linear relationship no longer holds, as equation (7) is no longer valid. Results obtained by solving equation (6) in full are presented in Fig. 3. For $m\delta/\rho d^2 \geq 100$ approximately, $U_c/fd$ varies linearly with $m\delta/\rho d^2$, while for $m\delta/\rho d^2 < 100$ the variation is no longer linear.

It should not be be inferred that the authors believe $U_c/fd$ to vary linearly with $m\delta/\rho d^2$ for a *full array of flexible cylinders*, even at high $m\delta/\rho d^2$. It has been shown [13] that for $m\delta/\rho d^2 \geq 300$ the fluidelastic coupling between cylinders becomes important, and in this region there will be a substantial difference between the critical flow velocities of a single flexible cylinder and a full array of flexible cylinders. To illustrate this point, the variation of $U_c/fd$ with $m\delta/\rho d^2$ for a double row of flexible cylinders in the middle of an array of rigid cylinders, as obtained in [13], is also presented in Fig. 3. The substantial differences between the two solutions for $m\delta/\rho d^2 > 300$ may easily be seen. If an attempt is made to express the dependence of $U_c/fd$ with $m\delta/\rho d^2$ in a Connors-type expression, then the exponent of $m\delta/\rho d^2$ will be less than 1 for $m\delta/\rho d^2 > 300$, this exponent decreasing as $m\delta/\rho d^2$ increases.

A very important consequence of the flow retardation parameter may be observed in Fig. 3; for $m\delta/\rho d^2 < 1.5$ there are bands of velocity above the minimum critical flow velocity for which the system is stable. For example, at $m\delta/\rho d^2 =$

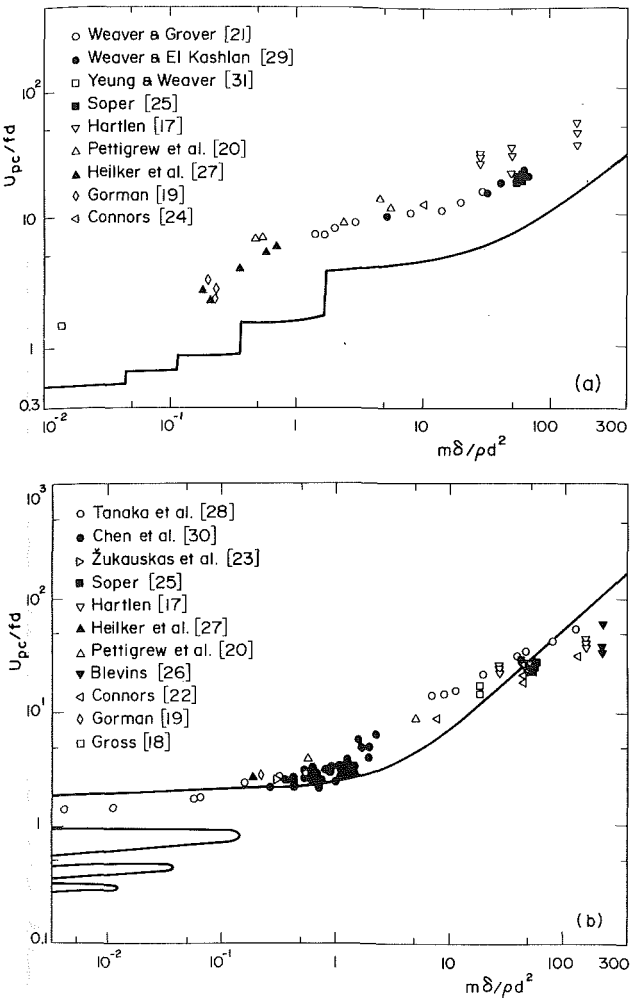


**Fig. 4 A comparison between the theoretical solution of a single flexible cylinder ($\delta$ = 0.05, $\mu$ = 1) with available experimental data. (*a*) a rotated triangular array with P/d 1.375; (*b*) an in-line square array with P/d = 1.5.**

0.5, with $\delta = 0.001$, the system becomes unstable at $U_c/fd = 0.40$; at $U/fd = 0.56$ it is restabilized, becoming unstable again for all $U/fd \geq 1.15$. This somewhat surprising behavior is a direct result of the periodicity in the fluid stiffness terms of equation (6) – which, in turn, is a result of the flow-retardation time lag being a function of $U/fd$. Thus, flow retardation is capable of producing regions of positive fluid damping for flow velocities above that which produces negative fluid damping. This behavior is, in fact, very similar to that obtained by Lever and Weaver [11].

Although the numerical results of this fluid-dynamically linearized analysis indicate that increasing flow velocity at low $m\delta/\rho d^2$ will produce alternate unstable and stable regions, the authors do not expect this to materialize in practice, the reason being that, once the system becomes unstable, linear theory is no longer applicable and "hard" oscillator effects will sustain instability in the regions indicated to be stable by linear theory. Thus, the instability boundary at any $m\delta/\rho d^2$ will be as indicated by the "minimum" critical flow velocity; note, that this will yield jumps in the instability boundary as $m\delta/\rho d^2$ is increased. A further question relates to how many of these "bounded" unstable regions can exist. In Fig. 3, four of these regions are shown, with the width of $U/fd$ for the lowest region being approximately 0.01, or less than 10 percent, of $U_c/fd$. It is to be expected that, in any real array, interstitial flow turbulence and turbulent buffeting would produce changes in the gap flow velocity of this order and, thus, these narrow unstable regions would not materialize.

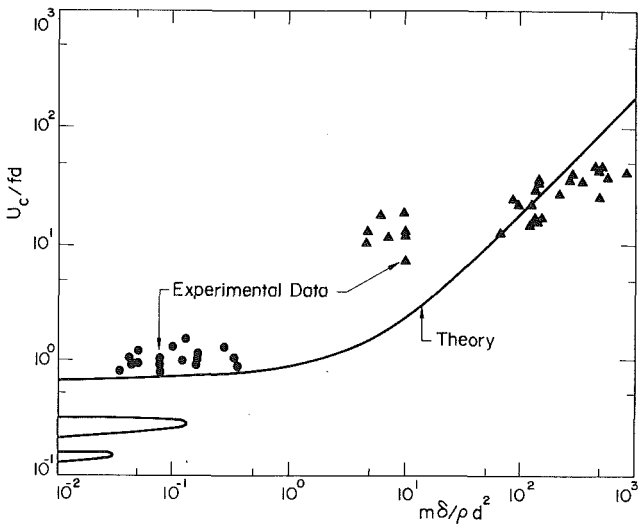


**Fig. 5 A comparison between experimental data [32, 33] and the theoretical stability boundary ($\delta$ = 0.05, $\mu$ = 1), for a single flexible cylinder in an in-line square array of rigid cylinders, with P/d = 1.5 (•, water flow; ▲, air flow).**

A last point of interest at low $m\delta/\rho d^2$ is the independence of $\delta$ and $m/\rho d^2$. Dimensional analysis suggests no reason why these two non-dimensional terms should be lumped together into one, although conventionally this is often done. The results of this analysis show that for $m\delta/\rho d^2 > 5$, approximately, there is little error in doing so. However, for $m\delta/\rho d^2 < 5$ the critical flow velocity for a fixed $m\delta/\rho d^2$ depends on the specific value of $\delta$. In Fig. 3 it is shown that increasing $\delta$ from 0.001 to 0.1 tends to reduce the area of the stable velocity bands.

**3.3 Comparison With Experiment for the Rotated Triangular Array.** The results from available experimental data for fluidelastic instability from fully flexible rotated triangular arrays are compared with results from this single-flexible-cylinder theory in Fig. 4(*a*). The theoretical data are for $P/d = 1.375$; the experimental ones are for $1.2 < P/d < 1.5$, but several sets (e.g., [21, 29]) are for exactly $P/d = 1.375$. As the majority of experimental data are presented in terms of the pitch flow velocity, $U_p = U_\infty P/(P-d)$, the theoretical solution has been converted accordingly, to make comparison possible.

It is seen in Fig. 4(*a*) that agreement between the single-flexible-cylinder theory and the experimental data is generally good. The theoretical curve gives a lower bound for fluidelastic instability, being lower than the experimental points by approximately 50 percent for $0.01 < m\delta/\rho d^2 < 300$. (If plotted in the same figure, results from single-flexible-cylinder experiments [33] intermingle with those of fully flexible arrays).

A further encouraging point in favor of this theoretical solution is that the form of the experimental variation of $U_{pc}/fd$ with $m\delta/\rho d^2$ is far better represented by this analysis than by any Connors-type expression.

**3.4 Results for the In-Line Array ($P/d = 1.5$) and Comparison With Experiment.** As shown in Table 1, all three arrangements involving in-line square arrays are fluidelastically unstable, the least stable being the case of a flexible cylinder in the middle row of the three-row array. It is of particular interest to note the dependence of $U_c/fd$, not only on the number of rows in the array, but also on the row in which the flexible cylinder is located; thus, a cylinder in the front row of the two-row array would become unstable at a flow velocity 2.3 times smaller than one in the back row. These theoretical predictions were confirmed by wind and water tunnel experiments.

The theoretical values of $U_{pc}/fd$ and $U_c/fd$, obtained from equation (6), for a flexible cylinder in the middle of a three-row array are given in Fig 4(*b*) and Fig. 5, respectively. They are similar to those of Figs. 3 and 4(*a*) and need not be discussed at length. The theoretical values of $U_{pc}/fd$ are compared with available experimental data from fully flexible arrays (in which $1.3 < P/d < 2.0$) in Fig. 4(*b*); and with the authors' experimental data [32, 33] involving a single flexible cylinder in interior rows of five- or six-row arrays ($P/d = 1.5$) in Fig. 5.

The experimental results of Fig. 5 are for the flexible cylinder in the second, third or fourth row of the five-row array in water flow, and in the second or fifth row of the six-row array in air flow; no effect of position could be detected in the results and so these different positions are unidentified in the figure.

It is seen that theory is in good agreement with experiment, both for fully flexible arrays (Fig. 4(*b*)) and for a single flexible cylinder (Fig. 5). Once again, at least for $m\delta/\rho d^2 < 100$, the theoretical curve gives an effective lower bound for the critical flow velocity.

## 4 Conclusions

A quasi-static analysis of a single flexible cylinder positioned either in a double row or in a full array of rigid cylinders has been presented. Although the analysis is quasi-static, a frequency-dependent term is obtained, arising from retardation of flow approaching the stagnation region of the cylinder. It is shown that the stability of the cylinder is strongly dependent on the geometrical pattern and spacing of the adjacent cylinders, even though they are rigid and play no part in the dynamic analysis. For those geometric patterns predicted to be unstable, the motion of the unstable cylinder is purely in the cross-flow direction.

Using this analysis, the effect of mechanical damping on the critical flow velocity is investigated. It is shown that for low $m/\rho d^2$ an increase in damping may not produce a change in $U_c/fd$, unless a "jump" in the instability boundary is encountered. However, for high $m/\rho d^2$ an increase in damping will always increase $U_c/fd$. If an attempt is made to express the stability boundary in a "Connors-type" expression, then the exponent of the $m\delta/\rho d^2$ term will be a function of $m\delta/\rho d^2$ itself. The results presented here suggest that this exponent will vary from approximately 0.0 to 1.0.

A comparison is made between the critical flow velocities obtained theoretically using this analysis and available experimental data for two types of array: a rotated triangular array and a square in-line array. In general, the agreement is good, especially for the in-line array. When it is realized how little experimental input is required for this analysis, as compared to either the complete quasi-static analyses [5, 9, 10, 13] or the unsteady type analysis [6–8], then the agreement between theory and experiment seems even more remarkable.

A major contribution of this work has been the exploration of the limitations of single-flexible-cylinder analyses, such as this one and Lever and Weaver's [11, 34].

The first limitation is that $m\delta/\rho d^2$ be not too high ($<300$, approximately). As shown previously by Chen [7, 8] and by the authors [13], there are two possible mechanisms producing instability: (i) a negative damping mechanism, prevalent at low $m\delta/\rho d^2$; (ii) a fluidelastic stiffness mechanism, which is dominant at high $m\delta/\rho d^2$. As shown in Fig. 3 for the rotated triangular array, for sufficiently high $m\delta/\rho d^2$, single-flexible-cylinder analyses seriously overestimate stability, because they neglect fluidelastic-stiffness effects between neighboring cylinders.

A second major limitation exposed here is that certain types of fully flexible arrays, notably rotated square arrays, cannot be analyzed at all by single-flexible-cylinder analysis. Thus, the single-flexible-cylinder analysis predicts that these arrays are unconditionally stable, and this was experimentally confirmed; yet, if more than one of the cylinders are flexible, fluidelastic instabilities are possible [13], suggesting that for such arrays fluidelastic-stiffness coupling effects are important for all values of $m\delta/\rho d^2$. This limitation of single-flexible-cylinder analysis is not recognized by Lever and Weaver [11, 34], who predict fluidelastic instability of *a single flexible cylinder* within rotated square arrays, indepedent of $P/d$, contrary to experimental evidence.

Another advantage of this type of analysis via-à-vis Lever and Weaver's is that it can easily be extended to deal with more than one flexible cylinder in the array [13, 35], whereas the Lever and Weaver model cannot.

## Acknowledgments

The authors gratefully acknowledge the financial support of the Natural Sciences and Engineering Research Council of Canada and Le programme FCAC of Québec.

## References

1 Paidoussis, M. P., "Flow-Induced Vibrations in Nuclear Reactors and Heat Exchangers; Practical Experiences and State of Knowledge," *Practical Experiences with Flow-Induced Vibrations* (eds. Naudascher, E. and Rockwell, D.), Springer-Verlag, Berlin, 1980, pp. 1–81.

2 Paidoussis, M. P., "Fluidelastic Vibration of Cylinder Arrays in Axial and Cross Flow," *Journal of Sound and Vibration*, Vol. 76, 1981, pp. 329–359.

3 Paidoussis, M. P., "A Review of Flow-Induced Vibrations in Reactors and Reactor Components," *Nuclear Engineering and Design*, Vol. 74, 1983, pp. 31–60.

4 Connors, H. J., Jr., "Fluidelastic Vibration of Tube Arrays Excited by Cross-Flow," *Flow-Induced Vibration in Heat Exchangers* (ed. Reiff, D. D.), ASME, New York, 1970, pp. 42–56.

5 Belvins, R. D., "Fluid Damping and the Whirling Instability of Tube Arrays," *Flow-Induced Vibrations* (eds. Chen, S. S., and Bernstein, M. D.), ASME, New York 1979, pp. 35–39.

6 Tanaka, H., and Takahara, S., "Unsteady Fluid Dynamic Force on Tube Bundle and its Dynamic Effects on Vibration," *Flow-Induced Vibration of Power Plant Components* (ed. Au-Yang, M. K.), ASME, New York, 1980, pp. 77–92.

7 Chen, S. S., "Instability Mechanisms and Stability Critieria of a Group of Circular Cylinders Subjected to Cross Flow. Part I: Theory," ASME *Journal of Vibration, Acoustics, Stress and Reliability in Design*, Vol. 105, 1983, pp. 51–58.

8 Chen, S. S., "Instability Mechanism and Stability Criteria of a Group of Circular Cylinders Subjected to Cross Flow. Part 2: Numerical Results and Discussion," ASME *Journal of Vibration, Acoustics, Stress and Reliability in Design*, Vol. 105, 1983, pp. 253–260.

9 Price, S. J., and Paidoussis, M. P., "Fluidelastic Instability of a Double Row of Circular Cylinders Subject to a Cross-Flow," ASME *Journal of Vibration, Acoustics, Stress and Reliability in Design*, Vol. 105, 1983, pp. 59–66.

10 Whiston, G. S., and Thomas, G. D., "Whirling Instabilities in Heat Exchanger Tube Arrays," *Journal of Sound and Vibration*, Vol. 77, 1982, pp. 1–31.

11 Lever, J. H., and Weaver, D. S., "A Theoretical Model for the Fluidelastic Instability in Heat Exchanger Tube Bundles," ASME *Journal of Pressure Vessel Technology*, Vol. 104, 1982, pp. 147–158.

12 Paidoussis, M. P., Mavriplis, D., and Price, S. J., "A Potential Flow Theory for the Dynamics of Cylinder Arrays in Cross Flow," *Journal of Fluid Mechanics*, Vol. 146, 1984, pp. 227–252.

13 Price, S. J., and Paidoussis, M. P., "An Improved Mathematical Model for the Stability of Cylinder Rows Subject to Cross-Flow," *Journal of Sound and Vibration*, Vol. 97, 1984, pp. 615–640.

14 Simpson, A., and Flower, J. W., "An Improved Mathematical Model for the Aerodynamic Forces on Tandem Cylinders in Motion with Aeroelastic Applications," *Journal of Sound and Vibration*, Vol. 51, 1977, pp. 183–217.

15 Paidoussis, M. P., Suss, S., and Pustejovsky, M., "Free Vibration of Cylinders in Liquid-Filled Channels," *Journal of Sound and Vibration*, Vol. 55, 1977, pp. 443–459.

16 Price, S. J., and Paidoussis, M. P., "The Aerodynamic Forces Acting on Groups of Two and Three Circular Cylinders when Subject to a Cross Flow," *Journal of Industrial Aerodynamics and Wind Engineering*, Vol. 17, 1984, pp. 329–347.

17 Hartlen, R. T., "Wind Tunnel Determination of Fluidelastic Vibration Thresholds for Typical Heat Exchanger Tube Patterns," *Ontario Hydro Report 74-309-K*, 1974.

18 Gross, H.-C., "Untersuchung Aerolastischer Schwingungs-mechanismen und deren Berücksichtigung bei der Auslegung von Rohrbündel-Wärmetauschern," Ph.D. Thesis, *Technical University of Hanover*, 1975.

19 Gorman, D. J., "Experimental Study of Peripheral Problems Related to Liquid Flow Induced Vibration in Heat Exchangers and Steam Generators," *Trans. 4th International Conference on Structural Mechanics in Reactor Technology*, Paper No. 4/g, San Francisco, 1977.

20 Pettigrew, M. J., Sylvestre, Y., and Campagna, A. O., "Vibration

Analysis of Heat Exchanger and Steam Generator Designs," *Nuclear Engineering and Design*, Vol. 48, 1978, pp. 97–115.

21 Weaver, D. S., and Grover, L. K., "Cross-Flow Induced Vibrations in a Tube Bank," *Journal of Sound and Vibtration*, Vol. 59, 1978, pp. 277–294.

22 Connors, H. J., "Fluidelastic Vibration of Heat Exchanger Tube Banks," ASME *Journal of Mechanical Design*, Vol. 100, 1978, pp. 347–353.

23 Žukauskas, A., and Katinas, V., "Flow-Induced Vibration in Heat-Exchanger Tube Banks," *Practical Experiences with Flow-Induced Vibrations* (eds. Naudascher, E. and Rockwell, D.), Springer-Verlag, Berlin, 1980, pp. 188–196.

24 Connors, H. J., "Fluidelastic Vibration of Tube Arrays Excited by Non-Uniform Cross Flows," *Flow-Induced Vibration of Power Plant Components*, (ed. Au-Yang, M. K.), ASME, New York, 1980, pp. 93–108.

25 Soper, B. M. H., "The Effect of Tube Layout on the Fluidelastic Instability of Tube Bundles in Cross Flow," *Flow-Induced Heat Exchanger Tube Vibration* (ed. Chenoweth, J. M.), ASME, New York, 1980, pp. 1–9.

26 Blevins, R. D., Gibert, R. J., and Villard, B., "Experiments on Vibration of Heat Exchanger Tube Arrays in Cross Flow," *Trans. 6th International Conference on Structural Mechanics in Reactor Technology*, Paper No. B6/9, Paris, 1981.

27 Heilker, W. J., and Vincent, R. Q., "Vibration in Nuclear Heat Exchangers due to Liquid and Two-Phase Flow," ASME *Journal of Engineering for Power*, Vol. 103, 1981, pp. 358–366.

28 Tanaka, H., and Takahara, S., "Fluidelastic Vibration of Tube Array in Cross Flow," *Journal of Sound and Vibration*, Vol. 77, 1981, pp. 19–37.

29 Weaver, D. S., and El-Kashlan, M., "The Effect of Damping and Mass Ratio on the Stability of a Tube Bank," *Journal of Sound and Vibration*, Vol. 76, 1981, pp. 283–294.

30 Chen, S. S., and Jendrzejczyk, J. A., "Experiment and Analysis of Instability of Tube Rows Subject to Liquid Cross Flow," ASME *Journal of Applied Mechanics*, Vol. 104, 1982, pp. 704–709.

31 Yeung, H. C., and Weaver, D. S., "The Effect of Approach Flow Direction on the Flow-Induced Vibrations of a Triangular Tube Array," ASME *Journal of Vibration, Acoustics, Stress and Reliability in Design*, Vol. 105, 1983, pp. 76–82.

32 Price, S. J., Mark, B., and Paidoussis, M. P., "An Experimental Stability Analysis of a Single Flexible Cylinder Positioned in an Array of Rigid Cylinders and Subject to Cross-Flow," *Symposium on Flow Induced Vibrations*, Vol. 2, (eds. Paidoussis, M. P., Au-Yang, M. K., and Chen, S.-S.), ASME, New York, 1984, pp. 179–194.

33 Price, S. J., Paidoussis, M. P., Candler, G., Mark, B., Macdonald, R., and Hagyard, K., Yet unpublished experimental data on the dynamics and stability of rotated square, in-line square and rotated triangular arrays in air and water cross-flow. Dept. of Mechanical Engineering, McGill University, 1985.

34 Lever, J. H., and Weaver, D. S., "On the Stability of Heat Exchanger Tube Bundles. Part I and II," *Symposium on Flow-Induced Vibrations*, Vol. 2, (eds. Paidoussis, M. P., Au-Yang, M. K., and Chen, S.-S.). ASME, New York, 1984, pp. 83–116.

35 Price, S. J., and Paidoussis, M. P., "Fluidelastic Instability of a Full Array of Flexible Cylinders Subject to Cross-Flow," *Fluid-Structure Interaction and Aerodynamic Damping*, (eds. Dowell, E. H. and Au-Yang, M. K.), ASME, New York, 1985, pp. 171–192.

**Sei-ichi Iida**
Professor.

**Akira Fujimoto**
Graduate Student.

Hokkaido University,
Department of Mechanical Engineering,
N13, W8, Sapporo,
060, Japan

# A Fast Approximate Solution of the Laminar Boundary-Layer Equations

*A new approximate method of calculating steady laminar boundary-layers is presented. This method is based on the mutual relationships between boundary-layer characteristic quantities. The governing equations are efficiently solved without assuming a specific velocity profile. Moreover, a method of estimating the velocity profile using the characteristic quantities is also proposed. Comparison of the results obtained for a wide variety of applications to boundary-layer flows with separations with exact solutions indicates that the present method enables one to obtain solutions with sufficient accuracy and shorter computational time when compared with existing computational techniques.*

## 1 Introduction

Today in calculating laminar boundary-layer flows, we can obtain highly accurate solutions using available finite-difference or finite-element schemes, but such schemes are rather complicated and take considerable computational time in comparison with approximate (integral) methods. Especially, in non-steady problems in which governing equations have to be solved repeatedly, it takes considerable computational time. Therefore, approximate methods are useful for many practical purposes [1]–[4].

One of the best-known approximate methods is the Kármán-Pohlhausen method [12] in which a fourth-degree polynomial is assumed as a velocity profile and a parameter $\Lambda(=(\delta^{*2}/\nu^*)(dU^*/dx^*))$ is introduced to connect the velocity profile to the boundary conditions. The momentum-integral equation is then solved by employing the assumed velocity profile. This method works well in an accelerated region, but cannot adequately predict the boundary-layer behavior near a separation point. An improved method was developed by Tani [5] who employed both the momentum- and the energy-integral equations. This method also assumes the velocity profile in the form of a fourth-degree polynomial, while a parameter $-a-$, which is proportional to skin friction, is introduced instead of $\Lambda$. The momentum thickness is evaluated from the energy-integral equation for a given external velocity distribution $U(x)$, and then the parameter $a$ is expressed as a function of $x$ while satisfying the momentum-integral equation. In both of these methods, however, the velocity profiles are not sufficiently accurate in comparison with its exact profiles because the profiles are introduced only to relate the boundary-layer characteristic quantities to the parameter $a$ or $\Lambda$. In most practical cases, our primary interest is in whether and where a boundary-layer separation occurs for a given external velocity distribution $U(x)$, and how the global quantities such as displacement thickness, momentum thickness and shape factors develop in the streamwise direction.

The present paper proposes an alternative method of calculating the boundary-layer characteristic quantities without assuming velocity profiles a priori. In this method, both the momentum- and the energy-integral equations are used as governing equations, and the characteristic quantities are mutually related simple formulas. A similar method was first reported by Tani and Yu [6] who studied boundary-layer flow on a flat plate suddenly moved in a still fluid. China and Kobashi [7] have applied a similar method to steady-state boundary-layer problems. Although they succeeded in obtaining solutions over a wide range of conditions with sufficient accuracy, further refinements of the method seem to be necessary to treat flows near a separation point. In the present method, the characteristic quantities are expressed as functions of $x$ and the Keller's box finite-difference formula [9]–[11] is applied to the one-dimensional flow governed by the two integral equations. As a result, a fairly rapid convergence was achieved even in the vicinity of a separation point.

In Section 2, the general formulation and the calculation scheme are presented. The relationships among the various characteristic quantities are approximated in Section 3 where the non-dimensional wall shear-stress $P$ is chosen as the independent variable. Other quantites are expressed as dependent variables of $P$ in simple formulas which are used to locally satisfy the exact solutions at a stagnation point, a flat plate condition and a separation point. For the last condition the value obtained from Howarth's retarded flow ($U = 1-x$) [8] at the separation point is employed. In Section 4, the present method is applied to several types of flow to demonstrate its usefulness in practical applications.

Since the method itself does not provide boundary-layer velocity profiles, a new calculation scheme is proposed in Section 5 in order to rapidly obtain velocity profiles from the characteristic quantities. Finally, this method of predicting velocity profiles is applied to typical flows. The profiles obtained show reasonable agreement with exact solutions.

## 2 Governing Equations and Computational Scheme

Let us consider both the momentum- and the energy-integral equations of a steady incompressible boundary-layer:

Contributed by the Fluids Engineering Division for publication in the JOURNAL OF FLUIDS ENGINEERING. Manuscript received by the Fluids Engineering Division, January 23, 1985.

$$(\partial u/\partial y)_w/U^2 = [(2\delta_2+\delta_1)/U](dU/dx) + d\delta_2/dx \quad (1)$$

$$d(U^3\delta_3)/dx = 2\int_0^\infty (\partial u/\partial y)^2 dy \quad (2)$$

where:

$$\left.\begin{aligned} &\delta_1 = \int_0^\infty (1-u/U)dy, \qquad \delta_2 = \int_0^\infty [u/U(1-u/U)]dy, \\ &\delta_3 = \int_0^\infty [u/U(1-u^2/U^2)]dy \end{aligned}\right\} \quad (3)$$

The variables in equations (1)–(3) have been normalized as:

$$x = x^*/L^*,\ y = y^*\sqrt{\mathrm{Re}}/L^*,\ u = u^*/Vr^*,\ U = U^*/Vr^*,$$

$$\delta_K = \delta_K{}^*\sqrt{\mathrm{Re}}/L^*(K=1,2,3,),\ \mathrm{Re} = Vr^*L^*/\nu^*$$

in which an asterisk denotes dimensional variables.
In addition, the characteristic quantites are defined as:

$$\left.\begin{aligned} &H = \delta_1/\delta_2, \qquad G = \delta_3/\delta_2, \\ &P = (2\delta_2/U)(\partial u/\partial y)_w, \qquad Q = (4\delta_3/U^2)\int_0^\infty (\partial u/\partial y)^2 dy \end{aligned}\right\} \quad (4)$$

Using these quantities, equations (1) and (2) may be rewritten as follows:

$$U(d\delta_2{}^2/dx) + 2(2+H)\delta_2{}^2(dU/dx) = P \quad (5)$$

$$U\delta_2{}^2(dG^2/dP)(dP/dX) + G^2P - 2G^2\delta_2{}^2(H-1)(dU/dx) = Q \quad (6)$$

Here, equation (5) is obtained directly from equation (1), and equation (6) is derived from both equations (2) and (5). Furthermore, the following quantities are introduced in order to simplify equations (5) and (6):

$$\Theta = \delta_2{}^2,\ \Gamma = G^2,\ V = dU/dx,\ \Omega = d\Gamma/dP \quad (7)$$

Finally, the two governing equations are obtained:

$$U(d\Theta/dx) + 2(2+H)\Theta V = P \quad (8)$$

$$U\Theta\Omega(dP/dx) + \Gamma P - 2\Gamma\Theta(H-1)V = Q \quad (9)$$

Since $H$, $G$, and $Q$ are regarded as functions of the independent variable $P$ (discussed later in Section 3), equations (8) and (9) constitute simultaneous ordinary differential equations for $P$ and $\Theta$, and thus can be easily solved by applying the box finite-difference scheme [9]–[11].

Considering $h_n$ as the nodal spacing between the $(n)$th and the $(n-1)$th nodal points in the $x$-direction, the quantities in these two equations may be approximated by the finite-difference formulation as follows:

$$\phi_{n-1/2} = (\phi_n + \phi_{n-1})/2 \quad (10)$$

$$(d\phi/dx)_{n-1/2} = (\phi_n - \phi_{n-1})/h_n \quad (11)$$

where $\phi$ denotes the quantity, such as $U$, $P$, $\Theta$, $(2+H)\Theta V$, $U\Theta\Omega$, etc., and $h_n$ is the spacing between $x_n$ and $x_{n-1}$. Moreover, for multiple iterations, revised quantities are expressed as:

$$\left.\begin{aligned} P_n{}^{i+1} &= P_n{}^i + \delta P_n{}^i \\ \Theta_n{}^{i+1} &= \Theta_n{}^i + \delta\Theta_n{}^i \end{aligned}\right\} \quad (12)$$

in which $\delta P_n{}^i$ and $\delta\Theta_n{}^i$ are small deviations.
The substitution of equations (10)–(12) into equations (8) and (9) while neglecting the quadratic terms of $\delta P_n{}^i$ and $\delta\Theta_n{}^i$ yield the following expressions:

$$\left.\begin{aligned} A_{11}\delta\Theta_n{}^i + A_{12}\delta P_n{}^i &= \Phi \\ A_{21}\delta\Theta_n{}^i + A_{22}\delta p_n{}^i &= \Psi \end{aligned}\right\} \quad (13)$$

where:

$$\left.\begin{aligned} A_{11} &= U_n + U_{n-1} + 2h_nV_n(H_n{}^i+2) \\ A_{12} &= -h_n \\ A_{21} &= U_n\Omega_n{}^i(P_n{}^i - P_{n-1}) - 2h_nV_n\Gamma_n{}^i(H_n{}^i-1) \\ A_{22} &= U_n\Omega_n{}^i\Theta_n{}^i + U_{n-1}\Omega_{n-1}\Theta_{n-1} + h_n\Gamma_n{}^i \end{aligned}\right\} \quad (14)$$

and:

$$\left.\begin{aligned} \Phi &= R_{n-1} - (A_{11}\Theta_n{}^i + A_{12}P_n^i) \\ \Psi &= S_{n-1} - (A_{21}\Theta_n{}^i + A_{22}P_n{}^i) + U_n\Omega_n{}^iP_n{}^i\Theta_n{}^i + h_nQ_n{}^i \end{aligned}\right\} \quad (15)$$

where:

$$\left.\begin{aligned} R_{n-1} &= [U_n + U_{n-1} - 2h_nV_{n-1}(H_{n-1}+2)]\Theta_{n-1} + h_nP_{n-1} \\ S_{n-1} &= (U_{n-1}\Omega_{n-1}\Theta_{n-1} - h_n\Gamma_{n-1})P_{n-1} \\ &\quad + h_n[Q_{n-1} + 2V_{n-1}\Gamma_{n-1}\Theta_{n-1}(H_{n-1}-1)] \end{aligned}\right\} \quad (16)$$

Here, the values with subscript $(n-1)$ indicate those at the point one-step upstream, which have been determined in the previous step.

The calculation begins with the specified initial condition,

## Nomenclature

Symbols without asterisk denote nondimensional quantities.

- $L^*$ = reference length
- $Vr^*$ = reference velocity
- $\nu^*$ = kinematic viscosity
- Re = Reynolds number = $Vr^*L^*/\nu^*$
- $u$ = velocity component in $x$ direction = $u^*/Vr^*$
- $U$ = local velocity outside boundary-layer = $U^*/Vr^*$
- $\bar{u}$ = $u/U$
- $x$ = abscissa along wall = $x^*/L^*$
- $y$ = ordinate normal to wall = $y^*\sqrt{\mathrm{Re}}/L^*$
- $\eta$ = scaled ordinate normal to wall = $y^*\sqrt{U^*/x^*\nu^*}$
- $\bar{\eta}$ = $\eta/\Delta$
- $\delta$ = boundary-layer thickness in $y$ scale
- $\delta_1$ = displacement thickness in $y$ scale
- $\delta_2$ = momentum thickness in $y$ scale
- $\delta_3$ = energy thickness in $y$ scale
- $\Delta$ = boundary-layer thickness in $\eta$ scale
- $\Delta_1$ = displacement thickness in $\eta$ scale
- $\Delta_2$ = momentum thickness in $\eta$ scale
- $P$ = wall shear-stress = $(2\delta_2/U)(\partial u/\partial y)_w$
- $H$ = shape factor = $\delta_1/\delta_2$
- $G$ = shape factor = $\delta_3/\delta_2$
- $Q$ = energy dissipation = $(4\delta_3/U^2)\int_0^\infty (\partial u/\partial y)^2 dy$

**Subscripts**

- $w$ = quantity at wall
- $st$ = value for two dimensional stagnation flow
- $fl$ = value for flat plate condition
- $sp$ = value for separation point
- $n$ = number of nodal point in $x$ direction
- $i$ = number of iterations
- $m$ = exponent of power
- $N$ = value obtained by numerical integration

Table 1 Fundamental data

| | | |
|---|---|---|
| $H_{sp}$= 3.82240 | $H_{fl}$= 2.59110 | $H_{st}$= 2.21623 |
| $G_{sp}$= 1.52698 | $G_{fl}$= 1.57258 | $G_{st}$= 1.62575 |
| $Q_{sp}$= 0.960492 | $Q_{fl}$= 1.09072 | $Q_{st}$= 1.35533 |
| $P_{sp}$= 0.0 | $P_{fl}$= 0.441048 | $P_{st}$= 0.720678 |

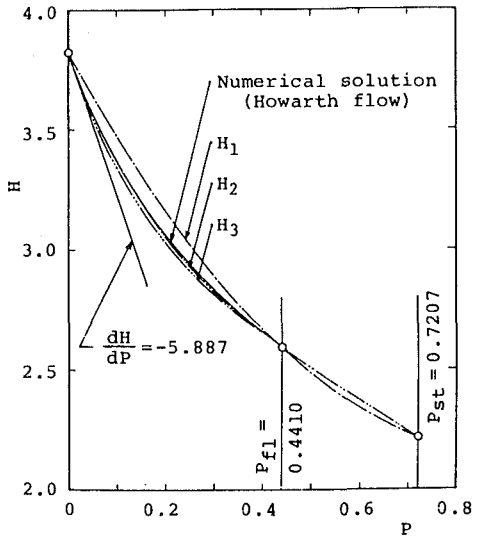


Fig. 1 H-P curves of approximate functions

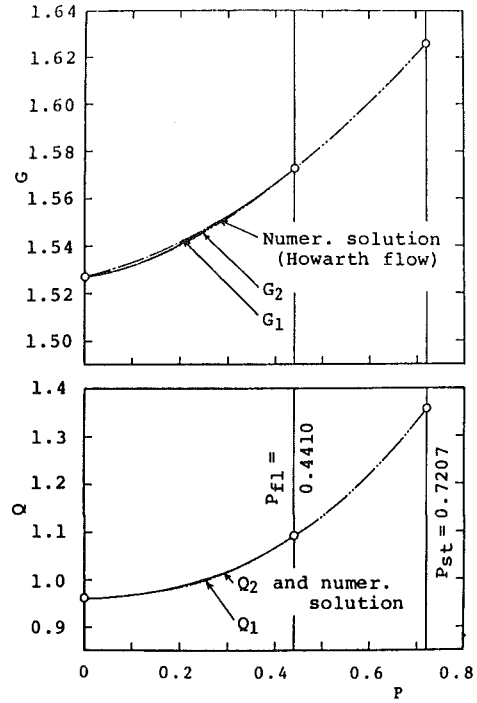


Fig. 2 G-P and Q-P curves of approximate functions

that is, the Hiemenz solution for a flow starting from a stagnation point ($P_0 = P_{st}$, $\Theta_0 = 0.0854648/(du/dx)_{st}$) or the Blasius solution for a flow starting from a flat plate at zero incidence ($P_0 = P_{fl}$, $\Theta_0 = 0.0$). In either case the initial values at $x = x_n$ are assumed to be:

$$P_n^{i=0} = P_{n-1},\ \Theta_n{}^{i=0} = \Theta_{n-1}$$

In equation (13), the deviation terms $\delta P_n{}^i$ and $\delta\Theta_n{}^i$ are given by:

$$\delta P_n{}^i = D_{pn}{}^i/D_n{}^i,\ \delta\Theta_n{}^i = D_{\Theta n}{}^i/D_n{}^i \tag{17}$$

in which:

$$\left.\begin{aligned} D_{\Theta n}{}^i &= \begin{vmatrix} \Phi & A_{12} \\ \Psi & A_{22} \end{vmatrix}, \quad D_{pn}{}^i = \begin{vmatrix} A_{11} & \Phi \\ A_{21} & \Psi \end{vmatrix} \\ D_n{}^i &= \begin{vmatrix} A_{11} & A_{12} \\ A_{21} & A_{22} \end{vmatrix} \end{aligned}\right\} \tag{18}$$

These values are substituted into equation (12) and the iterative procedures are continued until the following convergence conditions are met:

$$|\delta P_n{}^i| < 10^{-5},\ |\delta\Theta_n{}^i| < 10^{-7} \tag{19}$$

Here, it is noteworthy that the nodal spacing may be chosen arbitrarily. This is an advantage of the use of the box discretization scheme. Using these criteria, it turned out that the convergence was satisfactory for all the examples cited in Table 3. Moreover, only 2 or 3 iterations were needed in the range from the starting point to the streamwise section in the neighborhood of the separation point. Even in the vicinity of the separation point, the number of the iterations necessary never exceeded 12. It is apparent that the present method produces a much faster convergence than other approximate methods.

Since a solution is not obtained in the singular region where $P$ approaches to zero, say $P \leqq 0.001$, the value of $\Theta$ at $P = 0$ is extrapolated from those at several nodal points upstream in the neighborhood of the separation point.

## 3 Approximation of the Relations Among the Boundary-Layer Characteristic Quantities

**3.1 Fundamentals.** The primary concept of the present method is to express the relationships between $G$, $H$, $Q$, and $P$ in as simple a form as possible. These functions are determined from three kinds of exact solutions; (1) a two dimensional stagnation flow, (2) a flat plate flow with zero incidence and (3) a flow at a separation point. The first and the second solutions are obtained by solving the Falkner-Skan equation [12]:

$$f''' + (M+1)ff''/2 + M[1-(f')^2] = 0 \tag{20}$$

with boundary conditions:

$$f(0) = f'(0) = 0,\ f'(\infty) = 1$$

where $M$ is a pressure gradient parameter; $M = (x/U)(dU/dx)$. Two typical cases of $M = 1$ and $M = 0$ correspond to the Hiemenz solution (stagnation) and the Blasius solution (flat plate), respectively. For the third condition, the Howarth solution for retarded flow ($U = 1-x$) at the separation point is adopted. This flow is considered fundamentally important. The values of $H$, $G$, and $Q$ for these three conditions are shown in Table 1.

Although the solution of the Horwarth flow has already been given by Howarth himself [8] and later by Leigh [13], it was recalculated using the box method [9]-[11] to obtain a more accurate solution. The results yielded the location and the momentum thickness at the separation point as $x_{sp}$ = 0.1197765 and $\delta_{2sp}$ = 0.291434, respectively. Furthermore, the gradient of $H$ against $P$ at the separation point was found to be:

$$(dH/dP)_{sp} = -5.887 \tag{21}$$

This can be obtained from the condition that the set of equations (8) and (9) becomes singular at the separatin point; the condition being expressed as:

$$(dH/dP)_{sp} = [2\delta_{2sp}{}^2(dU/dx)_{sp}]^{-1}$$

In Figs. 1 and 2 curves of $H(P)$, $G(P)$ and $Q(P)$ are shown, where open circles denote the reference values in Table 1 and solid curves denote the numerical solutions obtained in 0

Table 2 Data of approximate functions in Figs. 1 and 2

| Curves of approximation | Coefficients | | | $\left(\frac{dH}{dP}\right)_{sp}$ |
|---|---|---|---|---|
| H - P curves | $A_H$ | $B_H$ | $C_H$ | |
| $H_1 = A_H + B_H P + C_H P^2$ | 3.82240 | -3.67986 | 2.01361 | -3.680 |
| $H_2 = A_H + B_H P + C_H (1-P)^6$ | 3.12833 | -1.26608 | 0.694066 | -5.430 |
| $H_3 = A_H + B_H P + C_H (1-P)^7$ | 3.15310 | -1.30011 | 0.669298 | -5.985 |
| G - P curves | $A_G$ | $B_G$ | $C_G$ | |
| $G_1 = A_G + B_G P + C_G P^2$ | 1.52698 | 0.0502975 | 0.120378 | |
| $G_2 = A_G + B_G P^{3/2} + C_G P^2$ | 1.52698 | 0.134984 | -0.0311644 | |
| Q - P curves | $A_Q$ | $B_Q$ | $C_Q$ | |
| $Q_1 = A_Q + B_Q P^2 + C_Q P^3$ | 0.960492 | 0.526348 | 0.324510 | |
| $Q_2 = A_Q + B_Q P^2 + C_Q P^4$ | 0.960492 | 0.615135 | 0.279334 | |

Table 3 Location of separation points for several types of flow

| No. | U(x) | Numerical solutions | | Approximate solutions | $\frac{x_{sp}}{x_{spN}} - 1$ |
|---|---|---|---|---|---|
| | | $x_{spN}$ | Author | $x_{sp}$ | |
| 1 | $1-x$ | 0.120 | Howarth[8] | 0.1195 | -0.0042 |
| | | 0.1198 | Leigh[13] | | -0.0025 |
| 2 | $1-x^2$ | 0.271 | Tani[15] | 0.2714 | 0.0015 |
| 3 | $1-x^4$ | 0.462 | " | 0.4653 | 0.0071 |
| 4 | $1-x^8$ | 0.640 | " | 0.6500 | 0.0156 |
| 5 | $x-x^3-0.12156\,x^5$ | 0.6245 | Curle[16] | 0.6354 | 0.0175 |
| 6 | $x-x^3$ | 0.6551 | " | 0.6578 | 0.0041 |
| 7 | $x-x^3+0.07885\,x^5$ | 0.6647 | " | 0.6759 | 0.0168 |
| 8 | $\sin x$ | 1.8230 | Terrill[14] | 1.8245 | 0.0008 |
| 9 | $x\exp(-x)$ | 1.3125 | Hayashi[17] et al. | 1.3108 | -0.0013 |

$\leqq P \leqq P_{fl}$. The additional separation condition of equation (21) is also shown in Fig. 1 for comparison.

**3.2 Approximate Expressions for the Relationships Between *H*, *G*, *Q*, and *P*.** As mentioned previously, the fundamental aim of the present method is to express the relationships between $H$, $G$, $Q$, and $P$ in simplest possible forms. Some examples of the formulas employed are given in Table 2. The curves of these formulas for the entire domain of $P$ ($0 \leqq P \leqq P_{sl}$) are shown in Figs. 1 and 2. Among these, the set consisting of $H_1$, $G_1$, and $Q_1$ is the simplest one. However, it can be seen from Figs. 1 and 2 that $H_1$ shows a large deviation from the numerical solution, and also $G_1$ does not agree well with the numerical solution for small $P$.

As will be discussed in Section 3.3, the value of $(dG/dP)_{sp}$, which is zero in the numerical solution, is very important because it is closely related to the characteristic behavior of $P$ which drops to zero steeply near the separation point. Thus, the second term of $G_1 (= B_G P)$ may have an exponent which is larger than 1 such as $B_G P^m$, where $m > 1$.

The formula for $H_3$, in which the exponent in the third term has been selected such that the slope at $P = 0$ agrees approximately with the condition of equation (21), deviates from the numerical solution in the middle range of $P$. For reference, the values of $(dH_K/dP)_{sp}$, $(K = 1, 2, 3)$ are shown in the right end-column of Table 2.

Among these functions, the set of $H_2$, $G_2$ and $Q_2$ appears to be the best fit to the numerical solutions over the entire range of $P$ ($0 \leqq P \leqq P_{fl}$).

**3.3 Application of the Formulas *H(P)*, *G(P)*, and *Q(P)* to Howarth's Retarded Flow.** In order to examine the validity of these approximate formulas, the following three sets of them were applied to Howarth's retarded flow:

($a$) $H_1$, $G_1$, $Q_1$
($b$) $H_2$, $G_2$, $Q_2$
($c$) $H_3$, $G_2$, $Q_2$

In Fig. 3, the distributions of non-dimensional skin friction $P(x)$ for the respective sets are compared with the numerical solutions in the neighborhood of the separation point.

Apparently, the set ($b$) gives the closest separation point to that of the numerical solution. It is also noted that this solution is in good agreement with the numerical solution even in the upstream stations. The set ($c$) predicts the separation point slightly downstream and gives poorer agreement with the exact solution than that of the set ($b$). This is due to the discrepancy between the curve of $H_3$ and the numerical solution in the middle part of $P$ in Fig. 1. It is also obvious from Fig. 3 that the curve based on the set ($a$) is much different from the numerical solution.

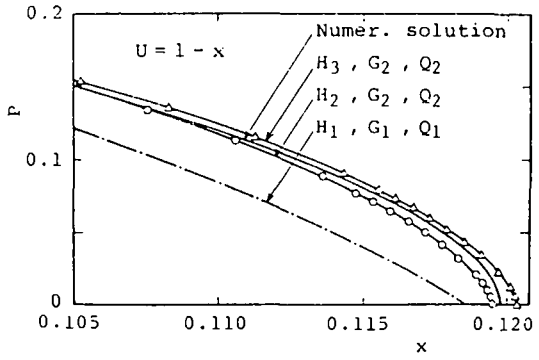


Fig. 3 Solutions of Howarth flow near separation point

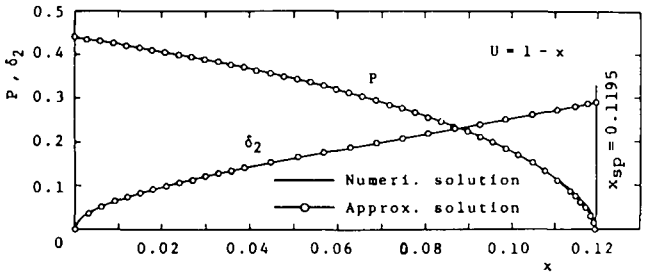


Fig. 4 Comparison of approximate and numerical solutions for Howarth flow

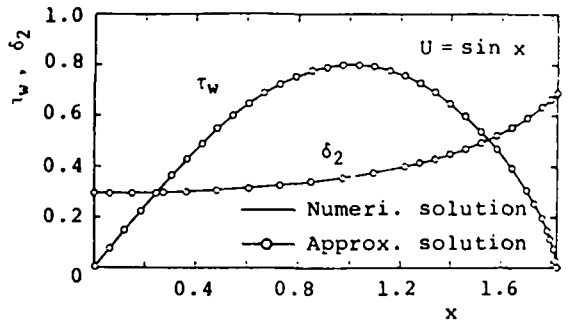


Fig. 5 Comparison of approixmate and numerical solutions for flow around circular cylinder

These considerations have led to the adoption of set ($b$) as the most suitable approximation. Using the formulas of set ($b$), the solutions of the Howarth flow are shown together with the numerical solutions in Fig. 4. One notes that the approximate solutions are in excellent agreement with the numerical solutions with the exception of the neighborhood of the separation point itself.

**3.4 Application to Flow Started From a Stagnation Point.** Although the present method works quite well for the Howarth flow, it is not surprising in the sense that the numerical solution of that flow has been used to determine the relationships between $G$, $H$, $Q$, and $P$. Therefore, in order to verify the validity of the method, it is necessary to examine the behavior applied to an essentially different kind of flow such as a flow started from a forward stagnation point. Here, the flow around a circular cylinder ($U = \sin x$) was selected, for which the exact solution has already been obtained by Terrill [14]. In order to compare the present method with the Terrill's results, a new non-dimensional shear-stress $\tau_w$ defined as:

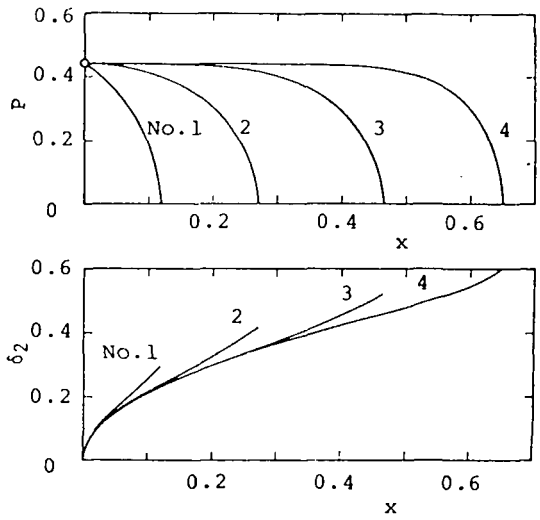


Fig. 6 Approximate solutions of various flows started form flat plate condition

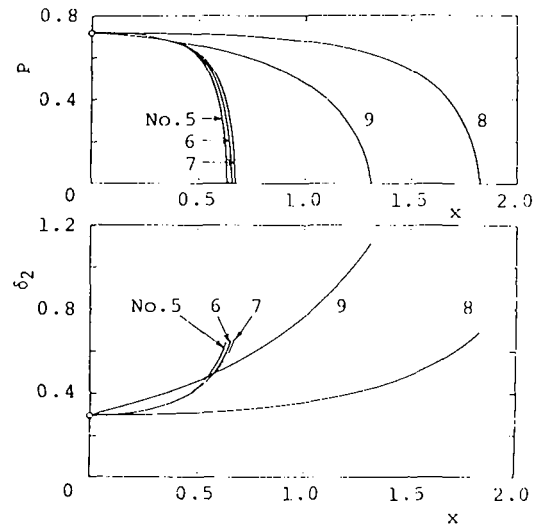


Fig. 7 Approximate solutions of various flows started from forward stagnation point

$$\tau_w = (\partial u/\partial y)_w = (P/2\delta_2)U \tag{22}$$

is introduced instead of $P(x)$. The result of the calculation is shown in Fig. 5 which again exhibits excellent agreement with the numerical solution.

## 4 Application to Additional Flows

The successes described above suggested the application of the present method to other types of flow. These are tabulated in Table 3 for case in which the location of the separation points is already known. In the table, flows 1-4 are cases started from the flat plate condition and cases 5-9 are flows started from the stagnation point. The results calculated for these two groups are shown in Figs. 6 and 7, respectively. Since the outer velocties $U(x)$ shown in Fig. 6 are of the form $U = 1 - x^m$, it is seen that the solutions vary systematically according to $m = 1, 2, 4, 8$. From Figs. 6 and 7 the location of the separation points ($P \rightarrow +0$), $x_{sp}$ has been estimated and is shown in Table 3. Introducing a quantity $(x_{sp}/x_{spN} - 1)$ to compare $x_{sp}$ with that of the exact solution, $x_{spN}$, the error is found to be less than 2 percent for all flow configurations.

Because the prediction of a separation point is one of the most important results of boundary-layer calculations, the present method seems to be suitable for practical applications having sufficient accuracy and simplicity.

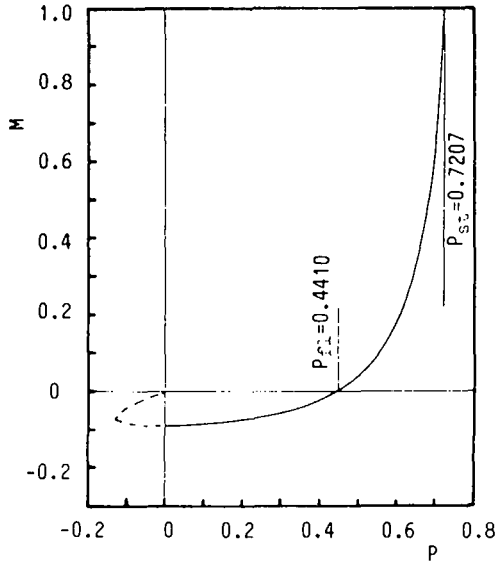


Fig. 8 Relation between M and P on Falkner-Skan equation

## 5 Method of Estimating Velocity Profiles From Boundary-Layer Characteristic Quantities

In previous sections, a new calculation method to obtain the characteristic quantities has been developed. Although in many practical cases these quantites provide sufficient information concerning the boundary-layer flow, the velocity profile is also sometimes needed in order to examine the structure of the boundary-layer in detail.

In this section a method will be presented for estimating velocity profiles when the characteristic quantities have been given.

**5.1 Introduction of Scaled Variables.** Let the ordinate normal to a wall and the scaled boundary-layer thicknesses be given by:

$$\eta = y\sqrt{U}/x \tag{23}$$

$$\Delta = \delta\sqrt{U}/x \tag{24}$$

$$\Delta_K = \delta_K\sqrt{U}/x \quad (K = 1, 2, 3) \tag{25}$$

In addition, various characteristic quantites are defined as:

$$\begin{aligned} E &= \Delta_2/\Delta \ (= \delta_2/\delta) \\ H &= \Delta_1/\Delta_2 \ (= \delta_1/\delta_2) \\ P &= 2\Delta_2 f_w'' \ (= (2\delta_2/U)(\partial u/\partial y)_w) \end{aligned} \tag{26}$$

where $f = \psi^*/\sqrt{\nu^* x^* U^*}$ means a scaled dimensionless stream function and prime denotes the derivative with respect to $\eta$.

**5.2 Approximate Velocity Profiles Based on Solutions of the Falkner-Skan Equation and a Polynomial Expression.** Usually, there are two ways to approximate velocity profiles; one is to employ the solutions of the Falkner-Skan equation and the other a polynomial expression.

First, a method using the Falkner-Skan solutions (evaluated from equation (20)) is demonstrated. Since the velocity profiles are described by only one parameter, $M$, the problem is reduced to relating this parameter to the characteristic quantities, especially to the non-dimensional skin friction $P$. The relationship between $P$ and $M$ can readily be obtained by solving equation (20), and is shown in Fig. 8. The equation is known to have two possible solutions in the region of $M \leqq 0$ [18], however, the effective range of $P$ in the present analysis is limited to $0 \leqq P \leqq P_{sp}$.

An example of this procedure was carried out for Howarth's retarded flow. The results obtained are shown in Fig. 9. The deviation from the exact solution is seen to in-

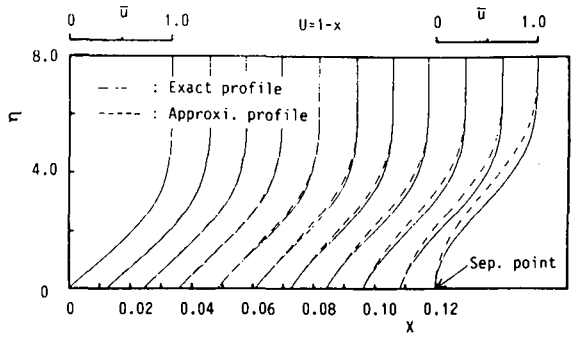


Fig. 9 Approximation of Howarth flow based on Falkner-Skan equation

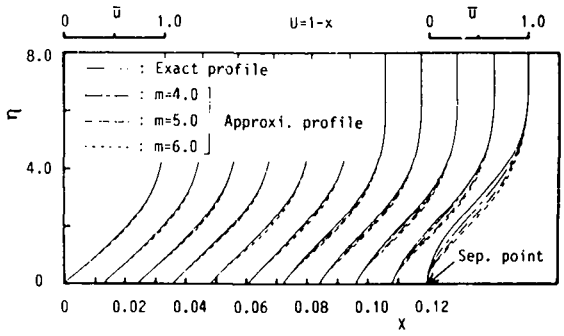


Fig. 10 Approximation of Howarth flow based on polynomial expression

crease as the boundary-layer develops. This deviation is due to the fact that the profiles are necessarily dependent only on $M$ and do not have any means to adjust the boundary-layer thickness.

A second method using a polynomial expression was also investigated. Here, Tani's approximate velocity profile [6] which contains one parameter, $a$, was employed:

$$\bar{u} = 1 - (1-\bar{\eta})^{m-1}[1 + (m-1-a)]u], \quad 0 < \bar{\eta} < 1 \tag{27}$$

where $m$ denotes the degree of the polynomial and $\bar{u} = u/U$ and $\bar{\eta} = \eta/\Delta$.

Equation (27) satisfies the following boundary conditions:

$$\left.\begin{aligned} &\bar{u} = 0, \quad \partial \bar{u}/\bar{\eta} = a \text{ at } \bar{\eta} = 0 \\ &\bar{u} = 1, \quad \bar{u}^{(k)} = 0 \quad \text{at } \bar{\eta} = 1 \end{aligned}\right\} \tag{28}$$

where $k < m-1$ and $k$ denotes the order of the derivative:

$$\bar{u}^{(k)} = \partial^k \bar{u}/\partial \bar{\eta}^k$$

In equation (28), the velocity profile parameter $\alpha$ is proportional to the skin friction. The characteristic quantities (equation (26)) are calculated by direct integration of equation (27). This procedure yields the following expressions:

$$E = \Delta_2/\Delta = [3m(m-1)/(m+1) + 3a/(m+1) - a^2/m]/(4m^2-1) \tag{29}$$

$$P = 2\Delta_2 f_w'' = 2aE \tag{30}$$

Therefore, if $P$ and $\Delta_2$ are known, the parameter $\alpha$ and the boundary-layer thickness $\Delta$ can be calculated from above relationships for a given value of $m$. $P$ is also written as follows:

$$P = 2a[3m(m-1)/(m+1) + 3a/(m+1) - a^2/m]/(4m^2-1) \tag{31}$$

In this example, three values of $m$, i.e., $m = 4$, 5 and 6 are investigated. The parameter $\alpha$ is calculated from equation (31) by using the Newton-Raphson method in which the initial value is selected in the range of $0 \leqq a \leqq 4.0$ (see Tani [5]). $\Delta$ can be calculated from equation (29).

The results obtained for the Howarth flow are shown in Fig. 10. It is seen that the best result is obtained for $m = 4$, even though agreement with the exact profile is not perfect.

**5.3 Velocity Profiles Employing an Exponential Function.** In this section, a new calculation method for velocity profiles employing an exponential function is proposed based on the idea that velocity profiles are characterized mainly by the non-dimensional skin friction $P$ and the shape factor $H = \Delta_1/\Delta_2$.

According to Iida [19] who studied secondary solutions of a flow around a circular cylinder, the velocity profile near the outer edge of a boundary-layer in the vicinity of a separation point may be expressed by an exponential form:

$$\bar{u} \fallingdotseq 1 - \exp(-\alpha\eta^\beta) \tag{32}$$

where $a$ is a parameter and $\beta = 2$.

In order to employ this profile over the entire region of $\eta$, $\beta$ is regarded as a parameter so that the profile agrees with the exact one at separation points of several types of flow (the determination procedure of $\alpha$ and $\beta$ will be discussed later). A further extention of equation (32) applicable to any streamwise location may be made in the form:

$$\bar{u} = 1 - \exp(-\alpha\eta^\beta) + f_w'' \eta \exp(-\gamma\eta) \tag{33}$$

where $\alpha$, $\beta$, $\gamma$ are parameters with conditions:

$$\alpha > 0, \quad \beta > 1, \quad \gamma > 0$$

Equation (33) satisfies the following boundary conditions:

$$\left.\begin{aligned} &\bar{u} = 0 \\ &\partial\bar{u}/\partial\eta = f_w'' \end{aligned}\right\} \text{at } \eta = 0$$
$$\bar{u} = 1 \qquad \text{at } \eta = \infty \tag{34}$$

If the values $P$ and $\Delta_2$ are given, $f_w''$ can be determined from the following expression (see equation (26)):

$$f_w'' = P/2\Delta_2 \tag{35}$$

Now, let us examine how the velocity profile, equation (33), is affected by the parameters $\alpha$, $\beta$ and $\gamma$. The parameter $\alpha$ principally effects the displacement thickness $\Delta_1$. The parameter $\beta$ mainly affects the curvature of the profile and the momentum thickness $\Delta_2$. On the other hand, the parameter $\gamma$ has no substantial effect on the shape of the profile. In most cases a fixed value of $\gamma$, say $\gamma = 1$, may be used. But when the boundary-layer thickness is too thin, the value ($\gamma = 1$) may cause $\bar{u} > 1$ in the boundary-layer. In this case a suitable value of $\gamma$ may be employed.

Numerical integration of equation (33) yields $\Delta_{1N}$ and $\Delta_{2N}$, which are then compared with available exact solutions $\Delta_1$ and $\Delta_2$ to determine $\alpha$ and $\beta$. For fixed $\beta$ and $\gamma$, $\Delta_{1N}$ becomes a monotonically decreasing function of $\alpha$, and $\Delta_{2N}$ also shows a monotonically decreasing trend with $\beta$ for fixed $\alpha$ and $\gamma$. Considering these facts, suitable values of $\beta$ and $\gamma$ are first assumed and then iteration is carried out until $\Delta_{1N} = \Delta_1$ is achieved using a binary chopping method. Outside of this iterative loop, another iteration is executed until $\Delta_{2N} = \Delta_2$ is satisfied for fixed values of $\alpha$ and $\gamma$. Finally, a further iteration is carried out outside the second loop to determine $\gamma$. The minimum value of $\gamma$ is selected such that the velocity profile $\bar{u}$ satisfies the condition of $\bar{u} - 1 < 10^{-5}$ for all $\eta$. Consequently, the parameters $\alpha$, $\beta$, and $\gamma$ are determined by executing this triple-loop of iterations.

An application of this method to Howarth flow produced remarkably accurate results. Nevertheless the procedure is rather complicated, therefore a more expedient method described below is recommended.

**5.4 A Fast Method for Estimating Velocity Profiles.** In this section, a simplified version of the method of determining the parameters $\alpha$, $\beta$, and $\gamma$ is presented.

First, the method of Section 5.3 is applied to the following types of flow. (Note that their exact solutions are available.)

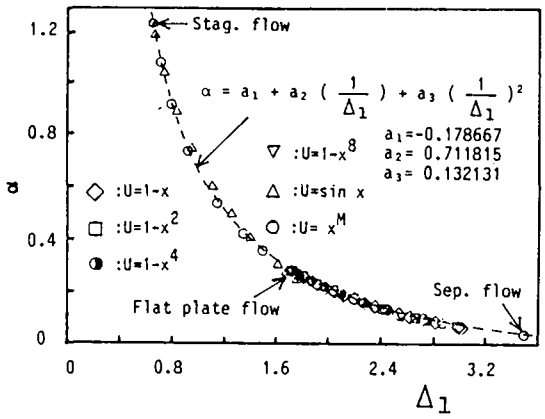


Fig. 11 $\alpha$-$\Delta_1$ curve

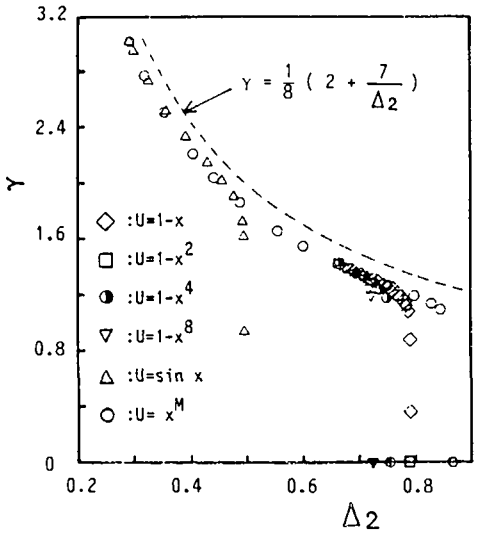


Fig. 12 $\gamma$-$\Delta_2$ curve

| | | |
|---|---|---|
| $(A)\, U = 1 - x^m$; | $m = 1$ | Howarth [8] |
| | ; $m = 2, 4, 8$ | Tani [15] |
| (B) $U = \sin x$ | ; flow around a circular cylinder | Terrill [14] |
| $(C)\, U = x^M$ | ; flow past a wedge | Hartree [20] |

Figure 11 shows the resulting plots of $\Delta_1$ versus $\alpha$. The data are clearly representable by a single curve which is approximated by:

$$\alpha = a_1 + a_2\Delta_1^{-1} + a_3\Delta_1^{-2} \tag{36}$$

where $a_1 = -0.178667$, $a_2 = 0.711815$, $a_3 = 0.132131$. Equation (36) also satisfies the three exact solutions; a two dimensional stagnation point flow, a flat plate flow and a zero-skin-friction flow due to the Falkner-Skan equation. Other plots of $\Delta_2$ versus $\gamma$ are shown in Fig. 12. It may be seen that $\gamma$ rapidly falls to zero near the separation point. In this region, however, the third term in equation (33) can be ignored due to its very small value of $f_w''$ and thus the value of $\gamma$ does not significantly affect the velocity profile. Furthermore, values of $\gamma$ less than those plotted yield velocity profiles with $\bar{u} > 1$, which should be excluded. Therefore the following approximate relationship is employed, which is also shown in Fig. 12.

$$\gamma = (2 + 7/\Delta_2)/8 \tag{37}$$

Meanwhile, $\beta$ has to be determined in the same way as in Section 5.3, because an accurate simplified relationship between $\beta$ and the characteristic quantities could not be found.

In summary, all of the parameters can be determined through the following procedures:

(1) specification of $P$, $\Delta_1$, and $\Delta_2$
(2) determination of $f_w''$ by equation (35)

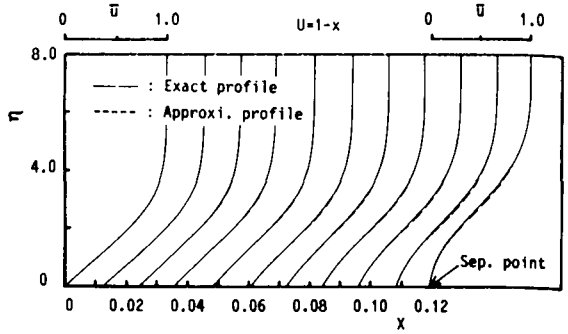


Fig. 13 Approximation of Howarth flow based on present method

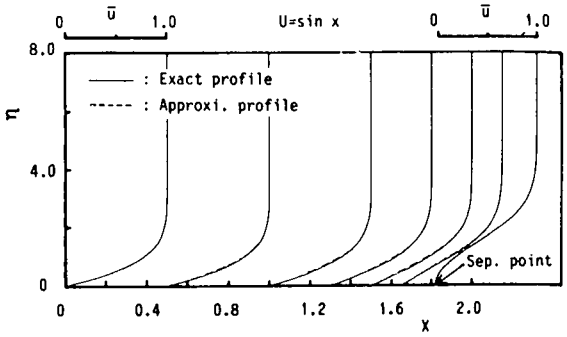


Fig. 14 Approximation of flow around circular cylinder based on present method

(3) determination of $\alpha$ and $\gamma$ by equations (36) and (37)
(4) iteration of $\beta$ until the condition of $\Delta_{2N} = \Delta_2$ is satisfied

In this simplified method, only a single-loop iteration procedure is needed, and the approximate velocity profile may be obtained considerably faster than in the triple-loop method.

Next, this simplified method was applied to the six types of flow ((A) to (C)), using the characteristic quantities ($P$, $\Delta_1$, $\Delta_2$) given by the approximate method in Section 2. As examples, the results of the Howarth flow and the flow around a circular cylinder are shown in Figs. 13 and 14 by broken lines, together with the corresponding exact profiles shown by solid lines. It is clear that excellent agreement is achieved.

Finally, for further verification, the present method was applied to a more sensitive case, a flow around an elliptic cylinder corresponding to Schubauer's famous experiment [21], in which the Pohlhausen method failed to predict the occurrence of separation. In this application, Schabauer's experimental data for the pressure distribution were fitted by a least-squares approximation using a 10th-degree polynomial expression. The result showed that the location of the separatin point was at $x_{sp} = 1.975$ which agreed very nicely with the experimental result. $x_{sp} = 1.99 \pm 0.02$. Furthermore, the velocity profiles also agreed well with those of the experiment at all sections. This tends to confirm that the present method can predict the location of separation and velocity profiles with sufficient accuracy and with considerable economy of computational time.

## 6 Concluding Remarks

A new approximate calculation method for steady laminar boundary-layers has been developed for practical applications. The results are summarized as follows:

(1) Both the momentum- and the energy-integral equations are satisfied without the assumptions of a specific velocity profile a priori.

(2) The boundary-layer characteristic quantities $H$, $G$, and $Q$ are related to the non-dimensional skin friction $P$ with simple approximate formulas which satisfy three exact solutions; a two dimensional stagnation point flow, a flat plate flow with

zero incidence and a separation point of Howarth's retarded flow. The most suitable set is shown to be $H_2$, $G_2$, and $Q_2$ reported in Table 2.

(3) The present method predicts the separation point with good accuracy for various types of flow shown in Table 3. Rapid convergence is achieved even in the vicinity of the separation point.

(4) A fast method of estimating the velocity profile has also been proposed. The formula representing the velocity profile consists of two exponential terms with three parameters. Only one parameter has to be estimated iteratively.

(5) The proposed method enables one to calculate velocity profiles with reasonable accuracy and with shorter computational time then traditional methods.

## Acknowledgment

The authors wish to acknowledge the invaluable advice and constructive criticism given by Professor Emeritus Itiro Tani, University of Tokyo, who suggested this work.

The numerical computations of this work were carried out by the HITAC M-280H computer system of Hokkaido University.

## References

1 Hayashi, N., "On the Approximate Solution of the Unsteady Quasi-Two-Dimensional Incompressible Laminar Boundary-Layer Equations," *Journal of Physical Society of Japan*, Vol. 17, No. 1, 1962, pp. 203.

2 Miller, R. W., and Han, L. S., "Analysis of Unsteady Laminar Boundary Layer Flow by an Integral Method," ASME JOURNAL OF FLUIDS ENGINEERING, Vol. 95, No. 2, 1973, pp. 237.

3 Fasler, K. S., and Danberg, J. E., "Boundary-Layer Separation on Moving Walls Using an Integral Theory," *AIAA Journal*, Vol. 15, No. 2, 1977, pp. 274.

4 Matsushita, M., Shimada, T., and Akamatsu, T., "Numerical Analysis of Unsteady Laminar Boundary Layers with Separation Using One Parameter Integral Method," *Trans. JSME*, Vol. 48, No. 426, 1982, pp. 195 (in Japanese).

5 Tani, I., "On the Approximate Solution of the Laminar Boundary-Layer Equations," *Journal of the Aeronautical Sciences*, Vol. 21, No. 7, 1954, pp. 487.

6 Tani, I., and Yu, N. J., "Unsteady Boundary Layer Over a Flat Plate Started from Rest," *International Union of Theoretical Applied Mechanics, Symposium*, (Eichelbrenner, E. A., ed.), Recent Research on Unsteady Boundary Layers, Quebec, 1972, pp. 886.

7 China, H., and Kobashi, Y., "An Approximate Method to Estimate the Laminar Boundary Layer Separation," *Bulletin of the Faculty of Engineering*, Hokkaido University, No. 98, 1980, pp. 31 (in Japanese).

8 Howarth, L., "On the Solution of the Laminar Boundary Layer Equations," *Proceedings of Royal Society of London*, Series A, Vol. 164, 1938, pp. 547.

9 Keller, H. B., and Cebeci, T., "Accurate Numerical Methods for Boundary Layer Flows," *Proceedings of the Second International Conference on Numerical Method in Fluid Dynamics, Lecture Notes in Physics*, 8, Springer-Verlag, 1970, pp.92.

10 Cebeci, T., and Smith, A. M. O., *Analysis of Turbulent Boundary Layers*, Academic press, 1974.

11 Keller, H. B., "Numerical Methods in Boundary-Layer Theory," *Annual Review of Fluid Mechanics*, Vol. 10, 1978, pp. 417.

12 Schlichting, H., *Boundary Layer Theory*, 7th ed., McGraw-Hill, 1979.

13 Leigh, D. C. F., "The Laminar Boundary-Layer Equation: A Method of Solution by Means of an Automatic Computer," *Proceedings of the Cambridge Philosophical Society*, Vol. 51, 1955, pp. 320.

14 Terrill, R. M., "Laminar Boundary-Layer Flow Near Separation with and without Suction," *Philosophical Transactions of the Royal Society of London*, Series A, Vol. 253, 1960, pp. 55.

15 Tani, I., "On the Solution of the Laminar Boundary Layer Equations," *Journal of Physical Society of Japan*, Vol. 4, No. 3, 1949, pp. 149.

16 Curle, N., *The Laminar Boundary Layer Equations*, Oxford Math. Monographs, 1962.

17 Hayashi, N., Inouye, K., and Tsuji, H., "Solutions of Laminar Boundary-Layer Equations Involving Separations," *Physics of Fluids*, Vol. 12, suppl. II, 1969, pp. 283.

18 Stewartson, K., "Further Solutions of the Falkner-Skan Equation," *Proceedings of the Cambridge Philosophical Society*, Vol. 50, 1954, p. 454.

19 Iida, S., "Second Order Boundary-Layer Solutions for the Stagnation Flow of a Circular Cylinder," *Bulletin of JSME*, Vol. 21, No. 151, 1978, pp. 104.

20 Hartree, D. R., "On an Equation Occurring in Falkner and Skan's Approximate Treatment of the Equations of the Boundary Layer," *Proceedings of the Cambridge Philosophical Society*, Vol. 33, Part II, 1937, pp. 223.

21 Schubauer, G. B., "Air Flow in a Separating Laminar Boundary Layer," NACA Report 527, 1935, pp. 369.

# Limitations of the Boundary-Layer Equations for Predicting Laminar Symmetric Sudden Expansion Flows

**J. P. Lewis**[1]
Research Assistant.

**R. H. Pletcher**
Professor.
Mem. ASME

Department of Mechanical Engineering and Computational Fluid Dynamics Center, Iowa State University, Ames, Iowa 50011

*A finite-difference solution scheme is used to study the limitations and capabilities of the boundary-layer equation model for flow through abrupt, symmetric expansions. Solutions of the boundary-layer equations are compared with previous numerical predictions and experimental measurements. Some flow parameters are not well predicted for Reynolds numbers below 200. Global iteration over the flow field to include upstream effects does not significantly influence the predictions. Axisymmetric and two-dimensional flows are investigated. The effect of initial conditions is discussed*

## 1 Introduction

Flow with separation is often encountered in fluid mechanics due to adverse pressure gradients and rapid changes in geometry. In the case of a rapid expansion, a zone of recirculating flow forms downstream of the abrupt expansion. This paper deals with the finite-difference solution of the boundary-layer equations for steady incompressible, laminar, isothermal flow through sudden symmetric expansions (Fig. 1).

Until fairly recently it was considered necessary to utilize the full Navier-Stokes equations to obtain a valid solution to flows with recirculation. There have been several numerical solutions of the Navier-Stokes equations for sudden symmetric expansions in the past twenty years (Hung [1], Macagno and Hung [2], Morihara [3], Durst et al. [4], Pollard [5, 6], Agarwal [7], and Osswald et al. [8]). The only symmetric planar expansion measurements with fully-developed flow at the expansion were done by Durst et al. [4] and Cherdron et al. [9]. However, the flow was symmetric only for the lowest Reynolds number examined by Durst et al. [4]. Cherdron et al. [9] emphasized flows with asymmetries and provided no quantitative data for symmetric flows. The flow is asymmetric for higher Reynolds numbers due to disturbances at the lip of the step being amplified in the shear layer between the recirculating region and the main flow region. Macagno and Hung [2] obtained the only detailed measurements of fully-developed laminar flow through an abrupt pipe expansion.

Recently, several investigators have used the boundary-layer equations to predict the flow through a sudden expansion. Kumar and Yajnik [10] and Plotkin [11] used approximating functions to reduce the partial differential equations to ordinary differential equations. Those who used a finite-difference discretization of the partial differential equations for flow through a symmetric sudden expansion include Acrivos and Schrader [12], and Kwon et al. [13]. Kwon et al. [13] only predicted the flow through planar expansions and Acrivos and Schrader [12] provided almost no comparison with experiment or solutions of the Navier-Stokes equations. Kwon and Pletcher [14] and Oosthuizen [15] used the boundary-layer equations to predict the flow through an asymmetric channel expansion. Oosthuizen was able to predict the additional separation region on the wall opposite the step that was first reported by Armaly and Durst [16]. The reattachment lengths and velocity profiles predicted by the boundary-layer equations of the previous studies are in good agreement with those of the Navier-Stokes equations for surprisingly low Reynolds numbers.

Clearly there must be limits to the validity of the boundary-layer equations for such geometries. In many configurations in which recirculation occurs, the use of the full Navier-Stokes equations is indeed required. However, the fully-developed, incompressible flow passing through a sudden expansion in a symmetric two-dimensional or axisymmetric channel appears to be an exception, and is yet another example of a flow which can, within limits, be accurately computed by solving the boundary-layer equations. Just as for other configurations in which the boundary-layer equations are commonly used, there exists an initial flow region for which the boundary-layer assumptions are not valid. In this initial low-Reynolds number region, the boundary-layer solution would be expected to deviate observably from experimental measurements and solutions to the full Navier-Stokes equations.

Since the previous studies that used the boundary-layer equations [12–15] provided only isolated comparisons with experiments and Navier-Stokes solutions, the limitations of the boundary-layer equations have not been previously defined. The purpose of the present paper is to more clearly define the limitations of such solutions for both two-dimensional and ax-

[1]Present address: Allison Gas Turbine Division, General Motors Corporation, Indianapolis, Ind.

Contributed by the Fluids Engineering Division for presentation in the JOURNAL OF FLUIDS ENGINEERING. Manuscript received by the Fluids Engineering Division, January 22, 1985.

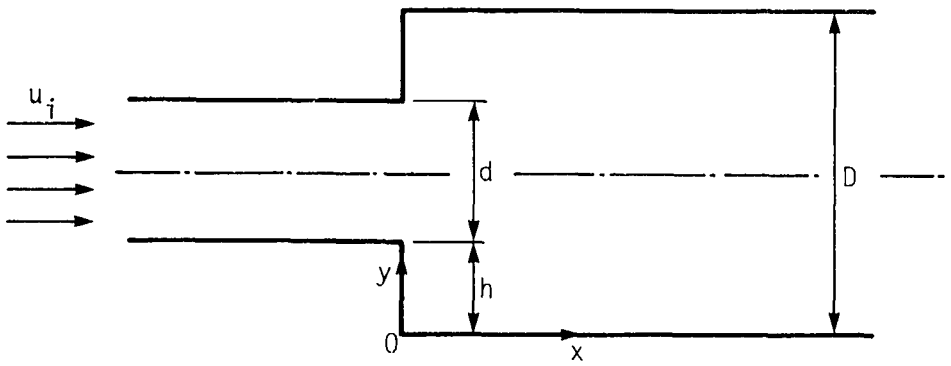


Fig. 1 Sudden expansion geometry

isymmetric expansion flows with respect to Reynolds number and expansion ratio. Determining the range of applicability of the boundary-layer equations is of practical importance since the effort required to solve the boundary-layer equations is an order of magnitude less than that required for the full Navier-Stokes equations. Furthermore, as will be indicated in the Analysis section, the constant property boundary-layer equations are independent of Reynolds number. Therefore, the boundary-layer equations need to be solved only once for any given expansion ratio and the solution can then be applied through proper scaling for any channel Reynolds number.

The computational scheme used in this study builds upon the "once-through" procedure used by Kwon et al. [13] for a two-dimensional channel expansion. However, both two-dimensional and axisymmetric geometries are considered here, with emphasis on axisymmetric geometries. Kwon et al. [13] employed the FLARE approximation [17] in their calculations. Accordingly, the streamwise convective derivative was neglected in regions of reversed flow. The effect of removing the FLARE approximation through global iterations is studied in the present work. In doing this, the solution of the boundary-layer equations is marched through the region of flow reversal using the FLARE approximation for only the first iteration. The FLARE approximation is then discarded. Flows that are fully developed at the expansion or step are considered. The paper compares the results of the boundary-layer calculations with solutions to the Navier-Stokes equations, other boundary-layer equation solutions, and available experimental measurements.

## 2 Governing Equations

The boundary-layer continuity and momentum equations can be written in the following nondimensional form by introducing the stream function for convenience.

$$U = \frac{1}{R^m}\frac{\partial \Psi}{\partial Y} \tag{1}$$

$$cU\frac{\partial U}{\partial X} - \frac{1}{R^m}\frac{\partial \Psi}{\partial X}\frac{\partial U}{\partial Y} = \chi + \frac{1}{R^m}\frac{\partial}{\partial Y}\left(R^m\frac{\partial U}{\partial Y}\right) \tag{2}$$

Where

$$U = \frac{u}{u_i};\quad X = \frac{x}{d\,\mathrm{Re}};\quad Y = \frac{y}{d}$$

$$\Psi = \frac{\psi}{d^{1+m}u_i};\quad R = \frac{r}{d};\quad \chi = -\frac{\mathrm{Re}\,d}{\rho u_i^2}\frac{dp}{dx}$$

The Reynolds number is based on the average inlet velocity $u_i$, and $d$. This is the same scaling commonly used for developing flows in channels. By nondimensionalizing in this manner, the solution of the boundary-layer equations is dependent only on the channel geometry and not the Reynolds number. These equations are applicable for two-dimensional or axisymmetric flow. When the geometry is two-dimensional, $m$ is taken as zero; when axisymmetric, $m$ is taken as one. The distance from the centerline of an axisymmetric problem is $r$. The coefficient of the convective term in the $X$-direction, $c$, is used in the FLARE approximation [17]. While using this approximation, if $U$ is negative, $c$ is taken as zero. If $U$ is nonnegative, $c$ is set to one. If the FLARE approximation is not being used, $c$ is taken as one regardless of the sign of $U$.

Fully developed inlet conditions were used at the step. Due to the parabolic characteristic of the boundary-layer equations, starting the calculations before the step in the entrance channel with fully-developed inlet conditions would have no

## Nomenclature

$A$ = constant
$c$ = FLARE coefficient
$c_f$ = skin-friction coefficient ($= 2\tau_w/(\rho u_i^2)$)
$d$ = inlet plate spacing or inlet pipe diameter
$h$ = step height
$l_r$ = $x$-distance to reattachment
$m$ = constant (= 1 or 0)
$p$ = pressure
$r$ = distance from the pipe centerline
$R$ = nondimensional distance from the pipe centerline ($= r/d$)
Re = Reynolds number ($= \rho u_i d/\mu$)
$u$ = $x$ component of velocity
$u_i$ = average $u$ at inlet
$U$ = nondimensional $x$ velocity component ($= u/u_i$)
$x$ = coordinate along the surface measured from the step
$X$ = nondimensional $x$ coordinate ($= x/(d\,\mathrm{Re})$)
$X_r$ = $X$ to reattachment
$\Delta X$ = $X^{i+1} - X^i$
$Y$ = nondimensional $y$ coordinate ($= y/d$)
$\tau_w$ = wall shear stress
$\rho$ = density
$\chi$ = nondimensional pressure gradient $\left(= -\frac{d\mathrm{Re}}{\rho u_i^2}\frac{dp}{dx}\right)$
$\psi$ = stream function
$\Psi$ = nondimensional stream function ($= \psi/(d^{m+1}u_i)$)
$\Psi_{\min}$ = minimum $\Psi$

**Superscripts**

$i$ = mesh index corresponding to $X$

**Subscripts**

$j$ = mesh index corresponding to $Y$
min = minimum value
$r$ = reattachment
$w$ = wall

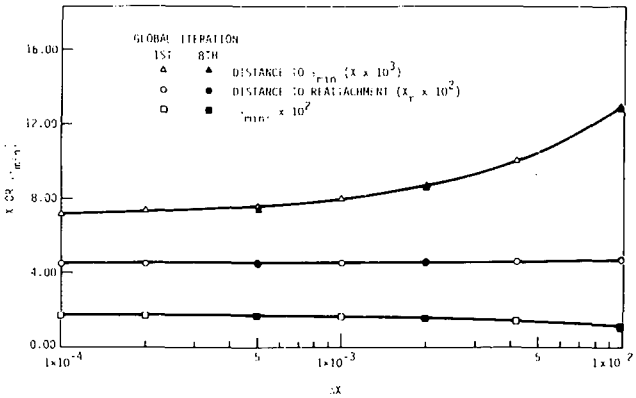


Fig. 2 The effect of reducing $\Delta X$ on reattachment length ($X_r$), minimum stream function ($\Psi_{min}$), and distance to $\Psi_{min}$ for an axisymmetric 1:2 expansion

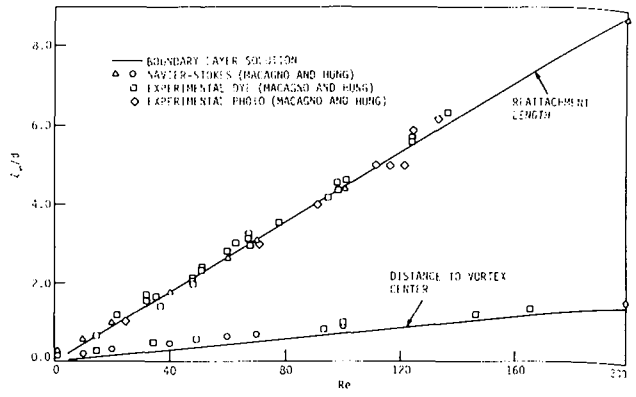


Fig. 3 Comparison of the distances to flow reattachment and vortex center for experiment [2], Navier-Stokes solutions [2], and boundary-layer equation solution with FLARE for a 1:2 pipe expansion

effect. The step would not be sensed by the equations until the step itself was reached. Experiments and Navier-Stokes solutions have shown that this is a good assumption. Armaly et al. [18] experimentally studied fully-developed flow over a backstep. The velocity profile they measured at the step had only a small variation from a parabolic profile. Macagno and Hung [2] used a parabolic inlet profile upstream of the step for their Navier-Stokes calculations. The velocity profile they predicted at the expansion varied insignificantly from the parabolic profile.

The velocity at the downstream face of the step was taken as zero in the present study except for a few cases in which a nonzero "collision velocity" was specified that was determined by the returning flow in the recirculating region as suggested by Acrivos and Schrader [12]. However, since the "collision velocity" algorithm predicted zero velocities on the face of the step as $\Delta X$ was reduced and did not have any significant effect on the flow field when nonzero velocities were predicted, it is of no real value and so was discarded.

The boundary conditions at the wall are

$$U(X,0)=0 \ ; \ \Psi(X,0)=0 \tag{3}$$

The boundary condition on the velocity is given by the symmetry condition at the centerline

$$\frac{\partial U}{\partial Y}=0 \tag{4}$$

The boundary condition for the stream function at the channel center is

$$\Psi_{\text{centerline}}=\frac{1}{2} \text{ two-dimensional geometry} \tag{5a}$$

$$\Psi_{\text{centerline}}=\frac{1}{8} \text{ axisymmetric geometry} \tag{5b}$$

## 3 Method of Solution

The partial differential equations were approximated with finite differences. When using the FLARE approximation, the $X$-derivatives were always differenced in an upwind manner with respect to the global flow. For multiple sweeps through the domain the $X$-derivatives were evaluated using one-sided upwind differencing with respect to the local flow direction. When $U$ at the $i+2$ station from a previous global iteration was negative, $U$ at the $i+2$ station, which was saved from a previous iteration, was used in the difference equations. This permitted the flow from downstream (in the global sense) to influence the solution at the $i+1$ level through the representation of the streamwise convective term in regions of reversed flow. The $Y$-derivatives were differenced with second order central differences. The nonlinear terms were linearized using Newton linearization.

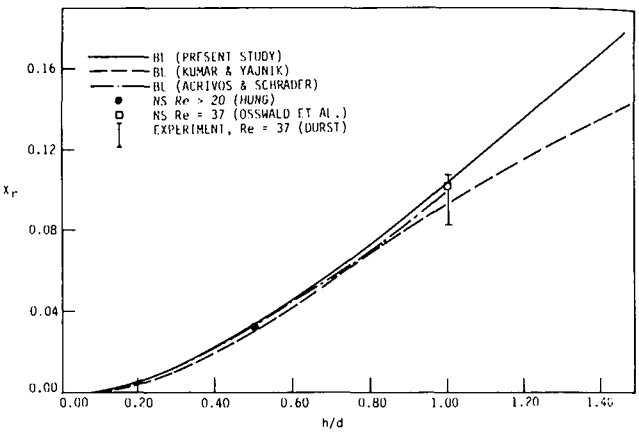


Fig. 4 Distance to reattachment for a two-dimensional channel expansion as a function of expansion ratio predicted by the boundary-layer equations [10, 12], the Navier-Stokes equations [1, 8], and experiment [4]

Uniform grid spacing was used in both directions. The channel half-width was divided into 80 equal increments. The $X$-grid spacing was smaller than 1/200 of the estimated distance to reattachment. Grid refinement studies showed that this grid was adequately fine and that the problem formulation was consistent. Figure 2 shows an example of grid refinement in the $X$-direction.

The continuity and momentum equations were solved implicitly in a coupled manner at each marching station. The resulting system of equations is block tridiagonal with each block of coefficients consisting of a two by two matrix as follows

$$\begin{bmatrix} B_j & 0 \\ b_j & 1 \end{bmatrix}\begin{Bmatrix} U_j^{i+1} \\ \Psi_{j-1}^{i+1} \end{Bmatrix}+\begin{bmatrix} D_j & E_j \\ b_j & -1 \end{bmatrix}\begin{Bmatrix} U_j^{i+1} \\ \Psi_j^{i+1} \end{Bmatrix}+\begin{bmatrix} A_j & 0 \\ 0 & 0 \end{bmatrix}\begin{Bmatrix} U_{j+1}^{i+1} \\ \Psi_{j+1}^{i+1} \end{Bmatrix}=\begin{Bmatrix} H_j\chi+C_j \\ 0 \end{Bmatrix} \tag{6}$$

The values of the coefficients are given in the Appendix. The method of solving the system then follows that reported in Kwon et al. [13].

The solution was obtained by marching from the step for a desired distance downstream using the FLARE approximation. Two to four Newton linearization iterations were required per step down the channel for the average solution change (the larger of $\Sigma\Delta U_j/\Sigma U_j$ or $\Sigma\Delta\Psi_j/\Sigma\Psi_j$) to be less than $5\times10^{-4}$ from a previous Newton linearization iteration. After the first global iteration, the FLARE approximation was discarded. Iterative, global sweeps were made through the

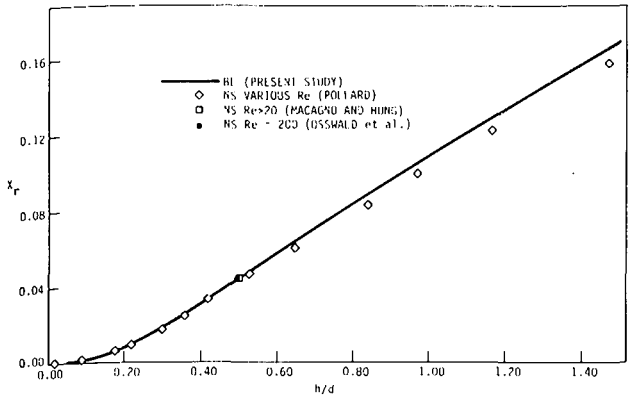


Fig. 5 Distance to reattachment for an axisymmetric expansion as a function of expansion ratio predicted by the boundary-layer equations and the Navier-Stokes equations [2, 5, 8]

**Table 1 Comparison of Navier-Stokes solution and boundary-layer solution for 1:3 plane expansion**

| Study | $X_r$ | $X$ to $\Psi_{min}$, $Y$ to $\Psi_{min}$ | $\Psi_{min}$ |
|---|---|---|---|
| Osswald et al. [8] | 0.1030 | 0.0290, 0.615 | 0.0515 |
| Present | 0.0981 | 0.0227, 0.647 | 0.0668 |

flow domain until the maximum change of any parameter was less than 0.5 percent. Eight to fifteen global iterations were adequate to meet the 0.5 percent criterion. Test runs with 100 global iterations showed that the solution did not change from the converged values. An average run required only 3–5 seconds of NAS AS/6 computer time per global sweep through the flow field. No artificial damping or smoothing was used.

## 4 Results

Calculations were made for expansion ratios of 1:1.2 ($d$:$D$ as in Fig. 1) through 1:4 for both two-dimensional and axisymmetric flows. This range of expansion ratios included the range of those studied by others with experimental tests and numerical solutions for this type of geometry. Comparisons were then made with available experimental results and solutions to the Navier-Stokes equations.

Reattachment length was well predicted over a wide range of expansion ratios and Reynolds numbers. Global iteration over the flow field had almost no affect on the reattachment length predicted by the boundary-layer method. Figures 3 through 5 compare the reattachment length ($X_r$) predicted by the boundary-layer equations without global iteration with those of experiment and other numerical predictions. Figure 3 shows the comparison between the reattachment length predicted by the boundary-layer equations and the results of Macagno and Hung. The agreement is excellent for Reynolds numbers above twenty. The reattachment length measured by Durst et al. [4] (see Fig. 4) was taken from a photo of smoke in air from which it was difficult to tell accurately where reattachment occurred. Figures 4 and 5 show that the distance to reattachment predicted by the boundary-layer equations is very good for $h/d$ from 0.0 to 0.5 and at least marginal from 0.5 to 1.0. Table 1 compares the predictions of the boundary-layer equations and the Navier-Stokes equations [8] for the location of flow reattachment. The ratio of the inlet to outlet plate spacing is 1/3; the Reynolds number is 37.3. Even for this large expansion ratio and low Reynolds number, the distance to reattachment predicted by the boundary-layer equations is within 5 percent of that predicted by the Navier-Stokes equations.

Velocity comparisons with the Navier-Stokes predictions were also encouraging. The velocity predicted by the boundary-layer equations compares well with the Navier-

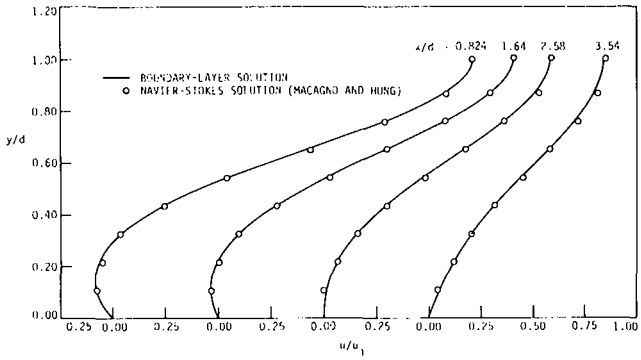


Fig. 6 Comparison of velocity profiles predicted by the boundary-layer equations and the Navier-Stokes equations [2] for Re = 60 and a 1:2 axisymmetric expansion

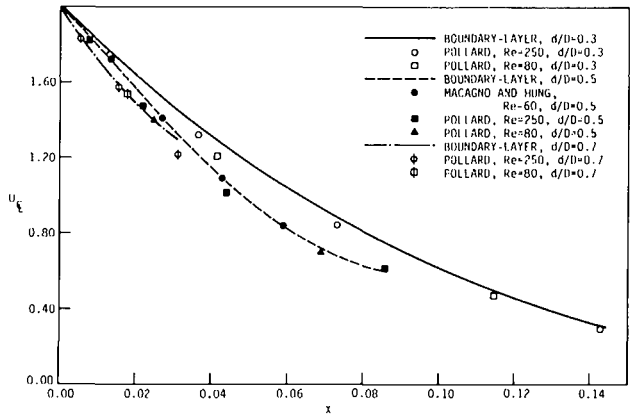


Fig. 7 Comparison of centerline velocity predicted by the boundary-layer equations and the Navier-Stokes equations [2, 5] for $d/D$ = 0.3, 0.5, and 0.7

Stokes solution of Macagno and Hung [2] (Fig. 6) for Re = 60 and a 1:2 pipe expansion. Even in the region of reversed flow the agreement is good. Figure 7 shows the centerline velocities for axisymmetric flow for three different expansion ratios. The boundary-layer solution used for this plot is again that for just one sweep down the channel since global iteration did not affect the centerline velocity. The agreement between the boundary-layer solution and the Navier-Stokes solution of Macagno and Hung [2] for the 1:2 expansion ratio is almost perfect. Pollard's [5] predictions don't compare as well.

The boundary-layer solution, which is independent of Reynolds number, appears as the asymptotic limit to the solution of the Navier-Stokes equations as the Reynolds number becomes large. Figure 8 shows the Reynolds number for which this approximation for symmetric expansions becomes valid. For Reynolds numbers above 200, the predictions of the two equation sets are almost identical. For Reynolds numbers below 100, the boundary-layer predictions of $\Psi_{min}$ are greatly in error. This trend is consistent with the $\Psi_{min}$ comparison shown in Table 1. For the case shown in Table 1 (Re = 37.3), the prediction of $\Psi_{min}$ by the boundary-layer equations was 30 percent higher than that predicted by the Navier-Stokes equations; the $X$-location of $\Psi_{min}$ was 22 percent lower. Figure 3 shows that the distance to the vortex center predicted by the boundary-layer equations is less than that predicted by the Navier-Stokes equations and measured experimentally by what appears to be a constant amount for all Reynolds numbers. The relative error becomes less at larger Reynolds numbers. Global iterative sweeps down the channel affected $\Psi_{min}$ by less than 1 percent.

Pollard [6] published the only explicit skin-friction coefficient data found by the present authors. Figure 9 shows that $c_f$ predicted by Pollard does not correlate well with the

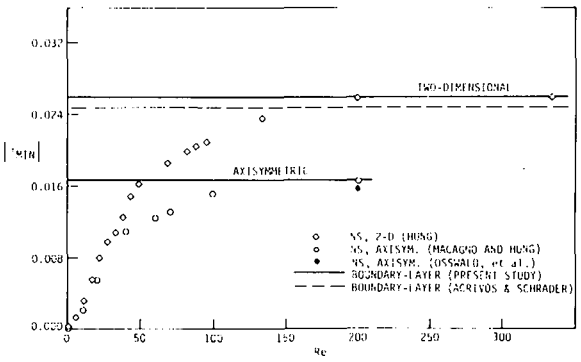


**Fig. 8 Comparison of the stream function at the center of the trapped vortex predicted by the boundary-layer equations and the Navier-Stokes equations (Hung [1], Macagno and Hung [2], and Osswald et al. [8]) for a 1:2 expansion**

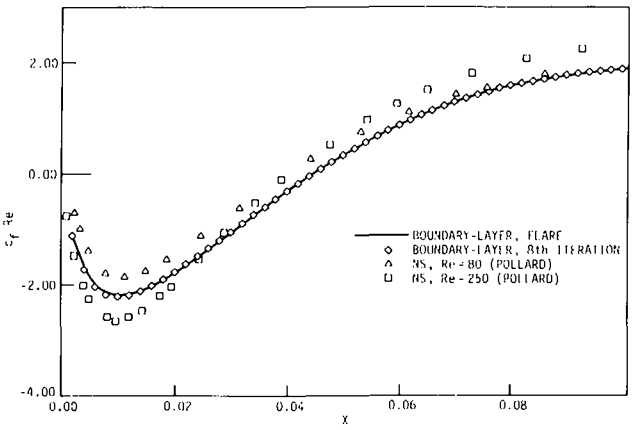


**Fig. 9 Friction coefficient predicted by the boundary-layer equations with and without global iteration compared with the Navier-Stokes solution by Pollard [6] for a 1:2 pipe expansion**

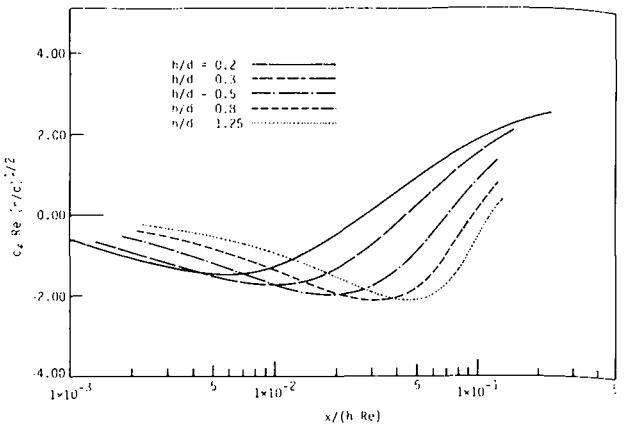


**Fig. 10 Friction coefficient predicted by the boundary-layer equations using FLARE for different expansion ratios for two-dimensional expansions**

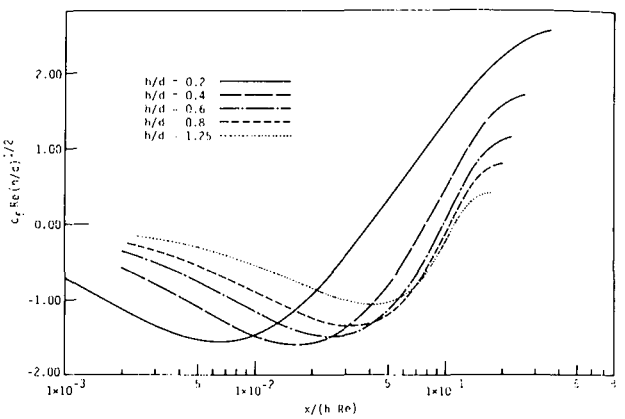


**Fig. 11 Friction coefficient predicted by the boundary-layer equations using FLARE for different expansion ratios for axisymmetric expansions**

boundary-layer prediction even when the Reynolds number is 250. For a Reynolds number this large, the agreement was expected to be better. It should be noted that Pollard's prediction using the Navier-Stokes equations shown in Fig. 9 for a Reynolds number of 250 overshoots the fully-developed $c_f$ Reynolds number product of 2.0 by 11.0 percent. Since Pollard provides very few details of his computational procedure other than it is similar to the SIMPLE method of Patankar and Spalding [19], it is not clear why $c_f$ exceeds the fully-developed values in some cases. Figure 9 also shows that global iteration has little effect on the boundary-layer prediction of $c_f$ for this expansion ratio. The skin-friction coefficient is based on the average inlet velocity $u_i$.

Figures 10 and 11 show predicted values of the skin-friction coefficient for different values of $h/d$. Both figures are results obtained using the "once-through" method with the FLARE approximation. When using these curves, one should realize that they may not be accurate for low Reynolds numbers (less than 100) and large values of $h/d$ (greater than 0.5). Figures 10 and 11 are included due to the lack of $c_f$ data in the literature.

The boundary-layer equations using FLARE predicted the existence of a small secondary eddy in the corner formed by the wall and the step. For $d/D = 0.5$, this eddy was less than 1/220th the length of the primary eddy. This eddy was discovered while using an extremely small $\Delta X$ for mesh refinement studies. The second eddy rotates in a direction opposite that of the large one. The flow situation very near the corner is similar to Stokes flow across the top of a wedge cut in a wall. The solution to this Stokes flow is a "stack" of eddies in the wedge, decreasing in size and intensity as one moves down in the wedge [20].

## 5 Conclusions

From the results mentioned in the previous section, one can draw the following conclusions.

1. The distance to flow reattachment and velocities outside of the trapped eddy are very well predicted by the boundary-layer equations for Reynolds numbers above 20 and expansion ratios below 1:3.
2. The eddy structure is not well predicted for low Reynolds numbers (Re < 200 for a 1:2 pipe and planar expansion). This is shown by the poor predictions of the magnitude and position of $\Psi_{min}$. For planar expansions, when the Reynolds number is approaching the point where the flow can be predicted by the boundary-layer equations, experiments have shown the flow tends to be asymmetric [9].
3. Reattachment length is a poor criterion to determine if the flow field is well predicted.
4. Global iteration over the flow field using the boundary-layer equations does not significantly change the predictions and offers little improvement over the "once through" method using FLARE.
5. A zero velocity initial condition on the face of the step is adequate. A nonzero velocity on the step face was not predicted by the algorithm of Acrivos and Schrader [12] as the grid was refined. A small nonzero velocity on the face of the step did not significantly affect the solution.

## Acknowledgments

This material is based on work supported by the National

Science Foundation under Grant CBT-8211713. Partial support from the National Aeronautics and Space Administration under Grant NGT-016-002-801 is also gratefully acknowledged.

## References


1 Hung, T.-K., "Laminar Flow in Conduit Expansions," Ph.D. thesis, University of Iowa, 1966.

2 Macagno, E. O., and Hung, T.-K., "Computational and Experimental Study of a Captive Annular Eddy," *J. Fluid Mech.*, Vol. 28, No. 1, 1967, pp. 43-64.

3 Morihara, H., "Numerical Integration of the Navier-Stokes Equations," Ph.D. thesis, University of New York at Buffalo, 1972.

4 Durst, F., Melling, A., and Whitelaw, J. H., "Low Reynolds Number Flow over a Plane Symmetric Sudden Expansion," *J. Fluid Mech.*, Vol. 64, No. 1, 1974, pp. 111-128.

5 Pollard, A., "Entrance and Diameter Effects on the Laminar Flow in Sudden Expansions," *Momentum and Heat Transfer Processes in Recirculating Flows*, Edited by B. E. Launder and J. A. C. Humphrey, ASME, New York, 1980, pp. 21-26.

6 Pollard, A., "A Contribution on the Effects of Inlet Conditions when Modeling Stenoses Using Sudden Expansions," *J. Biomech.*, Vol. 14, No. 5, 1981, pp. 349-355.

7 Agarwal, R. K., "A Third-Order-Accurate Upwind Scheme for Navier-Stokes Solutions at High Reynolds Numbers," AIAA Paper No. AIAA-81-0112, 1981.

8 Osswald, G. A., Ghia, K. N., and Ghia, U., "Unsteady Navier-Stokes Simulation of Internal Separated Flows over Plane and Axisymmetric Sudden Expansions," AIAA Paper No. AIAA-84-1584, 1984.

9 Cherdron, W., Durst, F., and Whitelaw, J. H., "Asymmetric Flows and Instabilities in Symmetric Ducts with Sudden Expansions," *J. Fluid Mech.*, Vol. 84, 1978, pp. 13-31.

10 Kumar, A., and Yajnik, K. S., "Internal Separated Flows at Large Reynolds Number," *J. Fluid Mech.*, Vol. 97, No. 1, 1980, pp. 27-51.

11 Plotkin, A., "Spectral Method Solutions for some Laminar Channel Flows with Separation," *AIAA Journal*, Vol. 20, No. 12, 1982, pp. 1713-1719.

12 Acrivos, A., and Schrader, M. L., "Steady Flow in a Sudden Expansion at High Reynolds Numbers," *Phys. Fluids*, Vol. 25, No. 6, 1982, pp. 923-930.

13 Kwon, O.-K., Pletcher, R. H., and Lewis, J. P., "Prediction of Sudden Expansion Flows Using the Boundary-Layer Equations," ASME JOURNAL OF FLUIDS ENGINEERING, Vol. 106, No. 3, 1984, pp. 285-291.

14 Kwon, O.-K., and Pletcher, R. H., "Prediction of the Incompressible Flow over a Rearward-Facing Step," Technical Report No. HTL-26, CFD-4, ISU-ERI-Ames-82019, Engineering Research Institute, Iowa State University, 1981.

15 Oosthuizen, P. H., "A Numerical Study of Laminar Flow through a Stepped Channel Using the Boundary Layer Equations with Particular Emphasis on 'Secondary' Separation," ASME Paper No. 84-FE-7, 1984.

16 Armaly, B. F., and Durst, F., "Reattachment Length and Circulation Regions Downstream of a Two-Dimensional Single Backward Facing Step," *Momentum and Heat Transfer Process in Recirculating Flows*, Edited by J. A. C. Humphrey and B. E. Launder, ASME, New York, 1980, pp. 1-7.

17 Reyhner, T. A., and Flugge-Lotz, I., "The Interaction of a Shock Wave with a Laminar Boundary Layer," *Int. J. Nonlinear Mech.*, Vol. 3, 1968, pp. 173-199.

18 Armaly, B. F., Durst, F., Pereira, J. C. F., and Schonung, B., "Experimental and Theoretical Investigation of Backward-Facing Step Flow," *J. Fluid Mech.*, Vol. 127, 1983, pp. 473-496.

19 Patankar, S. V., and Spalding, D. B., "A Calculation Procedure for Heat, Mass and Momentum Transfer in Three-Dimensional Parabolic Flows," *Int. J. Heat Mass Transfer*, Vol. 15, 1972, pp. 1787-1806.

20 Moffat, H. K., "Viscous and Resistive Eddies Near a Sharp Corner," *J. Fluid Mech.*, Vol. 18, No. 1, 1964, pp. 1-18.


## APPENDIX

The elements of the coefficient matrices in equation (6) vary depending on the circumstance. The following equations apply when $U$ is positive and when $U$ is negative if the FLARE approximation is being used.

$$A_j = -\frac{(\hat{\Psi}_j^{i+1} - \Psi_j^i)}{\Delta X\, \phi_j} - 2.0\, \frac{(R_{j+1/2}^{i+1})^m M_{j+1/2}^{i+1}}{\Delta Y\, \phi_j}$$

$$B_j = \frac{(\hat{\Psi}_j^{i+1} - \Psi_j^i)}{\Delta X\, \phi_j} - 2.0\, \frac{(R_{j-1/2}^{i+1})^m M_{j-1/2}^{i+1}}{\Delta Y\, \phi_j}$$

$$C_j = c\, \frac{(\hat{U}_j^{i+1})^2 +}{\Delta X} + \frac{\hat{\Psi}_j^{i+1}}{\phi_j \Delta X}\, (U_{j-1}^{i+1} - U_{j+1}^{i+1})$$

$$D_j = c\, \frac{(2\hat{U}_j^{i+1} - U_j^i)}{\Delta X} + \frac{2}{\phi_j} \left[ \frac{(R_{j+1/2}^{i+1})^m M_{j+1/2}^{i+1}}{\Delta Y} + \frac{(R_{j-1/2}^{i+1})^m M_{j-1/2}^{i+1}}{\Delta Y} \right]$$

$$E_j = -\frac{(\hat{U}_{j+1}^{i+1} - \hat{U}_{j-1}^{i+1})}{\phi_j \Delta X}$$

$$H_j = 1$$

$$b_j = \frac{\Delta Y}{2}\, (R_{j-1/2}^{i+1})^m$$

where

$$\phi_j = 2\Delta Y (R_j^{i+1})^m \quad ; \quad M = \frac{\nu}{\nu_i}$$

$\nu_i$ is the reference kinematic viscosity used in the Reynolds number.

For axisymmetric geometry, the boundary-layer equations are singular as $R$ approaches zero. The equations obtained by taking the limit of the boundary-layer equations as $R$ goes to zero replaced the regular set when $R$ was zero. The different set of coefficients used for the nodes at the centerline (when $j = NJ$) follow.

$$A_{NJ} = 0.0$$

$$B_{NJ} = -\frac{2^{m+1} M_{NJ-1/2}^{i+1}}{(\Delta Y)^2}$$

$$C_{NJ} = \frac{c}{\Delta X} (\hat{U}_{NJ}^{i+1})^2$$

$$D_{NJ} = \frac{c}{\Delta X} (2\hat{U}_{NJ}^{i+1} - U_{NJ}^i) + \frac{2^{m+1} M_{NJ-1/2}^{i+1}}{(\Delta Y)^2}$$

$$E_{NJ} = 0$$

The coefficients $H_j$ and $b_j$ remain unchanged from the previous set of coefficients.

When iterating globally by making repetitive sweeps through the flow field, the following coefficients were used only when $U$ was negative. The following equations were obtained from using a one-sided local upwind differencing scheme.

$$A_j = -\frac{(\Psi_j^{i+2} - \hat{\Psi}_j^{i+1})}{\phi_j \Delta X} - \frac{2}{\phi_j}\, \frac{(R_{j+1/2}^{i+1})^m M_{j+1/2}^{i+1}}{\Delta Y}$$

$$B_j = \frac{1}{\phi_j} \left[ \frac{\Psi_j^{i+2} - \hat{\Psi}_j^{i+1}}{\Delta X} - \frac{2}{\Delta Y}\, (R_{j-1/2}^{i+1})^m M_{j-1/2}^{i+1} \right]$$

$$C_j = -\frac{(\hat{U}_j^{i+1})^2}{\Delta X} + \frac{\hat{\Psi}_j^{i+1}}{\phi_j \Delta X} (\hat{U}_{j+1}^{i+1} - \hat{U}_{j-1}^{i+1})$$

$$D_j = \frac{U_j^{i+2} - 2\,\hat{U}_j^{i+1}}{\Delta X} + \frac{2}{\phi_j} \left[ \frac{(R_{j+1/2}^{i+1})^m M_{j+1/2}^{i+1}}{\Delta Y} + \frac{(R_{j-1/2}^{i+1})^m M_j^{i+1}}{\Delta Y} \right]$$

$$E_j = \frac{1}{\phi_j \Delta X}\, (\hat{U}_{j+1}^{i+1} - \hat{U}_{j-1}^{i+1})$$

$$H_j = 1.0$$

$$b_j = (R_{j-1/2}^{i+1})^m\, \frac{\Delta Y}{2}$$

The resulting system of linear equations were solved in the same way as reported in Kwon et al. [13].

# Developing Turbulent Flow in a U-Bend of Circular Cross-Section: Measurement and Computation

**J. Azzola**
Mem. ASME

**J. A. C. Humphrey**
Mem. ASME

Department of Mechanical Engineering,
University of California,
Berkeley, Calif. 94720

**H. Iacovides**

**B. E. Launder**
Mem. ASME

Department of Mechanical Engineering,
UMIST,
Manchester, U.K.

*Laser-Doppler measurements of the longitudinal and circumferential velocity components are reported for developing turbulent flow in a strongly curved 180 deg pipe and its downstream tangent. In the bend, the mean longitudinal velocity component changes little after $\theta = 90$ deg, but the circumferential component never achieves a fully-developed state. Similar behavior is observed in the normal stresses, with large levels of flow anisotropy arising everywhere in the bend and downstream tangent. Between $\theta = 90$ deg and $X/D = 5$, the circumferential velocity profiles display reversals of the secondary flow which are essentially independent of the Reynolds number. Predictions of the flow development are presented based on a "semi-elliptic" truncation of the Reynolds equations in the main part of the flow with the standard k-$\epsilon$ effective viscosity model used to approximate the turbulent stress field. In the immediate vicinity of the wall a simpler treatment, PSL, is adopted that allows the inclusion of the very fine mesh needed to resolve the viscous sublayer without excessive computer storage. The calculated behavior displays reasonably good agreement with the measurements in the bend, including the secondary flow reversals. Downstream of the bend, however, the rate of recovery of the flow is too slow, which points to the same weakness in the turbulence model as found in the recovery region of the flow over a backward-facing step.*

## 1 Introduction

**1.1 The Problem of Interest and Earlier Work.** Over the last ten years, approximately, a substantial amount of experimental information has been obtained for developing turbulent flows in curved ducts of rectangular cross-section [1–7]. Detailed measurements in these important flow configurations, in particular of the secondary motions and complex turbulent characteristics which they induce, have been made possible by the non-intrusive laser-Doppler velocimetry technique. In contrast, turbulent flow-field measurements in curved pipes appear to be relatively sparse [8]. This is surprising given the practical importance of the curved pipe configuration. The lack of detailed data is partly explained by the greater difficulties associated with optical alignment through transparent curved surfaces.

The dominant influence of the flat walls on the secondary motion induced in rectangular ducts precludes the use of data obtained in these configurations to interpret accurately the characteristics of flow developing in curved pipes. For example, Cuming [9] shows analytically that, for equal radius of curvature to diameter ratio and dimensionless streamwise pressure drop, the ratio of the relative intensity of the secondary flow in a duct of square cross-section to that in a pipe of circular cross section is 2.47 at the center line location. This result is strictly valid only for fully developed laminar flow. Comparisons between present results and corresponding measurements by Chang et al. [5] in a curved duct of square cross-section with similar developing turbulent flow characteristics show that the secondary motion ratio can be considerably larger than 2.47, depending on the streamwise location. This point has been quantified and discussed in [10].

Among the early measurements of secondary turbulent flow patterns developing in and downstream of curved pipes are the total pressure and yaw results obtained by Rowe [11] in a 180 deg bend and the attached downstream tangent. In Rowe's experiment $Rc/D = 12$ and $Re = 2.36 \times 10^5$, where $Rc$ is the bend mean radius of curvature, $D$ its diameter and Re is the Reynolds number based on the bulk fluid velocity. An upstream tangent of length $X/D = 69$ was used to provide a fully developed axisymmetric turbulent velocity profile at the bend inlet plane. Among Rowe's findings were that: secondary flow is most intense at about $\theta = 30$ deg, as of which point the total pressure gradient induces a streamwise component of vorticity opposite in sense of rotation to the streamwise vorticity produced at the start of the bend; the curved flow is essentially fully developed past $\theta = 90$ deg; there is evidence of local reversal in the secondary flow direction along the bend symmetry plane between $\theta = 90$ deg and $X/D = 5$.

Because of the nature of the variables measured in Rowe's study, and because of the influence of the mechanical probes used in the flow, an accurate determination of the fully developed flow streamwise location was not possible. (A combination of weak secondary motions, undetected by the yawmeter, with unchanging relatively large total pressure measurements, would certainly have given the impression of fully developed flow.) Due to experimental uncertainty, Rowe was not able to define precisely the magnitude and extent of

Contributed by the Fluids Engineering Division for publication in the JOURNAL OF FLUIDS ENGINEERING. Manuscript received by the Fluids Engineering Division April 4, 1985.

secondary flow reversal in the vicinity of the bend symmetry plane. Although valuable for helping to understand the behavior of the mean flow, particularly in relation to inviscid effects, the pressure and yaw contours obtained by Rowe shed no light on the turbulent characteristics of the flow.

Enayet et al. [12] have investigated developing turbulent flow in a 90 deg curved pipe with $Rc/D = 2.8$ and Re = 43,000. Relatively thin boundary layers were induced at the bend inlet plane by means of a smooth contraction. The mean longitudinal (streamwise) velocity component and the corresponding turbulence intensity were measured using a laser-Doppler velocimeter. This information was supplemented by wall-pressure measurements. The relatively flat inlet velocity profile and small value of $Rc/D$ in [12] enhanced streamwise acceleration of the flow at the inner radius wall relative to the outer wall. As a result, throughout the bend and up to $X/D = 6$ in the downstream tangent, the maximum in the stream-wise velocity component remained between the bend center line and the inner radius wall. This finding contrasts strongly with Rowe's observation that the maximum was always located between the bend center line and the outer radius wall. Because the Dean numbers of these two flows are very similar, being De = Re $(D/Rc)^{1/2} \simeq 6.8 \times 10^4$ in Rowe's bend and $2.6 \times 10^4$ in the bend of Enayet et al., the difference in the maximum velocity location must be due to the different inlet flow boundary layer thicknesses. A similar finding has been reported in [3] for the flow through a curved duct of square cross section.

The problem of numerical simulation of developing flow in curved pipes has been the subject of considerable research effort for the past twenty years. The extensive literature on laminar flow has been recently reviewed in [8, 13]. The first serious attempt to compute turbulent flow was reported by Patankar et al. [14] who applied their three-dimensional parabolic (noniterative) procedure to simulate Rowe's experiment. The parabolic approximation enforces, at any station, the same streamwise pressure over the whole cross section. In view of the relatively large radius ratio for the case in question, such a numerical approximation was satisfactory over much of the bend. At the inlet to and exit from the bend, however, the sign of the pressure gradient is in fact different on the inside and outside of the bend and the adjustments to the flow that this causes cannot be mimicked by a parabolic solver.

Although for laminar flow several workers have discretized the full elliptic form of the equations of motion [15, 16], provided there is no flow reversal in the streamwise direction, a semielliptic treatment [17] is more attractive as only the pressure field then requires storing over the solution domain. The approach was applied by its originators [17] to flow in a rectangular-sectioned bend. Recently two of the authors [18] have applied a procedure of the same type to predict turbulent flow in coils and in the 90 deg bend of [12]. For the former case only heat-transfer data were available for comparison; these indicated that the predictions correctly reproduced the monotonic increase in local Nusselt number from the inside to the outside of the bend, though the inner-to-outer variation was only about 60 percent of that measured. Agreement with the streamwise velocity profiles of [12] was broadly satisfactory, though the boundary layer development on the inside of the bend did not proceed as far toward separation as the experiment showed, nor was the rate of recovery downstream as fast. There was, moreover, some uncertainty on the degree of difficulty provided by this test case as the boundary layers were rather thin and the pressure disturbance so large that inviscid effects would have dominated over much of the flow.

**1.2 The Present Contribution.** The above brief review has identified substantial deficiencies in our knowledge of the physics of turbulent flow through curved pipes and of the relaxation processes undergone by fluid passing from a curved to a straight pipe section. A full understanding will require many experiments with different ratios of bend to pipe radii and different flow conditions at entry. In comparison with [18], we have selected a somewhat larger bend radius, 180 deg rather than 90 deg of turning, and a fully-developed flow at the bend entry plane. All these differences are designed to make the resultant flow pattern in the bend more strongly dependent on the turbulent stress field. Downstream of the bend, the turbulent stresses provide the only substantial agency for restoring the flow towards that associated with a straight pipe. The initial stages of this restoration have been documented at one diameter intervals.

Finally, in order to gain an impression of how successful or otherwise the widely used $k$-$\epsilon$ eddy viscosity model is in predicting this flow's behavior, the solving scheme developed in [18] has provided the basis for a numerical simulation.

## 2 The Experiment

**2.1 Flow System and Instrumentation.** The experimental system was composed of: a water rig (described in detail in [5]), of which the most important component was the flow test section; a DISA 55X modular series laser-Doppler velocimeter and its associated electronic instrumentation; and a PDP 11/34 Digital Equipment Corporation minicomputer.

The basic components of the flow test section are shown schematically in Fig. 1. They comprised two straight pipes and a 180 deg curved pipe, constructed from transparent plexiglass. The pipe cross-section was circular throughout with a 4.45 cm ± 0.02 cm inner diameter ($D$). The ratio of bend mean radius of curvature to pipe diameter was $Rc/D = 3.375$. Both tangents were of length $X = 54.7\ D$, being, respectively, attached to the 0 deg (inlet) and 180 deg (outlet) planes of the bend by means of flanges. Special care was taken to avoid

## Nomenclature

$D$ = pipe diameter
$\mathrm{De}(\equiv \mathrm{Re}(D/Rc)^{1/2})$ = Dean number
$k$ = turbulent kinetic energy
$r$ = radial (cross-stream) coordinate
$Rc$ = curved pipe radius of curvature
$\mathrm{Re}(\equiv DU_b/\nu)$ = Reynolds number
$u'(\equiv\sqrt{\overline{u^2}})$ = rms of the longitudinal velocity fluctuations
$\overline{u^2}$ = longitudinal component of normal stress
$U$ = longitudinal component of mean velocity
$U_b$ = bulk average velocity through the pipe
$v'(\equiv\sqrt{\overline{v^2}})$ = rms of the circumferential velocity fluctuations
$v^2$ = circumferential component of normal stress
$\overline{vw}$ = turbulent shear stress in $r$, $\phi$ plane
$V$ = circumferential component of mean velocity
$W$ = radial component of mean velocity
$X$ = longitudinal (streamwise) coordinate in a straight pipe section
$\epsilon$ = dissipation of turbulent kinetic energy
$\theta$ = longitudinal (streamwise) coordinate in a curved pipe section
$\nu$ = fluid kinematic viscosity
$\phi$ = circumferential (cross-stream) coordinate

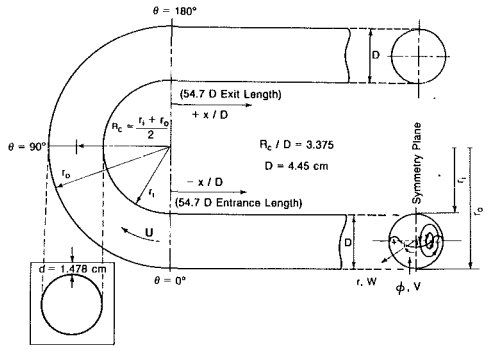


**Fig. 1 The test section configuration and definition of coordinate system**

possible mismatches between the component cross sections that otherwise might disturb the flow. A stainless steel (20 mesh) screen and a 3.5 cm long flow straightening honeycomb section were placed upstream of the entrance tangent. They were held in place by a thin circular plexiglass plate. The plate was 3.175 mm thick and had 85 holes of 3.175 mm diameter arranged in a rectangular array spaced 4.495 mm on the centers in each direction. The purpose of the screen-honeycomb-plate combination was to make uniform the cross-stream plane distribution of the flow and accelerate its streamwise development.

The curved pipe section was constructed by fitting together two symmetrical half sections of plexiglass, each respectively machined on one of the two flat faces to contain the shape of a semicircular open channel. This method of construction ensured that when matched at the common symmetry plane the cross-section of the resulting curved pipe was accurately circular. When assembled, the curved pipe section had flat outer surfaces of thickness $d = 1.48 \pm 0.02$ cm (see Fig. 1). The straight pipe sections had a circumferentially uniform wall thickness of $0.32 \pm 0.02$ cm. The entire test section was supported horizontally by a metal frame with the bend symmetry plane parallel to the floor.

The test section was part of a closed loop through which water was made to flow by gravity from a constant head tank. From this tank the flow passed through the test section, and then into a large sump tank from where it was pumped back to the constant head tank. Flow to the head tank was controlled by a gate valve and measured using a venturi meter connected to a differential mercury manometer. The possibility of propagating disturbances through the test section was eliminated by avoiding the use of valves, sharp bends and metering devices in the test section flow loop. Flow to and from the test section tangents was channeled through 2 in (5.08 cm) i.d. gently bent tygon tube pieces. Baffles and screens located in the constant head tank served to dampen the swirling motion of the flow leaving the tank. Residual swirl and weak secondary motions induced by the mild curvature of the tygon tube upstream of the test section were eliminated by the flow straightening section.

Measurements of the mean flow and turbulence characteristics were made using a DISA 55X modular series laser-Doppler velocimeter in backscatter mode. The system has already been described in full detail in reference [5]. A 2-watt Lexel Argon-Ion water-cooled laser was used as the light source. The laser and velocimeter optics were mounted to the top of a thick aluminum table which was itself firmly bolted to an $x$, $y$, $z$ traversing mechanism. The traversing mechanism could displace the table top $\pm$ 7.5 cm in 5 $\mu$m increments along any of the coordinate axes by means of three linearly encoded stepping motors monitored by the PDP 11/34 minicomputer. The minicomputer functioned as the central data acquisition and reduction controller of data validated and measured by a DISA 55L96 Doppler signal processor or "counter." Directional ambiguity in the circumferential (or tangential) velocity component was resolved by means of a Bragg cell combined with electronic downmixing.

**2.2 Experimental Methodology.** Prior to an experimental run, water was allowed to flow through the rig until it was purged of air bubbles and had attained a steady thermal state corresponding to about 20°C. Experiments were performed for two values of the bulk average velocity corresponding to $U_b = 1.29 \pm 0.03$ m/s and $U_b = 2.47 \pm 0.04$ m/s, respectively. During the course of an experimental run the fluid temperature rose from 18°C to 22°C, approximately. Values for the Reynolds numbers of these two flows, based on physical properties of water at 20°C, are Re = 57,400, and 110,000, respectively. The associated Dean numbers are De = 31,300, and 59,900.

The velocimeter optical probe volume was formed by the intersection of two 514.5 nm (green) light beams with a half-angle in air of 3.28 deg. The measurement volume characteristics were: a diameter of 0.1 mm, a length of 1.6 mm, and a fringe spacing of 4.50 $\mu$m with about 18 fringes contained in the optical probe. In reality spatial filtering and threshold settings on the counter reduced the dimensions of the optical probe. The probe volume was positioned by fine control of the motorized traversing table. The details of the optical alignment procedure are provided in [10]. Cornstarch particles ranging in size from 1 to 10 $\mu$m were added to the flow so that validated particle data rates of 1 kHz were achieved.

With a reference position established, usually on the outer surface of the test section, the computer software was activated which controlled the signal acquisition and data processing. An initial check on flow symmetry was performed at $X/D = -2$ in the upstream tangent. Measurements of the streamwise velocity component and its normal stress at this station (half profiles are shown in Figs. 2 and 3) are in good agreement with the data of Laufer [19]. Measurements of the circumferential velocity component (not plotted) showed that it was everywhere less than $\sim$ 1.5 percent of the bulk average velocity at this station. Calculations of $U_b$, obtained by integrating the measured velocity distributions at $X/D = -2$, yielded values in good agreement (to within $\sim$ 3 percent) with the values obtained from the venturi meter pressure drop readings.

Following the symmetry and mass flow confirmations, all subsequent measurements were restricted to vertical (radial) scans in the surface $\phi = \pi/2$ in the symmetrical upper half of the test section. Scans were made at $X/D = -2, -1, 1, 2, 3, 4$, and 5 in the straight pipes and $\theta = 3, 45, 90, 135$, and 177 deg in the bend. At each of these stations 15 radial positions were probed, starting at the centerline and moving in increments of 1.5 mm toward the wall, with a 16th position fixed at 0.7 mm from the inside pipe wall. At each measurement point the mean velocity and normal stress were statistically determined from populations of 1 to 3 samples consisting of 1000 individual measurements each. More than 90 percent of all the measurements consisted of at least 2 samples per point. Each individual measurement was required to satisfy the counter 5/8 validation comparison to within a preset tolerance of 6 percent. At every validation of a Doppler burst a "data ready" signal was issued by the counter to a logic conversion circuit. This circuit then sent a triggering pulse to the computer parallel line interface module which was checked for data availability by a software loop approximately every 20 $\mu$s.

Although the velocimeter is capable of two-component measurements, curvature of the test section surfaces precluded dual-channel operation. Values for the streamwise component of the mean and fluctuating velocities, $U$ and $u'$, were derived from measurements obtained with the probe volume fringes aligned normal to the longitudinal coordinate direction. Values for the circumferential components, $V$ and $v'$, were

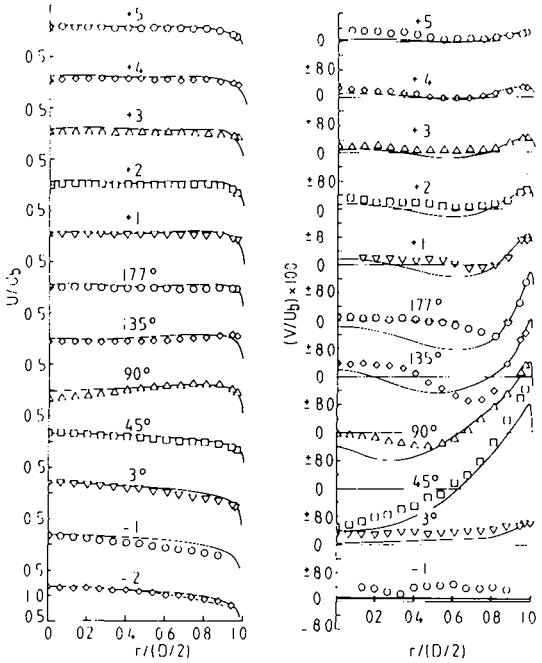


Fig. 2 Measurements (points) and calculations (continuous lines) of the longitudinal ($U$) and circumferential ($V$) mean velocity components at sequential longitudinal stations in a 180 deg curved pipe with straight tangents. Dashed line at $X/D = -2$ corresponds to Laufer's [19] developed flow data.

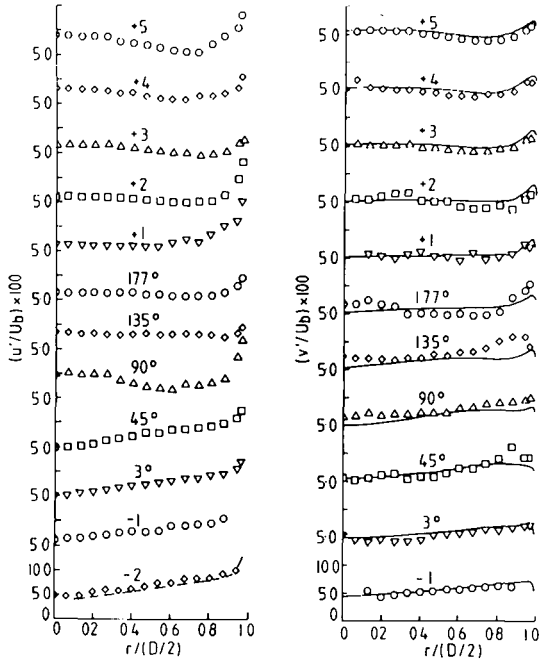


Fig. 3 Measurements (points) and calculations (continuous lines) of the longitudinal ($u'$) and circumferential ($v'$) turbulence intensity components at sequential longitudinal stations in a 180° curved pipe with straight tangents. Dashed line corresponds to Laufer's [19] developed flow data. In the calculations $u' = v' = (2k/3)^{1/2}$.

obtained through a rotation of the optics by 90 deg, thus placing the fringes normal to the circumferential component direction.

Because of the large positive magnitudes of the streamwise velocity component, frequency shifting was unnecessary for measurements of this component. By contrast, the circumferential velocity component exhibited low magnitudes, with signs both positive and negative. To resolve this directional ambiguity, a net frequency shift of 500 kHz was imposed using a DISA 55N10 Bragg cell combined with electronic downmixing.

**2.3 Measurement Error.** Error sources affecting the accuracy (systematic error) and precision (random error) of laser-Doppler measurements have been discussed in [20-22]. In this study the most serious potential systematic errors were attributed to probe volume positioning, velocity gradient broadening and velocity bias, respectively. The main sources of random error affecting the precision of the measurements were due to: (*a*) statistical sampling uncertainty (due to the finite size of sample populations); and (*b*) uncertainty in the determination of the normalizing bulk average velocity, $U_b$. Estimates of the first uncertainty were derived from the measurements themselves. For both mean velocity components, this uncertainty was always less than ± 2-3 percent (rms error), while for the turbulence intensities it was always less than ± 2-5 percent. The error in $U_b$ was ± 2 percent and arose principally from uncertainties in the manometer pressure readings.

The initial probe volume location uncertainty was estimated to be half the effective probe volume length, or ± 0.5 mm approximately. This error is altered as the beams traverse the pipe because of changes in index of refraction (at the air/plexiglass and plexiglass/water interfaces) and wall curvature effects. To calculate the actual probe volume location, and to estimate the uncertainty in this location, it is necessary to know the relevant trigonometric relations. These are derived in [10]. The relations depend on the velocity component of interest and on the shape of the surfaces at the measurement station in question. In regions of surface curvature, both the probe volume location and the half angle between the beams in water depend nonlinearly on the probe volume virtual radial location (the location in air). Calculations of the error incurred in $\gamma$, the half angle of the beams in water, due to a ± 0.5 mm positioning error in the initial probe volume location showed that this source of inaccuracy was negligible. Similarly, calculations showed that the initial positioning uncertainty was only significant very near the pipe walls, in regions with steep field gradients. Thus, estimates of the maximum (absolute) systematic errors in the measurements obtained nearest the walls gave: ~ 4 percent for $U/U_b$; ~ 10 percent for $u'/U_b$; ~ 15 percent for $V/U_b$, and ~ 10 percent for $v'/U_b$. In the bulk of the flow all these errors were significantly less than ~ 2 percent.

Velocity gradient broadening has been analyzed by Melling [23] who proposed a simple method for estimating its magnitude. For the conditions of this study, gradient broadening in the measurements was estimated to be less than 1 percent everywhere in the flow.

Various weighting methods have been proposed to correct for the velocity bias effect [21, 22], but none of these is entirely satisfactory. They all involve assumptions regarding the statistical distribution of particles in the flow. In addition, the corrections can be influenced by the problem of "incomplete-signal bias." The use of the weighting scheme proposed by McLaughlin and Tiederman [24], in which the particle residence time is taken to be inversely proportional to the modulus of the measured velocity, was investigated in this study. For the longitudinal velocity component, differences between weighted and unweighted data sets were relatively small (less than 1 percent). For the circumferential component the differences were much larger, with the weighted data giving a less realistic (overdamped) picture of the flow field. The reason for this is attributed to an overcorrection in the weighting scheme which, for the circumferential component, amounts to a disproportionate weighting of slow moving particles. This occurs as a consequence of taking the particle residence time as $t_{res} \sim V^{-1}$ instead of $t_{res} \sim (U^2 + V^2 + W^2)^{1/2}$. The latter, more accurate, weighting could not be performed with the present single component measurement system.

For turbulence intensities less than 10 percent Drain [21] shows that velocity bias corrections of the mean and rms velocities should not amount to more than ~ 2 percent. In this study the measured turbulence intensities never exceed ~ 12 percent. As a result, plots of the unweighted data only are presented here. Listings of both weighted and unweighted measurements are provided in [10].

## 3 The Computational Method

The numerical procedure developed by the authors to predict laminar or turbulent flow in pipe bends has been described in [13, 18]. Here, therefore, we simply summarize its main features.

The method is based on a semi-elliptic discretization of the Reynolds equations expressed in toroidal coordinates in which the three components of velocity and the static pressure form the set of dependent variables. Following the methodology of the TEACH family of computer programs, [25], a finite-volume approach to forming the difference equations is adopted with a staggered mesh for the different dependent variables. The quadratic upstream weighted approximation is adopted for convective transport, [26], while a modified version of Patankar's SIMPLER algorithm [27] is used to secure a pressure field in compliance with the continuity equation.

Although in a shear flow as complex as this one might well expect to have to adopt some nonequilibrium, nonisotropic model of turbulence to secure close agreement with experiment, the (relative) computational simplicity of using isotropic effective diffusion coefficients persuaded us that in this study the turbulent stresses should be obtained by the standard $k \sim \epsilon$ model [18, 28]. However, in place of the wall functions that usually provide a link between near-wall velocities and shear stresses and supply effective boundary conditions for the turbulence energy ($k$) and its viscous dissipation ($\epsilon$), a fine mesh has been incorporated to cover the viscous sublayer and "buffer" regions. In this sub-region we have for simplicity adopted the mixing-length hypothesis using van Driest's [29] damping function. Of course, to resolve accurately the very rapid variation of effective transport coefficients across this near-wall sublayer a fine mesh is required. In order that this requirement should not impose a substantial core penalty, the variation of pressure across the sublayer was obtained by radial equilibrium (instead of by continuity); the technique, known as PSL, is described in [30].

Computations were made over the semi-circular cross section bounded by the plane of symmetry passing through the center of the pipe and the bend center. Starting inlet profiles were obtained by computing the development of the flow in a straight pipe over a distance of 53 diameters. The downstream profiles of the dependent variables were then used as the inlet profiles for the computation of the U-bend flow at a position 2 diameters upstream of the bend. The mesh comprised 28 radial and 24 uniformly-spaced circumferential nodes mapping the semi-circular section and 160 streamwise planes. This mesh density has been found from our previous work to give essentially grid independent results[1] when used with the third-order accurate quadratic upstream approximation for convection. The computations extended a total of 8 diameters into the tangent downstream of the bend where, at the exit plane, zero-streamwise gradient constraints were applied to all variables. Successive streamwise passes over the domain were made until momentum and mass residuals summed over all planes were below 1 percent of the entering momentum and mass flow rates. Convergence required about 6 hours cp time on a Cyber 205 (with an unvectorized code) though in practice only very small changes resulted over the second half of the computation.

[1] For example, in [18] an increase in the number of radial nodes from 28 to 40 altered the predicted level of Nusselt number by less than 1 percent.

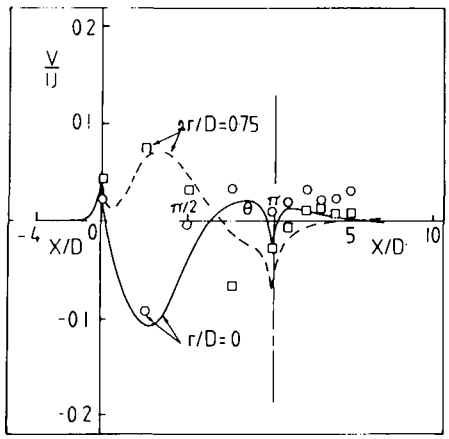


**Fig. 4 Measurements (points) and calculations (lines) of developing secondary flow at two radial locations contained in the symmetry plane, $\phi = \pi/2$, of a 180 deg curved pipe with straight tangents.**

## 4 Results and Discussion

Measurements of the longitudinal ($U/U_b$) and circumferential ($V/U_b$) velocity components and their respective turbulence intensities ($u'/U_b$), $v'/U_b$) are shown in Figs. 2-3. Only the data at the lower Reynolds number (Re = 57,400) are here included. Except for relatively small differences, the dimensionless profiles show that flow development is essentially the same at Re = 110,000 [10]. This is an important point since all the calculations reported here were performed for Re = 65,000 (with $Rc/D$ = 3.375). Tabulations of the measurements are available in [10].

The $U$ and $u'$ component measurements at $X/D = -2$ show good agreement with the developed flow measurements obtained by Laufer [19] in a straight pipe. At $X/D = -2$ the $V$ component is less than (+) 0.015 $U_b$ (not plotted). However, at $X/D = -1$ and $\theta = 3$ deg, the $V$ component is ~ (+) 0.04 $U_b$. With reference to the coordinate system in Fig. 1, this implies that the inlet flow is gradually (but only slightly) accelerated toward the inner radius of the pipe, a result expected from potential flow theory and previously observed by others.

In the first half of the bend ($\theta$ = 3 to 90 deg), the $U$-profiles show the core of the streamwise flow losing speed while the flow near the wall accelerates. $V$-profiles at corresponding stations reveal the development of a strong secondary flow. This secondary flow is induced by the transverse pressure gradient set up between the outer ($r_o$) and inner ($r_i$) wall regions of the bend. In the pipe center, it works to overcome and reverse the sense of the cross-stream motion in the inlet flow. Near the wall the original sense of cross-stream motion is preserved and intensified, with $(V/U_b)_{max} \sim 0.30$ at $\theta$ = 45 deg. Nevertheless, the levels of secondary flow found in the present study are lower than those obtained in a square sectioned duct for equivalent curvature ratio and entering flow conditions [5].

Between $\theta$ = 45 and 135 deg the $V$-profiles reveal a striking feature of the flow. In the fluid core, $r/(D/2) < 0.5$, the cross-stream flow undergoes a *second reversal* in its sense of motion and is redirected toward the pipe inner radius. As a result, a region of negative cross-stream flow (directed from $r_i$ toward $r_o$) is trapped between the core and the wall; for example, $V/U_b \sim -0.06$ at $\theta$ = 135 deg. Between $\theta$ = 135 deg in the bend and $X/D$ = 5 in the downstream tangent, the region of negative cross-stream flow gradually disappears. Notwithstanding, an imprint of its presence remains in all the subsequent $V$-profiles.

The occurrence of a second cross-stream flow reversal past $\theta$ = 90 deg in the bend supports the concept proposed by Rowe [11], that each symmetrical half section of the bend develops *two* counter-rotating vortical structures. The more intense of

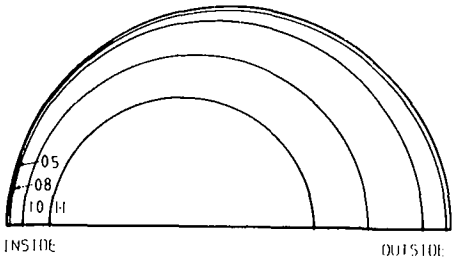


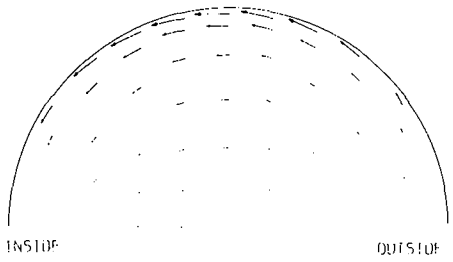


(L/R) = 0.35 ; Θ = 3°

Fig. 5(*a*)

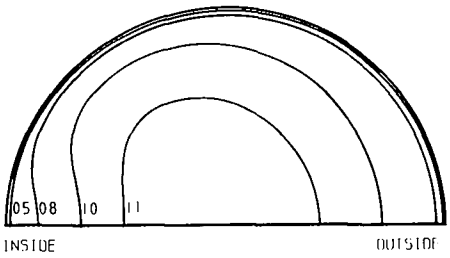


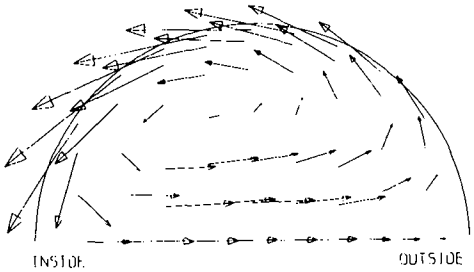


(L/R) = 5.30 ; Θ = 45°

Fig. 5(*b*)

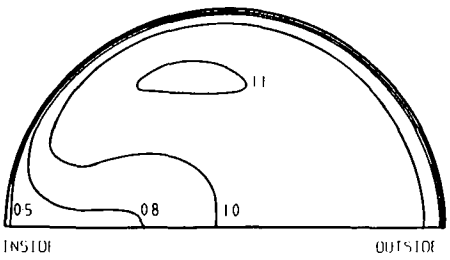


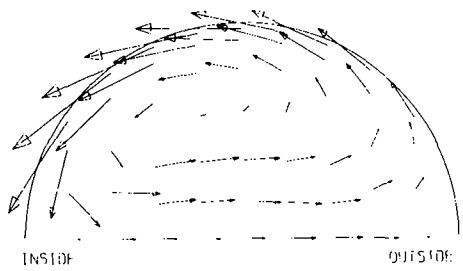


(L/R) = 10.60 ; Θ = 90°

Fig. 5(*c*)

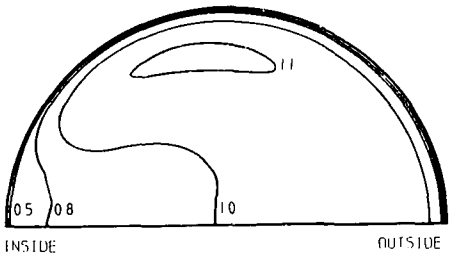


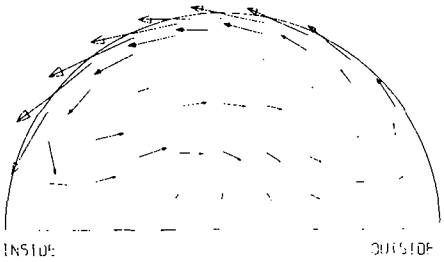


(L/R) = 15.91 ; Θ = 135°

Fig. 5(*d*)

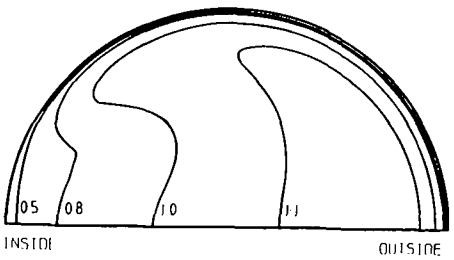


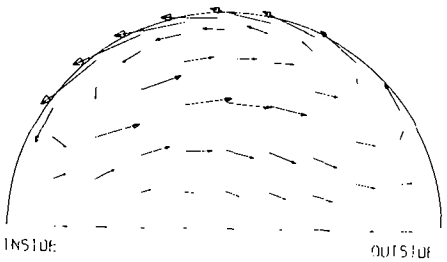


(L/R) = 20.95 ; Θ = 177°

Fig. 5(*e*)

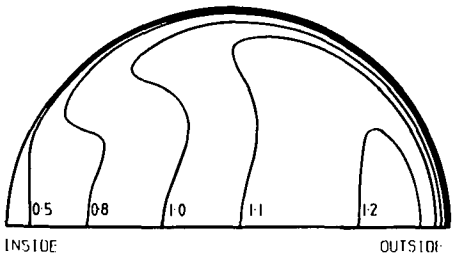


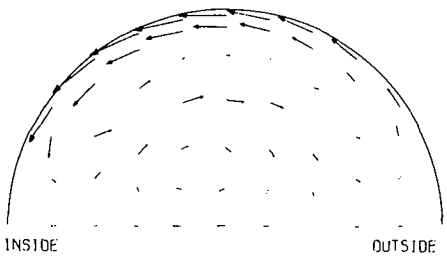


(L/R) = 23.21 ; X/D = 1

Fig. 5(*f*)

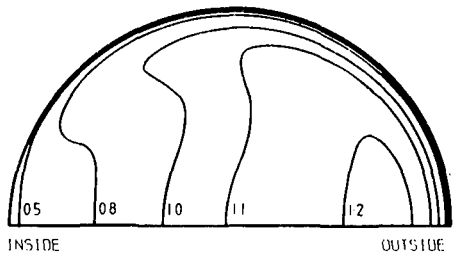


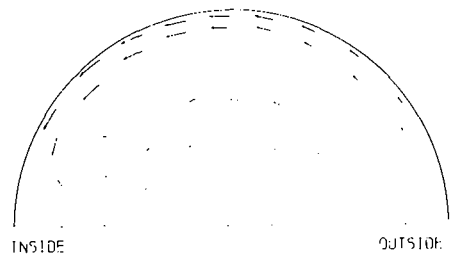


Fig. 5(g)

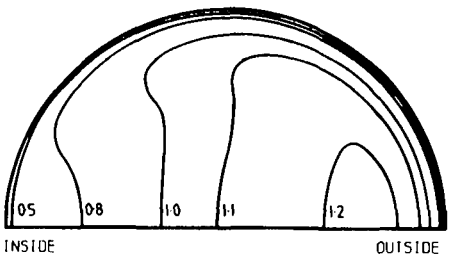


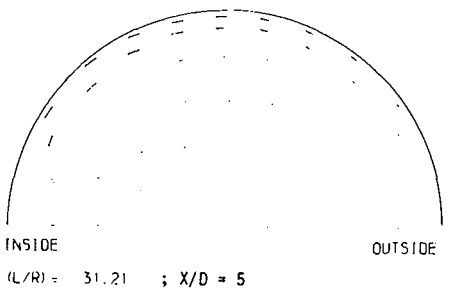


Fig. 5(h)

**Fig. 5 Calculated flow development in a 180 deg curved pipe with straight tangents. Top figures show streamwise ($U/U_b$) velocity component contours. Bottom figures show cross-stream vector velocities. In bottom figures, 0.10 $D$ corresponds to 0.08 $U_b$.**

the two, located between the pipe wall and the core of the flow, preserves the sense of cross-stream motion induced by the transverse pressure gradient at the start of the bend. The smaller, weaker, structure is mainly confined to the core and is attributed to the formation of a transverse pressure gradient opposite in sign to that at the start of the bend.

The present mean flow measurements place on a firm quantitative basis the interpretation by Rowe of his total pressure and yaw measurements. However, in contrast to Rowe's results, the $V$-profiles provided here show that fully developed mean flow conditions are not established in the present bend.

The computed distribution of longitudinal velocity shown in Fig. 2 actually mirrors very closely the measured development. Only at 90 deg is there a discernible difference between the two, the experiments indicating a larger dip in velocity at the axis. This measure of agreement, while encouraging, at least partly reflects that the mean velocity profile along this $\phi = \pi/2$ surface does not offer a particularly sensitive test. This is not the case with the secondary flow shown in Fig. 2. The computations do not reproduce as strong an increase in the $V$ velocity component, directed towards the inside of the bend, as the data at $X/D = -1$ and $\theta = 3$ deg. However they do predict very well the strong, single-cell secondary flow that develops by 45 deg. They also capture broadly the way the "return" flow near the mid-plane is brought to a halt and reverses by 135 deg. Interestingly, the computations suggest that the sign of the secondary velocity on the symmetry plane reverses yet again at 177 deg and at one diameter downstream. While the measuremens at 177 deg still show marginally positive $V$ for small $r$, the sign of the acceleration is evidently correct. The differing development of the secondary flow at different radial positions is brought out in Fig. 4 which shows the progress of $V/U$ on the $\pi/2$ surface at $2r/D = 0.75$ and at the pipe axis. The flow reversals exhibited by the measurements are generally well captured by the numerical computation, at least within the bend itself.

A more complete picture of the computed flow development in the U-bend is provided in Fig. 5 which shows both the secondary flow vectors in the cross-sectional plane and the streamwise flow contours. The modifications that the former bring to the latter are readily discernible. Particularly interesting are the 90 and 135 deg contours where the maximum streamwise velocity is displaced off axis (as in the experiment, Fig. 2), and those at 177 deg where the contours $U/U_b = 0.8$ and 1.0 show clearly the effect of the reversal of the secondary flow on the mid-plane. In Fig. 5, $R$ and $L$ are, respectively, the bend radius of curvature and length of the pipe "centerline" measured from the inlet plane.

Downstream of the bend the computations do not mimic the steady cross-stream movement of fluid towards the side of the pipe corresponding with the inside of the bend (Fig. 3). This reflects a significantly too slow recovery of the computed streamwise velocity from the strong adverse pressure gradient that the fluid on the inside of the bend encounters at the bend exit. Computations for the 90 deg bend of Enayet [18] with precisely the same model show a similar too slow recovery. It is also relevant to mention that several groups adopting the same (or a very similar) turbulence model to compute the flow downstream of the reattachment point behind a backward-facing step for the 1981 Stanford Conference also found a too sluggish recovery [31]. The behavior here predicted thus seems an endemic feature of the model that needs to be removed.

In flow through a straight pipe, the circumferential normal stress is approximately equal to the arithmetic mean of the other two components. Accordingly, on Fig. 3, showing the measured distribution of $v'$, have been added the profiles of $\sqrt{2k/3}$ using the $k$-levels generated by the computations. As expected, at the inlet there is close agreement between computation and measurement. There is, moreover, reasonably close agreement between the two over the whole flow domain. We note, however, that measured levels of $v'$ are rather higher than those computed near the wall between 45 and 177 deg. This difference, we believe, arises mainly from the direct generation of $\overline{v^2}$ by the strongly sheared secondary flow (i.e., large $\partial V/\partial r$); although generation of $k$ by this agency also appears in the turbulence energy transport equation, it is a less important process there. At 90 and 135 deg the computed levels of $\sqrt{2k/3}$ are lower than the measured levels of $v'$ over the whole radius by amounts ranging from 1 to 30 percent. It seems likely that at these positions the computed energy dissipation rate, $\epsilon$, has become too large, preventing the rise in fluctuating velocity levels that the experimental values indicate. The experimental values of $v'$ decrease markedly beyond the bend exit, and the subsequent downstream development shows remarkable agreement between the computations and the measurements.

Plots of the ratio $v'/u'$, a measure of turbulent flow anisotropy, are given in [10]. The results suggest that, between $X/D = -1$ and $\theta = 90$ deg, near the outer radius wall, the

term $-\overline{vw}\,\partial V/\partial r$ contributes strongly to the generation of $\overline{v^2}$. Beyond $\theta = 90$ deg this contribution decreases, allowing dissipation and redistribution mechanisms to reduce the level of $\overline{v^2}$ near the wall, as observed.

## 5 Concluding Remarks

This study places on a firm quantitative basis some of Rowe's [11] qualitative interpretations of the behavior of turbulent flow through a 180 deg curved pipe. Specifically, the existence of two cross stream flow reversals has been confirmed both experimentally and by the numerical simulations. The results support the notion of an additional (symmetrical) pair of counter-rotating vortical structures embedded in the core of the flow within the curved pipe. The levels of secondary flow are on the whole lower than in the corresponding square duct flow [5]. This underlines the dominant effect of the flat walls in the curved square duct in driving the secondary motion. No cross-stream flow reversals were measured in the latter case, which further indicates how different are the structures in what superficially appear to be two very similar flows.

The rms level of velocity fluctuations is substantially raised as the flow passes around the bend due to the additional mean strain associated with the turning of the primary flow and, particularly, the secondary-flow velocity gradients thus created. There are, in addition, changes in the structure of the turbulent field in the core – notably the large increase of streamwise fluctuations at 90 deg and the rise in $v'$ observed between 135 and 177 deg – whose cause cannot be unravelled with any certainty from measurements on the $\phi = \pi/2$ surface alone.

The numerical simulations have reproduced with a gratifying degree of fidelity the measured evolution of the flow. It strengthens the impression formed in [5] that often the $k \sim \epsilon$ eddy viscosity model does better in simulating *really* complex flows, such as those found within the 180 deg bend, than it does in less strongly perturbed flows. For example, in the present case the prediction of the flow recovery *downstream* of the bend shows the largest disagreement with the measured behavior even though secondary velocities are there very weak. No general conclusions may be drawn, however, for computations of the square bend with the same model of turbulence used here [32, 33] display spectacular disagreement with the data of [5].

Future work on bend flows needs to be aimed at providing a more complete mapping of the primary and secondary mean flow and stress distributions over the entire conduit cross-section. This data should help in clarifying the role of the additional pair of vortical structures in curved pipe flow and the relaxation process occurring in the downstream tangent.

## Acknowledgments

The experimental work at the University of California, Berkeley, was initially supported by the Office of Naval Research through Contract Number N 00014-80-C-0031 and, more recently, by the Office of Fossil Energy of the U.S. Department of Energy under Contract Number DE-AC03-76SF00098. The computational work at UMIST was also sponsored by the U.S. Office of Naval Research through Grant Number N00014-83-G-0021. We are grateful to these agencies for their respective support. Thanks go to Ms. Loris C-H Donahue for the typing of this manuscript. The authors' names are listed in alphabetical order.

## References

1 Humphrey, J. A. C., Whitelaw, J. H., and Yee, G., "Turbulent Flow in a Square Duct with Strong Curvature," *J. Fluid Mech.*, Vol. 103, 1981, pp. 443-463.

2 Enayet, M. M., Gibson, M. M., and Yianneskis, M., "Measurements of Turbulent Developing Flow in a Moderately Curved Square Duct," *Int. J. Heat and Fluid Flow*, Vol. 3, No. 4, 1982, pp. 221-224.

3 Taylor, A. M. K. P., Whitelaw, J. H., and Yianneskis, M., "Curved Ducts with Strong Secondary Motion: Velocity Measurements of Developing Laminar and Turbulent Flow," ASME JOURNAL OF FLUIDS ENGINEERING, Vol. 104, 1982, pp. 350-359.

4 Anderson, B. H., Taylor, A. M. K. P., Whitelaw, J. H., and Yianneskis, M., "Developing Flow in S-shaped Ducts," *Proc. Int. Symposium on Applications of Laser-Doppler Anemometry to Fluid Mechanics*, Lisbon, July 1982.

5 Chang, S. M., Humphrey, J. A. C., and Modavi, A., "Turbulent Flow in a Strongly Curved U-Bend and Downstream Tangent of Square Cross-Sections," *PhysicoChemical Hydrodynamics*, Vol. 4, No. 3, 1983, pp. 243-269.

6 Rojas, J., Whitelaw, J. H., and Yianneskis, M., "Flow in Sigmoid Diffusers of Moderate Curvature," *Proc. Fourth Symposium on Turbulent Shear Flows*, Karlsruhe, FDR, Sept. 1983.

7 Brunn, H. H., "An Experimental Investigation of Secondary Flow Losses in Bends with Rectangular Cross Sections," Department of Engineering, Report CUED/A-Turbo/TR 95, University of Cambridge, 1979.

8 Berger, S., Talbot, L., and Yao, L.-S., "Flow in Curved Pipes," *Ann. Rev. Fluid Mech.*, Vol. 15, 1983, pp. 461-512.

9 Cuming, H. G., "The Secondary Flow in Curved Pipes," NPL, UK, Reports and Memoranda, No. 2880, Feb. 1952.

10 Azzola, J., and Humphrey, J. A. C., "Developing Turbulent Flow in a 180° Curved Pipe and its Downstream Tangent," Report LBL-17681, Materials and Molecular Research Division, Lawrence Berkeley Laboratory, University of California, 1984.

11 Rowe, M., "Measurements and Computations of Flow in Pipe Bends," *J. Fluids Mech.*, Vol. 43, 1970, pp. 771-783.

12 Enayet, M. M., Gibson, M. M., Taylor, A. M. K. P., and Yianneskis, M., "Laser-Doppler Measurements of Laminar and Turbulent Flow in a Pipe Bend," *Int. J. Heat and Fluid Flow*, Vol. 3, 1982, pp. 211-217.

13 Humphrey, J. A. C., Iacovides, H., and Launder, B. E., "Some Numerical Experiments on Developing Laminar Flow in Circular-Sectioned Bends," *J. Fluid Mech.*, Vol. 154, 1985, p. 357.

14 Patankar, S. V., Pratap, V. S., and Spalding, D. B., "Prediction of Laminar Flow and Heat Transfer in Helically Coiled Pipes," *J. Fluid Mech.*, Vol. 62, 1974, p. 539.

15 Humphrey, J. A. C., "Numerical Calculation of Developing Laminar Flow in Pipes of Arbitrary Curvature Radius," *Can. J. Chem. Eng.*, Vol. 56, 1978, p. 151.

16 Soh, W. Y., and Berger, S. A., "Laminar Entrance Flow in a Curved Pipe," *J. Fluid Mech.*, Vol. 148, 1984, p. 109.

17 Pratap, V. S., and Spalding, D. B., "Numerical Computations of the Flow in Curved Ducts," *Aero. Quart*, Vol. 26, 1974, p. 219.

18 Iacovides, H., and Launder, B. E., "The Computation of Momentum and Heat Transport in Turbulent Flow Around Pipe Bends," *Proc. 1st UK National Heat Transfer Conference*, Vol. 2, 1097, I. Chem. Engrs. Symposium Series 86, 1984.

19 Laufer, J., "The Structure of Turbulence in Fully Developed Pipe Flows," NACA Technical Report No. 1174, 1954.

20 Durst, F., Melling, A., and Whitelaw, J. H., *Principles and Practice of Laser-Doppler Anemometry*," Academic Press, London, 1976.

21 Drain, L. E., *The Laser Doppler Technique*, Wiley, New York, 1980.

22 Buchave, P., "The Measurement of Turbulence with the Burst-Type Laser-Doppler Anemometer – Errors and Correction Methods," Ph.D. thesis, State University of New York at Buffalo, 1979.

23 Melling, A., "Investigation of Flow in Non-Circular Ducts and Other Configurations by Laser-Doppler Anemometry," Ph.D. thesis, University of London, 1975.

24 McLaughlin, D. K., and Tiederman, W. G., "Biasing Correction for Individual Realization of Laser Anemometer Measurements in Turbulent Flows," *Physics of Fluids*, Vol. 16, 1973, pp. 2082-2088.

25 Gosman, A. D., and Ideriah, F. J. K., "TEACH-2E: A General Computer Program for Two-Dimensional, Turbulent Recirculating Flows," Mech. Eng. Dept., Imperial College, 1976.

26 Leonard, B., "A Stable and Accurate Convective Modelling Procedure Based on Quadratic Upstream Interpolation," *Com. Meth. Appl. Mech. Engrg.*, Vol. 19, 1979, p. 59.

27 Patankar, S. V., *Numerical Heat Transfer and Fluid Flow*, Hemisphere, 1980.

28 Launder, B. E., and Spalding, D. B., "The Numerical Computation of Turbulent Flows," *Comp. Meth. Appl. Mech. Engrg.*, Vol. 3, 1974, p. 269.

29 van Driest, E. R., "On Turbulent Flow Near a Wall," *J. Aero Sci.*, Vol. 23, 1956, p. 1007.

30 Iacovides, H., and Launder, B. E., "PSI – An Economical Approach to the Numerical Analysis of Near-Wall Elliptic Flows," ASME JOURNAL OF FLUIDS ENGINEERING, Vol. 106, 1984, p. 245.

31 Kline, S. J., Cantwell, B., and Lilley, G. (eds.), *Proc. AFOSR-HTTM-Stanford Conference on Complex Turbulent Flows*, Stanford University 1982.

32 Chang, S. M., Humphrey, J. A. C., Johnson, R. W., and Launder, B. E., "Turbulent Momentum and Heat Transport in Flow Through a 180° Bend of Square Cross-Section," *Proc. 4th Turbulent Shear Flow Symposium*, Karlsruhe, 1983.

33 Choi, Y. D., Personal Communication, 1984.

# Analysis of Subsonic Transitory Stalled Flows in Straight-Walled Diffusers

**W. Wysocki**

**Z. Kazimierski**

Department of Mechanical Engineering,
Technical University of Lodz,
Poland

*A simple, semi-empirical procedure is presented for computation of subsonic, turbulent, attached, and transitory-stalled flows in straight-walled diffusers with plenum exit. The procedure employs a zonal model while using the concept of a dividing streamline and integral methods for boundary layer calculations on diverging and parallel side walls. The dividing streamline separates the transitory stall zone, having zero mass flow rate, from the effective flow channel. The procedure predicts the pressure as a function of streamwise location with modest computation times, typically a few minutes on a personal computer and can be useful in design calculations.*

## 1 Introduction

According to the classification of diffuser flow regimes made in [1], the present work is concerned with an investigation of straight-walled diffuser performance of the first two regimes. These regimes contain the unstalled and transitory-stalled flows limited by the curve $b - b$ shown in Fig. 1. The cases investigated in this work are marked in Fig. 1 by means of thirty small crosses and circles.

The attempts made in [2] to compute diffuser flow using the time-averaged Navier-Stokes equations and the two-equation $k - \epsilon$ turbulence model are not particularly encouraging. Since the mentioned set of equations is elliptic in nature, the solution can be found only when the boundary conditions are given along a closed boundary of the computational domain. In the diffuser application the boundaries are the diffuser walls, the inlet and the exit planes. For diffusers with plenum exit the boundary condition at the exit plane, especially the velocity distribution, cannot be determined a priori. The diffuser considered in [2] was connected smoothly to a long parallel inlet and outlet channel for which the symmetric boundary conditions at the inlet and exit planes were applied. The solution has, therefore, the form of symmetrical stalls appearing at the transition from the diverging to the parallel section of the channel. It is well known that such a pattern of the detached diffuser flow does not exist in practice. The observed stall zone is usually not symmetric. This leads to the conclusion that the solution of the elliptic problem discussed in [2] is not stable with respect to small perturbations of the inlet flow parameters or diffuser geometry. Taking into account the computer time and the inadequacy mentioned above it seemed appropriate to try to construct another model of the diffuser flow.

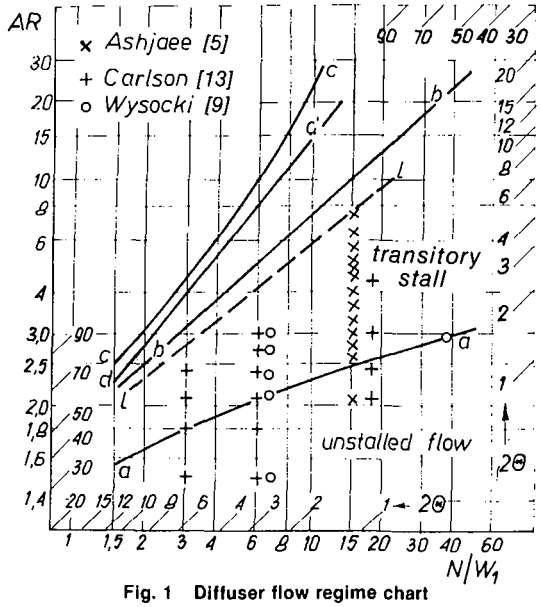


Fig. 1 Diffuser flow regime chart

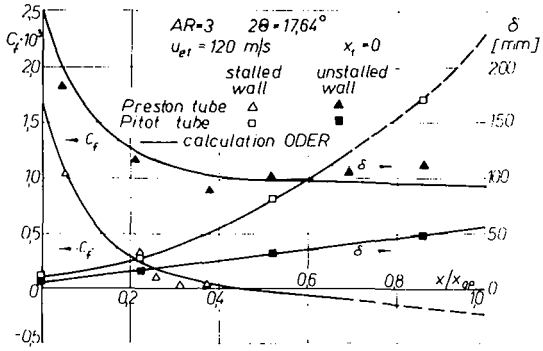


Fig. 2 Wall shear stress coefficient and boundary layer thickness along x-axis, [9]

Contributed by the Fluids Engineering Division for publication in the JOURNAL OF FLUIDS ENGINEERING. Manuscript received by the Fluids Engineering Division, June 28, 1984.

Recently, some predictive methods have been developed which rely on boundary layer integral relations to provide satisfactory results for the transitory-stalled regime of the diffuser flow. They have been presented in [4], [5] and [6]. The flow models used are zonal and steady. All methods use one-dimensional flow models for the potential core, momentum integral relations and an entrainment equation for the boundary layer zone. Simultaneous solution of these equations is employed to compute the different zones where the flow is detaching or detached. Special correlations of flow detachment and the boundary layer flow state approaching detachment are used in these works. In order to achieve good agreement with the experimental data, special correlations are formulated in the form of either the lag parameters for attached and detached flow used in [4] or the $\xi$ parameters which models the effect of the flow asymmetry, [6].

As it was proven experimentally in [9], a detachment existing at one diffuser wall creates not only an asymmetry of the boundary layers but causes this asymmetry to extend upstream to the inlet plane of the diffuser. This is shown in Fig. 2. The boundary layer thickness, $\delta$, is greater and the wall skin friction, $\tau_w$, lower on the detachment wall at the inlet, than those on the opposite side.

The theoretical calculation of the incompressible boundary layer, upstream and downstream of the separation region, was performed in [8]. The integral relations for the boundary layers, two-parameter universal mean velocity profile and eddy viscosity models valid upstream and downstream of the detachment were used in [8] to describe the problem. The initial conditions for this boundary layer calculation were specified on the basis of experimental data [8], [9] taking into account the differences in the boundary layer structure on the stalled and unstalled wall at the inlet to the diffuser, Fig. 2. The mean velocity profile in the form proposed by Kuhn and Neilsen [12] has been applied in this calculation. All comparisons between the velocity distributions mentioned above and experimental velocity profiles obtained in [9], [10] lead to the conclusion that Kuhn-Neilsen profile can be used in the regions upstream and downstream of the detachment in the diffusers.

The example of solutions [8] presented here in Fig. 2, and many others discussed in [8] allow us to conclude that the detachment of the turbulent boundary layer in diffusers can be fully described by means of the method presented in [8]. The method was realized in the form of the ODER computer program.

The results obtained by means of this program lead one to the conclusion that the detached diffuser flow asymmetry can be described in a different way than those presented in [4] and [6].

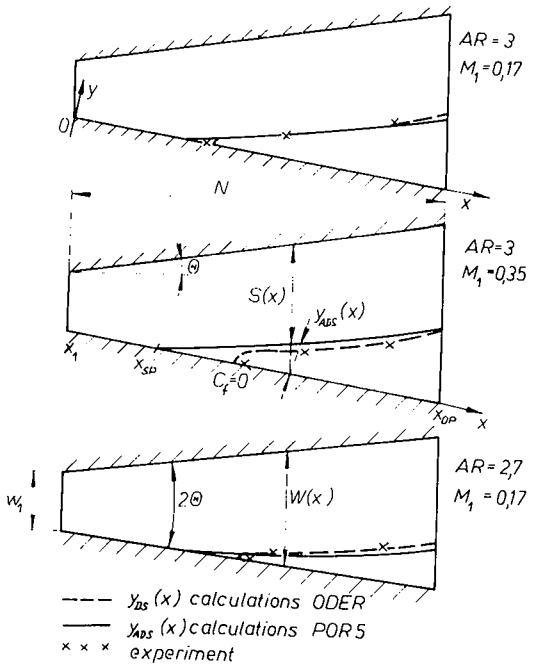


**Fig. 3 Dividing streamline shapes**

From the condition applied in [8] in the region downstream of the detachment:

$$\int_0^{y_{DS}(x)} u(x, y)dy = 0 \tag{1}$$

the dividing streamline $y_{DS} = y_{DS}(x)$ is determined. The dividing streamlines calculated in [8] for the examined transitory-stalled diffuser flows are shown with the dashed lines in Fig. 3. These results are compared with the experimental data, [9], shown in Fig. 3 by means of the small crosses.

The influence of the inlet Mach number $M_1$ on the dividing streamline shape, in the range of $M_1 \leq 0.35$ and $Re_1 \geq 6.6 \times 10^4$, respresentative for the discussed flow, is insignificant. This conclusion agrees very well with the results of Runstadler and Dolan [14].

## Nomenclature

ALFA = coefficient, equation (6)
AR($= W_{OP}/W_1$) = diffuser area ratio
$b$ = diffuser depth, m
$C_f$ = wall shear stress coefficient
$Cp$ = local pressure recovery coefficient
$D$ = coefficient, equation (7)
$H(=\delta^*/\delta^{**})$ = boundary layer shape factor
M = corestream Mach number
$N$ = diffuser axial length, Fig. 3, m
PO = coefficient, equation (6)
$p$ = pressure, N/m$^2$
$S$ = effective diffuser width, equation (2), m
$SK$ = Sandborne-Kline function, equation (4)
$u$ = velocity component in $x$ direction, m/s
$W$ = diffuser width, Fig. 3, m
$x, y$ = coordinates, Fig. 3, m
$y_{DS}$ = dividing streamline (streamsurface), equation (1)
$y_{ADS}$ = approximate streamline (streamsurface)
$\delta$ = boundary layer thickness, m
$\delta^*$ = boundary layer displacement thickness, m
$\delta^{**}$ = boundary layer momentum thickness, m
$\Theta$ = diffuser half angle, Fig. 3

**Subscripts**

$d$ = diverging walls
$e$ = boundary layer outer edge
$OP$ = outlet point
$P$ = parallel walls
$SP$ = starting point
1 = diffuser inlet

Table 1 Discrete values of ALFA and PO functions

| $D$ | 0.30 | 0.35 | 0.40 | 0.45 | 0.50 | 0.55 | 0.60 | 0.65 | 0.70 |
|---|---|---|---|---|---|---|---|---|---|
| ALFA | 0.040 | 0.047 | 0.063 | 0.080 | 0.100 | 0.123 | 0.150 | 0.180 | 0.213 |
| PO | 0.033 | 0.037 | 0.040 | 0.047 | 0.053 | 0.060 | 0.067 | 0.076 | 0.090 |

| $D$ | 0.75 | 0.80 | 0.85 | 0.87 | 0.90 | 0.92 | 0.94 | 0.96 | 1.0 |
|---|---|---|---|---|---|---|---|---|---|
| ALFA | 0.253 | 0.333 | 0.586 | 0.812 | 1.000 | 1.000 | 1.000 | 1.000 | 1.000 |
| PO | 0.103 | 0.123 | 0.153 | 0.172 | 0.266 | 0.429 | 0.713 | 0.924 | 1.000 |

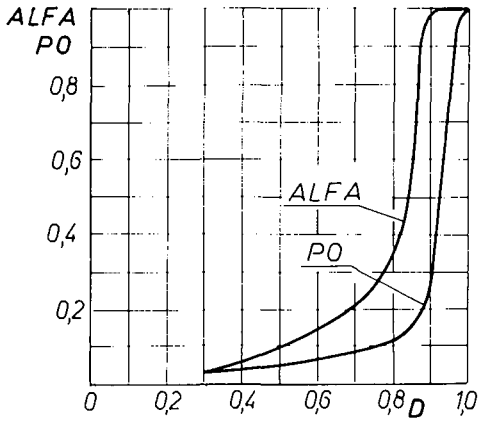

Fig. 4 Plots of PO = PO($D$), ALFA = ALFA($D$)

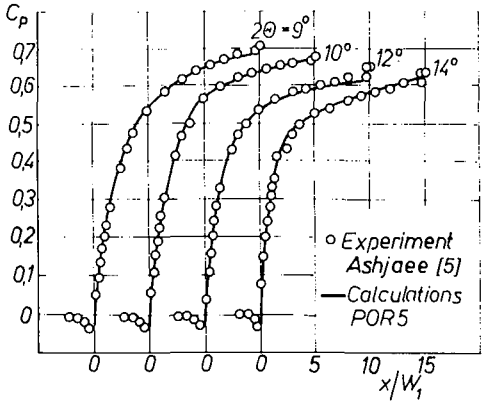

Fig. 5 Local pressure recovery diagrams

The concept of the dividing streamline was used in a new, simple diffuser flow model presented in the next section of this paper.

## 2 Model of the Diffuser Flow

The model presented employs a one-dimensonal flow representation of the inviscid core and an integral method (see Appendix) for boundary layer calculations. The three-dimensional character of the flow in the diffuser corners is neglected.

When the detachment zone occurs the accurate prediction of the pressure distrubution along the diffuser axis depends on the appropriate determination of the effective flow channel. The dividing streamline, whose approximate shape is defined below, separates the transitory stall zone (having zero net streamwise mass flow rate) from the effective flow channel of the diffuser. During diffuser design procedure, the method described in [8] cannot be used for the determination of the dividing streamline shape. The asymmetry of the boundary layers at the inlet plane which has to be introduced in the method given in [8], is not known during design calculations. The results obtained in [8] allow us, however, to recognize the character of the dividing streamline. The approximate shape of this line is correlated experimentally as follows.

It is assumed that the dividing streamline, $y_{DS}(x)$ can be approximated by a segment of a parabola $y_{ADS}(x)$. The segment begins on the wall somewhat upstream from the point determined as the Sandborne-Kline intermittent separation point [8], [10], etc. The starting point location is marked $x_{SP}$. It is also assumed that the tangent to $y_{ADS}(x)$ at $x_{SP}$ may vary in its direction from being parallel to the wall of detachment to being parallel to the opposite wall. The tangent to $y_{ADS}(x)$ at the outlet point $x_{OP}$ is assumed to be parallel to the opposite wall, (Fig. 3). The starting point location, $x_{SP}$, and the direction of the tangent to $y_{APS}(x)$ at this point are correlated experimentally, utilizing two coefficients described here.

The effective width of the diffuser, $S(x)$, is defined as follows:

$$S(x) = W(x) \text{ for } x_1 \le x < x_{SP}, \quad \text{and}$$

$$S(x) = W(x) - y_{ADS}(x) \cdot \cos \Theta \text{ for } x \ge x_{SP} \tag{2}$$

For $x \ge x_{SP}$ the dimension $S(x)$ is determined by the formula:

$$S(x) = ax^2 + bx + c \tag{3}$$

The location of the starting point, $x_{SP}$, is calculated from the condition:

$$(\mathrm{PO})' + SK(x) = 0$$

where:

$$SK(x) = 1 + \left(1 - \frac{\delta^*}{\delta}\right)^{-1} - \frac{\delta^*}{\delta^{**}} . \tag{4}$$

(PO)′ is the first experimental coefficient enabling the specificaton of $y_{ADS}(x)$. For (PO)′ = 0 the equation (4) reduces to the well-known Sandborne-Kline intermittent separation criteria, $SK(x) = 0$. Thus, the coefficients of the parabola $a$, $b$, $c$ introduced in (3) are calculated according to the assumptions mentioned before:

$$\begin{aligned} &ax_{SP}^2 + bx_{SP} + c = S(x_{SP}) \\ &2\,ax_{SP} + b = (\mathrm{ALFA})' \cdot \mathrm{tg}\, 2\Theta \\ &2\,ax_{OP} + b = 0, \end{aligned} \tag{5}$$

where $0 \le (\mathrm{ALFA})' \le 1$ is the second experimental coefficient describing the value of the derivative $dS/dx$ at $x = x_{SP}$.

The experimental coefficients PO′ and (ALFA)′ are finally expressed as follows:

$$\mathrm{PO} = \frac{SK(x_1) + (\mathrm{PO})'}{SK(x_1)} \; ; \; \mathrm{ALFA} = (\mathrm{ALFA})' \cdot \mathrm{PO}, \tag{6}$$

where $SK(x_1)$ is the value of $SK(x)$ at the diffuser inlet and $\delta(x_1)$, $\delta^*(x_1)$, $\delta^{**}(x_1)$ are determined for symmetrical boundary layers developed in the diffuser inlet channel.

The dividing streamline $y_{ADS}(x)$ should be understood as the projection of the dividing streamsurface extending between the diffuser parallel side walls. The three-dimensional character of this surface at the side walls is neglected.

The coefficients PO and ALFA are determined on the basis

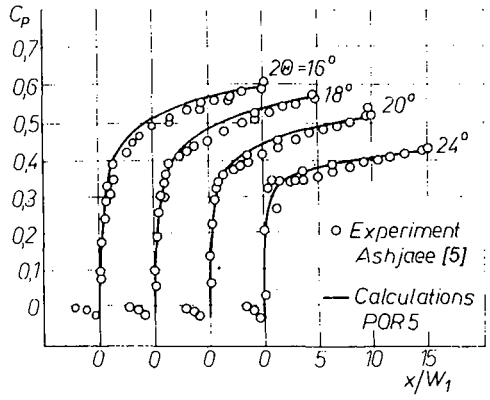


Fig. 6 Local pressure recovery diagrams

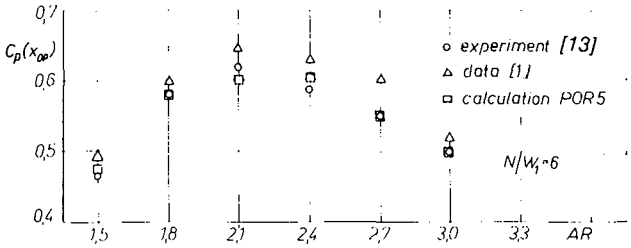


Fig. 7 Overall pressure recovery diagrams

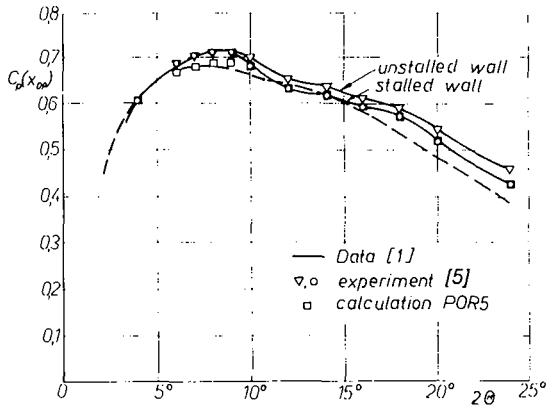


Fig. 8 Overall pressure recovery diagrams

of the investigations of 30 diffusers marked in Fig. 1 by means of small crosses and circles. It is possible to present coefficients PO and ALFA as functions of a single parameter:

$$D = \frac{AR_b - AR}{AR_b - AR_a} \tag{7}$$

According to the chart shown in Fig. 1, for given values of $N/W_1$, the $AR$, $AR_a$, $AR_b$ denote actual area ratio, area ratio on a $a - a$ line and $b - b$ line, respectively. Thus, the parameter $D$ locates a diffuser geometry on the map shown in Fig. 1. The available data allowed the authors to determine PO and ALFA in the range $0.3 \le D \le 1.0$. The presented experimental functions PO = PO($D$) and ALFA = ALFA($D$) ensure the best correlation between experimental and calculation results in the scope of the pressure distribution along the diffusers axis for all cases discussed. These functions are specified in Table 1 and are plotted in Fig. 4.

The calculation method is finally formulated as follows:

Having PO and ALFA for given $D$ and $\delta(x_1)$, $\delta^*(x_1)$, $\delta^{**}(x_1)$, the coefficients (PO), (ALFA) and $a$, $b$, $c$ can be calculated according to (4), (5), (6) and the effective width of the diffuser, $S(x)$, according to (2) and (3) is determined.

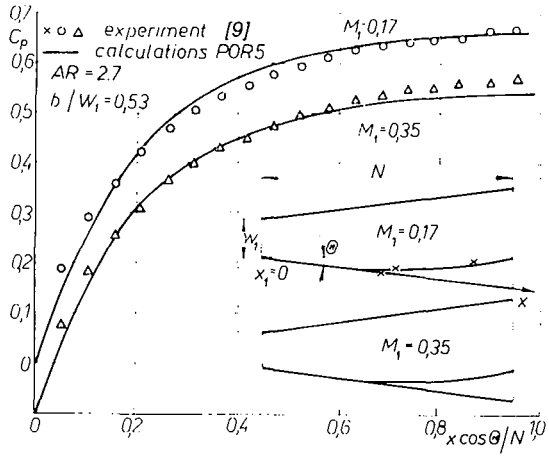


Fig. 9 Local pressure recovery diagrams

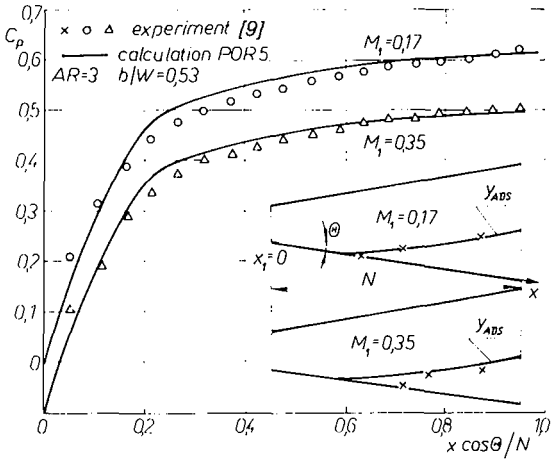


Fig. 10 Local pressure recovery diagrams

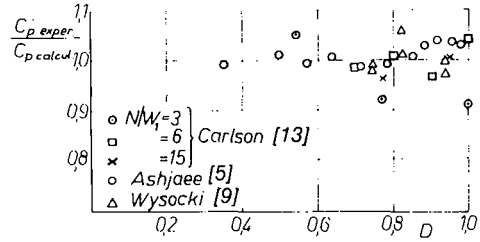


Fig. 11 Relative discrepancies of calculated and measured overall pressure recovery coefficients

Having $u_e(x_1)$ and $M_1(x_1)$, the compressible turbulent boundary layers existing on the diverging and parallel diffuser walls are then calculated using a procedure explained in the Appendix.

The influence of the inlet Mach number, in the range of $M_1 \le 0,35$, on PO and ALFA was neglected, according to [14] and to the authors' experiences. The dividing streamline for $x > x_{SP}$ is treated as a wall, and in spite of its real character the zero slip condition is assumed at this boundary. The inaccuracy resulting from this assumption is small and is corrected by PO and ALFA coefficients.

## 3 Results and Comparisons

In order to verify the results obtained by the calculating procedure described in this paper, comparisons were made with experiment. Figures 5, 6, 7 show comparisons with the results of experiments from [5], [13]; Fig. 8 with the experimental

results presented in [1] and [5]. Comparisons with experimental data obtained in our laboratory are given in Figs. 9 and 10.

Figure 11 illustrates the relative discrepancies between the calculated and measured outlet pressure recovery coefficient, $Cp(X_{op})$, for 26 cases discussed. For the majority of the compared cases the agreement between calculated and experimentally received results is very good. The comparisons for the pressure distributions along the diffuser axis shown in Figs. 5, 6, 9, 10 can be characterized as satisfactory. The results discussed above refer to the transitory-stalled flows. In the range of unstalled flows (below the curve $a - a$ in Fig. 1) the discrepancies between calculated and measured $Cp(X)$ are lower than for the stalled flows.

## 4 Conclusions

A calculation method has been developed that successfully predicts unstalled and transitory-stalled diffuser flows. The method is based on the experimental data correlations. The investigation concerns straight-walled diffusers working in the range of subsonic, ($M_1 \leq 0, 35$), unstalled and transitory-stalled flows limited by the curve 1 – 1 shown in Fig. 1, which is equivalent to $D = 0.3$, (Fig. 4). The presented method allows one to calculate diffusers of different $b/W_1$ ratio. For the comparisons made, $b/W_1$ was varied in the range $0.5 \leq b/W_1 \leq 4$.

The calculation procedure is realized by means of the POR5 computer program with very modest computational times, typically about four minutes on a personal computer. The comparisons made show good agreement between experimental results and computational predictions, and give confidence to the application of the method to the design calculations and optimization of the considered diffusers.

## References


1 Reneau, L. R., Johnston, J. P., and Kline, S. J., "Performance and Design of Straight, Two-Dimensional Diffusers," ASME *Journal of Basic Engineering*, Mar. 1967, p. 141.

2 Pope, S. B., "The Calculation of Turbulent Recirculating Flows in General Orthogonal Coordinates," *Journal of Computational Physics*, Vol. 26, No. 2, 1978, pp. 197-217.

3 Reneau, L. R., and Johnston, J. P., "A Performance Prediction Method for Unstalled, Two-Dimensional Diffusers," ASME *Journal of Basic Engineering*, Sept. 1967, p. 643.

4 Ghose, S., and Kline, S. J., "The Computation of Optimum Pressure Recovery in Two-Dimensional Diffusers," ASME JOURNAL OF FLUIDS ENGINEERING, Dec. 1978, p. 419.

5 Ashjaee, J., and Johnston, J. P., "Straight-Walled, Two-Dimensional Diffusers—Transistory Stall and Peak Pressure Recovery," ASME JOURNAL OF FLUIDS ENGINEERING, Sept. 1980, p. 275.

6 Bardina, J., et al., "A Prediction Method for Planar Diffuser Flows," ASME JOURNAL OF FLUIDS ENGINEERING, June 1981, p. 315.

7 Wooley, R. L., and Kline, S. J., "A Procedure for Computation of Fully Stalled Flows in Two-Dimensional Passages," ASME JOURNAL OF FLUIDS ENGINEERING, June 1978, p. 180.

8 Kazimierski, Z., Wysocki, W., and Smolny, A., "Investigations of Turbulent Boundary Layer in the Vicinity of Separation," *Archives of Mechanics*, Vol. 36, No. 4, 1984, pp. 523-538.

9 Wysocki, W., "Turbulent Diffuser Flows," Ph. D. thesis, The Technical University of Lodz, Dept. of Mechanical Engineering, 1984, in Polish.

10 Simpson, R. L., et. al., "The Structure of a Separating Turbulent Boundary Layer, Part 1, Mean Flow and Reynolds Stresses," *Journal of Fluid Mechanics*, Vol. 113, 1981, p. 23.

11 Assasa, G. M., and Gay, B., "Prediction numerique des ecoulements turbulents au voisinage du point de decollement," *Entropie*, Vol. 81, Mai-Juin, 1978.

12 Kuhn, G. P., and Nielsen, J. N., "Prediction of Turbulent Separated Boundary Layer," *AIAA Journal*, July 1974, p. 881.

13 Carlson, J., Johnston, J. P., and Sagi, C. J., "Effects of Wall Shape on Flow Regimes and Performance in Straight, Two-Dimensional Diffusers," ASME *Journal of Basic Engineering*, Mar. 1967, p. 151.

14 Rundstadler, P. W., and Dolan, F. X., "Further Data on the Pressure Recovery Performance of Straight-Channel, Plane-Divergence Diffusers at High Subsonic Mach Numbers," ASME JOURNAL OF FLUIDS ENGINEERING, Sept. 1973, p. 373.


## APPENDIX

The compressible, turbulent boundary layers existing on the diverging and parallel side walls of the diffuser are calculated based on a known integral method [3]. Parameters of the boundary layers related to the diverging and parallel walls are designated by the subscripts $d$ and $p$, respectively. In the region of the transitory stall, the dividing streamsurface defined by $y_{APS}(x)$ is treated as a wall. The equations are nondimensionalized on inlet throat width $W_1$ and inlet free-stream velocity $U_{e1}$.

For the unknowns:

$$\delta_d^{**}, \delta_p^{**}, \delta_d^{*}, \delta_p^{*}, H_d, H_p, u_e, M$$

the set of eight following equations was formulated:

$$\frac{d\delta_p^{**}}{dx} = \alpha_p - \delta_p^{**}\left[2(S-2\delta_d^{*})^{-1}\frac{d}{dx}\left(\frac{S}{2}-\delta_d^{*}\right) + (H_p+2-M^2)\frac{1}{u_e}\frac{du_e}{dx}\right] \tag{1A}$$

$$\frac{d\delta_d^{**}}{dx} = \alpha_d - \delta_d^{**}\left[-2(b-2\delta_p^{*})^{-1}\frac{d\delta_p^{*}}{dx} + (H_d+2-M^2)\frac{1}{u_e}\frac{du_e}{dx}\right] \tag{2A}$$

$$\frac{dH_p}{dx} = \left(\beta_p\frac{1}{u_e}\frac{du_e}{dx}+\zeta_p\right)(1+0.1145M^2)+\Phi_d\frac{dM}{dx} \tag{3A}$$

$$\frac{dH_d}{dx} = \left(\beta_d\frac{1}{u_e}\frac{du_e}{dx}+\zeta_d\right)(1+0.1145M^2)+\Phi_d\frac{dM}{dx} \tag{4A}$$

$$\frac{d\delta_p^{*}}{dx} = \delta_p^{**}\frac{dH_p}{dx}+H_p\frac{d\delta_p^{**}}{dx} \tag{5A}$$

$$\frac{d\delta_d^{*}}{dx} = \delta_d^{**}\frac{dH_d}{dx}+H_d\frac{d\delta_d^{**}}{dx} \tag{6A}$$

$$\frac{1}{u_e}\frac{du_e}{dx}[1-0.4M_1^2u_e^2] = -2(S-2\delta_d^{*})^{-1}\frac{d}{dx}\left(\frac{S}{2}-\delta_d^{*}\right) + 2(b-2\delta_p^{*})^{-1}\frac{d\delta_p^{*}}{dx} \tag{7A}$$

$$\frac{dM}{dx} = \frac{1}{u_e}\frac{du_e}{dx}u_e[1+0.2M_1^2(1-u_e^2)]^{1/2}(1-0.08M_1^2u_e^2)M_1 \tag{8A}$$

where: $S = S(x)$ is given by (2), and

$$\alpha = 0.123e^{-1.56H}(\mathrm{Re}_{\delta^{**}})^{-0.268} \tag{9A}$$

$$\beta = -2e^{4.68(H-2.975)}[2.558\ln(4.075\,\mathrm{Re}_{\delta^{**}})]^2 \tag{10A}$$

$$\zeta = -e^{4.68(H-2.975)}[H-1.286]\frac{2.035}{\delta^{**}} \tag{11A}$$

$$\Phi = 0.545M + 0.229M\frac{H-0.2728M^2}{1+0.1145M^2} \tag{12A}$$

The presented formulas compose the algorithm realized in the form of the computer program POR5.

# A Study of the Internal Forces in a Variable-Displacement Vane-Pump—Part I: A Theoretical Analysis

**A. M. Karmel**
Project Trilby,
General Motors Research Laboratories,
Warren, MI 48090

*Growing energy costs continue to motivate the use of variable-displacement pumps in hydraulic systems with varying flow requirements. This study presents an analysis of the internal pressure-distribution in variable-displacement vane-pumps, and of the resulting forces and torques applied to their mechanisms and shafts. This analysis is essential to the study of the pump dynamics and control, the pump design, and the selection of the pump bearings. These forces are shown to be a function of the line pressure, the pump eccentricity, the shaft rotational speed, the fluid bulk modulus, the fluid viscosity, and the design geometry. These forces are composed of two periodic components: a continuous component due to the exposure of chambers to the line port, and an intermittent component due to a hydraulic-lock phenomenon. A design criterion is formulated which eliminates magnitude variations in the continuous component of the radial shaft-load.*

## 1 Introduction

Growing energy costs continue to motivate the use of variable-displacement pumps in hydraulic systems with varying flow requirements. Variable-displacement pumps are already used widely in various industrial and automotive applications [1–3]. To fully realize their economic potential, these pumps should be carefully designed and controlled, accounting for the internal forces that develop during operation. These forces generate the loads and the torques applied to the shaft and the mechanism in both fixed- and variable-displacement pumps. In addition, they can determine the dynamics of the mechanism of variable-displacement pumps and affect the dynamics of the entire hydraulic system.

Piston-type variable-displacement pumps are used extensively in high-pressure applications such as hydrostatic transmissions and airborne systems, and have received much attention in the technical literature [3–7]. In contrast, variable-displacement vane-pumps (VDVP's), which are often used in the mid-pressure range, have not been investigated thoroughly. At present, there are no analytical models in the public domain for evaluation of their internal forces. The VDVP model that was developed by DeGarcia et al. [3] includes the dynamics of the regulator only, and does not account for the internal forces applied to the mechanism and the shaft of the pump.

With no analytical models available for these pumps, their regulation and their related system design are often conducted experimentally. Since a large number of operating variables and design parameters influence the dynamic behavior of the pump, this approach may lead to rather frustrating results. Solutions which are applicable to one set of parameters at a given operating point, may worsen performance under different conditions, and minor design changes may lead to unpredictable results. Moreover, the lack of analytical models for the VDVP impairs the engineer's ability to estimate the dynamic behavior of a new system.

This paper presents an analysis of the internal pressure-distribution in variable-displacement vane-pumps, and of the resulting forces applied to their mechanisms and shafts. Specifically, expressions are presented for calculating the force applied to the cam and its pivot, the radial load applied to the shaft and its bearings, the torque applied to the cam about its pivot, the radial load applied to the shaft and its bearings, the torque applied to the cam about its pivot, and the torque applied to the shaft. A design criterion has been developed that limits the magnitude variations of the radial shaft-load in vane pumps. The characteristics of these forces and their dependence on the design and operating parameters are the subject of the second part of this study [8].

## 2 Description

Figure 1 displays a schematic of the VDVP analyzed in this study. The pump consists of a circular cam which pivots about a point fixed with respect to the housing. The vanes move radially in slots machined in the rotor and are pressed against the inner surface of the cam by the centrifugal forces. In order to provide proper sealing between the chambers (which depends on the contact forces between the vanes and the cam inner surface), the centrifugal forces must overcome the radial forces applied by the fluid pressure to the vane cross-sections.[1]

Contributed by the Fluids Engineering Division for publication in the JOURNAL OF FLUIDS ENGINEERING. Manuscript received by the Fluids Engineering Division, November 7, 1984.

[1] In some configurations, to improve sealing at low shaft-speeds, the centrifugal forces are augmented by fluid pressure or by spring forces applied to the vane inner tips.

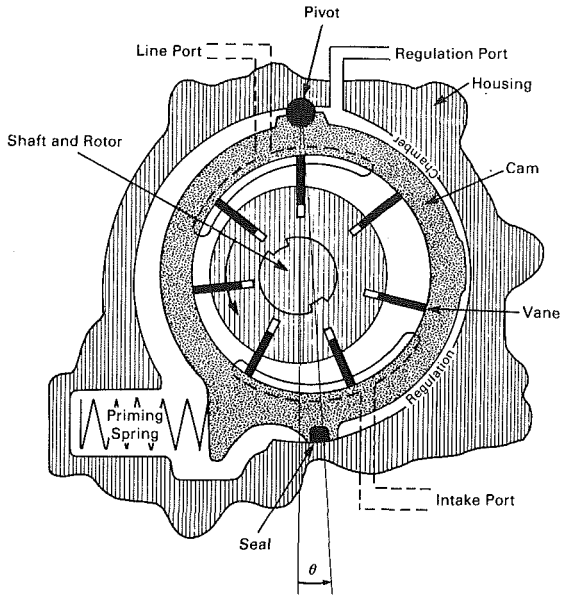


**Fig. 1 Schematic of a VDVP**

Consequently, the VDVP in this configuration must operate at sufficiently high rotational speeds.

Fluid is pumped from the intake to the line port as the volume of a chamber decreases while moving toward the latter. This volume decrease is modulated by the offset of the cam center from the shaft center. This offset, known as eccentricity, can be measured by either the linear distance between the centers of the cam and the shaft, or by the angle $\theta$ shown in Fig. 1. In this study, the eccentricity will be measured by the angle $\theta$ only. With this definition, eccentricity appears directly in the equation of motion of the pump and is therefore more suitable for dynamic analyses. Furthermore, some variables, which exhibit a highly non-linear dependence on linear eccentricity, are virtually linearly dependent on angular eccentricity.

In some applications, the centers of the shaft and the cam do not coincide, even at 0° eccentricity, due to an intentional offset of the cam. This offset is defined positive for those cams in which the pivot/cam-center distance is longer than the pivot/shaft-center distance (cam center "below" shaft center). A priming spring attempts to push the cam to its maximum eccentricity position (maximum output flow). It is opposed by a regulator pressure applied to the outer surface of the cam (an area designated as the "regulation chamber"). Sealing is provided by an O-Ring mounted in a circular groove on the cam upper surface (between this surface and the pump cover) and by a seal on the cam tip which defines the boundary of the regulation chamber.

Except for a limited travel range, a chamber is always connected to the line or the intake ports, either directly (with the chamber overlapping a port) or indirectly through relief undercuts at the bottom of the cam (which extend the reach of each port). Since these undercuts are machined in the cam, the extension of the ports becomes a function of the eccentricity.

Through two limited angular sections between the ports, a chamber is isolated from both ports, a characteristic which is inherent in the operation of any vane pump. In this paper, such a section, in which hydraulic-lock phenomena are taking place, is referred to as "dead-volume."

## 3 The Internal Pressure-Distribution

**General.** The internal forces in a vane pump (forces that are applied to either the mechanism or the shaft) result primarily from fluid pressure. This pressure develops due to the exposure of chambers to the line port, and due to a hydraulic-lock phenomenon (compression or expansion of fluid) in the dead-volume zones. The contribution of the

## Nomenclature

$D$ = distance from cam center to its pivot
$d$ = vane width
$\bar{F}_{Ci}$ = the force applied by a pressurized chamber to the cam
$\bar{F}_{Rfi}$ = the force applied by a pressurized chamber to the rotor and shaft, excluding vane forces
$\bar{F}_{Ri}$ = the force applied by a pressurized chamber to the rotor and shaft, including vane forces
$\bar{F}_{v_{i+1}}, \bar{F}_{v_{i-1}}$ = the fluid forces applied to the leading and trailing vanes of a chamber
$h_r, h_v, h_s$ = clearances between cover and rotor, cover and vane, and vane and slot in rotor, respectively
$L_r, L_v, L_s$ = leakage path lengths between cover and rotor, cover and vane, and vane and slot in rotor, respectively
$l$ = distance from a point on the cam inner surface to the shaft center
$l_o, l_f$ = initial and final values of $l$ of a chamber (moving in the direction of rotation, i.e., initial value corresponds to trailing-vane location)
$m$ = maximum number of chambers exposed to the line port
$n_c$ = number of VDVP chambers
$P$ = fluid pressure
$P_{DV1}$ = pressure in $DV_1$
$P_{DV2}$ = pressure in $DV_2$
$P_{i+1}, P_{i-1}$ = pressure in the chambers leading and trailing chamber #i
$R$ = inner radius of cam
$r$ = rotor radius
$\bar{T}_i$ = the torque applied by a pressurized chamber to the cam
$\bar{T}_{si}$ = the torque applied by the vane forces to the shaft
$VDVP$ = variable-displacement vane-pump
$W$ = axial width of the pump ring (cam)
$\alpha_{i\ i=1,4}$ = angular reference of relief undercuts relative to the cam
$\beta_{i\ i=1,4}$ = angular reference of the ports relative to the housing
$\gamma$ = average included angle of a chamber (from one vane center to the next)
$\gamma'$ = average included internal angle of a chamber (from one vane inner surface to the next)
$\theta$ = cam eccentricity
$\delta$ = included angle of a vane
$\phi$ = angular reference relative to the housing (shaft angular position)
$\theta$ = angular reference relative to the cam
$\Omega$ = shaft rotational speed
$\beta$ = hydraulic-fluid bulk modulus
$\mu$ = fluid viscosity
$\eta, \tau$ = integration variables

Appendix A provides additional details for some design parameters.

**Table 1 Pressure variation in a chamber**

| $\phi$ From | $\phi$ To | Pressure |
|---|---|---|
| $\gamma$ | $\beta_1+\gamma-\frac{\delta}{2}$ | Line |
| $\beta_1+\gamma-\frac{\delta}{2}$ | $\phi(\alpha_3,\theta)+\frac{\delta}{2}$ | $DV_1$ |
| $\phi(\alpha_3,\theta)+\frac{\delta}{2}$ | $\beta_3+\gamma-\frac{\delta}{2}$ | Intake |
| $\beta_3+\gamma-\frac{\delta}{2}$ | $\phi(\alpha_2,\theta)+\frac{\delta}{2}$ | $DV_2$ |
| $\phi(\alpha_2,\theta)+\frac{\delta}{2}$ | $\gamma$ | Line |

chambers exposed to the line port is continuous; however, while the shaft rotates, the number of chambers exposed to the line port may vary, which changes both the magnitude and the direction of this component. In contrast, the dead-volume contribution is intermittent as it develops only when a chamber is in a dead-volume zone. Because of the rotary nature of the pump operation, both components are periodic.

**Assumptions.** The analysis of the internal pressure-distribution in a VDVP is based on the following assumptions:

- The internal forces that are applied to the cam, the vanes, and the shaft, are the result of fluid pressure only.
- Pressures are uniform within each chamber. Centrifugal and local flow effects in a chamber (that exist primarily when a chamber is pressurized or depressurized) are neglected. A chamber therefore experiences pressures which correspond to line, intake or dead-volume pressures.
- When inside a dead-volume zone, pressure in a chamber changes according to volume variations, fluid compressibility, and leakage.
- Fluid mass is negligible.
- Vanes are equally spaced[2].
- Temperature is constant.
- Pressure drops below atmospheric level are negligible. The intake pressure reduction and partial vacuum developed due to volume expansion in the dead-volume zone are not accounted for.

**Pressure Variation in a Chamber.** At a constant shaft velocity, shaft angular position may replace time as the free variable. This spatial variable can be referenced by the position of the leading vane of a chamber. The pressure in a chamber then becomes a function of its leading-vane location. The intersection points of this vane with the edges of the ports, or the relief undercuts, determine the transition from one pressure zone to the next. A transition that is determined by an intersection with a port is a function only of the shaft angular position since the ports are fixed with respect to the housing. On the other hand, a transition that is determined by an intersection with a relief undercut in the cam becomes a function of both the shaft angular position and the eccentricity. The analysis therefore requires the ability to transfer coordinates between the fixed housing and the pivoting cam. The relationships between these references, along with the applicable transformation equations are developed in Appendix A. These equations facilitate the construction of the VDVP pressure table (Table 1) which gives the pressure in a chamber as a function of the leading-vane position. In this table, transitions

[2]Deviations on the order of a few degrees are intentionally introduced to the spacing of the vanes in order to reduce noise.

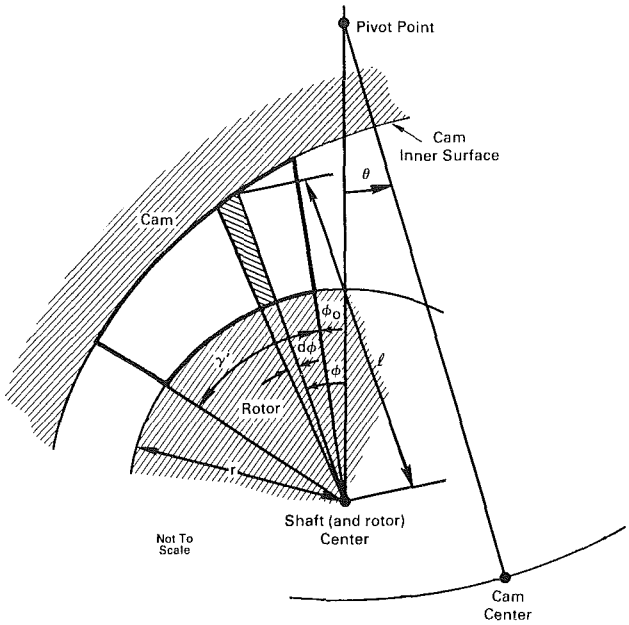


**Fig. 2 Calculation of a chamber volume**

determined by an intersection of a vane with a relief undercut do not include the effect of the angular deviation from radial contact; this deviation shifts the contact point sideways from the vane centerline along the vane-tip profile.

**Dead-Volume Pressure.** As discussed earlier, the operation of the VDVP requires the existence of two dead-volume zones: one into which a chamber enters moving from line port to intake-port contact (designated $DV_1$), and a second into which a chamber enters moving from intake to line port (designated $DV_2$). A chamber is in a dead-volume zone when it is not connected to either port. The fluid is locked between the vanes, the rotor and the cam and is constrained to follow the volume variations determined by the geometry. Figure 2 shows a schematic which was used to calculate the volume of a chamber:

$$V=\frac{W}{2}\left[\int_{\phi_0}^{\phi_0+\gamma'} l^2\cdot d\phi - r^2\gamma'\right] \tag{1}$$

where $l$ is given in Appendix A. Assuming a vane may be approximated by an angular section $\delta$:

$$\gamma'=\gamma-\delta=\frac{2\pi}{n_c}-\frac{d}{r} \tag{2}$$

Assuming that no cavitation or leakage occurs, the pressure rises or drops during the sweep through the dead-volume zone due to the volume variation and fluid compressibility:

$$\Delta P=-\beta\frac{\Delta V}{V} \tag{3}$$

where $V$ represents a volume and $\Delta V$ represents its variation, and $\beta$ is the bulk modulus of the fluid.[3]

Pressure variations, as predicted by equation (3), are considerably reduced due to leakage. Fluid may leak radially over and under the cam into the regulation chamber; radially over and under the rotor toward the shaft; tangentially over and under vanes to adjacent chambers; tangentially past vane contact line with the cam inner surface to adjacent chambers; and radially between the vane and the rotor slot clearances toward the shaft. In each of these paths, leakage is modeled by a stationary[4] slot equation:

[3]Different fluid-air ratios can be represented by different bulk moduli.

[4]The stationary slot equation properly models the radial leakage over the moving rotor, whereas for tangential leakage over vanes, a leakage term due to vane velocity must be added [9]. However, for each chamber, the velocity leakage terms of its two vanes will practically cancel each other. Consequently, they are neglected.

$$Q=\frac{Dh^3}{12\mu L}\,\Delta P \tag{4}$$

where $h$ is the slot clearance, $D$ is the slot width, $L$ is the length of the leakage path, $\mu$ is the fluid viscosity, and $\Delta P$ is the pressure difference along the path. Simplifying assumptions are made which expedite the calculations while retaining the overall effect of leakage on the dead-volume pressure: The O-Ring between the cam and the pump cover eliminates leakage through this path; and the centrifugal force minimizes the clearance between the vane tips and the cam inner surface to a level that leakage along this path may also be neglected. The overall leakage flow becomes:

$$Q_{DV1}=\frac{1}{6\mu}\left[\left(\frac{r}{L_r}\,\gamma' h_r^3+\frac{l_f-r}{L_v}\,h_v^3+\frac{W}{L_s}\,h_s^3\right)\cdot P_{DV1}+\frac{l_o-r}{L_v}\cdot h_v^3\cdot(P_{DV1}-P_0)\right] \tag{5}$$

in $DV_1$, and

$$Q_{DV2}=\frac{1}{6\mu}\left[\left(\frac{r}{L_r}\,\gamma' h_r^3+\frac{l_0-r}{L_v}\,h_v^3+\frac{W}{L_s}\,h_s^3\right)\cdot P_{DV2}+\frac{l_f-r}{L_v}\cdot h_v^3\cdot(P_{DV2}-P_0)\right] \tag{6}$$

in $DV_2$.

Cam motion, while a chamber is in a dead-volume zone, should also affect the dead-volume pressure.

## 4 The Resultant Internal Forces and Torques

Figure 3 shows the forces applied to the cam and the shaft by a single pressurized chamber. The direction of these forces is either indicated in Fig. 3 or can be readily derived. Their magnitude and the torques they produce are given in the following paragraphs.

The magnitude of the force applied to the cam and its pivot is given by:

$$|\bar{F}_{Ci}|=\int_{-\frac{\psi_2-\psi_1}{2}}^{\frac{\psi_2-\psi_1}{2}} P\cdot\cos\eta\cdot 2\pi r\cdot\frac{d\eta}{2\pi}W=2\cdot P\cdot R\cdot W\cdot\sin\frac{\psi_2-\psi_1}{2} \tag{7}$$

The magnitude of the forces applied to the vanes is given by:

$$\begin{aligned}|\bar{F}_{v_{i-1}}| &= (P-P_{i-1})\cdot(l_0-r)\cdot W\\ |\bar{F}_{v_{i+1}}| &= (P-P_{i+1})\cdot\{l_f-r)\cdot W\end{aligned} \tag{8}$$

excluding centrifugal and friction forces.

The magnitude of the radial force applied to the shaft, excluding the contribution of the vanes is given by:

$$|\bar{F}_{Rfi}|=\int_{-\frac{\gamma'}{2}}^{\frac{\gamma'}{2}} P\cdot\cos\tau\cdot 2\pi r\cdot\frac{d\tau}{2\pi}W=P\cdot r\cdot W\int_{-\frac{\gamma'}{2}}^{\frac{\gamma'}{2}}\cos\tau d\tau=2\cdot P\cdot r\cdot W\cdot\sin\frac{\gamma}{2} \tag{9}$$

The radial force applied to the shaft, including the contribution of the vanes is given by:

$$\bar{F}_{Ri}=\bar{F}_{Rfi}+\bar{F}_{v_{i-1}}+\bar{F}_{v_{i+1}} \tag{10}$$

or by:

$$\bar{F}_{Ri}=-\bar{F}_{Ci} \tag{11}$$

The magnitude of the resultant torque applied to the cam about its pivot is given by:

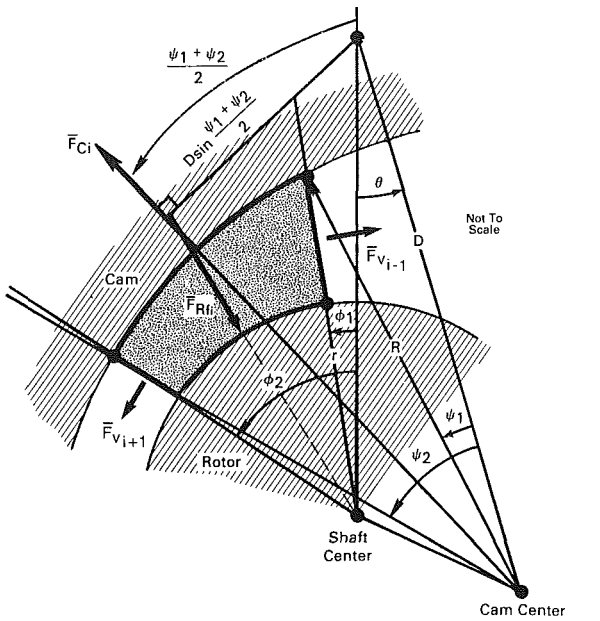


**Fig. 3 Forces and torques applied by a single pressurized chamber to the cam, the shaft, and the vanes**

$$|\bar{T}_i|=-2\cdot P\cdot R\cdot W\cdot\sin\frac{\psi_2-\psi_1}{2}\cdot D\cdot\sin\frac{\psi_2+\psi_1}{2}=P\cdot R\cdot W\cdot D(\cos\psi_2-\cos\psi_1) \tag{12}$$

The magnitude of the torque applied to the shaft due to the vane forces is given by:

$$|\bar{T}_{si}|=|\bar{F}_{v_{i+1}}|\cdot\left(r+\frac{l_f-r}{2}\right)-|\bar{F}_{v_{i-1}}|\cdot\left(r+\frac{l_0-r}{2}\right) \tag{13}$$

or by:

$$|\bar{T}_{si}|=-|\bar{F}_{Ci}|\cdot l\cdot\sin(\theta+\psi-\phi) \tag{14}$$

At any shaft angular position $\phi_1$, the corresponding cam reference $\psi_1$ is determined using equations (A-2), (A-3). Note that while $\phi_1-\phi_2$ is constant (based on the equally spaced vanes assumption), $\psi_1-\psi_2$ is a function of the eccentricity.

Hence, equations (7)–(14), together with the transformation equations and with the pump pressure table (Table 1), determine the contributions of a single pressurized chamber to the internal forces in a VDVP. These forces are periodic with respect to shaft rotation with a period of $1/n_c$ of a revolution for equally spaced vanes.

**Design for a Constant-Magnitude Radial Shaft-Load.** Shaft-bearing fatigue limits depend on the radial-load magnitude (average and peak levels), its duty cycle, and the shaft speed [10–12]. Figure 4 shows the components of the radial shaft-load: the main component (due to the exposure of chambers to the line port) is always directed inward, while the dead-volume components may be directed inward or outward, depending on whether compression or expansion takes place.

These components of the radial shaft-load vary with shaft position. The dead-volume contributions are inherently intermittent. Because of their potentially high peaks, their level and duration must be closely controlled to minimize their adverse effect on bearing life. This point is discussed in detail in the second part of this study [8]. The main component is continuous but may undergo periodic fluctuations in both its magnitude and direction, if the number of chambers exposed to the line port varies with shaft position. Fixed-displacement pumps can be designed to maintain a fixed number of chambers exposed to the line port, i.e., the transition of one chamber out of the line-port zone is synchronized with the transition of another chamber into the line-port zone. However, in variable-

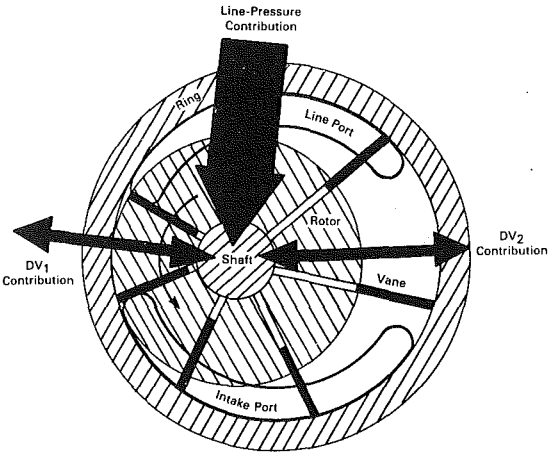


Fig. 4 The components of the radial shaft-load

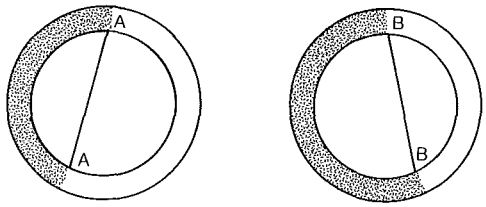


Fig. 5 Different size pressure zones applying equal-magnitude radial loads

displacement pumps, the transition points from one pressure zone to the next vary with the position of the cam and their synchronization may become extremely difficult to control.

This section presents the development of a design criterion which guarantees a fixed-magnitude radial shaft-load in spite of variation in the number of chambers exposed to the line port, and without the need to synchronize the transition points. This criterion imposes a limit on the angular extension of the line port as a function of the number of pump chambers. This limit is set so that the length of the chord of the pressure zone does not change when the number of the pressurized chambers vary, thus maintaining the magnitude of the resultant force. Figure 5 shows an example of two different-size pressure zones with equal-length chords (AA = BB).

The following paragraphs outline the criterion development. Define:

$m-$ maximum number of chambers exposed to the line port (the number of chambers exposed to the line port then varies between $m$ and $m-1$)

Based on the assumption of a uniform pressure in a chamber, and neglecting the vane width, chambers exposed to the line port may be regarded as in a continuous uniform pressure zone. The resultant radial shaft-load of this zone is given by equation (11) applied to the combined arc of the chambers. Therefore, the magnitude of the resultant radial shaft-load due to $m$ chambers exposed to the line port is given by:

$$|\bar{F}_R|_m \sim 2 \cdot P \cdot R \cdot W \cdot \sin \frac{\psi_2 - \psi_1}{2}\bigg|_m \sim 2 \cdot P \cdot R \cdot W \cdot \sin \frac{m\gamma}{2}$$

and the magnitude of the resultant radial shaft-load due to $m-1$ chambers exposed to the line port is given by:

$$|\bar{F}_R|_{m-1} \sim 2 \cdot P \cdot R \cdot W \cdot \sin \frac{(m-1)\gamma}{2}$$

[5]The final result holds even without this assumption since it depends on the resultant forces of adjacent chambers being $\gamma$ degrees apart – a condition that is met also for finite width vanes.

For equal magnitudes of radial shaft-load under both conditions:

$$|\bar{F}_R|_{m-1} = |\bar{F}_R|_m$$

which requires that

$$\sin \frac{m-1}{2}\gamma = \sin \frac{m\gamma}{2}$$

which leads to

$$m = \frac{\pi}{\gamma} + \frac{1}{2}$$

Since

$$\gamma = \frac{2\pi}{n_c}$$

the condition for a fixed-magnitude radial shaft-load due to exposure to the line port becomes:

$$m = \frac{n_c + 1}{2} \tag{15}$$

To realize this condition $n_c$ must be an odd number; this requirement conforms with a recommended design practice since an odd number of chambers minimizes pressure ripples resulting from the pulsating-type operation of the pump [13].

## 5 Summary

The analysis of the internal forces in a VDVP is summarized as follows:

1. Analytical expressions for the pressure distribution inside a VDVP have been formulated. They were used to model the forces and torques which are applied to the pump internal mechanism and its shaft. They should be utilized:

   (*a*) to model the dynamics of this type of pump for control, regulation, and system simulation.
   (*b*) to optimize the pump design.

2. The internal forces and torques in a VDVP are functions of the line pressure, the pump eccentricity, the shaft rotational speed, the fluid bulk modulus, the fluid viscosity (temperature dependence), the design geometry, and the cam motion. These functions are periodic with respect to the shaft angular position and can be separated into:

   (*a*) a continuous component due to the exposure of chambers to the line port (with an amplitude proportional to the line pressure).
   (*b*) an intermittent component due to fluid compression in a chamber while it is sealed from either port.

3. These periodic components are superimposed on the pump pulsations inherent in the operation of both fixed- and variable-displacement pumps, due to their finite number of pumping elements. The frequency content of the torque applied to the pump mechanism must be considered in the pump regulation and control.
4. The periodic variation in the magnitude of the continuous component of the radial shaft-load can be eliminated by a correct design.

## References

1 Stefanides, E. J., "Pump/Valve System Upgrades Mobile Vehicle Hydraulics," *Design News*/2-15-82.

2 Hydra-matic Division Service Department, "THM200-4R Principles of Operation," General Motors Corportion, 1980.

3 DeGarcia, H., et al., McDonnell Douglas Co. "Aircraft Hydraulic Systems Dynamic Analysis," Report AFAPL-TR-78-77, Oct. 1978.

4 Beswarick, W. J., and Bhinder, F. S., "A Performance Prediction

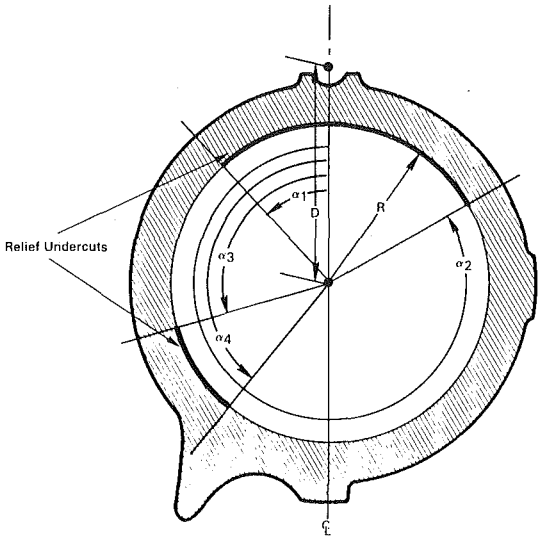


Fig. 6 Geometrical parameters of the VDVP

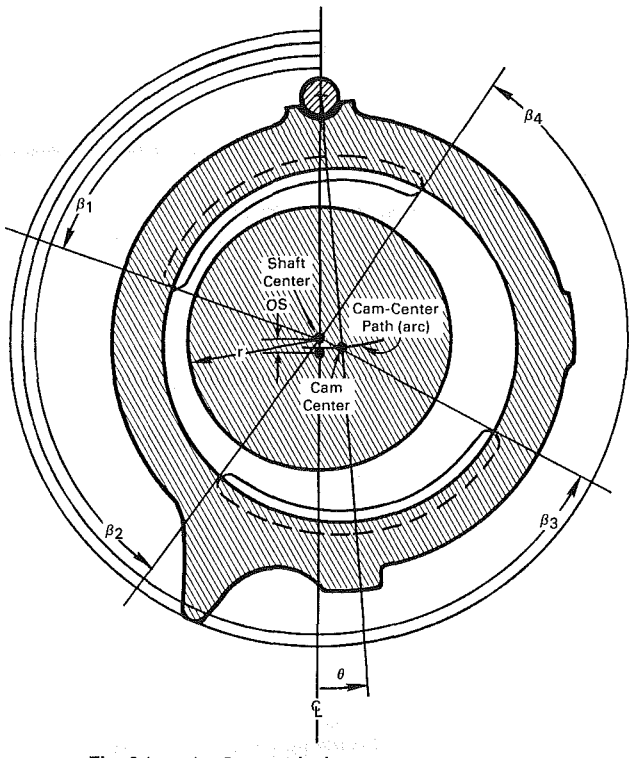


Fig. 6 (cont.) Geometrical parameters of the VDVP

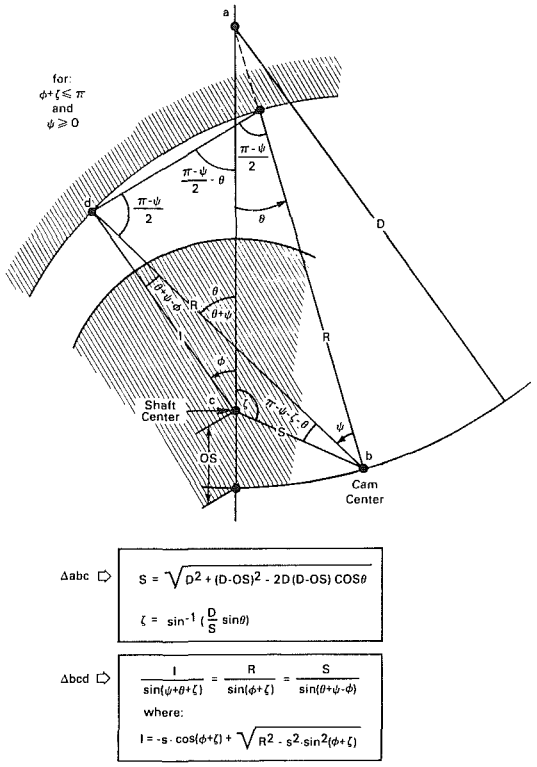


$$\Delta abc \Rightarrow \quad S = \sqrt{D^2 + (D\text{-}OS)^2 - 2D(D\text{-}OS)\cos\theta}$$

$$\zeta = \sin^{-1}\left(\frac{D}{S}\sin\theta\right)$$

$$\Delta bcd \Rightarrow \quad \frac{l}{\sin(\psi+\theta+\zeta)} = \frac{R}{\sin(\phi+\zeta)} = \frac{S}{\sin(\theta+\psi-\phi)}$$

where:

$$l = -s\cdot\cos(\phi+\zeta) + \sqrt{R^2 - s^2\cdot\sin^2(\phi+\zeta)}$$

Fig. 7 Kinematic relationships between shaft and cam angular references


Method for Axial Piston of the Swashplate Type," SAE Paper No. 821090, 1982.

5 Taplin, L. B., "Dynamic Performance of Variable Delivery Constant Pressure Pumps," presented at the SAE Sub Committee A-6C Meeting, Detroit, Mich., Apr. 1961.

6 Polozov, A. V., "Analysis of Dynamic Properties of a Pump Delivery Control System," *Russian Eng. Journal*, Vol. 54, Issue 2, 1974, pp. 7–13.

7 Lin, S. J., Akers, A., and Zeiger, G., "The Effect of Oil Entrapment in an Axial Piston Pump," ASME *Journal of Dynamic Systems, Measurement and Control*, Vol. 107, Dec. 1985.

8 Karmel, A. M., "A Study of the Internal Forces in Variable-Displacement Vane-Pump – Part II: A Parametric Study," ASME JOURNAL OF FLUIDS ENGINEERING, published in this issue, pp. 233–237.

9 Rothbart, H. A., Editor-in-Chief, *Mechanical Design and Systems Handbook*, Chapters 12, 37 (Eqs. 12.8, 37.46), McGraw-Hill, 1964.

10 Martin, F. A., and Booker, J. F., "Influence of Engine Inertia Forces on Minimum Film Thickness in Con-Rod Big-End Bearings," The Institute of Mechanical Engineers, Lubrication and Wear Group, Proceedings 1966-67, Volume 181, Part 1.

11 Harris, T. D., *Rolling Bearing Analysis*, Wiley, 1966.

12 The Timken Roller Bearing Company, *The Timken Engineering Journal*, Section 1, Ohio.

13 Hadekel, R., *Displacement Pumps and Motors*, London, Sir Issac Pitman and Sons Ltd., 1951.


## APPENDIX A

### VDVP Kinematic Relationships

The transformation equations between the housing and the cam coordinates are developed in this Appendix. Figure 6 defines the geometrical parameters required for the kinematic analysis.

Figure 7 presents the geometrical relationships between the shaft angular reference, the cam angular reference, the eccentricity and the design parameters, under different kinematic configurations. These relationships can be summarized by a single equation which holds throughout the entire angular range:[6]

$$\frac{l}{\sin(\psi+\zeta+\theta)} = \frac{R}{\sin(\theta+\zeta)} = \frac{S}{\sin(\theta+\psi-\phi)} \tag{A-1}$$

which is further reduced into:

$$\phi = \tan^{-1}\left[\frac{R\cdot\sin(\theta+\psi) - s\cdot\sin\zeta}{S\cdot\cos\zeta + R\cdot\cos(\theta+\psi)}\right] \tag{A-2}$$

$$\psi = \phi - \theta + \sin^{-1}\left[\frac{S}{R}\cdot\sin(\phi+\zeta)\right] \tag{A-3}$$

Equations (A-2) and (A-3) are the transformation equations between the shaft and cam coordinates.

[6] For negative eccentricities, $\zeta$ should be assigned a negative value.

# A Study of the Internal Forces in a Variable-Displacement Vane-Pump—Part II: A Parametric Study

**A. M. Karmel**
Project Trilby,
General Motors Research Laboratories,
Warren, MI 48090

*This is the second part of an analytical study of the internal forces in a variable-displacement vane-pump. It presents a parametric study of the forces and torques applied to the mechanism and the shaft of this pump, as functions of line pressure, the eccentricity, and the design geometry. It is shown that the continuous components of the torque and of the direction of the radial shaft-load vary as a saw-tooth wave at twice the vane-frequency while the magnitude of the radial shaft-load varies as a square wave at vane-frequency. The design criterion developed in the first part of this study is used to demonstrate the elimination of the magnitude variations in the radial shaft-load. The intermittent components of the internal forces vary as a pulse train at vane frequency and may produce high-peak pressure pulses which must be closely controlled. The variable-capacity feature of variable-displacement vane-pumps has a significant effect on the torque applied to the mechanism, but only a secondary effect on the overall radial shaft-load.*

## 1 Introduction

This is the second part of an analytical study of the internal forces in a variable-displacement vane-pump (VDVP). It presents a parametric study of the forces and the torques applied to the mechanism and to the shaft of this type of pump, based on the theory developed in the first part [1]. Both operating and design parameters are assessed in terms of their effect on the internal forces.

The dead-volume contribution was analyzed under fixed-eccentricity conditions thereby excluding dynamic effects, i.e., eccentricity variations while a chamber is within a dead-volume zone. These effects should be reexamined once a dynamic model for this pump is completed.

### Nomenclature

See Part I of this paper [1].

## 2 The Internal Forces in a VDVP

Equations (10)–(12) in conjunction with Table 1 from reference [1] were used to calculate the internal forces and torques in a 100 mm diameter VDVP shown in Fig. 1.

Results are shown as functions of the shaft angular position at fixed eccentricities, thereby excluding dynamic effects due to eccentricity variations in the dead-volume zones. All plots are given for a $(2\pi/7)$ spatial period, which results from the seven chamber design of this pump (assuming equally spaced vanes). Also note that for this chamber configuration, the design criterion [1] for a fixed-magnitude radial shaft-load requires that the number of chambers exposed to the line port should vary between 3 and 4 ($m = 4$)

With a positive cam offset in the above design, a chamber in

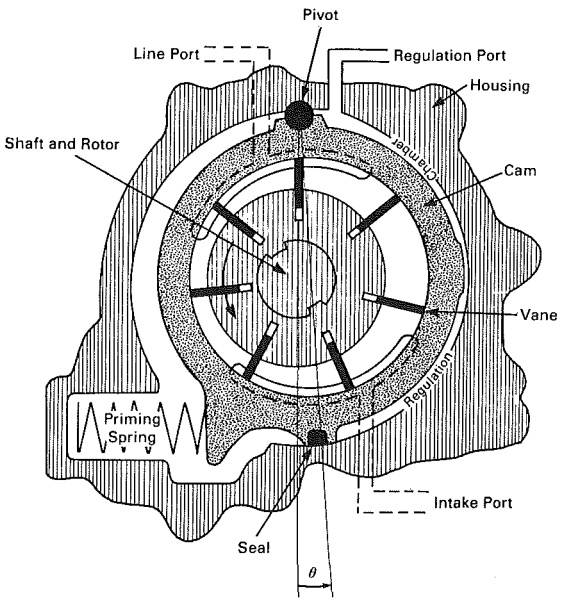


Fig. 1 Schematic of the VDVP

Contributed by the Fluids Engineering Division for publication in the JOURNAL OF FLUIDS ENGINEERING. Manuscript received by the Fluids Engineering Division, November 7, 1984.

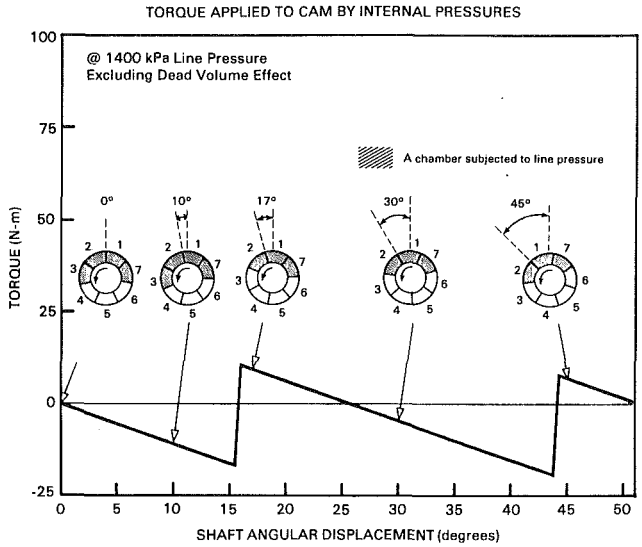


Fig. 2 The continuous component of the torque applied to the cam

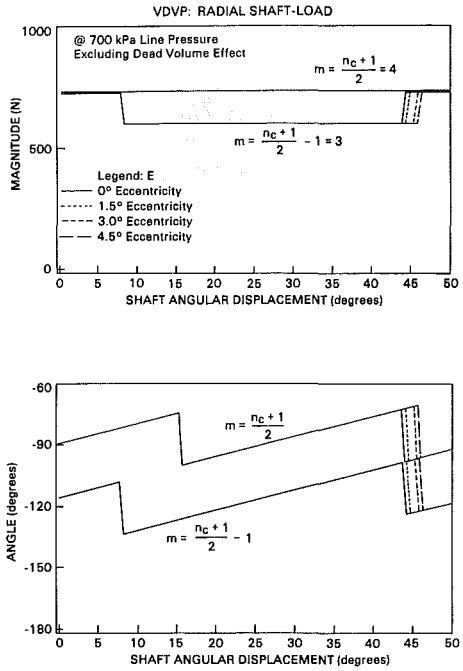


Fig. 3 The continuous component of the radial shaft-load

$DV_1$ undergoes a continuous volume increase which results in partial vacuum for all eccentricities (see Appendix A); Consequently, pressure in $DV_1$ is taken as atmospheric. In contrast, $DV_2$ undergoes a continuous volume decrease for all eccentricities which boosts the fluid pressure from the intake (atmospheric) level it has entering this zone.

**The Continuous Component of the Internal Forces.** Figures 2 and 3 display the spatial histories of the torque on the cam and of the radial shaft-load with only the contribution due to the exposure of the chambers to the line port; i.e., excluding the dead-volume effect. Figure 2 shows a sawtooth pattern at twice the vane frequency[1]. This pattern results from a varying number of pressurized chambers, depending on the shaft angular position. Initially, at $\phi = 0°$, because of the symmetry associated with zero eccentricity, the resultant-force of the

[1] "Vane frequency" is the product of the number of chambers and the shaft rotational speed.

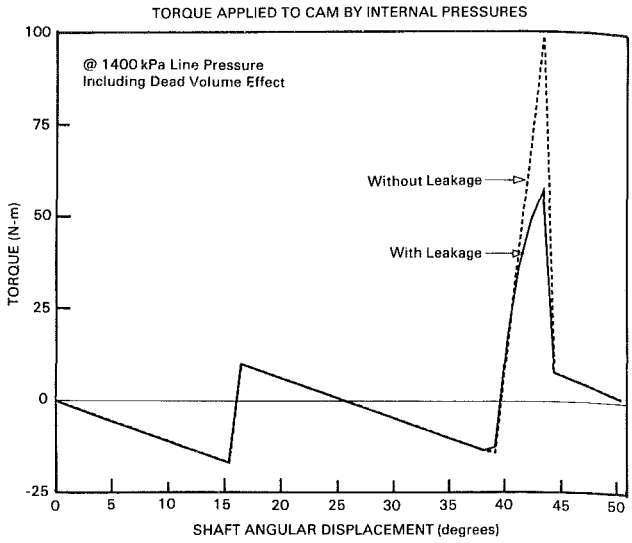


Fig. 4 The torque applied to the cam by the internal pressures

four pressurized chambers passes through the pivot point and results in a zero torque. As the shaft rotates, a lever arm for the resultant force develops and creates a net negative torque on the cam. This negative trend is almost linear with shaft rotation and it ends as the leading pressurized chamber (chamber #3) enters $DV_1$. The pressure drop associated with $DV_1$ reduces the number of pressurized chambers to three, significantly changing the overall torque distribution. A positive torque is now applied to the cam by the remaining three chambers. The torque jump due to the transition from four to three pressurized chambers creates the sawtooth shape. Subsequent rotation of the shaft generates an almost identical slope as before, which ends in another positive torque-jump as chamber #6 is pressurized entering the line-port zone.

The radial shaft-load in Fig. 3 is plotted for two design configurations:

- A port design which conforms to the design criterion [1] for a fixed-magnitude radial shaft-load ($m = 4$).
- A port design which does not conform to the above design-criterion ($m = 3$).

As predicted, the magnitude of the continuous component of the radial shaft-load is constant over the entire period for $m = 4$. For $m = 3$, the magnitude of the radial shaft-load varies as a square wave at vane frequency, with $\sim 25$ percent change in magnitude. Moreover, the transition points shift with eccentricity, somewhat changing the duty-cycle of the load.

The direction of the radial shaft-load follows a sawtooth pattern over that same period, oscillating at twice the vane frequency. The shape is identical for both cases except for an angular bias between them. Both exhibit the same dependence on eccentricity.

The remainder of this discussion assumes a configuration which conforms to the design criterion for a fixed-magnitude radial shaft-load.

**The Dead-Volume Component of the Internal Forces.** Figures 4 and 5 display the spatial histories of the torque on the cam and of the radial shaft-load, including dead-volume effects with and without leakage. The pressure in $DV_2$ may become much higher than the line pressure, particularly when leakage is not taken into account. As chamber #6 enters $DV_2$, high pressure develops in this chamber which leads to spikes in the torque applied to the cam and the radial shaft-load. Note the strong influence leakage has in reducing these spikes. Since leakage is proportional to the cube of the clearance, it may vary dramatically between production units due to manufacturing tolerances. The effect of the leakage on the pump

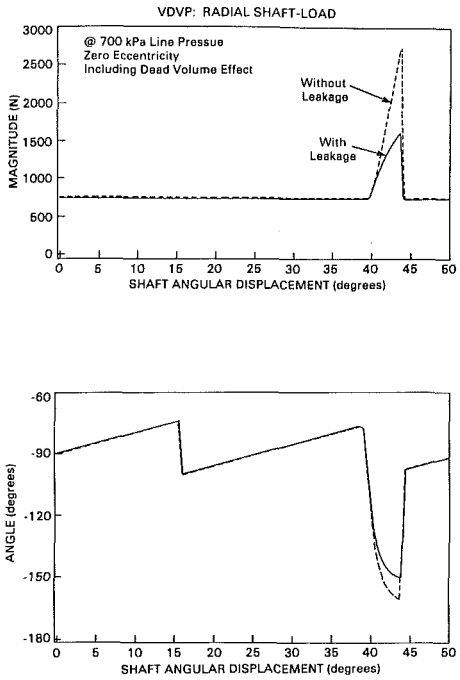


Fig. 5 The radial shaft-load due to the internal pressures

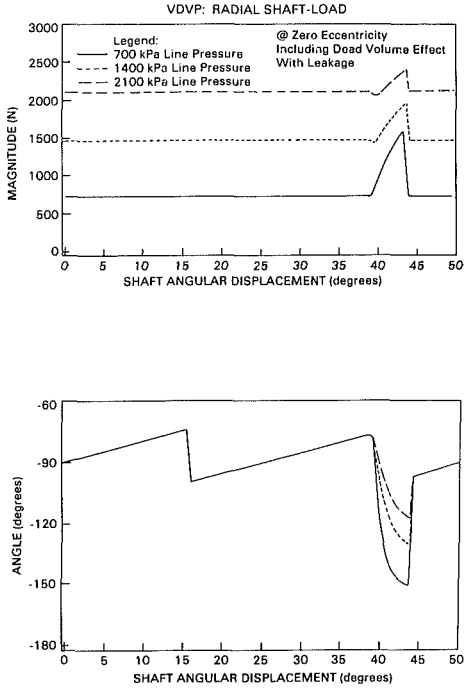


Fig. 7 The radial shaft-load—variation with line pressure

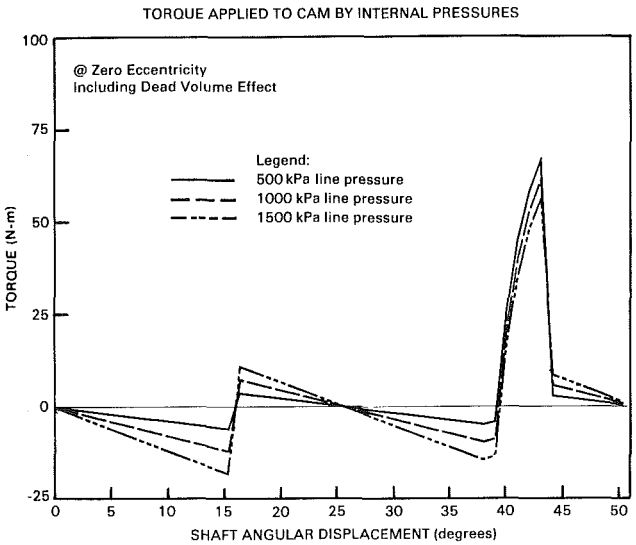


Fig. 6 The torque applied to the cam by the internal pressures—variation with line pressure

dynamics will vary accordingly. However, the overall dynamic characteristics of the pump will be less affected by these leakage variations since they do not influence the major contribution of the continuous component.

**The Line Pressure Effect on the Internal Forces.** Figures 6 and 7 display the spatial histories of the torque on the cam and of the radial shaft-load as line pressure is varied at zero eccentricity. Most significant is the change in the continuous components of the loads with only minor changes in the dead-volume spikes (if leakage were not considered, dead-volume spikes would not be affected at all by line-pressure variations). Variations in the overall torque while a chamber is in a dead-volume zone result primarily from the variations in the continuous contribution onto which dead-volume spikes are superimposed.

Since the amplitude of the torque sawtooth is proportional to the line pressure so is its net negative contribution to the mean torque, i.e., the higher the line pressure the more negative it becomes. Higher line-pressure tends to reduce the effect of the dead-volume pulses on the radial shaft-load, since the continuous load approaches its peak level. The direction of the radial shaft-load does not vary with line pressure, except for the contribution of the dead-volume pulses. As line pressure increases, the overall direction approaches the values predicted by the continuous contribution of the chambers exposed to the line port.

**The Eccentricity Effect on the Internal Forces.** Figures 8 and 9 display the spatial histories of the torque on the cam and of the radial shaft-load for different eccentricities. Eccentricity affects the torque sawtooth as well as the dead-volume spike. Under higher eccentricity conditions, the contribution of the torque sawtooth to the mean torque becomes less negative. However, eccentricity has a much more significant effect on the dead-volume spikes as it influences both their level and spatial duration. In contrast, the continuous component of the radial shaft-load is independent of eccentricity variations.

**The Effect of the Dead-Volume Range on the Internal Forces.** The impact of the dead-volume pulses on bearing life increases with their level and spatial duration [2–4]. The dead-volume pressure-spikes invariably relate to their angular range, as logner zones usually compress (or expand) the fluid more. Such compression, aside from excessive loading of the shaft, also contributes to additional leakage and efficiency loss. Expansion, such as occurs in $DV_1$, creates a partial vacuum, and may cause local cavitation. Figure 10 shows the range of the dead-volume zones as a function of eccentricity. Both $DV_1$ and $DV_2$ increase with eccentricity. Note that the variation of $DV_1$ range is lower compared to that of $DV_2$, a feature which relates to the distance of their transition points (as determined by the relief-undercuts at the bottom of the cam) from the cam pivot.

Figure 11 displays the spatial history of the radial shaft-load for different eccentricities, with reduced $DV_2$ range. The dead-volume range is reduced to vane width for all eccentricities by an extension of the line port, which eliminates the dead-volume dependence on the cam relief-undercuts. The

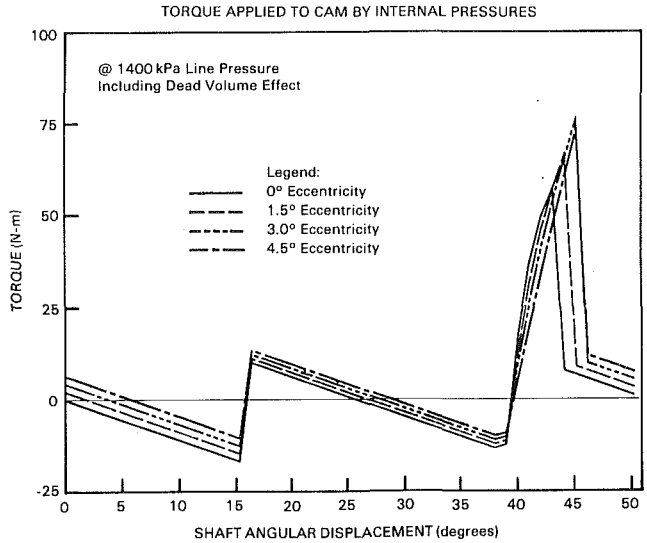


Fig. 8 The torque applied to the cam—variation with eccentricity

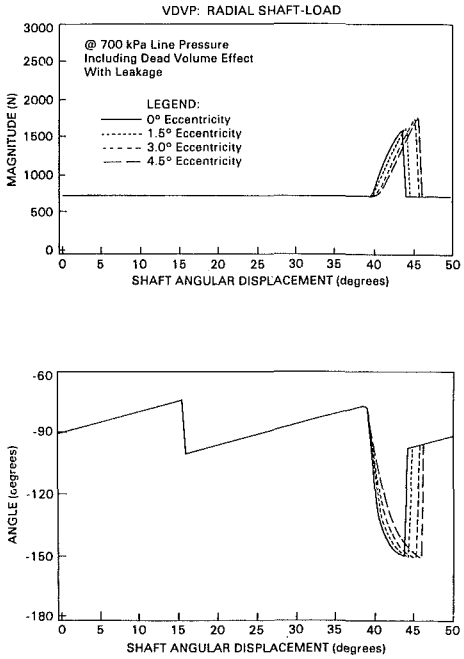


Fig. 9 The radial shaft-load—variation with eccentricity

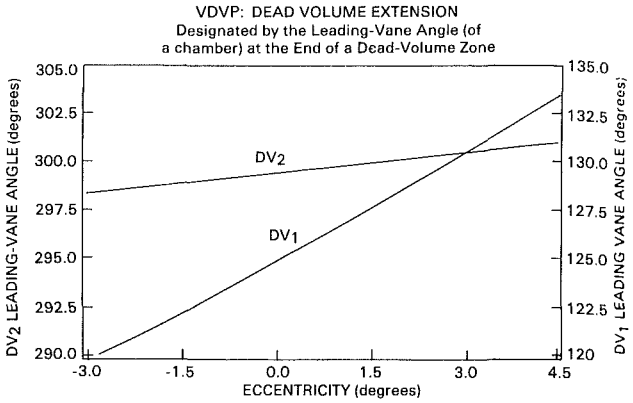


Fig. 10 $DV_1$ and $DV_2$ range—variation with eccentricity

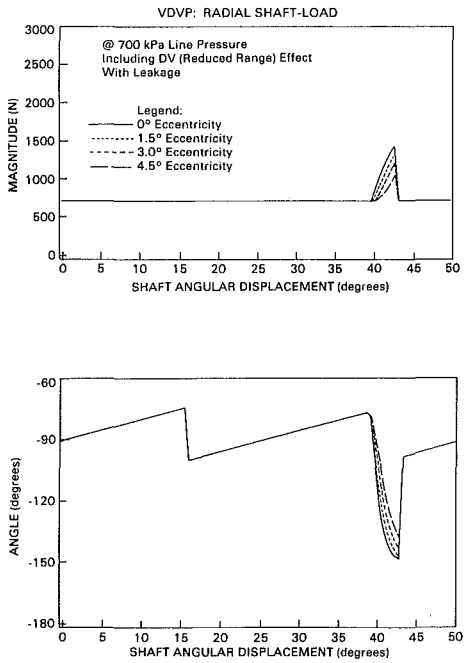


Fig. 11 The radial shaft-load—variation with eccentricity for a reduced $DV_2$ range

reduction of the dead-volume pulses is beneficial in terms of both their magnitude and spatial duration.

## 3 Summary

The parametric study of the internal forces in a VDVP is summarized as follows:

1. The internal forces which develop due to fluid pressure have the following characteristics:
   (*a*) The continuous component (due to the exposure of chambers to the line port) of the torque applied to the cam and of the direction of the radial shaft-load varies as a sawtooth wave at twice the vane-frequency, while the magnitude of the radial shaft-load varies as a square wave at vane-frequency. These variations are the result of the varying number of chambers exposed to the line port. The periodic variation in the magnitude of the continuous component of the radial shaft-load cam be eliminated by correct design.
   (*b*) The intermittent component (due to a hydraulic-lock phenomenon) appears as a pulse-train at vane frequency—a result of fluid compression in a chamber as it passes through a zone in which it is sealed from either port. These pulses develop through a limited zone of angular displacement. Their magnitude may be much greater than the average load and should be closely controlled, along with their duration. In addition to their relationship to the angular range of the dead-volume zone, these pulses strongly depend on leakage; i.e., they are functions of clearance, viscosity (temperature) and shaft speed. The $DV_2$ effect on the radial shaft-load is reduced at high line-pressure, since the continuous contribution of the line pressure approaches the peak level of the $DV_2$ pulses.
2. Higher eccentricities result in significantly higher amplitude torques on the cam; however, they have only a marginal effect on the radial shaft-load.

3. The dead-volume contribution was analyzed under fixed-eccentricity conditions thereby excluding dynamic effects, i.e., eccentricity variations while a chamber is within a dead-volume zone. Such effects are expected to reduce the peak of the dead-volume pressure spikes, and reduce the adverse result of longer dead-volume zones.
4. Compression and expansion in the dead-volume zones may lead to leakage, mechanical and volumetric-efficiency losses, and a certain degree of cavitation. Because of production tolerances, these characteristics may vary drastically among production units.
5. The design of the dead-volume zones in vane-pumps should be carefully conducted. Ideally, dead-volume zones should be designed to compress fluid from intake pressure up to line pressure, but no higher. Such a design must consider varying clearances and different fluid-air ratios. It is especially important in fixed-displacement pumps where dynamic effects cannot relieve excessive spikes in pressure.

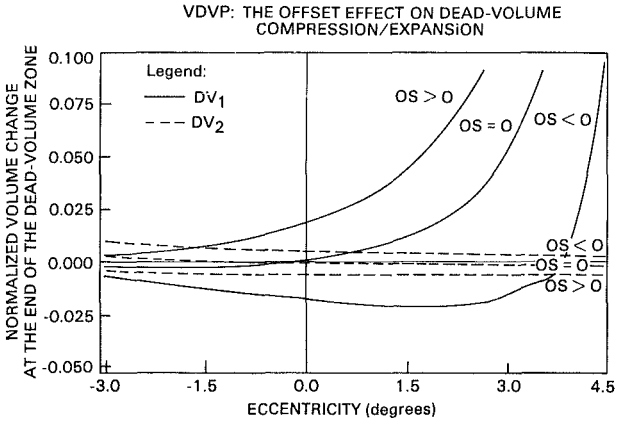


**Fig. 12 The offset effect on the dead-volume zones**

## References


1 Karmel, A. M., "A Study of the Internal Forces in a Variable-Displacement Vane-Pump—Part I: A Theoretical Analysis," ASME JOURNAL OF FLUIDS ENGINEERING, published in this issue pp. 227-232.

2 Martin, F. A., and Booker, J. F., "Influence of Engine Inertia Forces on Minimum Film Thickness in Con-Rod Big-End Bearings," The Institute of Mechanical Engineers, Lubrication and Wear Group, *Proceedings 1966-67*, Vol. 181, Part 1.

3 Harris, T. D., *Rolling Bearing Analysis*, Wiley, 1966.

4 The Timken Roller Bearing Company, *The Timken Engineering Journal*, Section 1, Ohio, USA.


## APPENDIX A

### The Offset Effect in the Design of Variable-Displacement Vane-Pumps

The offset of the cam center from the rotor center at $\theta = 0°$ is crucial to the effect of the two dead-volume zones. Figure 12 shows the normalized volume-change of the dead-volume zone (normalized with respect to its initial value as it enters such a zone) at the end of the dead-volume range, as a function of eccentricity. The offset is defined positive for pivot/cam-center longer than pivot/shaft-center distances (cam center "below" shaft center). Note how the normalized volume changes its sign for nonpositive offset values, which indicates that a dead volume may compress or expand the fluid as the eccentricity varies. The contribution to the radial shaft-load of such a dead volume will shift directions. For a positive offset, however, either compression or expansion occurs for all eccentricities, which determines a fixed-direction load for each zone.

D. M. Webber

P. W. M. Brighton

Safety and Reliability Directorate,
UKAEA,
Culcheth,
Warrington WA3 4NE
UK

# Inviscid Similarity Solutions for Slumping From a Cylindrical Tank

## 1 Introduction

Bai et al. [1] have recently considered the slumping behavior of an unconfined, cylindrical column of liquid on a smooth, flat surface. This problem is relevant to the prediction of consequences of major accidents in the chemical and petroleum industries. The aim of this note is to point out errors in that work and to clarify the theory of this flow, in the inviscid approximation. We shall present explicit self-similar solutions to the shallow-water equations with specific reference to the relevant boundary conditions.

## 2 The Governing Equations

The shallow water equations [2, 3] governing the behavior of an inviscid shallow pool are:

$$\frac{\partial h}{\partial t} + \nabla \cdot (\mathbf{u}h) = 0 \tag{1}$$

$$\frac{\partial u}{\partial t} + (\mathbf{u} \cdot \nabla)\mathbf{u} + g\nabla \mathbf{h} = 0 \tag{2}$$

The depth $h$ of the pool and the two-component horizontal velocity $\mathbf{u}$ are functions of time $t$ and the (two) horizontal coordinates $\mathbf{x}$. Specialising to axisymmetric, purely radial flow taking $|\mathbf{x}| \equiv r$ and $|\mathbf{u}| \equiv v$, these equations become

$$\frac{\partial h}{\partial t} + \frac{1}{r}\frac{\partial}{\partial r}(rvh) = 0 \tag{3}$$

$$\frac{\partial v}{\partial t} + v\frac{\partial v}{\partial r} + g\frac{\partial h}{\partial r} = 0 \tag{4}$$

For a liquid spreading on a flat surface and unresisted by any ambient medium, then $g$ is the acceleration due to gravity. Equation (3) is the same as (2.1) by Bai et al. [1], but in their equation (2.2) the gravity driving term is wrong.

These equations have a wider applicability: for a light liquid of density $\rho$ spreading on (and immiscible with) calm water of density $\rho_w$, then $g = \tilde{g}\,(\rho_w - \rho)/\rho_w$ where $\tilde{g}$ is the acceleration due to gravity; for a heavy liquid spreading on a flat, solid surface under deep water then $g = \tilde{g}\,(\rho - \rho_w)/\rho$. The last case is directly analagous to that of a heavy gas cloud spreading in air in the limit where air entrainment into the cloud is neglected.

Contributed by the Fluids Engineering Division for publication in the JOURNAL OF FLUIDS ENGINEERING. Manuscript received by the Fluids Engineering Division May 20, 1985.

In fact hitherto equations (3) and (4) have been considered mainly in the literature on oil slicks on water [4, 5] and in the context of heavy gas clouds (see [6] for a review), rather than for liquids slumping axisymmetrically on land. In the case of plane geometry equations (1) and (2) form the basis of the classic "dam-break" model (see [7] for a review).

The most significant difference between the problems defined above is not in the definition of $g$, but in the appropriate boundary conditions at the edge of the pool. We shall discuss these after presenting the self-similar solutions, but we stress that the relevance of these solutions is only established when they are shown to satisfy the boundary conditions.

## 3 Self-Similar Solutions

Let us consider then a circular pool of overall radius $R(t)$ and fixed volume $Q$, and look for self-similar solutions of the form

$$v(r,t) = \frac{dR}{dt} \cdot u(\xi) \tag{5}$$

$$h(r,t) = \frac{Q}{\pi R^2} \cdot \phi(\xi) \tag{6}$$

with

$$\xi \equiv \frac{r}{R(t)} \tag{7}$$

The total volume $Q$ is just the integral of $h$ over the area of the pool and so

$$\int_0^1 d\xi \cdot \xi\phi(\xi) = \tfrac{1}{2} \tag{8}$$

Equations (3,4) now become

$$\frac{d}{d\xi}[\xi\phi(u-\xi)] = 0 \tag{9}$$

$$\ddot{R}u + \frac{\dot{R}^2}{R}(u-\xi)\frac{du}{d\xi} + \frac{gQ}{\pi R^3}\frac{d\phi}{d\xi} = 0 \tag{10}$$

Equation (9) integrates trivially giving $\xi\phi(u-\xi)$ to be constant. Furthermore if the depth is to be finite at the origin ($\xi = 0$) then this constant must be zero and hence

$$u = \xi \tag{11}$$

This simplifies (10) so that the method of separation of variables yields

$$\frac{d^2R}{dt^2} = \frac{4gQ(1-s)}{\pi R^3} \tag{12}$$

$$\frac{d\phi}{d\xi} = -4(1-s)\xi \tag{13}$$

where $s$ is a constant. The integral of (13) which satisfies (8) is

$$\phi = (2-s) - 2(1-s)\xi^2 \tag{14}$$

Thus our solution is

$$v(r,t) = \frac{r}{R}\frac{dR}{dt} \tag{15}$$

$$h(r,t) = \frac{Q}{\pi R^2}\left\{(2-s) - 2(1-s)\left(\frac{r}{R}\right)^2\right\} \tag{16}$$

where $R(t)$ satisfies (12). Note that we have chosen the constant $s$ such that

$$h(R,t) = s \cdot \frac{Q}{\pi R^2} \tag{17}$$

The solution is valid for $0 \le s \le 2$.[1]

The general solution of (12) is

$$R^2 = at^2 + bt + c \tag{18}$$

where $a$, $b$, and $c$ are constants which must satisfy

$$b^2 - 4ac = \frac{-16gQ(1-s)}{\pi} \tag{19}$$

These self-similar solutions corresponding to different values of $a$, $b$, $c$, and $s$ cover a large enough range of conditions to illustrate the rôle of the boundary conditions in determining the form of the solution.

## 4 Boundary Conditions

The boundary conditions at the front will consist of equations involving the values $v_f$ and $h_f$ of the fields at the front ($r = R(t)$). The form of the boundary conditions will depend on the problem in hand, and there is no guarantee that they will admit a self-similar solution at all. However, as we shall see, self-similar solutions are admitted for a number of problems of interest.

One of the conditions common to all the problems which we shall consider is

$$v_f = \frac{dR}{dt} \tag{20}$$

This ensures that no liquid is "lost" at the front, and that (1) is exactly integrable to give conserved volume $Q$. The self-similar solutions satisfy this condition.

The second boundary condition must depend on the nature of any force acting on the front. We shall examine three cases

$$v_f = 0 \tag{21a}$$

$$v_f = K\sqrt{gh_f} \tag{21b}$$

$$h_f = 0 \tag{21c}$$

where, in (21$b$), $K$ is a constant.

Condition (21$a$) is appropriate for the trivial case of a pool confined in a circular tank. The boundary conditions (20), (21$a$) are consistent with the self-similar solution with $a = b = 0$, $s = 1$ and a tank radius of $\sqrt{c}$. The pool depth $h$ is uniform and constant. (This solution agrees with experience in contrast to the corresponding solution $v = 0$, $h \sim r^{-1/2}$ of the equations of reference [1], which even denies the possibility of a finite depth of liquid at rest in a circular tank.)

Condition (21$b$) has been used [4, 5] to model the behavior of a liquid pool spreading on a denser liquid – in particular an oil slick on calm water. This condition may be derived by equating the hydrostatic pressure drop across the front of the pool (proportional to $\tilde{g}(\rho_w - \rho)h_f$) with the resistance pressure from the displaced water (proportional to $\rho_w v_f^2$).

The fields (15), (16) satisfy (21$b$) provided that

$$\frac{dR}{dt} = K\left(\frac{gsQ}{\pi}\right)^{1/2}\frac{1}{R} \tag{22}$$

This is consistent with (18) only if $a = 0$ and $\pi b^2 = 4K^2 sgQ$. (Note that this is a very particular case of (18) where $R \sim \sqrt{t}$.) The constant $s$ is now found from (19) and $c$ determines the zero of time. The solution has $s > 1$ and hence a depth profile (16) with a raised front. This solution is also relevant for the slumping of a heavy gas cloud resisted by the ambient air.

The rate at which work is done on the ambient fluid can be clarified by considering the kinetic energy per unit area $T = \frac{1}{2}\rho h(\mathbf{u}\cdot\mathbf{u})$ and the potential energy per unit area $P = \frac{1}{2}g\rho h^2$, for which

$$\frac{\partial}{\partial t}(T+P) + \nabla\cdot(\mathbf{u}(T+P)) = -\nabla\cdot(\mathbf{u}P) \tag{23}$$

is implied directly by (1) and (2). Thus the rate of change of the total pool energy is just the area integral of the right-hand size, or the integral of $-vP$ around the circumference of the pool. Thus the rate at which work is done is $\pi R\dot{R}g\rho h_f^2$.

In the case of a pool unresisted by any ambient fluid then (21$c$) is the relevant boundary condition and no work is done. This is the case for a liquid spreading on a flat solid surface in the approximation that air resistance is negligible. Now (21$c$) implies $s = 0$ in our self-similar solution, and so (18) and (19) imply $a > 0$, $c > 0$. In fact $a$, $b$, and $c$ may be found from (19) and from the conserved total energy

$$E = 2\pi\int_0^R dr\cdot r(T+P) \tag{24}$$

The remaining degree of freedom is the choice of the zero of time. Note that the conservation of energy is more general than the self-similar solution and so (24) may be used to estimate "$a$" for the large-time self-similar solution even for a release which does not initially have the similarity profiles (15), (16). For a cylindrical release from rest at uniform depth $h_0$ [1] we find $a = 3gh_0$. The large time behavior is $R \sim a^{1/2}t$.

## 5 The Time-Scale for Onset of Self-Similarity

The self-similar solutions given above do not describe the details of acceleration from rest with an arbitrary initial height profile. However at large times the flow is expected to settle down to the self-similar behavior. The time-scale over which this happens is

$$t_0 = R_0/(gH_0)^{1/2} \tag{25}$$

where $R_0$ is the initial radius and $H_0$ the initial height-scale. Grundy and Rottman [8] have recently confirmed that this will happen for the case of boundary condition (21$b$). Also experiments on radial heavy-gas cloud spreading have shown that the behavior $R \propto \sqrt{t}$, suggested by the similarity analysis, is indeed established after a time of 10 $t_0$ (see reference [14] for example).

We also note that much work on the dam-break problem [2, 7, 9–11] has focused on the early-time regime $t \lesssim 0(t_0)$, when waves reflected from the back of the reservoir (or in our case waves that have propagated through the axis of symmetry) have not had time to affect the flow. This is a different flow régime from the one discussed here and in reference [1]. Also Greenspan and co-workers [12, 13] have studied the interac-

[1] There are also solutions for an annular pool corresponding to $s > 2$, but in this case (8) and (14) must be modified slightly.

tion of instantaneous releases with containing walls on timescales of order $t_0$.

## 6 Discussion

The self-similar solutions given here contrast strongly with those of Bai et al. [1]. In that work it is concluded that a slumping liquid column on a smooth surface behaves as $R \sim \sqrt{t}$, and numerical solutions for the depth and velocity profiles are discontinuous.

We have shown that the correct equations, together with a proper consideration of the boundary conditions, give different spreading laws for different flows, and lead to a spreading law with $R \sim t$ in Bai et al.'s [1] case.[2] Also there is always a perfectly adequate self-similar profile without hydraulic jumps.

Like reference [1], this work has been concerned only with solutions of the inviscid equations. The magnitude of resistance effects may be estimated as follows.

Turbulent resistance may be incorporated into the model by replacing the right-hand side of (4) by $-Cv^2/h$ where $C$ is a friction coefficient [7]. For the energy-conserving solution given above the ratio of this term with the gravity driving term is of order $[CR_0/h_0][R/R_0]^5$. Thus for any release with $h_0 \lesssim R_0$ the inviscid approximation can only be valid until $(R/R_0) \sim C^{-1/5}$. Taking a typical value of $C \sim 10^{-3}$ means until $R \sim 4R_0$.

We have recently described the effects of both turbulent and laminar resistance elsewhere [15], where we illustrate how long the inviscid phase may be expected to last, and we hope to publish a fuller account of that work in due course.

[2] Indeed conservation of energy arguments lead directly to this conclusion in this inviscid limit.


## Acknowledgment

This paper is based on work carried out on behalf of the UK Health and Safety Executive.


## References


1 Bai, Y., Johnson, W., Low, R. G. M., and Ghosh, S. K., "Asymptotic Behavior in Slumping From a Cylindrical Tank," ASME JOURNAL OF FLUIDS ENGINEERING, Vol. 106, 1984, pp. 279–284.

2 Stoker, J. J., *Water Waves*, Interscience, 1957, Section 2.4.

3 Landau, L. D., and Lifshitz, E. M., *Fluid Mechanics*, Pergamon Press, 1959, Section 100.

4 Hoult, D. P., "Oil Spreading on the Sea," *Ann Rev Fluid Mech*, Vol. 4, 1972, pp. 341–368.

5 Fannelop, T. K., and Waldman, G. D., "Dynamics of Oil Slicks," *AIAA Journal*, Vol. 10, 1972, pp. 506–510.

6 Wheatley, C. J., and Webber, D. M., "Aspects of the Dispersion of Denser-Than-Air Vapours Relevant to Gas Cloud Explosions," Published by the Commission of the European Communities EUR 9592 en., 1984.

7 Henderson, F. M., *Open Channel Flow*, MacMillan, 1966.

8 Grundy, R. E., and Rottman, J. W., "The Approach to Self-Similarity of the Solutions of the Shallow Water Equations Representing Gravity Current Releases," *J Fluid Mech*, Vol. 156, 1985, pp. 39–53.

9 Dressler, R. F., "Hydraulic Resistance Effect Upon the Dam-Break Functions," *J Research of the National Bureau of Standards*, Vol. 49, 1952, pp. 217–225.

10 Dressler, R. F., "Comparison of Theories and Experiments for the Hydraulic Dam-Break Wave," Assoc Int d'Hydrologie Scientifique, Assemblée Générale de Rome, Vol. III, 1954, pp. 319–328.

11 Whitham, G. B., "The Effects of Hydraulic Resistance in the Dam-Break Problem," *Proc Roy Soc*, Series *A227*, 1955, pp. 339–407.

12 Greenspan, H. P., and Young, R. E., "Flow Over a Containment Dyke," *J Fluid Mech*, Vol. 87, 1978, pp. 179–192.

13 Greenspan, H. P., and Johansson, A. V., "An Experimental Study of Flow Over an Impounding Dyke," *Stud Appl Math*, Vol. 64, 1981, pp. 211–223.

14 Brighton, P. W. M., Prince, A. J., and Webber, D. M., "Determination of Cloud Area and Path from Visual and Concentration Records," *J. Hazardous Materials*, Vol. 11, 1985, pp. 155–178.

15 Webber, D. M., and Brighton, P. W. M., "A Mathematical Model of a Spreading, Vaporising Liquid Pool," in "Heavy Gas and Risk Assessment III," ed. S. Hartwig, D. Reidel Publishing Company, 1986, pp. 223–232.

**M. F. Hamilton**
Former Graduate Student,
Engineering Mechanics and Science Department.

**D. E. Thompson**
Senior Research Associate,
Applied Research Laboratory.

**M. L. Billet**
Senior Research Associate,
Applied Research Laboratory.

The Pennsylvania State University,
State College, PA 16804

# An Experimental Study of Travelling-Bubble Cavitation Noise

*High-frequency travelling-bubble cavitation noise generated on a Schiebe headform is analyzed with reference to several existing noise theories which are based on the collapse of a single spherical bubble. After normalizing the noise level by a bubble event rate, the normalized cavitation number based on the minimum pressure coefficient provides a reasonable scaling factor, for the noise level radiated per collapse. At frequencies above 10 kHz and for free-stream velocities between 9.1 and 12.2 mps (30 and 40 fps), the trend of noise level per collapse versus normalized cavitation number correlated well with noise theories and was constant with flow velocity for constant normalized cavitation number. The energy density spectra were flat from 10 to 100 kHz regardless of the cavitation number or free-stream velocity for the range of these experiments.*

## Introduction

Although there have been many experimental investigations of cavitation noise, most studies are generally concerned with well-developed forms such as wake, vortex or fixed-patch cavitation. In those cases, the entire cavitating region is regarded as a single complex noise source as opposed to considering the collapse of each individual bubble. Near inception when the bubbles are collapsing independently, the radiated noise is often more intense than when the cavitation becomes developed. Such incipient cavitation noise has already been analyzed previously on hydrofoils by Barker [1] and Blake et al. [2] but because of the typically narrow ranges of flow parameters which support incipient conditions, relations indicating how the noise depends on the flow parameters have been determined for these cases. Noise studies have also been conducted for the collapse of a single bubble. This was accomplished by Harrison [3], Mellen [4], and more recently by Chahine et al. [5] where spark gaps were used to generate the bubbles, and also by Hentschel [6] who employed a focused laser beam for that purpose. However, the parameters involved in those investigations do not reflect those typically encountered in flow-induced cavitation.

Therefore, the present study examines travelling-bubble cavitation which is easily generated on a Schiebe headform. In travelling-bubble cavitation each bubble collapses independently, while the Schiebe headform allows for a relatively wide operating range, in terms of flow parameters, for this type of cavitation to exist. Measurements of cavitation noise generated in this way are compared to the relevant theories for noise radiation due to bubble collapse.

Cavitation noise analysis essentially began in 1917 with Rayleigh's solution [7] to the problem posed by Besant [8] of calculating the pressure field generated by the collapse of a spherical cavity in an incompressible fluid. The extension of this analysis by Plesset [9] resulted in the Rayleigh-Plesset equation governing the dynamics of a bubble in an arbitrary time-varying pressure field. It has been shown by Fitzpatrick and Strasberg [10] how this classical analysis predicts an energy spectrum which raises as roughly $f^4$ to a peak at a frequency near the reciprocal of the bubble lifetime, after which it rolls off as $f^{-2/5}$. Both Mellen [11] and Blake et al. [2] obtained noise spectra which exhibited this type of spectral response, except that their spectra rolled off as $f^{-2}$. A review of the hydroacoustic variables that control the ideal sound spectrum of cavitation is given by Blake and Sevik [12].

Subsequent theoretical advances in modelling cavitation noise were few and far between. Not until World War II was an analysis of the propagation of weak shocks developed by Kirkwood and Bethe [13] which enabled Gilmore [14] in 1952 to derive an equation for the collapse of a bubble in a compressible fluid. Both experiment [4] and numerical analysis [15] have demonstrated the accuracy of Gilmore's theory, particularly around the final stage of collapse where bubble wall velocities are sonic and the effects of compressibility become important. However, solutions of that equation must be obtained by numerical methods, and as such it does not yield useful analytical predictions of the radiated sound field.

Another important parameter during the final collapse stage is the presence of any noncondensable gas contained in the bubble. In addition, acoustic pressure waves may be generated by the high bubble wall velocities. Using Whitham's method [16] of describing shock wave propagation, Baiter [17] derived an expression for the pressure pulse in the far field of the bubble, including the effects of noncondensable gas pressure but not of compressibility with respect to bubble dynamics. Esipov and Naugol'nykh [18], using the Kirkwood-Bethe approximation, did include the effects of compressibility and arrived at a solution similar to Baiter's. Both solutions assume a shock wave having an exponential profile, and consequently depict a flat energy spectrum which eventually rolls off at the high end around a frequency determined by the time constant of the wave profile. A number of experiments [1, 2, 11] yielded noise spectra which hinted at such a high frequency spectral plateau.

Thus, these noise theory results are compared to the ex-

Contributed by the Fluids Engineering Division for publication in the JOURNAL OF FLUIDS ENGINEERING. Manuscript received by the Fluids Engineering Division, March 8, 1983.

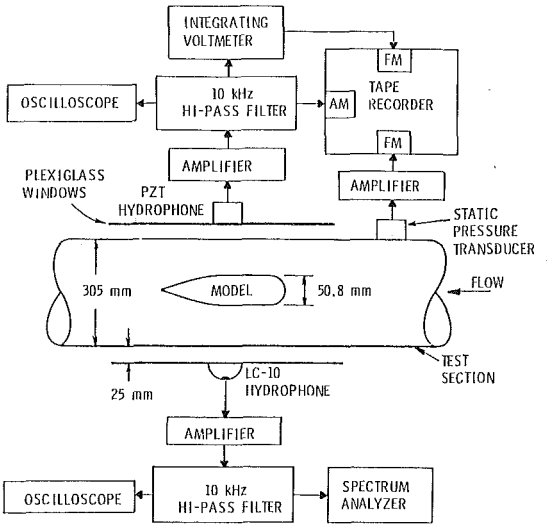


**Fig. 1 Schematic of experimental apparatus**

perimentally measured sound radiated by travelling-bubble cavitation. Comparisons are based on how the noise level per collapsing bubble depends on the cavitation number ($\sigma$) and the flow velocity ($V_\infty$). The independent behavior of the bubbles permits the measured frequency spectra to be qualitatively compared with those predicted by the single spherical bubble noise theories [19].

## Experimental Apparatus and Procedure

This investigation was conducted in the 305 mm (12-in.) diameter water tunnel of the Applied Research Laboratory at The Pennsylvania State University. The headforms used were two 50.8 mm (2-in.) diameter Schiebe noses which were identical except for modifications that provided measurements of either static or acoustic pressure. Schiebe headforms have been shown to experience no laminar separation in the Reynolds number range considered [20] and thus support travelling-bubble cavitation for a relatively wide pressure range, provided there are enough microbubbles available in the free stream [20].

To measure the pressure distribution along the surface of the Schiebe nose, one headform was equipped with ten flush-mounted pressure taps at various distances from the stagnation point. These pressures were compared with the free-stream static pressure, for flow velocities ranging from 6.1 to 18.3 mps (20 to 60 fps), to determine the pressure coefficient $C_p$ defined as:

$$C_p = \frac{P - P_\infty}{\frac{1}{2}\rho V_\infty^2}. \tag{1}$$

With the cavitation number ($\sigma$) given by

$$\sigma = \frac{P_\infty - P_v}{\frac{1}{2}\rho V_\infty^2} \tag{2}$$

measurements of the incipient and desinent cavitation number, $\sigma_i$ and $\sigma_d$ respectively, were determined visually with the aid of a stroboscope by adjusting the test section pressure at constant flow velocities.

A study of bubble dynamics was accomplished with a high-speed photographic system which consisted of a Redlake Hycam camera and an EG & G type 501 stroboscope. A Schiebe nose was modified with a small barium-titanate transducer which was mounted flush with the surface of the model 60 mm downstream from the stagnation point. Thus, at the same time that the high-speed films of bubble collapse were taken, the resulting noise bursts were being monitored by that transducer. After high-pass filtering at 10 kHz, the noise was recorded on a Bell and Howell type CPR-4010 tape recorder. The tape recording was synchronized with the films via voltage spikes input to a second channel which marked the points in time where the strobe would fire to create each successive picture.

Additional studies of bubble dynamics were realized by filming the cavitation on videotape. Voltages corresponding to the pressure and velocity in the test section were noted as recorded on the audio track of the tape so that the effects of a wide range of flow parameters could be observed.

To measure the cavitation noise occurrences, a 25 mm (1-in.) diameter lead-zirconate-titanate (PZT) hydrophone was coupled to the outside of the test section window. The specific acoustic impedance of the window was near that of water such that minimum sound reflection occurred at the interface formed by the two media. The hydrophone was aimed at a location on the model about 50 mm downstream of the stagnation point. With a separation of about 150 mm (6-in.) between the face of the hydrophone and the surface of the model, the measured beamwidth on that surface was about 70 mm at its halfpower points.

After highpass filtering at 10 kHz, the output from the hydrophone was input to one channel of the tape recorder. A DC voltage output from an rms voltmeter, which represented the cavitation noise level above 10 kHz, was input to a second channel. On yet a third channel, a DC voltage was recorded which was proportional to the free stream static pressure in the test section. The entire arrangement is illustrated in Fig. 1.

Tests were run at flow velocities ranging from 9.1 to 12.2 mps (30 to 40 fps) in increments of 0.76 mps (2.5 fps). With the velocity held constant, the pressure in the test section was lowered from an initial point above $\sigma_i$. As soon as noise bursts due to bubble collapses were witnessed on an oscilloscope, tape recording would begin as the pressure was continuously lowered until the travelling-bubble cavitation transformed into an attached cavity. This procedure was repeated at each

## Nomenclature

$a$ = radius of Schiebe body
$c$ = speed of sound
$C_p$ = pressure coefficient
$\bar{C}_p$ = average pressure coefficient where $P < P_v$
$C_{p_{\min}}$ = minimum pressure coefficient
$f$ = frequency
$L$ = noise level
$L_c$ = noise level per collapse
$M$ = shock wave parameter
$N$ = number of collapses per second
$p$ = acoustic pressure
$P$ = pressure
$P_g$ = noncondensable gas pressure
$P_s$ = peak shock wave pressure
$P_v$ = vapor pressure
$\ddot{R}$ = bubble wall acceleration
$R_m$ = minimum bubble radius
$R_M$ = maximum bubble radius
$s$ = length of surface of Schiebe body
$s_v$ = length of region where $P < P_v$
$S$ = spectral energy density
$t$ = time
$V$ = bubble volume
$\ddot{V}$ = second derivative of bubble volume
$V_\infty$ = free-stream velocity
$\theta$ = time constant
$\rho$ = mass density of water
$\sigma$ = cavitation number
$\sigma_d$ = desinent cavitation number
$\sigma_i$ = incipient cavitation number
$\tau$ = bubble collapse time

velocity. In addition, noise spectra from 10 to 100 kHz were obtained using a Celesco LC-10 hydrophone mounted in a parabolic reflecting dish on the test section window. Adjustments for natural resonances due to the test section geometry were made on the basis of spectra generated by a calibrated LC-10 source located adjacent to the model. The spectra were analyzed with a Spectral Dynamics SD-360 real time FFT processor. Using two hydrophones permitted simultaneous measurement of noise occurrences and noise level spectra.

Finally, the effect of the velocity and pressure on the sound transmission path was investigated. The temperature of the water used throughout this investigation was approximately 2°C, while the total gas content was roughly 10 parts per million on a molar basis as measured with a van Slyke apparatus. To determine how sound was absorbed by free-stream bubbles as a function of pressure, white noise was projected into the test section through the window opposite the PZT hydrophone. This test was conducted at 7.6 mps (25 fps) since lower pressures are required to support cavitation at correspondingly lower velocities, and hence any effects due to free-stream bubbles should be prevalent under these conditions. Attenuation of less than 1 dB was observed above 10 kHz after lowering the pressure from a state of no cavitation until the cavitation noise itself obscured the projected white noise. Consequently, this effect was ignored.

There were essentially two reasons for high-pass filtering all noise measurements at 10 kHz. First, the water tunnel itself generated so much noise at low frequencies as to render making adjustments for the background noise almost impossible. Second, near-field effects make interpretation of measurements below 10 kHz questionable. The wavelength of sound in water at that frequency is already about 150 mm (6 in.), which is approximately the distance from the region of cavitation to the hydrophone.

## Mathematical Models

The dynamics of a spherical bubble in an incompressible fluid are described by the Rayleigh-Plesset equation [9],

$$R\ddot{R}+\frac{3}{2}\dot{R}^2=\frac{P(R)-P_\infty}{\rho} \tag{3}$$

where $P(R)$ represents the pressure applied by the contents of the bubble to the bubble wall located at radius $R=R(t)$, and $P_\infty$ is the pressure field experienced by the bubble. Very often $P(R)$ is considered to be constant and equal to the vapor pressure of water, $P_v$. This approximation becomes unacceptable only at the very beginning and end of the bubble life cycle where gas content must be considered for small bubble volumes. Also, effects of viscosity and surface tension have been shown to exert only a minor influence on bubble dynamics [22].

Equation (3) yields several analytical expressions describing various stages of growth and collapse for a bubble in a local pressure field defined by $P$. During vaporous bubble growth, it can be shown [23] that the bubble wall velocity remains essentially constant. Thus, setting $\ddot{R}=0$ and $P(R)=P_v$ in equation (3), an approximate formula for the maximum bubble radius $R_M$ is easily derived and given by

$$R_M=s_v\sqrt{\frac{1}{3}\,\frac{\bar{C}_p+\sigma}{\bar{C}_p-1}}, \tag{4}$$

where $s_v$ is the length of the bubble path along which $P<P_v$. It is assumed here that bubble growth occurs only in that region, with the average pressure represented by $\bar{C}_p$.

Even during collapse, the noncondensable gas pressure becomes significant only for $R<<R_M$. However, at this point the bubble wall velocity is so high that it violates the assumption of incompressibility, invalidating Rayleigh's analysis. Nevertheless, Rayleigh calculated the collapse time of a bubble for $P(R)=P_v$ to be

$$\tau=1.3\,\frac{R_M}{V_\infty\sqrt{C_p+\sigma}}. \tag{5}$$

Hickling and Plesset [15] have shown equation (5) to agree within 1 percent of their numerical analysis for a compressible liquid in the absence of any vapor pressure.

In the far field of the bubble, the Rayleigh-Plesset equation provides input for calculating the acoustic pressure [24]

$$p(r,t)=\frac{\rho}{4\pi r}\,\ddot{V}\left(t-\frac{r}{c}\right), \tag{6}$$

where $V=(4/3)\,\pi R^3$ is the bubble volume. Using the Rayleigh-Plesset equation again to derive an asymptotic expression for the radius $R(t)$ of a collapsing bubble for $R<<R_M$, the acoustic pressure becomes

$$p(r,t)\alpha\left(\frac{\rho}{r}\right)V_\infty{}^{6/5}R_M{}^{9/5}(C_p+\sigma)^{3/5}t^{-4/5}. \tag{7}$$

Taking the Fourier transform of equation (7) and squaring the result, the energy density is then

$$S(f)\alpha\left(\frac{\rho}{t}\right)^2V_\infty{}^{12/5}R_M{}^{18/5}(C_p+\sigma)^{6/5}f^{-2/5}. \tag{8}$$

Any noncondensable gas contained in a bubble cushions the collapse and for small amounts of gas the collapsing bubble can rebound into another growth stage. This requires an abrupt change in the movement of the surrounding fluid and produces a compression wave. This compression wave propagates outwards and can possibly form a shock front. Shock formation is caused by nonlinear compressibility effects on sound radiation. It occurs when the initial pulse amplitude is high enough so that the shock is formed before the nonlinear effects are neutralized through geometric attenuation and propagation losses. Assuming that an exponentially shaped shock wave occurs, Baiter [17] followed Whitham's analysis [16] and derived

$$p(r,t)=P_se^{-t/\theta}, \tag{9}$$

to arrive, via the Rayleigh-Plesset equation, at values of $P_s$ and $\theta$ given by

$$P_s=\rho c^2\,\frac{R_M}{r}\left(\frac{P_g}{\rho c^2}\right)^{1/4}\ln\left(\frac{r}{R_m}\right)^{-1/2} \tag{10}$$

and

$$\theta=5.9\,\frac{R_M}{c}\left(\frac{P_g}{\rho c^2}\right)^{1/4}\ln\left(\frac{r}{R_m}\right)^{1/2}. \tag{11}$$

$R_m$ is the minimum radius of the bubble at the instant when rebound occurs, and $P_g$ refers to the gas pressure in the bubble when $R=R_M$. The above relations require $P_g<<P$ for a gas behaving adiabatically with a specific heat ratio equal to 4/3.

Considering again a noncondensable adiabatic gas but accounting for compressibility of the fluid, Esipov and Naugol'nykh [18] used the Kirkwood-Bethe approximation [13] to arrive at an expression in the form of equation (9) where the pressure is again given by equation (10), but now

$$\theta=\frac{R_M}{c}\left(\frac{P_g}{\rho c^2}\right)^{1/4}\left[M^{-3/2}+2\sqrt{2}\ln\left(\frac{r}{R_m}\right)^{1/2}\right]. \tag{12}$$

They define the parameter $M$ as

$$M=\left[\frac{1}{2}+\frac{3P_g{}^{3/4}(\rho c^2)^{1/4}}{P}\right]^{-1} \tag{13}$$

Shock wave pulses are often modelled by an exponential pulse. The energy density spectrum of equation (9) is

$$S(f)=\frac{(P_s\theta)^2}{1+(2\pi\theta f)^2} \tag{14}$$

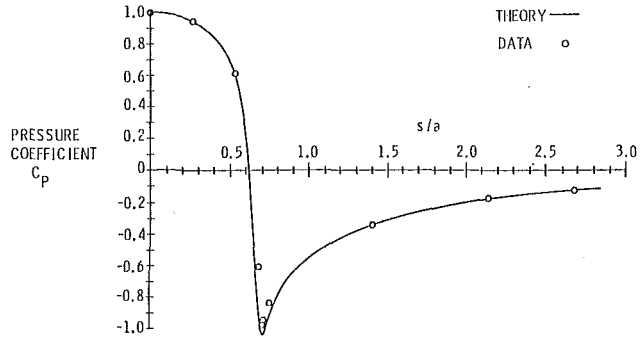


**Fig. 2 Theoretical and experimental pressure distribution of Schiebe nose (uncertainty in $C_p = \pm 0.01$, in $s/a = \pm 0.010$ at 20:1 odds)**

Equation (14) implies a flat spectrum up to a cutoff frequency given by

$$f = \frac{1}{2\pi\theta}. \tag{15}$$

after which the spectrum will roll off as $f^{-2}$. Thus, to find the energy density below the cutoff frequency, it is sufficient to determine

$$S(f) = (P_s\theta)^2. \tag{16}$$

For the range of flow parameters used in this investigation, the bubbles experience pressures between 0.2 and 0.5 atm during their collapse stage. Consequently, the $M^{-3/2}$ term in equation (12) may be neglected for $P_g < 0.001$ atm. In fact, such low gas pressure is required for using equations (9) through (12) because of the assumption that shock formation does indeed occur. Hickling and Plesset [15] showed that, with a pressure of 1 atm forcing collapse, shock formation just barely occurs for an initial gas pressure of 0.01 atm. Higher gas pressures will cushion the collapse sufficiently to prohibit shock formation altogether. Thus, equation (12) becomes almost identical to equation (11) so that the energy density below cutoff becomes, from equation (16),

$$S(f) \approx \frac{\rho}{f^2} R_M{}^4 P_g. \tag{17}$$

## Results and Discussion

No closed-form solution describing the pressure distribution along the surface of a Schiebe headform [25] exists, so a computer-generated solution appears in Fig. 2. The experimental values of $C_p$ appearing in Fig. 2 result from averaging a number of runs through the range of flow velocities. Good agreement between measured and predicted pressure coefficients was obtained.

Figure 3 gives values obtained for the incipient and desinent cavitation number, $\sigma_i$ and $\sigma_d$ versus velocity. The error is often larger at lower velocities where the free-stream pressure must be correspondingly lower to cause cavitation. At those lower pressures, free-stream air bubbles can become large enough to be confused with cavitation on the model.

An interesting feature of Fig. 3 results from a comparison with Fig. 2. Classical theory predicts $\sigma \leq -C_{p_{\min}}$ for vaporous cavitation, implying that vaporous cavitation should not exist for any $\sigma > -C_{p_{\min}}$ as there is then no location on the model where $P \leq P_v$. With $C_{p_{\min}} = -1.0$ on the headform, an alternative type of cavitation above $\sigma = 1.0$ must be suggested to account for the values of $\sigma_i$ and $\sigma_d$ at velocities below 11.4 mps.

The trend for $\sigma_i$ and $\sigma_d$ to decrease with increasing velocity is not uncommon at high air contents such as 10 ppm. At this air content level there are approximately 20 nuclei/cc in the range of 10 to 100 $\mu$m in this tunnel. Since this phenomenon is discussed more thoroughly in reference [26], it is sufficient

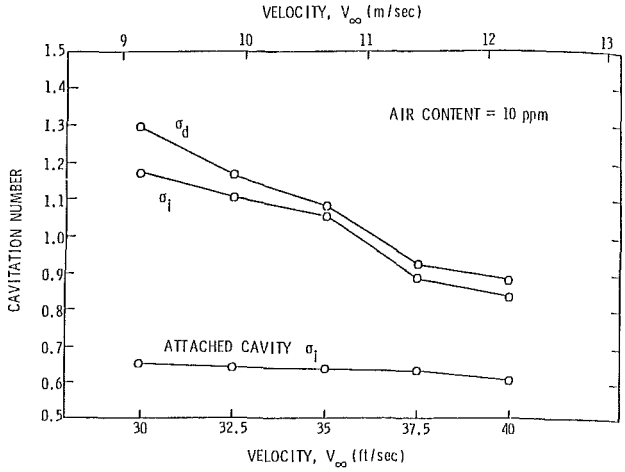


**Fig. 3 Incipient and desinent cavitation numbers (uncertainty in $\sigma_i$ and $\sigma_d = \pm 0.03$, in $V_\infty = \pm 0.1$ at 20:1 odds)**

here to note that the effect of any gas content is to increase the point of inception for decreasing flow velocities.

Data resulting from the high-speed films and videotapes were compared with the equations describing bubble growth and collapse. Photographs show that in most cases the bubbles were asymmetric due to the severe pressure gradients; however, a maximum radius ($R_m$) was determined from the equivalent volume (see reference [21]). Measurements of $R_M$ exceeded the predictions of equation (4) by factors ranging from 2 to 4. It is interesting that Blake et al. [2] performed similar calculations for travelling-bubble cavitation on a hydrofoil and found equation (4) to overestimate their maximum bubble radii by about 20 percent.

A critical parameter in equation (4) is the distance $S_v$ travelled by the bubble where it experiences a local pressure $P < P_v$. Blake's investigation [2] shows $S_v$ to be greater than 30 mm, such that the bubbles have almost attained their maximum radii by the time they leave that low pressure region. For this investigation this low pressure region extends far less than 4 mm along the Schiebe headform. High-speed films show that bubble growth did not usually begin until about the time that the nucleus was leaving the low pressure region, most of the bubbles occurred outside of the boundary layer and most of the bubbles were asymmetric.

Thus it is not surprising that differences occur with equation (4) which represent an asymptotic solution to the Rayleigh-Plesset equation when the bubble experiences a low pressure impulse. Subsequent bubble growth calculations gave a good correlation between $R_m$ and photographic data. More detailed discussions on asymmetric bubble growth and collapse are given in references [27] and [28]. What is not certain is whether equation (4) correctly describes the functional dependence of $R_m$ on $\sigma$ and $C_p$ for cavitation noise correlation despite an inability to predict specific values.

Similarly, measurements of collapse times were compared with the predictions of equation (5). The measured times were generally longer than those calculated using equation (5) by a factor of 2 to 3, while Blake et al. observed collapse times only 15 percent in excess of the predicted values. Air content is one basic difference here; Blake et al. held the air content below 2.5 ppm, but in this investigation it was approximately 10 ppm. Higher air content yields an increased noncondensable gas content which will retard the rate of collapse, while equation (6) assumes the pressure in the bubble to be constant and equal to $P_v$. It is interesting that Harrison [3], observing bubble cavitation in a venturi nozzle where he maintained an air content of about 5 ppm, recorded data for bubble collapse corresponding exactly to Rayleigh's theory.

A second difference is the shape of the pressure curve on the body. The Schiebe headform has a very steep rise in pressure

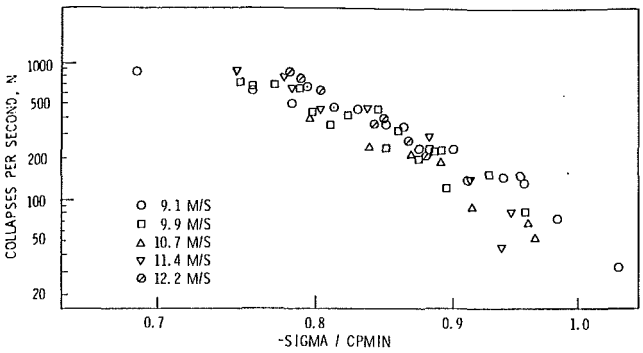


Fig. 4 Rate of bubble collapse versus $-\sigma/C_{p_{min}}$ (uncertainty in $-\sigma/C_{p_{min}} \approx \pm 0.04$)

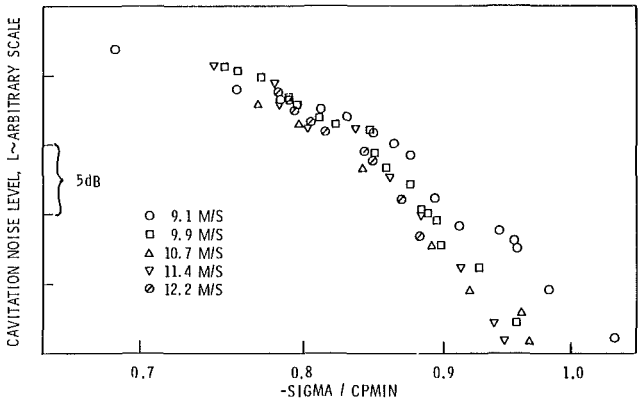


Fig. 5 Noise level versus $-\sigma/C_{p_{min}}$ (uncertainty in $L \approx \pm 2$ dB, in $-\sigma/C_{p_{min}} = \pm 0.04$ at 20:1 odds)

downstream of the location of the minimum pressure. This can be contrasted to a gentle rise in pressure downstream of the location of the minimum pressure on the hydrofoil used by Blake et al. Equation (5) estimates the collapse time on the assumption of an averaged constant pressure; but to be realistic, one must allow for a changing pressure.

The noise radiation per collapse was analyzed by digitizing tape recordings of the cavitation noise and viewing the output on an oscilloscope. Digitization was performed at an effective sampling rate of 200 kHz such that the acoustic signal was analyzed for continuous intervals of 185 msec in real time. For each time segment, the noise level and pressure in the test section were determined by voltages recorded on separate channels, which were sampled immediately before and after every 185 msec interval. Thus, by counting the number of noise bursts occurring in each segment, the manner in which the noise level per collapse depended on the pressure was determined. This procedure was repeated at different velocities.

It should be noted that this measured event rate is not necessarily the same as the number of cavitation bubbles being created at that time. However, acoustic reflections off the tunnel walls were found to be insignificant by observing the response of acoustic impulses generated in the test section. Also, since the noise tests were conducted at velocities between 9.1 and 12.2 mps where the high-speed films and videotapes indicated negligible rebounding action, this factor was ignored. Finally, the collapse of some bubbles may be accompanied by an insignificant sound output, but these cases were assumed to represent anomalous behavior. Thus it may be assumed that the number of noise bursts adequately represents the actual number of cavitation bubbles. More importantly, good relations for the noise per collapse are obtained which can then be compared with the relevant theories. In what follows, it is assumed that each noise burst counted represents a single collapse.

It was initially thought that $\sigma/\sigma_d$, or equivalently $\sigma/\sigma_i$, would serve as an appropriate scaling factor for the noise per collapse. The reason that this is not the case relates to the discussion of why $\sigma_i$ and $\sigma_d$ are not constant in Fig. 3 where predominantly gaseous cavitation was assumed to exist above $\sigma = 1.0$ at all velocities. This does not mean that nuclei with gas pressures as high as 0.1 atm will not give rise to bubbles that will eventually collapse with sufficient violence to generate appreciable sound. After all, for adiabatic expansion the nuclei need only grow to a maximum radius just over three times their initial radius to attain $P_g = 0.001$ atm at $R = R_M$, such that shock formation is almost inevitable. However, since gaseous bubble growth is not nearly as explosive as that of vaporous cavitation, cavitation above $\sigma = 1.0$ may indeed produce negligible sound output. In view of this, it is not surprising that the noise does not scale with $\sigma_d$ or $\sigma_i$. Instead, $-C_{p_{min}}$ was chosen to be the normalization factor since it corresponds in theory to the values of $\sigma$ marking vaporous cavitation inception.

The number of bubble collapses per second and the noise level are plotted in Figs. 4 and 5 against $-\sigma/C_{p_{min}}$, where $-C_{p_{min}}$ seems a reasonable choice for the normalization factor. In fact, the curves for the total noise level in Fig. 5 appear to have collapsed quite well. The somewhat greater scatter associated with the curves in Fig. 4 may simply be a reflection of the difficulties inherent in counting the noise bursts, especially with increasing cavitation activity. The cavitation noise levels measured were greater than the background noise levels by at least 6 dB, hence, no correction for background levels was applied.

The choice of $-C_{p_{min}}$ for the normalizing factor is based on the theory that vaporous cavitation begins at values of $\sigma$ corresponding to less than $-C_{p_{min}}$. To further verify this choice of normalizing factors, a series of tests should be conducted, following the present scenario, with a series of bodies having different values of $-C_{p_{min}}$. Correlation of the results using $-C_{p_{min}}$ would then establish its validity as the proper normalizing factor.

To derive results for the noise level per collapse, $L_c$, the data for each velocity in Fig. 5 were normalized by the corresponding data in Fig. 4. The resulting data are displayed in Fig. 6. The salient feature of Fig. 6 is that the noise per collapse appears to scale with $-\sigma/C_{p_{min}}$ alone, with apparently no contribution from $V_\infty$. Thus, for each free-stream velocity, the functional dependence of the noise on $-\sigma/C_{p_{min}}$ is roughly the same. Additionally, the dependence of $\sigma$ itself on $V_\infty$ is such that for a constant value of $-\sigma/C_{p_{min}}$, the noise per collapse is practically equivalent for any value of $V_\infty$.

Aside from difficulties in counting bursts, another possible reason for the scatter of the data in Fig. 6 is that the conditions in the tunnel change slightly from one run to the next. This was borne out by the different values of both $\sigma_i$ and $\sigma_d$ when measured at different times. An important parameter affecting those results is the statistical nature of the free-stream nuclei, which is known to change significantly even during a single test.

To compare the results of Fig. 6 with the available noise theories, equation (4) was used to describe $R_M$. Here $s_v$ is assumed to be constant, which seems reasonable after inspecting the pressure distribution curve of Fig. 2 for $-\sigma/C_{p_{min}}$ between 0.8 and 0.9. In equation (4), $\bar{C}_p$ was set equal to $C_{p_{min}} = -1.0$, while the high-speed films and videotapes shows $\bar{C}_p = -1/3$ to adequately represent the average pressure experienced by the bubbles during collapse. Employing these values in the classical incompressible noise theory given by equation (8), a comparison is made in Fig. 6 with the experimental results. For the range of $\sigma$ observed in this study, the combination of equations (4) and (8) appear to provide a reasonable model for the functional dependence on $\sigma$. However, equation (8) also predicts the noise per collapse to

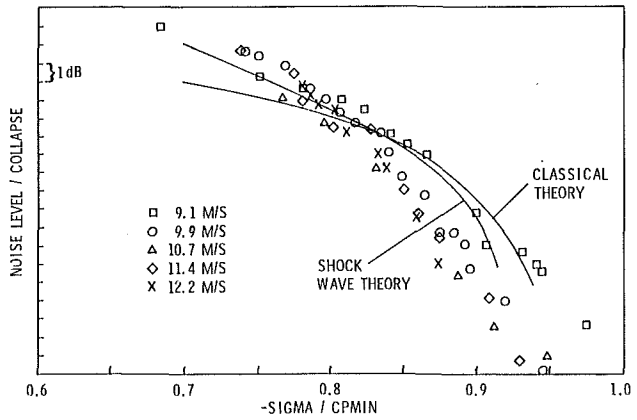


**Fig. 6 Experimental and theoretical noise level per collapse versus $-\sigma/C_{p_{min}}$ (uncertainty in $-\sigma/C_{p_{min}} = \pm 0.04$ at 20:1 odds)**

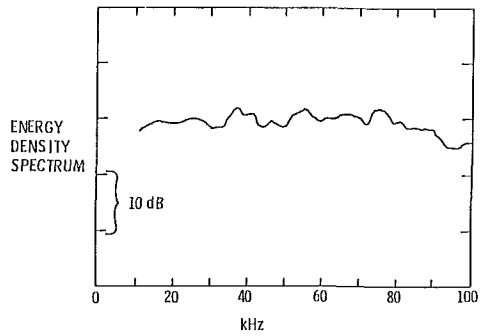


**Fig. 7 Energy density spectrum at $V_\infty = 9.1$ mps, $\sigma = 0.8$ (uncertainty in energy density level $= \pm 2$ dB, in frequency 0 Hz)**

vary as $V_\infty^{2.4}$ for constant $-\sigma/C_{p_{min}}$, a trend which was not revealed in the experimental results of Fig. 6.

Assuming a maximum value for $P_g$ of 0.001 atm and using estimates of $R_M$ from the videotapes, both equations (11) and (12), after insertion in equation (15), show cutoff frequencies lying above 100 kHz in the shock wave spectrum. Hence, equation (16) should be a valid approximation for the two shock wave noise theories. Setting $\bar{C}_p = -1.0$ again in equation (4) and inserting it into equation (17), the two theories are compared with the measured trend in Fig. 6. These models show a more reasonable correlation to the experimental trends of the noise with $\sigma$ than the classical incompressible noise theory. Furthermore, the results indicating that $L_c$ is independent of $V_\infty$ for constant $-\sigma/C_{p_{min}}$ is correctly implied by using the combination of equations (4) and (17).

Quite possibly, equation (4) is inadequate for modelling the actual maximum bubble radii observed in this investigation. Using the videotapes, attempts were made to investigate the dependence of $R_M$ on $\sigma$ and $V_\infty$. Unfortunately, valid results were hampered by difficulties in obtaining radius measurements for any significant range of $\sigma$. These difficulties were due to the limited resolution capabilities of the video system, in addition to the asymmetries of the bubbles in the flow field. Because $R_M$ is a critical parameter in each of the noise theories, it is thus difficult to arrive at a valid appraisal of any of the models given the uncertainty of this parameter as measured in this investigation. Since no other known studies provide this necessary data, equation (4) stands as the only functional approximation of $R_M$, despite its apparent inadequacies.

Constant bandwidth energy density spectra of the cavitation noise were found to be flat from 10 to 100 kHz for all values of $\sigma$ and $V_\infty$. A typical example, after corrections were made for the hydrophone response and tunnel resonances, is shown in Fig. 7. The spectra will increase uniformly in level for decreasing $\sigma$. Morozov [19] proved that the shape of the cavitation noise spectrum is identical to that of a single bubble collapse when the occurrence of noise bursts follows a Poisson distribution. Studies of the tape recordings indeed showed such a distribution to exist.

The low-frequency roll-off predicted by equation (8) was not observed in the spectra. With bubble life times typically around 4 ms, a spectral peak might be expected near .25 kHz such that a roll-off would then be anticipated above 10 kHz. Mellen [11], and more recently Blake et al. [2], reported an $f^{-2}$ trend at frequencies immediately above the spectral peak which was located near the reciprocal of the bubble life time. However, the spectra obtained by Blake et al. appear to rise again to a new plateau following the initial roll-off. Moreover, both Barker [1] and Mellen [11] reported spectra which levelled off after the low-frequency roll-off to a plateau extending from 10 to 100 kHz. Barker also noted that the noise level between 10 and 100 kHz was essentially independent of velocity when $\sigma$ was held constant, even though it increased as $V_\infty^6$ between 1 and 10 kHz. Although the rate of collapse of individual bubbles was not measured in that study, the data were obtained for incipient conditions where the collapse rates should have been comparable. Nevertheless, Barker's results are also supported by Fig. 5.

The presence of a high-frequency spectral plateau implies the existence of pressure pulses, the time constants of which are short compared to the reciprocal of the upper cutoff frequency with spectra described by formulas such as equation (14). That the noise does not increase with $V_\infty$ for constant $-\sigma/C_{p_{min}}$ in the high-frequency regime seems to support the analyses of Baiter and Esipov and Naugol'nykh if one assumes that the maximum bubble radius depends only on $\sigma$. Also, the $\sigma$ dependence of the noise power collapse is predicted reasonably well by the shock wave models.

On the other hand, Barker's results suggest that different mechanisms generate noise at low and high frequencies. Both Mellen and Blake et al. observed spectral behavior supporting the classical model at low frequencies. In addition, the increased velocity dependence at low frequencies reported by Barker is predicted by a comparison of equation (8) to equation (17).

## Summary

An experiment was conducted to determine the bubble dynamics and the resulting high frequency noise above 10 kHz, associated with travelling bubble cavitation on a headform. Where appropriate, the experimental results are compared to available theoretical results. A summary of those results and comparisons is given in the following:

(1) Measurements of maximum bubble radius exceeded the predictions, based on an asymptotic solution to the Rayleigh-Plesset equation, by factors ranging from 2 to 4,

(2) Measurements of bubble collapse times were longer than those calculated by a factor of 2 to 3, based on an asymptotic solution to the Rayleigh-Plesset equation,

(3) The travelling bubble cavitation noise per collapse does not scale with $\sigma_i$ or $\sigma_d$, but instead with $C_{p_{min}}$, since gaseous cavitation is present at certain conditions,

(4) Classical incompressible noise theories provide a crude model for the functional dependence of noise level above 10 kHz per collapse on $\sigma$,

(5) Shock wave noise theories provide a reasonable model for the functional dependence of noise level per collapse above 10 kHz on $\sigma$,

(6) Travelling bubble cavitation noise level per bubble above 10 kHz is independent of velocity for constant $\sigma$,

(7) Classical incompressible noise theories do not predict a flat noise spectrum from 10 kHz to 100 kHz as was measured

but shock wave noise theories do predict such a spectral shape, and

(8) Classical incompressible noise theories show a velocity to the 2.4 power dependence for noise levels per bubble while shock wave noise theories show the noise level per bubble to be independent of velocity, as was measured.

## Acknowledgment

This work was performed at the Applied Research Laboratory under the sponsorship of the Naval Sea Systems Command. The authors would also like to acknowledge the helpful comments of Mr. H.-J. Baiter at the Fraunhofer Institut für Hydroakustik, Ottobrunn, West Germany.

## References

1 Barker, S. J., "Measurements of Radiated Noise in the Caltech High-Speed Water Tunnel – Part II: Radiated Noise From Cavitating Hydrofoils," Graduate Aeronautical Laboratories, California Institute of Technology, Mar. 1975.

2 Blake, W. K., Wolpert, M. J., and Geib, F. E., "Cavitation Noise and Inception as Influenced by Boundary Layer Development on a Hydrofoil," *Journal of Fluid Mechanics*, Vol. 80, May 23, 1977, pp. 617–640.

3 Harrison, M., "An Experimental Study of Single Bubble Cavitation Noise," *Journal of the Acoustical Society of America*, Vol. 24, Nov. 1952, pp. 776–782.

4 Mellen, R. H ., "An Experimental Study of the Collapse of a Spherical Cavity in Water," *Journal of the Acoustical Society of America*, Vol. 28, May 1956, pp. 447–454.

5 Chahine, G. L., Courbiere, P., and Garnaud, P., "Correlation Between Noise and Dynamics of Cavitation Bubbles," 6th Conference on Fluid Machinery, Budapest, Sept. 1979.

6 Hentschel, W., "Acoustic and Optical Investigation on the Dynamics of Holographically Generated Cavitation Bubble Systems," Ph.D. thesis, Third Physical Institute of the Universität, Göttingen, 1979.

7 Rayleigh, L. (Strutt, J. W.), "On the Pressure Developed in a Liquid During the Collapse of a Spherical Cavity," *Philosophical Magazine*, Vol. 34, Aug. 1917, pp. 94–98.

8 Besant, W. H., *Hydrostatics and Hydrodynamics*, Art. 158, London, Cambridge University Press, 1859.

9 Plesset, M. S., "The Dynamics of Cavitation Bubbles," ASME *Journal of Applied Mechanics*, Sept. 1949, pp. 277–282.

10 Fitzpatrick, H. M., and Strasberg, M., "Hydrodynamic Sources of Sound," *1st Symposium on Naval Hydrodynamics*, Publication 515, Sept. 1956.

11 Mellen, R. H., "Ultrasonic Spectrum of Cavitation Noise in Water," *Journal of the Acoustical Society of America*, Vol. 26, May 1954, pp. 356–360.

12 Blake, W. K., and Sevik, M. M., "Recent Developments in Cavitation Noise Research," ASME *International Symposium on Cavitation Noise*, Winter Annual Meeting, Phoenix, AZ, Nov. 14–19, 1982.

13 Kirkwood, J. G., and Bethe, H. A., "The Pressure Wave Produced by an Underwater Explosion," National Defense Research Committee of the Office of Scientific Research and Development, Report 588, 1942.

14 Gilmore, F. R., "The Growth and Collapse of a Spherical Bubble in a Viscous Compressible Liquid," California Institute of Technology, Report 26-4, 1952.

15 Hickling, R., and Plesset, M. S., "Collapse and Rebound of a Spherical Bubble in Water," *Physics of Fluids*, Vol. 7, Jan. 1964, pp. 7–14.

16 Whitham, G. B., "On the Propagation of a Weak Shock Wave," *Journal of Fluid Mechanics*, Vol. 1, 1956, pp. 290–38.

17 Baiter, H.-J., "Aspects of Cavitation Noise," *Proceedings of Symposium on High Powered Propulsion of Ships*, Wageningen, The Netherlands, Dec. 1974.

18 Esipov, I. B., and Naugol'nykh, K. A., "Collapse of a Bubble in a Compressible Liquid," *Soviet Physics-Acoustics*, Vol. 19, 1973, pp. 187–188.

19 Morozov, V. P., "Cavitation Noise as a Train of Sound Pulses Generated at Random Times," *Soviet Physics-Acoustics*, Vol. 14, 1969, pp. 361–365.

20 Gates, E. M., and Billet, M. L., "Cavitation Nuclei and Inception," *Proceedings of the 10th Symposium of the IAHR*, Tokyo, Japan, Sept. 1980.

21 Hamilton, M. F., "Trvelling-Bubble Cavitation and Resulting Noise," M.S. thesis, Acoustics Dept., The Pennsylvania State University, May 1981.

22 Ivany, R. D., and Hammitt, F. G., "Cavitation Bubble Collapse in Viscous, Compressible Liquids – Numerical Analysis," ASME *Journal of Basic Engineering*, Vol. 87, Dec. 1965, pp. 977–985.

23 Ross, D., *Mechanics of Underwater Noise*, New York, Pergamon Press, 1976, p. 206.

24 Fitzpatrick, H. M., "Cavitation Noise," *2nd Symposium on Naval Hydrodynamics*, ACR-38, Aug. 1958.

25 Schiebe, F. R., "Measurements of the Cavitation Susceptibility of Water Using Standard Bodies," St. Anthony Falls Hydraulic Laboratory, University of Minnesota, Report No. 118, Feb. 1972.

26 Holl, J. W., "An Effect of Air Content on the Occurrence of Cavitation," ASME *Journal of Basic Engineering*, Vol. 82, Dec. 1960, pp. 941–946.

27 Knapp, R. T., Daily, J. W., and Hammitt, F. G., *Cavitation*, McGraw-Hill, New York, 1970.

28 Hammitt, F. G., *Cavitation and Muliphase Flow Phenomena*, McGraw-Hill, New York, 1980.

**Myung Kyoon Chung**
Associate Professor.

**Hyung Jin Sung**[1]

**Kye Bock Lee**
Research Assistant.

Department of Mechanical Engineering,
Korea Advanced Institute of
Science and Technology,
Seoul, Korea

# Computational Study of Turbulent Gas-Particle Flow in a Venturi

*A "two-fluid" model has been applied to predict turbulent dilute gas-particle flow through a Venturi tube. Bulk motion of particles is considered as a secondary fluid flow which exchanges mass and momentum with the primary conveying air stream. Closure of the time-averaged equations is achieved by modelling turbulent second-order correlations with an extended mixing-length theory. Proposed closure model is found to aptly simulate the dependency of the static pressure drop on the particle size, flow rate and the loading ratio.*

## 1 Introduction

Measurement of particle feedrates in gas-particle turbulent flows is frequently encountered in the energy-related industries. For example, pneumatic transport of pulverized coal to boiler needs accurate information in order to control combustion economy. The Venturimeter was expected to be potentially attractive device as a flow meter because of its simplicity and versatility. Previous studies and applications of the two phase Venturimeter are briefly summarized by Sharma and Crowe [1].

The experimental study on the applicability of the Venturimeter as a device for measuring particle flow rate was originated by Carlson, Frazier, and Engdahl [2]. A more extensive experimental study was undertaken by Farbar [3], who developed a simple model for measuring the pressure drop. Recently, Lee and Crowe [4] carried out experiments to find a scaling law of the Venturimeter for a dilute gas-particle flow. They identified the Stokes number and gas particle loading ratio as key scaling parameters.

As a numerical analysis of gas-particle flows, Sharma and Crowe [1] have developed an implicit quasi one-dimensional numerical scheme for dilute gas-particle flow (CONVAS). In this case, governing equations are written in conservative forms for mass, momentum and energy with gas velocity, temperature and pressure as the dependent variables. The mass and momentum coupling terms due to the presence of particles in the gas flow appear as source terms to the gaseous phase. The Stokesian drag force due to the velocity difference between gas and particles was considered as a dominant source term to the gaseous momentum. Wall friction was assumed negligible in the momentum transfer process of the gaseous phase. Lee and Crowe [4] extended the one-dimensional CONVAS model to a two-dimensional case for gas-particle flow. This approach, called PSI cell (Particle Source In cell) model, is also based on treating the particles as sources of mass and momentum to the gaseous phase.

Another approach to modelling gas-particle flows is to regard the conveying gas phase (primary fluid) and particle phase (secondary fluid) as two interactive fluids which exchange momentum, energy and mass with each other. There are, however, prevailing controversies in physical modelling about the pressure gradient and the constitutive relations in the secondary fluid, which results in several different derivations of the "two-fluid" equation [5–8]. A brief summary on the previous applications of the "two-fluid" equations is given by Crowe [9].

Marble [10] has formulated two-fluid momentum equations for a dilute suspension based on the collisionless Boltzman equation for the evolution of the distribution function describing the particle cloud in the following forms:

(primary fluid)

$$\rho_f \frac{\partial u_i}{\partial t} + \rho_f u_j \frac{\partial u_i}{\partial x_j} = -\frac{\partial p}{\partial x_i} + \frac{\partial \tau_{ij}}{\partial x_j} + F_{pi}$$

(secondary fluid)

$$\bar{\rho}_p \frac{\partial v_i}{\partial t} + \bar{\rho}_p v_j \frac{\partial v_i}{\partial x_j} = -F_{pi} + \frac{\partial S_{ij}}{\partial x_j} ,$$

where $F_{pi}$ is the force per unit volume due to interaction between two phases and $S_{ij}$ is the stress tensor due to particle motion at velocities different from the local mean.

Melville and Bray [11] applied these equations to a turbulent free jet of dilute gas-particle mixture. Providing that $\bar{\rho}_p/\rho_f$ is in the order of unity and that the Stokesian relaxation time scale, $t^*(=\rho_s d_p^2/18\mu)$, is of the same order as turbulent time scale of the primary fluid, they assumed that the mean velocities of the primary fluid and the secondary fluid are the same; thus, $F_{pi}=0$. Choi and Chung [12] extended and modified Melville and Bray's [11] model in order to apply it to a wall-bounded shear flow. They also assumed that the relative velocity between the two phases was negligible. In developing flows, however, the relative velocity is not zero and the time scale ratio, $t^*/t_l$, varies widely depending on the locations. Therefore, the Stokesian drag force, which is a principal contributor to $F_{pi}$, plays an important role in the momentum transfer process.

Basic assumption in modelling eddy viscosity of the primary

[1]Present address: Assistant Professor, Department of Mechanical Engineering, Korea Institute of Technology.

Contributed by the Fluids Engineering Division and presented at the International Symposium on Gas-Solid Flow, Atlanta, Ga., May 12–14, 1986. Manuscript received by the Fluids Engineering Division, January 24, 1984.

fluid in [11] and [12] is the local equilibrium between the rate of turbulence energy production and its dissipation. But, the balance equation for the local equilibrium was intuitively formulated. A theoretical budget equation of the turbulence kinetic energy has been developed by Elghobashi and Abou-Arab [13].

Purpose of the present study is to carry out a numerical analysis for a gas-particle flow in a Venturi solving the "two-fluid" model equations with further modification and refinement of the previous extended mixing-length model [12]. The numerical results are compared with Farbar's and Lee and Crowe's experimental data, particularly about the dependency of the static pressure drop on the particle size, flow rate and the loading ratio.

## 2 Physical Models for Gas-Particle Flows

A dilute gas-particle flow is a flow in which a particle motion is controlled by local aerodynamic forces. In the "two-fluid" model, bulk motion of the particles is considered as a continuum, and both phases are regarded as two mutually interacting fluids. Governing equations for both phases are closely coupled with each other through mass, momentum and energy source terms.

The mean continuity equations, and volume-averaged momentum equations for the primary and secondary fluids, neglecting gravity force, added mass effect of the accelerated fluid and Basset forces, are given by [14] in two-dimensional cylindrical coordinates, as follows:

(primary fluid)

$$\frac{\partial \bar{U}_f}{\partial x}+\frac{1}{r}\frac{\partial}{\partial r}(r\bar{V}_f)=0 \tag{1}$$

$$\bar{\rho}_b\bar{U}_f\frac{\partial \bar{U}_f}{\partial x}+\bar{\rho}_b\bar{V}_f\frac{\partial \bar{U}_f}{\partial r}=-\frac{\partial P}{\partial x}+\bar{\rho}_b\frac{1}{r}\frac{\partial}{\partial r}\left[r\left(\nu_{fl}\frac{\partial \bar{U}_f}{\partial r}-\overline{u_f'v_f'}\right)\right]+F_{pi} \tag{2}$$

(secondary fluid)

$$\bar{U}_p\frac{\partial \bar{\rho}_p}{\partial x}+\bar{V}_p\frac{\partial \bar{\rho}_p}{\partial r}=-\frac{1}{r}\frac{\partial}{\partial r}(r\overline{\rho_p'v_p'})-\bar{\rho}_p\frac{\partial \bar{U}_p}{\partial x}-\frac{\bar{\rho}_p\bar{V}_p}{r}-\bar{\rho}_p\frac{\partial \bar{V}_p}{\partial r}-\frac{\partial}{\partial x}(\overline{\rho_p'v_p'}) \tag{3}$$

$$\bar{\rho}_p\bar{U}_p\frac{\partial \bar{U}_p}{\partial x}+\bar{\rho}_p\bar{V}_p\frac{\partial \bar{U}_p}{\partial r}=-\alpha\frac{\partial p}{\partial x}+\frac{1}{r}\frac{\partial}{\partial r}\left[r\bar{\rho}_p\left(\nu_{pl}\frac{\partial \bar{U}_p}{\partial r}-\overline{u_p'v_p'}\right)\right]-\frac{1}{r}\frac{\partial}{\partial r}(r\bar{U}_p\overline{\rho_p'v_p'})-F_{pi} \tag{4}$$

$$\bar{\rho}_p\bar{U}_p\frac{\partial \bar{V}_p}{\partial x}+\bar{\rho}_p\bar{V}_p\frac{\partial \bar{V}_p}{\partial r}=-\frac{1}{r}\frac{\partial}{\partial r}(2r\bar{V}_p\overline{\rho_p'v_p'})-\frac{\partial}{\partial x}(\bar{V}_p\overline{\rho_p'u_p'})-\frac{\partial}{\partial x}(\bar{\rho}_p\overline{u_p'v_p'})-\frac{\partial}{\partial x}(\bar{U}_p\overline{u_p'v_p'})-\frac{1}{t^*}[(\bar{V}_p-\bar{V}_f)\bar{\rho}_p] \tag{5}$$

It is assumed that the secondary fluid consists of particles of spherical shape and uniform size, and also the effect of inter-particle collisions are neglected. If the volume fraction ($\alpha = \bar{\rho}_p/\rho_s$) is large, the bulk density of the primary fluid $\bar{\rho}_b = \rho_f(1-\alpha)$ should be considered as a variable. However, for the case at hand, $\alpha$ is about $3\times10^{-3}$. Therefore, the bulk density of the primary fluid can be assumed to be constant (i.e., $\bar{\rho}_b = \rho_f$), whereas, the dispersed particle density ($\bar{\rho}_p$) is treated as a variable [11].

For the particle Reynolds number less than 700, $F_{pi}$ can be written as the forms [1, 14],

$$F_{pi}=(\bar{U}_p-\bar{U}_f)\frac{\bar{\rho}_p}{t^*}(1+0.15\ \mathrm{Re}_p^{0.687}) \tag{6}$$

In the above equations (1)–(5), the upper cases $U$ and $V$ denote the mean velocity components in the axial and the radial directions, respectively. Primed lower cases $u'$ and $v'$ are the fluctuating turbulent velocity components and subscripts $f$ and $p$ refer to the primary fluid and secondary (particle) fluid, respectively. $\nu_{fl}$ and $\nu_{pl}$ stand for the laminar

## Nomenclature

$A_d$ = cross-sectional area of the pipe
$A_f$ = cross-sectional area of the computed flow
$a,b,C_{p\epsilon}$ = model constants
$D$ = Van Driest damping function
$d_p$ = particle diameter
$F_{pi}$ = Stokesian drag force, equation (6)
$F'$ = retarding force per unit length exerted by the wall, equation (18)
$l_f$ = characteristic length scale for primary fluid flow
$\dot{m}$ = mass flow rate of fluid, equation (18)
$p$ = static pressure
$R$ = pipe radius
$r$ = radial distance from the pipe axis
Re = Reynolds number based on pipe diameter
$\mathrm{Re}_p$ = particle Reynolds number ($\mathrm{Re}_p = |\bar{U}_p-\bar{U}_f|d_p\rho_f/\mu$)
St = Stokes number (St = $\rho_s^2 d_p\bar{U}_f/36\,\mu R$)
$t^*$ = Stokesian relaxation time scale
$t_l$ = Lagrangian integral time scale
$u',v'$ = fluctuating velocity components in axial and radial directions
$\bar{U},\bar{V}$ = averaged mean velocity components in axial and radial directions
$u$ = reference value of velocity, equation (18)
$\alpha$ = volume fraction ($=\bar{\rho}_p/\rho_s$)
$\delta_{.99}$ = boundary layer thickness
$\epsilon_f,\epsilon_{f0},\epsilon_p$ = kinematic eddy viscosity
$\nu_{fl},\nu_{pl}$ = kinematic laminar viscosity
$\kappa,\lambda$ = model constants
$\bar{\rho}_b$ = bulk density of primary fluid ($\bar{\rho}_b=\rho_f(1-\alpha)$)
$\bar{\rho}_p$ = average density of secondary fluid defined by average mass of particles per unit volume

**Subscripts**

*eff* = effective
$f$ = primary fluid
$l$ = laminar
0 = of clean fluid
$p$ = particle laden, or secondary fluid
$s$ = solid

kinematic viscosity of the primary fluid and the virtual laminar kinematic viscosity of the secondary fluid [12]. Among the turbulence correlation terms in the above differential equations, the second order terms, $\overline{u_f'v_f'}$, $\overline{u_p'v_p'}$, $\overline{\rho_p'v_p'}$ and $\overline{\rho_p'u_p'}$ are known to be predominant over molecular contributions to momentum and mass transfer for high Reynolds number flows. Third-order diffusive transport terms, $\overline{\rho_p'u_p'v_p'}$ and $\overline{\rho_p'v_p'^2}$, have been omitted in equations (4) and (5), respectively, simply due to lack of information.

As a simple gradient turbulence model at first-order closure level, the Boussinesq eddy viscosity models are applied,

$$\overline{u_f'v_f'} = -\epsilon_f \frac{\partial \bar{U}_f}{\partial r}, \quad \overline{u_p'u_p'} = -\epsilon_p \frac{\partial U_p}{\partial r} \qquad (7), (8)$$

$$\overline{\rho_p'v_p'} = -\frac{\epsilon_p}{\sigma_\phi}\frac{\partial \bar{\rho}_p}{\partial r}, \quad \overline{\rho_p'u_p'} = -\frac{\epsilon_p}{\sigma_\phi}\frac{\partial \bar{\rho}_p}{\partial x} \qquad (9), (10)$$

where $\epsilon_f$ is the scalar eddy viscosity of the primary fluid, $\epsilon_p$ is that of the secondary fluid, and $\epsilon_p/\sigma_\phi$ is an eddy diffusivity of the secondary fluid. The Schmidt number, $\sigma_\phi$, of 0.7 is selected as was used by Melville and Bray [11]. Turbulence models for the scalar eddy viscosities, $\epsilon_f$ and $\epsilon_p$, were developed and tested successfully in a wall-bounded pipe flow of Choi and Chung [12], thus, similar modelling method is adopted in the present study.

Owen [15] states that the presence of solid particles decreases the eddy viscosity of the primary fluid arising from dissipation of turbulence energy at the interface between solid particles and the fluid. In order to derive a formula for scalar eddy viscosity, $\epsilon_f$, in the particle laden flow, he considered a state of local equilibrium between the production and the rate of dissipation of the turbulent kinetic energy. It was assumed that the turbulent kinetic energy is generated only by the primary fluid, but it is dissipated by both the primary and the secondary fluids.

However, according to the Boothroyd's [14] experimental observations, the production of the turbulent kinetic energy by the secondary fluid is also significant, and Choi and Chung proposed the eddy viscosity as follows:

$$\frac{\epsilon_f}{\epsilon_{f_0}} = \left[\frac{1+\dfrac{\bar{\rho}_p}{\rho_f}\dfrac{\epsilon_p}{\epsilon_f}}{1+\dfrac{\bar{\rho}_p}{\rho_f}}\right]^{1/2} \qquad (11)$$

This model was derived from a balance equation based on crude physical models for the rates of production and dissipation by both fluids.

Recently, a theoretical approximate balance equations for $k$ and $\epsilon$ in the gas-particle flow have been derived by Elghobashi and Abou-Arab [13]. It turns out that the turbulent kinetic energy production by the secondary fluid is proportional to

$$\rho_f \epsilon_f \left(\frac{k}{\epsilon}\right)\frac{d}{dr}\left[\epsilon_f \frac{d}{dr}\left(\frac{\bar{\rho}_p}{\rho_s}\right)\right]\left(\frac{d\bar{U}}{dr}\right)^2,$$

and that the turbulent kinetic energy of the primary fluid is dissipated by the relative motion between two phases as well as by the primary fluid itself. Applying the simple mixing length model to terms of the approximate equations for $k$ and using the isotropic approximations, $k = 3/2u_f^2$ and $\epsilon = 0.08k^{3/2}/l_f$, the following balance equation may be obtained.

$$\rho_f u_f l_f\left[1+1.02l_f^2\frac{d^2(\bar{\rho}_p/\rho_s)}{dr^2}\right]\left(\frac{d\bar{U}}{dr}\right)^2 = 0.147\rho_f\frac{u_f^3}{l_f} + C_{p\epsilon}\frac{\bar{\rho}_p}{t^*}u_f(u_f-u_p) \qquad (12)$$

where, $u_f$ and $u_p$ are the turbulent characteristic velocity scales for the primary and secondary fluids, and $l_f$ is the length scale for the primary fluid. The model constant of $C_{p\epsilon}$ is in the order of unity.

$$\epsilon_f = u_f l_f, \quad \epsilon_{f_0} = l_f^2\left|\frac{d\bar{U}}{dr}\right|,$$

and equation (12), the ratio of the scalar eddy viscosity in the particle laden flow to that in the clean flow is,

$$\frac{\epsilon_f}{\epsilon_{f_0}} = \left[\frac{1+1.02l_f^2\dfrac{d^2}{dr^2}\left(\dfrac{\bar{\rho}_p}{\rho_s}\right)}{1+C'_{p\epsilon}\dfrac{\bar{\rho}_p}{\rho_f}\dfrac{t_l}{t^*}\left(1-\dfrac{\epsilon_p}{\epsilon_f}\right)}\right]^{1/2} \qquad (13)$$

where $C'_{p\epsilon}$ is a model constant to be determined and $t_l$ is the Lagrangian integral time scale. For a case when $\bar{\rho}_p/\rho_s << 1$, the second term in the numerator in equation (13) may be neglected.

The eddy viscosity of the clean fluid flow without suspension of solid particles, $\epsilon_{f0}$, is estimated by the following conventional mixing length model.

$$\epsilon_{f_0} = \kappa^2(R-r)^2D^2\left|\frac{dU}{dr}\right| \quad \text{for } (R-r) < \frac{\lambda\delta_{.99}}{\kappa} \qquad (14)$$

$$= \nu_{fl}a\mathrm{Re}^b \quad \text{for} (R-r) > \frac{\lambda\delta_{.99}}{\kappa} \qquad (15)$$

where $D$ is the Van Driest damping function, and model constants are; $a = 0.005$, $b = 0.9$, and $\kappa = 0.41$. The boundary layer thickness, $\delta_{.99}$, is replaced by the local pipe of radius $R$ and $\lambda$ is selected so that the numerical value of $\epsilon_{f_0}$ should be matched smoothly between equation (14) and (15) at their interfaces.

The eddy viscosity of the secondary fluid, $\epsilon_p$, has been expressed in various ways by previous researchers [16, 17]. The following form (16) proposed by Choi and Chung [12] turned out to yield more correct results for the pressure drop in this particular study.

$$\frac{\epsilon_p}{\epsilon_f} = \frac{1}{1+\left(\dfrac{t^*}{t_l}\right)^2} \qquad (16)$$

The turbulent time scale $t_l$ is estimated by a relation, $t_l = l_f^2/\epsilon_f$. Equation (16) is valid only for high turbulent Reynolds number flow. The equation (16) predicts that $\epsilon_p/\epsilon_f$ becomes smaller near the wall region, which is in contradiction to Soo's [18] theoretical and experimental observations of solid-boundary effect which asserts that $\epsilon_p/\epsilon_f$ is nearly constant across the stream. Accordingly, as in Choi and Chung [12], we assumed that $\epsilon_p/\epsilon_f$ in the inner region has a constant value which is same as that in the outer region.

Near the wall region, a model of the virtual laminar kinematic viscosity of the secondary fluid, $\nu_{pl}$ introduced by Choi and Chung [12] is also used in the following form,

$$\frac{\nu_{pl}}{\epsilon_p} = \frac{\nu_{fl}}{\epsilon_f} \qquad (17)$$

## 3 Numerical Procedure

A forward marching technique by Patankar and Spalding [19] is used to solve the governing parabolic differential equations. Each equation is transformed by a streamfunction derived from the continuity equation of the primary fluid (von Mises transformation).

Since we do not know how the distributions of velocity will change during the forward marching step, the pressure gradient in equations of the primary and secondary fluids can not be determined a priori. In the Patankar and Spalding scheme,

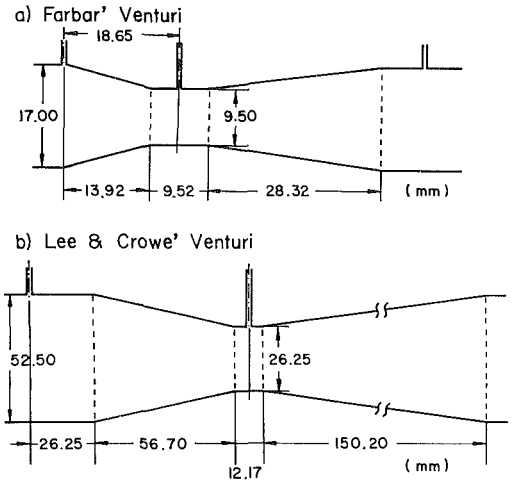


Fig. 1 Geometric details of experimental Venturis, (a) Farbar; (b) Lee and Crowe

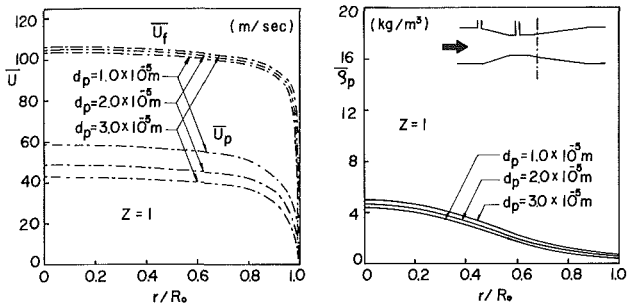


Fig. 2 Predicted distributions of $\bar{U}_p$, $\bar{U}_f$, and $\bar{\rho}_p$ at the diffuser section in a Venturi as a function of particle diameter (for $z = 1$)

the pressure gradient is estimated from the information in the previous calculation step. Then, the momentum equation is solved for the next downstream step. After computation is completed, the nondimensional coordinate $\omega$, which is normal to the marching direction, is converted to physical coordinate, i.e., radial coordinate $r$. In this case, due to the approximate estimation of the pressure gradient, the computed boundary, $R_f$, which corresponds to $\omega = 1$, is not coincident with the physical boundary, $R_d$. In order to minimize such discrepancy, Patankar and Spalding [19] proposed the following form to estimate the pressure gradient.

$$\frac{dp}{dx} = -\frac{F'}{A_d} - \frac{\dot{m}\bar{u}}{A_d^2}\frac{dA_d}{dx} \tag{18}$$

where $F'$ is the retarding force per unit length exerted by the wall, and $A_d$ stands for the cross-sectional area of the pipe. The term $dA_d/dx$ can be calculated from

$$\frac{dA_d}{dx} = \frac{A_{d,D} - A_{f,U}}{\Delta x} = \frac{[(A_{d,D} - A_{d,U}) + (A_{d,U} - A_{f,U})]}{\Delta x} \tag{19}$$

where, $A_f$ stands for the cross-sectional area of the computed flow. Subscripts $D$ and $U$ denote downstream and upstream conditions.

The initial velocity profiles of the primary and secondary fluids at the inlet of a Venturi are assumed to be fully developed with the same velocity distributions. By summation of equation (2) and (4), the following relation is obtained for the case in which $\bar{U}_f = \bar{U}_p$ [20],

$$\frac{dp}{dx} = \frac{1}{r}\frac{d}{dr}\left[(\epsilon_{eff,f} + \epsilon_{eff,p})r\frac{d\bar{U}}{dr}\right] \tag{20}$$

where $\epsilon_{eff}$ is the effective eddy viscosity and is defined as the laminar kinematic viscosity plus the turbulent eddy viscosity. From this relation, the fully developed velocity profile is obtained by substituting the turbulent models (13–16) and by integrating the equations with an assumed $dP/dx$ estimated from Choi and Chung [12]. The initial particle density profile at the inlet of the Venturi is assumed to be uniform across the section and is taken from the given particle loading, $\bar{\rho}_p = z\bar{\rho}_f$. The boundary conditions at the wall for the primary fluid are $\bar{U}_f = \bar{V}_f = 0$. And those for the secondary fluid are assumed to be $\bar{V}_p = 0$, $d\bar{\rho}_p/dr = 0$ (as in Di Giacinto et al. [8]) and $(d\bar{U}_p/dr)_{\text{wall}} = (d\bar{U}_f/dr)_{\text{wall}}$. A reason of this last boundary condition is explained as follows. Since the particles are known to slip over the wall surface [14], $\bar{U}_p$ does not vanish at the wall. Another logical choice may be such that its gradient is zero at the wall. However, our basic assumption is that the overall pressure drop is due to the secondary fluid flow over the wall as well as due to the primary air flow. If the velocity gradient of the secondary fluid is assumed to be zero, our mixing length model would negate any contribution of the secondary fluid to the overall pressure drop, which is in contradiction to our basic assumption. Although the particles and the air flows are not in kinetic equilibrium, the boundary condition for $\bar{U}_p$ assumed above may be a reasonable choice between the two logical extremes, $\bar{U}_p = 0$ and $d\bar{U}_p/dr = 0$.

**Table 1**

| Particle diameter (micron) | Mass (percent) |
|---|---|
| 4.84 | 2.5 |
| 7.43 | 5.5 |
| 11.45 | 6.0 |
| 19.03 | 10.8 |
| 29.42 | 40.2 |
| 43.26 | 32.5 |
| 76.60 | 2.5 |

## 4 Computational Results and Discussions

In order to access the computational accuracy of our theory, experiments by Farbar [3] and Lee and Crowe [4] are numerically analyzed. The geometrical details of both experimental Venturis are shown in Fig. 1. The solid particles used in Farbar's experiment are powdered alumina silica whose specific gravity is 2.45. A discretized particle size distribution used in the CONVAS [4] is also adopted in the present computation. For Lee and Crowe's experiment, the solid particles are spherical glass beads (specific gravity is 2.90) whose discrete size distribution is given in Table 1.

Figure 2 shows representative profiles of $\bar{U}_p$, $\bar{U}_f$, and $\bar{\rho}_p$, depending on the variation of the particle size. The mean velocity profile of the secondary fluid is much more dependent on the particle size than that of the primary fluid is. It may be seen that the secondary fluid flows substantially slower than the primary fluid and that the dispersed particle density $\bar{\rho}_p$ is higher in the core region. The slip velocity of the particles at the wall turns out to be about 2.8 ~ 4.0 m/s, which is about 10 percent to the centerline particle velocity.

Figure 3 illustrates the effect of particle size on the pressure drop, which is obtained by a series of computations with a single particle size. The pressure drop due to the particles is strongly dependent on smaller particles, but the pressure drop in the limit $d_p \to 0$ is less than that predicted by CONVAS. The influence of the loading ratio $z$ on the pressure drop is also shown in Fig. 3. As noted by Sharma and Crowe [1] for incompressible equilibrium flow (Stokes number equals to zero), the augmented nondimensional pressure is nearly proportional to the loading ratio $z$. A nondimensional pressure drop versus the loading ratio at the throat is plotted for various air flowrates in Fig. 4, which shows that the Venturi flowmeter is a convenient linear device for the measurement of particle flowrates. The slope of the straight line is sensitive to the model constant $C'_{p\epsilon}$ in equation (13); here, $C'_{p\epsilon} = 0.7$ which

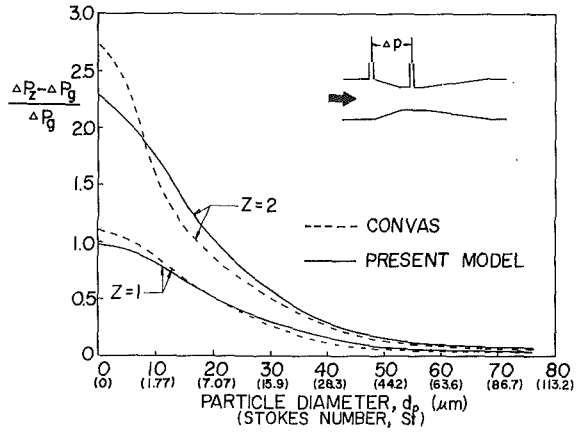


Fig. 3 Comparisons of predicted pressure drop ratios by present model with those by CONVAS [1]

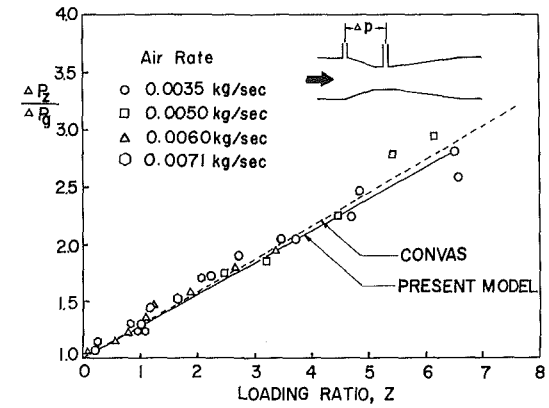


Fig. 4 Comparisons of predicted pressure drop ratios with experiment. Predictions: — — —, CONVAS; ———, Present model. Symbols: data of Farbar [3]

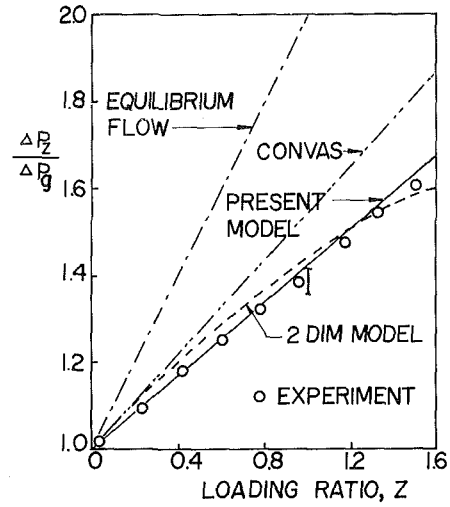


Fig. 5 Comparisons of predicted pressure drop ratios with experiment. Predictions: —·—·—, Equilibrium flow model; — — — —, Two dimensional model by Lee and Crowe [4]; —··—··—, CONVAS; ———, Present model. Symbol o, data of Lee and Crowe [4], experimental uncertainty 5 percent.

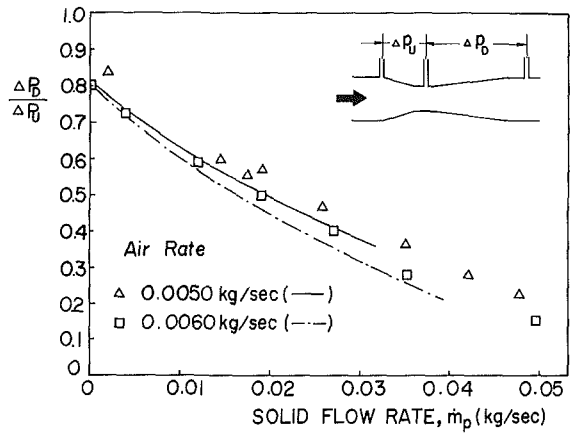


Fig. 6 Comparisons of predicted pressure recovery with experiment Curves; Prediction by present model. Symbols, data of Farbar [3]

is chosen such that best agreement be obtained between theory and experiments.

Figure 5 shows comparison between Lee's [4] experiments for low loading ratios and various theories. It is noted that the incompressibility assumption does not give any nonlinearity in the result for the pressure drop vs loading ratio as has been explicitly indicated in Lee and Crowe [4] and Sharma and Crowe [1]. From both Figs. 4 and 5, it turns out that the overall accuracy of the present model is better than other theories. In these experiments, the mean velocities of the primary fluid are very high, exceeding 100m/sec. According to Schlichting [21], this value is an outside limit for a gaseous flow to be considered incompressible. Since consideration of the compressibility effect requires more modelling works for the energy equation, we treated the flows as incompressible ones, though may it be upper extreme boundary of the incompressibility. Finally, the pressure recovery by the divergent section in percent of the pressure drop through the Venturi throat is calculated and compared with Farbar's experiment in Fig. 6. The results were obtained by a mass-weighted linear sum of the pressure drop for each particle size. A difficulty in calculating the pressure recovery in this way is that, when the particle size is large, the flow of the primary fluid separates in the divergent section. Only the pressure recovery up to the point of separation for large particles can be accounted for in the final estimation of the total pressure recovery; hence, under-prediction is inevitable. However, its dependency on the solid particles flowrate and on the air flowrate is in good agreement with experimental data. The percentage recovery decreases rapidly with increasing particles flowrate, and the rate of change of this decrease being greater for higher air flowrate.

## 5 Conclusions

A "two-fluid" model has been applied to investigate the turbulent dilute gas-particle flows through a Venturi tube. Bulk motion of the cloud of particles is treated as a secondary fluid which is fully mixed with the conveying primary air flow. Governing equations for the two phases contain turbulent shear stresses $\overline{u_f' v_f'}$, $\overline{u_p' v_p'}$ and turbulent mass transfers $\overline{\rho_p' u_p'}$ and $\overline{\rho_p' v_p'}$. Eddy viscosity models for the primary and the secondary fluids and a virtual laminar kinematic viscosity of the secondary fluid are introduced to close the Reynolds-averaged momentum equations and continuity equation. The results are compared with experimental data and with other theoretical predictions. Computed total pressure drop through the Venturi throat and the pressure recovery in the divergent section are in satisfactory agreements with available experimental data. Influences of the particle size, solid particle flowrate and the air flow-rate on the pressure drops are similarly reproduced by our numerical method as has been experimentally or numerically observed by other investigators. Advantages of the present method in comparison with a trajectory model [22] are that, it does not need any empirical information about the interactive exchanges of momentum and energy between the

conveying fluid and particles; momentum loss due to the wall friction is naturally incorporated in the computational scheme; it gives more detailed information about particles in the turbulent flow field such as $\bar{U}_p$, $\bar{U}_f$, and $\bar{\rho}_p$; it can be easily extended to multi-dimensional recirculating geometries; and more importantly, the method is easily extended to higher order turbulence modelling such as $k-\epsilon$ model or algebraic Reynolds stress model, for better computational accuracy.

## References


1 Sharma, M. P., and Crowe, C. T., "A Novel Physico-Computational Model for Quasi One Dimensional Gas-Particle Flows," ASME JOURNAL OF FLUIDS ENGINEERING, Vol. 100, Sept., 1978, pp. 343–349.

2 Carlson, H. M., Frazier, P. M., and Engdahl, R. B., "Meter for Flowing Mixtures of Air and Pulverized Coal," *Trans. ASME*, Feb. 1948, p. 65.

3 Farbar, L., "The Venturi as a Meter for Gas-Solids Mixtures," *Trans. ASME*, July 1953, pp. 943–951.

4 Lee, J., and Crowe, C. T., "Scaling Laws for Metering the Flow of Gas-Particle Suspensions through Venturis," ASME JOURNAL OF FLUIDS ENGINEERING, Vol. 104, Mar. 1982, pp. 88–91.

5 Drew, D. A., "Averaged Field Equations for Two-Phase Media," *Studies in Applied Mathematics*, Vol. 1, No. 2, 1971.

6 Soo, S. L., "On One-Dimensional Motion of a Single Component in Two Phases," *Int. J. of Multiphase Flow*, Vol. 3, 1976, p. 79–82.

7 Nigmatlin, R. I., "Spatial Averaging of Heterogeneous and Dispersed Phase Systems," *Int. J. of Multiphase Flow*, Vol. 5, 1979, pp. 353–385.

8 Di Giacinto, M., Sabetta, F., and Piva, H., "Two-Way Coupling Effects in Dilute Gas-Particle Flow," ASME JOURNAL OF FLUIDS ENGINEERING, Vol. 104, Sept. 1982, pp. 304–312.

9 Crowe, C. T., "Review-Numerical Models for Dilute Gas-Particle Flows," ASME JOURNAL OF FLUIDS ENGINEERING, Vol. 104, Sept. 1982, pp. 297–303.

10 Marble, F. E., "Dynamics of a Gas Containing Small Solid Particles," in *Proceedings of the 5th AGARD Combustion and Propulsion Symposium*, New York, Pergamon Press, 1963.

11 Melville, W. K., and Bray, K. N. C., "A Model of the Two Phase Turbulent Jet," *Int. J. of Heat and Mass Transfer*, Vol. 22, 1979, pp. 647–656.

12 Choi, Y. D., and Chung, M. K., "Analysis of Turbulent Gas-Solid Suspension Flow in a Pipe," ASME JOURNAL OF FLUIDS ENGINEERING, Vol. 105, Sept. 1983, pp. 329–334.

13 Elghobashi, S. E., and Abou-Arab, T. W., "A Two-Equation Turbulence Model for Two-Phase Flows," *Phys. of Fluids*, Vol. 26, Apr. 1983, pp. 931–938.

14 Boothroyd, R. G., *Flowing Gas-Solids Suspension*, Chapman and Hall, 1981.

15 Owen, P. R., "Pneumatic Transport," *J. Fluid Mech.*, Vol. 39, 1969, pp. 407–432.

16 Soo, S. L., "Statistical Properties of Momentum Transfer in Two Phase Flow," *Chem. Engr. Sci.*, Vol. 5, Apr. 1956, pp. 57–64.

17 O'Brien, R. W., "A Method for the Calculation of Effective Transport Properties of Suspensions of Interacting Particles," *J. Fluid Mech.*, Vol. 91, 1979, pp. 17–39.

18 Soo, S. L., and Tien, C. L., "Effect of the Wall on Two-Phase Turbulence Motion," ASME *Journal of Applied Mechanics*, Vol. 27, Mar. 1960, pp. 5–15.

19 Patankar, S. V., and Spalding, D. B., *Heat and Mass Transfer in Boundary Layers*, Int. Ed., Intertext Books, London, 1967.

20 Sung, H. J., "Computational Study of Turbulent Gas-Particle Flow in a Venturi," Ph.D. thesis, Korea Advanced Institute of Science and Technology, 1984.

21 Schlichting, H., *Boundary-Layer Theory*, McGraw-Hill, 1979.

22 Crowe, C. T., Sharma, M. P., and Stock, D. E., "The Particle-Source-in-Cell Method for Gas Droplet Flow," ASME JOURNAL OF FLUIDS ENGINEERING, Vol. 99, 1977, pp. 325–332.

**J. William Holl**
Professor of Aerospace Engineering.

**Michael L. Billet**
Senior Research Associate.

**Masaru Tada**
Former Graduate Student
in the Department of
Aerospace Engineering.

**David R. Stinebring**
Research Assistant.

Applied Research Laboratory,
The Pennsylvania State University,
State College, PA. 16804

# The Influence of Pressure Gradient on Desinent Cavitation From Isolated Surface Protrusions

*An experimental investigation was conducted to study the desinent cavitation characteristics of various sizes of two-dimensional triangular and circular arc protrusions in a turbulent boundary layer for favorable, zero, and unfavorable pressure gradients. The roughness height* (h) *varied from 0.025 cm (0.01 in.) to 0.762 cm (0.30 in.) and the relative height* (h/δ) *varied from 0.026 to 2.53. Desinent cavitation numbers* ($\sigma_d$) *were obtained visually over a velocity range of 9.1 mps (30 fps) to 18.3 mps (60 fps) at an average total air content of 3.8 ppm (mole basis). The data for zero pressure gradient were in fair agreement with data obtained for the same protrusion shapes by Holl (1958). The cavitation number* ($\sigma_d$) *was correlated with relative height* (h/δ), *Reynolds number* ($U\delta/\nu$) *and Clauser's (1954) equilibrium boundary layer shape factor* (G) *which includes the effect of pressure gradient. The data show that* $\sigma_d$ *increases with pressure gradient. This result was not expected since it appears to contradict the trends implied by the so-called characteristic velocity theory developed by Holl (1958).*

## Introduction

Systematic investigations of the limited cavitation characteristics of isolated surface irregularities were conducted at ARL/PSU in the 1950's and reported in the doctoral work of Holl in 1958 [1] and [2]. Subsequently, investigations were conducted at the Massachusetts Institute of Technology on distributed roughness and reported in the doctoral work of Arndt in 1967 [3] and [4]. Later, these investigations were augmented by additional studies at ARL/PSU and were reported by Arndt, Holl, Bohn, and Bechtel [5] together with the earlier investigations. These investigations were all conducted under essentially flat plate conditions, i.e., $dP/dx = 0$.

The results of the aforementioned flat plate studies for isolated protrusions were employed by Billet, Holl, and Parkin [6] to analyze a cavitation scale effect on families of hydofoils and hemispherical headforms. The results suggested that it would be prudent to investigate the effect of pressure gradient on the limited cavitation characteristics of an isolated surface protrusion. Consequently, the present investigation was conducted to satisfy this need. Two-dimensional surface protrusions with triangular and circular arc cross sections similar to those employed by Holl [1] were studied in the 11.43 cm × 50.8 cm (4.5 in. × 20 in.) water tunnel at ARL/PSU for various values of pressure gradient, velocity, and relative roughness height. A sketch of the protrusions is given in Fig. 1. A detailed description of the investigation of the triangular protrusions is given in reference [7].

## Description of the Investigation

**Test Arrangement.** The tests were conducted in the 11.43 cm × 50.8 cm (4.5 in. × 20 in.) water tunnel at ARL/PSU. The characteristics of this facility have been described by Lehman [8]. Major features of the test setup are shown in Fig. 2. The test arrangement utilized the two walls of the rec-

| TYPE | HEIGHT (h) (cm) | HEIGHT (h) (in.) |
|---|---|---|
| TRIANGLE | 0.762 | 0.30 |
| " | 0.381 | 0.15 |
| " | 0.254 | 0.10 |
| " | 0.178 | 0.07 |
| " | 0.127 | 0.05 |
| " | 0.051 | 0.02 |
| " | 0.025 | 0.01 |
| CIRCULAR ARC | 0.686 | 0.27 |
| " | 0.229 | 0.09 |
| " | 0.076 | 0.03 |
| " | 0.025 | 0.01 |

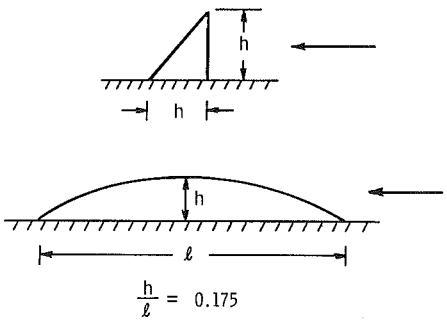


**Fig. 1 Cross sections and heights of triangular and circular arc protrusions**

Contributed by the Fluids Engineering Division for publication in the JOURNAL OF FLUIDS ENGINEERING. Manuscript received by the Fluids Engineering Division, October 15, 1984.

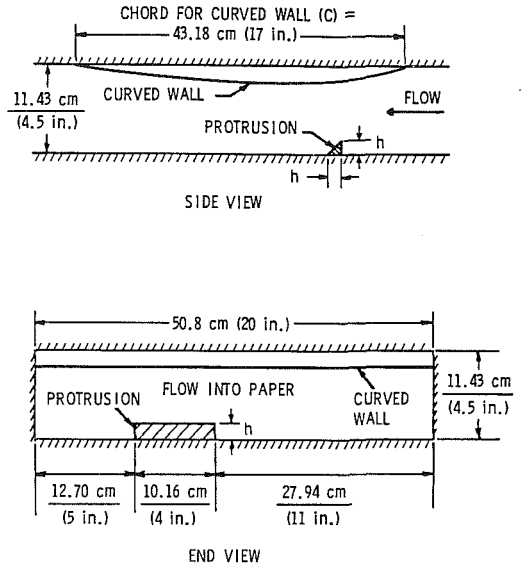


**Fig. 2 Test section arrangement in the 11.43 cm × 50.8 cm water tunnel**

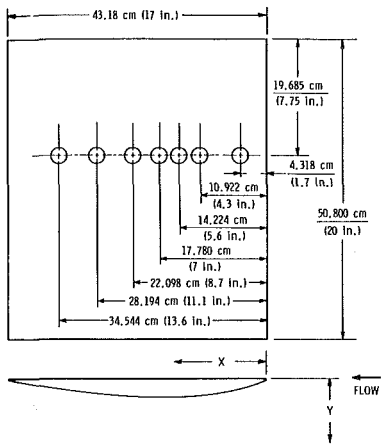


| X (cm) | Y (cm) | X (in.) | Y (in.) |
|---|---|---|---|
| 0 | 0 | 0 | 0 |
| 0.541 | 0.325 | 0.213 | 0.128 |
| 1.080 | 0.483 | 0.425 | 0.190 |
| 2.159 | 0.719 | 0.850 | 0.283 |
| 3.239 | 0.902 | 1.275 | 0.355 |
| 4.318 | 1.052 | 1.700 | 0.414 |
| 6.477 | 1.293 | 2.550 | 0.509 |
| 8.636 | 1.456 | 3.403 | 0.577 |
| 12.954 | 1.669 | 5.100 | 0.657 |
| 17.272 | 1.727 | 6.809 | 0.680 |
| 21.590 | 1.676 | 8.500 | 0.660 |
| 25.908 | 1.532 | 10.200 | 0.693 |
| 30.226 | 1.290 | 11.930 | 0.508 |
| 34.544 | 0.955 | 13.600 | 0.376 |
| 38.862 | 0.538 | 15.300 | 0.212 |
| 41.021 | 0.295 | 16.150 | 0.116 |
| 43.180 | 0 | 17.000 | 0 |

**Fig. 3 Details of the curved wall**

tangular test section which were 50.8 cm (20 in.) in width and 11.43 cm (4.5 in.) apart. A curved wall was installed on one side of the test section in order to produce various pressure gradients. The protrusions were inserted in various slots along the flat wall of the test section which was opposite to the curved wall. The curved wall made of plexiglass consisted of a hydrofoil with a 50.8 cm (20 in.) span and 43.18 cm (17 in.) chord. The cross section of the hydrofoil was one-half of a symmetrical hydrofoil section. Details of the curved wall are shown in Fig. 3. In order to measure the velocity profile at each location on the flat wall, i.e., the wall opposite to the curved wall, seven holes were drilled in the curved wall for the insertion of a total head tube. These seven locations were designated STA. I, II, III, IV, V, VI, and VII as shown in Fig. 4.

**Protrusions.** The triangular and circular arc protrusions were made of plexiglass. The cross sections and heights of the protrusions are shown in Fig. 1. These are the same cross-sections as those employed by Holl [1]. The span of each protrusion was 10.16 cm (4 in.) and slots were machined in a flat wall insert at the seven stations shown in Fig. 4. The top of the insert was flush with the wall when the insert was installed in the tunnel wall. When a protrusion was tested at any given station, such as Station I in Fig. 4, the remaining slots were filled with small plexiglass plates. As indicated in Fig. 1, seven triangular and four circular arc protrusions were employed in the tests. The roughness locations shown in Fig. 4 correspond

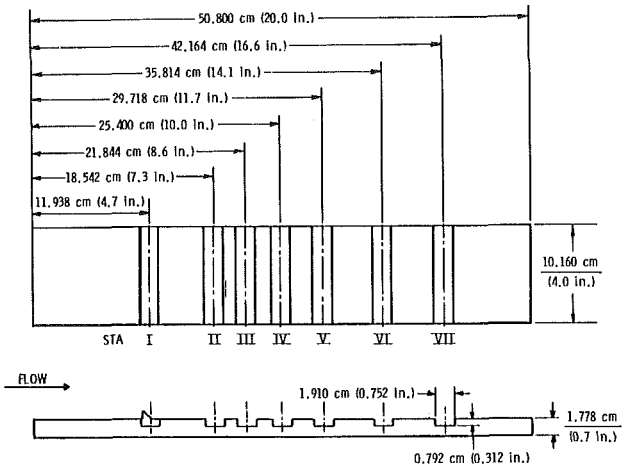


**Fig. 4 Schematic of tunnel wall insert showing test stations for the protrusions**

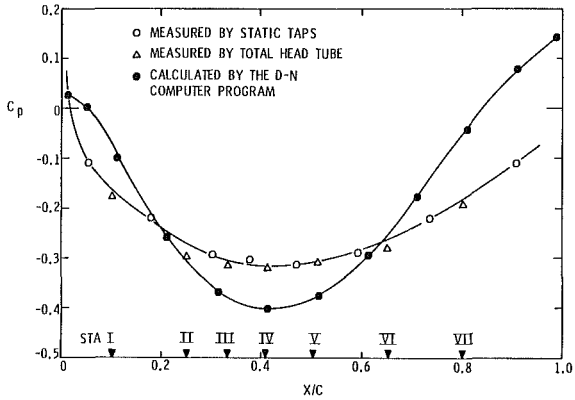


**Fig. 5 Pressure coefficient on the flat wall in the test section**

to the leading edge of the total head tube which was inserted into the flow through the seven holes in the curved wall shown in Fig. 3.

**Measurement of the Velocity at Infinity.** The wall pressure ($P_\infty'$) 16.26 cm (6.4 in.) upstream of the curved wall together with the pressure in the settling section ($P_0$) was used to find a nominal velocity at infinity ($U_\infty'$). However, the measuring station at 16.26 cm (6.4 in.) was influenced by the curved wall so that it was not possible to determine the actual velocity at infinity ($U_\infty$) by measurement. This was determined by an application of the Douglas-Neumann method which indicated that $U_\infty'/U_\infty = 0.9833$.

**Measurement of the Pressure Distribution on the Flat Wall.** The pressure distribution along the flat wall was measured by static pressure taps located between the measuring stations along the wall. The data were expressed in coefficient form, i.e.,

$$C_p = \frac{P - P_\infty}{1/2\rho U_\infty{}^2}. \tag{1}$$

These data are shown by the open circular symbols in Fig. 5.

The velocity at the edge of the boundary layer ($U$) was measured by a total head tube as described in the next section. These data are shown in Fig. 6. The wall pressure coefficient was calculated by the relation

$$C_p = 1 - \left(\frac{U}{U_\infty}\right)^2. \tag{2}$$

These values of $C_p$ shown by the open triangular symbols in Fig. 5 are in good agreement with $C_p$ obtained by wall pressure taps.

**Table 1 Boundary layer parameters at each station**

| Station | $x/c$ | $\delta$ (cm) | $\delta$ (in.) | $\delta^*$ (cm) | $\delta^*$ (in.) | $\theta$ (cm) | $\theta$ (in.) | $H$ |
|---|---|---|---|---|---|---|---|---|
| I | 0.10 | 0.315 | 0.124 | 0.031 | 0.0122 | 0.0231 | 0.0091 | 1.34 |
| IV | 0.41 | 0.424 | 0.167 | 0.046 | 0.0183 | 0.0348 | 0.0137 | 1.335 |
| VII | 0.80 | 0.950 | 0.374 | 0.090 | 0.0354 | 0.0648 | 0.0255 | 1.39 |

These parameters correspond to $U_\infty = 12.2$ mps (40 fps).

**Table 2 Shape factor ($G$) and wake parameter ($\Pi$) at each station**

| Station | $x/c$ | $\delta^*$ (cm) | $\delta^*$ (inch) | $\tau_w$ (kPa) | $\tau_w$ (lb/ft$^2$) | $dP/dx$ (kPa/m) | $dP/dx$ (lb/ft$^2$) | $\beta$ | $\Pi$ | $G$ |
|---|---|---|---|---|---|---|---|---|---|---|
| I | 0.10 | 0.031 | 0.0122 | 0.1612 | 3.366 | −91.77 | −584.2 | −0.176 | 0.344 | 6.100 |
| IV | 0.41 | 0.046 | 0.0183 | 0.1619 | 3.381 | − 9.175 | − 58.4 | −0.026 | 0.457 | 6.448 |
| VII | 0.80 | 0.090 | 0.0354 | 0.1149 | 2.401 | +68.84 | +438.2 | +0.538 | 0.823 | 7.647 |

The shape factor ($G$), wake parameter ($\Pi$) and Clauser's equilibrium parameter ($\beta$) were calculated by using equations (8), (9), and (10), respectively. Data are for $U_\infty = 12.2$ mps (40 fps).

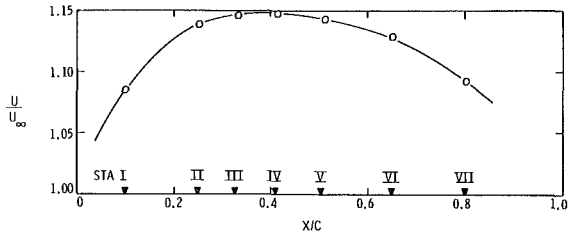


**Fig. 6 Velocity at the edge of the boundary layer on the flat wall in the test section**

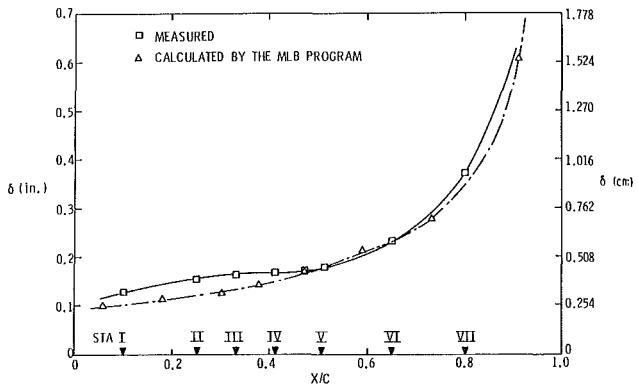


**Fig. 7 Boundary layer thickness on the flat wall in the test section**

The theoretical pressure distribution on the wall as obtained by the Douglas-Neumann (DN) computer program is shown by the solid circular symbols in Fig. 5.

**Determination of Velocity Profile Characteristics.** The velocity profiles were measured by traversing the boundary layer with a probe which was fabricated from a tube of rectangular cross section with an external size of 0.0457 cm (0.018 in.) × 0.211 cm (0.083 in.). A traversing device allowed the positioning of the total head tube within 0.0025 cm (0.001 in.). The edge of the boundary layer was attained when the total pressure became constant. The measured values of boundary layer thickness ($\delta$) are compared with values determined by the method of E. Truckenbrodt [9] in Fig. 7. It was necessary to shift the origin of the theoretical calculation in order to agree with the measured data.

The velocity profile data were not obtained sufficiently close to the wall to determine momentum thickness ($\theta$), displacement thickness ($\delta^*$), boundary layer shape parameters ($H = \delta^*/\theta$) and wall shear stress ($\tau_w$). Thus, $\delta^*$, $\theta$, and $H$ were determined by the Truckenbrodt method [9] and $\tau_w$ was determined from the Ludwieg-Tillman (10) relation

$$\frac{\tau_w}{1/2\rho U^2} = 0.246 \times 10^{-0.678H} \left(\frac{U\theta}{\nu}\right)^{-0.268} \tag{3}$$

where $U$ is the velocity at the edge of the boundary layer.

Measured values of $\delta$ together with calculated values of $\delta^*$, $\theta$, and $H$ are given in Table 1. The wall shear stress, pressure gradient and the parameters $\beta$, $\Pi$, and $G$ are given in Table 2. All data are shown for a nominal velocity ($U_\infty$) of 12.2 mps (40 fps). Experimental values of $\delta$ were scaled to 12.2 mps (40 fps) by the equation

$$\delta = 0.37 \left(\frac{UX}{\nu}\right)^{-0.2}. \tag{4}$$

**Cavitation Experiments.** There was not sufficient time available to conduct cavitation experiments at all seven stations so that three representative stations were selected for the experiments. These were Station I ($dP/dx < 0$), Station IV ($dP/dx \simeq 0$) and Station VII ($dP/dx > 0$).

During the experiments the total gas content was maintained at approximately 4 moles of air per million moles of water (ppm). The mean value for all tests was 3.8 ppm. The gas content was determined by a Van Slyke apparatus.

The primary purpose of the cavitation experiments was to determine the limited cavitation number ($\sigma_l$) defined as

$$\sigma_l = \frac{P_{\infty_l} - P_v}{1/2\rho U_\infty{}^2}. \tag{5}$$

This cavitation number can be determined experimentally by either the inception or desinence procedure. The desinence procedure was employed in this investigation. Thus $\sigma_l = \sigma_d$ where $\sigma_d$ is the desinent cavitation number given by

$$\sigma_d = \frac{p_{\infty_d} - P_v}{1/2\rho U_\infty{}^2}. \tag{6}$$

The desinence procedure consists of holding the velocity constant and increasing the pressure until the cavitation disappears.

A strobe light was used to aid in visually observing cavitation. When cavitation occurred along the top edge of the triangular protrusion, which appeared as luminous streaks originating several inches downstream of the protrusion, another type of cavitation appeared at both ends of the protrusion. These two types of cavitation joined together downstream. Special care was taken to see that the cavitation caused by the ends was not mistaken for that caused by the top edge of the triangular protrusion.

Desinent cavitation was defined as the absence of cavitation at the top edge of the protrusion for more than 30 seconds. Throughout the experiment, the observations were done by the same person. The pressure was lowered and raised from four to seven times for each velocity setting. The desinent cavitation number was based on the average pressure obtained from those readings. The gas content and temperature were measured before and after each run.

As indicated in a subsequent section $\sigma_d$ was correlated with several parameters which were characteristic of the flow. Two parameters which included the pressure gradient effects were employed in this analysis. These were the Coles' [11] wake parameter $\Pi$ and Clauser's [12] shape parameter $G$. The parameter $G$ is defined as

$$G = \left(1 - \frac{1}{H}\right)\sqrt{\frac{2}{C_f}} \tag{7}$$

where $H = \delta^*/\theta$ and $C_f = \tau_w/1/2\rho U^2$. The values of $G$ tabulated in Table 2 were calculated by Nash's (13) approximation

$$G \simeq 6.1\sqrt{\beta + 1.81} - 1.7. \tag{8}$$

Coles' wake parameter was approximated by the relation

$$\Pi \simeq 0.8(\beta + 0.5)^{0.75} \tag{9}$$

where

$$\beta = \frac{\delta^*}{\tau_w}\frac{dP}{dx}. \tag{10}$$

In establishing a correlation for the cavitation number it is prudent to calculate the cavitation number under essentially flat plate conditions ($\sigma_{lfp}$), i.e., the wall pressure ($P$) and velocity at the edge of the boundary layer ($U$) become the "local" infinity condition in the equation for cavitation number. Thus we have

$$\frac{P_\infty - P_v}{1/2\rho U_\infty{}^2} = -\frac{P - P_\infty}{1/2\rho U_\infty{}^2} + \frac{P - P_v}{1/2\rho U_\infty{}^2} \tag{11}$$

or

$$\sigma_l = -C_p + \left(\frac{U}{U_\infty}\right)^2\left(\frac{P - P_v}{1/2\rho U^2}\right) \tag{12}$$

or

$$\sigma_l = -C_p + (1 - C_p)\sigma_{lfp} \tag{13}$$

which is the superposition equation developed by Holl [1]. Solving for $\sigma_{lfp}$ yields

$$\sigma_{lfp} = \frac{\sigma_l + C_p}{1 - C_p}. \tag{14}$$

Thus in the experiment, $\sigma_l$ was determined by the desinence procedure, $C_p$ was determined from Fig. 5 and $\sigma_{lfp}$ was then calculated from equation (14).

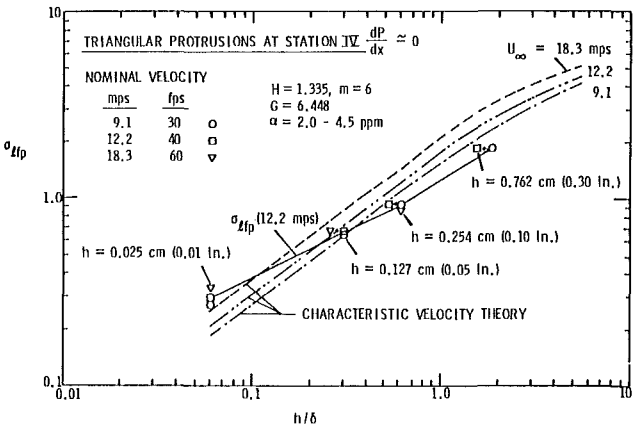


**Fig. 8 Cavitation data for triangular protrusions in zero pressure gradient—comparison with characteristic velocity theory**

## Results of the Cavitation Tests – Triangular Protrusions

The major results of the cavitation experiments for the triangles are shown in Figs. 8 through 11. The data from Station IV ($dP/dx \simeq 0$) are compared with the characteristic velocity theory in Fig. 8. The same data are compared with the earlier results of Holl [1] in Fig. 9. The cavitation number for all three stations are shown in Fig. 10 as a function of relative height ($h/\delta$). A power-law correlation is shown in Fig. 11 for all of the data at the three stations.

Referring to Fig. 8, $\sigma_{lfp}$ is shown as a function of $h/\delta$ for various velocities. These data were obtained at Station IV where $dP/dx \simeq 0$. They display a strong dependence upon the relative height ($h/\delta$) and are in fair agreement with the characteristic velocity theory (CVT) developed by Holl [1] and [14]. This theory assumes that if one knows $\sigma$ for the case $\delta = 0$ one can correct $\sigma$ by the proper choice of a characteristic velocity ($U_c$). This leads to

$$\sigma_{lfp} = \left(\frac{U_c}{U}\right)^2 \sigma_{lfp}' \tag{15}$$

where $\sigma_{lfp}'$ corresponds to the case $\delta = 0$. Assuming that $U_c{}^2$ is the average of the square of the velocity profile over the height

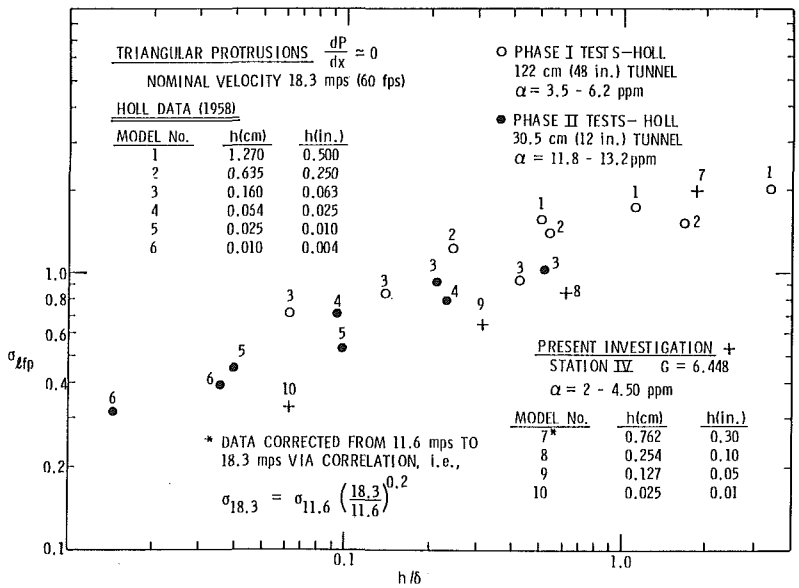


**Fig. 9 Cavitation data for triangular protrusions in zero pressure gradient—comparison with Holl's data (1958)**

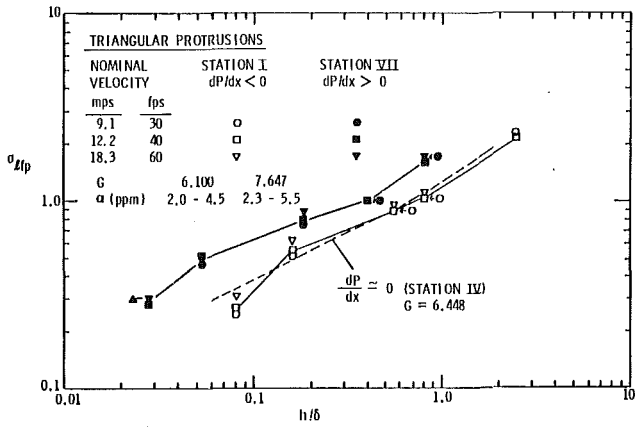


Fig. 10 Cavitation data for triangular protrusions in three different pressure gradients

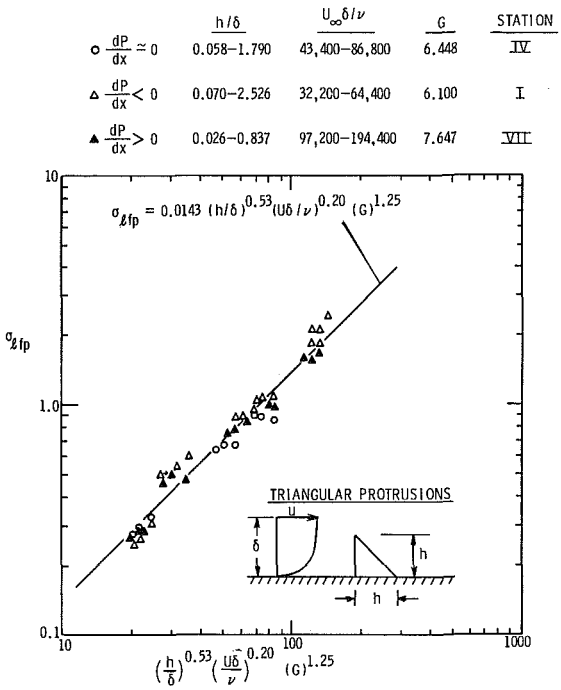


Fig. 11 Power law cavitation number correlation for an isolated triangular protrusion

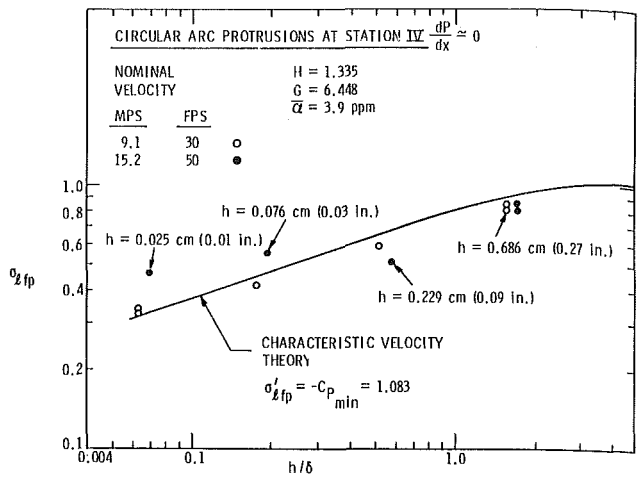


Fig. 12 Cavitation data for circular arc protrusions in zero pressure gradient—comparison with characteristic velocity theory

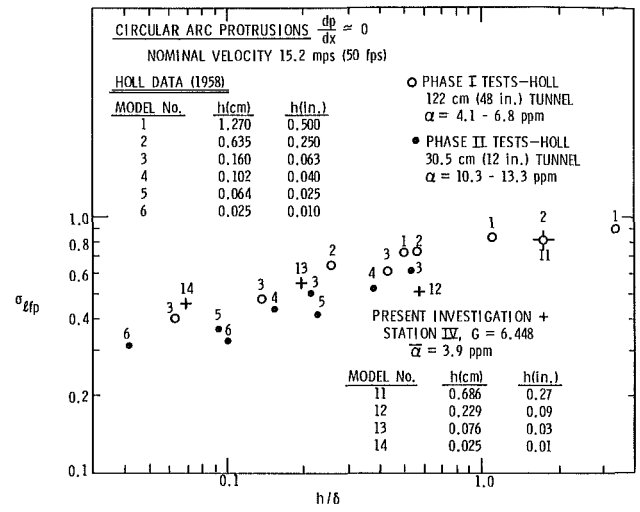


Fig. 13 Cavitation data for circular arc protrusions in zero pressure gradient—comparison with Holl's data (1958)

of the protrusion ($h$) and employing power-law type velocity profiles, i.e., $u/U = (Y/\delta)^{1/m}$, we can write

$$\sigma_{lfp} = \frac{1}{H}\left(\frac{h}{\delta}\right)^{2/m} \sigma_{lfp}' \quad \text{for } h/\delta \le 1 \tag{16}$$

and

$$\sigma_{lfp} = \left[1 - \frac{\delta}{h}\left(1 - \frac{1}{H}\right)\right]\sigma_{lfp}' \quad \text{for } h/\delta \ge 1 \tag{17}$$

where $H = \delta^*/\theta = 1 + 2/\mathrm{m}$. The cavitation number $\sigma_{lfp}'$ for the triangles has been determined by J. W. Holl and C. B. Baker at ARL/PSU by testing a family of sharp edged flat plates in a uniform stream. The data were correlated reasonably well by the equation

$$\sigma_{lfp}' = 0.0214\ \mathrm{Re}_h^{0.424} \tag{18}$$

where $h$ is one-half the height of the flat plates which was taken to be equivalent to the roughness height when $\delta \simeq 0$. $\mathrm{Re}_h$ is the Reynolds number $Uh/\nu$.

The data from the present investigation for Station IV where $dP/dx = 0$ are compared with that of Holl [1] in Fig. 9. In most cases the Holl data are above the data for the current investigation. This may be due either to the higher air contents employed in Holl's tests or differences in the definition of desinent cavitation. Tada [7] has attempted to correct Holl's data to the lower air content employed in the current investigation.

The cavitation data for all three of the measuring stations are shown in Fig. 10. The data from Station IV ($dP/dx \simeq 0$) and Station I ($dP/dx < 0$) are fairly close together. However, the data for Station VII ($dP/dx > 0$) where we have an adverse pressure gradient are significantly higher. This was an unexpected result since, as indicated by equation (15), the CVT would predict a decrease in $\sigma_{lfp}$ due to the smaller value of $U_c$ produced by the less uniform velocity profile characteristic of the adverse pressure gradient. However, the experimental data may contain significant effects related to the separating flow over the protrusion which are not adequately accounted for in the CVT.

Cavitation data for the zero-pressure gradient case were successfully correlated by Arndt, Holl, Bohn, and Bechtel [5] with relative height ($h/\delta$) and Reynolds number ($U\delta/\nu$) using a power-law equation. In the current investigation it was necessary to include a shape parameter to account for pressure gradient effects. Both the $G$ parameter of Clauser and Coles' wake parameter $\Pi$ were employed. As indicated by Tada [7], it was determined that by using $G$ one obtains a somewhat better

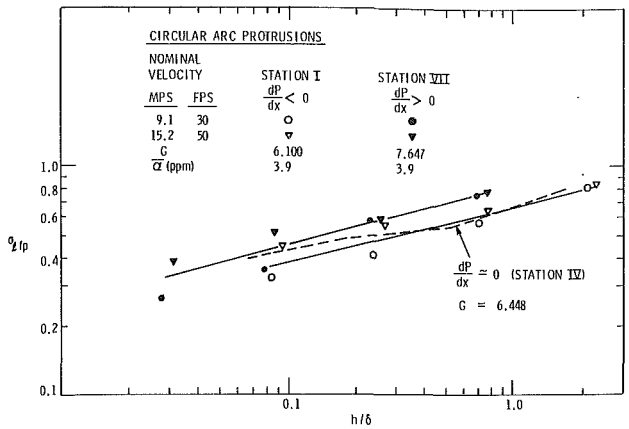


Fig. 14 Cavitation data for circular arc protrusions in three different pressure gradients

**Table 3 Comparison of constants in the correlation equation**

$$\sigma_{lfp} = d\left(\frac{h}{\delta}\right)^{a}\left(\frac{U\delta}{\nu}\right)^{b}(G)^{c}$$

| Protrusion | Source | d | a | b | c |
|---|---|---|---|---|---|
| Triangles | Holl 1958* | 0.1520 | 0.361 | 0.196 | 0** |
| Triangles | This Inv. | 0.0143 | 0.530 | 0.200 | 1.25 |
| Circular Arcs | Holl 1958* | 0.0410 | 0.344 | 0.267 | 0** |
| Circular Arcs | This Inv. | 0.0158 | 0.253 | 0.318 | 0.162 |

*Constants for these data are given in the paper by Arndt, Holl, Bohn, and Bechtel (1979).
**G = constant for all of the Holl data where $dP/dx \simeq 0$.

correlation. The results are shown in Fig. 11 where the data are correlated by the relation

$$\sigma_{lfp} = 0.0143\left(\frac{h}{\delta}\right)^{0.53}\left(\frac{U\delta}{\nu}\right)^{0.20}(G)^{1.25}. \tag{19}$$

The relation appears to be a reasonable correlation for these data.

## Results of the Cavitation Tests – Circular Arc Protrusions

The major results of the cavitation experiments for the circular arcs are shown in Figs. 12 through 15. The data from Station IV ($dP/dx \simeq 0$) are compared with the characteristic velocity theory in Fig. 12. The same data are compared with the earlier results of Holl [1] in Fig. 13. The cavitation number is shown as a function of relative height ($h/\delta$) for all three stations in Fig. 14. A power-law correlation is shown in Fig. 15 for all of the data at the three stations.

Referring to Fig. 12, the data obtained at Station IV where $dP/dx \simeq 0$ are compared with the characteristic velocity theory and it is seen that experimental and theoretical data are in fair agreement. The cavitation number for the circular arcs for the case $\delta = 0$, i.e., $\sigma_{lfp}'$, was assumed to be equal to the negative of the minimum pressure coefficient from perfect fluid theory. Thus

$$\sigma_{lfp}' = -C_{p_{\min}} = 1.083. \tag{20}$$

The data obtained at Station IV are compared with Holl's data in Fig. 13. These data correspond to the condition $dP/dx \simeq 0$. In contrast to the comparison displayed by the triangular data in Fig. 9, the circular arc data from this investigation are in better agreement with Holl's data. This suggests that desinent cavitation on the circular arc protrusion is less sensitive than desinent cavitation on the triangular protrusion to variations in air content.

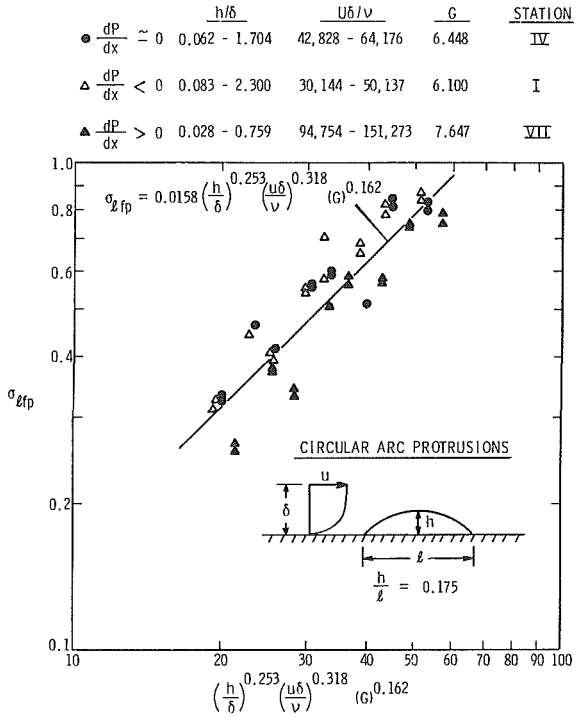


Fig. 15 Power law cavitation number correlation for an isolated circular arc protrusion

The cavitation data for all three of the measuring stations are shown in Fig. 14. These data display trends which are similar to those shown by the data for the triangular protrusions in Fig. 10, i.e., the data for $dP/dx \simeq 0$ and $dP/dx < 0$ tend to overlap over a significant portion of the range whereas the data obtained at Station VII for $dP/dx > 0$ are higher for all values of $h/\delta$. As indicated previously, this was an unexpected result because of the implications of the characteristic velocity theory.

The correlation of all of the circular arc data is shown in Fig. 15 where the correlation equation is

$$\sigma_{lfp} = 0.0158\left(\frac{h}{\delta}\right)^{0.253}\left(\frac{U\delta}{\nu}\right)^{0.318}(G)^{0.162}. \tag{21}$$

The exponent on $G$, i.e., 0.162, is considerably smaller than the 1.25 power which is characteristic of the triangular data in Fig. 11. The explanation of this result is not forthcoming at this time.

Equations (19) and (21) can be written in the general form

$$\sigma_{lfp} = d\left(\frac{h}{\delta}\right)^{a}\left(\frac{U\delta}{\nu}\right)^{b}(G)^{c}. \tag{22}$$

All of the constants $a$, $b$, $c$, and $d$, which occur in this equation, are compared with those of Holl in Table 3. There does not appear to be a consistent trend suggested by these comparisons. However, a statistical analysis of the data has indicated that this power law equation is too simple to accurately describe the phenomena. Nevertheless, the power law relation is a convenient relation for engineering approximations.

**Uncertainty Estimates.** The data shown in Figs. 5, 6, and 7 are for flow field measurements obtained with pressure probes. The uncertainty for $C_p$ given in Fig. 5 is ±1.5 percent, the uncertainty for $U/U_\infty$ given in Fig. 6 is ±1.5 percent, and the uncertainty for $\delta$ given in Fig. 7 is ±1.5 percent. The cavitation data ($\sigma_{lfp}$) plotted in Figs. 8 to 15 were obtained by pressure measurements; however, the cavitation state was determined by visual observations. The uncertainty of cavita-

tion as determined for many samples at a specified flow condition was determined to be ±5 percent.

## Acknowledgments

This investigation was sponsored by the Naval Sea Systems Command, Code NSEA 63R31, which is administered by Dr. Thomas E. Peirce. The authors would like to acknowledge the contributions of Ms. Donna Angotti to the analysis of the data for the circular arc protrusions.

## References

1 Holl, J. W., "The Effect of Surface Irregularities on Incipient Cavitation," Ph.D. thesis, The Pennsylvania State University, State College, PA, June 1958.

2 Holl, J. W., "The Inception of Cavitation on Isolated Surface Irregularities," ASME *Journal of Basic Engineering*, Vol. 82, 1960, pp. 169–183.

3 Arndt, R. E. A., "Cavitation Near Surfaces of Distributed Roughness," Ph.D. dissertation, Department of Civil Engineering, Massachusetts Institute of Technology, June 1967.

4 Arndt, R. E. A., and Ippen, A. T., "Rough Surface Effects on Cavitation Inception," ASME *Journal of Basic Engineering*, Vol. 90, 1968, pp. 249–261.

5 Arndt, R. E. A., Holl, J. W., Bohn, J. C., and Bechtel, W. T., "Influence of Surface Irregularities on Cavitation Performance," *Journal of Ship Research*, Vol. 23, No. 3, September 1979.

6 Billet, M. L., Holl, J. W., and Parkin, B. R., "Scale Effects on Cavitating Flows due to Surface Roughness and Laminar Separation," *AIAA Journal*, Vol. 20, May 1982, pp. 632–637.

7 Tada, M., "Effect of Pressure Gradient on Cavitation Inception from an Isolated Surface Roughness," Master of Science thesis, Department of Aerospace Engineering, The Pennsylvania State University, May 1983.

8 Lehman, A. F., "The Garfield Thomas Water Tunnel," ORL Report No. NOrd 16597-56, 1957, The Pennsylvania State University, State College, PA.

9 Truckenbrodt, E., "A Method of Quadrature for Calculation of the Laminar and Turbulent Boundary Layer in Case of Plane and Rotationally Symmetrical Flow," NACA TM 1379, May 1955.

10 Ludwieg, H., and Tillmann, W., "Investigations of the Wall-Shearing Stress in Turbulent Boundary Layers," NACA TM 1285, 1950; Translation from *Z. Angew. Math. Mech.*, Vol. 29, 1949.

11 Coles, D. E., "The Law of the Wake in the Turbulent Boundary Layer," *Journal of Fluid Mechanics*, Vol. 1, July 1966, pp. 191–226.

12 Clauser, F. H., "The Turbulent Boundary Layer," *Advances in Applied Mechanics*, Vol. 4, 1956, pp. 1–51.

13 Nash, J. F., National Physics Laboratory Aeronautical Report, Report No. 1137, England, 1965.

14 Holl, J. W., "The Estimation of the Effect of Surface Irregularities on the Inception of Cavitation," *Proceedings of Symposium on Cavitation in Fluid Machinery*, ASME, 1965.

# The Effects of Turbulence Stimulators on Cavitation Inception of Axisymmetric Headforms

**T. T. Huang**
Naval Architect,
David W. Taylor Naval Ship Research and Development Center,
Bethesda, Md. 20084-5000

*Cavitation inception observations were made in the DTNSRDC 36-inch water tunnel on three axisymmetric headforms with and without various turbulence stimulators installed. Direct transition measurements, made on two of the headforms with and without distributed surface roughness, were found to correlate reasonably well with the computed spatial amplification factors, $e^N$, at the separation locations. The computed $e^N$ factors were then used to estimate transition at other test conditions (without direct transition measurements). The predicted transition locations on all three smooth headforms occur at positions considerably aft of the minimum pressure locations. The three smooth headforms have different types of incipient cavitation—small band, transient spot, traveling bubble, and attached spot. The measured cavitation inception numbers for those cases are all significantly smaller than the computed negative values of the minimum pressure coefficient, $-C_{pmin}$. The predicted transition locations on the three headforms with densely and loosely packed 60-μm distributed roughness occur at a considerable distance upstream of the minimum pressure locations. Therefore, the flows over all three headforms with distributed roughness are turbulent at the $C_{pmin}$ locations for the Reynolds numbers tested. Under this condition, the measured cavitation inception numbers are found to approximate well with the values of $-C_{pmin}$. The incipient cavitation is in the form of attached small bubble lines evenly distributed around the minimum pressure locations. The measured cavitation inception numbers for the three headforms with an isolated roughness band located upstream of the minimum pressure locations are found to approximate the computed values of $-C_{pmin}$ when the roughness Reynolds number ($R_k = u_k K/\nu$) is equal to 600 and to be smaller than the values of $-C_{pmin}$ when the value of $R_k$ is less than 600. The incipient cavitation observed is attached patch type cavitation occurring in the vicinity of the minimum pressure location. The uncertainty of the measured cavitation inception numbers, in terms of the maximum deviations form the mean values of repeated measurements, is generally less than 0.02.*

## Introduction

Inception of cavitation in liquids is the condition under which cavitation is first detected, either visually or acoustically, with a simple measuring device. The simple assumption that equilibrium conditions are reached instantaneously and that the cavitation inception occurs immediately when the static pressure reaches the vapor pressure is often made in engineering predictions of cavitation inception. This assumption is probably valid for most full-scale bodies. However, the Reynolds number at model scale is one or two orders of magnitude smaller than the prototype value. The measured cavitation numbers $\sigma_i$ on small smooth models are generally significantly smaller than the negative value of the minimum pressure coefficient, $-C_{pmin}$ (see Huang [1], Arakeri and Acosta [2], Holl and Carroll [3], Van der Meulen [4], and Van der Meulen and Ye [5]). The boundary layers on the smooth models are usually laminar at the location of the minimum static pressure and remain laminar for a considerable length downstream. In contrast, transition from laminar to turbulent flow is most likely to take place upstream of a prototype minimum pressure location. Extensive reviews of the viscous effects on cavitation inception have been made by Acosta and Parkin [6, 7], and by Acosta [8]. Detailed numerical evaluations of the influence of viscous effects on model and full-scale cavitation inception correlation have been made by Huang and Peterson [9]. Prediction techniques and a large amount of data covering the scale effects on various types of cavitation have also been presented by Billet and Holl [10]. The viscous characteristics of the flow regime (whether laminar, laminar separated, transitional, or fully turbulent), at and upstream of the cavitation-prone minimum pressure location, play extremely important roles in the small model cavitation inception process, and the differences in flow regimes between model and full-scale are the major sources of so-called "scale effects" on cavitation inception.

Contributed by the Fluids Engineering Division and presented at the International Symposium on Cavitation Inception, ASME Winter Annual Meeting, New Orleans, La., December 9-14, 1984, of THE AMERICAN SOCIETY OF MECHANICAL ENGINEERS. Manuscript received by the Fluids Engineering Division, April 9, 1985.

Another controlling factor in cavitation inception is the size and population of the free-stream microscopic air bubbles in the flow facility. Large exposed free surface areas in the facility may result in an over-deaerated fluid during prolonged low pressure operation. The resulting lack of microbubbles has been found to delay the development of cavitation inception. Artificial seeding of the fluid with microbubbles has been found to stimulate cavitation inception, by Albrecht and Bjorheden [11] in the KaMeWa (KMW) Marine Laboratory free-surface cavitation tunnel, and by Noordzij [12] in the Netherland Ship Model Basin depressurized towing tank. Increasing microbubble population in most close-loop water tunnels has been found to promote traveling bubble inception (Gates and Acosta [13], and Ling et al. [14]). However, the effects of gross gas content on the attached types of cavitation (bubble-ring, band, transient spots, or fixed patch) are, in general, rather small [1, 3].

A high free-stream turbulence level is known to promote an early boundary-layer transition and, in certain conditions, early transition can lead to complete elimination of laminar separation [13]. It is expected that the effect of free-stream turbulence on cavitation inception becomes important when the turbulence level can cause significant change in transition and/or laminar separation.

Neither a high free-stream turbulence level nor a microbubble seeding is a reliable and practical technique for stimulating boundary-layer transition on models in cavitation tunnels. The magnitude of turbulence levels in water tunnels varies from 0.05–0.2 percent (good quality) to 0.2–1 percent (normal) and up to a maximum of 2 percent (in some tunnels). If a tunnel has a turbulence level higher than 2 percent, the result is usually a significant degradation of the tunnel's capability and flow quality to the point where cavitation experiments are usually difficult to be performed. To seed microbubbles uniformly across the test section without generating excessive vortices is also not a simple task. Furthermore, a proper seeding technique to assure model-to-full-scale correlation is not yet available and would be difficult to develop.

Scale effect prediction techniques [9, 10] may only be used to estimate the trend and the order of magnitude of the scale effects on cavitation inception and are not sufficiently accurate to give quantitative results. In addition, the prediction techniques require accurate knowledge of the pressure distribution. Such detailed information is often not available for three-dimensional bodies and propellers. Reliable and practical techniques to eliminate scale effects in the experimental procedure would be of great value to cavitation model testing in water tunnels. One promising technique is the use of a boundary-layer turbulence stimulator consisting of a microscopic distributed roughness from the leading edges of the propellers and hydrofoils, or the noses of bodies to an appropriate location upstream or downstream of the minimum pressure location. In the following, recent research relative to these techniques is summarized. Further research to perfect the techniques for model applications will also be proposed.

**Previous Relevant Research on Cavitation Inception on Bodies Using Turbulent Stimulators.** A boundary-layer tripping technique using a strip of approximately 53 to 62 $\mu$m irregular Carborundum particles about 1 mm from the leading edges of model propeller blades has been developed by Kuiper [15–18] to stimulate boundary-layer turbulence and thus to reduce viscous effects on propeller cavitation. A paint flow visualization technique showed the roughness to be quite effective in producing turbulent boundary layers over almost the entire chord length of the blades. Furthermore, Kuiper [16–18] concluded that the microbubble nuclei generated by the leading edge roughness apparently promoted the inception of bubble cavitation further downstream. Thus, the application of leading edge roughness is capable apparently of not only reducing viscous effects, but also providing needed nuclei. However, the leading edge roughnesses could also produce an undesired pressure perturbation near the minimum pressure location that might cause early cavitation on the roughness elements.

Propeller cavitation research is one of the most important areas of cavitation research. However, the pressure distributions and the three-dimensional boundary-layer properties of propellers are often not available or, if available, not accurately determined. Therefore, basic understanding of the effects

## Nomenclature

$A$ = computed spatial amplification ratio of a disturbance in the boundary layer to its amplitude at point of neutral stability

$A_s$ = $A$ at the position of laminar boundary-layer separation

$C_p$ = pressure coefficient given by $(P-P_0)/(1/2\rho U_0^2)$

$C_{p\min}$ = minimum value of $C_p$

$C_{ps}$ = $C_p$ at the position of laminar boundary-layer separation

$C_{ptr}$ = $C_p$ at the location of transition of laminar boundary-layer

$D$ = diameter of the axisymmetric headform

$K$ = $3K_s$, for distributed roughness about the average value of the maximum roughness depth in a single measuring length of 1 cm
or average vertical distance between the tip of the largest roughness in a circumferential distance of 1 cm and the smooth surface at the leading-edge of an isolated stimulator

$K_s$ = measured rms value of the roughness heights

$P$ = local static pressure on the headform

$P_0$ = free-stream tunnel static pressure

$P_v$ = vapor pressure of water at its bulk temperature

$R_D$ = Reynolds number given by $U_0D/\nu$

$R_{Dcrit}$ = critical Reynolds number at which transition takes place at the position of laminar boundary-layer separation

$R_k$ = $u_kK/\nu$, the roughness Reynolds number

$U_0$ = free-stream tunnel velocity

$u_K$ = local streamwise velocity component evaluated at the roughness height, $K$

$x$ = axial distance from the stagnation point

$x_s$ = axial distance from the stagnation point to the laminar separation point

$x_{tr}$ = axail distance from the stagnation point to the transition location

$Y$ = radial distance from the stagnation point to the transition location

$y$ = distance along the surface normal

$\alpha/\alpha_0$ = dissolved gas content in terms of percent of saturation at 21°C water temperature and atmospheric pressure

$\alpha/\alpha_{TS}$ = dissolved gas content in terms of percent saturation at test section water temperature and pressure

$\nu$ = kinematic viscosity of water

$\rho$ = mass density of water

$\sigma$ = cavitation number given by $(P-P_v)/(1/2\rho U_0^2)$

$\sigma_i$ = incipient cavitation number

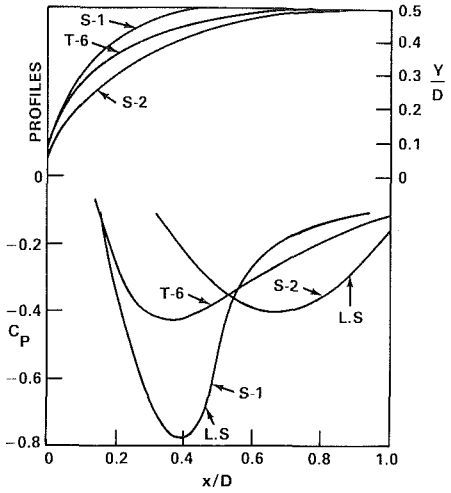


Fig. 1 Surface profiles and pressure coefficients of three headforms

of the leading-edge roughness tripping on cavitation is difficult to obtain from propeller model tests. More definitive experiments must be made on simpler models such as axisymmetric headforms or hydrofoils. For such models, accurate information on the pressure distributions and boundary-layer properties are relatively easy to obtain. The cavitation results obtained with such models are given next.

Billet and Holl [19] used distributed roughnesses having mean diameters of 30 $\mu$m and 66 $\mu$m on two small Schiebe headforms ($D$ = 2.54 and 50.8 mm). It is important to note that the effects on cavitation of distributed roughness on the nose of the model depend upon the extent of roughness upstream of the $C_{p\min}$ location; one case seems to trip the boundary layer and the other is not effective at all. Experimental investigations were conducted by Van der Muelen and Ye [5] on a slightly tapered NACA 4412 hydrofoil at an angle of attack of 2 deg with $-C_{p\min} = 1.105$ at $x/C = 0.28$. Without the application of roughness, the boundary layer was laminar up to a midchord position where transition to turbulence (at low speeds laminar flow separated at midchord) occurred. The types of cavitation observed were traveling-bubble or transient-spot cavitation. When roughness was applied, early transition to turbulence occurred, but this had no effect on the inception or appearance of traveling-bubble cavitation. However, when nuclei generation ahead of the foil was applied or when the roughness elements on the foil were cavitating, the type of cavitation changed to attached bubble cavitation. The measured incipient caviation number $\sigma_i$ on the foil having a leading-edge roughness band trip was found to simulate very closely the value of $-C_{p\min} = 1.105$, wheras the measured value of $\sigma_i$ on the smooth foil was 0.99.

A new foil section (YS-920) was designed by Shen and Eppler [20] to have a wider cavitation-free bucket at full-scale Reynolds number than that of the NACA 66 (MOD) section. A natural transition to turbulence near the leading edge will occur at the full-scale Reynolds number. However, at model scale, the boundary layer will be laminar near the leading-edge. A uniformly distributed roughness, consisting of spherical glass beads of 90-$\mu$m diameter covering the first 1.5 percent of the chord length on both the upper and lower surfaces, was used to simulate the high Reynolds number cavitation phenomenon [21]. The computed cavitation-free boundaries of the two foils at various angles of attack (based on the assumption that $\sigma_i = -C_{p\min}$ at full-scale) agreed very well with the measured boundaries of the two foils using leading-edge roughness but did not agree with the measured boundaries of the smooth foils [21]. Shen [21] also found that the termination of roughness at $x/C = 0.015$ caused a pressure disturbance there and that, at an angle of attack having $C_{p\min}$

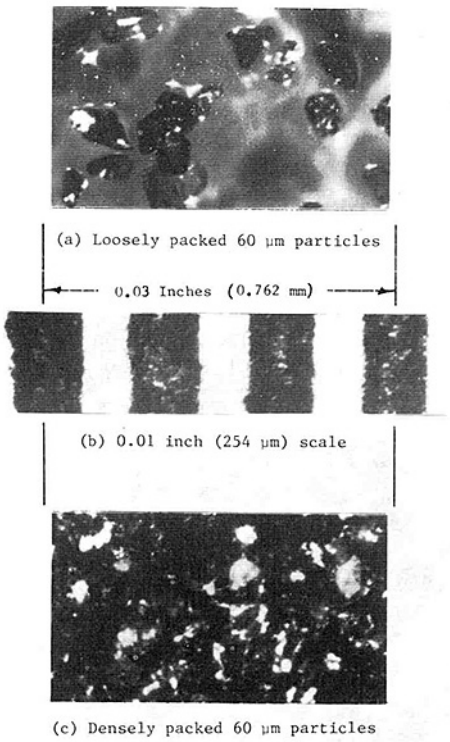


Fig. 2 Distributed roughness (amplified × 110)

located at about $x/C = 0.015$, the measured incipient cavitation number was slightly larger than the value of $-C_{p\min}$. Similar to the results of Van der Meulen and Ye [5], Shen [21] found that the scale effects on the midchord cavitation inception are effectively eliminated by using leading-edge roughness.

In order to gain further insight into the physics of cavitation inception on bodies with turbulence stimulators, and to obtain hydrodynamic parameter for selecting effective turbulence stimulators to reduce scale effects on cavitation inception, three axisymmetric headforms with distributed roughness and isolated strip rougnesss were tested in the DTNSRDC 36-inch water tunnel. A brief summary of this work is reported in the following sections (for details see report by Juang et al. [22]).

**Three Smooth Headforms and Turbulence Stimulators.** Two axisymmetric headforms having laminar separation and a third having natural flow transition were selected to investigate the effect of various boundary-layer turbulence stimulators on cavitation inception. The headform designated T-6 has natural transition without any possiblity of laminar separation. The other two headforms, designated S-1 (hemispherical nose) and S-2, exhibit laminar separation. The body contours and the distributions of the potential-flow pressure coefficients of the three headforms are shown in Fig. 1. Headforms T-6 and S-1 have the same maximum diameter ($D$ = 10.2 cm). Three scales of Headform S-2 were constructed with maximum diameters of $D$ = 10.2 cm, 7.63 cm, and 2.54 cm. All the headforms were constructed of plexiglas to avoid corrosion and the surface finish was kept at 0.4 $\mu$m.

Three types of turbulence stimulators were used. The first type was a single band of roughness, 2.5 mm wide with 30-$\mu$m or 60-$\mu$m particles distributed evenly on the band. The second type consisted of densely packed particles of distributed roughness that started at the stagnation point and extended downstream of the $C_{p\min}$ location. The same 60-$\mu$m irregular Carborundum particles used by Kuiper [15–18] and the 90-$\mu$m spherical glass beads used by Shen [21] were used to produce the distributed roughness. In addition, some of the headforms were tested with a third type of roughness where the

distributed roughness particles were not so densely packed. The difference between the densely and loosely packed distributed roughness is shown in Fig. 2. The rms values of the rougness profile within a single measuring length of 1 cm as measured by a roughness meter (Perthometer Model C5D) are 15-$\mu$m and 10-$\mu$m for the densely and losely packed distributed roughness, respectively.

**Headforms Cavitation Experiments.** Headform experiments were carried out in the DTNSRDC 36-inch Variable Pressure Water Tunnel (VPWT) with a closed-jet test section. Total air content was measured by a standard Van Slyke apparatus. All cavitation measurements were made with a dissolved air content of 9 parts per million by weight, corresponding to 40 percent of saturation at 21°C water temperature at atmospheric pressure. No quantitative measurements of free-gas bubble distribution were made in the present experiment.

The headforms were attached to the housing of the propeller shaft located at the centerline of the test section and were illuminated by an EG&G Xenon Stroboscope (Model LS 148). The system allowed the visual observation of cavitation bubbles. Traveling-bubble cavitation inception is defined in this report as the onset of dectable cavitation events which occur about once per second. Transient spot, band, and attached cavitation inceptions usually occur very suddenly and are quite repeatable. Therefore, their inception values are rather easy to obtain. Incipient cavitation numbers were determined by slowly lowering the tunnel pressure at constant tunnel velocity until cavitation events occurred. The cavitation number, $\sigma$, is given by

$$\sigma = \frac{P_0 - P_v}{1/2\rho U_0^2} \tag{1}$$

where $P_v$ = vapor pressure of the water
$P_0$ = static pressure at the centerline of the test section
$\rho$ = mass density of water
$U_0$ = tunnel velocity

The incipient cavitation number is denoted by $\sigma_i$.

Three to five independent measurements, obtained by two different observers, were used to establish the uncertainty of the cavitation inception numbers. They were denoted by $\sigma_i \pm \Delta\sigma$ in this paper, where $\sigma_i$ are the mean values of the different measurements and $\Delta\sigma$ are the maximum deviation from the

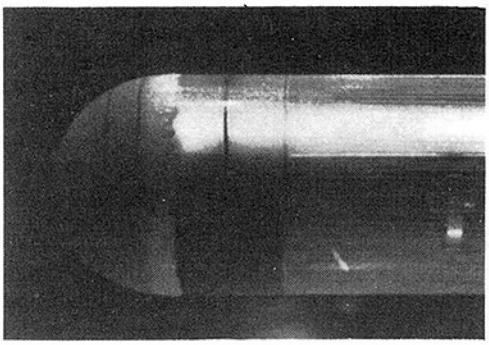

Fig. 3(a) Oil-film flow visualization show loosely packed 60 $\mu$m particles on the upper half of the model and densely packed 60$\mu$m particles on the lower half of the model

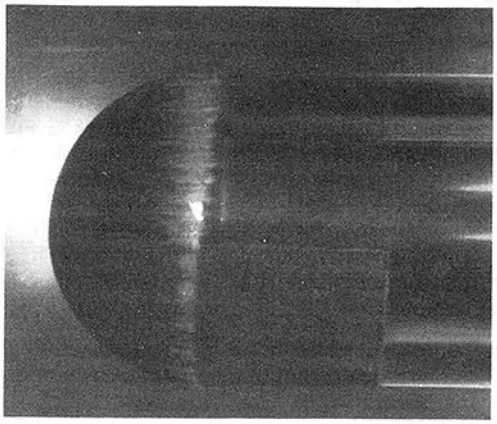

Fig. 3(b) Cavitation inception, $\sigma_i$ = 0.78 at the $C_{Pmin}$ location

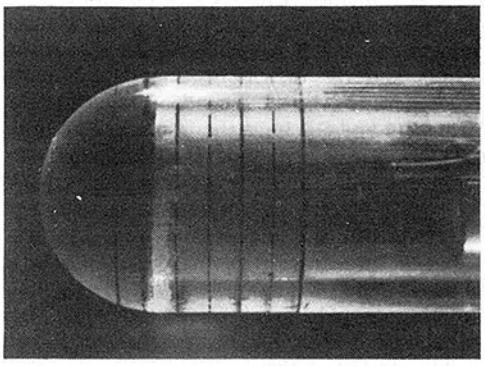

Fig. 3(c) Oil-film flow visualization show a boundary-layer tripping band (2.5 mm wide and 0.03 mm high) located at $x/D$ = 0.15 ($C_p$ = 0) on the upper half of the model and loosely packed 60 $\mu$m particles on the lower half

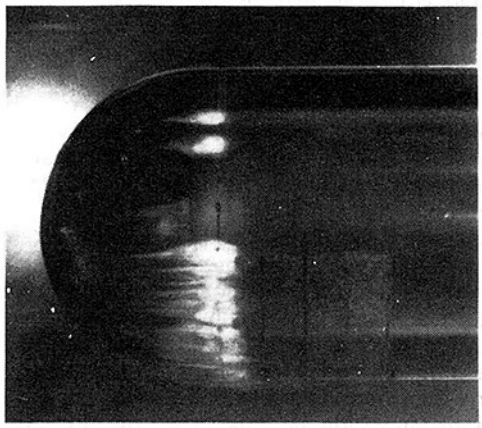

Fig. 3(d) Cavitation inception at $\sigma_i$ = 0.70 at the $C_{pmin}$ of the upper half

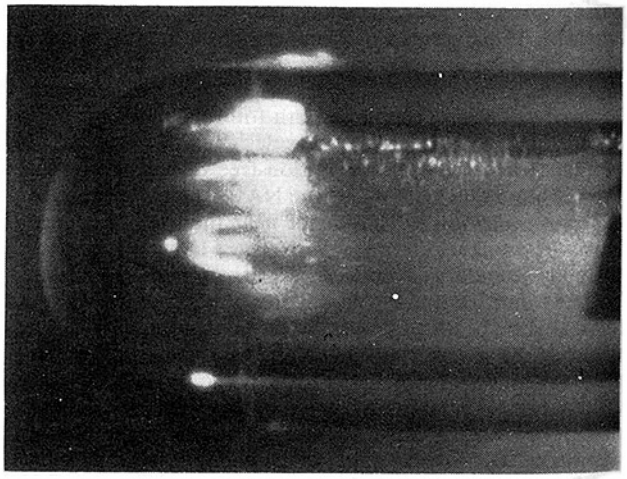

Fig. 3(e) Cavitation inception ($\sigma_i$ = 0.70) at the $C_{Pmin}$ of the headform with a boundary-layer tripping ring (2.5 mm wide and 0.03 mm high) located at $x/D$ = 0.2 ($C_P$ = −0.33)

Fig. 3 Cavitation inception on headform S-1 with boundary-layer turbulence stimulators

Table 1 Computed and measured critical Reynolds numbers for two laminar separated headforms with and without turbulence stimulators

| Headform | Surface Condition | Computed | | Measured |
|---|---|---|---|---|
| | | $R_{D_{crit}} \times 10^{-5}$ | $A_s$ | $R_{D_{crit}} \times 10^{-5}$ |
| Hemispheric Nose, S-1 | Smooth, rms finish < 0.4 μm | 90 | $e^9$ | > 19 |
| $C_{p,min} = -0.78$ at $(x/D)_{min} = 0.39$, $C_{ps} = -0.63$ at $x_s/D = 0.47$ | Densely packed 60-μm Distributed roughness | 3.6 | $e^9$ | 3.6 |
| | Loosely packed 60-μm Distributed roughness | 5.4 | $e^8$ | 5.4 |
| | Tripping band of 2.5 mm wide and 0.3 mm high at x/D=0.15 | – | – | 5.7 |
| S 2 $C_{p,min} = -0.41$ at $(x/D)_{min} = 0.68$, $C_{ps} = -0.30$ at $x_s/D = 0.89$ | Smooth, rms finish < 0.4-μm | 13<br>19 | $e^7$<br>$e^9$ | ≥ 13 |
| | Densely packed 60-μm Distributed roughness | 4.0 | $e^7$ | 4.0 |
| | Tripping band of 4 mm wide and 0.06 mm high at x/D=0.125 | – | – | 3.2 |

mean values. It should be noted that the small deviations of $\Delta\sigma$'s, generally in the range of 0.01 to 0.02, result from the small uncertainties of measuring the tunnel pressure and velocity. The cavitation inception measurements reported in this paper can be considered quite repeatable.

**Computed Boundary-Layer Characteristics.** The laminar boundary-layer on a small smooth model is quite stable from the stagnation point up to the location of $C_{p\min}$. Further downstream, the flow may or may not be separated depending upon the magnitude of the adverse pressure gradient. For a body having laminar separation, the Reynolds number at which natural flow transition first appears upstream of the laminar separation position is designated as the critical Reynolds number [23], $R_{D\text{crit}}$. Flows for which the Reynolds number is smaller or larger than $R_{D\text{crit}}$ are called "subcritical" and "supercritical," respectively [23]. Use of fluorescent oil-film visualization on Headforms S-1 and S-2 in the 36-inch water tunnel verified the existence of laminar separation at the predicted locations [1]. The Smith [24] spatial amplification factor has often been chosen as a simple yardstick to correlate the instability charateristics of the boundary layers with the various measured stages of transition. Satisfactory correlation between the computed amplification factors and measured transition processes on smooth bodies has been obtained by Huang [1] and Arakeri [25] in water tunnels; by Huang and Hannan [26] and Huang [27] in a wind tunnel; and by Power [28] in the towing basin. Similar transition correlation techniques for bodies with distributed roughness will be developed in the following.

Distributed surface roughness is known to promote the early onset of boundary-layer transition. Kosecoff et al. [29] developed an analytical model to simulate the effects of distributed surface roughness on transition. Merkle et al. [30] incorporated the Kosecoff analytical model into a computer program. The same analytical model has also been incorporated into an existing standard boundary-layer code at DTNSRDC to calculate: 1) the entire boundary-layer characteristics, 2) linear boundary-layer instability, and 3) the spatial amplification of disturbances in the boundary layers on the bodies with distributed roughness. The distributed roughnesses used in the experiments are the irregular particles glued on the surfaces of the headforms. In the following calculations, the roughness height $K$ is selected to be $3K_s$, where $K_s$ is the measured rms value of the roughness heights. The roughness height $K$ is about equal to the average value of the maximum individual roughness depth, which is the vertical distance between the highest and lowest points of a roughness profile within a single measuring length of 1 cm. For an isolated ring of rougness, the roughness Reynolds number $R_k = u_k K/\nu$ is also used, where $u_k$ is the smooth laminar boundary-layer velocity at the leading edge of the roughness band evaluated at a height of $K$.

The critical Reynolds number, $R_{D\text{crit}}$, at which laminar separation disappears as a result of the occurrence of natural transition at the separation point was estimated by observing the disappearance of a band of oil-film following the separation location. Shown in Figs. 3(*a*) and 3(*c*), the band of oil-film was visible at lower tunnel speeds and disappeared at high speeds. The measured value of $R_{D\text{crit}}$ for Headforms S-1 and S-2, as shown in Table 1, correlated well with the computed spatial amplification $A_s = e^7 \sim e^9$ at the separation point not only for the smooth headforms but also for the headforms with distributed roughness. The value of $R_{D\text{crit}}$ for the S-1 model occurs beyond the maximum speed capability of the 36-in. water tunnel. Thus, the measured value of $R_{D\text{crit}}$ was not obtained for the smooth S-1 model. The correlations shown in Table 1 imply that the spatial amplification factor $A$ can be used as a simple yardstick to correlate transition on bodies with and without distributed roughness. In order to determine the flow transition upstream of the minimum pressure location, an arbitrary conservative estimate of $A = e^{13}$ was used. It was believed that flow transition was quite certain to occur at a location where the computed value of $A$ reached $e^{13}$. The predicted transition locations on the three headforms with densely and loosely packed distributed roughness were found [22] at $0.04 < x/D < 0.13$ for the range of $1.9 \times 10^6 \geq R_D \geq 4 \times 10^5$. All the predicted transition locations on the headforms with distributed roughness were at a small distance from the stagnation point and a considerable distance upstream of the minimum pressure locations. Therefore, all the flows over the headforms with distributed roughness are definitely turbulent at the $C_{p\min}$ location. However, the computed amplification factor at the $C_{p\min}$ locations for the three smooth headforms were less than $e^5$ at the maximum test value of $R_D = 2 \times 10^6$. The flows over the three smooth headforms were laminar at the $C_{p\min}$ locations and the estimated transition locations were considerably aft of the $C_{p\min}$ locations. As shown in Table 1 the flow at the highest values of $R_D$ ($\cong 1.9 \times 10^6$) investigated was laminar at the separation point of the smooth S-1 model and was transitional at a small distance downstream of the separation point of the smooth S-2 model.

**Results of Cavitation Inception Measurements.** Cavitation inception observations on the smooth headforms were reported by Huang [1]. Repeat measurements of cavitation inception on the three smooth headforms were in agreement with the early observations [1]. Band cavitation inception with small parallel bubble lines distributed evenly at the laminar separation of the smooth hemispheric Headforms S-1 was found at $\sigma_i = 0.61 \cong -C_{ps}\ (= 0.63) < -C_{p\min}\ (= 0.78)$. The flow was predicted to be laminar at the separation point of the smooth Headform S-1 for the highest value of Reynolds number tested. Large transient attached cavitation spots appear and disappear randomly on the smooth Headform S-2 at $\sigma_i = 0.30 = -C_{ps} < -C_{p\min}\ (= 0.41)$ for the two large ($D$ = 10.2 cm and 7.63 cm) models and at $\sigma_i = 0.23 < -C_{ps}$ for the small ($D$ = 2.54 cm) model. For the range of $1.3 < R_D \times 10^{-6} < 1.9$, flow transition was predicted at a small distance downstream from the laminar separation point of the two large smooth S-2 models. The laminar separation was found to be intermittent with a short separation bubble, whereas a long laminar separation bubble was predicted on the small smooth S-2 model at $R_D = 4 \times 10^5$ using the criterion given in Reference [9]. On smooth Headform T-6 [1], traveling-bubble cavitation inception with $-C_{ptr}\ (0.25 \sim 0.30) < \sigma_i = (0.33) < -C_{p\min}\ (= 0.43)$, was observed initially and then attached patch cavitation with $\sigma_i = (0.23) \cong -C_{ptr} < -C_{p\min}$, was observed in the transition region. The predicted transition locations occur a considerable distance downstream of the minimum pressure locations for all three smooth headforms, the measured incipient cavitation numbers are all significantly smaller than the values of $-C_{p\min}$, and the cavitation inception is observed as small band, transient spot, and traveling-bubble or attached spot depending upon the nature of boun-

dary layer characteristics in the vicinity of cavitation inception.

Cavitation inception measurements were made on the three headforms with various combinations of turbulence stimulators. The variation of the observed cavitation inception within the limited range of Reynolds numbers tested was found to be small. Therefore, cavitation inception data were obtained at only two values of Reynolds number for most of the headforms. In order to reduce water tunnel testing time, two different turbulence stimulators were applied on the upper and lower halves of the same headform during one experiment. On hemispheric Headform S-1, three types of turbulence stimulators were used: 1) densely packed; 2) loosely packed 60-$\mu$m distributed roughness; and 3) boundary-layer tripping bands (2.5 mm wide and 0.03 mm high) located at an $x/D$ value of either 0.15 or 0.20. Cavitation inception observations on Headform S-1 with the three types of turbulence stimulators are shown in Fig. 3. Attached small cavitating bubble lines evenly distributed around the $C_{p\min}$ location were observed on the S-1 model with the two distributed roughnesses (Fig. 3($b$)). The measured cavitation inception numbers vary from 0.77 to 0.79 ($\sigma_i = 0.78 \pm 0.01$), which is approximately equal to the $-C_{p\min}$ value of 0.78. As shown in Figs. 3($d$) and 3($e$), large attached patch cavitation was observed on Headform S-1 with the boundary-layer tripping band (located at both $x/D = 0.15$ and 0.20). The measured cavitation inception numbers are 0.70 for the two-band locations and are slightly smaller than the $-C_{p\min}$ value. the leading edges of the cavitation patches were located at a small distance downstream of the $C_{p\min}$ location. A densely packed 60-$\mu$m distributed roughness and a boundary-layer tripping band (4 mm wide and 0.06 mm high) located at $x/D = 0.125$ were used on the 10.2 cm Headform S-2 (Fig. 4($a$)). Cavitation inception on the distributed roughness surface was in the form of attached small cavitating bubble lines evenly distributed around the $C_{p\min}$ location, whereas cavitation inception downstream of the tripping band was in the form of attached cavitating spots at the $C_{p\min}$ location. The measured cavitation numbers for the two cases are $\sigma_i = 0.42 \pm 0.01$, which is again very close to the $-C_{p\min}$ value of 0.41. The three types of turbulence stimulators used on the small ($D$ = 2.54 cm) S-2 Headform were: 1) densely packed 60-$\mu$m distributed roughness (Fig. 4($b$)), 2) evenly packed 90-$\mu$m sphetical glass beads (Fig. 4($c$)), and 3. A boundary layer tripping band (1.3 mm wide and 0.04 mm high) located at $x/D = 0.25$ (Fig. 4($d$)). The measured caviation inception numbers for the distributed roughness are $\sigma_i = 0.42 \pm 0.02$. Again, the measured value of $\sigma_i$ is very close to the $-C_{p\min}$ value of 0.41 and is located at the $C_{p\min}$ location. The measured cavitation inception number downstream of the tripping band is $\sigma_i = 0.38$, which is slightly smaller than the $-C_{p\min}$ value. The two types of turbulence stimulators used on Headform T-6 were: 1) densely packed 60-$\mu$m distributed roughness, and 2) a boundary-layer tripping band (2.5 mm wide and 0.03 mm high) located at $x/D = 0.125$. Cavitation inception in the form of attached cavitating bubble lines evenly distributed around the $C_{p\min}$ location was observed on Headform T-6 with the densely packed distributed roughness. The measured cavitation inception number is 0.42 which again is very close to the $-C_{p\min}$ value of 0.43. Large attached cavitation patches downstream of the tripping band were observed on Headform T-6 with the isolated stimulation ring. The measured cavitation number is slightly smaller than the $-C_{p\min}$ value.

For all of the headforms with densely packed 60-$\mu$m distributed roughness, cavitation inception was observed at the $C_{p\min}$ location and the measured cavitation inception numbers were found to be very close to the $-C_{p\min}$ values of ($\sigma_i = -C_{p\min} \pm 0.02$). In each case, cavitation inception was observed to be in the form of attached small cavitation bubble lines evenly distributed around the location of $C_{p\min}$ and the transition location was predicted to occur at a small distance

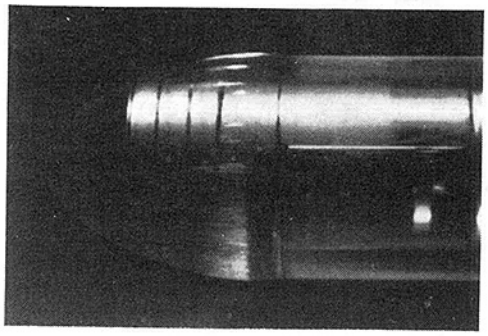

Fig. 4(*a*) Cavitation inception ($\sigma_i = 0.42$) on both halves of the headform ($D$ = 10.2 cm), with densely packed 60 $\mu$m particles on the lower half of the model and a tripping ring (4 mm wide and 0.06 mm high) at $x/D = 0.125$ ($C_P = 0.3$) on the upper half

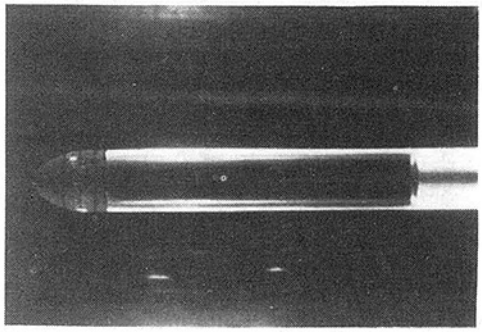

Fig. 4(*b*) Cavitation inception ($\sigma_i = 0.42$) on the small headform with densely packed 60 $\mu$m particles

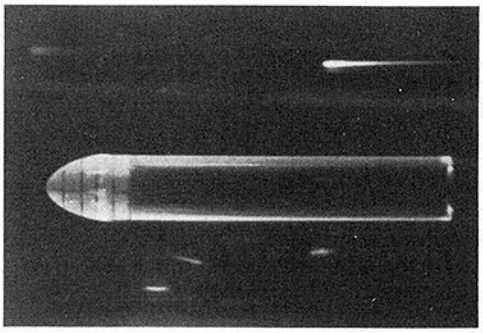

Fig. 4(*c*) Cavitation inception ($\sigma_i = 0.42$) on the small headform with evenly packed 90 $\mu$m spherical glass beads

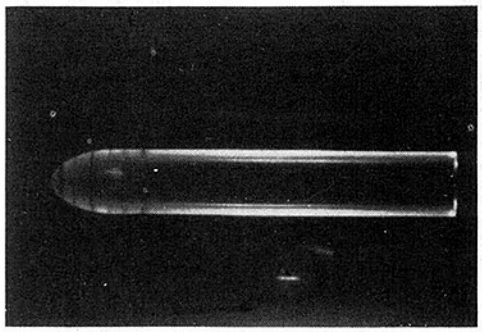

Fig. 4(*d*) Cavitation inception ($\sigma_i = 0.38$) on the small ($D$ = 2.54 cm) headform with a tripping ring (1.3 mm wide and 0.04 mm high) at $x/D = 0.25$ ($C_P = 0.05$)

Fig. 4 Cavitation inception on headform S-2 with boundary-layer turbulence stimulators

Table 2 **Measured cavitation inception on the three headforms with isolated boundary-layer tripping bands**

| Headform | Isolated Boundary-Layer Tripping Band | $R_D=\frac{U_\infty D}{\nu}\times 10^5$ | $R_k=\frac{u_k K}{\nu}$ | Figure | Measured $\sigma_i$ | $-C_{p\min}$ |
|---|---|---|---|---|---|---|
| S-1 | 2.5 mm wide and 0.03 mm high at x/D=0.15 or 0.20 | 13 | 190~210 | 3d | $\sigma_i=0.70\pm0.03$ | 0.78 |
| | | 19 | 330~360 | 3e | $\sigma_i=0.70\pm0.02$ | |
| S-2 | 4 mm wide and 0.06 mm high at x/D=0.125 | 13 | 520 | 4a | $\sigma_i=0.42\pm0.01$ | 0.41 |
| | | 19 | 570 | ~ | $\sigma_i=0.42\pm0.01$ | |
| | 1.3 mm wide and 0.04 mm high at x/D=0.25 | 4 | 520 | 4d | $\sigma_i=0.38\pm0.02$ | |
| T-6 | 2.54 mm wide and 0.03 mm high at x/D=0.125 | 13 | 200 | ~ | $\sigma_i=0.35\pm0.02$ | 0.43 |
| | | 19 | 340 | ~ | $\sigma_i=0.37\pm0.02$ | |

from the stagnation point ($0.04 < x/D < 0.13$) and a considerable distance upstream of the minimum pressure locations. Therefore, all the flows over the headforms with distributed roughness are definitely turbulent at the $C_{p\min}$ locations for the Reynolds numbers tested. However, for headforms with an isolated ring of roughness, attached cavitation inception numbers were found to be slightly smaller than the $-C_{p\min}$ values except for the large ($D = 10.2$ cm) Headform S-2 ($\sigma_i = -C_{p\min}$). The measured cavitation inception indices for the headforms with isolated roughness bands located upstream of the $C_{p\min}$ location are presented in Table 2. The width of the roughness band is small (< 4 mm). The computed roughness Reynolds numbers based on the roughness height $K$ at the leading edge of the roughness band, $R_k = u_k K/\nu$, are also given in the tables, where $u_k$ is the smooth laminar boundary-layer velocity at the band leading-edge evaluated at a height $K$. As shown in Table 2, the measured cavitation inception numbers for models with the roughness band approximate the values of $-C_{p\min}$ well ($-C_{p\min} = \sigma_i - 0.01$ for $R_k = 570$ and 520, and $-C_{p\min} = \sigma_i + 0.03$ for $R_k = 520$) when the computed values of $R_k$ are equal to or greater than 520. However, when the computed values of $R_k$ are less than 360 the measured values of $\sigma_i$ are smaller than the computed value of $-C_{p\min}$. The incipient cavitation observed was attached patch type occurring near the $C_{p\min}$ location. A minimum $R_k$ value of 600 had been recommended to stimulate laminar boundary layers to turbulent flows by Preston [33] for circular wire trips and also by Braslow et al. [34] for sand trips. The same threshold value of $R_k$ of 600 is recommended on the basis of the present investigation for the isolated roughness bands to promote earlier transition and to simulate proper cavitation inception. Furthrmore, the roughness bands must be located upstream of the minimum pressure location to assure a fully-developed turbulent boundary layer at $C_{p\min}$.

The application of an isolated boundary-layer tripping band on the leading edge of thin propeller blades could produce an undesired pressure disturbance near the minimum pressure location that might cause premature cavitation. Furthermore, the effects of this turbulence stimulator on propeller trip vortex cavitation, and lift/drag characteristics of the propeller blades is not fully understood. Further fundamental research is required to provide proper turbulence stimulators for propeller cavitation testing and is beyond the scope of this paper.

## Conclusions

Cavitation inception observations were made in the DTNSRDC 36-in. water tunnel on three axisymmetric headforms with and without various turbulence stimulators. The experiments were designed to identify conditions under which the cavitation inception number could be approximated by the negative of the minimum pressure, $-C_{p\min}$. The following conclusions may be drawn.

Potential-flow theory may be used to predict the minimum pressure value and location. For such models and models with distributed roughness, a correlation exists between the transition location, the location and value of minimum pressure, and the cavitation inception number. For models with isolated roughness bands upstream of the negative pressure location, a correlation may be made between the roughness Reynolds number $R_k = u_k K/\nu$, the location and value of minimum pressure, and the cavitation inception number. Furthermore, analytical methods may be sufficient to predict the correlations. Computed values of spatial amplification factors, $e^N$, of laminar boundary layer disturbances in the range of $7 < N < 10$ were found in this investigation to correlate reasonably well with the locations of measured flow transition on Headforms S-1 and S-2 with and without distributed roughness. Transition is predicted to occur considerably aft of $-C_{p\min}$ for the smooth models and the cavitation inception number was found to be much smaller than the value of the negative pressure coefficient. On the models with distributed roughness, transition occurred ahead of $-C_{p\min}$ and the cavitation number was approximately equal in value to the negative of the minimum pressure coefficient. Incipient cavitation numbers on the models with isolated roughness bands were found to approximate the computed values of $-C_{p\min}$ when the roughness Reynolds numbers were about equal to 600.

The type of incipient cavitation may vary with the use of a turbulence stimulator. Incipient cavitation on the smooth models was observed as small band, transient spot, and traveling bubble or attached spot on Headforms S-1, S-2, and S-3, respectively. On the models with distributed roughness, incipient cavitation occurred as attached small cavitating bubble lines evenly distributed about the minimum pressure location. Attached patch type cavitation was observed in the vicinity of the minimum pressure location for the headforms having the isolated roughness band. In order to assure that the flow is fully turbulent at the minimum pressure location, a conservative computed spatial amplification factor $A$ about equal to $e^{13}$ is recommended when using distributed roughness as a turbulence stimulator. Excessively large distributed roughness heights which cause extremely large increases of $A$ (i.e., $A > e^{20}$) should not be used. Furthermore, it is recommended that the roughness be distributed between the stagnation point and a location downstream of the minimum pressure location so that no surface discontinuity may be caused by the roughness. Under these conditions, the measured cavitation inception number $\sigma_i$ can be expected to closely approximate the value of $-C_{p\min}$. When a threshold roughness Reynolds number $R_k$ of 600 is satisfied for isolated turbulence stimulators located upstream of the minimum pressure location, the measured value of $\sigma_i$ is also expected to closely approximate the value of $-C_{p\min}$.

## Acknowledgments

This work was funded by the David W. Taylor Naval Ship R&D Center's General Hydrodynamics Research Program, Program Element 61153N, Task Area SR0230101. The author would like to thank Mr. G. S. Belt and Mrs. N. C. Groves for their assistance.

## References

1 Huang, T. T., "Cavitation Inception Observations on Six Axisymmetric Headforms," ASME JOURNAL OF FLUIDS ENGINEERING, Vol. 103, No. 2, 1981, pp. 273-278.

2 Arakeri, V. H., and Acosta, A. J., "Cavitation Inception Observations on Axisymmetric Bodies at Supercritical Reynolds Numbers," *Journal of Ship Research*, Vol. 20, No. 1, 1976, pp. 40-50.

3 Holl, J. W., and Carroll, J. A., "Observations of the Various Types of Limited Cavitation on Axisymmetric Bodies," ASME JOURNAL OF FLUIDS ENGINEERING, Vol. 103, No. 3, 1981, pp. 415-423.

4 Van der Meulen, J. H. J., "Boundary Layer and Cavitation Studies of

NACA16-012 and NACA-4412 Hydrofoils," *Proc. 13th Symposium on Naval Hydrodynamics*, Tokyo, Japan, Oct. 6–10, 1980, published by Shipbuilding Research Association of Japan, 1981, pp. 195–217.

5 Van der Meulen, J. H. J., and Ye, Yuan-Pei, "Cavitation Inception Scaling by Roughness and Nuclei Generation," paper presented at the 14th Symposium on Naval Hydrodynamics, Ann Arbor, Michigan, Aug. 23–27, 1982, published by National Academy Press, Washington, D.C., 1983, pp. 507–545.

6 Acosta, A. J., and Parkin, B. R., "Cavitation Inception—A Selective Review," *Journal of Ship Research*, Vol. 19, No. 4, 1975, pp. 193–205.

7 Acosta, A. J., and Parkin, B. R., "Report of the ATTC Cavitation Inception Committee," Proc. 19th ATTC, Ann Arbor, Michigan, 1981.

8 Acosta, A. J., "Cavitation Inception and Internal Flows with Cavitation," The Fourth David W. Taylor Lecture, Report DTNSRDC-78/011, 1979.

9 Huang, T. T., and Peterson, F. B., "Influence of Viscous Effects on Model Full-Scale Cavitation Scaling," *Journal of Ship Research*, Vol. 20, No. 4, 1976, pp. 215–223.

10 Billet, M. L., and Holl, J. W., "Scale Effects on Various Types of Limited Cavitation," ASME JOURNAL OF FLUIDS ENGINEERING, Vol. 103, No. 3, 1981, pp. 405–414.

11 Albrecht, K., and Bjorheden, O., "Cavitating Testing of Propellers in a Free Surface Tunnel Utilizing Micro Air Bubble Control," ASME JOURNAL OF FLUIDS ENGINEERING, Vol. 97, 1975, pp. 523–532.

12 Noordzij, L., "Some Experiments on Cavitation Inception with Propellers in the NSMB—Depressurized Towing Tank," *International Shipbuilding Progress*, Vol. 23, No. 265, 1976, pp. 300–306.

13 Gates, E. M., and Acosta, A. J., "Some Effects of Several Freestream Factors on Cavitation Inception on Axisymmetric Bodies," paper presented at the 12th Symposium on Naval Hydrodynamics, Washington, D.C., June 5–9, 1978, published by National Academy of Sciences, Washington, D.C., 1979, pp. 86–110.

14 Ling, S. C, Gowing, S., and Shen, Y. T., "Inception of Cavitation Over Headforms and Hydrofoils," paper presented at the 14th Symposium on Naval Hydrodynamics, Ann Arbor, Michigan, Aug. 23–27, 1982, published by National Academy of Sciences, Washington, D.C., 1983, pp. 547–579.

15 Kuiper, G., "Scale Effects on Propeller Cavitation Inception," paper presented at 12th Symposium on Naval Hydrodynamics, Washington, D.C., June 5–9, 1978, published by National Academy of Sciences, Washington, D.C., 1979, pp. 401–429.

16 Kuiper, G., "Cavitation Inception on Ship Propeller Models," Ph.D. thesis, Delft, Netherlands, 1981.

17 Kuiper, G., "Some Experiments with Specific Types of Cavitation on Ship Propellers," ASME JOURNAL OF FLUIDS ENGINEERING, Vol. 104, No. 1, 1982, pp. 105–114.

18 Kuiper, G., "A Comparison Between Cavitation Inception Phenomena in a Cavitation Tunnel and in a Depressurized Towing Tank," *International Journal of The Royal Institute of Naval Architects*, May 1983, pp. 93–107.

19 Billet, M. L., and Holl, J. W., "The Use of Distributed Roughness for Scaling Cavitation Inception," *Proc. 19th Attc, Ann Arbor, Michigan*, July 9–11, 1980, pp. 971–988.

20 Shen, Y. T., and Eppler, R., "Wing Sections for Hydrofoils—Part 2: Nonsymmetrical Profiles," *Journal of Ship Research*, Vol. 25, 1981, pp. 39–45.

21 Shen, Y. T., "Cavitation-Free Buckets of YS-920 and NACA-66 (MOD) Foil Section," Report DTNSRDC/SPD-1049-01, 1982.

22 Huang, T. T., Belt, G. S., and Groves, N. C., "Cavitation Inception Observations on Axisymmetric Headforms with Turbulence Stimulators," Report DTNSRDC-83/071, 1983.

23 Arakeri, V. H ., and Acosta, A. J., "Viscous Effects in the Inception of Cavitation on Axisymmetric Bodies," ASME JOURNAL OF FLUIDS ENGINEERING, Vol. 96, No. 4, 1973, pp. 519–527.

24 Smith, A. M. O., "Transition, Pressure Gradient, and Stability Theory," *Proceedings of the Ninth International Congress of Applied Mechanics*, Brussels, Belgium, Vol. 4, 1957, pp. 234–243.

25 Arakeri, V. H., "A Note of Transition Observation on an Axisymmetric Body and Some Related Fluctuating Wall Pressure Measurements," ASME JOURNAL OF FLUIDS ENGINEERING, Vol. 97, No. 1, 1975, pp. 82–87.

26 Huang, T. T., and Hannan, D. E., "Pressure Fluctuations in the Regions of Flow Transition," NSRDC Report 4723, 1975.

27 Huang, T. T., "Pressure Fluctuations in the Transition Regions of Forebodies of Revolution," *Proceedings of Low-Speed Boundary-Layer Transition Workshop II*, The Rand Corporation P-6119 (ed. by W. S. King and M. Kokata), 1978.

28 Power, J. L., "Drag, Flow Transition, and Laminar Separation on Nine Bodies of Revolution Having Different Forebody Shapes," DTNSRDC Report 77-0065, 1977.

29 Kosecoff, M. A., Ko, D. R. S., and Merkle, C. L., "An Analytical Study of the Effect of Surface Roughness on the Stability of a Heated Water Boundary Layer," Physical Dynamics, Inc., PDT-76-131, 1976.

30 Merkle, C. L., Tzou, K. T. S., and Kubota, T., "An Analytical Study of the Effect of Surface Roughness on Boundary-Layer Stability," Dynamics Technology, Inc., Report DT-7606-4, 1977.

31 Cecebi, T., and Smith, A. M. O., *Analysis of Turbulent Boundary Layers*, Academic Press, New York, 1974.

32 Okamura, T. T., "A Method for Calculating Laminar Boundary-Layer Profiles and Their Spatial Stability Properties for Two-Dimensional and Axisymmetric Bodies," Douglas Aircraft Company, Report MDC-J0097, Dec. 1971.

33 Preston, J. H., "The Minimum Reynolds Number for a Turbulent Boundary Layer and the Selection of a Transition Device," *Journal of Fluid Mechanics*, Vol. 3, Part 4, 1958, pp. 373–384.

34 Braslow, A. L., Hicks, R. M., and Harris, R. V., Jr., "Use of Grit-Type Boundary-Layer Transition Trips on Wind-Tunnel Models," National Aeronautics and Space Administration, Report TN D-3579, 1966.

Journal of Fluids Engineering

Technical Briefs

# Transition to Meandering Rivulet Flow in Vertical Parallel-Plate Channels

A. Anand[1] and A. Bejan[1]

## Background

The dynamics of rivulet flow has attracted considerable attention during the past two decades, in view of the position occupied by this flow in many engineering and geophysical applications. The need for high-flux surfaces for heat transfer and mass transfer in two-phase flow has served as stimulus for fundamental research on the hydrodynamic stability and on the surface wetting ability of rivulet flow. In the fluid mechanics literature, these problems have been dealt with experimentally by Kern [1, 2], Dussan and Davis [3] and Culkin [4]. In geophysics, considerable attention has been paid to the meanders executed by high-Reynolds-number rivulets: starting with the "stream-plate" experiments designed by Tanner [5, 6], meandering rivulets have been used as small-scale simulations of the meander formation mechanism in rivers (Gorycki [7, 8]).

The objective of the present note is to report a series of experimental observations of the rivulet flow sandwiched between two parallel plates. Relative to the single plate rivulet flow addressed in the above studies, the rivulet flow through a narrow parallel-plate channel is virtually unknown. The focus of the present experiments is on the rivulet transition from laminar flow to turbulent flow. The transition is marked by an abrupt shift to a meandering flow that, at least geometrically, looks similar to the buckling of thin fluid layers and filaments [9-14]. This geometric similarity and the growing interest in buckling flow phenomena served as additional incentives for conducting the present study.

## Experimental Apparatus

The downward flow of a water rivulet was observed between two vertical glass plates with adjustable plate-to-plate spacing (Fig. 1). The water stream enters the parallel-plate channel through a nozzle of rectangular cross-section formed by the top portion of the spacer material sandwiched between the glass plates. After falling vertically as a rivulet, the water stream leaves the parallel-plate channel through a similar opening cut into the bottom portion of the spacer. The dimensions of each glass plate are: height = 76 cm, width = 15.2 cm, and thickness = 1.3 cm. In an early version of the experiment we constructed the parallel-pate channel using plexiglas plates: this choice proved unsatisfactory, because in spite of the constant-thickness spacer and the strong clamps distributed around the edges of the rectangular plates the surface of each plate was not perfectly flat. Glass plates provided a much better alternative for creating uniform gaps whose sizes varied from 1 mm to 1.6 mm.

The role of constant pressure source for the rivulet flow was played by a cylindrical water reservoir of height 1.83 m and with an internal diameter of 14 cm. The water exited the reservoir through a nozzle with rounded internal profile, and was led to the parallel-plate channel of Fig. 1 through a tube with internal diameter of 6.4 mm.

The experiments were conducted using a single working fluid: distilled water mixed with 40 parts per million of the surfactant sodium lauryl sulfate [15] (viscosity = $(9 \pm 0.5) \times 10^{-3}$ g/(cm s), surface tension = $(58.5 \pm 2)$ dyn/cm). Without surfactant, the parallel-plate channel would retain small water beads in the place once occupied by exaggerated meanders of the kind visible in the lower section of Figs. 2.

The objective of this experimental study was to determine the conditions under which the rivulet flow shifts from the smooth, nearly-straight, course exhibited in the upper half of the first of the photographs of Fig. 2, to the fluctuating meandering course shown in the lower half of the photograph. The transition region of each rivulet was recorded photographically. As illustrated by the overall view presented in the first of the photographs of Fig. 2, the upper section of the rivulet was nearly straight and steady, whereas the transition section fluctuated laterally at practically the same vertical position in the parallel-plate channel. In each case, the transition height was defined as the distance from the vertical inlet port to the first elbow of the meander (the first elbow was regarded as the first "30 deg or greater" deviation of the

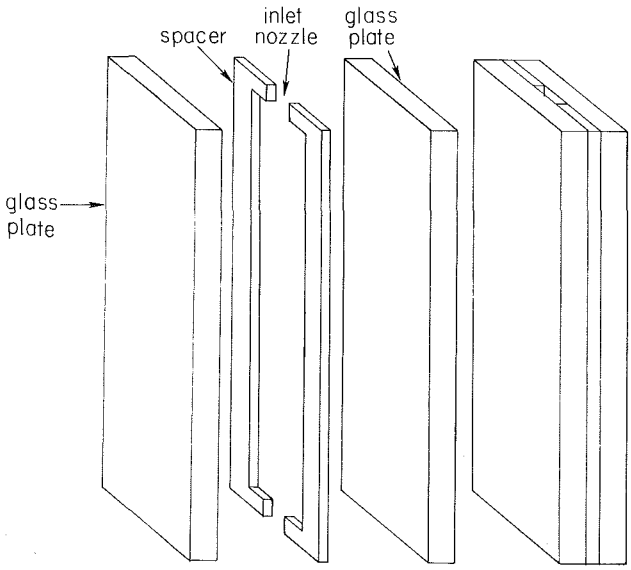


Fig. 1 Parallel-plate channel assembly principle

[1]Department of Mechanical Engineering and Materials Science, Duke University, Durham, NC 27006.

Contributed by the Fluids Engineering Division of The American Society of Mechanical Engineers. Manuscript received by the Fluids Engineering Division, November 5, 1984.

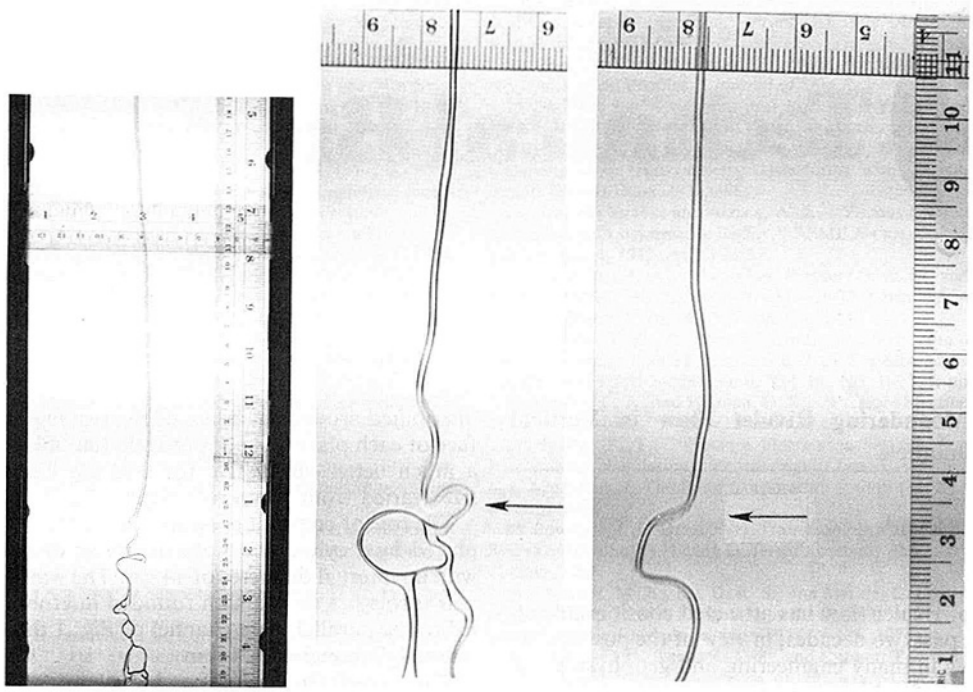

Fig. 2 Transition to meandering flow in a rivulet flow through a parallel-plate channel ($d$ = 1.45 mm, $Q$ = 1.36 m/s, transition Reynolds number = 1975)

rivulet from the vertical). This measurement technique was judged to be 10 percent accurate.

Transition observations were recorded for each rivulet defined by a certain volumetric flowrate $Q$[$ml/s$] and plate-to-plate spacing $d$[mm]. The rivulet flowrate was varied by means of an adjustable clamp attached to the tube preceding the parallel-plate channel. The flowrate was measured several times during each experiment by timing the filling of a calibrated container at the bottom of the apparatus. The plate-to-plate spacing was varied by changing the spacer material (Fig. 1). The total number of rivulets produced and studied in this manner was 121.

## Results

The transition from straight and steady flow to meandering flow is related to the monotonic increase in the local Reynolds number

$$\mathrm{Re} = \frac{Wd}{\nu} \tag{1}$$

as the rivulet is accelerated by gravity downward through the parallel-plate channel. In equation (1), $W$ is the rivulet velocity averaged over the rivulet cross-section, $W = Q/(Dd)$, where $D(z)$ is the local width of the rivulet (see Fig. 3). In principle, the local Reynolds number could be calculated directly by photographing and measuring the local width $D(z)$, and writing $\mathrm{Re} = Q/(\nu D)$. In practice, this simple approach is not feasible because in the transition region the local $D$ is ill-defined (Fig. 2).

Much better defined and easier to measure is the length of the nearly straight stable region, whose lower end is indicated by arrows in Fig. 2. There exists a one-to-one relationship between the length of the straight region and the local rivulet width $D$ (or $W$, or Re) corresponding to the location of "beginning of transition." This relationship is the equation for the draw-down shape of the rivulet accelerated by gravity and restrained by wall friction. An integral solution for the

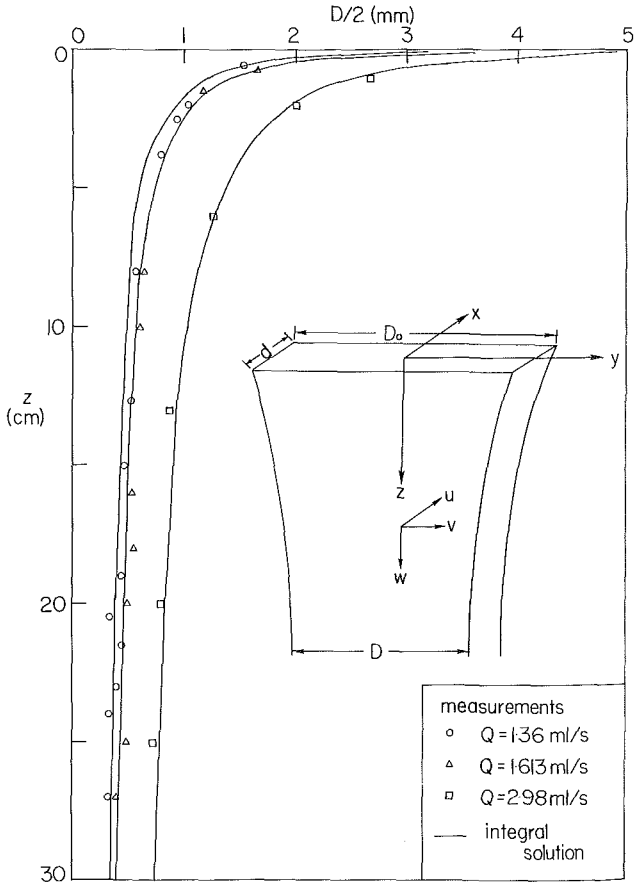


Fig. 3 Two-dimensional model for gravity-driven rivulet flow between two parallel plates, and the draw-down shape of the laminar section of the rivulet (the integral solution, eq. (8), versus experimental measurements)

$D(z)$ or $W(z)$ can be derived by considering the mass conservation equation and the momentum equation in the vertical direction, in the notation and coordinate system of Fig. 3,

$$\frac{\partial u}{\partial x}+\frac{\partial v}{\partial y}+\frac{\partial w}{\partial z}=0 \tag{2}$$

$$u\frac{\partial w}{\partial x}+v\frac{\partial w}{\partial y}+w\frac{\partial w}{\partial z}=\nu\nabla^2 w+g-\frac{1}{\rho}\frac{\partial P}{\partial z} \tag{3}$$

where $g$ is the gravitational acceleration acting in the positive $z$ direction, and $P$ is the pressure. By focusing on rivulet columns that are long and narrow enough we are permitted to assume that:

(i) the pressure gradient term $(\partial P/\partial z)/\rho$ is negligible in equation (3), because according to the boundary layer theory $\partial P/\partial z$ inside the slender water column is equal to $\partial P/\partial z$ outside the column, i.e., in the air that surrounds the experiment.

(ii) the fluid motion in the gap is two-dimensional, $u = 0$,

(iii) the velocity distribution versus $x$ resembles the Poiseuille profile

$$w=\frac{3}{2}W\left[1-\left(\frac{x}{d/2}\right)^2\right], \tag{4}$$

(iv) the gap averaged velocity $W$ is such that it is not a function of $y$. Together, equations (2, 3) reduce to

$$\frac{\partial w^2}{\partial z}+\frac{\partial(vw)}{\partial y}=\nu\left(\frac{\partial^2 w}{\partial x^2}+\frac{\partial^2 w}{\partial z^2}\right)+g \tag{5}$$

which, integrated over the rivulet cross-section ($-d/2 \le x \le d/2$, $-D/2 \le y \le D/2$), yields

$$\frac{6}{5}\frac{d}{dz}(DdW^2)=-12\frac{\nu DW}{d}+\nu dD\frac{d^2W}{dz^2}+gdD \tag{6}$$

Noting that the orders of magnitude of the four terms of equation (6) relative to the first term on the right-hand side are

$$\frac{Wd^2}{\nu H},\ 1,\ \left(\frac{d}{H}\right)^2,\ \frac{gd^2}{W} \tag{7}$$

we conclude that the second term on the right-hand-side can be neglected due to the slender-column geometry, $(d/H)^2 \ll 1$, where $H$ is the column height. Integrated, the three-term simplified version of equation (6) yields an implicit solution for the dimensionless average velocity,

$$1-W_*-\frac{b}{a}\ln\left(\frac{\frac{b}{a}-W_*}{\frac{b}{a}-1}\right)=az_* \tag{8}$$

where

$$W_*=W/W_0,\ z_*=z/D_0,\ a=10\frac{\nu D_0}{W_0 d^2},$$

$$b=\frac{5}{6}\frac{gD_0}{W_0^2},\ Q=WDd=W_0D_0d \tag{9}$$

and where $(\ )_0$ denotes conditions at $z = 0$.

Equation (8) provides a relationship between the vertical position along the stable rivulet section, $z$, and the local average velocity $W$ or the local width $D$. That equation (8) is valid is demonstrated in Fig. 3, which compares the theoretical draw-down shape $z(D)$ with experimental $z(D)$ measurements based on photographs of the stable rivulet column.

The local Reynolds number corresponding to the beginning of transition was calculated using equations (1) and (8), after measuring the total length of the stable and straight rivulet column preceding the transition zone. The results of these calculations are summarized in Fig. 4. Transition to meandering flow was observed when the plate-to-plate spacing was 1.45 mm and 1.6 mm. In a given rivulet (i.e., for $Q$ and $d$ fixed), the local Re value for the beginning of transition does not vary substantially from one observation to another: this is a restatement of the visual observation that despite the whiplash motion executed by the meanders of the transitional flow, the vertical location of the first meander does not vary appreciably in time.

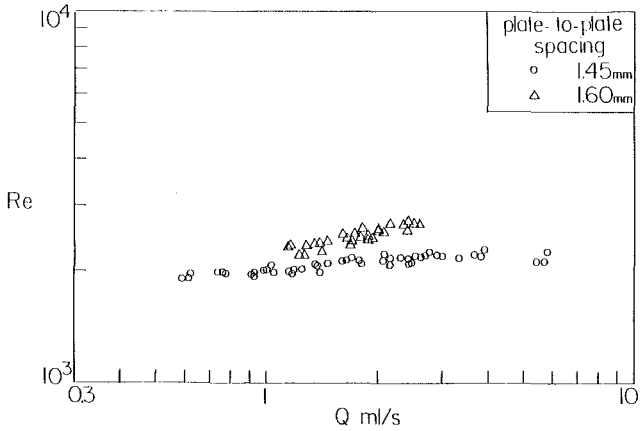


**Fig. 4 Transition Reynolds number versus rivulet flowrate**

## Conclusions

Figure 4 shows that the beginning of transition is characterized by local Reynolds numbers of order $2\times10^3$, which are consistent with the transition range traditionally associated with Poiseuille flow through a parallel-plate channel. Further evidence that the transition Reynolds number is of order $2\times10^3$ is provided by observations in an apparatus with plate-to-plate spacing of 1 mm, where the rivulet remained steady and straight for volumetric flowrates in the range 0.6–4 lm/s. If we substitute the height of the apparatus for $z$ in (8), we find that the maximum Reynolds number in the $d = 1$ mm channel (i.e., at the bottom extremity of the rivulet) is consistently of order 800 if $Q$ takes values between 0.6 and 4 ml/s. In other words, the 1 mm-wide channel is too narrow, and our flowrate capability too low, to permit the observation of transition.

The fact that the Reynolds number of transition to meandering rivulet flow is comparable with the Reynolds number associated with the onset of turbulence in fully developed laminar duct flow does not mean that the two transition phenomena are "equivalent." Much remains to be done both on the parallel-plate rivulet transition (see below) and on the parallel-plate Poiseuille flow transition in order to fully understand the relationshp between these two phenomena. At this stage, however, the numerical Reynolds number results of Fig. 4 are sufficiently similar to those of transition in fully developed duct flow to suggest that a connection between the two phenomena is possible and that such a connection deserves additional scrutiny.

Since only a single fluid was employed in the experiments, the present results do not document the possible effects of surface tension and gravity (or fluid density) on the transition Reynolds number. The study of these additional effects may prove interesting, indeed, one of the objectives of the present experimental study has been to draw attention to the parallel-plate rivulet geometry and to trigger future studies. Interesting is also the apparent similarity between some of the meandering flows observed in this study (e.g. the first photograph in Fig. 2) and the shape of buckled fluid filaments as they approach an obstacle (e.g., references [10, 11]).

## Acknowledgment

This experiment study was conducted with the support of the Office of Naval Research. Mr. Karl Rupp constructed the experimental apparatus. We offer special thanks to Professor William B. Krantz of the Chemical Engineering Department, University of Colorado, for continued advice on the use of water-surfactant mixtures.

## References

1 Kern, J., "Zur Hydrodynamik der Rinnsale," *Verfahrenstechnik*, Vol. 3, 1969, pp. 425–430.

2 Kern, J., "Stabilitätsprobleme der Rinnsalströmung," *Verfahrenstechnik*, Vol. 5, 1971, p. 289.

3 Dussan, V. E. B., and Davis, S. H., "On the Motion of a Fluid-Fluid Interface Along a Solid Surface," *J. Fluid Mech.*, Vol. 65, 1974, pp. 71–95.

4 Culkin, J. B., "Preliminary Experiments on Rivulet Instabilities," M.S. thesis, The Johns Hopkins University, Baltimore, Maryland, 1979.

5 Tanner, W. F., "Helical Flow, a Possible Cause of Meandering," *J. Geophys. Res.*, Vol. 65, 1960, pp. 993–995.

6 Tanner, W. F., "Inexpensive Models for Studying Helical Flow in Streams," *J. Geol. Education*, Vol. 10, No. 4, 1962, pp. 116–118.

7 Gorycki, M. A., "Hydraulic Drag: A Meander Initiating Mechanism," *Geol. Soc. Am. Bull.*, Vol. 84, No. 1, 1973, pp. 175–186.

8 Gorycki, M. A., "Hydraulic Drag: A Meander Initiating Mechanism," *Geol. Soc. Am. Bull.*, Vol. 84, No. 9, 1973, pp. 3119–3122.

9 Cruichshank, J. O., "Viscous Fluid Buckling: A Theoretical and Experimental Analysis With Extension to General Fluid Stability," Ph.D. dissertation, Iowa State University, Ames, Iowa, 1980.

10 Cruickshank, J. O., and Munson, B. R., "Viscous Fluid Buckling of Plane and Axisymmetric Jets," *J. FLuid Mech.*, Vol. 113, 1981, pp. 221–239.

11 Suleiman, S. M., and Munson, B. R., "Buckling of a Thin Sheet of a Viscous Fluid," *Phys. Fluids*, Vol. 24, 1981, pp. 1–5.

12 Cruickshank, J. O., and Munson, B. R., "An Energy Loss Coefficient in Fluid Buckling," *Phys. Fluids*, Vol. 25, 1982, pp. 1935–1937.

13 Cruickshank, J. O., and Munson, B. R., "A Theoretical Prediction of the Fluid Buckling Frequency," *Phys. Fluids*, Vol. 26, 1983, pp. 928–930.

14 Blake, K. R., and Bejan, A., "Experiments on the Buckling of Thin Fluid Layers Undergoing End-Compression," ASME JOURNAL OF FLUIDS ENGINEERING, Vol. 106, 1984, pp. 74–78.

15 Davies, J. T., and Rideal, E. K., *Interfacial Phenomenon*, Academic Press, New York, 1963, p. 195.